

SAPIENZA
UNIVERSITÀ DI ROMA

Investigating the nature of dark matter and of the Higgs boson with jets and missing transverse momentum at the LHC

Scuola di dottorato Vito Volterra

Dottorato di Ricerca in Fisica – XXXIV Ciclo

Candidate

Guglielmo Frattari

ID number 1594597

Thesis Advisors

Valerio Ippolito

Marumi Kado

31 October 2021

CERN-THESIS-2021-286
22/02/2022



Thesis defended on 22 February 2022
in front of a Board of Examiners composed by:

Maura Pavan (chairman)
Irene Di Palma
Riccardo Bellan

Investigating the nature of dark matter and of the Higgs boson with jets and missing transverse momentum at the LHC
Ph.D. thesis. Sapienza – University of Rome

© 2022 Guglielmo Frattari. All rights reserved

This thesis has been typeset by LaTeX and the Sapthesis class.

Author's email: guglielmo.frattari@cern.ch

A Giacomo, Ilaria ed Antonio

Abstract

Dark matter (DM) is one of the outstanding questions to which the Standard Model of particle physics (SM) still has no answer. Indeed, numerous evidences point to the existence of a non-baryonic matter component in the Universe that interacts with ordinary matter only through gravity. Under the hypothesis of the existence of a new interaction, three types of searches have been developed, among them collider searches represent a promising way of discovering and characterizing the properties of dark matter.

In this thesis, the search for DM is carried out in final states where a highly-energetic hadronic jet recoils against a large missing transverse momentum. The latter would be the signature of the production of weakly-interacting particles, which can be tagged in the final states thanks to the emission of radiation from the initial state of the collisions. The results were obtained with the data collected by the ATLAS experiment during the Run 2 of the LHC, corresponding to $139\,\text{fb}^{-1}$ of proton-proton collisions at a centre-of-mass energy of 13 TeV. The main SM background of the presented search, also called *monojet* search, is the $Z(\to \nu\bar{\nu})$+jets process, which has the same signature as the searched signal. A semi-data-driven technique is used to correct the Monte Carlo (MC) background predictions using data in independent control regions. Together with the adoption of accurate predictions for SM W/Z+jets processes, the background estimation technique allows to reduce the uncertainty of SM predictions to the percent range. The results presented in this thesis are interpreted in simplified DM models and compressed SUSY scenarios. The monojet analysis is also used to study the properties of the Higgs boson. An upper limit is set on its branching fraction into invisible final states, and the parameters of models that foresee the production of long-lived particles (LLPs) in its decay are also constrained.

Final states with jets and missing transverse momentum can also be produced by the decay of a Higgs boson into a $b\bar{b}$-pair, if the Higgs boson is produced in association with an invisibly-decaying Z-boson. The $Z(\nu\bar{\nu})H(b\bar{b})$ process is one of the leptonic channels of the $V(\to \textit{lep.})H(b\bar{b})$ process, where V can be either a W or Z boson. This allows the $H(b\bar{b})$ decay mode to be studied by exploiting the leptons to trigger and identify the events. The ATLAS collaboration has published two results with the full statistics collected during LHC Run 2, studying the $VH(b\bar{b})$ process in both well-resolved and boosted $H \to b\bar{b}$ decays. However, the two analyses are not statistically independent and rely on preliminary particle reconstruction and identification techniques. In this thesis, the work towards a Run 2 legacy result is presented, based on state-of-the-art reconstruction algorithms and an optimal combination of the two kinematic regimes. The performance of flavour tagging with new jet reconstruction algorithms is presented, along with an innovative method, based on graph-neural-networks, for performing an event-weighting technique called *truth tagging*, which helps to reduce systematic uncertainties due to limited Monte Carlo statistics. Finally, a first fiducial differential cross-section measurement of the $H(b\bar{b})$+$E_{\text{T}}^{\text{miss}}$ process is presented. This result forms the basis for more complete and refined work that will be included in the Run 2 Legacy result on the $VH(b\bar{b})$ process by the ATLAS collaboration.

The leading background process of the two analyses presented in this thesis is the production of a leptonically-decaying W or Z boson in association with hadronic jets. In the final part of the thesis, the implication of recent developments in the SHERPA MC event generator for ATLAS analyses are presented. The impact on the modelling of physical quantities thanks to the improvements of the matrix element and parton shower models is presented. The effect of changes in the description of the production fractions of heavy-flavour-hadrons is shown, and the performance of a preliminary setup based on the *fusing* of a $Z + bb$ calculation done in a four number-of-flavours scheme (NFS) with the inclusive 5NFS Z+jets calculation is presented. In addition, the performance of a technique for generating events based on the bias of the cross-section is discussed, and the studies leading to the final configuration adopted by the ATLAS collaboration for the generation of V+jets events are presented.

Contents

Introduction **xi**

1 Theoretical framework **1**
1.1 Standard Model overview . . . 1
1.1.1 Quantum field theory formulation of the SM . . . 2
1.2 Phenomenology of particle collisions . . . 10
1.3 State-of-the-art Standard Model measurements . . . 13
1.3.1 Higgs sector . . . 14
1.4 Limitations of the Standard Model . . . 17
1.5 The mystery of dark matter . . . 18
1.5.1 Experimental evidence of dark matter existence . . . 18
1.5.2 Dark matter freeze out . . . 23
1.6 Weakly Interacting Massive Particles . . . 24
1.6.1 WIMP searches . . . 25
1.7 The dark sector . . . 35
1.7.1 Theoretical models . . . 35

2 ATLAS and the LHC **39**
2.1 The Large Hadron Collider . . . 39
2.2 A Toroidal LHC ApparatuS . . . 42
2.2.1 The sub-detector systems . . . 44
2.2.2 The trigger system . . . 49
2.2.3 Data taking in Run 2 . . . 51
2.2.4 Events simulation . . . 52

3 Event reconstruction performance **55**
3.1 Inner detector tracks . . . 55
3.2 Leptons and photons . . . 56
3.2.1 Electrons and photons . . . 56
3.2.2 Muons . . . 59
3.2.3 Tau leptons . . . 62
3.3 Jets . . . 64
3.3.1 Pileup jet tagging . . . 72
3.3.2 Heavy-flavour jet tagging . . . 73
3.4 Missing transverse momentum . . . 77

4 The *Monojet* search **81**
4.1 The idea . . . 81
4.2 Background processes . . . 82
4.2.1 Monte Carlo simulation . . . 83
4.2.2 Event weights . . . 87
4.3 Object definition . . . 88
4.3.1 Overlap removal . . . 89
4.4 Event pre-selection . . . 89
4.5 Region definition . . . 91
4.5.1 Signal region . . . 91
4.5.2 Control regions . . . 91
4.5.3 Trigger debug stream . . . 99
4.6 Improvements with respect to the 36.2 fb^{-1} search . . . 100
4.7 Background estimation . . . 101
4.7.1 Data driven backgrounds . . . 101
4.7.2 Statistical model . . . 103
4.7.3 Fit strategies . . . 105
4.8 Systematic uncertainties . . . 105
4.8.1 Experimental uncertainties . . . 105
4.8.2 Modelling uncertainties . . . 112
4.9 Background estimation results . . . 117
4.9.1 Post-fit systematic uncertainties . . . 122
4.9.2 Inclusive fit . . . 127
4.10 Interpretation of the results . . . 128
4.10.1 Model-independent limits . . . 128
4.10.2 Constraints on simplified dark matter models . . . 129
4.10.3 Constraints on compressed SUSY scenarios . . . 138
4.10.4 Constraints on the $H \to$ inv. branching ratio . . . 141
4.11 Monojet and Long-Lived-Particles . . . 142

5 Measurement of the $VH(b\bar{b})$ process **151**
5.1 The $H \to b\bar{b}$ observation . . . 152
5.2 The starting point: preliminary $VH(\to b\bar{b})$ analyses . . . 153
5.2.1 Signal and background simulations . . . 153
5.2.2 Object definition . . . 154
5.2.3 Flavour tagging strategy . . . 157
5.2.4 Event selection and categorization . . . 159
5.2.5 Statistical model and fit strategies . . . 163
5.2.6 Main limitations . . . 167
5.3 Towards a Run 2 VH *legacy* analysis . . . 170
5.3.1 Improving flavour tagging . . . 170
5.3.2 Enhancing the truth tagging method . . . 173
5.3.3 Solving the overlap between resolved and boosted decays . . . 182
5.4 A first fiducial cross-section measurement . . . 195
5.4.1 Particle-level definitions . . . 195
5.4.2 Fiducial phase-space definition . . . 196
5.4.3 Fit model and unfolding strategy . . . 203

5.4.4 Results 209

6 Next generation V+jets Monte Carlo simulations 215
6.1 The impact of improved calculations 215
6.1.1 Next-to-leading-order virtual electroweak corrections 216
6.1.2 Electroweak parameter input scheme 218
6.1.3 Improved performance of the parton shower model 219
6.1.4 Heavy flavour modelling 221
6.1.5 Heavy flavour fusing 223
6.2 Towards a more efficient event generation 226
6.2.1 Phase-space slicing 228
6.2.2 Phase-space biasing 228
6.2.3 Assessing the statistical power 233
6.2.4 Mass enhancement for new physics searches 236

7 Conclusions 239

Appendix 243

A New Small Wheels for the upgrade of the ATLAS experiment 243
A.1 Motivation and system overview 243
A.2 SM1 modules of MicroMegas detectors 245
A.3 Validation of SM1 modules at LNF 247
A.3.1 Preliminary checks 248
A.3.2 Cosmic ray stand results 252

B Popular scientific description 257

Bibliography 267

Acknowledgements 285

Introduction

The Standard Model of particle physics (SM) [1] describes three of the four fundamental interactions of nature, the strong, electromagnetic, and weak force. The interactions between elementary particles are studied at the highest energy available in a laboratory at the CERN Large Hadron Collider (LHC), where proton-proton collisions (pp) are performed at a centre-of-mass energy ($\sqrt{s}$) of up to 13 TeV .

The most recently discovered particle of SM, the Higgs boson (H), was found in 2012 by the ATLAS and CMS experiments [2, 3] and completes the theory. However, several outstanding issues remain to be solved. In particular, the relatively small mass of the Higgs boson and its scalar nature require fine-tuning of the SM parameters. Moreover, the SM does not describe gravitational interactions and does not provide any candidate to describe the nature of dark matter (DM). Indeed, several cosmological observations suggest the existence of a non-baryonic form of matter that interacts with ordinary matter through gravity and is therefore referred to as dark. To satisfy the constraints imposed by astrophysical observations, Weakly Interacting Massive Particles (WIMPs) have been proposed as one of the possible solutions. These particles are assumed to interact with SM particles via new forces.

The search for WIMPs is carried out in different experimental ways which yield complementary results. The direct search targets elastic or inelastic scattering between WIMPs and SM particles. The indirect search looks for annihilation of WIMP pairs in SM particles, and tries to measure either an excess in the flux of antiparticles measured on Earth from the Cosmos or an excess in neutrino interactions. The collider search for WIMPs is based on the hypothesis that WIMP pairs can be produced in high-energy collisions at the LHC, leaving the experiments undetected and resulting in a large missing energy in the final states.

The golden channel for searching for DM particles at the LHC is the monojet channel, in which SM particles are produced in the initial state of the collisions and recoil against large missing transverse momentum in the final state. The kinematic of the collisions is indeed closed in the transverse plane, as the particles collide head-on. Therefore the production of non-interacting particles can be studied by considering unbalanced events.

The monojet search presented in this thesis is performed on the entire data set collected by the ATLAS experiment during LHC Run 2, which took place between 2015 and 2018 and in which pp collisions at $\sqrt{s} = 13$ TeV have been provided. The analysis uses a semi-data-driven technique to estimate the irreducible SM background process, $Z(\nu\bar{\nu})$+jets, that leads to the same signature of the sought signal, and to correct the Monte Carlo (MC) simulations adopted to estimate the other background processes such as the production of a vector boson associated with jets (V+jets)

or top-quark related processes. Precise QCD and EW predictions for the V+jets processes, together with highly statistical Control Regions allow the uncertainty on the SM backgrounds in the signal region to be reduced to the percent level, thus paving the field for precision searches. For this reason, particular attention is given to the effects of systematic uncertainties.

No significant deviations of the data from the SM predictions are observed, so both model-independent upper-limits on the visible cross-section and model-dependent constraints on the parameters of different BSM theories have been established. In this thesis, simplified dark matter models have been investigated. These provide a simple way to introduce WIMP particles into the SM, which are produced in pairs via new mediators. Limits on the parameters of such models can be transformed into constraints on the interaction cross-section between WIMPs and SM particles, or into limits on the annihilation rate of WIMP pairs. Therefore, the limits obtained in this analysis are also compared with the most stringent ones achieved by direct and indirect searches of WIMP DM. Limits are also set on the masses of particles predicted by supersymmetry, which produce in their decay stable and non-interacting particles which can also be identified as WIMP candidates.

Furthermore, monojet final states are used to study the properties of the Higgs boson. The invisible decays of such particle are predicted by the SM to be about 0.1% of the total decay modes. The monojet analysis presented in this thesis sets an upper limit on the Higgs branching fraction to invisible final states, and is used to study exotic scenarios in which long-lived-particles are produced in Higgs boson decays.

The Higgs boson can be associated to new physics phenomena. For this reason, it is interesting to study its properties to see if they are consistent with those predicted by the Standard Model. To target the dominant decay mode of the Higgs boson, $H \to b\bar{b}$, its associated production with a leptonic-decaying vector boson (VH) can be exploited. Indeed, this production mode allows to tag the events and extract the signal from the large QCD backgrounds of the LHC.

The topology of the final states is determined by the transverse momentum (p_{T}) of the produced Higgs boson. At a p_{T} of $75 \div 400\,\mathrm{GeV}$, the decay products appear well resolved in the detector. At a large transverse momentum, referred to as boosted topology, a different experimental approach is required to identify and measure the Higgs boson candidates. In this thesis, the state of the art of current measurements is briefly presented, and the main limitations of the published results are reviewed. So far, the two topologies have been treated independently. These two aspects motivate the on-going effort towards a Run 2 legacy analysis, which aims to make a combined measurement of the two regimes. Future improvements are discussed in this thesis.

The measurement of Higgs boson can be interpreted in the Simplified-Template-Cross-Section (STXS) framework, which provides a simple way to combine different decay modes of the Higgs boson to measure the production modes. However, possible complementary results can also be provided by fiducial differential cross-section measurements. In this thesis, the first result of such a measurement of the $H(b\bar{b})+E_{\mathrm{T}}^{\mathrm{miss}}$ final state is presented. An in-likelihood unfolding procedure is chosen to propagate in a simple way the correlation and constraints on the systematic uncertainties, central to the measurement of $VH(b\bar{b})$ processes at the LHC.

Monte Carlo simulations of the V+jets processes are a crucial part of both the analyses presented in this thesis and of the ATLAS physics programme in general. It is therefore important to rely on MC predictions that provide good modelling of the physical quantities of interest. In the last part of this thesis, the impact of the recent developments of the SHERPA MC generator on the physics modelling is presented. Another important aspect related to the generation of simulated events is the statistical power of the samples. The cross-section biasing approach introduced in the latest versions of the SHERPA generator is illustrated and the studies that lead to the choice of the ATLAS collaboration for the next generation of V+jets MC events are presented.

The thesis is structured as follows. Chapter 1 introduces the theoretical framework, the Standard model of particle physics and the DM problem. Chapter 2 discusses the experimental apparatus used to obtain the results shown in this thesis, while Chapter 3 presents the algorithms used to reconstruct the final states of particle collisions and their performance. Chapter 4 is devoted to the monojet analysis performed with the entire LHC Run 2 data set collected by the ATLAS experiment. In Chapter 5 the $VH(b\bar{b})$ analysis is presented, studies on the improvements towards a Run 2 legacy result are illustrated, and the measurement of the fiducial differential cross-section of $H(b\bar{b})$+$E_{\mathrm{T}}^{\mathrm{miss}}$ final state is presented. Finally Chapter 6 describes the modelling and computational improvements in the simulation of V+jets processes.

Personal contributions

All figures with the ATLAS label are included in ATLAS published papers, while figures with ATLAS PRELIMINARY label are included in ATLAS conference notes or public notes. A reference to the original publications is provided in the caption of each figure presented in this thesis. Figures without any ATLAS label are referenced accordingly, while all figures without any reference in the caption have been produced by me. This holds also for the tables presented.

My personal contributions to the results presented in this thesis are highlighted below.

I have been the main analyser of the *monojet* search [4] presented in Chapter 4, for which I contributed to the development of the offline software used to process official ATLAS simulations and to analyse both data and simulated events. I optimised the definition of the *Top control region* presented in Section 4.5.2, and I derived the effect of modelling uncertainties on the electroweak V+jets processes and diboson processes presented in Section 4.8.2. I have been responsible for the background estimation procedure presented in Section 4.9. For this stage of the analysis I optimised the statistical model, the smoothing and pruning algorithms adopted to improve the numerical accuracy of the fit, and I derived the effect of systematic uncertainties on the background predictions. Furthermore, I have been responsible for the interpretation of the results in terms of simplified dark matter models presented in Section 4.10.2, excluding the DMV interpretation and the indirect-detection re-interpretation of the DMP model, results derived from inputs I produced.

I coordinated the effort for the Long-Lived-Particles interpretation of the monojet

analysis results presented in Section 4.11. I contributed to fit studies and I have been editor of the public note [5] which documents the results.

The studies presented in Section 5.3.1, which show the performance of flavour tagging using particle-flow jets, excluding the training of the multivariate algorithms, and the studies on the Monte Carlo to Monte Carlo scale factors have been performed by me. Moreover, I have been the main analyser and editor of the public note [6] which documents these results.

I contributed to the validation phase for the results presented in Section 5.3.2, which documents the development of a neural network to perform truth tagging.

All the studies presented in Section 5.3.3 on the solution of the overlap between the resolved and boosted $VH(b\bar{b})$ analyses have been produced by me, as well as the results presented in Section 5.4 on a first fiducial differential cross-section measurement of the $H(b\bar{b})+E_{\mathrm{T}}^{\mathrm{miss}}$ final states.

I reviewed and organised the ATLAS internal documentation of the results presented in Chapter 6. The studies on the HF modelling presented in Section 6.1.4 have been performed by me, as well as the studies of the modelling of the SHERPA *fused* setup in the resolved $VH(b\bar{b})$ phase space. The studies presented in Section 6.2 on the phase space biasing technique adopted for the generation of V+jets events have been performed by me, along with the studies on the assessment of the statistical power of the samples, excluding the studies on the achieved equivalent luminosity.

My work has been included in the following publications:

- ATLAS Collaboration. "Search for new phenomena in events with an energetic jet and missing transverse momentum in pp collisions at $\sqrt{s} = 13\,\mathrm{TeV}$ with the ATLAS detector", *Phys. Rev. D, 103(11):112006*, 2021.
- ATLAS Collaboration. "Dark matter summary plots for s-channel mediators", ATL-PHYS-PUB-2021-006, 2021.
- ATLAS Collaboration. "Constraining the Dark Sector with the monojet signature in the ATLAS experiment", ATL-PHYS-PUB-2021-020, 2021.
- ATLAS Collaboration. "Monte Carlo to Monte Carlo scale factors for flavour tagging efficiency calibration", ATL-PHYS-PUB-2020-009, 2020.
- F. A. Di Bello, J. Shlomi, C. Badiali, G. Frattari, E. Gross, V. Ippolito, M. Kado. "Efficiency Parameterization with Neural Networks", *Comput. Softw. Big Sci., 5(1):14*, 2021.
- ATLAS Collaboration. "Modelling and computational improvements to the simulation of single vector-boson plus jet processes for the ATLAS experiment", *Submitted to JHEP*, 2021.

Chapter 1

Theoretical framework

The theoretical context in which this thesis is embedded is presented in this chapter. An overview of the Standard Model (SM) of particle physics and of the phenomenology of particle collisions is given in Section 1.1 and Section 1.2, respectively. The success of the SM in predicting the interaction cross-sections of elementary particles is presented in Section 1.3, where measurements performed by the ATLAS experiment are compared to state-of-the-art theoretical predictions. In particular, Section 1.3.1 focuses on the Higgs sector. The limitations of the SM are briefly discussed in Section 1.4, along with possible extensions of the theory proposed to address current problems. The mystery of dark matter (DM) is presented in Section 1.5, where evidence for its existence is reviewed, and the Weakly Interact Massive Particles (WIMPs) paradigm is presented. WIMPs searches are discussed in Section 1.6.1. Last, in Section 1.7 dark-sector models are introduced, and benchmark signatures proposed to search for the production of Long Lived Particles (LLPs) are presented.

1.1 Standard Model overview

The Standard Model of particle physics describes three out of the four fundamental forces of nature, the strong, electromagnetic and weak force, respectively. Gravitational effects appear to be on a significantly different energy scale, and are currently not described by the SM.

The fundamental components of the Universe are called elementary particles, and can be divided in *matter* component and *forces* components, with the latter mediating the interactions between the former. An overview is presented in Figure 1.1.

The matter component includes 12 spin 1/2 particles, *fermions*, which are organised in three *generations* of increasing proper mass. Each generation includes one electrically charged (e^-, μ^-, τ^-) and one neutral lepton, also called neutrino (ν_e, ν_μ, ν_τ), and an up type (u, c, t) and a down type (d, s, b) quark. Up- and down-type quarks have a fractional electromagnetic charge of $+2/3$ and $-1/3$, respectively. They also carry an additional *colour charge* which is a property of the theory of the strong interactions, the quantum chromo dynamics (QCD). For each matter particle, an anti-matter one is present, with all the charges of inverted sign.

The interactions between matter particles are governed by spin 1 vector bosons.

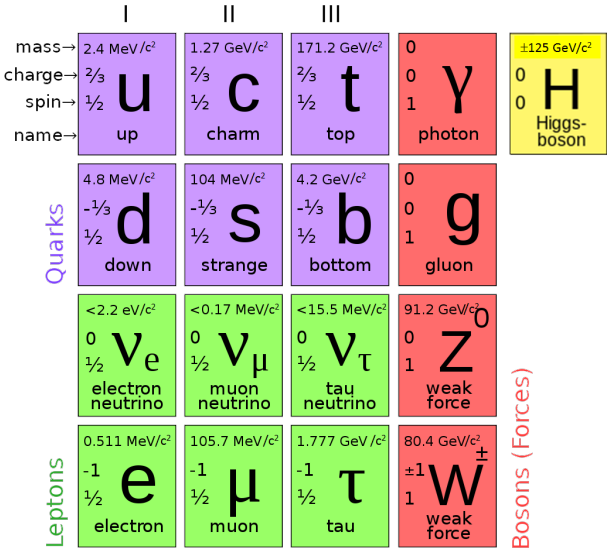


Figure 1.1. Summary of the elementary particles included in, and described by, the Standard Model, along with their properties. This figure was not produced by me, the original source is unknown.

Three are associated to the weak interactions, the $W^{\pm}$ and Z bosons, one is associated to the electromagnetic interaction, the photon (γ), and eight are associated to the strong force, the gluons g. Only one spin-0 particle is included in the SM, the Higgs boson (H). This particle is related to the mechanism which describes the mass of the elementary particles, which is presented in the next Section.

1.1.1 Quantum field theory formulation of the SM

A formulation of the SM was developed in the past 80 years in terms of four-dimensional[1] quantum fields, whose localised excitation results in the realisation of elementary particles. The dynamics of the SM can be described by the following Lagrangian density

$$\mathscr{L}_{\mathrm{SM}} = -\frac{1}{4}F_{\mu\nu}F^{\mu\nu} - i\bar{\psi}\not{D}\psi + (D_\mu\phi)^\dagger(D^\mu\phi) - V(\phi) + \bar{\psi}_i y_{ij}\psi_j\phi + h.c., \qquad (1.1)$$

which is invariant under local gauge transformations of the symmetry group $\mathrm{SU}(3)\otimes\mathrm{SU}(2)\otimes\mathrm{U}(1)$. Along with the Poincaré symmetry, such group guarantees that the physics described by the SM is independent of arbitrary choices of the reference frame or of a re-definition of the quantum fields.

Each term of Equation 1.1 is discussed further below. In summary, the first term on the right hand side (r.h.s.) of Equation 1.1 is an abbreviation of the kinematic term which describes the free propagation in the vacuum of gauge bosons. The second term is related to fermionic fields (ψ), and describes both their free propagation and their interaction with vector bosons. The following three terms are entirely associated with the Higgs boson, and describe how it interacts with vector

[1] Three spatial and one temporal dimensions.

bosons, its self-interaction and the interactions with fermions, which provide also a mass term for them.

Quantum electrodynamics

The free propagation of fermions in vacuum can be described by the Dirac Lagrangian [7]

$$\mathscr{L} = \bar{\psi} i \gamma_\mu \partial^\mu \psi - m \bar{\psi} \psi, \tag{1.2}$$

where ψ is the fermionic spinor, μ is the Lorentz index and runs from 0 to 3, ∂^μ is the covariant derivative and γ_μ are the Dirac matrices. A mass term, $m\bar{\psi}\psi$, is also included. In the following this will be neglected in the following because it is not invariant under the gauge transformations of the electroweak theory. However, as already mentioned, an invariant mass term for fermions is introduced in the SM Lagrangian via the Brout-Englert-Higgs mechanism.

This Lagrangian is invariant under a $U(1)$ global gauge transformation, $\psi \rightarrow \psi^{'} = e^{-ie\alpha}\psi$, where e is a parameter of the transformation itself, but not under a local one, depending on $\mathbf{x} = (x_0, x_1, x_2, t)$, of the form $\psi \rightarrow \psi^{'} = e^{-ie\alpha(\mathbf{x})}\psi$. The introduction of a covariant derivative of the form

$$D_\mu = \partial_\mu + ieA_\mu, \tag{1.3}$$

and of an additional field A_μ, which under a gauge transformation changes as

$$A_\mu \rightarrow A_\mu - \partial_\mu \alpha(\mathbf{x}), \tag{1.4}$$

guarantees the gauge invariance. Such transformation introduces an interaction term between fermions and the additional field, A_μ, which is identified as the electromagnetic field, and the parameter e is the electric charge. Since a new field has been introduced in the Lagrangian, a kinetic term has to be included. This is done by the introduction of the electromagnetic tensor $F_{\mu\nu} = \partial_\mu A_\nu - \partial_\nu A_\mu$. The quantum electrodynamics (QED) Lagrangian can thus be written as

$$\mathscr{L}_{\text{QED}} = \bar{\psi} i \not{\partial} \psi - \frac{1}{4} F_{\mu\nu} F^{\mu\nu} - ie\bar{\psi} \not{A} \psi, \tag{1.5}$$

where $\not{\partial} \coloneqq \gamma_\mu \partial^\mu$, and the same definition holds for $\not{A}$. The right-most term describes the interaction between charged fermions and photons.

Quantum chromodynamics

The QCD Lagrangian [8] can be derived in a similar way to the QED one, by requiring the Dirac Lagrangian to be invariant under a gauge transformation of the SU(3) symmetry group. This is motivated by the experimental observation of multiplets of hadrons, whose properties can be described under the assumption of the existence of a strong force characterized by a colour charge, which can assume three values. Only quarks, which carry the colour charge, interact via the strong force trough the exchange of gluons. The Lagrangian can be written as

$$\mathscr{L}_{\text{QCD}} = \bar{\psi} i \not{D} \psi - \frac{1}{4} G^a_{\mu\nu} G^{\mu\nu}_a, \tag{1.6}$$

where the covariant derivative is defined as

$$D_\mu = \partial_\mu \delta_{ij} + igT_{a,ij}A^a_\mu. \tag{1.7}$$

The δ_{ij} function imposes that the colour charge is conserved in the free propagation of quarks. Such colour index is implied in Equation 1.6 for the spinors ψ. The QCD coupling constant is indicated by g, while T_a, with $a = 1 \dots 8$, are the generators of the SU(3) symmetry and A^a are the gluon fields. As for the QED case, a gluon field tensor $G^a_{\mu\nu}$ is defined as

$$G^a_{\mu\nu} = \partial_\mu A^a_\nu - \partial_\nu A_\mu + g f^{abc} A^b_\mu A^c_\nu, \tag{1.8}$$

with f^{abc} representing the structure constants of the SU(3) symmetry group. The right-most term included in the definition follows from the gauge invariance requirement under a local transformation of the form $\psi \to \psi' = e^{-igT^a\alpha_a(\mathbf{x})}\psi$.

The second term of Equation 1.6 is the kinetic term of the gluon fields. Substituting Equation 1.8 in it, a crucial difference of QCD with respect to QED is highlighted. In fact, it can be written

$$\begin{aligned} -\frac{1}{4}G^a_{\mu\nu}G^{\mu\nu}_a = &-\frac{1}{4}(\partial_\nu A^a_\mu - \partial_\mu A^a_\nu)(\partial^\nu A^\mu_a - \partial^\mu A^\nu_a) + \\ &-\frac{1}{2}gA^b_\nu A^c_\mu(\partial^\nu A^\mu_a - \partial^\mu A^\nu_a)f_{bca} + \\ &+\frac{1}{4}g^2 A^b_\nu A^c_\mu f_{bca} A^\nu_d A^\mu_e f_{dea}, \end{aligned} \tag{1.9}$$

where the first line on the r.h.s. describes the propagation of free gluons. The second one describes three gluon self-interaction vertices, while the last line describes interaction vertices involving four gluon fields. The fact that the gauge bosons of the strong force self-interact is due to the non-abelian nature of the SU(3) symmetry group. Such self-interaction is not present in QED, and has an impact on the showering of coloured partons, as described in Section 1.2.

QCD predictions can be expressed in terms of a renormalized coupling constant $\alpha_s(\mu_\mathrm{R}) = g^2(\mu_\mathrm{R})$, which depends on a non-physical scale μ_R, the renormalization scale. Such quantity is defined to integrate out divergences which appear in predictions beyond the LO. The effective strength of the interaction is provided when evaluating the coupling constant at the scale at which the interaction takes place, typically referred to as Q.

The evolution of the coupling constant as a function of the scale μ_R is provided by the renormalization group equation (RGE) [9]

$$\mu^2_\mathrm{R}\frac{d\alpha_s}{d\mu^2_\mathrm{R}} = \beta(\alpha_s) = -\alpha_s^2\sum_{i=0}^{\infty} b_i \alpha_s^i. \tag{1.10}$$

The first term of the beta-function is given by

$$b_0 = -\frac{33 - 2n_f}{12\pi}, \tag{1.11}$$

where n_f indicates the number of quark flavours considered. The minus sign in front of the r.h.s. of equation 1.10 implies that the the coupling constant tends to 0 at high energies. Such phenomenon takes the name of *asymptotic freedom*. The leading-order solution of the RGE is given by

$$\alpha_s(Q^2) = \alpha_s(\mu)^2 \frac{1}{1 + b_0 \alpha_s(\mu^2) \ln(Q^2/\mu^2)}, \tag{1.12}$$

where Q is the scale at which the coupling constant is probed, and μ is a reference scale at which it is measured. It is possible to re-parameterize Equation 1.12 introducing an invariant mass scale Λ_{QCD}, defined as

$$\Lambda^2_{\mathrm{QCD}} \equiv Q^2 \exp\left(-\frac{b_0}{\alpha_s(Q^2)}\right), \tag{1.13}$$

such that it remains invariant if Q and μ are varied in Equation 1.12. This allows to rewrite the running coupling constant as

$$\alpha_s(Q^2) = -\frac{b_0}{\ln\left(\frac{Q^2}{\Lambda^2_{\mathrm{QCD}}}\right)}. \tag{1.14}$$

Again it is possible to see that at high energies the theory is asymptotically free. At low energies instead, the coupling constant increases and diverges at the so-called *Landau pole*, when $Q^2 = \Lambda^2_{\mathrm{QCD}}$. In this regime, non perturbative effects lead to the formation of stable and unstable hadrons.

Electroweak interactions

Fermions in the SM can be described by two independent components based on their chirality. Charged weak interactions couple to left handed fermions only, while the neutral currents couple to both the left and right handed ones.

The gauge symmetry group of electroweak interactions is the SU(2) $\otimes$ U(1). Left handed fermions are organised in SU(2) doubles, where for each fermionic generation $L = (\nu, \ell^-)$ and $Q = (u, d)$. Right handed fermions are instead singlets, and transform only under the U(1) symmetry. Anti-fermions are characterised by inverted properties: right handed anti-fermions transform as doublets, and left handed anti-fermions as singlets.

The quantum number associated with the electroweak interaction is the hypercharge, Y, which is determined by the charge of the particle (Q) and the value of the third component of its isospin. The latter is 0 for singlets, and $\pm 1/2$ for the components of the doublets. Electroweak interaction acts only on particles with non zero weak *hypercharge*, thus right handed neutrinos are neutral under this force.

The gauge transformation of the SU(2) and U(1) groups act on the left (ψ_L) and right handed fields (ψ_R) as

$$\begin{aligned} \psi_L &\to \psi_L e^{ig\alpha(\mathbf{x})^a \tau^a + ig'\beta(\mathbf{x})Y} \psi_L \\ \psi_R &\to \psi_R e^{ig'\beta(\mathbf{x})Y} \psi_R, \end{aligned} \tag{1.15}$$

where τ^a, with $a = 1..3$, are the generators of the SU(2) symmetry group, and $\alpha(\mathbf{x})$ and $\beta(\mathbf{x})$ are local phases; g and $g^{'}$ are the coupling constants associated to the two

interactions. The gauge invariance of the Lagrangian is restored by the introduction of a covariant derivative, such that

$$\begin{aligned}\mathscr{L}_{\mathrm{EW}} = &\sum_f \bar{\psi}_L^f \gamma_\mu (i\partial_\mu - gW_\mu^a \tau^a - g' B_\mu Y)\psi_L^f + \bar{\psi}_R^f (i\partial_\mu - g' B_\mu Y)\psi_R^f \\ &- \frac{1}{4} W_{\mu\nu}^a W_a^{\mu\nu} - \frac{1}{4} B_{\mu\nu} B^{\mu\nu}\end{aligned} \tag{1.16}$$

where the sum runs over the three fermionic generations, and the kinetic terms of the gauge fields are included under the form of strength tensors. These are defined as

$$W_{\mu\nu}^a = \partial_\mu W_\nu^a - \partial_\nu W_\mu^a + g\varepsilon^{abc} W_\mu^b W_\nu^c, \tag{1.17}$$

being ε^{abc} the totally anti-symmetric tensor. The $B_{\mu\nu}$ tensor is defined in the same way of the QED case. As for QCD, also in the electroweak case a self-interaction between W gauge bosons is present.

A rotation between the W_μ^a and B_μ fields allow to identify the physical observable fields associated to the SM photon and the SM $W^\pm$ and Z vector bosons. The charged W bosons are given by a combination of the W_μ^1 and W_μ^2 ones as

$$W^\pm = \frac{1}{\sqrt{2}} \left(W^1 \mp i W^2 \right), \tag{1.18}$$

while the Z^0 and γ bosons fields are given by

$$\begin{pmatrix} \gamma \\ Z \end{pmatrix} = \begin{pmatrix} \cos\theta_W & \sin\theta_W \\ -\sin\theta_W & \cos\theta_W \end{pmatrix} \begin{pmatrix} B \\ W_3 \end{pmatrix}. \tag{1.19}$$

The θ_W parameter is the Weinberg, or weak-mixing, angle. This relates the electromagnetic coupling constant to the ones of weak interactions, as

$$\begin{aligned} e &= g \sin\theta_W, \\ e &= g' \cos\theta_W. \end{aligned} \tag{1.20}$$

Moreover, the weak mixing angle is also responsible for the polarization of leptons in Z boson decays.

Every experimental observation of the electroweak interactions is consistent with a gauge theory. However, as for the fermionic fields, to not spoil the invariance an explicit mass term for the weak bosons cannot be written. This is in contrast with experimental observations, which require the W and Z bosons to be massive, thus a mechanism external to the gauge sector is needed. This is the Brout-Englert-Higgs mechanism, presented in the next Section.

The Brout-Englert-Higgs mechanism

The Brout-Englert-Higgs mechanism introduces a complex scalar field, ϕ, which transforms as a doublet under SU(2) gauge transformations, and have an hypercharge $Y = 1/2$. This allows to give a mass to all the particles with non-zero weak hypercharge.

The Lagrangian can be written as

$$\mathscr{L} = (D_\mu \phi)^\dagger (D^\mu \phi) - V(\phi) - \mathscr{L}_{\text{Yukawa}}, \tag{1.21}$$

with

$$\phi = \frac{1}{\sqrt{2}} \begin{pmatrix} \phi_1 + i\phi_2 \\ \phi_3 + i\phi_4 \end{pmatrix}, \tag{1.22}$$

and $\mathscr{L}_{\text{Yukawa}}$ describing the couplings between fermions and the Higgs boson. The potential $V(\phi)$ is gauge-invariant under SU(2) symmetry, and is given by

$$V(\phi) = -\mu^2 \phi^\dagger \phi + \lambda \left(\phi^\dagger \phi\right)^2, \tag{1.23}$$

with $-\mu^2$ and λ constant. To have an energetically bounded theory, λ must be positive. If $-\mu^2$ is greater than 0, the excitations of the ϕ field appear around 0. For $-\mu^2 < 0$, the potential takes the shape represented in Figure 1.2.

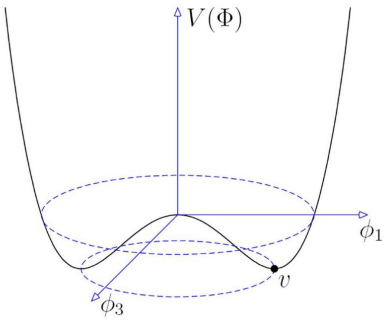


Figure 1.2. Representation of the Higgs potential $V(\phi)$. This figure was not produced by me, the original source is unknown.

The minimum of the potential is obtained for a non-zero field value. The Lagrangian is still gauge invariant, but the vacuum expectation value (vev, v), $v = \langle 0|\phi|0\rangle$ is not null. The value of the field in the minimum of the potential is given by $\phi^\dagger\phi = \frac{\mu^2}{2\lambda} = \frac{v}{2} > 0$. The vev value can be evaluated from the relation

$$\frac{G_F}{\sqrt{2}} = \frac{g^2}{8m_W^2}, \tag{1.24}$$

which can be derived from the description of the muon decay lifetime in the Fermi and SM theories, and is found to be $v = 246\,\text{GeV}$.

A gauge transformation allows to set three out of the four components of the ϕ field at 0, thus it can be written

$$\phi = \frac{1}{\sqrt{2}} \begin{pmatrix} 0 \\ v + h(\mathbf{x}) \end{pmatrix}, \tag{1.25}$$

where v is the vacuum expectation value of the ϕ field, and h is the scalar Higgs field. The fact that a gauge transformation allows to set to zero the ϕ_1, ϕ_2 and ϕ_4 components means that these are not representative of real fields. The electroweak

symmetry is, in this way, broken and a mass term for the gauge bosons and the fermions appears naturally.

Introducing the definition of ϕ provided in Equation 1.25, in Equation 1.21 we find

$$\begin{aligned}\mathscr{L} =& \frac{g^2v^2}{4}W^+_\mu W^{-,\mu} + \frac{g^2v}{2}hW^+_\mu W^{-,\mu} + \frac{g^2}{4}hhW^+_\mu W^{-,\mu} \\ & \frac{(g^2+g'^2)v^2}{8}Z_\mu Z^\mu + \frac{(g^2+g'^2)v}{4}hZ_\mu Z^\mu + \frac{(g^2+g'^2)}{8}hhZ_\mu Z^\mu.\end{aligned} \tag{1.26}$$

The first term of each line of the r.h.s. term can be identified as a mass term for the gauge bosons, thus

$$m_W^2 = \frac{g^2v^2}{4} \text{ and } m_Z^2 = \frac{(g^2+g'^2)v^2}{4}, \tag{1.27}$$

while the second term is a coupling between a pair of either W or Z boson and one Higgs boson. In particular this coupling can be rewritten in terms of the weak boson masses, and it is found to be equal to $y_V = 2m_V^2/v$. The latter term of each line of the r.h.s. term of Equation 1.26 is a coupling between two Higgs boson and two vector bosons. These terms show how the strength of the coupling of the Higgs boson to gauge bosons is proportional to their mass values. The mass of the Higgs boson itself is a free parameter of the theory, and depends on the parameters of the potential,

$$m_h = \sqrt{2\lambda v^2}. \tag{1.28}$$

The Yukawa Lagrangian which couples leptons to the Higgs boson can be written as

$$\mathscr{L}_{\text{leptons}} = -\sum_i \frac{g_i v}{\sqrt{2}}\bar{\psi}^i_L\psi^i_R + \frac{g_i h}{\sqrt{2}}\bar{\psi}^i_L\psi^i_R + h.c.\ . \tag{1.29}$$

The sum is performed over the three leptonic generations, ψ^i_L indicates the SU(2) left-handed doublets, and ψ^i_R the right-handed singlet. The first part is a mass term for leptons $m_\ell = g_i v/\sqrt{2}$, while the second one describes the coupling between the Higgs boson and the charged leptons, with a coupling strength proportional to the lepton mass, $y_\ell = m_\ell/v$. Since right-handed neutrinos has zero weak hypercharge, they do not couple to the Higgs boson, thus are considered mass-less in the SM.

The interaction between quarks and the Higgs boson can be derived in a similar way. However, since both the components of the $\text{SU}(2)_L$ doublet have non-zero weak hypercharge, to obtain an invariant Lagrangian the conjugate ϕ_C field, defined as

$$\phi_C = -i\sigma_2\phi^* = \frac{1}{\sqrt{2}}\begin{pmatrix} v + h(\mathbf{x}) \\ 0 \end{pmatrix}, \tag{1.30}$$

is introduced. The Yukawa Lagrangian involving quarks can be written by multiplying the SU(2) doublet from one generation with a singlet from another one, and each term, a priori, can have a different value of the coupling, indicated in the following by y. Thus the most general form is given by

$$\mathscr{L}_{\text{quark}} = -\sum_{i=1}^{3}\sum_{j=1}^{3}\left[y^u_{ij}\bar{u}^i_R\phi^\dagger_C Q^j_L + y^d_{ij}\bar{d}^i_R\phi^\dagger Q^j_L\right] + h.c.\,, \tag{1.31}$$

where Q_L^i indicate the SU(2) quark doublets, and u_R^i and d_R^i the singlets associated to up- and down-type quarks, respectively. From this equation the quark mass terms are derived, and part of the Lagrangian can be written as

$$\mathscr{L}_{\text{quark}} \supset -(\bar{u}_1, \bar{u}_2, \bar{u}_3)_R M^u \begin{pmatrix} u_1 \\ u_2 \\ u_3 \end{pmatrix}_L - (\bar{d}_1, \bar{d}_2, \bar{d}_3)_R M^d \begin{pmatrix} d_1 \\ d_2 \\ d_3 \end{pmatrix}_L + h.c.\,, \tag{1.32}$$

where $M^{u,d}$ are the quark mass matrices, or Yukawa matrices, given by $y_{ij}^{u,d}$ times $v/\sqrt{2}$. The eigenstates of such matrices are the physical quark fields. The diagonalization can be achieved by two unitary transformations applied to the $M^{u,d}$ matrices, which can be also seen as a transformation $U_{L,R}$ applied to the quark vectors. For the up type quarks one can write

$$\begin{pmatrix} u_1 \\ u_2 \\ u_3 \end{pmatrix}_{L,R} = U_{L,R} \begin{pmatrix} u \\ c \\ t \end{pmatrix}_{L,R}, \tag{1.33}$$

and similarly for the down-type quarks. $U_{L,R}$ are unitary transformations. The transformed matrices are diagonal and the eigenvalues are the quark masses. Moreover, the Higgs boson coupling to quarks is found to be

$$h\bar{q}q : \quad \frac{y_q}{\sqrt{2}} = \frac{m_q}{v}, \tag{1.34}$$

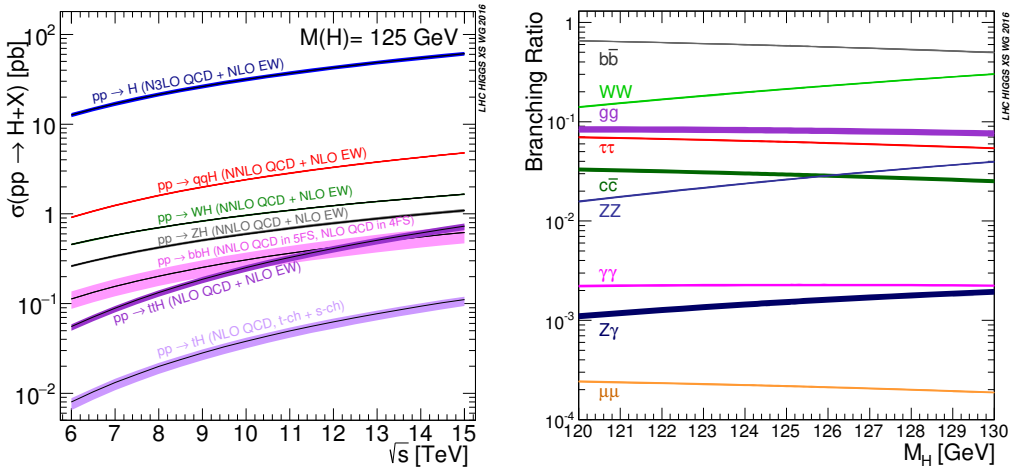
without any flavour-changing couplings. Thus, we can conclude also for quarks that their coupling to the Higgs boson is proportional to their physical mass. This property determines the Higgs boson decay modes in the SM.

Due to the nature of the Yukawa coupling, the dominant production mechanism for a SM Higgs boson involves the W and Z vector bosons, and third generation fermions.

As already mentioned, the Higgs boson does not couple directly to particles with zero weak hypercharge such as the photon or gluons. However, such coupling can be loop-induced by considering either W bosons or top quarks, respectively. In proton-proton collisions at the TeV scale, such as the ones produced at the Large Hadron Collider, the dominant production mode of the Higgs boson is the gluon-gluon fusion (ggF) process. This is due to the composite nature of the proton, which is described by parton-density functions (cf. Section 1.2); at the LHC energy, proton appear to be made mostly of gluons, thus the cross-section of the ggF process is enhanced. The second-leading Higgs boson production mode is the vector boson fusion (VBF), followed by the associated production with a vector boson (VH). A lower cross-section characterizes the associated production of either a single or a pair of top quarks (tH, ttH).

Cross-sections as a function of the centre-of-mass energy ($\sqrt{s}$) of proton-proton collisions are presented in Figure 1.3(a), assuming $m_H = 125\,\text{GeV}$.

An overview of the branching fraction of a SM Higgs boson with mass in the range $[120, 130]\,\text{GeV}$ is presented in Figure 1.3(b), instead. The main decay mode is in a $b\bar{b}$ pair, followed by a WW^* one. The third decay mode is in a pair of gluons



(a) (b)

Figure 1.3. Standard Model Higgs boson production cross section, as a function of the center-of-mass energy of pp collisions (a), and Higgs boson branching fraction (b), as a function of its mass in the range $[120, 130]$ GeV. Figures adapted from Ref. [10].

which, as already mentioned, happens via a top-quark loop. The $ZZ^* \to 4\ell$, $\gamma\gamma$ and $WW^* \to \ell\nu\ell\nu$ final states are the so called golden-channel, and were exploited by the ATLAS and CMS collaborations to achieve the discovery in 2012 of a boson with a mass of 125 GeV [2, 3], compatible with the one predicted by the Brout-Englert-Higgs mechanism. A summary of recent Higgs sector results are presented in Section 1.3.1.

1.2 Phenomenology of particle collisions

At the LHC protons are accelerated and collided in bunches. Further details on on the experimental side are provided in Chapter 2, while in this Section the phenomenology of hadron-hadron collisions is described. An example of the production of a Z boson in association with one parton, in proton-proton collision, is presented in Figure 1.4.

As described by the factorisation theorem [11], collisions happen between different proton constituents, the partons, which are either quarks or gluons, or with much lower probabilities photons [12] or even leptons [13]. Partons carry only a fraction of the total proton momentum, x_i, thus a partonic centre-of-mass energy is defined as $\sqrt{\hat{s}} = \sqrt{s x_1 x_2}$. The non-interacting components of the two protons are called spectator partons, and lead to minor energy deposits in the detector, referred to as *underlying event*. Quarks and gluons produced in the hard interaction are accelerated, and as electrically charged particles do, they emit multiple QCD radiation in a showering process. In such phenomenon the energy of each parton is split among an increasing number of other elementary particles. At energies of the order of the Λ_{QCD} constant, pole of the QCD running coupling ($\Lambda_{\text{QCD}} \simeq 0.2 \div 0.3$ GeV), bounding potentials between coloured partons intervene, and unstable and stable hadrons are formed through the *hadronisation* process. Free coloured particles are in fact not observed in nature. Such a property of the strong interactions goes under

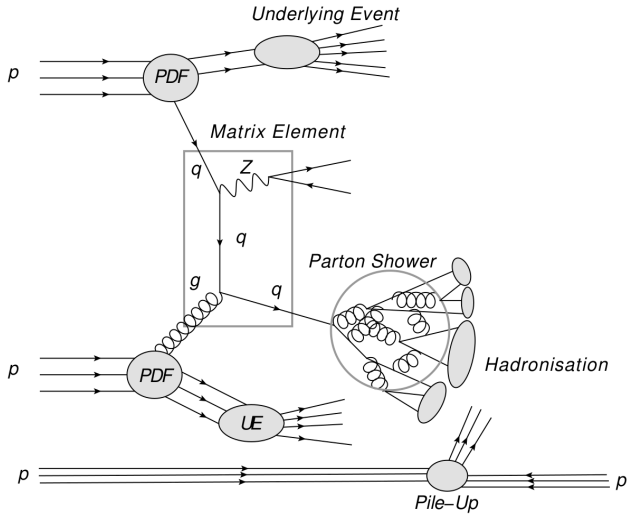


Figure 1.4. Representation of the production of a Z boson in association with one parton in pp collision. More details are provided in the text. Credits to Stephen Jiggins.

the name of *colour confinement*, and lead to the formation of hadronic jets in the final states. These are collimated sprays of charged and neutral hadrons produced in the parton showering, called *jets*.

Jet sequential recombination algorithms are defined to cluster the produced particles into a single object, the jet, which is a proxy of the parton produced in the hard-scattering interaction. In this thesis the k_t [14] and anti-k_t [15] algorithms are adopted. For each constituent considered in the jet clustering process, the distance with another constituent, d_{ij}, and with respect to the *beam* (B) are evaluated as

$$d_{ij} = \min\left(k_{\mathrm{T},i}^{2p}, k_{\mathrm{T},j}^{2p}\right) \frac{\Delta R_{ij}^2}{R^2}\,, \tag{1.35a}$$

$$d_{iB} = k_{\mathrm{T},i}^{2p}\,. \tag{1.35b}$$

$k_{\mathrm{T},i}$ corresponds to the transverse (with respect to the beam direction) momentum of the constituent i, R is a parameter of the algorithm, and ΔR is a Lorentz invariant angular distance between two different constituents (cf. Section 2.2). In the algorithm, the two distances are evaluated and compared: if the smallest of the two is d_{ij} then the two constituents are clustered together to form a single object, and their four momenta are combined. If $d_{iB} < d_{ij}$, the input i is considered as a jet, and removed from the ones available for the clustering. The value of the parameter p determines the type of algorithm: the k_t algorithm corresponds to the choice $p = 1$. In this case, soft particles are clustered first. For $p = -1$ the anti-k_t one is obtained. This is the standard choice of LHC experiments, since in this case jets are identified by the hardest emissions in the event, and a significantly lower dependency on the products of additional collisions, overlapping with the hard scatter interaction, is achieved. In fact, additional partons, and thus stable hadrons, can be produced either in multi-parton interaction between the same pair of colliding protons, or between different protons. Such phenomenon, later referred to as *pileup*,

is due to the fact that, as explained in more detail in Section 2.1, protons at the LHC are accelerated in bunches, thus there is non-zero probability to have multiple interactions in a single bunch-bunch collision.

Hard-scattering cross-sections calculation. The already mentioned factorisation theorem states that in such a collision the various processes happen at different energy scales, thus the interaction cross-section can be written as

$$d\sigma_{pp\to m} = \sum_{i,j} \int_0^1 dx_i \int_0^1 dx_j \int d\phi_m f_{i/p_1}(x_i, \mu_F^2) f_{j/p_2}(x_j, \mu_F^2) \frac{d\hat{\sigma}_{ij\to m}}{dx_i dx_j d\phi_m}. \quad (1.36)$$

The sum is performed over all the constituents of the proton which may initiate the hard scattering process. The functions $f_{i/p}(x_i, \mu_F)$ are called *parton density functions* (PDF), and describe the fraction of proton momentum, x_i, carried by a parton i, when the protons $p_{1,2}$ are probed at an energy scale μ_F. This is also called *factorization scale* and is introduced to regularise UV divergences which appear in partonic cross-section calculations beyond the LO into a re-definition of the PDF. The factorization scale is usually chosen to be equal to the energy scale of the process being evaluated, usually referred to as Q, since in the hard-scattering cross-section calculations terms of the form $\ln(\mu_F/Q)$ arise. Such choice is made to not spoil the convergence of the perturbative series, and avoids the appearing of large logarithms in the calculations. PDFs are non perturbative functions, and their evolution as a function of the energy scale $Q = \mu_F$ is provided by the DGLAP equation [16, 17, 18]. The form of PDF is determined experimentally in deep-inelastic-scattering, jets production and Drell Yan events [19, 20].

The partonic cross-section, indicated by $d\hat{\sigma}_{ij\to m}/dx_i dx_j d\phi_m$ is calculated in perturbation theory in QFT by squaring the matrix element term. Divergent contributions appearing in the calculations beyond the leading order (LO) can be controlled via the renormalization procedure, which consists in a redefinition of the strong coupling constant, α_s, to keep the predictions finite. In this procedure, the renormalization scale previously introduced (μ_R) arises, and it can be varied when modelling such calculation in Monte Carlo simulations to derive an uncertainty on the predicted cross-section. In general, differential cross-sections are finite only if calculated with respect to *infrared-safe observables*, i.e. that are insensitive to the emission of additional *soft* ($p_{\text{emiss.}} \to 0$) or *collinear* ($\theta_{\text{emiss.}} \to 0$) radiation from the outgoing partons. Observable quantities built using an infrared-safe definition of hadronic jets are, by construction, IR safe.

Event simulation. SM predictions compared to data are frequently obtained via Monte Carlo simulations, which allow to implement the picture presented in Figure 1.4. Different algorithms are adopted to calculate the matrix elements (ME), to perform the parton showering, to model the effect of the underlying event and the hadronization process. ME generators are able to describe with high accuracy the hard-scattering process, even if accompanied by few hard QCD emissions. To better describe multiple emissions parton shower (PS) algorithms are adopted. These describe such emissions in the soft and collinear approximations, which is the regime that dominates the cross-section. An optimal description of the events is achieved by

matching the predictions provided by ME generators and PS algorithms in multijet *merged* calculations. A comprehensive overview of the methods commonly adopted to model LHC physics is presented in Ref. [21].

1.3 State-of-the-art Standard Model measurements

The success of the SM in predicting interaction cross-sections is highlighted in Figure 1.5. It shows a comparison between measurements performed with the ATLAS experiment at Large Hadron Collider (cf. Chapter 2) and the theory predictions of a multitude of phenomena spanning the QCD, electroweak and Higgs sectors. Measurements have been performed at various centre-of-mass energies, and span over 10 orders of magnitude, as can be seen from the horizontal axis. Measured values are in good agreement in all sectors with state-of-the-art theoretical predictions, most of which are obtained at NLO or higher perturbative accuracy. Recent results related to the Higgs sector are presented in the next Section.

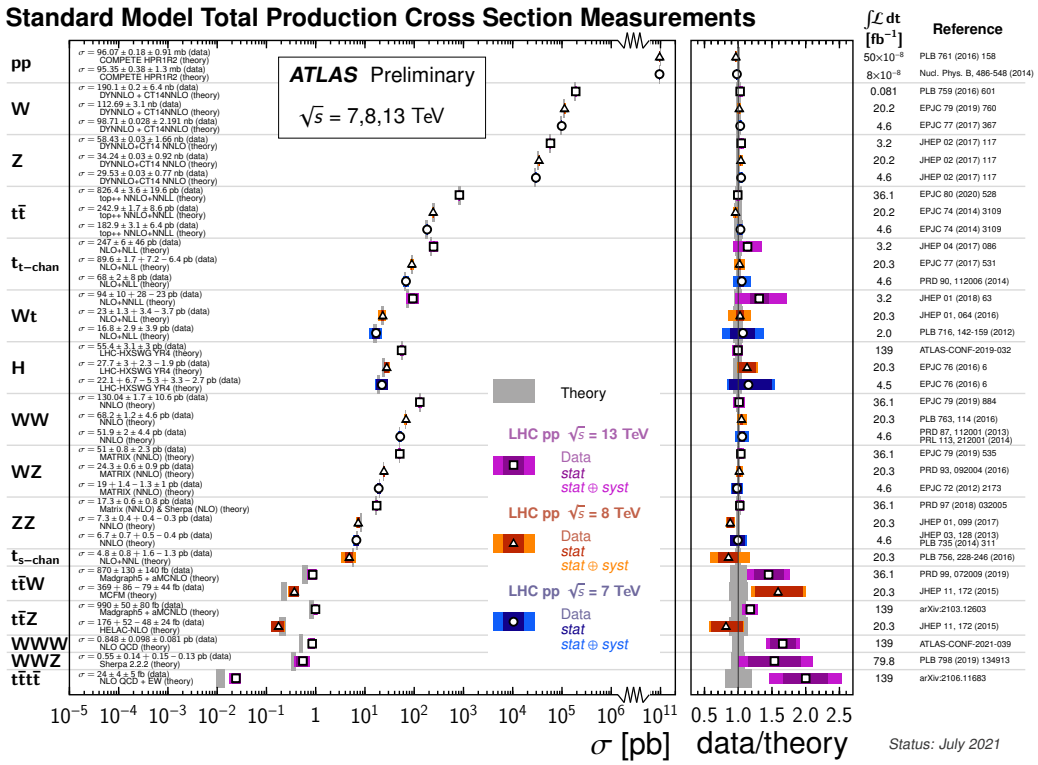


Figure 1.5. Summary of Standard Model cross-sections measured by the ATLAS collaboration in pp collisions at different $\sqrt{s}$ values. On the left the measured values of the cross-sections are compared to the state-of-the-art theoretical predictions. In the right pad the ratio to theory predictions is reported, while references to the measurements shown are given in the right-most column. Figure from Ref. [22].

1.3.1 Higgs sector

As already mentioned, the first observation of the Higgs boson was achieved by the ATLAS and CMS experiments in $\gamma\gamma$ and $ZZ^* \to 4\ell$ final states. After that, spin and CP measurements were performed to confirm that the observed particle was in agreement with the scalar boson predicted by the SM [23].

Moreover, LHC data collected between the 2015 and 2018 at $\sqrt{s} = 13\,\text{TeV}$ allowed to observe the Higgs boson coupling to vector bosons and third generation quarks. Couplings to τ-leptons [24, 25], top quark in $t\bar{t}H$ production mode [26, 27], and bottom quark in $H \to b\bar{b}$ decays [28, 29] were observed by both the ATLAS and CMS experiments. The latter decay mode is object of this thesis. To enhance the sensitivity to such a process, the associated production of the Higgs boson with a leptonically-decaying vector boson (VH) is exploited. Though the cross-section of such a process is much lower than the gluon-gluon fusion one, it allows to tag the events due to the presence of either a large amount of missing energy from the $Z \to \nu\bar{\nu}$ decay, or of electron or muons from the W/Z bosons. The $VH(\to b\bar{b})$ process is further discussed in Chapter 5 of this thesis.

First- and second-generation fermions are characterised by significantly lower couplings due to the nature of the Yukawa interaction. Evidence for the $H \to \mu^-\mu^+$ decay has been reported recently by the CMS collaboration in Ref. [30], with a rejection of the background-only hypothesis of 3σ (2.5σ expected). A similar result was achieved by the ATLAS collaboration, reported in Ref. [31], though the background only hypothesis is rejected with a significance of 2σ (1.7σ expected), thus more data are needed to declare evidence for such a process.

Direct constraints on the coupling between c quarks and the Higgs boson have been recently updated by the ATLAS collaboration [32]. To achieve a large sensitivity to the $H \to c\bar{c}$ decay, the $V(\to \text{leptons})H$ production mode is exploited, since it allows to strongly suppress the QCD background and tag the production of the Higgs boson via the leptonic decay of the associated vector boson. The analysis is performed in a similar way to the $VH(\to b\bar{b})$ one, described in this thesis in Chapter 5. The combined upper limit at 95% confidence level (CL) on the cross-section for the $VH \to c\bar{c}$ process is of 26 (31 expected) times the Standard Model.

A summary of the couplings of the Higgs boson to SM particles, including gauge bosons, measured by the ATLAS collaboration [33] is presented in Figure 1.6.

Couplings are parameterized in the so-called κ-framework [34], in terms of SM expected value times a strength modifier. These are defined for each Higgs boson production and decay mode as $\kappa_j^2 = \sigma_j/\sigma_j^{\text{SM}}$ and $\kappa_j^2 = \Gamma_j/\Gamma_j^{\text{SM}}$, where Γ_j is the partial decay width of the Higgs boson in the channel j. Such coupling modifiers impact also the total decay width of the Higgs boson. To this quantity, also undetectable final states, such decays to first-generation quarks and the $H \to ZZ^* \to \nu\bar{\nu}\nu\bar{\nu}$ process contribute.

After the observation of the Higgs boson couplings to SM particles, the focus shifted on the cross-section measurements, which are reported either in fiducial volumes or in the simplified template cross-sections framework (STXS) [35, 36]. The latter is presented in the next Section, while a first fiducial cross-section measurement of the $VH(\to b\bar{b})$ process is presented in in Chapter 5 of this thesis. Both kinds of measurements allow to test the Standard Model by comparing to state-of-the-art

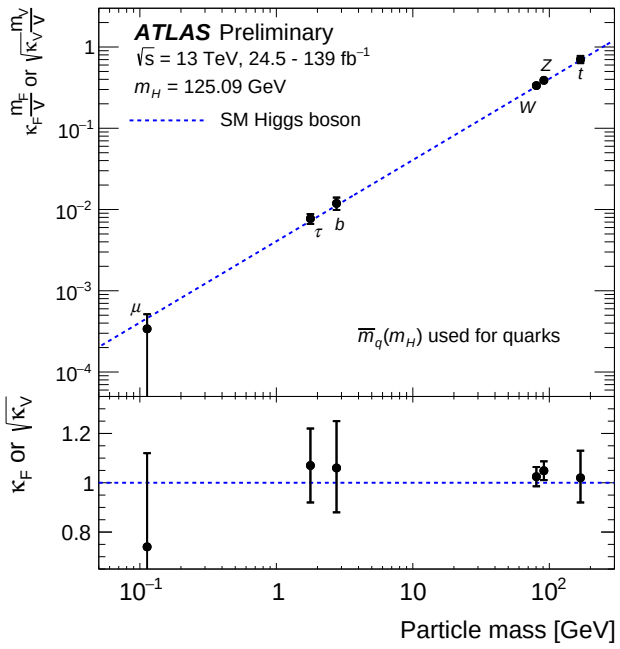


Figure 1.6. Higgs boson couplings to SM particles, as measured by the ATLAS collaboration. The vacuum expectation value of the Higgs field is taken to be $v = 246\,\text{GeV}$. Public plot of the ATLAS Higgs group.

calculations. STXS measurements allow also to set limits on the parameters of the Standard Model Effective Field Theory (SMEFT) framework [35].

Invisible decays of the Higgs boson allow to speculate on beyond the Standard Model effects. The SM expected branching fraction $\mathcal{B}_{\text{inv.}}$ is of the order of $\sim 0.1\%$, thus any deviation from such value would imply new physics phenomena. The production of long-lived particles in exotic decays of the Higgs boson is discussed in Section 1.7. The most sensitive topology to the $H \to$ inv. decay is provided by the vector-boson-fusion production mode, and the latest ATLAS analysis [37] of these events reached $\mathcal{B}_{\text{inv.}} < 13\%$ at 95% CL. A combination of this result with the one obtained in $t\bar{t}H$ topology [38, 39] and Run 1 results [40], reported in Ref. [41], allowed to exclude invisible branching fractions above 11% at 95% CL. An upper limit at the same CL value $\mathcal{B}_{\text{inv.}} < 34\%$ is set by the ATLAS monojet analysis presented in this thesis in Chapter 4.

Simplified template cross-sections

In the STXS framework, signal templates are built in fiducial volumes defined by means of a minimal number of particle-level selections focused on the production of the Higgs boson. These allow to measure the cross-section values in mutual exclusive phase spaces, and combine different decay modes in a straightforward way.

A set of STXS *bins* are identified such that the theoretical uncertainties associated to the predictions are minimized, and that possible BSM effects, like enhancements

of the cross-sections at high transverse momentum which can be parameterized in the SMEFT framework, can be easily isolated. A re-interpretation of the results is made possible since in addition to the cross-section measurement, the correlations between different STXS bins is usually provided.

Typically, the analyses separate the events in orthogonal categories based on the signal to background ratio, as for example the $VH(\to b\bar{b})$ analysis, discussed in Chapter 5 of this thesis, does in different $p_{\mathrm{T}}(V)$ bins. STXS bins are defined in a similar way, such that reconstruction-level categories adopted to maximise the sensitivity to the signal can be kept.

As already mentioned, signal templates of each category are defined by particle-level selections. The definition of the physics objects is harmonized among the different production modes, and the Higgs boson is considered to be a final state particle for these definitions. Since ATLAS and CMS are limited by the respective inner detector (ID) acceptances (cf. Section 2.2.1 for details on the ATLAS ID), a rapidity cut on H, $|y_H| < 2.5$, is applied. No rapidity or minimum p_{T} cuts are applied to the leptons. In the reconstruction of $p_T(H)$, photons in a $\Delta R < 0.1$ of the leptons are clustered together with them, to take into account the possible QED radiation. Moreover, all τ-lepton decay modes are considered in the final states. Candidates are built from the sum of all their decay products. Particle-level jets are reconstructed applying the anti-k_t algorithm with $R = 0.4$ on all stable particles ($c\tau > 10\,\mathrm{mm}$) excluding Higgs boson and vector boson decay products. No rapidity cut is applied, but jets are defined with a minimum p_{T} of 30 GeV.

Consecutive stages are defined in the STXS framework, which foresee an increased granularity of the categories based on cuts on the p_{T} of the Higgs boson, or on the particle-level jet multiplicity. The number of categories depends on two aspects: the sensitivity of the analyses which can provide such a measurement, and the amount of available data. STXS stage 0 is almost equivalent to a signal strength measurement in inclusive bins. For the VH production mode, in stage 0 three bins are defined: $qq' \to WH$, $q\bar{q} \to ZH$ and $gg \to ZH$. However, the separation between the quark- and gluon-initiated ZH process is not performed since the available statistics is not enough to discriminate between the two processes. Furthermore, to avoid ambiguous definitions of the categories which could arise when considering higher perturbative orders, the leptonic decay of the vector boson is explicitly required. The VH process with an hadronic decay of the vector boson is considered part of the VBF production mode, while the $gg \to Z(\to \mathrm{had.})H$ process is part of the ggF category.

Stage 1 of the STXS scheme, presented in Figure 1.7 for the VH production mode, is the target of LHC Run 2 analyses, modulo the possibility to merge some of the bins if the sensitivity is not large enough. These are indicated by the (+) symbol in the figure.

Latest ATLAS $VH(\to b\bar{b})$ measurements adopted a slightly modified scheme, as discussed in Ref [42], since the available data statistics did not allow to resolve all the categories. In particular, the $gg \to ZH$ and $qq \to ZH$ processes are merged, and no splitting in jet multiplicity is done.

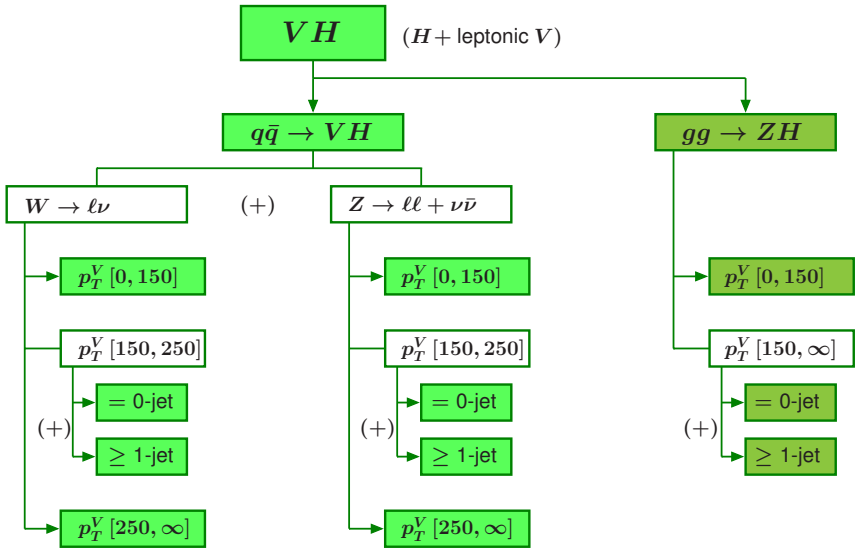


Figure 1.7. STXS stage 1 for the VH production mode. Figure adapted from Ref. [36].

1.4 Limitations of the Standard Model

Despite its success, the SM lacks an explanation for multiple phenomena, such as the masses of neutrinos [43], the strong CP problem [44], the *hierarchy* problem, and most importantly for this thesis, the nature of dark matter (DM). The latter is discussed in the next Section, while the hierarchy problem is briefly discussed below, since it can be solved in an elegant way by the supersymmetry theory, an extension of the SM, which provides also candidate DM particles.

The hierarchy problem is related to the value of the Higgs boson mass. Being a scalar particle, such quantity can receive very large radiative corrections, indicated by Δm_h, from all the SM particles which couple to it when considering beyond LO effects. In fact, such corrections are of the form

$$\Delta m_h^2 = \frac{\lambda_f}{16\pi^2}\left(2\Lambda^2 + \mathcal{O}\left[m_f^2 \ln\frac{\Lambda}{m_f}\right]\right), \tag{1.37}$$

where λ_f is the Yukawa coupling of the fermions, m_f their mass and Λ is an arbitrary large scale up to which the SM is assumed to be valid. If new phenomena are not present up to the Planck scale[2] ($\mathcal{O}(10^{19}\text{GeV})$), at which quantum gravitational effects are expected to dominate with respect to other SM forces, to obtain the measured Higgs boson mass large cancellations between different terms need to arise in such radiative correction. This *fine tuning* of the SM parameters appears innatural and could be solved by supersymmetry (SUSY) [46, 47].

[2]The Planck scale is defined as the equivalent energy of a Planck mass, $E_P = m_P c^2$, with m_P the Planck mass and c the speed of light. This latter quantity is the mass of a black-hole whose Schwarzschild radius [45] is equal to its Compton wave length, $\lambda = h/mc$ with h the Planck constant. The Planck scale is therefore given by $\Lambda = \sqrt{\hbar c^5/G} \sim 10^{19}$ GeV, where $\hbar = h/2\pi$ and G is the Newton constant.

Supersymmetry. The simplest extension of the SM is the Minimal Supersymmetric Standard Model (MSSM) [48], which introduces for each SM fermion a bosonic super-symmetric partner, and for each SM gauge boson, a corresponding super-symmetric fermion. Due to the fact that in QFT fermionic and bosonic loops are characterised by opposite sign, radiative corrections to the Higgs boson mass would cancel in a natural way if both contributions are taken into account. Since no super-symmetric partners of SM particles (also called *sparticles*) have been observed so far, it is hypothesised that supersymmetry is broken but in a soft way, such that sparticle masses differ of the order of the TeV with respect to SM ones. If this is not the case, the radiative corrections to the Higgs boson mass would again be large.

The MSSM model includes three generations of sfermions and a set of gauginos. Moreover, to give mass to both up- and down-type quarks, an extension of the SM Higgs sector is needed, such that a total of five Higgs bosons (two charged and three neutral) is needed. In the MSSM the gauginos fields mix and lead to four electrically neutral fermions, the neutralinos $\tilde{\chi}_0^{1,2,3,4}$, and two charginos $\chi_{1,2}^{\pm}$ of different mass. The heavier chargino can decay into the lighter one via the emission of a Z boson, or to a neutralino via the emission of a $W^{\pm}$ boson.

The interactions introduced by the MSSM should not violate the conservation of the baryon and lepton numbers, which is observed in several experiments looking for proton and $\mu \to e\gamma$ decays. For this reason a new symmetry which forbids such couplings is introduced, the R-parity. For each quantum field this is given by $R = (-1)^{3(B-L)+2s}$, where s is the spin of the particle, and B and L are their baryonic and leptonic numbers, respectively. All SM particles have $R = 1$, while supersymmetric particles have $R = -1$. In the MSSM the R-parity is conserved, thus the lightest neutralino is a stable particle, and supersymmetric decay chains lead to their production. As presented in the next Section, such particle can be interpreted as a dark matter particle candidate. Details on the models investigated by the monojet analysis presented in Chapter 4 of this thesis are presented in Section 1.6.1.

1.5 The mystery of dark matter

As introduced in the previous section, currently the SM does not provide an explanation for the nature of DM. Several astronomical observation hint in fact at the existence in the Universe of a large amount of energy density which behaves as ordinary matter, but does not interact with SM particles via neither the strong, nor the electroweak forces. Only gravitational effects due to its presence have been measured so far, thus no direct observation has been made, yet. A brief review of experimental evidence for the existence of DM is presented in the next Section. Further details are discussed in Ref. [49].

1.5.1 Experimental evidence of dark matter existence

Galaxy rotational curves. The first hint at the existence of DM dates back to 1932, when J. H. Oort measured via the Doppler shift of spectral lines the rotational velocity of stars located in the Milky Way. His results [50] showed how the observed amount of luminous matter, providing a gravitational field, was not enough to keep

the stars on their orbit. Similar results were obtained on larger spatial scales from the measurement of the rotational velocity of galaxies and cluster of galaxies [51, 52]. The expectation behaviour from classical mechanics, and the Gauss theorem, is that matter located at a distance r from the galactic center has a rotational velocity $v_{\text{rot.}} = \sqrt{GM(r)/r}$, where G is the gravitational constant and M the mass included in a sphere of radius r. Given astronomical observations of the luminous matter, for large enough r the mass value should tend to a constant, thus the asymptotic behavior of $v(r)$ should go as $1/\sqrt{r}$. This is in contrast with the experimental observations presented in Figure 1.8, which show a roughly constant behavior for $v(r)$ in the asymptotic regime. Such behaviour can be explained by a constant mass density $\rho(r)$, an *halo* of dark matter in which the galaxies are immersed.

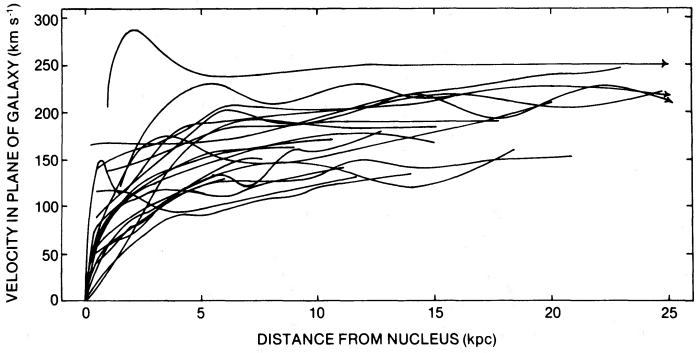


Figure 1.8. Rotational velocities of stars as measured in different galaxies. Figure from Ref. [51].

Strong gravitational lensing. Further experimental evidence for the existence of DM is provided by the observation of strong gravitational lensing effects of highly resolved source galaxies [53]. A detailed description of such phenomenon is presented in Ref. [54]. The effect consists in the observation of luminous arcs, or even closed rings, located around a foreground galaxy cluster and produced by the light of a background galaxy. Such phenomenon can be explained by the fact that a large amount of mass shapes the space-time around itself, thus light rays are deviated from their original propagation direction. An example of strong gravitational lensing is shown in Figure 1.9.

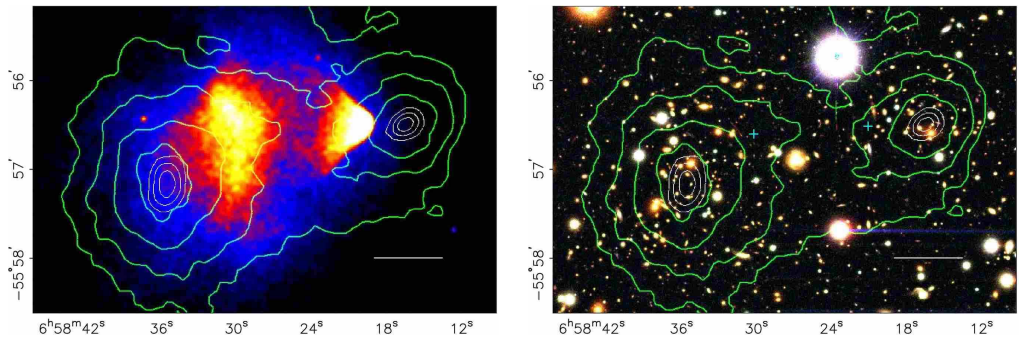
A detailed map of the mass distribution of the CL 0024+1654 cluster exploiting gravitational lensing has been produced [55]. This result, matched to an image produced by the Hubble Space Telescope, showed that visible stars are immersed in an homogeneous amount of matter, which does not emit electromagnetic radiation, hence dark. Similar effects were observed in other galaxy clusters. Such phenomenon is in agreement with the hypothesis of the existence of a dark matter halo in which galaxies are immersed.

The bullet cluster. Another experimental observation which proves the existence of DM is provided by the 1E0657-56 galaxy cluster, also called *bullet cluster*. This name comes from the fact that X-ray observations show that a collision between



Figure 1.9. Strong gravitational lensing effect from the SDSS J1152+3313 galaxy cluster. The blue ringlet is the result of light emitted from a background galaxy and deviated by the foreground one. Credits: ESA/Hubble, NASA, Judy Schmidt.

one larger galaxy cluster and a smaller *bullet* one happened. Results presented in Ref. [56] compared such emission spectra with a mapping of the mass distribution, obtained via the study of the gravitational lensing. In Figure 1.10(a) the X-ray spectrum is presented. The cone observed for the smaller bullet cluster on the right is the result of the emissions of baryonic matter, under the form of highly-energetic gases.



(a) (b)

Figure 1.10. Observations of the 1E0657-56 galaxy clusters, in the X-ray (a) and visible (b) spectrum, respectively. The green lines represent zones of same gravitational lensing effect intensity. The white line in each figure represents a distance of 200 kpc. Figures adapted from Ref. [56].

The shape and intensity of such emissions, also compared to the ones observed in the larger cluster, is compatible with what expected from a collision. Figure 1.10(b) shows, for the same clusters, the result of the gravitational lensing study. Matching the two images it is possible to see how most of the mass content of the two galaxies is displaced with respect to electromagnetic emissions. This hints at the fact that the dark matter halos of the two galaxies interacted very weakly in the collision event, and continued to move in the original directions.

Cosmic microwave background radiation. In 1965 A. Penzias and R. Wilson observed for the first time the radiation left over in the process of the formation of

the Universe [57]. The cosmic microwave background radiation (CMB) [58] consists in an almost homogeneous and isotropic source of low energetic photons at an energy of the eV level. Its observation corroborated the hypothesis of the Big Bang, the process from which the Universe originated.

A standard description of the evolution of the Universe is provided by the so called ΛCDM model. This is built from the Einstein field equation [59], which links the geometry of the space-time with the energy content of the Universe. This equation includes a constant term, referred to as the *cosmological constant* Λ, introduced to obtain a stationary solution for the Universe. This hypothesis was later found not to be true by the discovery of the Hubble's law [60]. However, such constant term is actually one of the central parameters of the ΛCDM model, as described later in this Section.

Under the hypothesis of an homogeneous and isotropic Universe [61], confirmed by multiple astrophysical observations, the Einstein equation can be simplified, and the Friedmann equations [62] obtained. The first Friedmann equation describes the expansion rate of the Universe in terms of its total energy density (referred to as Ω), including the Λ component, while the second one describes the evolution in time of the energy density components.

Friedmann equations allow to project back in time the energy densities associated to the matter, radiation and constant components, such that a picture of the primordial Universe can be obtained as a function of a temperature parameter T. This model leads to the conclusion that the large energy density of initial conditions diluted due to the expansion of the Universe.

At the very beginning of the Universe, the energy scale is supposed to be above the Planck one where quantum gravitational effects dominate. The dilution of the energy density, due to the expansion of the Universe, led to the electroweak symmetry era, which ended with the electroweak symmetry breaking at $T \sim 10^2\,\text{GeV}$. At energies of the order of Λ_{QCD}, quarks and gluons started to hadronize, while with further expansion, at energies of the order of the electronvolt, electromagnetic radiation (photons) and baryonic matter decoupled. The CMB is representative of this latter stage, and allows to study the matter distribution of the Universe at such epoch in time.

Later experimental observations of the CMB [63] reported that its spectrum corresponds now to the emissions of a black-body with a temperature of $\sim 2.73\,\text{K}$. Further observations identified in the CMB tiny fluctuations of the order of hundreds of μK, as represented in Figure 1.11 as measured by the Planck collaboration [64].

Such fluctuations are related to the presence of gravity wells in the early era of the Universe which allowed for the formation of structures of galaxies. To be explained, the presence of a matter component which produced gravitational wells is required. However, it is also required that such component decoupled from the ordinary matter before the CMB era via a *freeze out* mechanism, described in the next Section.

The fluctuations observed in the CMB temperature field map can be described by the ΛCDM model and the cosmological parameters, such as the cosmological energy densities, can be extracted. The temperature field reported in Figure 1.11

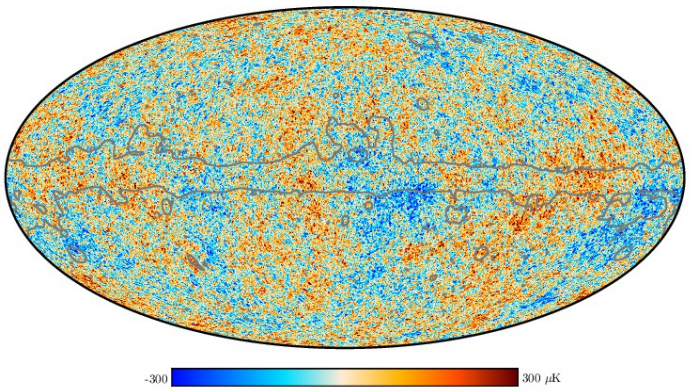


Figure 1.11. Temperature map, after the subtraction of backgrounds due to the emissions of foreground galaxies (like the Milky way), of the CMB as measured by the Planck collaboration. The colour scale represent the variation with respect to the mean value of the measured temperature. Figure adapted from Ref. [64].

can be described by a series of spherical harmonics of the form

$$T(\hat{n}) = \sum_{\ell,\, m} a_{\ell m} Y_{\ell m}(\hat{n}), \tag{1.38}$$

where $\hat{n}$ indicates a direction in the sky, $Y_{\ell m}$ are the spherical harmonics functions, and $a_{\ell m}$ are complex coefficients. The power spectrum is defined as the module of the coefficient of the series reported in Equation 1.38, $C_\ell = \langle a_\ell a_\ell^* \rangle$. Under the hypothesis of an isotropic Universe, the power spectrum is rotationally invariant and can therefore be averaged over m, and studied as a function of the index l. In Figure 1.12, the quantity $\mathcal{D}_l^{TT} = \ell(\ell+1)C_\ell^{TT}/2\pi$ is reported. The superscript TT indicates that the the function is referred to the intensity of the CMB. The acoustic oscillations of the primordial baryonic fluid result in such a peak structure. From the global shape of the power spectrum it is possible to extract information on the total matter component of the Universe. From an analysis of the location of the peaks (in the variable ℓ) and of their amplitude, the cosmological densities of different energy components can be extracted. The various terms, ρ_x, are by convention reported normalised to a critical density ρ_c, such that the total density Ω can be expressed as

$$\Omega \equiv \sum_x \frac{\rho_x}{\rho_c} = \sum_x \Omega_x. \tag{1.39}$$

The resulting values for the matter (m) and dark energy (Λ) density terms, reported in Ref. [65], are

$$\Omega_\Lambda h^2 = 0.3107 \pm 0.0082 \quad \text{and} \quad \Omega_\mathrm{m} h^2 = 0.1430 \pm 0.0011, \tag{1.40}$$

where $h = H_0/100\,\mathrm{km\,s^{-1}\,Mpc^{-1}}$ is the reduced Hubble constant. Other terms, such as the energy density of radiation or neutrinos, are today a negligible component. These results indicate that only 30% of the total energy component of the Universe is associated with matter. This component can be further divided in baryonic and non-baryonic ones, which are measured as

$$\Omega_\mathrm{c} h^2 = 0.1200 \pm 0.0012 \quad \text{and} \quad \Omega_\mathrm{m} h^2 = 0.02237 \pm 0.00015, \tag{1.41}$$

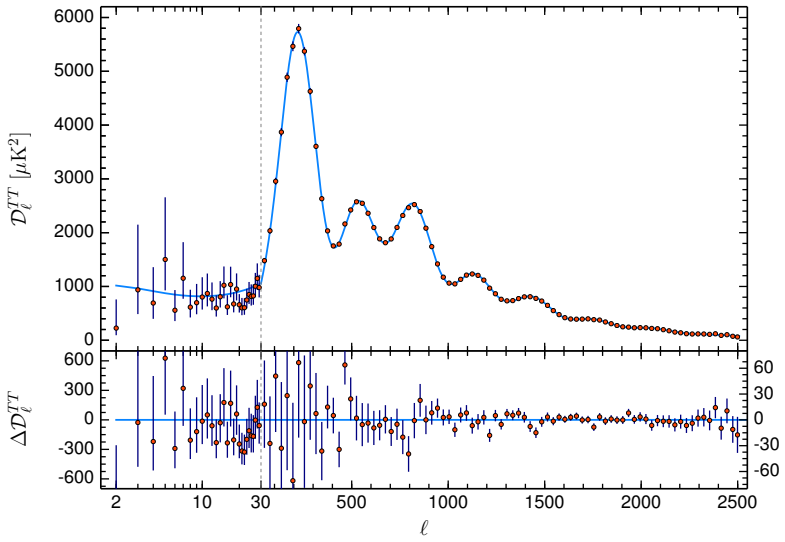


Figure 1.12. CMB intensity power spectrum, as measured by the Plank Collaboration. Experimental data are fitted by the ΛCDM model described in the text. Figure adapted from Ref. [65].

where the Ω_c refers to the cold dark matter energy density, while Ω_m refers to the baryonic matter. These results indicate that only 18.6% of the matter component of the universe is due to ordinary baryonic matter, while the rest is due to the presence of relic dark matter.

1.5.2 Dark matter freeze out

The observed relic density of dark matter in the Universe is hypothesised to be the result of a *freeze out* mechanism. Considering a stable and non-relativistic species of DM particles χ, the evolution in time (t) of its number density n in an expanding Universe can be described by the Boltzmann equation [66]

$$\frac{dn}{dt} = -3\mathcal{H}n - \langle\sigma v\rangle(n^2 - n_{\rm eq}^2). \tag{1.42}$$

$\mathcal{H}$ is the Hubble parameter (cf. Ref. [67]), which provides a measure of the Universe expansion rate, $\langle\sigma v\rangle$ is the thermal average of the product of the particle velocity and the annihilation cross-section of DM particles into SM ones, and n_{eq} is the particle number density at the thermal equilibrium. The time evolution of such equation can be visualised in Figure 1.13, where the particle number density n is reported as a function of the ratio between the DM particle mass m and its initial density T.

In the early era of the Universe the energy density is such that $T \gg m$, thus the production and annihilation rates exceed the expansion governed by $\mathcal{H}$. In this regime, the particle number density follows the expectation from the equilibrium density. For values of $T \leq m$ the pair production of DM particles is suppressed, and annihilation rate also is reduced, due to a decreased production rate of DM particles. When this process ceases, the number of particles stops evolving [67] and a relic

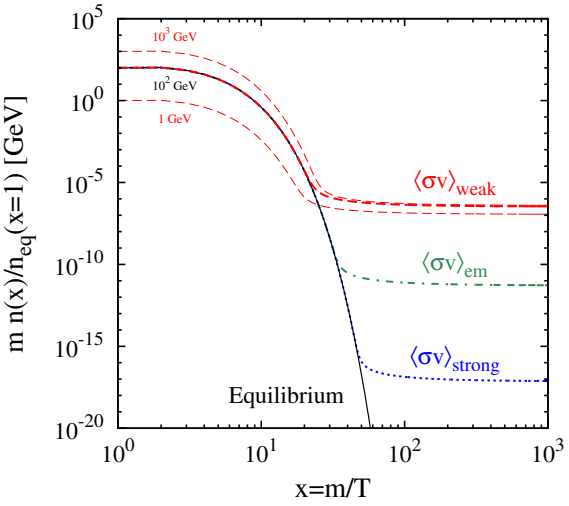


Figure 1.13. Evolution of the DM particle number density as a function of x $= m/T$ as defined in the text. The black line indicates the equilibrium abundance for $m_{\mathrm{DM}} = 100\,\mathrm{GeV}$. Asymptotically it tends to different constant values based on different hypothesis on the magnitude of the interaction cross-section σ, indicated by different colours. Figure adapted from Ref. [67].

density of DM particles is left. The final value of such density is proportional to the scale of the interaction cross-sections, and in particular it is found that weak-scale ones match the observed cosmological DM density when considering particles with masses in the GeV ÷ TeV range.

1.6 Weakly Interacting Massive Particles

If dark matter is of particle nature, candidates must fulfill the constraints imposed by the cosmological observation. These can be summarised in three points:

- candidates must be stable or long-lived, since it is supposed that DM was produced in the early era of the Universe but its effects are observed still today;
- candidates must be neutral under all the SM forces, except for gravity;
- the mass and interaction cross-section of DM candidates must lead to a relic density consistent with its measured value.

In the SM, except for neutrinos, there are no particles that satisfy such criteria. Moreover, the observations hints at a cold dark matter, thus relativistic neutrinos are also ruled out. Thus, new phenomena are required. Weakly Interacting Massive Particles have been proposed to naturally satisfy these requirements. Assuming interaction cross-sections of the order of electroweak processes, WIMPs are required to have a mass in the GeV ÷ TeV, thus are within the sensitivity region of several different experiments. The searches for such particles are discussed below.

1.6.1 WIMP searches

Three kind of searches, adopting different experimental techniques, are carried out to look for the interaction of a WIMP (χ) with SM particles. Complementary sensitivity to the scattering cross-section and WIMP masses are provided by the different methods, which can be divided in:

- direct detection experiments, which assume a lepto-phobic $\chi\,\mathrm{SM} \to \chi\,\mathrm{SM}$ scattering interaction, look for nuclear recoils of low-background experiments;
- indirect detection searches, which look for an excess of the production of SM anti-particles or an excess of high energetic photons in $\chi\chi \to \mathrm{SM}\,\overline{\mathrm{SM}}$ annihilation processes;
- collider searches, which hypothesise that high energy collisions of SM particles allow to produce WIMP pairs in the final states; such particles do not interact with the detector, thus a SM object is needed to tag the event in a $\mathrm{SM}\,\mathrm{SM} \to \chi\chi + \mathrm{X}$ process.

A brief overview of the direct and indirect searches is provided below. One collider search for WIMPs is presented in this thesis in Chapter 4. The models tested in such context are discussed in this Chapter.

Direct detection experiments

Direct detection (DD) experiments look for the recoil of SM particles caused by elastic or inelastic scattering of WIMPs with them. To probe WIMPs with masses of the order of GeV, nuclear recoils are targeted since provide the largest sensitivity. For sub-GeV WIMPs, no detectable nuclear recoils are produced, but it is possible to look at the excitation or ionization of the recoiling atom, caused by the WIMP-nucleus interaction. In the following, only nuclear recoils (NR) are presented.

The motion of the Earth, and in general of the Solar System, within the Milky Way, with an average velocity $\langle v \rangle \sim 10^{-3} \cdot c$ is expected to generate a flux of WIMPs. In fact, the Milky Way is hypothesised to be immersed in an halo of DM particles with a local density $\rho_\chi \sim 0.3\,\mathrm{GeV/cm^3}$. The expected interaction rate of WIMPs with a target is

$$R \simeq \frac{\rho_\chi}{m_\chi} N \langle \sigma_{\chi N} v \rangle, \tag{1.43}$$

where m_χ is the WIMP mass, N is the number of nuclei in a target ($N = m_{\mathrm{tar.}}/m_A$, with m_A nuclear mass), and $\sigma_{\chi N}$ the WIMP-nucleon interaction cross-section. The differential cross-section with respect to the nuclear recoil energy [68] is given by

$$\frac{d\sigma(E_{nr})}{dE_{nr}} = \frac{m_N}{2\langle v \rangle \mu^2} \left[\sigma_{SI} F_{SI}^2(E_{nr}) + \sigma_{SD} F_{SD}^2(E_{nr}) \right], \tag{1.44}$$

where μ is the reduced mass of the WIMP-nucleus system. The total cross-section σ of the new interaction can be divided in a component which is independent of the total spin of the nucleus (SI), and and a dependent (SD) one. The former corresponds to a scalar or vector effective four-fermion Lagrangian. The latter correspond to a pseudo-scalar or axial-vector interaction. The functions F_{SI} and F_{SD} are form

factors which take into account that at high energies the WIMP does not interact with the entire nucleus coherently.

In SI interactions, the WIMP coupling is proportional to the square of the mass number (A^2). Thus, experiments looking for SI interactions adopt heavy nuclei as targets, such as Ar, Ge or Xe. SD interactions foresee a coupling between WIMPs and nuclei independent of the target mass, but proportional to the total spin content of the nucleon (J). Since the cross-section depends explicitly on the expectation value of the total spin operators for protons and neutrons [68], results are usually quoted assuming that WIMPs couple to neutrons or protons only. For this purpose, experiments targeting SD interactions adopt as target elements with an odd number of protons (^{7}Fe, ^{19}F, ^{23}Na, ^{127}I) or neutrons (^{17}O, ^{27}Al, ^{29}Si, ^{73}Ge, $^{129/131}$Xe, ^{183}W).

For masses of the WIMPs of the order of $10 \div 100\,\text{GeV}$, current experiments are sensitive to WIMP-nucleon scattering cross-section of the order of $10^{-4}\,\text{pb}$. Moreover, the expected nuclear recoil in this mass range is of the order of tens of keV. Therefore, high background suppression and very large targets are the key element of the DD searches. The sensitivity is expected to increase for larger value of the masses due higher energy recoils, but the expected WIMPs flux is suppressed as $1/m_\chi$. At lower WIMP masses the sensitivity drops due to the low recoil energy. For these reasons, experiments are located in underground laboratories, and shielded against the natural radiation of the rocks, and are built with radio-pure materials.

To identify nuclear recoils, different experimental techniques are usually adopted. Detectors are often based either on cryogenic bolometers, to detect the phonons produced in the scattering, or are designed to look for a signal in scintillation light produced in liquid noble-gas detectors. Cryogenic systems are also adopted to detect ionisation charges of scattered nuclei. Typically, two of such technologies are adopted to discriminate in a better way potential signal candidates from background events.

Latest results from DD experiments for a SI WIMP-nucleon interaction are reported in Figure 1.14. The most stringent results for $m_\chi > 4\,\text{GeV}$ are set by the XENON1T experiment [69]. For lower values, the most current most stringent results are provided by the DarkSide-50 [70], CDMSLite [71] and CRESST [72] experiments.

The boundary to these kind of searches is given by the so called *neutrino floor*. Neutrinos produced in nuclear reactions which take place in the Sun, or in the interactions between cosmic rays and the Earth atmosphere, can in fact scatter against the nuclei of the experiments targets, leading to background interactions indistinguishable from the ones which might be due to WIMPs. To overcome such a limitation, directional searches which are sensitive to the expected modulation of the WIMP flux [74], induced by the Earth motion around the Sun, are being developed. Results from such experiments are not discussed in this thesis, thus the reader is referred to Ref. [75] for further details.

Indirect detection experiments

The annihilation of WIMP pairs into SM particles is the target process of indirect detection (ID) searches for DM. In particular, what experiments look for is an excess in the flux, as measured on earth, of anti-particles from different sources in the Universe. In fact, it is hypothesised that WIMPs gravitationally captured by heavy

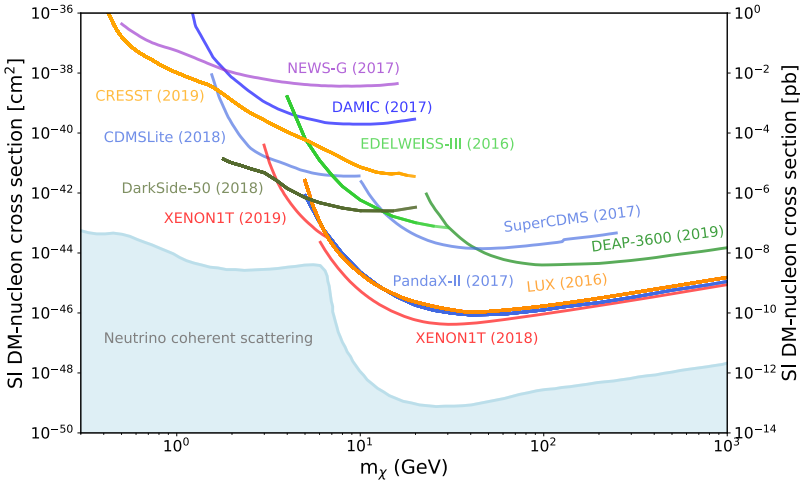


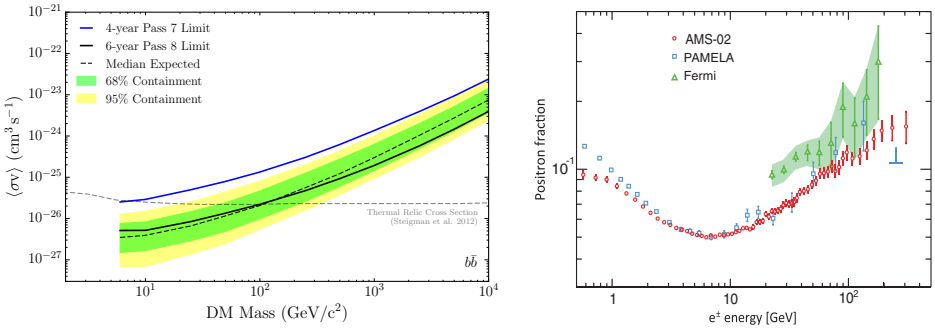
Figure 1.14. 90% CL limits on the SI WIMP-nucleon interaction cross-section, as a function of the WIMP mass. Figure adapted from Ref. [73].

objects can interact as $\chi\chi \to e^+e^-$, $p\bar{p}$, $\nu\bar{\nu}$, $\gamma\gamma$. The expected flux is proportional to the local density of DM, thus experiments look for signals from high density environments such as the Sun and the center of various galaxies.

The final states involving two neutrinos or two photons are particularly interesting, since low-velocity annihilations of WIMP pairs lead to nearly mono-energetic final state particles [73]. Moreover, neutrinos in particular are a good candidate to search for such processes. Indeed, these particles interact only weakly with the medium they cross to reach the Earth, and therefore can be detected by special experiments such as IceCube [76] or Super-Kamiokande [77]. Neutrinos can be also produced in the decay of hadrons produced in the $\chi\chi \to q\bar{q}$ processes, trough the subsequent decay chain of the final state hadrons. Energetic pairs of photons can be produced in the decay of neutral pions, or emitted as final state radiation from other particles. This signature is probed by the Fermi-LAT satellite [78], which targets fluxes of photons produced in the center of the Milky Way, or in satellite galaxies.

The constraint on the WIMP pair annihilation cross-section times the particle velocity, averaged over this latter quantity, obtained by the Fermi-LAT experiment is presented in Figure 1.15(a) as a function of the WIMP mass. Results have been obtained under different hypotheses which considering an annihilation of WIMP pairs 100% of the times into a single SM particle specie. The plot shows the case in which $b\bar{b}$ pairs are considered, and values above the black line are excluded at 95% CL.

Anti-particle fluxes are the target of the AMS-02 [79] and PAMELA [80] experiments, but also investigated by the aforementioned Fermi-LAT. In particular, an excess of high energetic positrons is observed by the three experiments, as reported in Figure 1.15(b). This excess could be explained by annihilation of WIMPs pairs with a mass of $\mathcal{O}(10\,\text{GeV})$. A similar excess in the flux of anti-protons has been reported also by the AMS experiment [81] which might be consistent with the same WIMP hypothesis. However several cosmological phenomena could also explain the observed distributions, thus no statements on WIMPs observation can be made at



(a) (b)

Figure 1.15. (a) 95% CL upper limit on $\langle\sigma v\rangle$ as a function of the WIMP mass, as obtained by the Fermi-LAT experiment [78]. (b) Positron to electron plus positron rate as measured by the AMS-02, Pamela and Fermi-LAT experiments, exhibiting an increasing fraction at high energy. Figure adapted from Ref [79].

the moment.

Collider searches

WIMP searches carried out at particle colliders are based on the hypothesis that it is possible to pair-produce them via a new mediator, which couples the SM and a new dark sector of particles. Such final states would be undetectable unless they are produced in association with one or more SM particles which allow to tag such events. This signature is referred to as mono-X, and is characterised by a large amount of missing energy, carried away by the non-interacting WIMPs. Exploiting the fact that in the plane transverse to the beam the total initial momentum of the collisions is zero, a powerful variable to look for such phenomena is the missing transverse momentum, $E_{\mathrm{T}}^{\mathrm{miss}}$. At an hadron collider, the emission of QCD initial state radiation (ISR) is favoured with respect to the emission of a photon, or the production of a vector boson. Thus, monojet final states, with the jet produced by the hadronisation of QCD ISR, are the golden channel to look for WIMPs at colliders.

A possible approach to collider based WIMP searches is to describe the interaction between SM particles and WIMPs via an effective field theory (EFT) [82]. This approach is valid if the mass of the mediator is much larger than the energy scale probed, thus it cannot be produced on-shell in the collisions. EFT interpretations have been the main outcome of dark matter searches carried out in monojet final states in proton-proton collisions during Run 1 of the LHC by the ATLAS and CMS experiments [83, 84].

Simplified dark matter models. For the Run 2 of LHC, simplified DM models which foresee the exchange of a spin 0 or spin 1 mediator between WIMP and SM particles have been proposed [85]. Such models allow to study further the kinematics of the WIMPs pair production process. The interactions foreseen by simplified DM models should not violate neither the exact nor the accidental symmetries of the SM,

like the conservation of the leptonic and baryonic number, otherwise the space of the allowed parameters would be heavily constrained. Such constraints can be avoided by imposing the Minimal Flavour Violation (MFV) requirement. This foresees that the additional interactions in the quark sector respect the SM flavour symmetry, or that any violation is associated with the quark Yukawa matrices, as for the SM Higgs sector.

These models are referred to as simplified since depend on only few parameters, the mass of the WIMPs (m_χ), the mass of the new mediator (m_{med}), and the couplings of this with SM (g_{SM}) and WIMP particles (g_χ), respectively. The mediators are assumed to have the minimal decay width, Γ, that allows the decay to one species of WIMP particle and to the SM particles to which they are coupled. Moreover, in simplified models only one type of new interaction is considered at the time. The masses of the WIMPs and of the new mediator are assumed to be generated in a dark Brout-Englert-Higgs mechanism, which is not considered in the predicted interactions with SM particles.

In the monojet analysis presented in Chapter 4 of this thesis, only the exchange of a lepto-phobic mediator in the s-channel has been considered, thus $g_{\text{SM}} = g_q$. The zero coupling to leptons is commonly introduced to evade the constraints imposed by di-lepton searches.

In an s-channel interaction, the propagator can be expressed as [86]

$$\frac{1}{Q^2 - m_{\text{med}}^2 + i\Gamma m_{\text{med}}}, \tag{1.45}$$

where Q is the transferred momentum in the interaction. When the mediator is produced on-shell, $Q^2 \simeq m_{\text{med}}^2$, the cross-section is enhanced, and considering the narrow width approximation [87] ($\Gamma \ll m_{\text{med}}$) it scales as $\sigma \sim g_q^2 g_\chi^2/\Gamma$. In the off-shell regime, $Q^2 \gg m_{\text{med}}^2$, the cross-section is suppressed, and scales simply as the square of the couplings g_q and g_χ. In the case in which the mediator mass is much larger than the energy scales probed, $Q^2 \ll m_{\text{med}}$, the predictions converge to the ones from the EFT approach, and the cross-section scales as $1/m_{\text{med}}^4$.

An overview of the models tested in the monojet analysis presented in this thesis is given below.

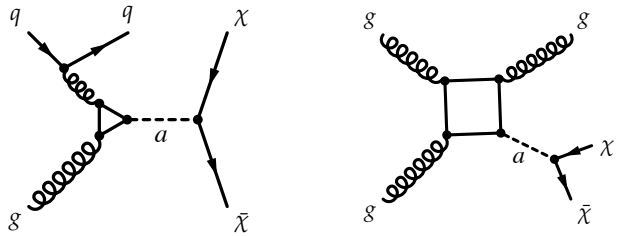
Spin 0 mediators. The production of a pair of WIMPs via a spin 0 pseudo-scalar mediator, a, is referred in the following as DMP model. The Lagrangian term which describes the interaction can be written as [86]

$$\mathscr{L}_a \supset -g_\chi a i\bar{\chi}\gamma_5\chi - \frac{ia}{\sqrt{2}}\sum_i \left(g_u y_i^u \bar{u}_i\gamma_5 u_i + g_d y_i^d \bar{d}_i\gamma_5 d_i\right), \tag{1.46}$$

where the sum runs over the three generations of up- and down-type quarks, and $y_i^f = \sqrt{2}m_i^f/v$ is the Yukawa coupling normalized to the Higgs vev (v). The Yukawa-like interaction is required to satisfy the MFV constraint. The coupling constant between the mediator and SM particles is scaled by the parameter g_q, while g_χ parameterizes the interaction strength between the new mediator and DM particles. For the benchmark models tested, both values of the couplings are set to unity. As previously mentioned, the width of the mediator is fixed, given the decay into SM

quarks and into the single WIMP particle species considered, and the couplings g_q and g_χ. The minimal decay width for a scalar or pseudo-scalar mediator is reported in Section 2.2. of Ref. [86].

Due to the presence of the Yukawa coupling, the dominant production mode of such mediator is via a top-quark loop. Such property suppresses the sensitivity of resonant searches, which would require two loops to produce dijet final states. The leading order (LO) Feynman diagrams for the DMP model are reported in Figure 1.16. Simulated events have been produced for different value of the parameters following the model described in Ref. [88], using POWHEG [89] and PYTHIA 8.1 [90] for the parton showering. Details on the signal samples adopted in the monojet analysis presented in this thesis are given in Section 4.10.2 instead.



(a) (b)

Figure 1.16. Feynman diagrams representing WIMPs (χ) pair production via a spin 0 pseudo-scalar mediator (a) in association with QCD radiation, which allows to tag the events in the final state of pp collisions. Figure adapted from Ref. [86].

In Figure 1.17 the distribution of the expected $E_{\mathrm{T}}^{\mathrm{miss}}$, defined in the transverse plane with respect to the collisions axis as the negative vectorial sum of the momenta of final state SM particles, is presented for various choices of the mass of WIMPs (here referred to as m_{DM}) in the case in which the mass of the mediator (m_{med}) is fixed to 100 GeV. The distribution is obtained considering a scalar mediator, but, as shown in Ref. [86], only a flat offset is observed in the $E_{\mathrm{T}}^{\mathrm{miss}}$ distribution when a scalar or pseudo-scalar mediator is considered. For a mediator mass of 300 GeV and $m_\chi = 10$ GeV, the cross-section obtained considering a pseudo-scalar is a factor 3 larger. Such factor increases for growing m_χ values. The hardness of the spectrum also increases for larger m_χ values, and saturates to a constant shape for $2m_\chi > m_{\mathrm{med}}$.

In Figure 1.18 a comparison of the $E_{\mathrm{T}}^{\mathrm{miss}}$ distribution is presented for different values of the mass of the mediator, fixing the mass of the WIMP to 10 GeV. No significant differences in the kinematics are observed for mediators with a mass smaller (300 GeV) or larger (500 GeV) than twice the mass of the top quark (~ 350 GeV).

The constraints on the parameters of simplified dark matter models involving the exchange of a pseudo-scalar mediator can be converted in limits on the annihilation cross-section of WIMPs pairs into SM particles ($\langle \sigma \cdot v \rangle$), and compared to the results obtained by the Fermi-LAT experiment. The annihilation rate is proportional to

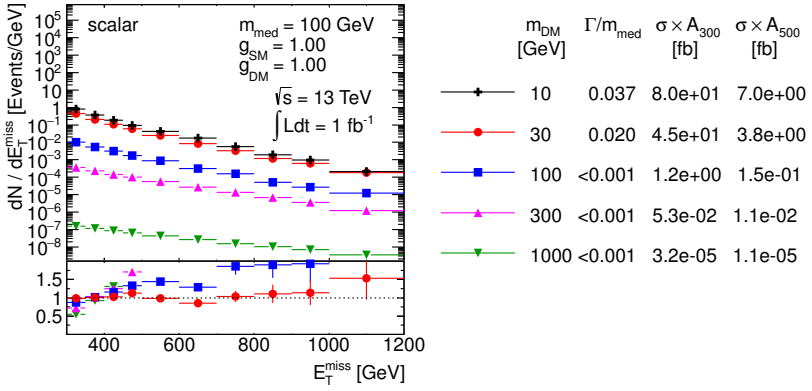


Figure 1.17. Missing transverse momentum distribution for the DMP model for different values of the WIMP mass (here referred to as m_{DM}) fixing the mass of the mediator at 100 GeV. On the right part, the ratios between the mediator decay width and mass are reported, along with the inclusive fiducial cross-sections values obtained imposing a truth $E_{\mathrm{T}}^{\mathrm{miss}}$ cut at 300 and 500 GeV. Figure adapted from Ref. [86].

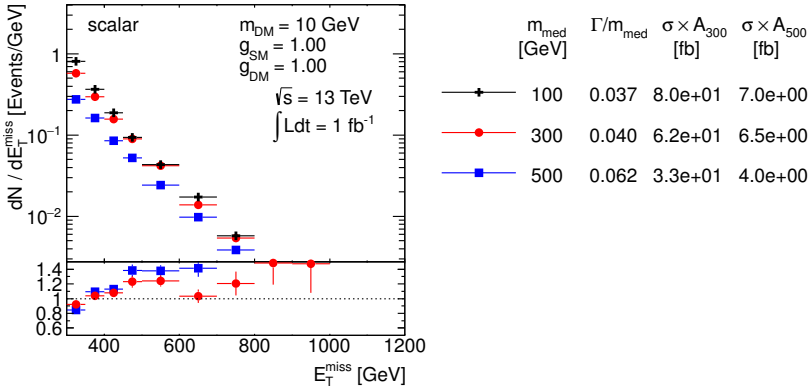


Figure 1.18. Missing transverse momentum distribution for the DMP model for different values of the mediator mass, fixing the WIMP mass (here referred to as m_{DM}) at 10 GeV. On the right part, the ratios between the decay width of the mediator and its mass are reported, along with the inclusive fiducial cross-sections values obtained imposing a truth $E_{\mathrm{T}}^{\mathrm{miss}}$ cut at 300 and 500 GeV. Figure adapted from Ref. [86].

the quark masses squared, and is given by [91]

$$\langle \sigma v \rangle = \frac{g_q^2 g_\chi^2 m_\chi^2}{(m_{\mathrm{med}} - 4m_\chi^2)^2 + m_{\mathrm{med}}^2 \Gamma^2} \cdot \\ \cdot \left[\frac{3 m_q^2 m_\chi^2}{2\pi v^2} \sqrt{1 - \frac{m_q^2}{m_\chi^2}} + \frac{\alpha_s^2}{2\pi^3 v^2} \left| \sum_q m_q^2 \tau \arctan^2 \left(\frac{1}{\sqrt{\tau - 1}} \right) \left(\frac{m_q^2}{m_\chi^2} \right) \right|^2 \right], \tag{1.47}$$

with $\tau = 4m^2_{\text{top-quark}}/m_a^2$. The first term of the second line of the r.h.s. is referred to the annihilation of WIMPs into quark pairs, while the second part to the annihilation

into gluon pairs via a quarks loop.

Spin 1 mediators. A new vector or axial-vector mediator can be included in the SM by considering an additional $\mathrm{U}(1)^{'}$ symmetry, under which the WIMP and some of the SM particles are charged. The interaction Lagrangian of this model can be written as [85]

$$\mathscr{L}_{V,A} \supset g_\chi V_\mu \bar{\chi}\gamma^\mu \left(g_\chi^V - g_\chi^A\gamma^5\right)\chi + \sum_i V_\mu \bar{q}\gamma^\mu \left(g_q^V - g_q^A\gamma^5\right) q, \tag{1.48}$$

where the sum runs over the three generation of SM quarks. In this formulation both the vector and axial vector couplings have been included with the constants are g_χ^V and g_χ^A, respectively. In the monojet analysis presented in this thesis the two cases have been considered independently. The DMV model foresees the production of a vector mediator, thus g_χ^A is set to 0. The production of an axial-vector mediator instead is referred to as DMA model, and in this case g_χ^V is set to 0. As for the spin-0 mediator, the decay width of the mediator is fixed by the allowed decays into SM quarks, given its mass, and by the values of the couplings g_q and $g_\chi^{A,V}$. The minimal decay width are reported in Section 2.1 of Ref. [86]. The LO Feynman diagram representing the production of a spin 1 mediator in association with QCD ISR is reported in Figure 1.19.

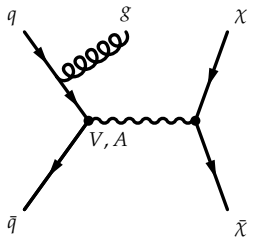


Figure 1.19. Feynman diagram representing WIMP (χ) pair production via a spin 1 vector (V) or axial-vector (A) mediator in association with QCD radiation. Figure adapted from Ref. [86].

Unlike the DMP model, in the DMV/DMA ones the resonant production of the new mediator with its subsequent decay back into SM particles is not suppressed. For this reason, strong constraints on the parameter space are set by dijet searches. This motivated the choice of $g_q = 0.25$ as the benchmark value for LHC Run 2 searches. However, as it can be seen in Figure 1.20, the $E_{\mathrm{T}}^{\mathrm{miss}}$ shape is unchanged when either only g_q, or g_q and g_χ are varied.

A comparison between the vector and axial-vector mediated interactions is presented in Figure 1.21. The shape of the $E_{\mathrm{T}}^{\mathrm{miss}}$ distribution is the same in the two cases, but a flat offset as a function of $E_{\mathrm{T}}^{\mathrm{miss}}$, is observed. The difference in the total cross-section between the two models becomes larger when increasing the mass of the WIMP particles.

Limits on the parameters of simplified dark matter models involving a vector or an axial-vector mediator can be translated into boundaries on the interaction cross-section between WIMPs and nucleons. Under the assumption of the model dependence given by the choice of the coupling constants, collider search results

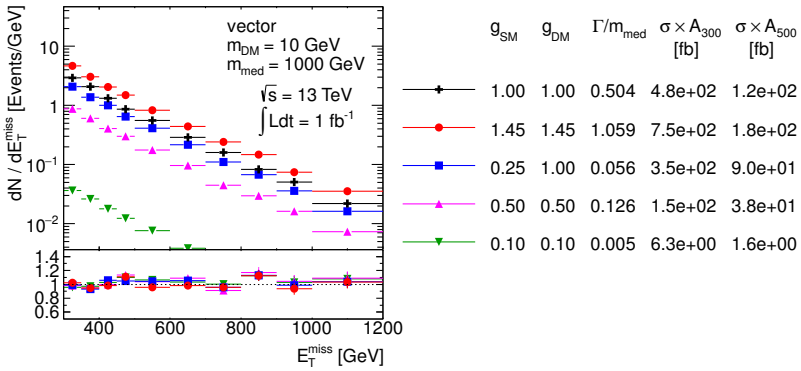


Figure 1.20. Missing transverse momentum distribution for the DMV model for different values of coupling parameters g_q and g_χ, fixing the WIMP (here referred to as DM) and mediator masses at 10 GeV and 1 TeV, respectively. On the right part the ratios between the decay width of the mediator and its mass are reported, along with the inclusive fiducial cross-sections values obtained imposing a $E_{\mathrm{T}}^{\mathrm{miss}}$ cut at 300 and 500 GeV. Figure adapted from Ref. [86].

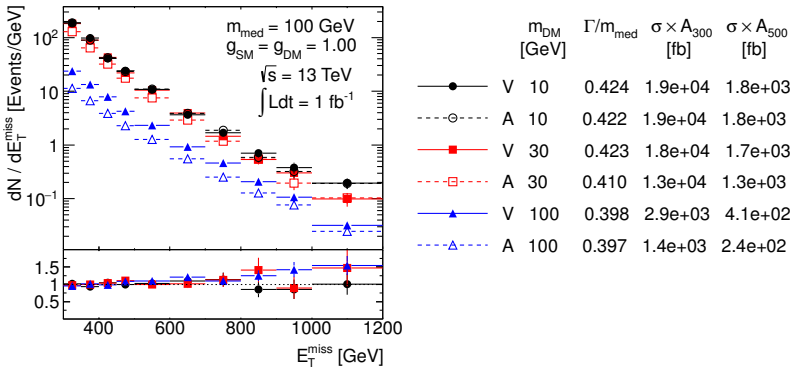


Figure 1.21. Comparison of the $E_{\mathrm{T}}^{\mathrm{miss}}$ distributions between the DMV and DMA models for fixed value of the mediator mass and different value of the WIMP mass. In the bottom pad, the ratio between the shape of the DMA and DMV distribution is presented. On the right part the ratios between the decay width of the mediator and its mass are reported, along with the inclusive fiducial cross-sections values obtained imposing a truth $E_{\mathrm{T}}^{\mathrm{miss}}$ cut at 300 and 500 GeV. Figure adapted from Ref. [86].

can be compared with the ones obtained by direct detection WIMP searches. As already mentioned, a vector mediator leads to a SI WIMP-nucleon interaction, while axial-vector mediators induce a SD one.

For the spin independent case, the scattering cross-section is given by [91]

$$\sigma_{\mathrm{SI}} = \frac{f^2(g_q) g_\chi^2 \mu_{n\chi}^2}{\pi m_{\mathrm{med}}}^4 , \tag{1.49}$$

where $\mu_{n\chi}$ is the reduced mass of the WIMP-nucleon system, and $f(g_q)^2$ is the mediator-nucleon coupling. For the vector mediator $f(g_q) = 3g_q$, thus the scattering

cross-section is given by

$$\sigma_{\mathrm{SI}} \simeq 6.9 \times 10^{-41}\mathrm{cm}^2 \cdot \left(\frac{g_q g_\chi}{0.25}\right)^2 \left(\frac{1\,\mathrm{TeV}}{m_{\mathrm{med}}}\right)^4 \left(\frac{\mu_{n\chi}}{1\,\mathrm{GeV}}\right)^2. \tag{1.50}$$

The scattering cross-section in the case of a SD interaction is of the same form of Equation 1.49, except for the fact that a factor 3 has to be considered in front of the r.h.s. term (cf. Ref. [91]). However, in the spin-dependent case the coupling between the mediator and the nucleon is $f(g_q) = 0.32 g_q$, since the mediator is sensitive to the spin content of the nucleus. Such a value is obtained under the assumption that g_q is equal for all quarks. Finally, the interaction cross-section is given in the SD case by

$$\sigma_{\mathrm{SD}} \simeq 2.4 \times 10^{-42}\mathrm{cm}^2 \cdot \left(\frac{g_q g_\chi}{0.25}\right)^2 \left(\frac{1\,\mathrm{TeV}}{m_{\mathrm{med}}}\right)^4 \left(\frac{\mu_{n\chi}}{1\,\mathrm{GeV}}\right)^2, \tag{1.51}$$

and is the same whether the WIMP-proton or WIMP-neutron scattering processes are considered.

The constraints on the parameters of simplified dark matter models obtained by the Run 2 monojet analysis are reported in Section 4.10.2 of this thesis.

Compressed SUSY scenarios. As already mentioned in Section 1.6, supersymmetry provides a WIMP cadidate, the lightest neutralino $\tilde{\chi}_1^0$. In R-parity conserving models, these particles are produced in the decay chain of squarks. Feynman diagrams representing such interactions are presented in Figure 1.22. The monojet analysis, object of this thesis, is particularly sensitive to the cases in which the mass splitting between the decaying squark and the neutralino is small ($\Delta m = m_{\tilde{q}} - m_{\tilde{\chi}_1^0} \sim 0$). In these cases, the transverse momentum of final state particles is low and the extraction of such signals from the large multijet background of hadron colliders is hard. However, the sensitivity to such processes can be enhanced if they are accompanied by an energetic jet produced by ISR, thus leading to a monojet-like topology.

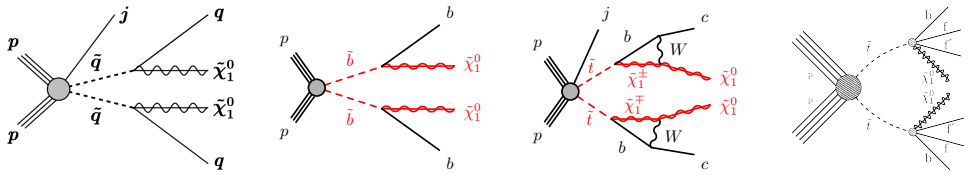


Figure 1.22. Feynman diagrams representing the SUSY processes investigated in the monojet analysis. (a) Squark pair production, (b) sbottom pair production, (c) stop pair production and direct decay and (d) four body decays of stops. These figures were not produced by me, the original source is unknown.

The processes considered are the pair production of stops $\tilde{t}$, sbottoms $\tilde{b}$, or squarks in general, considering all the supersymmetric partners of lighter SM quarks ($\tilde{q} = \tilde{u}$, $\tilde{d}$, $\tilde{s}$, $\tilde{c}$). The stop pair production can be investigated either in direct decays to a top quark and a neutralino, or in the so-called four-body-decay-mode, which

includes the production of two additional soft fermions f in a four point interaction, as represented in Figure 1.22(d). Constraints on the parameters of these models, obtained with the Run 2 monojet analysis, are presented in Section 4.10.3 of this thesis.

1.7 The dark sector

As already mentioned in the end of Section 1.3.1, the invisible branching fraction of the Higgs boson is predicted by the SM to be of the order of 0.1%. The current constraints set from ATLAS and CMS analyses are of the order of 10%, thus the possibility of new phenomena which lead to invisible final states is not ruled out completely yet. This motivates dark sector portal models which hypothesise the existence of an Hidden Sector (HS) of particles, decoupled from the SM, which is accessible via Higgs boson decays. Particles of the HS, or the mediator itself, could provide a solution to the hierarchy problem. Moreover, such models could provide an explanation to the mystery of dark matter. Some of these models are the Quirky Little Higgs [92], the Twin Higgs model [93] or Folded SUSY [94].

As done in the case of dark matter searches, to investigate the expected complex phenomenology of the HS simplified models have been introduced. These can be considered as the infrared limit of a more complete picture, and provide a signature to look for the production, and consequent decay, of the mediator between the SM and the dark sector. Such particles are hypothesised to be lighter than the Higgs boson, and to be long-lived (LLPs), i.e. characterized by a macroscopic lifetime such that they lead to displaced decays vertices within the ATLAS detector. In the limit of long proper lifetimes, such particles could even leave ATLAS without decaying, thus leading to missing energy in the final states as in the case of WIMPs.

1.7.1 Theoretical models

Falkowski Ruderman Volansky Zupan model. The first model investigated in the context of this thesis is the FRVZ [95, 96] one. It hypothesises the production of light long-lived dark photons (γ_d) in a decay chain initiated by the $H \rightarrow$ inv. decay. The process is initiated by a SM Higgs boson which decays into a pair of dark fermions (f_d). In turn, these decay into a γ_d and the Hidden Lightest Stable Particle (HLSP) which is undetected in the final states. The γ_d successively oscillate into a SM photon (γ) via a kinetic mixing governed by a parameter ε. Off-mass-shell photons then decay into pairs of fermions or light hadrons, producing displaced vertices.

The kinetic mixing parameter value is inversely proportional to the lifetime of the dark photon, thus the smaller the ε value, the more displaced the vertex of the photon decay from the interaction point. As already stated for the general LLP signature, if the proper lifetime of the γ_d ($c\tau_d$) is long enough, or the system is boosted by ISR, the γ_d decay products may not be reconstructed within the ATLAS detector, leading thus to a monojet signature.

ATLAS dark photon searches are typically divided into two categories, optimised for different ranges of the kinetic mixing parameter ε, thus of the lifetime of the γ_d [97]. Scenarios with $\varepsilon > 10^{-5}$ are probed by prompt searches [98], while displaced

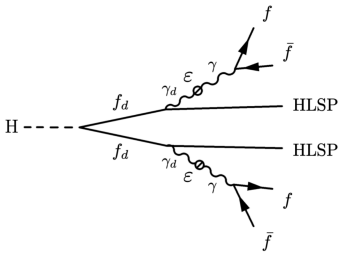


Figure 1.23. Decay chain predicted by the FRVZ model, leading to the production in displaced vertices of SM fermions, and missing transverse momentum due to the presence of undetected HLSPs. Figure adapted from Ref. [5].

dark-photon-jet searches, like the one in Ref. [99], target $\varepsilon < 10^{-5}$. This latter range is the one targeted by the monojet analysis, though some sensitivity at lower lifetimes could arise if the decay products of the γ_d are not properly identified.

The γ_d mass is assumed to be within the range [0.2, 2] GeV, thus the resulting off-shell SM photon can decay into electron or muon pairs, or light hadrons if $m_{\gamma_d} > 2m_{\pi}^{\pm}$. The description of the branching fraction of the $\gamma_d$as a function of its mass is presented in Figure 1.24. Below 500 GeV leptonic final states dominate, while above such threshold the main decay channel is in a $q\bar{q}$ pair, due to the presence of the $\rho(770)$, $\omega(782)$ and $\phi(1020)$ resonances which decay into pions or kaons.

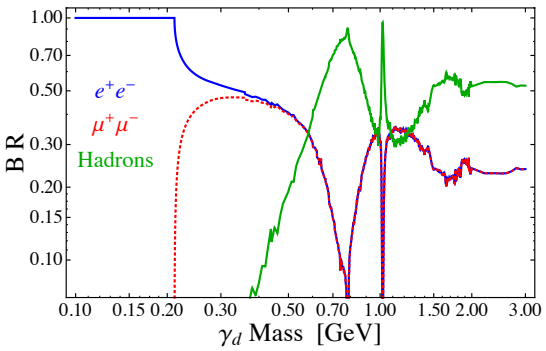


Figure 1.24. Dark photon branching fraction to electrons, muons and hadrons as a function of m_{γ_d}. Figure adapted from Ref. [95].

Hss model. The second model investigated involves a single additional BSM scalar particle, s, [100]. Such particles are characterised by a long mean proper lifetime, are pair-produced in Higgs boson decays, and can decay into SM fermions, as represented in the diagram reported in Figure 1.25.

A Yukawa-like interaction between the Higgs boson, the s particles and their decay products is assumed, and the s bosons are allowed to decay inclusively to all kinematically-allowed final states. The probability of the various decay modes of the additional s particle, as a function of its mass m_s, is presented in Figure 1.26.

For $m_s > 25$ GeV, the branching ratios to $b\bar{b}$, $c\bar{c}$, and $\tau^+\tau^-$ are approximately constant and amount to 86%, 5%, and 8%, respectively. For mass values in the

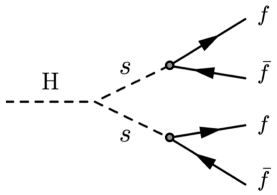


Figure 1.25. Diagram representing the production of a pair of long-lived scalar particles in the Higgs boson decay. The s particles successively decay into a pair of SM fermions, leading to displaced vertices in the ATLAS detector, or missing energy if the decay products are undetected. Figure adapted from Ref. [5].

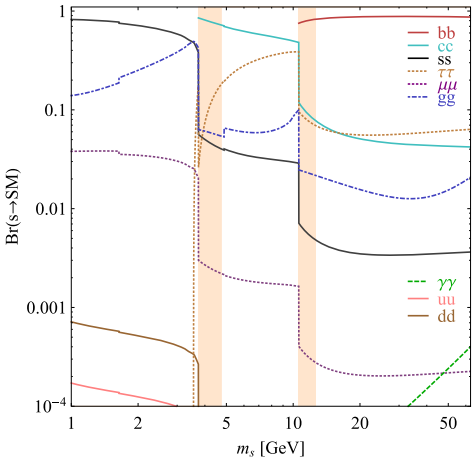


Figure 1.26. Branching ratio of the s scalar particle as a function of its mass m_s. The shaded regions indicate ranges in which the derivation of the simplified model, performed in Ref. [100], is not valid. Figure adapted from Ref. [100].

range between 5 and 10 GeV instead, the dominant decay mode is $s \to c\bar{c}$.

As in the case of the FRVZ model, if the Higgs boson is produced in association with ISR, and the lifetime of the scalar particles s is sufficiently long, the fermions produced in the final states might not be reconstructed within the ATLAS experiments, thus resulting in a monojet final state.

Constraints on both the LLPs models presented in this Section are shown in Section 4.11. Current limits set by the ATLAS collaboration have been extended at large lifetimes by the monojet analysis presented in this thesis.

Chapter 2

ATLAS and the LHC

In this chapter, the experimental facility where the data on which this thesis is based were collected is described. The Large Hadron Collider (LHC) was built with the purpose of colliding protons and heavy ions at a targeted centre-of-mass energy, $\sqrt{s}$, of respectively 14 TeV and 5.6 TeV. Such collisions are recorded by A Toroidal LHC ApparatuS, the ATLAS experiment. It is an almost hermetic detector, made by several sub-systems, optimised to fully reconstruct the particles produced in the collisions. Section 2.1 describes the LHC and its program, while in Section 2.2 the ATLAS experiment is described. In Section 2.2.3 an overview of the pp collisions data set collected by ATLAS at $\sqrt{s} = 13$ TeV during the LHC Run 2, which is used in this thesis, is presented.

2.1 The Large Hadron Collider

The LHC [101], installed at the CERN laboratories at the Swiss-French border near Geneva, is the world largest synchrotron. It is located between 45 and 175 m underground and has a circumference of about 27 km. LHC operations have been staged in Run and Long Shutdown (LS) periods. LHC Run 1 started in the Spring of 2010 and lasted until the end of 2012. In this period, pp collisions have been recorded at $\sqrt{s} = 7$ and 8 TeV. During LS1, the centre-of-mass energy of pp collisions was increased to 13 TeV, which was also chosen as COM energy throughout Run 2, which took place between the 2015 and 2018. Since the end of 2018 till today, the LS2 is ongoing. Work on magnets is being carried out to reach the designed target centre-of-mass energy of 14 TeV by the start of Run 3, which is expected to begin in March 2022.

LHC includes 1232 superconducting dipole magnets, able to provide a magnetic field of up to 8.3 T, which is needed to keep protons of up to 7 TeV of energy on the circular orbit. Additional magnets, 858 quadrupoles and around 6000 correctors, are located along the ring and act on the beam characteristics, such as its focus. Since same-sign particles are collided in the LHC, the two beams travel on separate vacuum chambers. Radio-frequency (RF) cavities, located in one point along the ring, provide an oscillating electric field which accelerates particles each time they pass by. The field oscillates at a fixed frequency of 400 MHz. Particles with the target energy, which pass trough the cavity while the field is zero, will not be accelerated,

while less (more) energetic particles will be accelerated (decelerated). This ensures that particles are kept in concentrated bunches. Beams are therefore accelerated by slightly increasing the magnetic field of the dipoles. This causes a higher bending, thus a shorter orbit. Particle bunches are formed at an earlier acceleration stage which involves several accelerators from the CERN complex. An overview of these systems is given in Figure 2.1. These particle bunches are then collided in the four main interaction points (IP) of the LHC, where the ATLAS [102], CMS [103], ALICE [104] and LHCb [105] experiments are located.

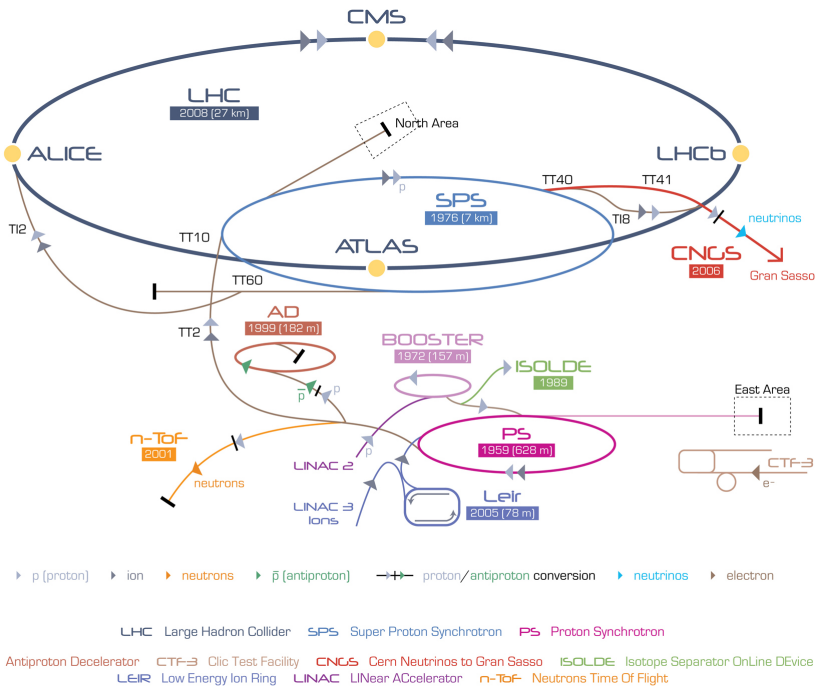


Figure 2.1. CERN accelerators complex. Figure adapted from Ref. [106].

During LHC Run 2, protons have been injected in the acceleration complex via the LINAC2 in six separate bunches at an energy of 50 MeV and enter the Proton Synchrotron Booster (PSB). The magnetic field is ramped up such that bunches of particles will travel on a shorter orbit and will get accelerated by a similar system to the RF of LHC. Once a kinetic energy (E_{kin}) of 1.4 GeV is reached, particles are transferred to the Proton Synchrotron (PS). Here, at E_{kin}= 2.5 GeV each bunch is split in 3 sub-bunches, which are further accelerated to the PS top energy, E_{kin} = 26 GeV. At this stage, each bunch is again split two times in two separate bunches. The 72 total bunches obtained in this way travel separated in time by 25 ns [107]. These bunches are then injected in the Super Proton Synchrotron (SPS) circular machine, which accelerates the protons up to 450 GeV. This is the injection energy of protons in the LHC. During Run 2 operations, the number of bunches per ring was 2556.

Run 2 machine performance

The number of pp collisions per second at the LHC is given by

$$\frac{dN}{dt} = \mathscr{L}\sigma_{pp}^{\text{tot}}, \tag{2.1}$$

where $\sigma_{pp}^{\text{total}}$ is the total interaction cross-section. This quantity is measured in *barn* ($1\text{b} = 10^{-24}$ cm^2). The instantaneous luminosity $\mathscr{L}$ is measured in cm^{-2}s^{-1}, depends on the beam characteristics, and can be expressed as

$$\mathscr{L} = f(\alpha)\frac{kfn_1n_2}{4\pi\sigma_x\sigma_y}. \tag{2.2}$$

In this equation, $f(\alpha)$ is a geometrical factor, lower than 1, which accounts for a non-zero collision angle (α) and other intra- and extra-beam effects. The interaction frequency is given by the term $k \cdot f$, where the former is the number of bunches injected in the ring, and the latter is the revolution frequency. The number of protons per bunch in each of the two colliding beams, referred to also as bunch intensity, is given by n_i. Assuming as z the direction in which the beam travels, $\sigma_x(y)$ is the rms of the beam size in the transverse plane. When the beam is accelerated, particles are confined by the magnetic field and tend to oscillate around the nominal propagation direction. The equation of motion in the transverse plane is given by an harmonic oscillator, whose amplitude is given by a parameter $\beta_{x(y)}$. This oscillations are reduced via triplet magnets, which are located near the interaction points, such that an higher luminosity is achieved where the collisions take place. In the interaction point this parameter takes the name of β^*, and it is measured in meters. The amount of data collected, the integrated luminosity over a time period, is instead expressed in terms of the inverse of a cross-section, in barns. An overview of the performance of the LHC during Run 2, in terms of the quantities introduced previously, is reported in Figure 2.2. Further details are reported in Ref. [108].

In each collision between the bunches, multiple pp interactions take place. The average number of these, μ, is directly related to the machine parameters, such as the transverse size of the beams and the intensity of the bunches, and to the total pp inelastic cross-section (σ_{tot}) which was measured to be 78.1 ± 2.9 mb by the ATLAS collaboration [109] $\sqrt{s} = 13$ TeV . These additional collisions tend to pile up to the hard scattering interactions, and can be a limiting factor for precision measurements. *Pileup* can affect the experiments in two ways: the *in-time pileup* is the one due to multiple collisions happening in the same bunch crossing. The *out-of-time pileup* is due to the fact that electric signals in particular detectors may last more than the time that separates two bunch crossings.

During LHC operations, the instantaneous luminosity decreases. The main reason are collisions taking place in the IPs, where experiment are located. Additional degradation is caused by intra-beam forces and by interactions of the proton bunches with residual gases in the beam pipe. Collisions are considered as *stable beams conditions* for a time which typically lasts between 5 and 15 hours. When the instantaneous luminosity goes below a fixed threshold, beams are dumped via a system installed along the ring, and a new injection is performed. The fill of the

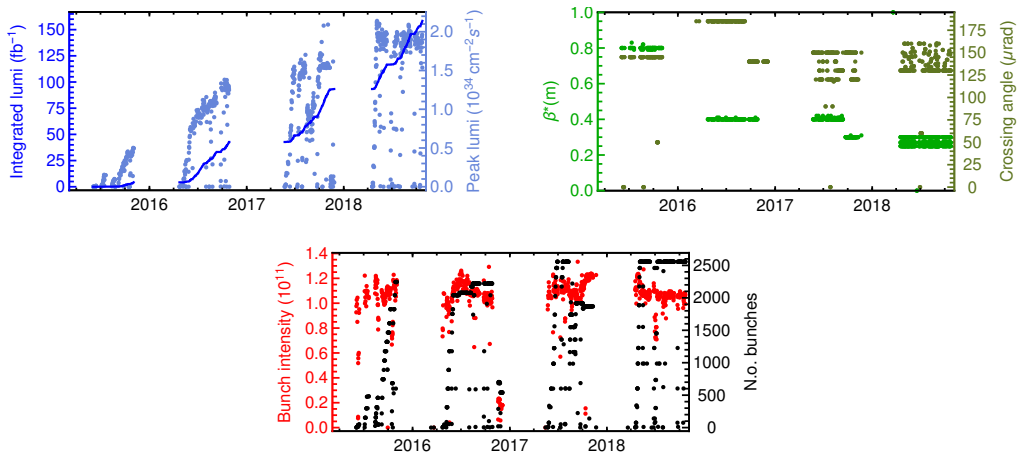


Figure 2.2. Summary of LHC performance during Run 2 as measured in the IP1 and IP5. In the top left pad are reported the integrated luminosity and the instantaneous luminosity measured when the fill of LHC is complete. In the top-right pad are reported the β^* and the crossing angle. The lower pad shows parameters related to the characteristics of the proton bunches. Figure adapted from Ref. [108].

rings with proton bunches and the ramping of the beam energy from 450 GeV to 6.5 TeV took between 90 and 120 minutes during Run 2. An example of a filling cycle of the LHC is shown in Figure 2.3.

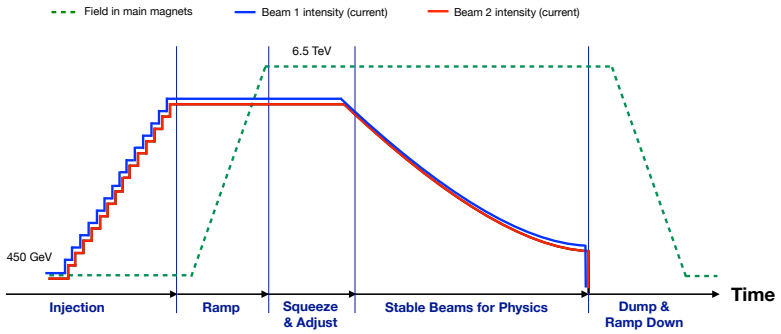


Figure 2.3. LHC filling cycle. Figure adapted from Ref. [110].

2.2 A Toroidal LHC ApparatuS

ATLAS [102] is a general-purpose detector built around IP1 of the LHC. An overview of the sub-detectors is shown in Figure 2.4. The experiment measures 44 m in length and 25 m in height, and is built with cylindrical symmetry around the beam pipe. The sub-detectors provide an almost hermetic coverage, and allow to reconstruct the final state particles produced in the collisions. From the interaction point and towards the outer part of the experiment there are a tracking system, an electromagnetic and an hadronic calorimeter, and the muon spectrometer. Further description of

each system and its performance are reported later in this Section. The experiment can be divided in a barrel (or central) part, and two end-caps.

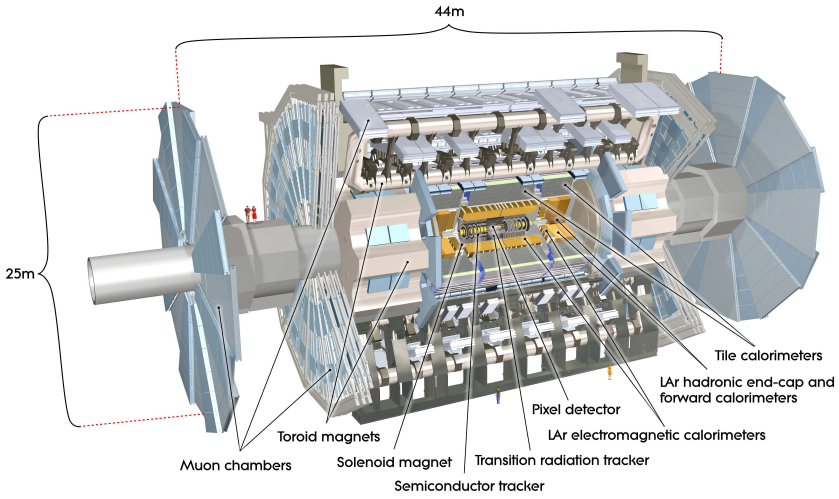


Figure 2.4. The ATLAS experiment. Figure from Ref. [102].

Superconducting magnets

Four different magnetic fields are used to bend charged particles such that a measurement of their momentum from the sagitta can be performed. The solenoid magnet, whose axis is parallel to the beam pipe, is located in the inner part of the experiment, as shown in Figure 2.4. It is 5.8 m long, it has an inner (outer) radius of 2.46 m (2.56 m), and provides a 2 T magnetic field. The external barrel toroid is made of 8 coils 25.3 m long. These form a cylindrical region of respectively 9.4 m and 20.1 m internal and external diameters, in which a magnetic field of mean value of 0.5 T is provided in air. In the two end-caps, similar coils provide a magnetic field in the range of [0.2,3.5] T in a radial zone between 0.8 and 5.3 m around the beam pipe. The bending power is not constant due to ferromagnetic structures present in the experiment. Hall probes installed in the system allows though for a mapping of the magnetic field with a precision of 0.01 mT.

Coordinate system

A cylindrical coordinate system is adopted, centered in the middle of the experiment. The z axis is defined along the beam pipe, the y axis is vertical, and the x axis is defined as pointing towards the LHC center. In the (x,y) plane, transverse to the beam direction, the azimuth angle ϕ and radius r are defined. The transverse momentum (p_{T}) of a particle is defined as the magnitude of the 2D projection of the momentum vector on this plane. The total transverse momentum after the collisions is expected to be almost zero, since the collisions are happening with a crossing angle of the order of micro-radiant. Residual differences are well covered by the resolution on the measurements of particles. The missing transverse momentum, $E_{\mathrm{T}}^{\mathrm{miss}}$, plays a central role in this thesis, and its definition is given in Section 3.4.

In the (z,y), or (z,r), plane the polar angle θ is taken starting from the z axis. The rapidity, y, is defined as

$$y = \frac{1}{2} \ln \left(\frac{E + p_z}{E - p_z} \right), \tag{2.3}$$

where p_z is the momentum component along the beam axis. For ultra-relativistic objects, this quantity is well approximated

$$\eta = -2 \ln \left(\tan \frac{\theta}{2} \right). \tag{2.4}$$

This quantity allows for an extended scale at low polar angles. Moreover, the coverage of the ATLAS sub-detectors is usually reported in terms of pseudo-rapidity. This quantity is also used to define the experimental cuts applied for the reconstruction of physics objects in the final states, since the Δy (approximate with $\Delta\eta$) is a Lorentz invariant quantity. With the pseudo-rapidity and the azimuth angle it is possible to define a geometrical distance

$$\Delta R = \sqrt{\Delta\eta^2 + \Delta\phi^2}, \tag{2.5}$$

which is used to express the separation between energy deposits, or more in general between two reconstructed physics objects in the final states of the collisions.

2.2.1 The sub-detector systems

Inner detector

The inner detector (ID) [111] is the closest system to the beam-pipe. Its purpose is to identify the hard-scatter and secondary vertices via the reconstruction of the tracks left by charged particles. From the bending of the track, a measurement of the momentum of such particles is also possible. An overall view of the system is presented in Figure 2.5, along with the dimensions of the entire structure.

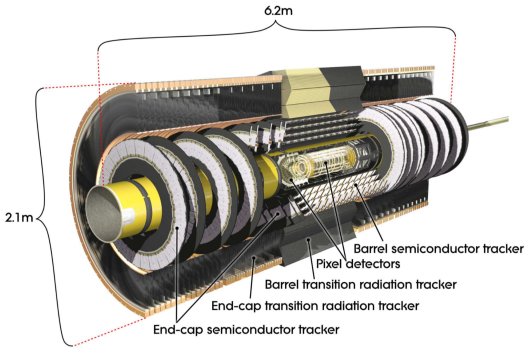


Figure 2.5. ATLAS inner detector. Figure from Ref. [112].

The system is composed by three different technologies: pixel sensors, semiconductor trackers (SCT), and transition-radiation-trackers (TRT). An additional layer of pixel, the insertable b-layer [113, 114], was installed during LS1 of the LHC to improve tracking performance and compensate the effects of radiation damages.

This innermost part is located at a radial distance of 3.3 cm to the beam, and includes 32×14 pixel readout circuits, with a $50 \times 250\,\mu m$ pitch size in the (ϕ,z) plane.

Pixel detector. The pixel sensors in the barrel are organised in three layers located between $R = 50.5$ mm and 123 mm. In the end-caps the sensors are installed on discs centered on the beam pipe. In both structures, sensors are mounted with a tilt angle such that the area where the read out electronics of one module is located, is covered by the active area of the following one. The spatial resolution of this detector was measured in test beams, and it is between 5 and 12 µm.

Semi-Conductor Tracker. The SCT [115] is organised in subsequent layers and disks as the pixel detector. The four barrel layers are located between $R = 30$ mm and 51 mm. In the end-caps the sensors are mounted on nine disks, and in three different radial sectors. The spatial resolution of the SCT alone is of around 15 µrad on the ϕ angle.

Transition Radiation Tracker. The TRT system [116] is located in the external part of the inner detector. Its purpose is to continuously track particles from the innermost layers up to the calorimeter system of the ATLAS detector. It also provides electrons identification based on the number of hits above the energy-deposit threshold corresponding to transition radiation. The active means of the detector are straw tubes which contain a mixture of Xenon-CO_2-O_2 (70%, 27%, 3%). These tubes are immersed in a matrix of polypropylene fibres, the radiator material which induces transition radiation. The barrel region covers the range $|\eta| < 1$, and provides a spatial resolution of $\phi \sim 130\,\mu m$. In the end-caps, straw tubes and activation material are organised in a disk structure.

Tracks within $|\eta| < 2.5$ and with a $p_T > 0.4$ GeV can be reconstructed by the ID. An overview of the performance of the inner tracking system is given in Ref. [117].

Calorimeters

The layout of the calorimetric system is shown in Figure 2.6. This system is located outside the superconducting solenoid, and its purpose is to measure the energy of the particles in a destructive way, via the reconstruction of electromagnetic and hadronic showers. The system has a coverage up to $|\eta| < 4.9$, and is formed by two sub-systems, an electromagnetic (EMC) and an hadronic part (HC), both based on the sampling technique. This foresees intervals of passive material, which induct the showers, alternated by active material where the deposited energy is read out by electronics.

A crucial point of the calorimetric system is that it has to fully contain the showers developed. This allows for the measurement of all the interacting particles produced in the collisions, while keeping a low probability of particles other than muons to provide signals in the muon spectrometers (a phenomenon denoted as *punch-through*). To match these requirements, materials with a high radiation length (X_0) and interaction length (λ) are adopted.

Electromagnetic calorimeter. The ATLAS electromagnetic calorimeter [118] is shaped as an accordion. It is formed by lead slabs (passive material) which

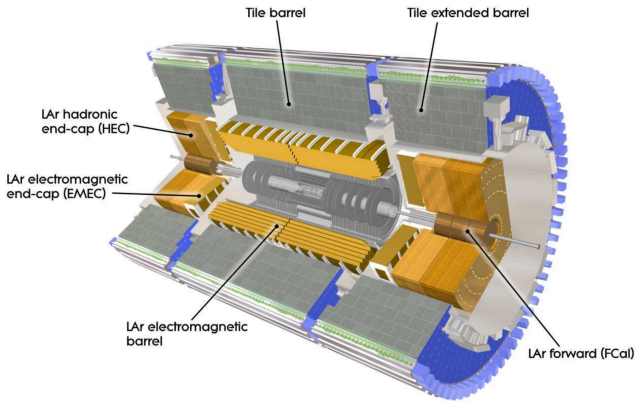


Figure 2.6. ATLAS calorimetric system. Figure from Ref. [102].

contains liquid Ar (the active material) kept at a temperature of 88.5 K. This geometry provides high sampling rates with a low read-out time. The system is symmetric around the interaction point, and is formed by a barrel part, which provides a coverage up to $|\eta| < 1.475$, and two end-caps covering the range between $1.375 < |\eta| < 2.5$. The separation region, between $1.37 < |\eta| < 1.52$, is called *crack-region* and is typically vetoed in the reconstruction of electrons or photons since it contains a large amount of inactive material. The barrel region extends for 6.4 m in total, and has an inner and outer radii of 1.4 and 2 m. The total depth of the calorimeter is between 22 X_0 and 33 X_0 depending on the $|\eta|$ value. Radially the system is segmented in three layers, which are read-out with different granularity. The first one is the most granular. Read-out cells have a dimension of $\Delta\eta \times \Delta\phi = 0.025/8 \times 0.1$ for $|\eta| < 1.40$, and 0.25×0.25 in the $|\eta|$ range $[1.40, 1.475]$. Such granularity is useful to identify the shower position and direction. The first layer, in terms of radiation lengths, is $4.3X_0$ long. In the second layer most of the energy of the EM showers is deposited, as it is $16X_0$ long. The readout cells here have a width of $\Delta\eta \times \Delta\phi = 0.025 \times 0.025$ and 0.075×0.025 respectively in the ranges $|\eta| < 1.40$ and $1.40 < |\eta| < 1.475$. The outer layer, which is $2X_0$ thick, collects the tails of the EM showers. Here, a coarser granularity of $\Delta\eta \times \Delta\phi = 0.05 \times 0.0245$ is adopted for the read-out. The end-cap EMC is formed by two wheels of 63 cm of width, with an inner (outer) radius of 33 cm (2.1 m). It covers the $|\eta|$ interval [1.375,3.2]. A total length between 24 and 38 X_0 is achieved for $1.475 < |\eta| < 2.5$, and between 26 and 36 X_0 in the more forward range up to $|\eta| < 3.2$. The outer part, in the range $1.5 < |\eta| < 2.5$, is segmented in 3 parts as for the barrel region with decreasing granularity. In the range $|\eta| < 1.8$ a pre-sampler layer with granularity $\Delta\eta \times \Delta\phi = 0.025 \times 0.1$ and made by 11 mm of LAr, is installed in front of the calorimeter. This allows to correct the energy measurement for the interactions of particles upstream of the EMC.

The energy resolution of the EMC was measured in test beams with electrons before the installation in the ATLAS experiment. In the interval between 15-150 GeV the measured energy is within 0.1% of the beam energy. The fractional energy resolution

was measured as a function of the beam energy, and was found to be

$$\frac{\sigma(\mathrm{E})}{\mathrm{E}} = \frac{10.1\%}{\sqrt{\mathrm{E(GeV)}}} \oplus 0.17\%, \tag{2.6}$$

where the first term is stochastic and the second one is related to the non-uniformity of the response of the detector.

Hadronic calorimeter. The hadronic calorimeter of the ATLAS experiment is formed by three subsystems: the tile calorimeter, located in the central region behind the EMC, a LAr hadronic end-cap calorimeter, located behind the end-caps of the EMC, and the LAr forward calorimeter. The tile calorimeter covers the range up to $|\eta| < 1.7$, and has an inner (outer) radius of 2.28 m (4.25 m). It is formed by a steel absorber and scintillating tiles, which are the active material from which the signal is read out. The absorber and scintillators are arranged in a periodic structure with a ratio of roughly 4.7:1. As the EMC, the tile calorimeter is segmented radially in three layers of different thickness. For $|\eta| < 1$ these equal 1.5, 4.1 and 1.8 interaction lengths, while 1.5, 2.6 and 3.3 λ are the thicknesses for $1.0 < |\eta| < 1.7$. The scintillating tiles produce UV light, which is captured by two wave-length-shifting optic fibers installed at the edges of each one. These allow for the conversion of the signal to visible light, to which photo-multipliers (PMTs), used for the readout, are more efficient. The HC end-caps cover instead the range $1.5 < |\eta| < 3.2$, and are built with planar geometry. The sampling is obtained alternating copper plates and LAr with a pitch of 8.5 mm. The system is subdivided in two modules of different granularity and therefore sampling rates, which are respectively 4.4% and 2.2%. Similarly to the EMC, the signal is induced in the LAr and read in a capacitive way in cells of $\Delta\eta \times \Delta\phi = 0.1 \times 0.1$ (0.2×0.2) for $|\eta| < 2.5$ ($|\eta| > 2.5$). The energy resolution of the HC is given by the convolution of three terms,

$$\frac{\sigma(\mathrm{E})}{\mathrm{E}} = \frac{52\%}{\sqrt{\mathrm{E(GeV)}}} \oplus \frac{1.6\,\mathrm{GeV}}{\mathrm{E}} \oplus 3\%. \tag{2.7}$$

The first one is related to the stochastic nature of the development of hadronic showers. The second one is due to noise from the read-out electronics. The last one is a constant term to account for unknown effects.

Forward calorimeters. The region closest to the beam pipe, in the range $3.1 < |\eta| < 4.9$, is covered by forward calorimeters (FCal). This system is flagged in Figure 2.6 by the label 'LAR forward', and is exposed to a high flux of particles since most of the collisions happen with low transferred momentum. FCal is formed by three sub-modules (FCal1, FCal2, FCal3), one electromagnetic and two hadronic calorimeters, each 45 cm thick. These calorimeters adopt LAr as the active material. The chosen passive medium for FCal1 is copper, and the total thickness achieved is of $27.6X_0$ and 2.66λ. Tungsten is instead adopted for FCal2 and 3, which allows to reach around $90X_0$ and 3.6λ in only 90 cm. The read-out is made in capacitive way from the LAr gaps, whose width varies in the three sub-systems between 269 µm and 508 µm.

Muon spectrometer

The muon spectrometer (MS) is located in the outer part of the ATLAS experiment. It provides tracking in the interval $|\eta| < 2.7$ of muons with momenta of at least 3 GeV. Trigger chambers are installed up to $|\eta| = 2.4$. A measurement of the momentum of muons is possible thanks to the magnetic fields present in the experiment. The target of the MS is to achieve a resolution of 10% on 1 TeV tracks. This is challenging since such tracks form a sagitta of about 500 µm. The layout of the system in the (z,r) plane is shown in Figure 2.7. This is orthogonal to the magnetic field provided by the barrel coils, and is therefore the plane in which charged particles are bent.

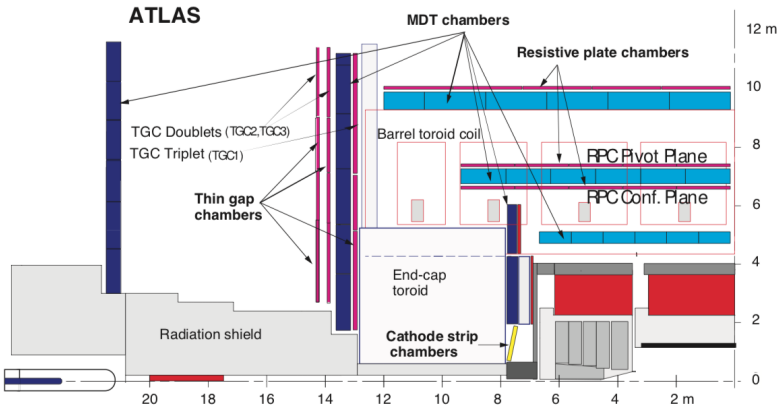


Figure 2.7. (z,r) view of the muon spectrometer. Figure adapted from Ref. [119].

Detectors are organised in 16 sectors, follow the symmetry of the barrel toroid coils, and provide almost full coverage around the IP. In the barrel, detectors are placed on three separate stations, respectively at 5, 7.5 and 10 m from the beam pipe. In the end-caps detectors are mounted on wheels, located at z 7.4, 10.8 and 14 m. The innermost one is called *small wheel*, while the two outer are the *big wheels*.

Tracking chambers. Monitored drift tubes (MDT) provide precision tracking of muons. These are operated with a gas mixture of Ar:CO_2 (93%, 7%), and allow for the measurement of the sagitta of muons with a precision of $\Delta s = 45$ µm when considering all the stations. A laser monitoring system is installed to control the alignment of the chambers. This is the dominant source of uncertainty when measuring high p_T muons ($p_T > 300$ GeV), while for low p_T particles the leading uncertainty is associated with the fluctuations in the energy deposited between the IP and the MS. MDT chambers are installed on all the MS stations, except for the small wheel, on which for $|\eta| > 2$ cathode strip chambers (CSC) are installed. CSC are able to cope with the high rate of particles, which can reach up to 150 Hz/cm^2 in this region of the detector. CSC chambers are installed on 8 sectors, are formed by four independent planes, and are divided in pads with a smaller pitch along the $|\eta|$ direction. Along this direction a precision of 60 µm can be achieved on each detection plane, while a coarser resolution of 5 mm is achieved on the ϕ direction.

Trigger chambers. The MS is adopted also to fire the trigger system of the ATLAS experiment, since muons can be produced in W, Z or Higgs boson decays and therefore indicate a potential interesting collision event. To provide a trigger, the detector response must be fast, and therefore the spatial resolution will be

only approximate. Moreover, the technology adopted in the barrel and in the end-caps regions is different because at fixed transverse momentum, particles at higher pseudo-rapidity will be in general more energetic, and therefore the bending by the magnetic field will be lower. Doublets of resistive plate chambers (RPC) are installed in the barrel region, on the middle and outer stations of the MS, as represented in Figure 2.7. These chambers provide triggers for the region up to $|\eta| < 1.05$, with a spatial resolution of 10 mm both in the z and ϕ direction, and have a time resolution of 1.5 ns. At larger pseudo-rapidity, one triplet of thin-gap chambers (TGC) is installed on the small wheel, while two TGC doublets are located on the big wheel closer to the IP. These chambers provide the trigger in the forward regions, for $1.05 < |\eta| < 2.4$. The spatial resolution of TGCs is of $2 - 6$ mm on the radial coordinate, and of $3 - 7$ mm on the ϕ direction. The time resolution of these chambers is of 4 ns.

2.2.2 The trigger system

The trigger system is used to identify possible interesting events among the 40 MHz collision rate of the LHC. During Run 2, the ATLAS trigger was based on two trigger levels [110]. These performed the read-out of the signals from the front end (FE) boards mounted on the detectors, converted the analog signals to digital ones and ran algorithms of increased complexity with an early rejection. This allowed to reduce the rate of events to be written to disk down to around 1 kHz. Figure 2.8 shows the data flow from the ATLAS FE boards to the CERN Tier-0 storage system.

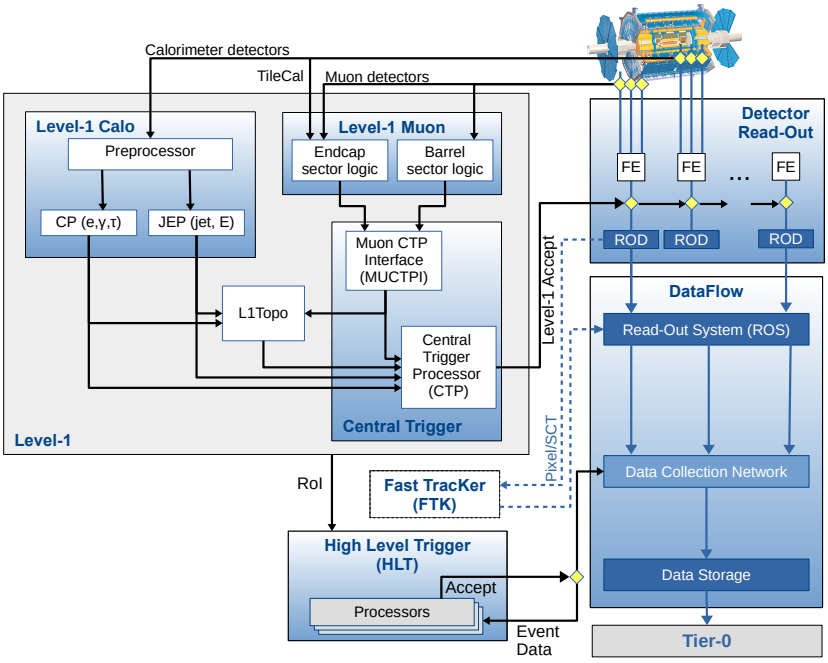


Figure 2.8. ATLAS Run 2 data flow in the trigger and read-out system. Figure taken from Ref. [110].

Level 1 trigger (L1). Potential interesting events are selected by either the Level-1 Calo (L1Calo) or Level-1 Muon (L1Muon) systems, which are both hardware-based. L1Calo takes as inputs the signals from the calorimeters with reduced granularity, performs analog-to-digital conversion, and sends them to the Cluster Processor (CP) and Jet/Energy-sum Processor (JEP). The first one identifies electrons, photons or τ-leptons, the latter identifies jet candidates and performs the calculation of the missing transverse momentum. L1Muon takes the inputs from the MS and the calorimeters: in the barrel regions signals are received from the RPC, while for the end-caps both signals from TGC and the tile calorimeter are used. Coincidence windows centered on the middle MS station are opened, and a hit in the inner and outer layers is sought. An estimate of the muon candidate p_{T} is provided by the width of the coincidence window in the η direction, since muons are bent in the (z,r) plane. Information from the L1Calo, L1Muon and from additional control sub-systems is sent to the central trigger processor (CTP) via the so-called L1Topo and Muon CTP interfaces. The CTP decides to accept or reject the events, and can also limit the number of accepted L1 candidates if the read-out rate exceeds the system capability, to prevent the overflowing of FE buffers. L1 trigger event selection can be based either on the number of muons above a certain p_{T} threshold, on the total energy measured in portions of the calorimeters, or not measured in the whole detector, as for the $E_{\mathrm{T}}^{\mathrm{miss}}$ triggers [120]. Additional triggers are based on more complex requirements, such as the angular distance between energy deposits in the calorimeters, or the invariant mass reconstructed from those. The rate of accepted events is reduced from the CTP down to 100 kHz, and the typical latency of L1 algorithms is below 2.5 µs.

High level trigger (HLT). Once the events are accepted by the L1 trigger, regions of interest (ROI), defined in the (η, ϕ) plane, are identified and the data are transferred from the FE boards of the sub-detectors to the read-out system (ROS) via the read-out drivers (ROD). The ROS is interfaced with a farm of processors on which the software-based HLT is ran. These take data from the ROS and apply algorithms which are designed to perform a decision in hundreds of milliseconds. The output rate of the HLT system during Run-2 has been of 1.2 kHz, with a typical disk writing rate of ∼1.2 GB/s.

Trigger menu and data streams. A combination of L1 trigger items and HLT algorithms, which apply kinematic selections on the preliminary reconstructed objects, form the so-called trigger chains. Different ones are used to select events with candidate leptons, photons, jets or to apply specific requirements as the isolation of identified leptons. Developed chains are typically used by multiple analysis groups in the ATLAS collaboration, and are stored in the so-called trigger menu. This evolved during the Run-2 of the LHC to cope with the improvements in the collision performance [121]. In particular, the goal is to keep the threshold of candidate objects as low as possible. To further control the trigger rate, a pre-scaling factor of N can be applied. For such a pre-scale factor, the probability for an event of being accepted by the trigger system is 1/N. Typically ATLAS analyses rely on the lowest un-prescaled triggers. This implies that the minimum p_{T} threshold on lepton triggers is of the order of 20 GeV, while for jets the threshold is around 400 GeV due to the large QCD processes cross-section. Events are written to storage via different streams, based on the trigger chain. During Run-2 pp operations, five

data streams were adopted. The *physics stream* stores full detector information, and is the one used to collect data used in analyses; the size of each event is around 1 MB. A *Trigger-Level Analysis (TLA) stream* stores only partial detector information and specific physics objects, which are reconstructed at HLT level. This significantly reduces the size of each event, to around 6.5 kB, and allows for lower trigger thresholds. The *debug stream* is used to recover events for which the HLT failed to be fully ran. This might happen for different reasons, such as a processing time exceeding limitations, a data transfer error or other similar issues. These events can then be fully recovered offline. A *calibration stream* is provided to collect data from specific sub-detectors or part of the trigger chain, while monitoring is provided via two streams. The *express stream* collects a restrained amount of data from the physics stream, applies offline reconstruction, and allows for data quality monitoring. The *monitoring stream* instead does not foresee data storage, and is only used to control the status of ATLAS sub-detectors.

2.2.3 Data taking in Run 2

During collisions, the instantaneous luminosity is monitored by dedicated detectors located in the forward arms of the ATLAS experiment. The primary measurement is provided by the LUCID2 Cherenkov detector [122]. This consists of 16 PMTs located at $z = \pm 17$ m from the IP, and is able to provide counts of particles in N out of 16 PMTs for all the colliding bunches. Counts are integrated over time periods of around one minute, which take the name of luminosity block (LB). In this period the instantaneous luminosity is assumed to be constant, therefore multiplying by the LB length it is possible to measure the integrated luminosity. The instantaneous luminosity is given by

$$\mathscr{L} = \frac{\mu_{\text{vis}} f_r}{\sigma_{\text{vis}}}, \tag{2.8}$$

where μ_{vis} is determined by PMT hits, as detailed in Ref. [123], and f_r is the LHC revolution frequency (40 MHz / 3564 LHC total bunch slots). σ_{vis} is a constant value, which is calibrated in special runs of the LHC which took place at the beginning of each year of data taking. In these runs, a *Van der Meer* scan is performed. This procedure, described in detail in Ref. [123], provides a value which needs to be corrected in normal physics runs due to the non-linear response of the LUCID detector. Figure 2.9 reports the integrated luminosity collected by the ATLAS experiment in pp collisions at $\sqrt{s} = 13$ TeV during Run-2 of the LHC. ATLAS was able to record over 94% of the collisions provided in the IP by the machine.

Not all the recorded collisions though can be used in physics analyses. LBs in which part of the detector was not functioning are excluded from the data set available by the definition of a *good-run-list*. This includes the LBs to be used to perform physics analyses, for which the total Run-2 integrated luminosity is 139 fb^{-1}. A total uncertainty of 1.7% is assigned to this value. The uncertainty, as reported in Ref. [123], is obtained by the combination of the measurements of each year of LHC run.

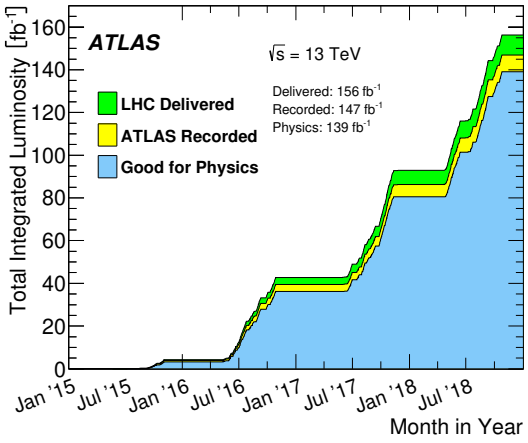


Figure 2.9. Total integrated luminosity by the ATLAS experiment of pp collisions at $\sqrt{s} = 13\,\text{TeV}$ provided by LHC Run-2. The longer plateaus correspond to the end-of-year shutdowns of the LHC. Figure from Ref. [124].

As already mentioned in the first part of this Chapter, the LHC machine has been improved throughout the years in terms of the collisions it was able to provide. This is directly reflected in the mean number of interactions per bunch crossing, $\langle\mu\rangle$, as represented in Figure 2.10. Its value increased during the Run-2 of the LHC from 13.4 to up to 37.8, with a total mean value of 33.7. The peak at low values represent dedicated runs of the LHC which provided collisions with very low pileup. Such conditions are ideal for example to measure properties of the W boson, since it is possible to reconstruct the neutrino in the events via a kinematic fit, thanks to the low occupancy of the detector.

2.2.4 Events simulation

The production of Monte Carlo samples is a crucial part of the ATLAS physics programme, since many analysis are based on a comparison between the measured data and the expected number of events. To perform meaningful comparisons, generated events need to be processed through the simulation of the ATLAS detector [125], implemented in GEANT4 [126, 127]. This is performed in two consecutive steps, the *simulation* and the *digitization* one.

In the simulation stage, each particle with a proper lifetime $c\tau > 10\,\text{mm}$ produced in the generation step is propagated through the GEANT4 model of the ATLAS detector. The energy deposits in sensitive portions of the detector, including the position and time information of each particle, referred to *hits*, are recorded and passed to the digitization stage.

In the digitization stage, the simulated signal hits are overlaid with cavern background events hits, and additional hits from soft QCD events to simulate the effect of pileup. In this stage, also detector noise is considered. The output of this stage is a byte-stream format file which emulates the data-taking procedure and conditions.

The same reconstruction algorithms applied to data can therefore be used to re-

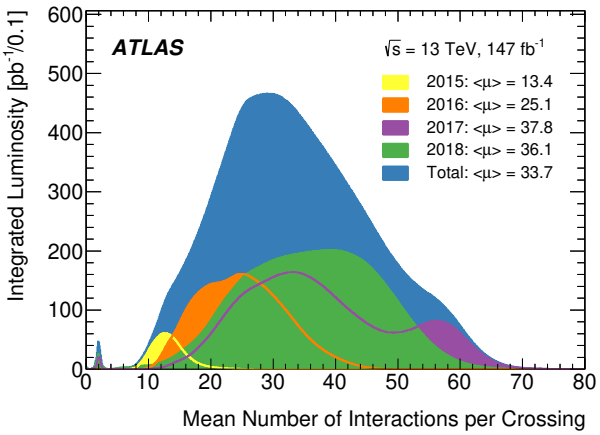


Figure 2.10. Mean number of interactions per bunch crossing during LHC Run 2 *pp* collisions at $\sqrt{s} = 13\,\text{TeV}$ as recorded by the ATLAS experiment, weighted by the integrated luminosity. Figure from Ref. [124].

construct simulated MC events. In the MC events, so-called 'truth-level' information are retained. These include the physics interactions which happen in both the generation and simulation stage, such as possible photon conversions in electron-positron pairs. These information can be used to quantify the performance of reconstruction algorithms and of the physics objects, as described in Chapter 3.

Simulated events are re-weighted to match the distribution of the average number of interactions per bunch crossing observed in the data.

Chapter 3

Event reconstruction performance

In this Chapter, the process of reconstruction of the final state physics objects used in this thesis, and their measurement performance, are described. This step involves several different sub-detectors, with tracks in the ID playing a central role for the identification of leptons and jets originating from heavy-flavour (HF) quarks. Section 3.1 introduces the track reconstruction process. In Section 3.2 the reconstruction of leptons and photons is described. The measurement and calibration procedure of hadronic jets, and their pileup and flavour tagging algorithms are described in Section 3.3. Lastly, in Section 3.4 the reconstruction of missing transverse momentum, which plays a central role in this thesis, is presented.

3.1 Inner detector tracks

Charged particles in the ATLAS ID travel inside a magnetic field. Therefore, their trajectory is helicoidal and can be described by five parameters, which are shown in Figure 3.1.

The five parameters are: the magnitude of the transverse momentum, p_{T}, the polar angle θ, the azimuth angle ϕ, the transverse impact parameter with respect to the beam direction, d_0, and the longitudinal impact parameter with respect to the nominal interaction point (IP), z_0. The last two parameters are expressed in mm, and are measured between the IP and the point of the closest approach in the transverse (d_0) and longitudinal plane (z_0).

The reconstruction of tracks in ATLAS during Run 2 is documented in Ref. [129]. Such process can be summarised in four consecutive steps. Hits in the pixel and SCT detectors, associated with an energy deposit above a fixed threshold, are grouped together in the *clustering* procedure to form space-points. *Track seeds* are formed by groups of three space-points. A combinatorial Kalman filter [130] is then run to build track candidates by the addition of hits which are compatible with this first estimate. In this step, tracks originating from the random association of space-points are removed. Since multiple tracks might share the same space-point, an ambiguity-solving algorithm is run. A score is assigned to each track, based on the χ^2 of the track fit, on its p_{T}, and on the number of holes in the track, which is defined as the

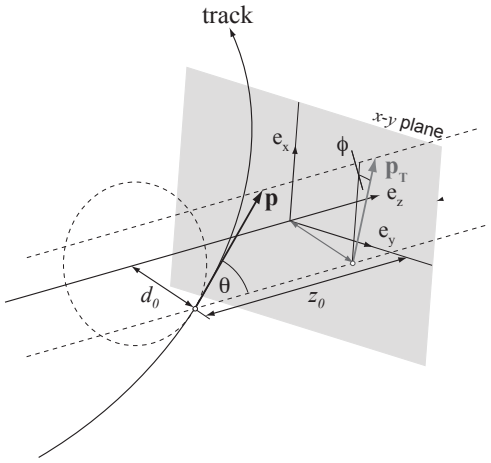


Figure 3.1. Schematic view of the parameters used to describe tracks in the ATLAS experiment. The e_z direction is taken along the beam direction. Figure from Ref. [128].

number of expected hits which are not present in one layer of the ID. Clusters of hits cannot be shared by more than two tracks, and each track cannot have more than two shared clusters on the same layer. If all the requirements in Table 3.1 are satisfied, a higher-resolution fit is performed to the track, which is then added to the collection of the available ones.

Table 3.1. Track characteristics requirements.

Requirement
$p_{\mathrm{T}} > 500\,\mathrm{MeV}$
$\lvert\eta\rvert < 2.5$
7 clusters in pixel or SCT detector
≤ 2 holes in the pixel or SCT detector
< 2 holes in the pixel detector
$\lvert d_0\rvert < 2\,\mathrm{mm}$ with respect to the beam-line
$\lvert z_0 \sin\theta\rvert < 3\,\mathrm{mm}$ with respect to the beam-line

Tracks are used to define the primary vertices of the interaction (PV). The one with the highest sum of the square of transverse momenta of the associated tracks is taken as the hard scatter (HS) vertex.

3.2 Leptons and photons

3.2.1 Electrons and photons

In this thesis only electrons[1] (e) and photons (γ) reconstructed in the barrel region ($|\eta| < 2.5$) are used. The reconstruction of such objects in the forward region is thus not discussed.

[1] Unless stated explicitly, electrons refers to both electrons and positrons.

The procedure starts with the identification of energy deposits on the form of topological clusters [131] in the EM and hadronic calorimeters. These are called *proto-clusters*, and are formed by summing calorimeter cells in which the energy deposit is equal or above four times the level expected from noise and pileup. The pre-sampling and the first EMC layers are excluded for the initial seeding. Proto-clusters then collect neighbouring cells with significance $E/\sigma(E) \geq 2$. If two local maxima, with $E_{\text{cell}} > 500\,\text{MeV}$ are found, the cluster is split into two. The resulting clusters are called *topo-clusters*. When initializing e/γ candidates, only the energy from the EMC layers is included: by applying a requirement on the fraction of energy in the EMC with respect to the total energy deposited in the calorimeters at 0.5, around 60% of pileup clusters are rejected.

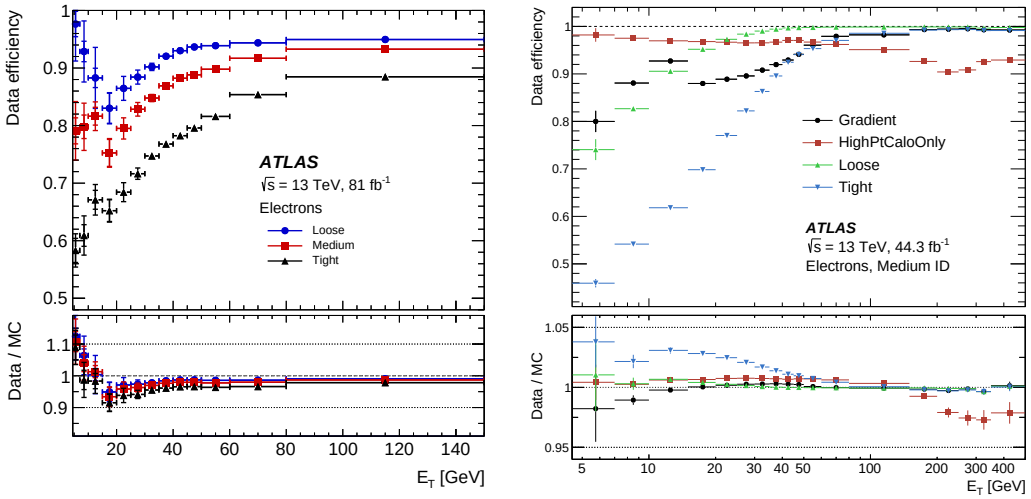
Hits in the ID are fitted, under the assumption of the track being originated from a pion, to build electron-candidate tracks. Energy losses for the interaction with the detector material are taken into account. If the fit fails, but the track candidate hits are close in the (η, ϕ) plane to a cluster candidate, a new fit is performed under the hypothesis of electron, which accounts for possible bremsstrahlung. If more than one track is matched to a energy deposit, only the one with most hits in the ID is retained. Otherwise, the one which once extrapolated to the second layer of the EMC is closer to the (η, ϕ) barycenter, is taken. Photon conversion vertices are reconstructed from two tracks which do not have hits in the innermost pixel detector, but only in the SCT and TRT detectors, and match a secondary vertex consistent with a mass-less particle. Conversion vertices are then matched to the EM topo-clusters.

Candidate clusters are further combined to form *superclusters*. EM topo-clusters are sorted based on the E_{T}, evaluated as $E_{\text{T}} = E/\cosh(\eta)$. If a cluster has $E_{\text{T}} > 1\,\text{GeV}$ and is associated with a track with at least four hits in the SCT detector, is classified as an electron seed cluster. Photon seeds are instead formed by clusters with $E_{\text{T}} > 1.5\,\text{GeV}$. Satellite clusters, i.e. the neighboring ones, are added to the seed one if they are found within $\Delta\eta \times \Delta\phi = 0.0075 \times 0.125$ of an electron seed. This window can be extended up to 0.125×0.3 if the best-matched track of the two clusters is the same. For photon seed clusters, instead, satellite clusters are added if the best-matched track is matched to one coming from a conversion vertex. After this categorizations an ambiguity resolution is performed. The obtained *supercluster* is labelled either as an electron candidate, a photon candidate, or ambiguous. This step is based on the number and type of tracks associated to the supercluster, and on the transverse momentum of those. Shower shape and additional discriminant variables, defined in Ref. [132], are then evaluated, and used in the e/γ identification process.

Electron identification and isolation criteria

A likelihood (LH) discriminant, which takes as input the aforementioned distributions of each electron candidate, is adopted to define identification working points (WP). This helps to discriminate between prompt electrons and the background of electrons originated in the $\gamma \to e^+e^-$ conversion, or in heavy-flavour hadron decays. Three mutually inclusive working points (*Loose*, *Medium*, *Tight*) are defined by a cut

which is optimised in different E_{T}, η bins. All the WPs require at least two hits in the pixel detector, and in total at least seven hits considering both the pixel and SCT detectors. This requirement reduces the contribution from photon conversions. An additional WP, which is used in this thesis, is defined requiring an hit in the insertable b-layer: it is called *Loose&Blayer*.
In Figure 3.2(a), the electrons identification efficiency is shown as a function of E_{T}. This is measured in data and MC simulation with the tag & probe (T&P) method using $J/\psi \to e^+e^-$ and $Z \to e^+e^-$ events. The first (latter) process is adopted in the $[5, 20]$ GeV ($> 15\,\mathrm{GeV}$) E_{T} range. The higher efficiency observed in data with respect to MC for $E_{\mathrm{T}} < 15\,\mathrm{GeV}$ is due to a mismodelling in the variables used in the LH discriminator. A correction factor, defined later as *scale factor*, takes into account such difference and correct the MC simulation to match the performance measured in data.



(a) (b)

Figure 3.2. (a) Electron identification efficiency (a) and isolation efficiency (b) as a function of the transverse energy. In the bottom pad the ratio between the efficiency measured in data and in the MC simulation is reported. Figures adapted from Ref. [132].

Electrons from W, Z, H bosons prompt decays are characterized by low activity around them, with respect to electrons coming from semi-leptonic decays of HF hadrons. Calorimeter and track-based isolation variables are defined to quantify the isolation of electron candidates. The former method is more sensitive to pileup. Topo-clusters are used to evaluate the energy in a cone of size ΔR around the electron candidate. The energy of the candidate particle is then subtracted, and corrections are applied to reduce the effect of pileup. The resulting variable is called $E_{\mathrm{T,cone}}^{\mathrm{isol}}$. The track based method instead uses tracks with $p_{\mathrm{T}} > 1\,\mathrm{GeV}$ within a variable-radius cone around the electron candidate, with a radial opening which depends on its p_{T} as $\Delta R = \min\left(\frac{10\,\mathrm{GeV}}{p_{\mathrm{T}}[\mathrm{GeV}]}, R_{\mathrm{max}}\right)$, where R_{max} is equal to either 0.2 or 0.4. The resulting variable is $p_{\mathrm{T,var}}^{\mathrm{isol}}$. Isolation working points are defined either to target a constant efficiency ($\varepsilon_{\mathrm{iso}}$) in (η, ϕ), a uniform $\varepsilon_{\mathrm{iso}}$ in η but dependent on the

electron E_{T} (*gradient*), or by imposing a fixed value to the isolation variable (*fixed*). In this thesis the *Loose* and *Tight* fixed working points, summarised in Table 3.2, are

Table 3.2. Definition of the electron isolation working points. Table adapted from Ref. [132].

Operating point	$E_{\mathrm{T,cone}}^{\mathrm{isol}}$ $(\Delta R = 0.2)$	$p_{\mathrm{T,var}}^{\mathrm{isol}}$ $(R_{\mathrm{max}} = 0.2)$
Loose	$E_{\mathrm{T,cone}}^{\mathrm{isol}}/p_{\mathrm{T}} < 0.20$	$p_{\mathrm{T,var}}^{\mathrm{isol}}/p_{\mathrm{T}} < 0.15$
Tight	$E_{\mathrm{T,cone}}^{\mathrm{isol}}/p_{\mathrm{T}} < 0.06$	$p_{\mathrm{T,var}}^{\mathrm{isol}}/p_{\mathrm{T}} < 0.06$

used. The performance of different WP are shown in Figure 3.2(b) as a function of E_{T}.

The total electron identification and reconstruction efficiency can be factorised as the product of different contributions,

$$\varepsilon_{\mathrm{total}} = \varepsilon_{\mathrm{cluster}} \times \varepsilon_{\mathrm{reco}} \times \varepsilon_{\mathrm{id}} \times \varepsilon_{\mathrm{iso}} \times \varepsilon_{\mathrm{trigger}}.$$

Each of this terms, except for the clustering efficiency ($\varepsilon_{\mathrm{cluster}}$), is evaluated in both data and MC simulation. *Scale factors* (SF), defined as the ratio of the efficiency measured in data and the one measured with MC, are derived to correct the simulation to match what is observed in data. SFs are typically close to 1, and systematic uncertainties on these are derived varying the method adopted to estimate each efficiency term.

Photons

The identification criteria of photon candidates are based on cuts on variables related to the shape of the EM shower, as reported in Ref. [132]. In fact, the energy deposits tend to be wider for converted photons. This is due to the fact that the aperture of the e^+e^- pair is amplified by the presence of the magnetic field. Three working points, *Loose*, *Medium* and *Tight*, are defined by an optimisation of the cuts applied on the discriminant distributions in different $|\eta|$ bins.
The identification efficiency is measured in data and compared to MC simulation in $Z \to \ell^+\ell^-\gamma$ and $Z \to e^+e^-$ events, following the methods described in Ref. [133]. Similar isolation criteria to the ones introduced for the electrons are defined for photons. Since no isolation requirement is applied to photons in this thesis, the reader is referred to Ref. [133] for further details.

3.2.2 Muons

Muons produced at the IP go trough roughly 100 to 190 interaction lengths before reaching the outer part of the ATLAS detector, where the muon spectrometer is located. At LHC energies muons are typically minimally-ionising particles (MIPs), which traverse the MS and leave the ATLAS experiment. The MS can provide a standalone reconstruction and measurements of muons with $p_T > 7\,\mathrm{GeV}$. The rejection of fake muons and the measurement of the transverse momentum of such particles can however be improved by exploiting the full ATLAS detector.

The muon reconstruction algorithm [134] starts with the identification of segments in the MS standalone. Starting from the hits in the external part of the ATLAS experiment, a χ^2 fit of the muon trajectory is then performed imposing a loose constraint from the IP location. This allows to take into account additional hits which initially where not included, and to remove spurious ones. The muon candidate is then extrapolated to the IP.

Six muon types are defined in ATLAS based on the detector used to perform the reconstruction. Muons which cannot be matched to a reconstructed track in the ID are defined as *muon-spectrometer extrapolated* (ME), and exploit the full coverage of the muon spectrometer up to $|\eta| = 2.7$. Tracks extrapolated from the MS and successfully combined to hits in the ID form *combined muon* candidates. A global χ^2 fit of the track is performed. Again, this allows the inclusion or the removal of hits from the MS or ID. Combined muons are reconstructed in the range $|\eta| < 2.5$. Short tracks from the additional coverage of some of the ID sub-detectors allows to form *silicon-associated forward* (SiF) muons. *Inside-out* (IO) muon candidates are formed by extrapolating the ID track to the MS, and looking for at least three aligned MS hits to be included in the track fit. *Segment-tagged* (ST) muons require instead at least one matching segment in the MS with the ID extrapolated track. In this case, the muon track parameters are taken from the measurement performed in the ID. If energy deposits consistent with a MIP are found along the extrapolated trajectory, these are used to tag the muon, which is defined as *calorimeter-tagged* (CT). Excluding the ME ones, every muon candidate is required to have tracks in the ID with at least one hit in the pixel detector, five hits in the SCT and less than three pixel or SCT missing hits. Additionally, at least 10% of the TRT hits originally assigned to the track must be included in the final fit [135].

On reconstructed muons, further requirements are applied to define different selection WPs, called *Loose*, *Medium* and *Tight*. These provide increased purity on the selection of prompt muons, at the cost of a lower efficiency. Two quantities are used to define the WP: the q/p significance, defined in Equation 3.1a and the ρ' variable, defined in Equation 3.1b. The latter is only defined when a measurement of the muon p_{T} is performed with the ID and the MS simultaneously.

$$q/p \text{ significance} = \frac{|q/p_{\mathrm{ID}} - q/p_{\mathrm{MS}}|}{\sqrt{\sigma^2(q/p_{\mathrm{ID}}) + \sigma^2(q/p_{\mathrm{MS}})}}, \tag{3.1a}$$

$$\rho' = \frac{|p_{\mathrm{T,ID}} - p_{\mathrm{T,MS}}|}{p_{\mathrm{T,CB}}}. \tag{3.1b}$$

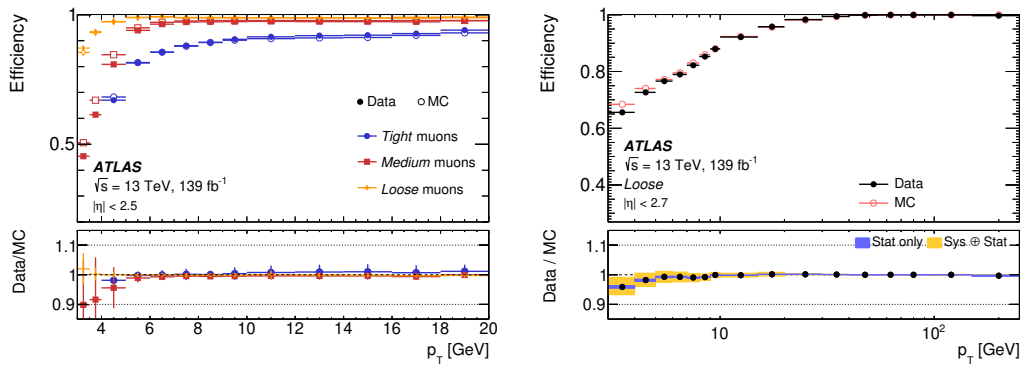
In the former equations, q indicates the charge of the muon, the ID (MS) suffix indicates that the quantity is measured using the inner detector (muon spectrometer), while CB indicates the combined measurement using both sub-detectors; $\sigma(q/p)$ indicates the uncertainty on the measurement of q/p.

Tight muons include CB and IO candidates which have been reconstructed with at least one segment formed by three hits in the MDT or CSC detectors in at least two MS stations. Moreover, they are required to pass selection criteria based on

both the previously introduced variables. The value of the cut has been optimised in p_{T} and η bins. *Medium* muons include only combined and IO candidates, but a flat cut q/p significance < 7 is applied instead. The requirement on the number of hits in the MS is kept. The identification efficiency increases from 93% to 97% for muons with $p_{\mathrm{T}} > 20\,\mathrm{GeV}$, but an increase of 50% of the efficiency of reconstructing muons from background processes, such as light hadrons or non-prompt decays, is observed. *Loose* muons include also CT and ST originated muon candidates, and provide higher efficiency for $|\eta| < 0.1$, where the number of MS chambers is lower due to the presence of shafts used to access the barrel part of the ATLAS experiment. Two additional WPs, *low* and *high-*p_{T}, have been developed [134] to provide improved resolution and efficiency for analyses targeting the extremes of the phase space.

As for the electrons, prompt muons are typically isolated, while the ones from semi-leptonic hadron decays are accompanied by close-by activity. Track- and calorimeter-based isolation variables are defined as described for the electrons in Section 3.2.1, and are both used in the definition of the muon isolation WPs [134]. The tightest one provides a mean isolation efficiency of 70% between 5 and 20 GeV of p_{T}, 89% in the range [20, 100] GeV, and 98% for $p_{\mathrm{T}} > 100\,\mathrm{GeV}$. The corresponding misidentification rates for light hadrons in the same p_{T} ranges are 11.9%, 1.0% and 1.6%, respectively.

Identification and isolation efficiencies are measured using the T&P method in $Z \to \mu^+\mu^-$ events. For $p_{\mathrm{T}} < 20\,\mathrm{GeV}$, the $J/\psi \to \mu^+\mu^-$ process is used instead. The method, described in detail in Ref. [134], is similar to the one adopted for the measurement of electron identification efficiencies. A *scale factor* is used to account for the differences observed in the efficiency measured in data and MC simulation. The identification and isolation efficiencies as a function of the muon p_{T} are shown in Figure 3.3(a) and 3.3(b), respectively. The *loose* isolation WP is shown.

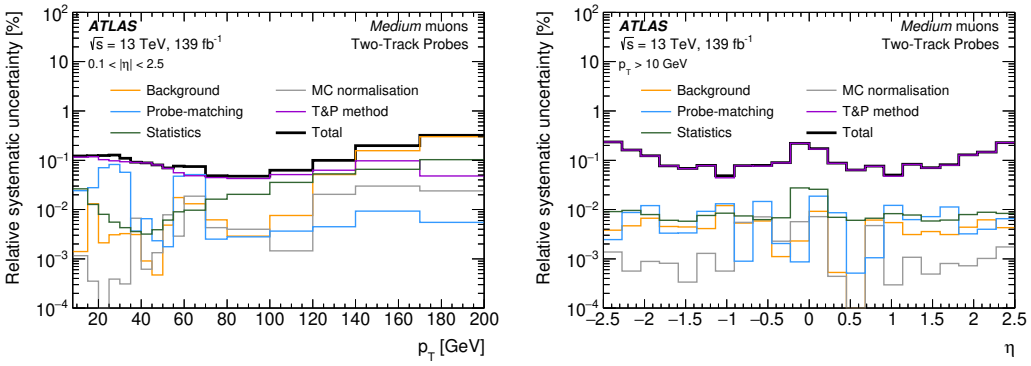


(a) (b)

Figure 3.3. Muon identification (a) and isolation efficiency (b) as a function of the muon transverse momentum. In the bottom pad the ratio between the efficiency measured in data and MC simulation is reported. Figures from Ref. [134].

Systematic uncertainties affect the value of the scale factors. These are related to the T&P method, to the matching between the ID tracks and the reconstructed

muon candidate (*probe matching*), and to the estimate of background processes in the T&P method.



(a) (b)

Figure 3.4. Breakdown of the systematic uncertainties affecting the efficiency scale factors as a function of muon p_{T} (a) and η (b) for the *medium* identification working point. Figures from Ref. [134].

In Figures 3.4(a) and 3.4(b) the breakdown of the uncertainties on the efficiency SF for *medium* muons is shown as a function of p_{T} and η, respectively. While the uncertainty on the T&P method dominates at low p_{T}, at high p_{T} the uncertainties related to the background estimation technique are the largest. The level of total uncertainty ranges between 0.1 and 0.3%. The uncertainty is almost independent on η. The increase at $\eta \sim 0$ is associated to the lower coverage of the MS.

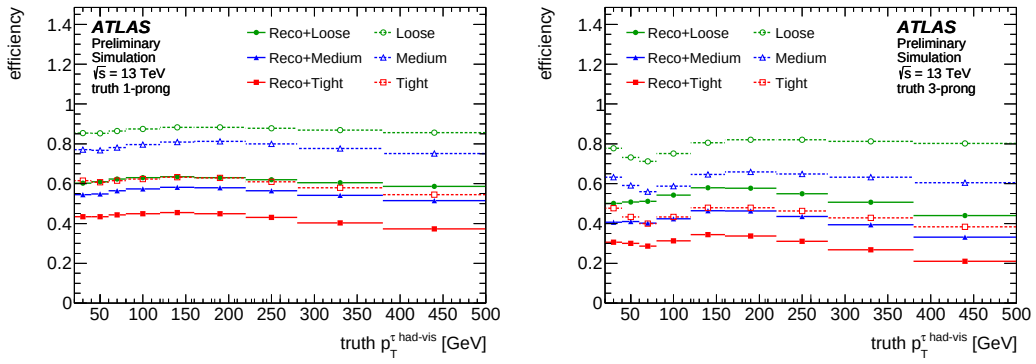
3.2.3 Tau leptons

τ leptons are not collider-stable particles, and decay via the processes $\tau \to \ell\nu_l\nu_\tau$ ($\ell = e, \mu$) or $\tau \to \nu_\tau$ + hadrons 34% and 66% of the times respectively. Leptonic τ decays are identified via the reconstruction of muons and electrons. Hadronic ones, labelled as τ_{had}, are categorised instead by the number of charged particles produced in the decay. Half of the total branching fraction of the τ lepton leads to a one charged track (*one-prong* topology), and roughly 15% of the decays are in *three-prong* final state.

The reconstruction starts with the identification of topological clusters, as done for the electrons. Tau candidates are required to have $p_{\mathrm{T}} > 10\,\mathrm{GeV}$ and to be within $|\eta| < 2.5$. Candidates reconstructed in the *crack-region* between the barrel and forward calorimeters, $1.37 < |\eta| < 1.52$, are vetoed. Among the primary vertices, the one with the largest fraction of p_{T} coming from tracks associated with the topo-clusters (with a requirement of $\Delta R < 0.2$) is defined as the τ vertex. Only tracks with $|d_0| < 1\,\mathrm{mm}$ and $|z_0 \sin\theta| < 1.5\,\mathrm{mm}$ with respect to such tau vertex are adopted.

The energy deposit of the τ candidate is corrected via MC simulation [136]. A subtraction to the measured energy, based on the position in the detector ($|\eta|$) of the τ candidate and on the number of reconstructed primary vertices (N_{PV}), is performed to take into account the pileup contribution. The detector response is

extracted from MC simulation. It is evaluated from the distribution of the corrected energy of τ candidates, divided by the truth energy of the τ. This is defined in simulation considering only the visible decay products, thus excluding the truth neutrinos. A gaussian fit is performed, and the mean of the distribution yields the detector response. The measured energy deposits are then divided by this correction factor. After the aforementioned calibration is performed, the p_{T} resolution is about 7.5% for 100 GeV candidates, and better than 5.5% above 250 GeV. At low p_{T} it degrades quickly. In this range, an alternative calibration based on a multi-variate-analysis (MVA) can be used. This method, not used in this thesis, is described in Ref. [136]. Systematic uncertainties on the calibration procedure are derived by altering the detector response in MC simulation, by testing different hadronization models in the simulated samples adopted, and by taking into account an alternative modelling of the passive material within the ATLAS detector. The leading source of uncertainty is due to the single-particle response of the detector. The total uncertainty is not uniform in p_{T} and $|\eta|$, and ranges between 2 and 6%.



(a) (b)

Figure 3.5. Identification and combined identification and reconstruction efficiency of τ_{had} candidates as a function of p_{T} for (a) one-prong and (b) three-prong τ lepton decays. Figures from Ref. [137].

The identification of τ_{had} candidates is done using a set of boosted-decision-tree (BDT) algorithms, which are trained to discriminate the one- or three-prong final states from the hadronic background. The discriminating variables, whose complete description can be found in Ref. [137], are based on the properties of the topo-clusters which form the candidate and of the tracks associated. From the BDT score distributions, WPs providing different efficiency values are defined. In Figure 3.5(a) and 3.5(b) the identification and combined reconstruction plus identification efficiency are shown for one- and three-prong τ_{had} decays, as a function of the truth visible τ p_{T}. The WPs are defined such that the efficiency is almost independent on p_{T} and pileup. The dip observed between 50 and 100 GeV in the identification of three-prong decays is made to compensate a p_{T} dependence in the reconstruction efficiency, such that overall the combined value is almost flat. The *Loose* ID working point, adopted in this thesis by the monojet analysis (see Chapter

4), has an average combined efficiency of 60% and 50% for one-prong and three-prong decays, respectively.
The leading source of systematic uncertainty in the τ_{had} identification below 100 GeV of p_{T} is due to the calibration of the calorimeter response. This has a large impact on the shape of the input variables of the identification BDT algorithms. For one-prong candidates, uncertainties in the interaction with the passive material of the ATLAS detector have the largest effect. Overall, identification uncertainties range between the 5% and 18%, with the largest value for three-prong decay modes in the $30 < p_{\text{T}} < 100\,\text{GeV}$ and $|\eta| < 1.37$ ranges, due to the calorimeter response.

3.3 Jets

The hadronisation of partons lead to sprays of collimated hadrons in the detector, called *jets*. Energy deposits in the calorimeters are clustered to form topo-clusters [131], as done for the reconstruction of the electrons. The energy of the topo-clusters used as inputs for the jet formation is not however representative of the total energy deposit, due to the large fraction of hadronic interactions. For this reason, at first topo-clusters are calibrated at the electromagnetic scale (EMscale). Then, once jets are clustered, a calibration of the Jet Energy Scale (JES) is performed. Jets are formed by clustering together the topo-clusters using the anti-k_t algorithm [15] with the radius parameter R set to 0.4. Before the calibration procedure, the four-momentum of the jets is corrected to take into account that these have been originated in the PV of the collision. These jets are called *EMTopo jets*.
The JES calibration is introduced to correct the measured jet energy using particle-level information available in MC simulations. The calibration procedure is formed by four consecutive steps, briefly described below: the pileup correction step, the absolute JES correction, the Global Sequential Calibration (GSC) and the final *in-situ* calibration. Further details can be found in Ref. [138].

Pileup corrections. An event-by-event subtraction to the energy of the jet candidate is performed, based on the average energy density (ρ) in the event, due to pileup, and the actual jet area, both evaluated as described in Ref. [139]. The ρ value is evaluated in the (y, ϕ) plane by looking at jets within $|\eta| < 2$ clustered using the k_t algorithm. This algorithm clusters first soft radiation, and includes in the jet definition the contribution of the soft background. A residual dependence on pileup is observed. This is due to the fact that ρ is evaluated in low-occupancy regions of the calorimeter and in a limited range of the detector. A second correction, derived from MC simulation and based on truth particle-level jets. These are defined by running the anti-k_T algorithm on charged and neutral truth collider-stable particles, i.e. with a $c\tau_0 > 10\,\text{mm}$, excluding neutrinos and muons.

Truth jets are matched to the reconstructed ones by requiring $\Delta R < 0.3$. The jet p_{T} is corrected as in Equation 3.2:

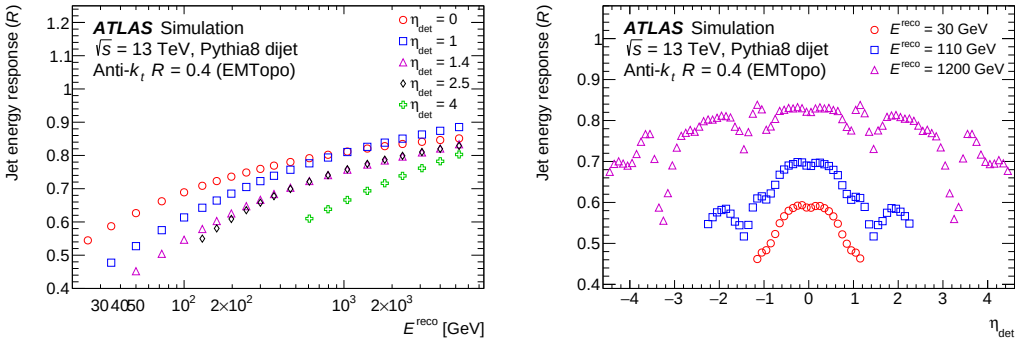
$$p_{\text{T}}^{\text{corr}} = p_{\text{reco}} - \rho \times \text{A} = \alpha(N_{\text{PV}} - 1) - \beta\mu, \tag{3.2}$$

where α and β are two parameters determined by a fit in bins of truth p_{T} and $|\eta_{\text{det}}|$[2],

[2] $|\eta_{\text{det}}|$ is the pseudo-rapidity evaluated by assuming that the jet originated from the nominal

and μ is the pileup value. Systematic uncertainties are defined to take into account the mismodelling of the aforementioned quantities by the MC simulation.

JES absolute calibration. The response of the detector is corrected using MC simulation to account for the presence of hadronic interactions with the passive material of the detector. Moreover, biases in the $|\eta|$ reconstruction arise due to the fact that the ATLAS calorimeter system is made by different technologies and of different granularity. Also in this case, corrections are derived by matching jets at reconstruction level with their truth particle level counterpart. The average jet energy response is evaluated with a gaussian fit to the distribution of the $E_{\text{reco}}/E_{\text{true}}$ ratio in different E_{true} and $|\eta_{\text{det}}|$ bins. The jet energy response is reported in Figure 3.6(a) (3.6(b)) as a function of the reconstructed energy (pseudo-rapidity). The drop at low E values is due to non-gaussian response and thresholds effects, while the dips in the $|\eta_{\text{det}}|$ distribution are in correspondence of the transition regions between the barrel, end-cap ($|\eta| \sim 1.4$), and forward systems ($|\eta| \sim 3.1$). Such biases are removed by an additional correction which impacts the p_{T} and η of the jet, but not its four-momentum. After the application of the JES absolute calibration the jets are considered at the EM+JES scale.



(a) (b)

Figure 3.6. Jet energy response as a function of jet energy and jet pseudo-rapidity at reconstruction-level as obtained from simulated events with at least two jets. Figures from Ref. [138].

Global sequential calibration. The detector response may depend on the energy distribution of jet components, on the flavour composition (i.e. the fraction of HF hadrons in the jet), or on the fact that the jet was initiated by a quark or a gluon. A set of multiplicative corrections are sequentially applied to correct for such effects, and impact only the resolution of the jet response function, but not the energy scale. These corrections are derived from energy measurements performed in specific parts of the detector such as the first layer of the HCAL, the last layer of the LAr calorimeter, or for example by counting the number of tracks associated to the jet and by looking at the muon spectrometer chambers aligned with the jet axis. This latter measurement allows to reduce the impact of the *punch trough* of hadrons in the MS in presence of highly-energetic jets. Such effect is negligible in

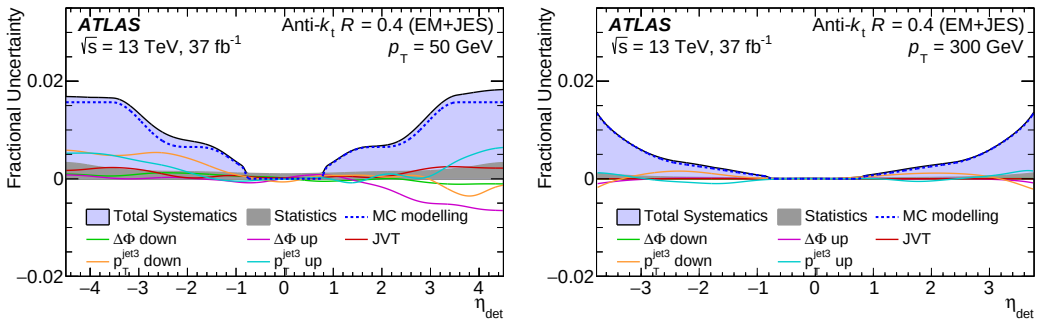
interaction point, (0,0,0).

the analyses presented in this thesis. After GSC is applied, the jet p_{T} resolution is improved by almost 30% in the entire range between 20 GeV and 2 TeV.

***In-situ* calibration.** A final correction to account for differences in the jet response as measured in data and MC is applied. Such differences might arise from a mismodelling of the hard-scatter interaction, underlying event or jet formation process. The correction relies on the measurement of the average jet response, which is performed both in data and MC simulation using Z+jets, γ+jets and multi-jet events by comparing the jet p_{T} to the one of a well-reconstructed and calibrated object. To reduce the dependency on the presence of extra jets in the event or on leakages in the reconstruction, the ratio between the response defined as in Equation 3.3

$$\mathcal{R}_{in\ situ} = \left\langle \frac{\text{jet}\, p_{\mathrm{T}}}{\text{reference object}\, p_{\mathrm{T}}} \right\rangle, \tag{3.3}$$

evaluated in both data and MC, is calculated. The correction is evaluated in three separate steps, described in detail in Ref. [138].
The first one is the η inter-calibration, and provides a correction to the JES to take into account the fact that the ATLAS calorimeter is made of different technologies in different η regions. This correction equalises the response of the forward region ($0.8 < |\eta| < 4.5$) to the one of the central part, $|\eta| < 0.8$, where jets are assumed to be well calibrated. Systematic uncertainties arising from this procedure are shown in Figure 3.7(a) and 3.7(b) for jets with a p_{T} of 50 GeV and 300 GeV respectively, as a function of the $|\eta_{\mathrm{det}}|$ variable. The leading source of uncertainty is related to the choice of the simulated MC samples adopted in the evaluation of the correction. Alternative ME and PS models are tested to derive such correction.



(a) (b)

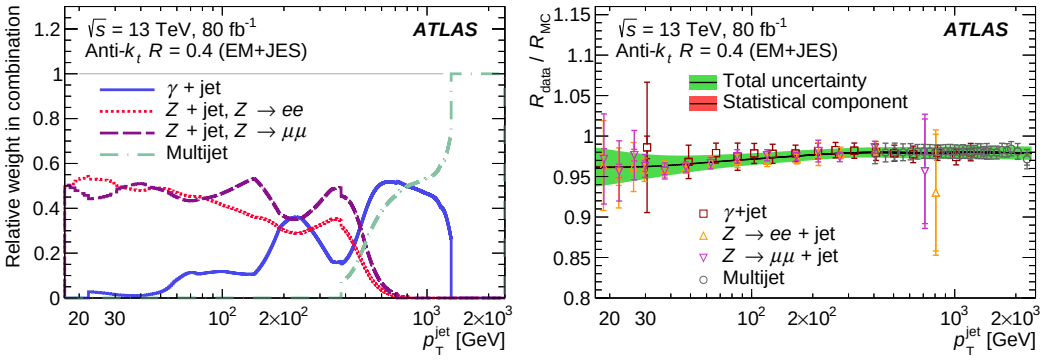
Figure 3.7. Systematic uncertainties associated to the jet η inter-calibration procedure for jets of 50 GeV (a) and 300 GeV (b) of transverse momentum as a function of the $|\eta_{\mathrm{det}}|$ variable. Figures from Ref. [138].

The second correction is performed as a function of the jet p_{T} and corrects for the response of the calorimeter to hadrons. It is based on the missing transverse momentum projection fraction method, described in Ref. [140]. This relies on the fact that at particle-level in a γ+jets event one has $\vec{p}_{\mathrm{T}}^{\,\gamma} + \vec{p}_{\mathrm{T}}^{\,\mathrm{recoil}} = \vec{0}$, where $\vec{p}_{\mathrm{T}}^{\,\mathrm{recoil}}$ is

the total hadronic momentum recoiling against the photon. At reconstruction-level, instead, under the assumption that the photon is well calibrated, one can write

$$\vec{p}_{\mathrm{T}}^{\,\gamma} + \mathcal{R}_{\mathrm{MPF}} \cdot \vec{p}_{\mathrm{T}}^{\,\mathrm{recoil}} = -\vec{E}_{\mathrm{T}}^{\,\mathrm{miss}}, \tag{3.4}$$

where $\mathcal{R}_{\mathrm{MPF}}$ indicates the calorimeter response to the hadrons and $\vec{E}_{\mathrm{T}}^{\,\mathrm{miss}}$ is evaluated from the topo-clusters and photon energy deposits. By projecting Equation 3.4 along the γ direction, it is possible to extract $\mathcal{R}_{\mathrm{MPF}}$. This is used to correct the response of the measured jet. The correction is evaluated in both $Z(\to e^+e^-/\mu^+\mu^-)$+jets and γ+jets events. Above 1 TeV, it is possible to evaluate the calibration factor by using other lower-energy jets recoiling against a single jet. This multi-jet balance (MJB) method allows to extend the calibration up to more than 2 TeV of jet p_{T}. A combination of the three measurements is performed to obtain a smooth correction function used to correct data.

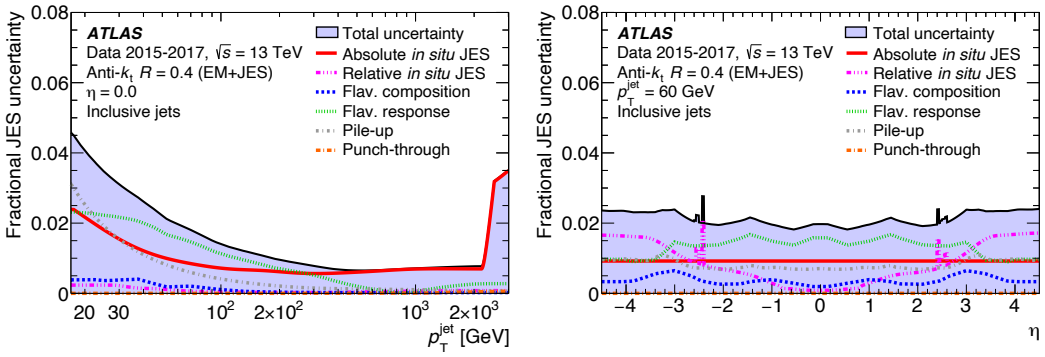


(a) (b)

Figure 3.8. (a) Relative weight of each measurement in the evaluation of the combined *in situ* calibration as a function of jet p_{T}. (b) Final *in situ* response factor as evaluated from the 2015, 2016 and 2017 ATLAS data set, as a function of the jet p_{T}. Figures from Ref. [138].

The relative importance of each measurement is shown as a function of the jet p_{T} in Figure 3.8(a). The Z+jets measurements are mainly used in the low-medium p_{T} regime, where the systematic uncertainties associated to the measurement of leptons are low. At $p_{\mathrm{T}} \sim 500$ GeV the γ+jets measurement becomes the dominant one in the combination, and the highest p_{T} regime is, as already stated, covered by the MJB method. In Figure 3.8(b) the ratio between the $\mathcal{R}_{\mathrm{MJB}}$ factor evaluated in MC simulation and in data, is shown as a function of the jet p_{T}.

The total uncertainty on the JES calibration is below 5% everywhere, and is shown as a function of the jet p_{T} and $|\eta|$ in Figures 3.9(a) and 3.9(b), respectively. The dominant contribution at low jet p_{T} is due to pileup and the different response of the detector to quark and gluon initiated jets. The absolute *in-situ* JES uncertainty becomes the dominant contribution for p_{T} higher than 400 GeV. At very high p_{T} the uncertainty is only due to the single-particle response. As a function of jet $|\eta|$, contributions are almost flat, except for the one due to the jet η inter-calibration procedure. The sharp increases at $\eta \pm 2.5$ are related to non-closure between the



(a) (b)

Figure 3.9. Total uncertainty on the JES determination and its sub-components shown as a function of jet p_{T} (a) and jet η (b). Figures from Ref. [138].

data and MC after the correction is applied. All the systematic uncertainties related to the JES can be parameterized by 125 nuisance parameters. Reduction schemes which make use of the eigenvector decomposition [141] are adopted by the analyses presented in this thesis to reduce the number of nuisance parameters. As shown in Ref. [138], a good description of the underlying uncertainty effects is kept.

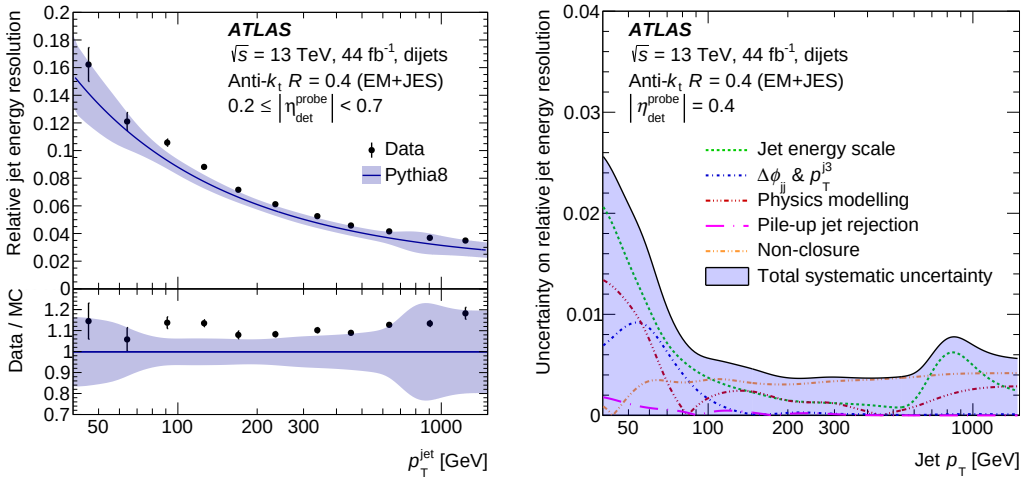
Jet energy resolution The jet energy resolution (JER) can be parameterized as a function of the jet p_{T} as done in Equation 3.5,

$$\frac{\sigma(p_{\mathrm{T}})}{p_{\mathrm{T}}} = \frac{N}{p_{\mathrm{T}}} \oplus \frac{S}{\sqrt{p_{\mathrm{T}}}} \oplus c, \tag{3.5}$$

where N, S and c are constant values. These represent respectively a noise term, a stochastic term due to fluctuations in the response of the detector. The constant term parameterize the fluctuations due to the jet formation position and its interaction with the detector. This latter term dominates above 400 GeV. JER is measured in multi-jet events, with the balance method described in Ref. [138]. The JER as a function of jet p_{T} is shown in Figure 3.10(a). The total systematic uncertainty and a breakdown of its main components is shown in Figure 3.10(b). At low p_{T}, and very high p_{T}, these components are directly related to JES uncertainties. At medium p_{T}, the largest contribution is due to the non-closure between the particle- and reconstruction-level when evaluating the JER on MC samples.

Particle-flow jets

The particle-flow algorithm, whose description can be found in Ref. [142], can be used to improve the reconstruction and calibration of jets. Before the anti-k_t is ran on the topo-clusters, the contribution of charged hadrons reconstructed in the ID and associated with the jet is subtracted from the energy deposit. Such energy contribution is replaced by the p_{T} measured in the ID, which provides a better measurement of charged hadrons with respect to the calorimeter. The assign of tracks to the jet is performed via the so called ghost-association. This procedure



(a) (b)

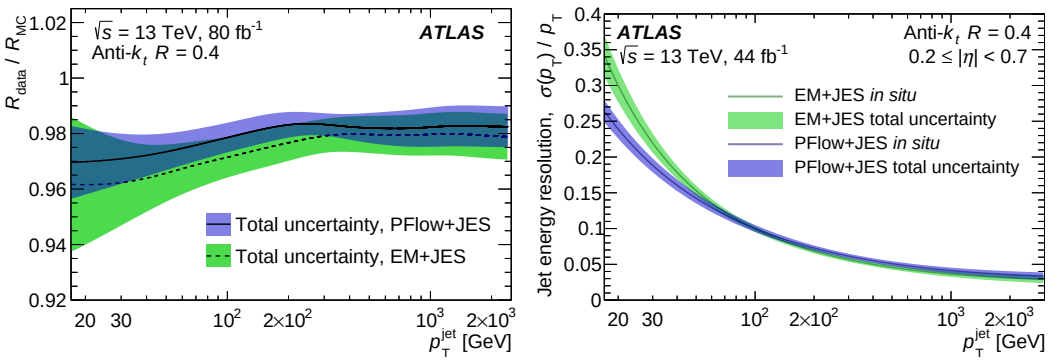
Figure 3.10. (a) Relative jet energy resolution as a function of the jet p_{T}, as measured in data and MC dijet events. (b) Breakdown of the JER relative uncertainty as a function of jet p_{T}. Figures from Ref. [138].

assign a very low transverse momentum to each track, i.e. $\mathrm{O}(10^{-100})$, and include those in the list of constituents on which the jet clustering algorithm is run. In this way, tracks are associated to the jets even if the shape of such objects is irregular. The subtraction of the energy associated to each track is not performed if this falls into a significant energy deposit [138]. This is evaluated by comparing the topo-cluster energy with the expected energy deposit from charged pions in the jet, evaluated from MC simulations. For jet $p_{\mathrm{T}} > 100\,\mathrm{GeV}$, no subtraction is performed, and the two jet reconstruction algorithms described coincide.

The calibration of particle-flow jets (*PFlow*) proceeds via the same steps already described for EMTopo jets. A better angular resolution is observed for PFlow jets [142], and the JES measurement is found to be affected by lower systematic uncertainties. Moreover, as shown in Figure 3.11(a), the response function as measured in data and MC simulation for the JES calibration is closer to unity at low jet p_{T}. Figure 3.11(b) shows that the JER can be improved at low jet p_{T} thanks to the better measurement of tracks with respect to topo-clusters in this regime. The usage of tracks also allows for a reduction of the dependence of the jet reconstruction algorithm on the pileup. PFlow jets are used in this thesis in Section 5.3, where studies to improve ATLAS $VH(\to b\bar{b})$ measurements are presented.

Large-radius jets

The reconstruction of jets with the anti-k_t algorithm with a larger radius parameter has been identified as one way of improving the sensitivity of LHC experiments to the $VH(\to b\bar{b})$ signal [143]. At high transverse momentum ($p_{\mathrm{T}}(H) \gg m_H$), Higgs boson decay products are expected to be separated by $\Delta R(b,b) \simeq 2m_H/p_{\mathrm{T}}(H)$. This



(a) (b)

Figure 3.11. Comparison between the JES (a) and JER (b) response functions for EMTopo and PFlow jets, defined as the ratio of each quantity as measured in data and MC, as a function of the jet p_{T}. Figures from Ref. [138].

topology can be used to significantly reduce the $t\bar{t}$ background, since these events are expected to have two $b-$jets in different detector hemispheres. Large-radius (large-R) jets have been used so far also in several studies of the top quark, electroweak bosons pair production and searches for heavy dibosons resonances.

Large-R jets reconstruction [144] starts as for EMTopo jets from the clustering of topoclusters with the anti-k_t algorithm. The default R parameter value chosen by ATLAS is 1.0. To reduce the contribution from initial-state-radiation (ISR) and pileup, a *trimming* procedure is performed following Ref. [145]. This procedure consists in the identification within the large-R jet of sub-jets, reconstructed with the k_t algorithm with a radius parameter $R = 0.2$, with a p_{T} below a fixed relative threshold with respect to the large-R jet. Such contributions are removed from the large-R jet candidate. The uncalibrated, i.e. before the application of JES corrections, p_{T} is required to be greater than 200 GeV, with $|\eta| < 2.5$.
The calibration procedure of large-R jets is close to the one performed for EMTopo jets. In addition to the absolute JES calibration, an additional correction to the jet mass scale (JMS), derived as a function of reconstructed jet energy and η_{det}, is applied. After these two steps the jets are said to be calibrated at the JES + JMS scale. To improve the mass resolution, a combined jet mass is defined exploiting the ID. Track-jets are built using reconstructed ID tracks as inputs of the anti-k_t and trimming algorithms. The track-jet mass is then defined as

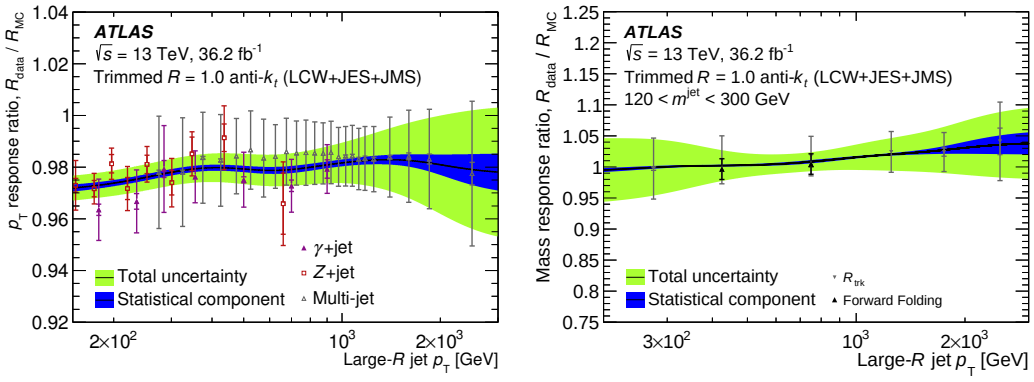
$$m_{\mathrm{TA}} = m_{\mathrm{track}} \frac{p_{\mathrm{T}}^{\mathrm{calo}}}{p_{\mathrm{T}}^{\mathrm{track}}}, \tag{3.6}$$

where quantities with the 'track' label are evaluated from the track-jet, while 'calo' to the large-R jet; m_{TA} is used to define the combined mass of the large-R jet

$$m_{\mathrm{comb}} = w_{\mathrm{calo}} m_{\mathrm{calo}} + w_{\mathrm{TA}} m_{\mathrm{TA}}, \tag{3.7}$$

where the w terms are weights defined such that the mass resolution is better than either the large-R jet and the track-jet mass resolution.

Large-R jets are further calibrated with the *in-situ* procedure. The JMS is also calibrated with an *in-situ* procedure. Two different methods are adopted: the calorimeter-to-track response ratio, and the forward-folding, both described in detail in Ref. [144]. The first method is only used to derive systematic uncertainties on the JMS, and is based on the mean of the gaussian distribution of the double ratio between data and MC simulation of $R_{\mathrm{TRK}} = \left\langle p_{\mathrm{T}}^{\mathrm{calo}}/p_{\mathrm{T}}^{\mathrm{track}} \right\rangle$. Deviations between data and MC simulation are taken as systematic uncertainties. The forward folding method instead performs a fit to the large-R jet mass in $t\bar{t}$ events. In particular, from the position and the shape of the W and top-quark peaks it is possible to extract the jet mass scale and jet mass resolution.



(a) (b)

Figure 3.12. Ratio of the response function as measured in MC simulation and data for the JES (a) and JMS (b) via the in-situ method for large R jets, as as a function of the large-R jet p_{T}. Figures from Ref. [144].

In Figure 3.12(a) the large-R jet p_{T} response ratio between data and MC is shown. As for EMTopo jets, the three *in-situ* measurements are combined to cover the p_{T} range from 200 GeV to about 2.4 TeV. The uncertainty is propagated from the *in situ* measurements, and is about 1% at low p_{T} and 2% at high p_{T}. The dominant one in this regime is the JES of the EMTopo jets used in the multijet balance method. Figure 3.12(b) reports the response function for the jet mass scale as a function of large R jet p_{T}. This ratio is consistent with unity within uncertainties, which are of the level of 2 to 5% in the 400 GeV-1 TeV p_{T} range. The dominant source of uncertainty on this quantity is due to the alternative modelling obtained from different ME and PS generators of the MC samples used in the calibration procedure.

Variable-radius track-jets

As already introduced, tracks which satisfy the quality criteria requirements described in Table 3.1 can be used to build track-jets. The opening angle of hadronisation products at high transverse momentum roughly scales as $\Delta R \sim 1/p_{\mathrm{T}}$. Variable-radius (VR) jets have been introduced to catch this dependence [146]. The anti-k_t

algorithm is ran with an effective R parameter defined as

$$R_{\text{eff}}(p_{\text{T}}, \rho) = \min\left\{0.4, \max\left\{0.02, \frac{\rho}{p_{\text{T}}}\right\}\right\}, \tag{3.8}$$

which depends on the jet p_{T} and on a parameter ρ. Tracks from the ID are used as inputs to build the VR track-jets.

The parameter ρ determines how quickly the jet radius changes. Its default parameter in ATLAS is 30 GeV. The dependence of R on the jet p_{T} is shown in Figure 3.13, overlaid to the leading VR track-jet p_{T} distribution observed in simulated $qq \to Z(\nu\nu)H(b\bar{b})$ events. As it can be seen, most of the events fall in the range in which the R parameter of the VR track-jet is lower than 0.4. VR track-jets are used by the boosted $VH(b\bar{b})$ analysis, described in Section 5.2, to identify the two b-jets from the H decay within the large-R jet.

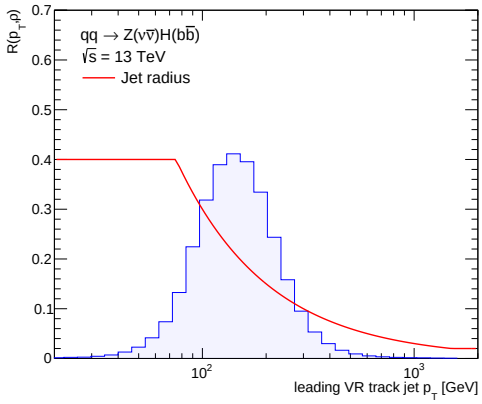


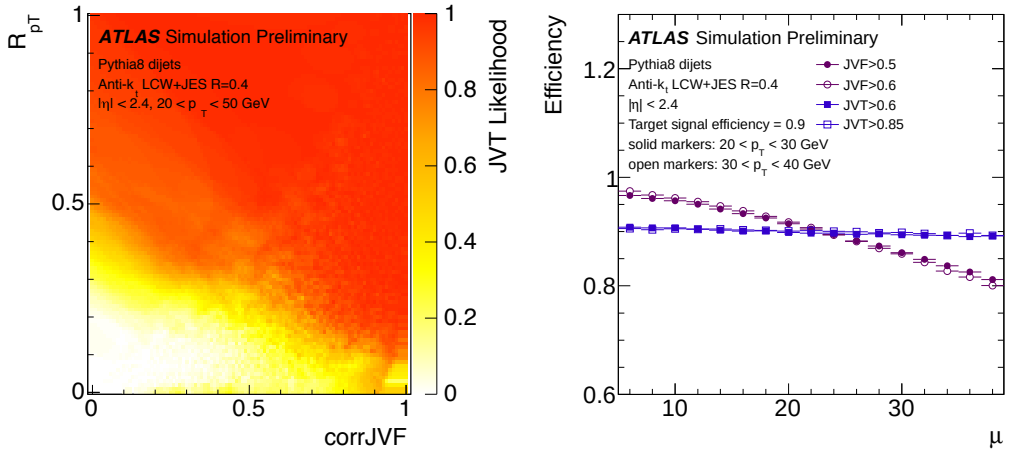
Figure 3.13. Effective R parameter of the anti-k_T algorithm adopted in the definition of VR track-jets shown as a function of p_{T}, and overlaid to the leading VR track jet p_{T} distribution obtained in $qq \to Z(\nu\nu)H(b\bar{b})$ simulated events (arbitrary normalisation).

3.3.1 Pileup jet tagging

At large average number of interaction per bunch crossing, local fluctuations may lead to the reconstruction of spurious low-p_{T} pileup jets. In order to reduce such contributions, the jet-vertex-fraction (JVF) [147] variable was developed. JVF is defined as the scalar sum of the transverse momenta of tracks belonging to the HS vertex and associated to a jet, divided by the same quantity, evaluated over all the interaction vertices reconstructed in the collision. This quantity though is not stable as a function of N_{PV}, as the denominator increases. A corrected version of JVF is introduced [147] to scale by N_{PV} the sum of the p_{T} of tracks associated with a jet but not with the HS vertex.

In order to build a 2D discriminant to reduce pileup jets, an additional variable is considered, $R_{p_{\text{T}}}$. This quantity is defined as the scalar sum of the p_{T} of the tracks associated with the jet and originating from the HS vertex, divided by the jet p_{T}, evaluated after the calibration. In fact, this includes already a subtraction of pileup contributions. This variable is peaked at low values for pileup jets, and tends to be

larger for the ones from the HS vertex, despite the fact the neutral component is not included in the numerator. Using the k-nearest-neighbour algorithm [148], from the 2D distribution of the corrected-JVF and $R_{p_{\mathrm{T}}}$ variables a likelihood discriminator called *jet-vertex-tagger*, JVT, is built. The JVT likelihood distribution, as a function of the two aforementioned variables, is shown in Figure 3.14(a). The hard-scatter identification efficiency is shown in Figure 3.14(b) as a function of average number of interaction per bunch crossing, as obtained from MC multi-jet events. One can observe how the efficiency for JVT is almost flat as a function of pileup, while it decreases for JVF. The implementation of JVT leads to improved pileup jet rejection, as $\langle\mu\rangle = 33.7$ in the Run-2 data set. The efficiency is measured in Z+jets events as described in Ref. [147], and scale factors are derived to take into account potential mismodelling in the simulation.



(a) (b)

Figure 3.14. (a) JVT likelihood function shown in the (JVF,$R_{p_{\mathrm{T}}}$) plane. (b) Dependence of the hard-scatter efficiency as a function of actual interaction per bunch crossing for JVF and JVT for different requirements on the discriminant variables. Both figures are obtained in simulated multi-jet events. Figures from Ref. [147].

3.3.2 Heavy-flavour jet tagging

The identification of jets initiated from b-quarks, also called *b-tagging*, plays a crucial role in this thesis. Without such procedure, the measurement of the $VH(b\bar{b})$ process would not be possible due to the large QCD backgrounds of the LHC. Moreover, b-tagging is also used in the search for dark matter in monojet final states, to build a top-quark enriched control region to constrain large modelling systematic uncertainties, as described in Section 4.9.

The long mean proper lifetime of b-hadrons[3], of the order of picoseconds, leads to

[3]In the following b-hadrons and c-hadrons will refer respectively to B and D mesons, produced in the hadronisation process of b and c quarks.

displaced secondary vertices where multiple tracks are produced. In MC simulation the truth flavour of each jet is identified in the following way: for each jet a truth $b-$hadron is sought within a fixed radius cone of $\Delta R = 0.3$; if such hadron is found the jet is b-labelled. If none is found, a truth c-hadron is looked for in the same way, and again, if found, the jet is said to be c-labelled. If also a c-hadron is not found, then a truth τ-lepton is sought, and if this is not found then the jet is light-flavour labelled, otherwise it is labelled as a τ-jet. At reconstruction-level, instead, the identification of b-jets relies on a set of low-level taggers which access the tracks in the event, or exploit kinematic constraint given by the b- and c-hadron masses, to produce inputs for higher level taggers. For such algorithms, tracks are ghost-associated to jets, assuming a variable radius parameter [149].

Four low-level taggers are defined:

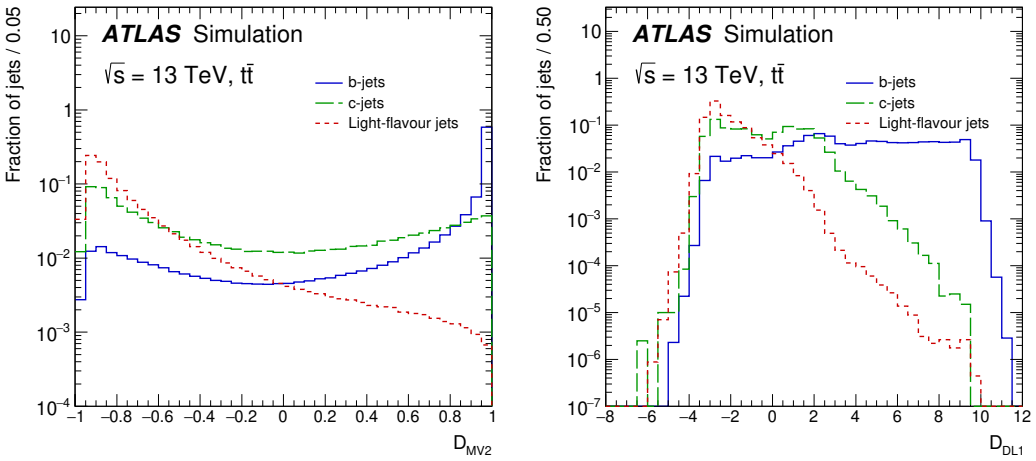
- **IP2D** and **IP3D** [150]: likelihood ratio (LLR) discriminants based on the transverse ($d_0/\sigma(d_0)$) and longitudinal ($z_0/\sigma(z_0)$) impact parameters signed significance. Such distributions are expected to be asymmetric for particles which do not decay promptly such as b-hadrons. The LLR of each tagger is built from the ratio of the probability density functions derived for the different truth jet flavours in MC simulation. Tracks are treated as independent from each other, thus their likelihood value is multiplied to obtain a final one for each tagger. The two values are given as input to the higher-level-taggers.

- **SV1** [151]: aims at the reconstruction of secondary vertices within the jets. The algorithm is seeded by a pair of tracks, and via a χ^2 fit more tracks are matched to the secondary vertices. The invariant mass of the system of tracks is required to be less than 6 GeV. If a higher value is found, the vertex is discarded. The algorithm outputs eight variables, such as the mass of the vertex, the significance of the decay length and other information related to the identified tracks.

- **JetFitter** [152]: aims at the reconstruction of the full b- and c-hadron decay chains, by the identification of a flight direction which matches subsequent decay vertices. It also outputs eight discriminant variables, mainly related to the track multiplicity associated to each vertex.

- **RNNIP** [153]: recurrent neural network which takes as an input the signed impact parameter significance of each track, the fraction of jet p_{T} carried by the track with respect to jet p_{T} and the angular distance with respect to the jet axis. It outputs four probabilities, one for each truth label discussed before, which are combined to provide a single score for the jet.

Three distinct high-level-taggers are then defined based on the architecture and inputs taken. **MV2c10** [150, 149] is a BDT which uses the outputs from all the above low-level-taggers, except for the RNNIP score. It is trained to separate b-jets from c- and light-flavour jets. The output of such BDT is a score between -1 and 1, whose distribution derived in simulated $t\bar{t}$ events is shown in Figure 3.15(a). During the training, the fraction of c-jets, with respect to the total background, is set to 7% [149]. This enhances the discrimination power with respect to b-jets.



(a) (b)

Figure 3.15. MV2c10 (a) and DL1 (b) score distributions as determined in simulated $t\bar{t}$ events. Figures from Ref. [149].

The **DL1** tagger uses the same input of MV2c10, with the addition of information from JetFitter on possible tertiary vertices. It is based on a deep neural network, and gives as an output three probabilities for each jet, p_b, p_c and p_l. These are combined *a-posteriori* to define a score which, in the case of b-tagging, is given by

$$D_{\mathrm{DL1}} = \ln\left(\frac{p_b}{f_c \cdot p_c + (1 - f_c) \cdot p_l}\right), \tag{3.9}$$

where f_c is fixed to 0.08. This parameter is tuned to achieve sufficient discrimination power between b- and c-jets. A c-tagger can be built in the same way by swapping p_b and p_c and re-tuning the parameter f. The output score distribution of DL1 is shown in Figure 3.15(b). The third tagger is called **DL1r**, and is an extension of DL1. It takes the same inputs of DL1, with the addition of the RNNIP output. Its perfomance on the tagging of PFlow jets are shown in Ref. [6], and further studies are reported in this thesis in Section 5.3.

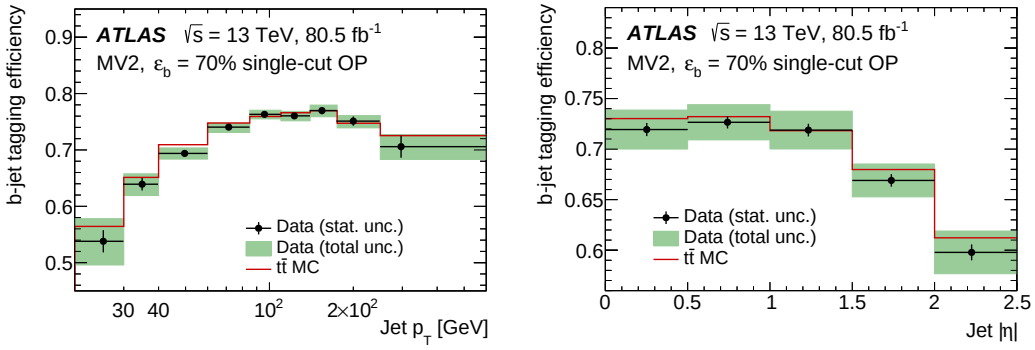
Single-cut operating working points (OP) are defined by applying a fixed cut on the output scores. These are designed to provide an average b-tagging efficiency of 60%, 70%, 77% and 85%. The cut values, together with the corresponding rejection factors are shown in Table 3.3. Pseudo-continuous b-tagging WPs can also be defined by requiring the efficiency of tagging a jet to be within an interval, e.g. between 77% and 70%. Such WPs are adopted in the $VH(\to b\bar{b})$ analysis since they allow for the determination of the quality with which a jet is identified as b-tagged.

Tagging algorithms are calibrated by comparing the efficiency and mistag rates, defined as the efficiency of tagging a c- or light-flavour jet as a b-jet, observed in MC samples to the same quantities measured in data. Such calibration is performed in $t\bar{t}$ dilepton events for b-jets [149] and c-jets [154]. To calibrate the light-flavour jet mistag rate, the calibration is performed on Z+jets events [155]. The b-tagging

Table 3.3. Definition of single-cut WPs, and performance in terms of selection efficiency and rejection factors, as evaluated on s $t\bar{t}$ MC sample, for MV2 and DL1 b-tagging algorithms. Table from Ref. [149].

ϵ_b	MV2				DL1			
	Selection	Rejection			Selection	Rejection		
		c-jet	τ-jet	Light-flavour jet		c-jet	τ-jet	Light-flavour jet
60%	> 0.94	23	140	1200	> 2.74	27	220	1300
70%	> 0.83	8.9	36	300	> 2.02	9.4	43	390
77%	> 0.64	4.9	15	110	> 1.45	4.9	14	130
85%	> 0.11	2.7	6.1	25	> 0.46	2.6	3.9	29

efficiency for the MV2c10 algorithm is shown as a function of jet p_{T} and $|\eta|$ in Figures 3.16(a) and 3.16(b), respectively.



(a) (b)

Figure 3.16. b-jet tagging efficiency as measured in $t\bar{t}$ dilepton events and in MC simulation for the MV2c10 tagging algorithm. Figures from Ref. [149].

The degradation of the efficiency at low jet p_{T} is due to the multiple scattering of particles. In the same way, this phenomenon affects the efficiency at high $|\eta|$ values, since in that region particles interact with more detector material. At high p_{T} , instead, the tracks become to be more collimated and the tracking efficiency is degraded.

SFs are derived from the ratio of the efficiency measured in data and in MC simulation. These are assumed to be independent among different jets, and are applied as a multiplicative correction to the event weights in the analyses. Additional MC-to-MC scale factors are derived by comparing different MC generators which adopt different ME generation algorithms, or alternative parton-shower models. These are needed to correct the SF when the MC sample used in the calibration procedure does not match the one adopted by an analysis. Further details on these MC-to-MC SFs, and studies carried out on PFlow jets in the context of this thesis are reported in Section 5.3. Systematic uncertainties on the flavour-tagging procedure are propagated from the calibration analyses. Different sources of uncertainties can affect the value of the SFs. An eigenvector decomposition is performed to reduce the number of uncertainties which are propagated trough physics analyses selections to derive the effect of flavour-tagging uncertainties. Different schemes can be adopted,

based on the level of detail needed on the description of such uncertainties.

3.4 Missing transverse momentum

Missing transverse momentum ($\vec{E}_{\mathrm{T}}^{\mathrm{miss}}$) is a 2D vector defined in the transverse plane of the collisions, proxy of the production of non-interacting particles. It is the key element of the searches of DM at particle colliders, since it is hypothesised that WIMPs produced in particle collisions at the LHC escape the experiment undetected. Moreover, it allows to identify $Z(\to \nu\bar{\nu})H(\to b\bar{b})$ candidate events, thus improving the sensitivity to the $H(\to b\bar{b})$ process.

The $\vec{E}_{\mathrm{T}}^{\mathrm{miss}}$ is defined as in Equation 3.10,

$$\vec{E}_{\mathrm{T}}^{\mathrm{miss}} = -\sum_{\text{obj. } i} \vec{p}_{\mathrm{T}}^{\,i} - \sum_{\substack{\text{soft} \\ \text{signals } j}} \vec{p}_{\mathrm{T}}^{\,j}, \tag{3.10}$$

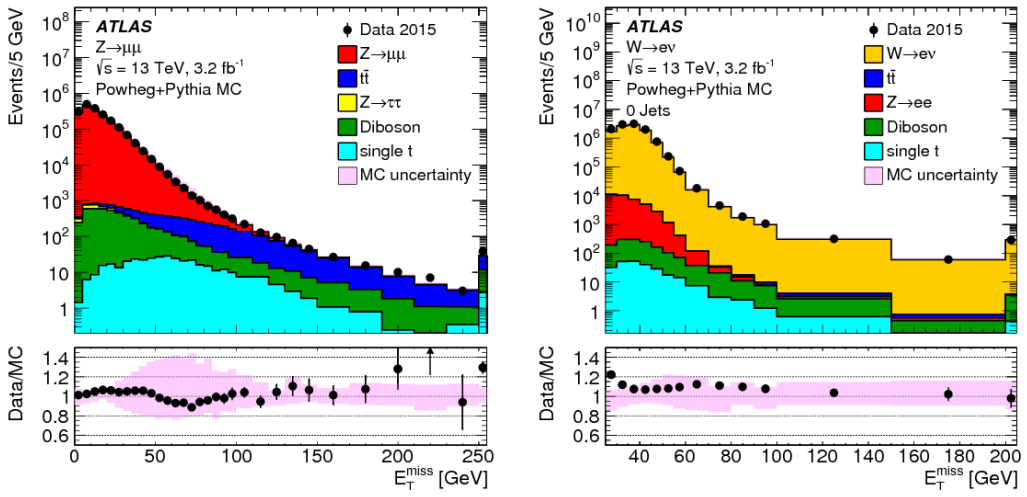
where the first term is called *hard term*, and includes all the reconstructed and calibrated objects, such as electrons, photons, hadronically decaying τ-leptons, jets and muons. A *soft term* is added to take into account all the signals not associated with any of the previous objects. This term can be evaluated considering ID tracks or topo-clusters in the calorimeter. The standard ATLAS choice [156] is to consider a *track soft term* (TST), which – although it does not take into account the presence of neutral particles – is insensitive to pileup due to the fact that only tracks associated to the HS vertex are considered.

The objects entering the definition of $\vec{E}_{\mathrm{T}}^{\mathrm{miss}}$ are independent from each other. An ambiguity solving procedure is followed to avoid the double-counting of detector signals [156]. The priority order is the following: electrons, photons, hadronically decaying τ-leptons, jets and muons. A partial overlap of jets and electrons or photons may happen. In this case, after the object selection for $E_{\mathrm{T}}^{\mathrm{miss}}$ calculation, the ratio $\kappa_E = E_e^{\mathrm{EM}}(\gamma)/E_{\mathrm{jet}}^{\mathrm{EM}}$ is evaluated. The superscript EM indicates that both objects are considered calibrated at the electromagnetic scale, as discussed in Section 3.3. If κ_E is lower than 0.5, the jet is included in $\vec{E}_{\mathrm{T}}^{\mathrm{miss}}$ calculation with its p_{T} scaled by $1-\kappa_E$, otherwise it is discarded, and the tracks associated only to the jet enter in the TST. The overlap between muons and jets is also considered. Ghost-association between the jet and the muon determines whether such two objects overlap. Requirements on the transverse momentum ratio and on the number of tracks of the HS vertex associated to the jet allow to understand if the jet is due to pileup, and therefore needs to be removed. Moreover, muons might radiate hard photons at small angles, which lead to a reconstructed jet in the calorimeter. In this case the number of tracks associated to the HS vertex and the energy deposit characteristics, e.g. the jet width[4], allow for the identification of such jets. These are included in the calculation of $\vec{E}_{\mathrm{T}}^{\mathrm{miss}}$. Lastly, reconstructed tracks associated to the PV and close-by any electron, photon, τ-lepton, or that are ghost associated to any jet, or match a muon ID track are not considered in the TST.

The modelling in simulation of the magnitude of the $\vec{E}_{\mathrm{T}}^{\mathrm{miss}}$, $E_{\mathrm{T}}^{\mathrm{miss}}$, of MC simulations of $E_{\mathrm{T}}^{\mathrm{miss}}$ in events with and without genuine $E_{\mathrm{T}}^{\mathrm{miss}}$ is shown in Figure 3.17.

[4]The jet width is defined by the number of associated calorimeter cells.

In this figure, data collected in 2015 are compared to MC in $Z(\rightarrow \mu\mu)$+jets and $W(\rightarrow e\nu)$+jets events. In the latter case, a requirement of 0 jets passing selection criteria, as defined in Ref. [156], is applied. To reduce the dependence of the comparison on the MC generators adopted, each process is normalized to the generator cross-section, and the overall distribution is scaled to the same integral of data. A good agreement is observed in dimuon events, with data compatible with MC within uncertainties. The mismodelling observed at low $E_{\mathrm{T}}^{\mathrm{miss}}$ in W+jets events is due to the fact that the contribution from multi-jetevents were not taken into account in simulation.



(a) (b)

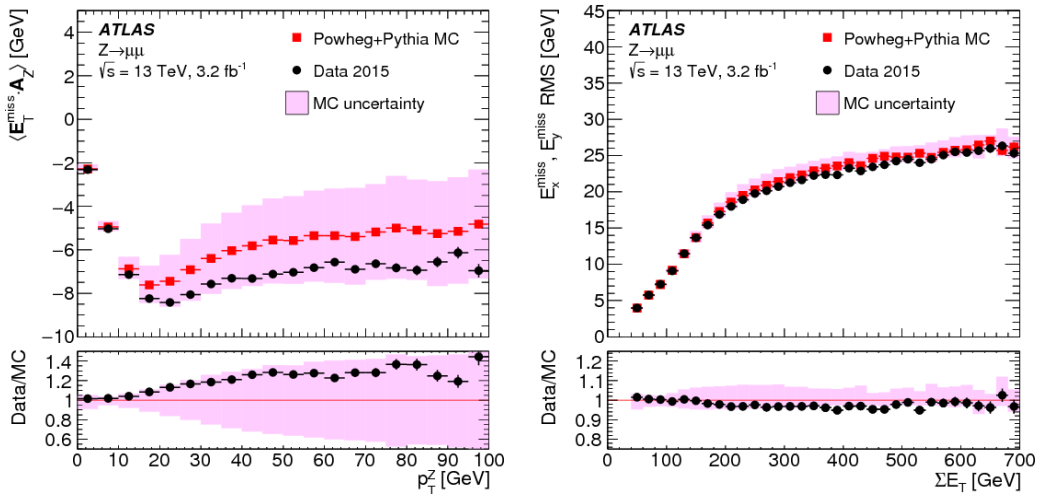
Figure 3.17. Comparison of the $E_{\mathrm{T}}^{\mathrm{miss}}$ distribution in (a) Z+jets events and (b) W+jets events, where genuine $E_{\mathrm{T}}^{\mathrm{miss}}$is expected from the non-reconstruction of the neutrino. Figures from Ref. [156].

Detector response to $E_{\mathrm{T}}^{\mathrm{miss}}$ can be evaluated in $Z(\rightarrow \mu\mu)$+jets decays where the expected $E_{\mathrm{T}}^{\mathrm{miss}}$ is zero. In each event, the projection of the $\vec{E}_{\mathrm{T}}^{\mathrm{miss}}$ onto the reconstructed flight direction of the Z boson ($\vec{A_Z}$) is built, $\left\langle E_{\mathrm{T}}^{\mathrm{miss}} \cdot \vec{A_Z} \right\rangle$. If no jets are present in the event, the expected value of such quantity is 0. Values below 0 are expected if the hadronic recoiling activity is underestimated. In Figure 3.18(a) the $E_{\mathrm{T}}^{\mathrm{miss}}$ response, as a function of the transverse momentum of the Z boson ($p_{\mathrm{T}}^{\mathrm{Z}}$), is shown. At low values, the missing neutral component in the soft term leads to an underestimation of the hadronic recoil activity. At higher p_{T} the jet term in the $\vec{E}_{\mathrm{T}}^{\mathrm{miss}}$ definition tends to dominate, and a flat offset is observed. Data and MC simulation are found to be in good agreement within uncetainties.

The resolution of $E_{\mathrm{T}}^{\mathrm{miss}}$ measurement is determined by the rms of the x and y components of the $\vec{E}_{\mathrm{T}}^{\mathrm{miss}}$ with respect to their expected value. This can be measured in data selecting $Z(\rightarrow \mu\mu)$ events, where $E_{\mathrm{T}}^{\mathrm{miss}}$ is expected to be zero. Figure 3.18(b) shows the rms of the two $\vec{E}_{\mathrm{T}}^{\mathrm{miss}}$ components as a function of the scalar sum of transverse energies of all objects reconstructed in $Z(\rightarrow \mu\mu)$ events, defined as $\sum E_{\mathrm{T}}$. At low values of $\sum E_{\mathrm{T}}$ the resolution is dominated by the measurement of the two

muons, while the logarithmic behaviour above $\sim 180\,\text{GeV}$ is related to the JER.

Systematic uncertainties on the $E_{\text{T}}^{\text{miss}}$ reconstruction are provided for both the scale and resolution measurement. The hard term uncertainty component is propagated from the objects used in its definition. Soft-term systematic uncertainties are evaluated from data and MC simulation by looking at $\vec{E}_{\text{T}}^{\text{miss,soft}}$ components parallel and perpendicular to the reconstructed direction of the hard term [156].



(a) (b)

Figure 3.18. (a) Comparison of the average projection of $\vec{E}_{\text{T}}^{\text{miss}}$ on the flight direction of the Z boson in Z + jets events. (b) Resolution on the measurement of $\vec{E}_{\text{T}}^{\text{miss}}$components as measured in data and obtained in MC simulation in $Z(\to \mu\mu)$ + jets events. Figures from Ref. [156].

$E_{\text{T}}^{\text{miss}}$ reconstruction variants. As already mentioned, alternatively to the TST, the soft term can be evaluated from calorimeter energy deposits not associated to any reconstructed objects. The calorimeter soft term (CST) can be used to define $\vec{E}_{\text{T}}^{\text{miss,calo}}$. However, such definition is highly sensitive to pileup. A lower resolution at low $E_{\text{T}}^{\text{miss}}$ is also expected due to worse performance of the calorimeter on the measurement of low-p_{T} objects with respect to the ID.
Another $\vec{E}_{\text{T}}^{\text{miss}}$ variant, adopted in the $VH(b\bar{b})$ analysis as an input to the final MVA, is the *track*-$E_{\text{T}}^{\text{miss}}$ ($\vec{p}_{\text{T}}^{\text{miss}}$). This is built using only tracks reconstructed in the ID associated to the HS vertex. Such $E_{\text{T}}^{\text{miss}}$ definition is insensitive to pileup. However, it has an intrinsic lower-scale response, due to the fact that no neutral components of jets, nor photons, are included. Moreover, while the $E_{\text{T}}^{\text{miss}}$ reconstruction uses jets with $|\eta|$ up to 4.5, the $\vec{p}_{\text{T}}^{\text{miss}}$ reconstruction is limited by the acceptance of the inner tracker, $|\eta| < 2.5$.

Chapter 4

The *Monojet* search

The production of new physics phenomena at the LHC might go undetected in the final state of the collisions, and lead to large missing energy. In order to overcome the large hadronic background of LHC collisions, the presence of SM particles reconstructed in the final state is often required. This leads to the so-called mono-X signatures. At an hadron collider in particular, the emission of QCD initial state radiation (ISR) is enhanced with respect to the emission of a photon, or the associated production of an electroweak boson. Gluons hadronize in the final state and lead to a monojet signature, a golden channel to look for new phenomena at the LHC. Events with jets recoiling against a significant amount of missing transverse momentum have been observed for the first time at CERN Sp$\bar{\text{p}}$S by the UA1 collaboration [157] in 1984. Since then, several searches have been performed in this final state.

In this Chapter, the monojet analysis carried out with the data collected by the ATLAS experiment, in pp collisions at $\sqrt{s} = 13\,\text{TeV}$, during LHC Run 2 is presented. These results have been published in Phys. Rev. D 103 (2021) 112006.
Section 4.1 presents a general overview of the analysis while in Section 4.2 the background processes are discussed. The objects and event selection adopted in the definition of the analysis regions are discussed in Section 4.3, 4.4 and 4.5. In Section 4.6 a summary of the improvements with respect to the previous iteration of this analysis in ATLAS is given. The background estimation is presented in Section 4.7, and a discussion of the systematic uncertainties is given in Section 4.8. Results are finally presented in Section 4.9. Model independent limits, constrains on the parameters of DM simplified models, and on the Higgs to invisible branching fraction are discussed in Section 4.10. A re-interpretation of the results in terms of long lived particles models is presented in Section 4.11. This work has been published as an ATLAS public note, ATL-PHYS-PUB-2021-020.

4.1 The idea

In this analysis we look for events in which up to four hadronic jets recoil against a large amount of missing transverse momentum, at least 200 GeV. Events in which leptons are reconstructed are not considered as part of the signal region (SR). An event display of a monojet like event is shown in Figure 4.1. This event has been recorded in 2017 ATLAS data. It includes a central jet with $p_{\text{T}} = 1924\,\text{GeV}$ and

$E_{\mathrm{T}}^{\mathrm{miss}} = 1913\,\mathrm{GeV}$. Such event might have been arisen from the associated production of jets with a Z boson, the latter decaying into a pair of neutrino anti-neutrino ($Z \to \nu\bar{\nu}$).

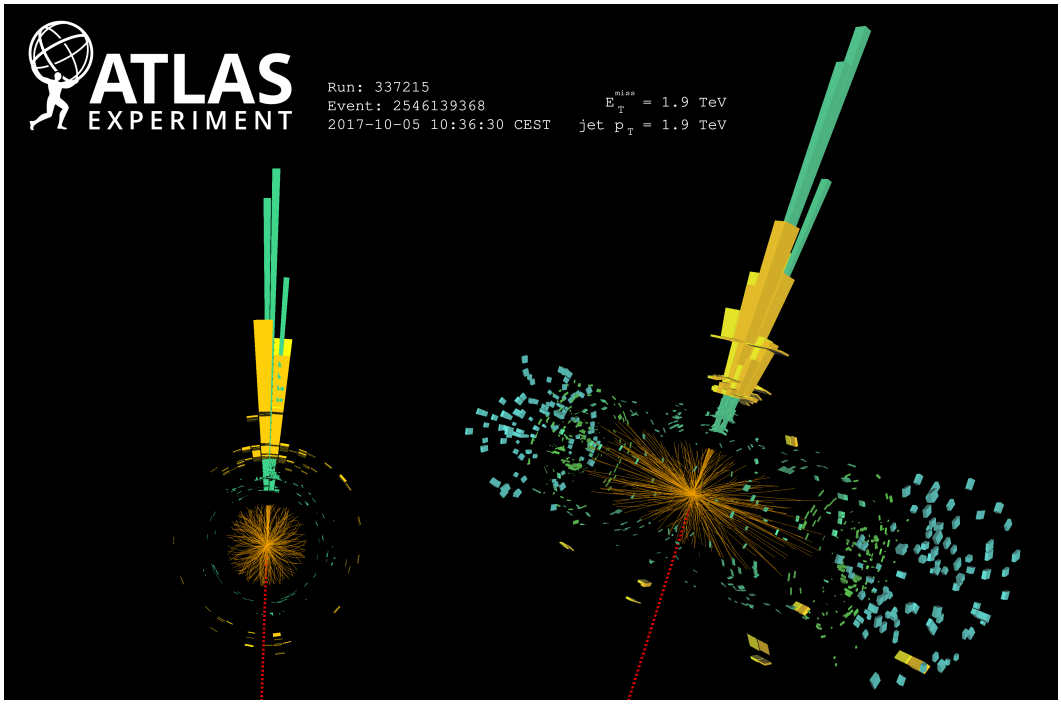


Figure 4.1. Monojet event recorded by the ATLAS experiment during 2017 data taking campaign. The length of the green (yellow) bars is proportional to the energy deposits in the electromagnetic (hadronic) calorimeter cells associated with the jet. Reconstructed tracks in the ID are represented by orange lines. The direction of missing transverse momentum is represented by the red dotted line. A view of the event in the transverse plane is presented on the left part of the figure. Figure from the auxiliary material of Ref. [4].

Other SM processes, like $W(\to \ell\nu)$+jets, lead to the same final state if the lepton is not correctly reconstructed. The goal is to look for deviations from the SM predictions. It is therefore crucial to identify all the possible background sources.

A semi data-driven approach, based on a simultaneous fit to statistically independent control regions (CR), is adopted to correct MC predictions of background processes using data. Moreover, such CR allow to reduce the systematic uncertainties associated with the predictions. The discriminant variable used in the search is the $E_{\mathrm{T}}^{\mathrm{miss}}$. A total uncertainty between 1.2% and 4.2% is achieved on the background predictions. Since no significant deviations from the SM are observed, upper limits on the visible cross-section and on new phenomena models are set. An upper limit on the branching fraction of the Higgs boson into invisible final states ($\mathcal{B}(H \to \mathrm{inv.})$ is also set.

4.2 Background processes

Background processes to the monojet search can be either irreducible or reducible.

Irreducible backgrounds these processes lead to the exact same final state of the sought signal. For this reason, it is not possible to apply a cut on kinematic variables of the event to improve the signal significance. The $Z(\to \nu\bar{\nu})$+jets process, produced via either strong or electroweak mode, is the main irreducible background of the search. Another irreducible background would be the production of a pair of Z bosons, both decaying into a pair of neutrinos. However, the cross-section of the latter process is negligible with respect to the former.

Reducible backgrounds leptonically decaying W bosons produced in association with jets, dibosons, $t\bar{t}$ and tW production include genuine $E_{\mathrm{T}}^{\mathrm{miss}}$ from one or more neutrinos in the final states. Such events include also leptons. If these are not reconstructed, events would enter the SR. It is therefore crucial to adopt efficient WP and loose cuts to identify any additional charged lepton, such that these events are rejected (or assigned to one of the control regions, as defined later in this Chapter). The $Z(\to \ell^+\ell^-)$ process is an almost negligible background of the search, though can be used to correct $Z(\to \nu\bar{n}u)$+jets predictions via a dilepton enriched CR.

Background processes are modelled with state of the art MC simulations, as described in Section 4.2.1. As already mentioned, a set of control regions, defined in Section 4.5.2, is used to correct their predictions and constrain the associated modelling uncertainties.

Additional background events arise from QCD multijet production. This process is particularly relevant at low $E_{\mathrm{T}}^{\mathrm{miss}}$, since one or more soft jets not correctly reconstructed in the final state lead to fake $E_{\mathrm{T}}^{\mathrm{miss}}$. Moreover, due to the large QCD cross-section, this is the largest background. However, it can be significantly reduced with an angular distance requirement between the $E_{\mathrm{T}}^{\mathrm{miss}}$ direction and any jet in the event. A monojet-like signature can be also emulated by high energetic particles produced in the interaction between the beam and LHC collimators located near the ATLAS interaction point. Muons can travel parallel to the beam pipe, and deposit a significant amount of energy in the calorimeters, which emulates a jet. This process is categorized as non-collision background (NCB). Cosmic muons are also a source of NCB, but their contribution is reduced by timing requirements on the calorimeters signals. Both the QCD background at low $E_{\mathrm{T}}^{\mathrm{miss}}$ and NCB are not well modelled in MC simulations. Their estimate, described in Section 4.7.1, is thus obtained in a data driven way.

4.2.1 Monte Carlo simulation

The MC calculations adopted for the nominal predictions are described in this section.

Single vector boson production. W/Z+jets (V + jets) processes, where the V production is not EW induced, are simulated using the Sherpa [158] 2.2.1 event generator. The matrix element (ME) calculations include up to 2 extra QCD emissions at next-to-leading order (NLO), and up to 4 extra emissions at leading order (LO), and are performed using the Comix [159] and Open Loops [160] libraries.

The NNPDF3.0NNLO parton density function set [161] is used in the five number of flavours scheme ME calculation. The ME generator is interfaced within SHERPA with a parton shower algorithm based on the Catani-Seymour dipole formulation [162], which adopts the cluster hadronisation model [163]. Matching is performed with the CKKW method [164] using a 20 GeV threshold, and it is extended at NLO accuracy with the ME+PS@NLO prescription [165]. To populate with enough statistical precision the entire phase space, events are generated in slices of the parton level $\max(H_{\mathrm{T}}, p_{\mathrm{T}}^{V})$ variable. H_{T} is defined as the scalar sum of the p_{T} of parton level jets with $p_{\mathrm{T}} > 20$ GeV, and p_{T}^{V} is the transverse momentum of the vector boson as calculated from ME leptons. A total of 6 samples, whose boundaries are set at [70, 140, 280, 500, 1000] GeV and the centre-of-mass energy, are obtained and merged together. Events, normalised to the generator cross-section, are initially re-weighted to an inclusive NNLO QCD calculation [166].

NNLO QCD and NLO EW virtual corrections to the production of vector bosons in association with jets are applied following the prescriptions of Ref. [167]. These include the effect of two-loop EW Sudakov logarithms evaluated at NLL accuracy. Such terms are relevant at high boson p_{T}, where the corrections to the cross-section are of the order of few percent. The cross-section is reweighted via a one-dimensional ratio between the differential cross-section as function of the boson p_{T} provided in theoretical predictions, and the one obtained with ATLAS MC simulations at particle-level. This quantity is defined by the sum of the transverse momenta of the leptons produced in the vector boson decay. To take into account the emission of QED radiation off charged leptons, photons found within $\Delta R < 0.1$ are reclustered with them, forming the so-called *dressed-leptons*.

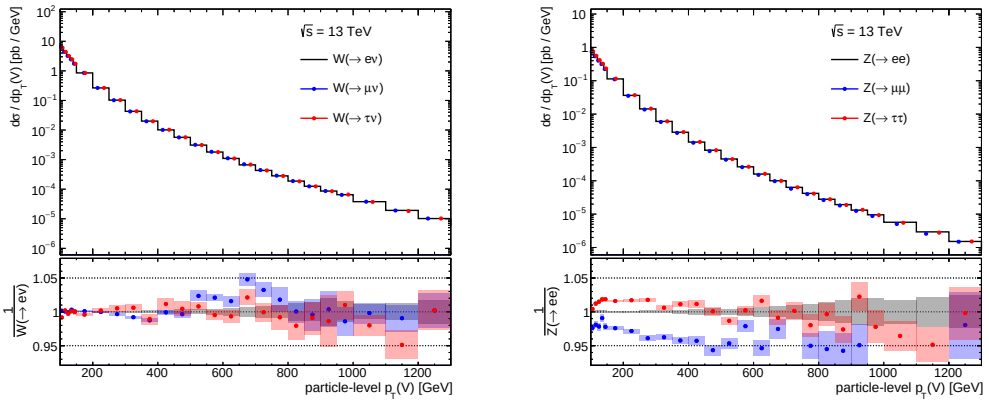
The reweighting is described by Equation 4.1

$$\frac{\mathrm{d}}{\mathrm{d}p_{\mathrm{T}}^{V}}\frac{\mathrm{d}}{\mathrm{d}\vec{y}}\sigma^{V}(\vec{\varepsilon}_{\mathrm{MC}}, \vec{\varepsilon}_{\mathrm{TH}}) = \frac{\mathrm{d}}{\mathrm{d}p_{\mathrm{T}}^{V}}\frac{\mathrm{d}}{\mathrm{d}\vec{y}}\sigma^{V}_{\mathrm{MC}}(\vec{\varepsilon}_{\mathrm{MC}})\frac{\frac{\mathrm{d}}{\mathrm{d}p_{\mathrm{T}}^{V}}\sigma^{V}_{\mathrm{TH}}(\vec{\varepsilon}_{\mathrm{TH}})}{\frac{\mathrm{d}}{\mathrm{d}p_{\mathrm{T}}^{V}}\sigma^{V}_{\mathrm{MC}}(\vec{\varepsilon}_{\mathrm{MC}})}, \tag{4.1}$$

where $\mathrm{d}/\mathrm{d}\vec{y}$ represents the dependency of the cross section on all the other variables. In the ratio on the right hand side of the equation, $\mathrm{d}/\mathrm{d}p_{\mathrm{T}}^{V}$ indicates that such dependency is integrated out. $\vec{\varepsilon}_{\mathrm{MC}}$ indicates the set systematic uncertainties associated to the MC predictions. A set of theoretical systematic uncertainties, $\vec{\varepsilon}_{\mathrm{TH}}$, are provided by the authors of Ref. [167] to take into account missing higher orders in the calculation, the extrapolation between low and high p_{T} and differences between W and Z boson corrections. These prescription allow to correlate the estimate of these two processes in a fit. Thus, in addition to $Z(\to \ell\ell)$+jets, $W(\to \ell\nu)$+jets events can be used to estimate the $Z(\to \nu\bar{\nu})$+jets background. More details on the fit model are provided in Section 4.7.2.

Corrections are provided by the authors separately for the $Z(\to \ell^{+}\ell^{-})$, $Z(\to \nu\bar{\nu})$ and $W(\to \ell\nu)$ processes. These can be applied to every lepton flavour if FSR of leptons is taken into account in the reconstruction of the boson p_{T}. However, in the MC samples used, the $p_{\mathrm{T}}(V)$ spectrum of the different lepton flavours is affected by statistical fluctuations. Moreover, the overall cross-sections used to normalize the events of different channels, extracted from the logs of the event generation stage,

can be slightly different between different leptonic channels, thus introducing overall relative shifts. These effects are not an issue, because the value given as an input simplifies, a posteriori, in the ratio of equation 4.1. In Figure 4.2 a comparison of the boson p_{T} spectrum is presented for $W(\to \ell\nu)$+jets and $Z(\to \ell^-\ell^+)$+jets evens, for the three different lepton flavours.



(a) (b)

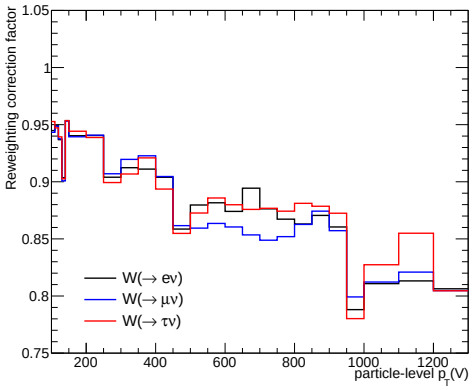
Figure 4.2. Comparison of cross-section predictions obtained in simulated V+jets events for different lepton flavour channels. Events are generated according to the setup described in this Section. Error bars shown in the bottom pane represent the relative statistical uncertainty on the predictions.

In order to absorb such statistical fluctuations, the ratio on the right hand side of Equation 4.1 is evaluated for each different lepton flavour. The obtained correction factors are shown in Figure 4.3.

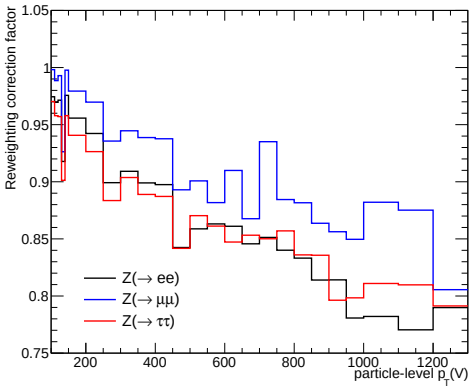
The size of the correction is compatible within different lepton flavours. Residual differences are due to the two effects already discussed: statistical fluctuations and slightly different values of the used cross-sections. While the latter effect is completely re-absorbed a posteriori, the former only partially.

A slightly larger correction for Z + jets processes, and a different slope between $W(\to \ell\nu)/Z(\to \ell^-\ell^+)/Z(\to \nu\bar{\nu})$, due to different EW corrections for each processes, are observed. The dips present in the correction factors at around 140 GeV, 280 GeV, 500 GeV and 1 TeV are due to the procedure with which the MC samples are generated. As already mentioned, Sherpa 2.2.1 V+jets samples have been produced by splitting the phase space integration in $\max(H_{\mathrm{T}},p_{\mathrm{T}}(V))$ slices. Once these are correctly weighted, the description of the cross-section is good, as already shown in Figure 4.2. In the ratio with the inputs provided from the authors of the prescriptions (i.e. smooth distributions) small steps appear. However, these are mostly reabsorbed in the application of the correction factor. In Figure 4.3(c) it is possible to see how a different choice of the slicing variable, used for the generation of part of the $Z(\to \nu\bar{\nu})$ + jets events, leads to a smoother correction factor.

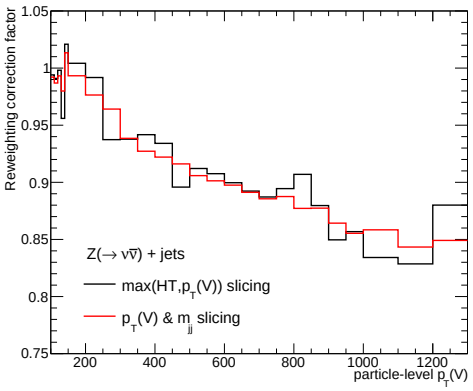
Details on the systematic uncertainties associated with the prescriptions, and their impact on the background estimate, are discussed in Section 4.8.2.



(a) $W(\to \ell\nu)$ + jets



(b) $Z(\to \ell^-\ell^+)$ + jets



(c) $Z(\to \nu\bar{\nu})$ + jets

Figure 4.3. Correction factors used to reweight the V+jets processes to higher order.

Electroweak V+jets production. Even if the cross section of the Vjj process including a t-channel propagator is subdominant with respect to the strong mode, this process becomes relevant on the tail of the $E_{\mathrm{T}}^{\mathrm{miss}}$ distribution, as shown later in Section 4.4. Thus, events not overlapping with the aforementioned ones are produced using Herwig 7.1.3 (7.2 for final states including muons) [168] at NLO accuracy, provided by the `VbfNLO` [169] package. The MMHT2014NLO PDF set [170] is used.

Top quark processes. $t\bar{t}$ events are simulated at NLO accuracy using the Powheg-Box v2 [89] generator with the NNPDF3.0NLO PDF set. The h_{damp} parameter, which regulates hard ISR emissions against which the $t\bar{t}$ system can recoil, is set to 1.5 times the mass of the top quark. The decay of such particle is handled by MadSpin [171] to preserve the spin correlations. The ME is interfaced with Pythia 8.230 [172] for the parton showering. The NNPDF2.3LO PDF set [173] is used, together with the A14 set of tuned parameters [174]. The production rate, branching fraction, and the kinematics of b- and c-hadrons decays are handled by EvtGen v1.6.0 [175].

Single top processes in the s-, t- and tW channels are simulated at NLO using Powheg-Box v2, with the NNPDF3.0NLO PDF set. The ME generator is interfaced with Pythia 8.2.30 for the parton showering. Also in this case, MadSpin, the A14 set of tuned parameters and EvtGen are used. To account for the interference with the $t\bar{t}$ process, the diagram removal (DR) scheme [176] has been chosen for the nominal tW sample. Modelling differences with respect to the diagram subtraction (DS) scheme have been included as a systematic uncertainty, as described in Section 4.8.2.

Dibosons production. Final states including the production of $Z(\to \ell\ell)Z(\to \ell\ell)$, $Z(\to \ell\ell)W(\to \ell\nu)$, $Z(\to \ell\ell)Z(\to \nu\bar{\nu})$ and $W(\to \ell\nu)Z(\to \nu\bar{\nu})$ have been simulated at NLO accuracy including one extra QCD emission, and at LO for up to 3 partons, using the Sherpa 2.2.2 event generator. The PDF set, merging and matching procedure are the same adopted in the V+jets setup described previously in this Section.

4.2.2 Event weights

Simulated MC events have an associated weight, used to take into account different aspects described below.

First, MC events generated beyond LO have a weight which is needed to achieve the correct cross-section distribution once a sufficient number of events is simulated. Negative weighted events are generated to correctly reproduce the cancellations which arise in the ME calculation. Weights are also associated to the PS part of the generation, to take into account the Sudakow form factors associated with QCD emissions. Each event need to be weighted by its associated value, and normalized by the sum of all the weights from the events generated. Once multiplied by the cross-section, the obtained distribution is correctly normalized. Higher order cross-section calculations might be available for some processes. An inclusive reweight can be implemented scaling the event weight for a k factor. Moreover, if the events are generated with a filter, an efficiency $\epsilon_{\text{filt.}}$ has to be taken into account in the event weight. This is needed, because to obtain such event $1/\epsilon_{\text{filt.}}$ have been generated.

Once event weights normalised as mentioned above are multiplied by the integrated luminosity, expected number of events is obtained.

A set of corrections related to the measurement procedure need to be taken into account in the event weight. As already introduced in Section 3, the reconstruction performance of physics objects in MC simulation is corrected by *scale factors*, SF. These correct the obtained efficiencies to the one measured in data. One SF needs to be applied each time a reconstruction, identification, isolation or tagging WP of the objects is required. Typical values of the SF are close to unity. In a similar way, *inefficiency scale factors*, also called anti-SF, are applied when a veto is set on the reconstruction or identification of particular objects. In the monojet analysis, anti-SF are introduced for the lepton veto applied in the SR and CR, and for the veto of b-tagged jets in the definition of the single lepton CR. The categorization of the events is discussed in Section 4.5.

Finally, an event weight is also derived to correct the distribution of the average

interaction per bunch crossing, such that the observed pileup distribution in data is correctly reproduced in the simulations.

The total event weight, which is used when histograms from MC events are produced to perform a data to MC comparison and a fit to the data with MC templates is given by the product of all the aforementioned components as

$$w_{\text{tot}} = \prod_i w_i. \tag{4.2}$$

The same technique is also applied for simulated signal samples.

4.3 Object definition

The reconstruction of final state jets, leptons, photons, hadronically-decaying τ leptons and of the $\vec{E}_{\text{T}}^{\text{miss}}$ in the event proceeds as described in Chapter 3. For some objects, two categories are defined: *baseline* and *signal*. This classification is used in the pre-selection of the events, and in their categorization in the different regions of the analysis. The definition of *baseline* objects is based on looser cut. It is meant to maximise the identification efficiency. *Signal* ones are defined using tighter working points or additional cuts instead, with the goal to identify well reconstructed objects.

Jets. No distinction between *baseline* and *signal* jets is made. They are required to have $p_{\text{T}} > 30\,\text{GeV}$ and $|\eta| < 2.8$. To suppress pileup jets, a requirement on the JVT variable defined in Section 3.3.1, JVT > 0.59 is applied for central jets ($|\eta| < 2.4$) with p_{T} below 120 GeV. To identify fake jets, e.g. due to NCB sources or noise bursts in the HEC, requirements on the topology of the energy deposits in the calorimeter system are applied. The *Loose* cleaning WP, defined in Ref. [177], is required. As an example, one jet is defined as *BadLoose* if one single layer of the calorimeters include more than 99% of the jet energy.

Jets originating from the decay of $b-$quarks are identified using the MV2c10 discriminant described in Section 3.3.2. Such jets are required to be within $|\eta| < 2.5$, and to pass the cut that defines the single OP cut WP which provides $\varepsilon \simeq 60\%$ on average.

Electrons. *Baseline* electrons are required to satisfy $E_{\text{T}} > 7\,\text{GeV}$, $|\eta| < 2.47$, and to be identified by the *Loose&Blayer* WP defined in Section 3.2.1. A requirement on $|z_0 \sin\theta| < 0.5\,\text{mm}$ is applied. *Signal* electrons need to satisfy the *baseline* quality criteria, and to pass the *Tight* identification WP. Moreover, they are required to have $d_0/\sigma(d_0) < 5$, $p_{\text{T}} > 30\,\text{GeV}$, and not to be within the *crack-region* of the EMC ($1.37 < |\eta| < 1.52$).

Muons. *Baseline* muons are required to pass the *Medium* identification WP defined in Section 3.2.2, and to have $p_{\text{T}} > 7\,\text{GeV}$ and $|\eta| < 2.5$. To be labelled as *signal*, muons are required to have $d_0/\sigma(d_0) < 3$, $|z_0 \sin\theta| < 0.5\,\text{mm}$ and a transverse momentum greater than 10 GeV.

τ leptons. Hadronically decaying τ leptons *baseline* definition requires $p_{\text{T}} > 20\,\text{GeV}$ and $|\eta| < 2.5$. As for *signal* electrons, the *crack-region* of the EMC is vetoed.

τ_{had} candidates are required to pass the *Loose* identification WP. As discussed in Section 4.4, τ_{had} are only used to veto events, thus no *signal* definition is applied.

Photons. *Baseline* photons are required to pass the Tight identification criteria (see Section 3.2.1), to have $E_{\text{T}} > 10\,\text{GeV}$ and $|\eta| < 2.37$. Also in this case, since photons are only used to veto events, no *signal* γ definition is applied.

Missing transverse momentum. The $\vec{E}_{\text{T}}^{\text{miss}}$ is calculated from the negative vectorial sum of all the baseline objects defined above. Jets are included if they satisfy the criteria $p_{\text{T}} > 20\,\text{GeV}$ and $|\eta| < 4.5$. The track soft term is used to take into account signals not associated to any of the aforementioned objects.

4.3.1 Overlap removal

To avoid double counting signals in the events, an overlap removal (OR) procedure is performed. It takes into account all the *baseline* objects defined above, except hadronically decaying tau leptons. Objects not passing the OR are removed from the event. It is performed following the order below:

- electron - muon: if they share the same ID track, remove the electron since the energy deposit in the calorimeter is likely to be originated from the muon;
- jet (j) - electron: if $\Delta R(j, e) < 0.2$ the jet is removed and the electron is kept. If $0.2 < \Delta R(j, e) < 0.4$ the jet is kept, and the electron discarded, since this is likely to have been originated in the displaced decay of one hadron in the jet.
- jet - muon: if $\Delta R(j, \mu) < 0.2$ and the jet has at least three ghost associated (GA) tracks, the muon is removed and the jet kept. If $\Delta R(j, \mu) < 0.2$ and less than three GA tracks are associated to the jet, or the muon itself is GA to the jet, then the latter is discarded. Finally, if $0.2 < \Delta R(j, \mu) < 0.4$, the muon is discarded and the jet is kept.

The last step of the OR procedure involve photons, which are discarded if reconstructed within $\Delta R < 0.4$ of an electron or a muon. If the separation between a jet and a photon is below 0.4, the jet is discarded and the photon is kept.

4.4 Event pre-selection

Events in data are selected with calorimeter based $E_{\text{T}}^{\text{miss}}$ triggers [120] and single electron ones [178]. The former do not use any hits from the muon spectrometer, therefore are suitable also to select $W(\to \mu\nu)/Z(\to \mu\mu)$+jets events.

The $E_{\text{T}}^{\text{miss}}$ triggers used in different periods of the Run 2 data taking campaign are reported in Table 4.1. Trigger chains with increasing thresholds have been used to cope with the evolving rates. The level 1 trigger threshold was kept at 50 GeV, except for the first part of 2017 data taking. The HLT threshold varied between 90 and 110 GeV. The 'mht' and 'pufit' labels refer to different algorithms adopted to reduced pileup contributions. These are described in Ref. [120].

Table 4.1. Missing transverse momentum triggers used to select events.

Period	Fraction of collected events	Trigger chain
2015	-	HLT_xe70_mht
2016		
$296393 \leq \text{run} < 302872$	4.6%	HLT_xe90_mht_L1XE50
$302919 \leq \text{run} \leq 303892$	4.7%	HLT_xe100_mht_L1XE50
$303943 \leq \text{run} \leq 311481$	90.7%	HLT_xe110_mht_L1XE50
2017		
$325713 \leq \text{run} \leq 331975$	12.6%	HLT_xe110_pufit_L1XE55
$332303 \leq \text{run} \leq 341649$	87.4%	HLT_xe110_pufit_L1XE50
2018		
$348197 \leq \text{run} \leq 350066$	0.8%	HLT_xe110_pufit_xe70_L1XE50
$350067 \leq \text{run} \leq 364400$	99.2%	HLT_xe110_pufit_xe65_L1XE50

Different single electron trigger chains have been used via a logical *or* to collect data, and are summarised in Table 4.2. The L1EM20VH trigger is fired if it finds a candidate electron with at least 20 GeV of transverse energy at level 1, and no energy deposits in the hadronic calorimeter; 'lhloose' indicates that the electron is required to satisfy the *loose* identification criterion (the same holds for 'medium' and 'tight'). The suffix 'nod0' indicates that no requirements are set on the d_0 parameter, and 'ivarloose' indicates that the electron is required to pass the *loose* isolation working point. The energy threshold at HLT is defined by the 'HLT_e' part of the trigger chain.

Table 4.2. Single electron triggers used to select events, combined via a logical *or*.

Period	Trigger chain
2015	HLT_e24_lhmedium_L1EM20VH *or* HLT_e60_lhmedium *or* HLT_e120_lhloose
2016, '17, '18	HLT_e26_lhtight_nod0_ivarloose *or* HLT_e60_lhmedium_nod0 *or* HLT_e140_lhloose_nod0

Only events collected while the ATLAS detector was fully functioning are analysed. The corresponding run numbers are stored in a *good run list*.

In the monojet analysis, all the events are required to have at least one primary vertex, as defined in Section 3.1, and to contain at least one central jet ($|\eta| < 2.4$) with $p_{\mathrm{T}} > 150$ GeV. On top of the *Loose* cleaning criterion, the jet is required to satisfy the condition $f_{\mathrm{ch}}/f_{\mathrm{max}} > 0.1$. f_{ch} indicates the fraction of charged particles included in the jet. f_{max} is the largest fraction of energy deposited in one single calorimeter layer. NCB sources tend to have f_{ch} close to 0 and f_{max} close to 1, thus are suppressed by this requirement. To reduce the multijet background, events with jet multiplicity greater than four are rejected.

4.5 Region definition

Events are categorized in six statistically independent regions, based on the number of reconstructed leptons in the event. Such division defines a signal (or search) region and the control regions (CR). These are enriched in background processes including leptons instead, and are used in a simultaneous maximum likelihood fit, described in Section 4.7, to correct the background predictions in the SR using data, without looking at the SR itself.

4.5.1 Signal region

Events passing the pre-selection cuts are assigned to the signal region (SR) if they have $E_{\mathrm{T}}^{\mathrm{miss}} > 200\,\mathrm{GeV}$ and no *baseline* leptons, including τ_{had}, nor photons are reconstructed. To suppress the multijet background, a requirement on the angular distance in the transverse plane between the $\vec{E}_{\mathrm{T}}^{\mathrm{miss}}$ direction and any jet in the event is applied. In the previous iteration of the analysis a $\min\Delta\phi(j, E_{\mathrm{T}}^{\mathrm{miss}}) > 0.4$ selection was applied. Since the multijet background increases significantly when the minimum $E_{\mathrm{T}}^{\mathrm{miss}}$ requirement is lowered to 200 GeV and it has a large associated uncertainty (cf. Section 4.7.1), a tighter selection is applied in the $200\,\mathrm{GeV} < E_{\mathrm{T}}^{\mathrm{miss}} < 250\,\mathrm{GeV}$ bin to reduce its contribution. This choice is further motivated in Section 4.7.1.

In Figure 4.4 the distributions of the missing transverse momentum, jet multiplicity, leading jet p_{T}, leading jet $|\eta|$ and the minimum angular distance between any jet and the direction of the $\vec{E}_{\mathrm{T}}^{\mathrm{miss}}$ are shown for data, and compared to the MC predictions. Events are normalized to the generator cross-sections, and at this stage the V+jets reweighting described in Section 4.2.1 is not applied yet as the purpose is to check the performance of the modelling. The background composition, estimated from MC simulation, shows that more than half of the total background is due to the $Z(\to \nu\bar{\nu})$+jets process. The second-leading background is $W(\to \tau\nu)$+jets. In the MC template both the leptonic and hadronic decays of the τ lepton are included. Top-quark-related backgrounds constitute altogether a subdominant component ($\sim 3\%$). Though, this processes are affected by large modelling uncertainties at high $E_{\mathrm{T}}^{\mathrm{miss}}$, as described in Section 4.8.2. The contribution of multijet and NCB backgrounds is not shown in the plots. These reduce the slight excess of data observed at low $E_{\mathrm{T}}^{\mathrm{miss}}$ and leading jet p_{T} values.

The modelling of the kinematic distributions presented is good. A slight offset is observed in all the distributions, due to known differences between the measured and Sherpa V+jets predicted cross-sections [179]. This motivates the use of CRs to correct the predictions of the simulated samples.

4.5.2 Control regions

A total of five CRs are defined. Four are dedicated to the estimate of the $Z(\to \nu\bar{\nu})$+jets process, and are enriched in V+jets events. The last CR is instead defined to constrain the modelling uncertainties associated with top-quark related processes.

Control regions are defined to be as close as possible to the SR. These are obtained by inverting the lepton veto present in the SR definition. The τ_{had} and γ

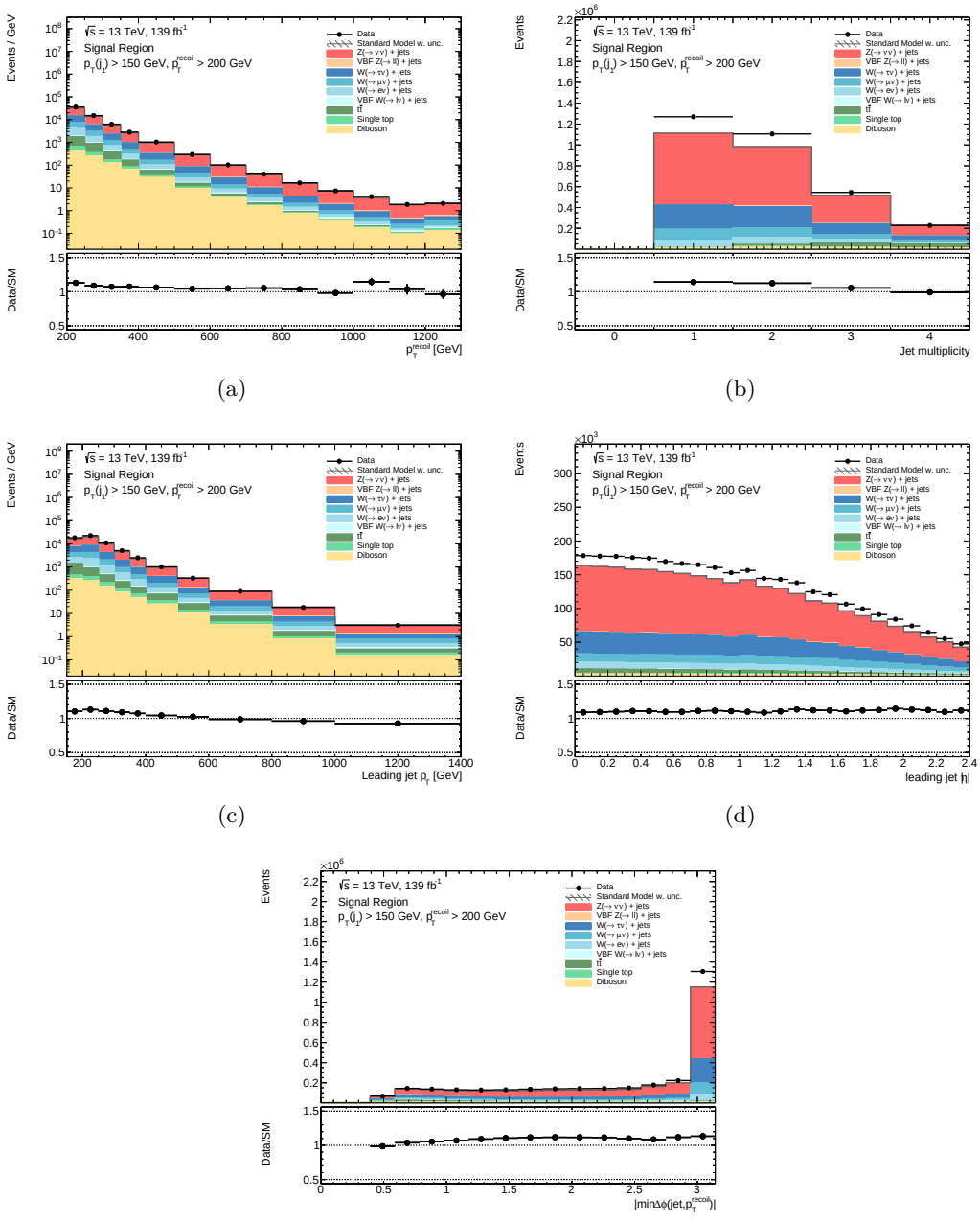


Figure 4.4. Signal region events distributions of the (a) $E_{\mathrm{T}}^{\mathrm{miss}}$, (b) jet multiplicity, (c) leading-jet p_{T} (d) leading-jet $|\eta|$ and (e) minimum $\Delta\phi(j, E_{\mathrm{T}}^{\mathrm{miss}})$. Only MC statistical uncertainties are shown. The generator cross-section is used to normalise the events, and the V+jets reweighting, described in Section 4.2.1, is not applied.

vetoes are kept. The variable used in the simultaneous likelihood fit is the differential distribution of $p_{\mathrm{T}}^{\mathrm{recoil}}$, the magnitude of the 2D vector

$$\vec{p}_{\mathrm{T}}^{\,\mathrm{recoil}} = \vec{E}_{\mathrm{T}}^{\mathrm{miss}} + \sum_{\text{all } \ell} \vec{p}_{\mathrm{T}}(\ell), \tag{4.3}$$

where the sum is performed over all the *signal* leptons identified in the events. The variable defined in this way is a proxy for the transverse momentum of the vector boson in all the regions considered.

The requirement on the angular distance between any jet and the $E_{\mathrm{T}}^{\mathrm{miss}}$ in the event applied in SR is defined in CRs applying the same requirements on $\vec{p}_{\mathrm{T}}^{\,\mathrm{recoil}}$.

Single-electron control region

A control region enriched in the $W(\to e\nu)$+jets process is obtained selecting events with the single electron triggers introduced in Section 4.4. Exactly one *signal* electron which satisfies the *Tight* fixed-cut isolation working point, defined in Section 3.2.1, is required. A veto on events with *baseline* muons, photons or τ leptons is imposed. Events are required to have $p_{\mathrm{T}}^{\mathrm{recoil}} > 200\,\mathrm{GeV}$. To target W+jets events, the transverse mass of the electron-$E_{\mathrm{T}}^{\mathrm{miss}}$ system, defined as $m_{\mathrm{T}} = \sqrt{2p_{\mathrm{T}}(e)E_{\mathrm{T}}^{\mathrm{miss}}\left[1-\cos(\Delta\phi(e, E_{\mathrm{T}}^{\mathrm{miss}})\right]}$, is required to be in the range [30, 110] GeV. To reduce the multijet contribution at high lepton p_{T} two additional cuts are applied: the $E_{\mathrm{T}}^{\mathrm{miss}}$ significance, defined as $\mathcal{S} = E_{\mathrm{T}}^{miss}/\sqrt{H_{\mathrm{T}}}$ with H_{T} the sum of jets p_{T} , is required to be greater than 5, and $E_{\mathrm{T}}^{\mathrm{miss}} > 70\,\mathrm{GeV}$. A b-jet veto is applied to keep the region statistically independent to the one defined to be enriched in top-quark related processes. Pre-fit $p_{\mathrm{T}}^{\mathrm{recoil}}$, leading jet p_{T}, lepton kinematic variables, transverse mass and jet multiplicity distributions are shown in Figure 4.5. The trend observed in the lepton pseudo-rapidity is a known mismodelling of the Sherpa V+jets sample. The dips observed around $\eta = \pm 1.4$ are due to the *crack-region* of the EMC, which is vetoed in the electron reconstruction. Overall a good modelling is observed, and the residual discrepancy is due to known mis-modellings of the Sherpa V+jets samples in part of the phase space.

Single muon control region

$W(\to \mu\nu)$+jets events are selected with the same $E_{\mathrm{T}}^{\mathrm{miss}}$ trigger adopted for the SR. Exactly one *signal* muon, and no other reconstructed *baseline* lepton or photon, is required in the event. Summing up the muon transverse momentum with the $\vec{E}_{\mathrm{T}}^{\mathrm{miss}}$, $\vec{p}_{\mathrm{T}}^{\,\mathrm{recoil}}$ is obtained. Its magnitude is required to be greater than 200 GeV. Also in this case, the transverse mass of the muon-$E_{\mathrm{T}}^{\mathrm{miss}}$ system is required to be $30\,\mathrm{GeV} < m_{\mathrm{T}} < 100\,\mathrm{GeV}$, and a b-jet veto is applied. The pre-fit $p_{\mathrm{T}}^{\mathrm{recoil}}$, leading jet p_{T}, kinematics variables of the lepton, transverse mass and jet multiplicity distributions are shown in Figure 4.6. The dip observed in the muon η distribution around 0 is related to the reduced coverage of the MS. This is due to the presence of shafts to allow the access to the inner part of the ATLAS detector. Also in this case, the muon η asymmetry is a know mismodelling of Sherpa v2.2.1.

Di-electron control region

The di-electron control region is included in the likelihood fit for the first time in this iteration of the ATLAS monojet search. It was already considered for the previous

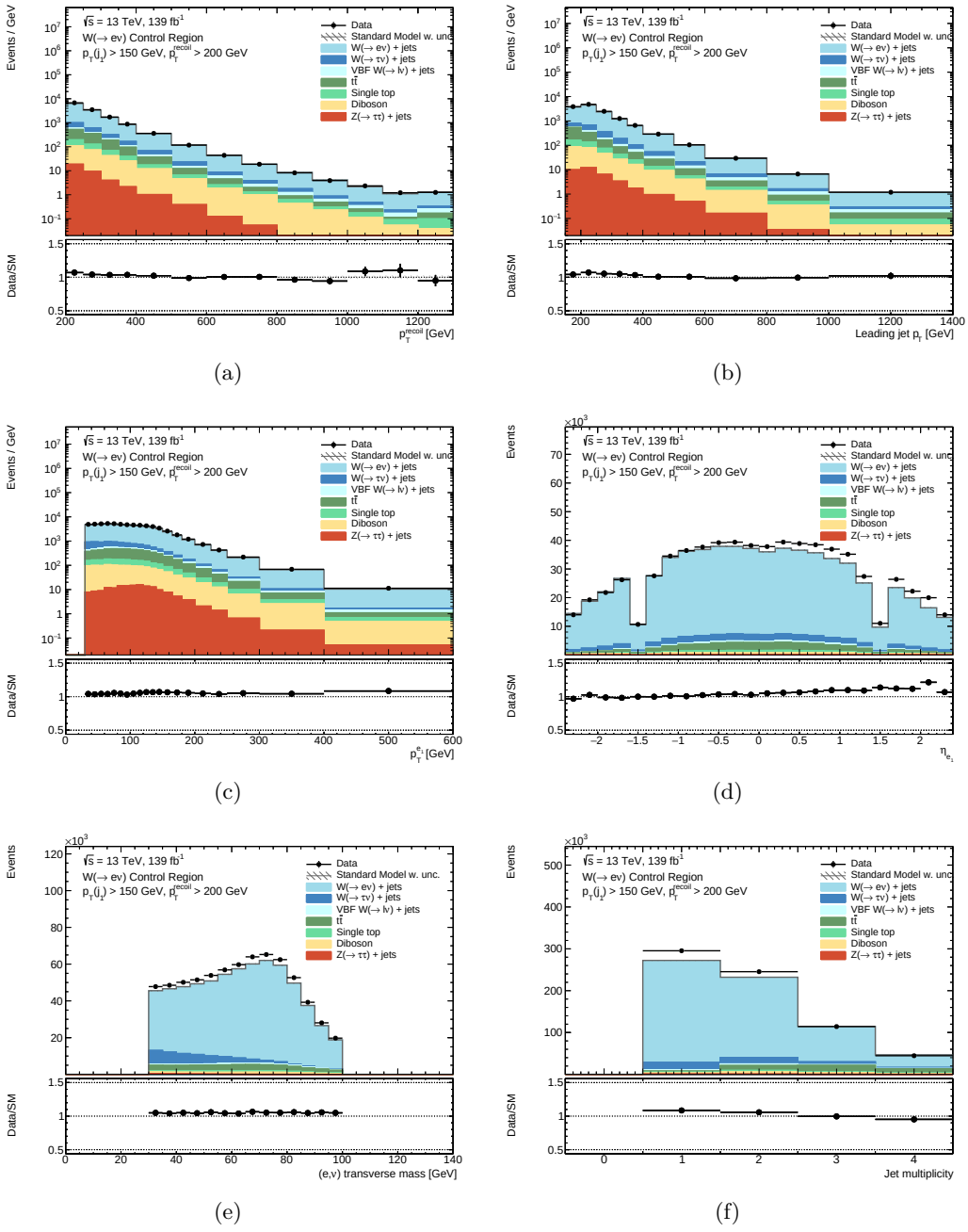


Figure 4.5. Pre-fit (a) $p_{\mathrm{T}}^{\mathrm{recoil}}$, (b) leading jet p_{T} (c) electron p_{T}, (d) electron η, (e) transverse mass of the electron-$E_{\mathrm{T}}^{\mathrm{miss}}$ system, (f) jet multiplicity distributions of the events selected in the single electron CR. Only MC statistical uncertainties are shown. The generator cross-section is used to normalise the events, and the V+jets reweighting, described in Section 4.2.1, is not applied.

one [180], performed with 36 fb^{-1}, but the available statistics was not sufficient to improve the SR backgrounds estimate. $Z(\rightarrow ee)$+jets events are targeted by requiring exactly two reconstructed *signal* electrons, and no other *baseline* lepton or photon.

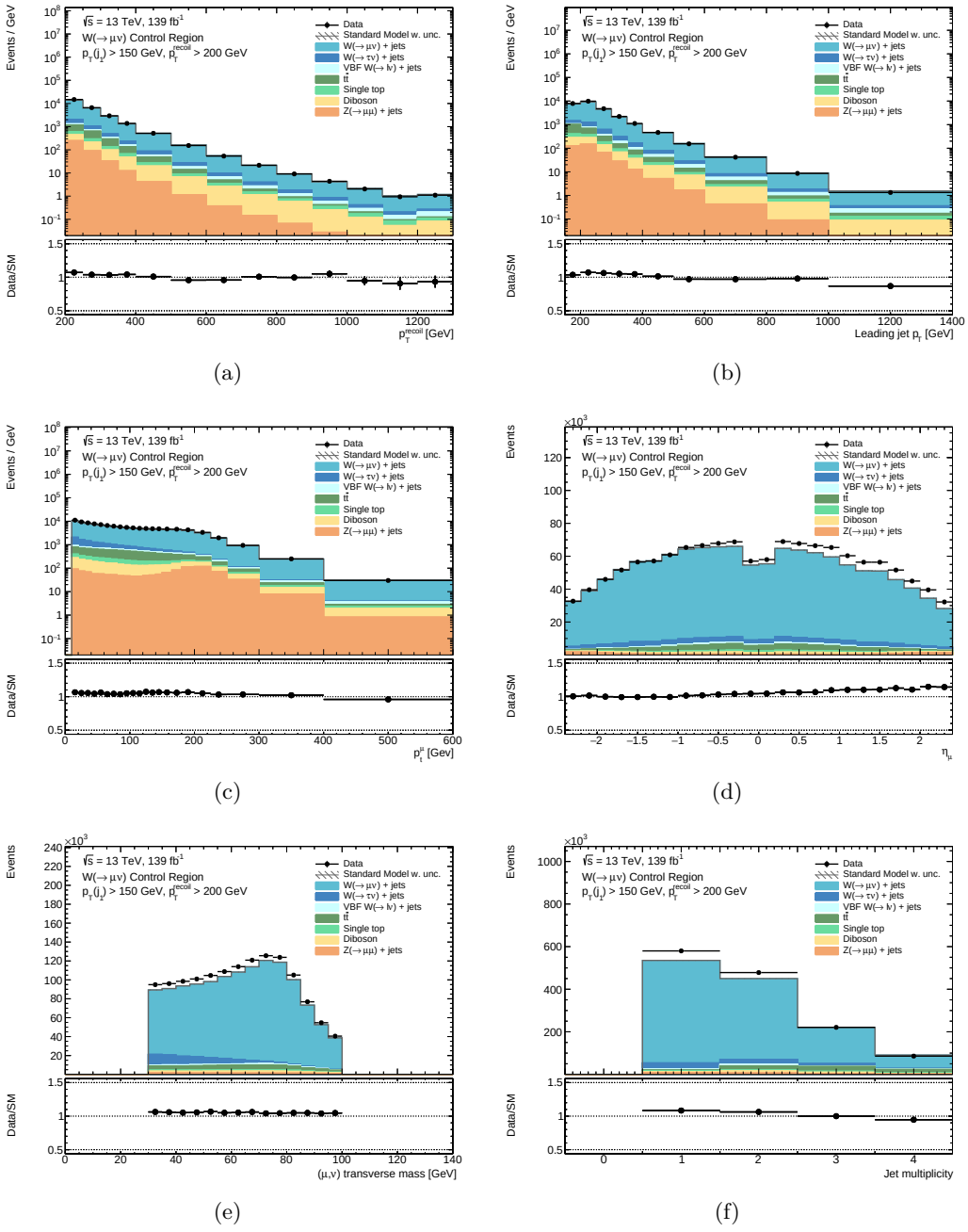


Figure 4.6. Pre-fit (a) $p_{\mathrm{T}}^{\mathrm{recoil}}$, (b) leading jet p_{T} (c) muon p_{T}, (d) muon η, (e) transverse mass of the muon-$E_{\mathrm{T}}^{\mathrm{miss}}$ system, (f) jet multiplicity distributions of the events selected in the single muon CR. Only MC statistical uncertainties are shown. The generator cross-section is used to normalise the events, and the V+jets reweighting, described in Section 4.2.1, is not applied.

No requirement on the charge of the leptons is applied. Single electron triggers are adopted to pre-select data events. The two leptons are required to have an invariant mass $66\,\mathrm{GeV} \leq m_{ee} \leq 116\,\mathrm{GeV}$, and the total $p_{\mathrm{T}}^{\mathrm{recoil}}$ is required to be greater than

200 GeV. The pre-fit modelling of selected kinematic variables, related to jets and the two leptons, is shown in Figure 4.7. This CR is highly pure in $Z(\rightarrow ee)$+jets events, which constitute more than 94% of the total expected background. The introduction of the di-electron CR increases the data statistics available in 2L CRs by $\sim 40\%$, therefore allowing to improve the background estimate.

Di-muon control region

A $Z(\rightarrow \mu\mu)$+jets enriched CR is defined by the selection of data events with the $E_{\mathrm{T}}^{\mathrm{miss}}$ trigger. Exactly two *signal* muons are required to be reconstructed. As for the di-electron CR, the invariant mass of the two muon system is required to be $66\,\mathrm{GeV} < m_{\mu\mu} < 116\,\mathrm{GeV}$. The total recoiling transverse momentum against hadronic activity, $p_{\mathrm{T}}^{\mathrm{recoil}}$, is required to be greater than 200 GeV. In Figure 4.8, the pre-fit distributions of selected kinematic variables regarding jets and the muons in the event are presented.

Top-quark processes control region

As described in Section 4.8.2, large modelling uncertainties affect the top-quark-related processes. One of the major improvements of the previous iteration of the ATLAS monojet analysis [180] was the introduction of a CR with a single muon plus at least one b-tagged jet. In the full Run 2 result presented here, the definition of the top CR has been extended. By the inclusion of events with a single electron plus at least one b-jet, an increase of more than 30% of the available statistics has been achieved. This allows to constrain further the modelling uncertainties associated with the simulation of top-quark-related processes.

The definition of the top CR follows exactly the one of the single electron and single muon CRs, except for the inversion of the b-jet veto. At least one b-tagged jet is required in the events. To improve the statistical power of the region, the electron and muon channels have been merged into a single one. Pre-fit distributions of jet and lepton kinematic variables are shown in Figure 4.9.

A significant mismodelling is observed at high transverse momentum. This is due to know mismodelling of the single-top process: the DR scheme in fact tends to over-estimate the cross-section of the tW process. The shape difference observed in the $p_{\mathrm{T}}^{\mathrm{recoil}}$ distribution between data and the MC prediction will be fixed in the likelihood fit by the single-top modelling systematic uncertainty. More details on this uncertainty are discussed in Section 4.8.2.

The MV2c10 score distribution of the leading jet is presented in Figure 4.10(a). As expected, a peak of events around 1 is observed. This is due to the requirement of at least one b-tagged jet in the events. In a sub-dominant portion of cases the leading jet is not a b-tagged one, as shown by the additional accumulation of events close to -1. Figure 4.10(b) shows instead the minimal angular distance between the $\vec{p}_{\mathrm{T}}^{\,\mathrm{recoil}}$ direction and any jet in the event. As expected, in semi-leptonic $t\bar{t}$ events genuine $E_{\mathrm{T}}^{\mathrm{miss}}$is present due to the neutrinos originated in $t \rightarrow W(\rightarrow \ell\nu)b$ decay. Moreover, in boosted events, the W is likely to be close to the b-jet in the event. W+jets production instead shows a distribution similar to the one observed in the SR, with typically one jet recoiling against the vector boson. The step observed between

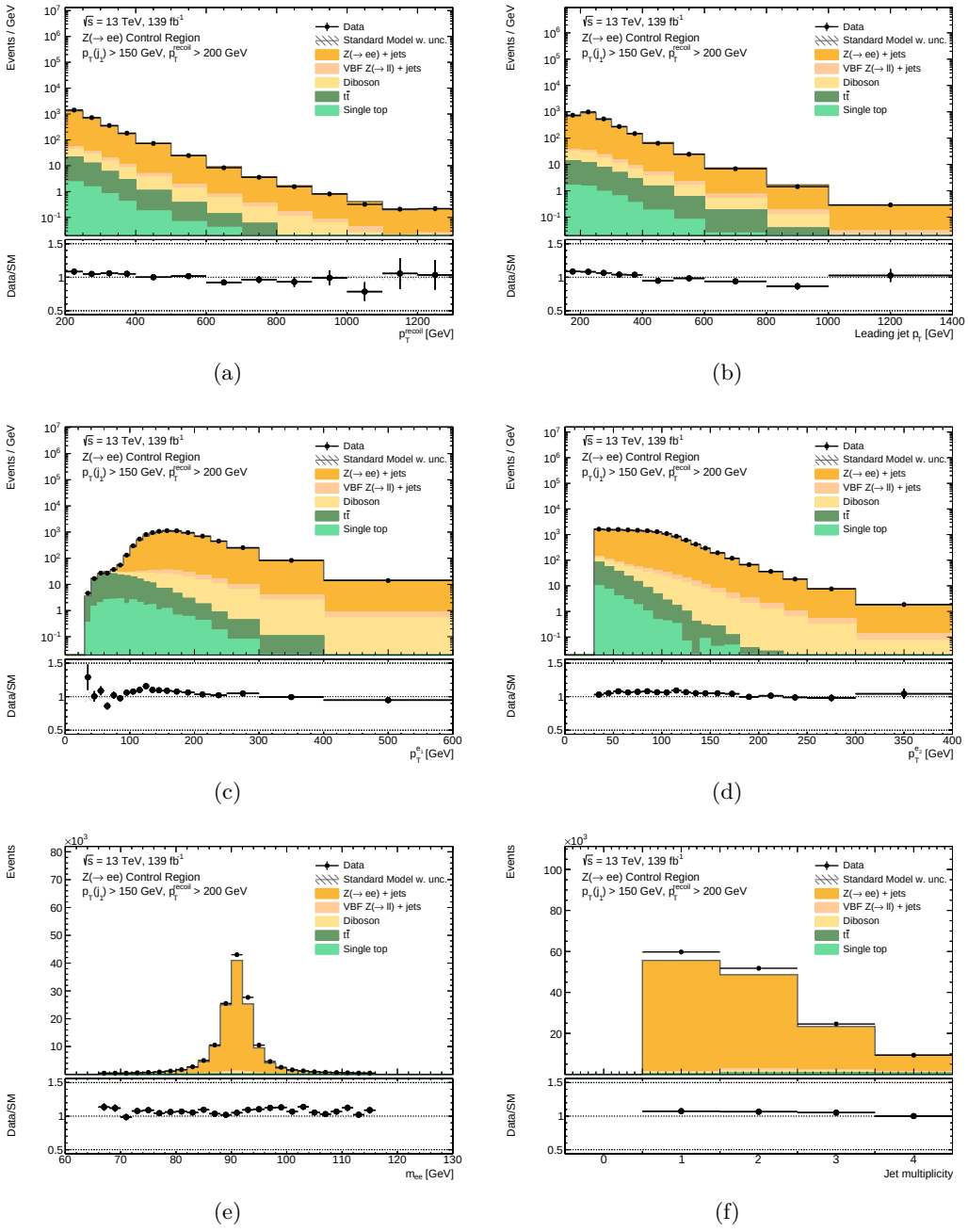


Figure 4.7. Pre-fit (a) $p_{\mathrm{T}}^{\mathrm{recoil}}$, (b) leading jet p_{T}, (c,d) leading and sub-leading electron p_{T}, (e) invariant mass of the di-electron system and (f) jet multiplicity distributions for events selected in the di-electron CR. Only statistical uncertainties are shown. The generator cross-section is used to normalise the events, and the V+jets reweighting, described in Section 4.2.1, is not applied.

the first two left bins of the distribution is due to the fact that the $\min\Delta\phi(j, E_{\mathrm{T}}^{\mathrm{miss}})$ cut is different between the $E_{\mathrm{T}}^{\mathrm{miss}} < 250\,\mathrm{GeV}$ and $E_{\mathrm{T}}^{\mathrm{miss}} < 250\,\mathrm{GeV}$ ranges.

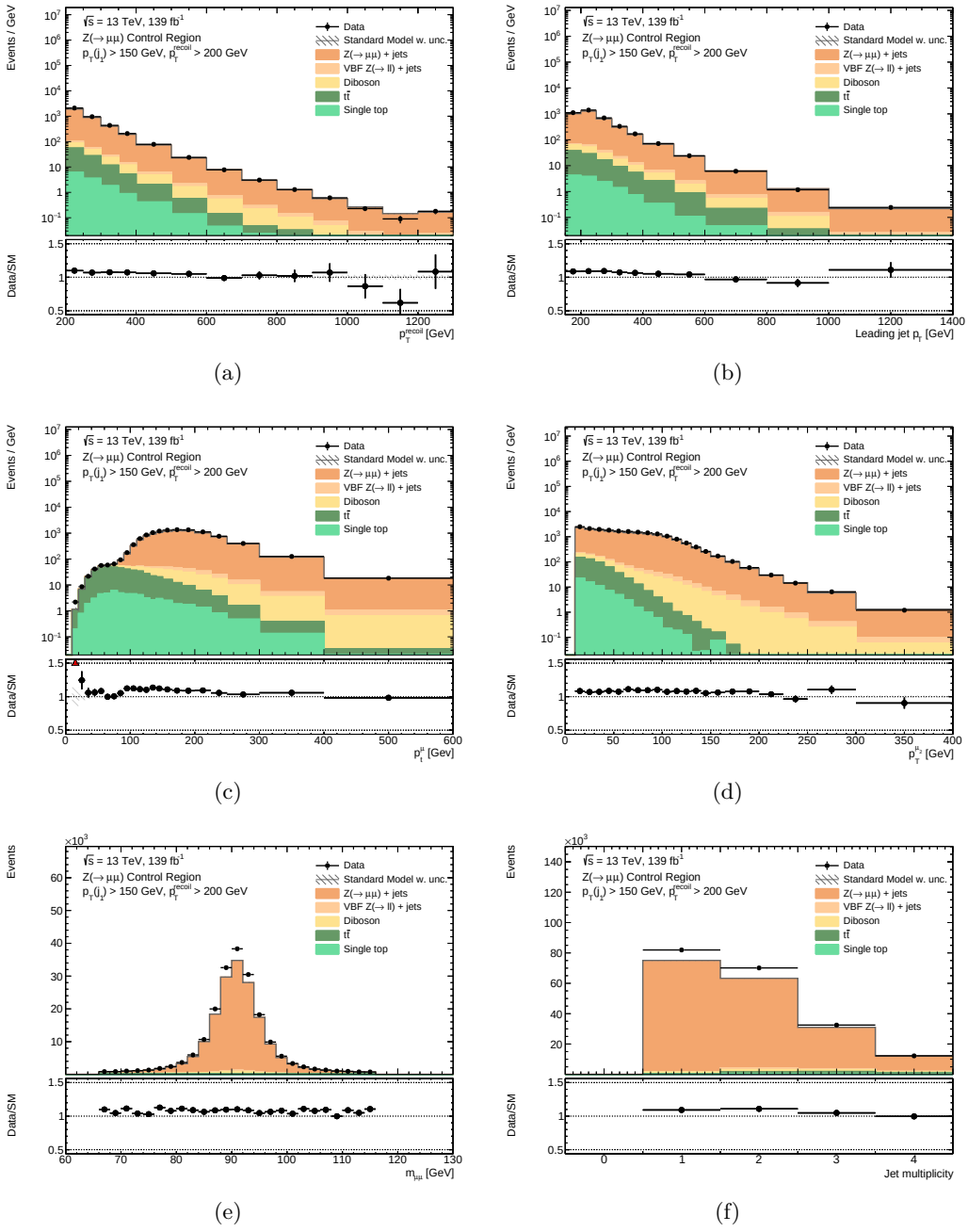


Figure 4.8. Pre-fit (a) $p_{\mathrm{T}}^{\mathrm{recoil}}$, (b) leading jet p_{T} ,(c,d) leading and sub-leading muon p_{T}, (e) invariant mass of the di-muon system and (f) jet multiplicity distributions for events selected in the di-muon CR. Only statistical uncertainties are shown. The generator cross-section is used to normalise the events, and the V+jets reweighting, described in Section 4.2.1, is not applied.

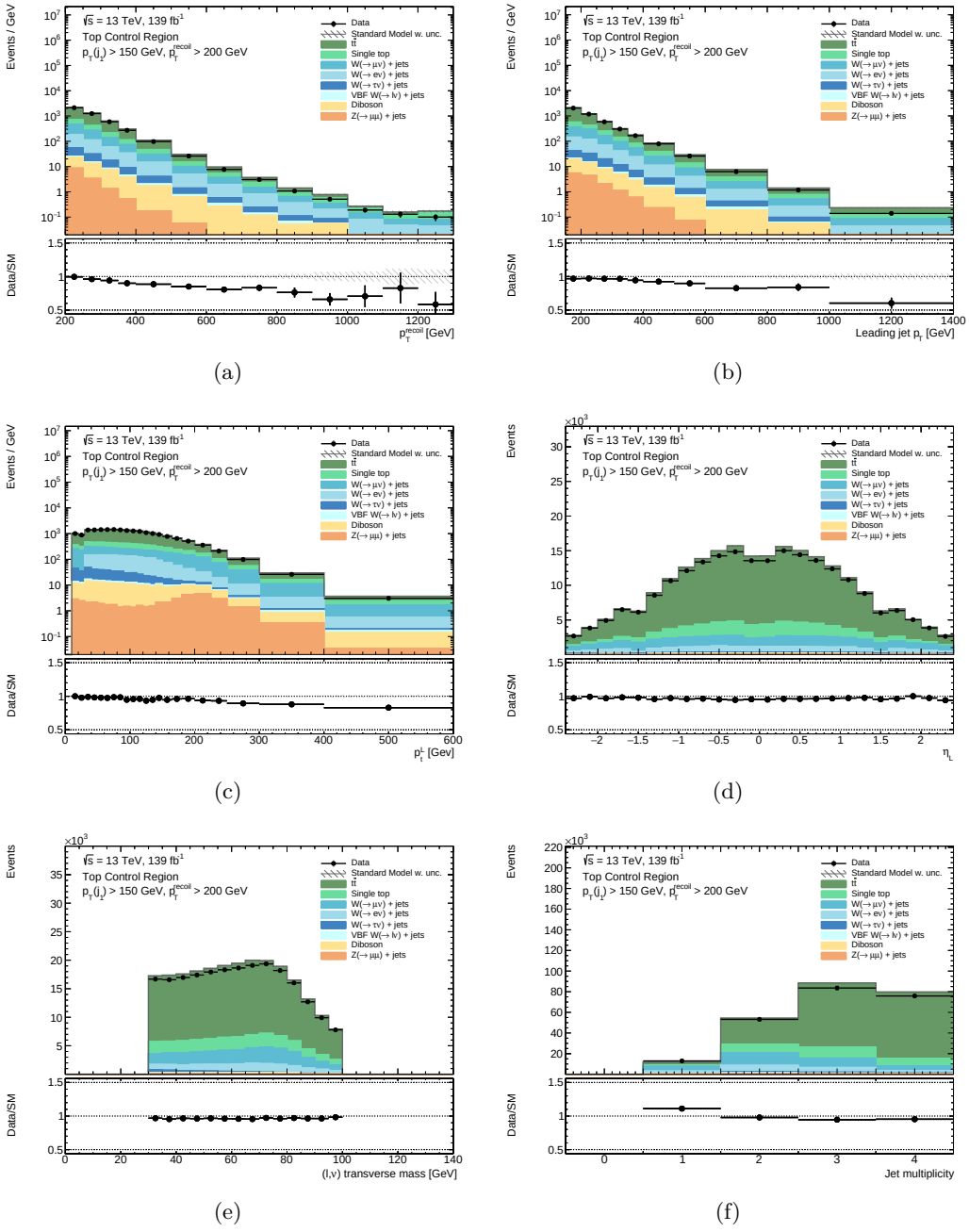
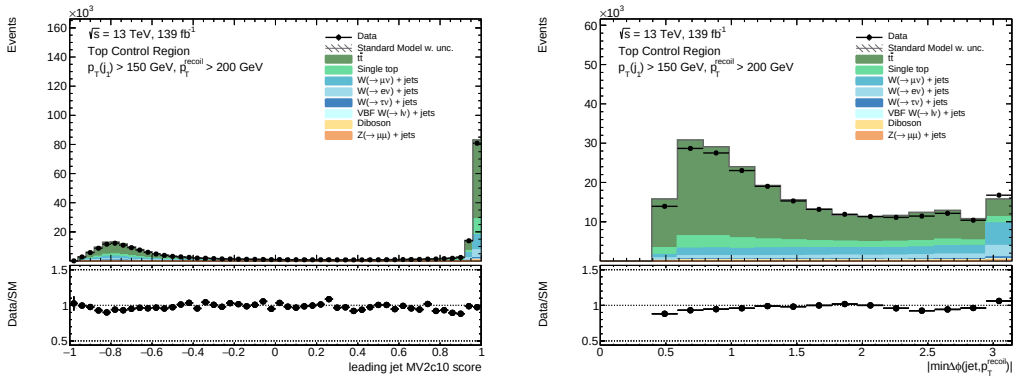


Figure 4.9. Pre-fit (a) $E_{\mathrm{T}}^{\mathrm{miss}}$, (b) leading jet p_{T} (c) lepton p_{T}, (d) lepton η, (e) transverse mass of the ℓ-$E_{\mathrm{T}}^{\mathrm{miss}}$ system and (f) jet multiplicity distributions of the events selected in the top CR. Only statistical uncertainties are shown. Events are normalized to generator cross-section, and the V+jets reweighting, described in Section 4.2.1, is not applied.

4.5.3 Trigger debug stream

As mentioned in Section 2.2.2, data events might cause the high-level trigger to timeout. Therefore, the associated hits are read out on a separate stream, called



(a) (b)

Figure 4.10. Pre-fit (a) leading jet MV2c10 score and (b) $\min\Delta\phi(j, E_{\mathrm{T}}^{\mathrm{miss}})$ distributions of the events selected in the top CR.

debug stream. Such events are reconstructed *offline* (i.e. while the detector is not recording the collisions). Then the usual event selection can be applied to look for any events which should enter one of the aforementioned regions.

A total of 10 events was found to be selected in the monojet analysis regions. Their category, data taking period and $p_{\mathrm{T}}^{\mathrm{recoil}}$ are reported in Table 4.3. No data from the 2017 and 2018 data taking campaign debug stream passed the event selection.

Table 4.3. List of events selected from the trigger debug stream.

Region	Run (year)	$p_{\mathrm{T}}^{\mathrm{recoil}}$ [GeV]
SR	279259 (2015)	209
	279345 (2015)	260
	280423 (2015)	230
	280500 (2015)	290
	280614 (2015)	264
Single muon CR	279169 (2015)	270
	279813 (2015)	252
	279984 (2015)	471
Single electron CR	303208 (2016)	432
Top CR	302137 (2016)	292

4.6 Improvements with respect to the $36.2\,\mathrm{fb}^{-1}$ search

With respect to the previous iteration of the monojet analysis [180], several improvements in the event selection and regions definition have been included.

The main one is the reduction of the $p_{\mathrm{T}}^{\mathrm{recoil}}$ threshold, which has been lowered from 250 GeV to 200 GeV, and of the leading jet p_{T} one, from 250 GeV to 150 GeV.

These two improvements increase the sensitivity of the monojet analysis to signals which have a softer spectrum than SM backgrounds. The sensitivity to WIMP production via pseudo-scalar mediators, described by simplified models introduced in Section 1.6.1, and to the $H \rightarrow$ invisible decays is expected to be improved.

Another significant change is the reduction of the p_{T} thresholds used to define *baseline* leptons. Previously, a minimum p_{T} of 20 GeV was required for both electrons and muons. This value is now 7 GeV. The impact of this change was quantified by looking at the expected background events in SR. Inclusively, a reduction of 8%, 13% and 41% is observed for the $W(\rightarrow \tau\nu)$, $W(\rightarrow \mu\nu)$ and $W(\rightarrow e\nu)$ backgrounds. Also top-quark and dibosons backgrounds are reduced by 19% and 8% respectively.

The introduction of the τ_{had} veto has no effect on the signal efficiency, but allows to reduce the total SR background by 11%. The highest reduction is observed for top-quark-related processes. A reduction in $W(\rightarrow \tau\nu)$ + jets events of around 20% is also observed. Minor reduction in the total background is also obtained in the CR, with an inclusive reduction between 1.5 and 2%.

From the modelling point of view, EW production of V+jets processes have been considered, as with the full Run 2 statistics their contribution is no more negligible in the tail of the $p_{\mathrm{T}}^{\mathrm{recoil}}$ distributions. Moreover, the V+jets theory reweighting, introduced in Section 4.2.1, has been updated according to the latest prescriptions, which promote the cross-section to NNLO QCD and NLO EW accuracy. In the previous iteration of the analysis, the reweight was performed to NLO QCD and NLO EW accuracy.

The extended definition of the top control region and the inclusion of the two-electron control region have been already discussed in the previous Section.

4.7 Background estimation

The main background of the search, V+jets production, is estimated in a semi-data-driven way by correcting MC predictions in the SR by means of the four statistically independent CR defined in the previous Section. The modelling of top-quark processes is corrected in the b-jets enriched CR. The subdominant dibosons and EW induced V+jets processes estimates are taken from MC predictions, and their $p_{\mathrm{T}}^{\mathrm{recoil}}$ distributions can vary only for the effect of systematic uncertainties. Multijet production and NCB contributions are instead estimated via a data driven technique. Further details on the statistical model adopted for the fit are given in Section 4.7.2, while in the next Section the estimate of the data driven backgrounds is presented.

4.7.1 Data driven backgrounds

Multijet production. MC simulations fail to model with sufficient accuracy the non gaussian response of the detector to low-p_{T} jets. Thus, the multijet background is estimated with the so-called jet smearing method. This has been already adopted in the previous iteration of the ATLAS monojet analysis [180], and is described below.

Data seed events are selected using single-jet triggers with thresholds in the [35, 380] GeV range. Since such triggers would exceed the available bandwidth to record

the events, they are pre-scaled with average factors[1] between 40000 and 1. This value depends on the luminosity block, and is available for each of those.

An ATLAS standard tool, which provides jet response functions constrained on data, is used to perform the background estimate. These functions, validated in di-jet and tri-jet final states, are used to smear well-reconstructed multijet seed events. Such sample is selected using a requirement on the $E_{\mathrm{T}}^{\mathrm{miss}}$ significance $\mathcal{S} = \frac{E_{\mathrm{T}}^{\mathrm{miss}} - 8\,\mathrm{GeV}}{\sqrt{E_{\mathrm{T}}}} < 0.05$. The correction factor -8 GeV is introduced to take into account the $E_{\mathrm{T}}^{\mathrm{miss}}$ TST response, which misses the neutral component of the soft term. In these seed events, jets are required to have at least $p_{\mathrm{T}} \geq 20\,\mathrm{GeV}$. A smearing of the four-momentum is performed one thousand times using the aforementioned response functions. The monojet SR selection is then applied. The shape of the multijet background is taken from the accepted events. The normalization of the template is instead extracted from a multijet-enriched CR, defined with the requirement $\min\Delta\phi(j, E_{\mathrm{T}}^{\mathrm{miss}}) < 0.3$. In such region, the contributions from the other SM backgrounds are subtracted using nominal MC predictions.

Due to the expected large contribution and large uncertainty associated with the estimate, the cut defined to reject such background, $\min\Delta\phi(j, E_{\mathrm{T}}^{\mathrm{miss}}) > 0.4$, is further optimized. In order to obtain a multijet background rejection of 97% in the SR, while keeping a 89% efficiency on $Z(\nu\bar{\nu})$+jets events, this quantity is required to be greater than 0.6 in the first $p_{\mathrm{T}}^{\mathrm{recoil}}$ bin. In the second SR $p_{\mathrm{T}}^{\mathrm{recoil}}$ bin, a cut $\min\Delta\phi(j, E_{\mathrm{T}}^{\mathrm{miss}}) > 0.4$ leads to a $Z(\nu\bar{\nu})$+jets efficiency of 92% and a multijet background rejection of 97%. The corresponding values for a threshold of 0.6 would be 89% and 98%, thus justifying the choice of a different cut between the first two $p_{\mathrm{T}}^{\mathrm{recoil}}$ bins.

The estimate of the multijet background is reported in Table 4.4. Negligible contribution is observed above 600 GeV. A conservative uncertainty of 100% is applied to the predictions.

Table 4.4. Multijet background SR estimates, obtained with the jet smearing method.

$E_{\mathrm{T}}^{\mathrm{miss}}$ bin [GeV]	Multijet yields ±100%
[200, 250]	18605
[250, 300]	5422
[300, 350]	1131
[350, 400]	387
[400, 500]	57
[500, 600]	5
$\sum$	25607

Non-collision background. As previously mentioned in Section 4.2, monojet-like topologies might arise from highly-energetic muons produced in the interaction between the beam halo and LHC collimators. These fake jets can be discriminated from the collision-originated ones by looking at the timing variable t_{jet}. This is defined as the average of the individual times of jet energy deposits, weighted by

[1] A pre-scaling factor of 10 means that on average one over 10 actual events is recorded.

their fraction to the total energy. The time is evaluated with respect to the one of the trigger. The distance with respect to the IP is taken into account by considering an offset corresponding to the time a light-speed particle would take to reach such detector element. NCB sources have $|t_{\text{jet}}| > 5\,\text{ns}$, as measured in unpaired bunches [181]. The estimate of NCB background is performed in four consecutive steps. A NCB enriched region is produced applying SR cuts, but inverting the tight cleaning requirement on the leading jet. The total number of events is N_{NCB}. In this region, the number of out of time (OOT) events with $t_{\text{jet}} < -5\,\text{ns}$ is counted, and a tagging efficiency is defined as $\varepsilon_{\text{NCB}} = N_{\text{NCB}}^{\text{OOT}}/N_{\text{NCB}}$. By counting the OOT events in SR, the final estimate of the NCB background is given by $\text{NCB}_{SR} = N_{\text{SR}}^{\text{OOT}}/\varepsilon_{\text{NCB}}$. The estimated yields for each data taking year are reported in Table 4.5. Negligible contribution is observed for $p_{\text{T}}^{\text{recoil}} > 700\,\text{GeV}$. As for the multijet background, a conservative 100% uncertainty is applied on the yields.

Table 4.5. NCB SR estimates obtained with the jet timing method.

$E_{\text{T}}^{\text{miss}}$ bin [GeV]	NCB yields ±100%
[200, 250]	3513
[250, 300]	781
[300, 350]	243
[350, 400]	87
[400, 500]	46
[500, 600]	15
[600, 700]	8
$\sum$	4693

4.7.2 Statistical model

The observable used in the simultaneous fit is the $p_{\text{T}}^{\text{recoil}}$ distribution. This coincides with $E_{\text{T}}^{\text{miss}}$ in the SR. The binning adopted in the maximum-likelihood fit is reported in Table 4.6. In the following, the bins are also referred to as EMX, with X from 0 to 12.

Table 4.6. Binning of the $p_{\text{T}}^{\text{recoil}}$ distribution chosen for the maximum-likelihood fit.

$p_{\text{T}}^{\text{recoil}}$ bins[GeV]						
[200, 250)	[250, 300)	[300, 350)	[350, 400)	[400, 500)	[500, 600)	[600, 700)
[700, 800)	[800, 900)	[900, 1000)	[1000, 1100)	[1100, 1200)	[1200+)	

Nominal background predictions can vary in the fit for the effect of free-floating normalisation factor, κ, and gaussian-constrained nuisance parameters (NPs), α. The latter are used to parameterize the effect of systematic uncertainties of experimental and theoretical nature. The NP, as taken fully correlated among the different $p_{\text{T}}^{\text{recoil}}$ bins, can affect both the normalization and the shape of the distributions. Additional gaussian-constrained NPs, γ *stat.* parameters, describe the effect of MC statistical uncertainty.

One single normalization factor, κ_V, multiplies the bin-by-bin event yield predictions for V+jets processes. The correlated estimate between W and Z+jets processes is possible thanks to a set of systematic uncertainties provided together with the V+jets reweighting procedure described in Section 4.2.1, which take into account differences between the W and Z processes. These are discussed further in Section 4.8.2, and allow to estimate the irreducible $Z(\to \nu\bar{\nu})$+jets irreducible background via W and Z enriched CR.

Two separate normalization factors are used to correct the predictions of the $t\bar{t}$, $\kappa_{t\bar{t}}$, and single top-quark, κ_t, processes. This is motivated by the fact that the two processes have two different $p_{\mathrm{T}}^{\mathrm{recoil}}$ differential distributions, as can be observed in Figure 4.9(a). Furthermore, this decorrelation improves the background modelling in the top CR. The three normalization factors are taken to be fully correlated among different bins and regions.

The complete likelihood model is given by the product of Poisson distributions ($\mathcal{P}$) of observing N_{ri}^{obs} data events given the expected number of total events in each bin $p_{\mathrm{T}}^{\mathrm{recoil}}$ bin i and of each region r, multiplied by gaussian distributions of parameters α and γ which introduce the effect of systematic uncertainties on the expected yields

$$\mathcal{L} = \prod_r \prod_i \mathcal{P}\left(N_{ri}^{\mathrm{obs}} | N_{ri}^{\mathrm{exp}}(\kappa, \vec{\alpha}, \vec{\gamma})\right) \prod_\alpha \mathcal{G}\left(\alpha|0,1\right) \prod_\gamma \mathcal{G}\left(\gamma|1,\delta_\gamma\right). \tag{4.4}$$

The expected number of events in each region and bin is given by the sum of expected signal and background events, $N_{ri}^{\mathrm{exp}} = \mu N_{ri}^{\mathrm{sig}} + N_{ri}^{\mathrm{bkg}}$. Signal predictions are scaled by a freely-floating normalisation factor, μ, which is called *signal strength*. Expected background yields can be expressed as

$$\begin{aligned} N_{ri}^{\mathrm{bkg}} = \kappa_V \Big(& N_{ri}^{Z(\nu\bar{\nu})+\mathrm{j}} + N_{ri}^{W(e\nu)+\mathrm{j}} + N_{ri}^{W(\mu\nu)+\mathrm{j}} + N_{ri}^{W(\tau\nu)+\mathrm{j}} + \\ & + N_{ri}^{Z(ee)+\mathrm{j}} + N_{ri}^{Z(\mu\mu)+\mathrm{j}} + N_{ri}^{Z(\tau\tau)+\mathrm{j}} \Big) + \\ & + \kappa_{t\bar{t}} N_{ri}^{t\bar{t}} + \kappa_t N_{ri}^{\mathrm{single}-t} + \\ & + N_{ri}^{\mathrm{diboson}} + N_{ri}^{\mathrm{EW}\,W+j} + N_{ri}^{\mathrm{EW}\,Z+j} + \\ & + N_{ri}^{\mathrm{multijet}} + N_{ri}^{\mathrm{NCB}}. \end{aligned} \tag{4.5}$$

As already mentioned, each term of Equation 4.5 can vary for the effect of systematic uncertainties as

$$N_{ri} = N_{ri}^{\mathrm{nominal}} \cdot (1 + \sum_j f(\alpha_j)\theta_{ri}^j) \cdot \gamma_{ri}, \tag{4.6}$$

where α_j is associated to a specific source of systematic uncertainty j, and θ_{ri}^j is the relative size of such uncertainty in the region r and bin i. Two values are given as input, and commonly referred to as $\pm 1\sigma$ variations, and a function f, a sixth-grade polynomial up to $\alpha = 1$, and an exponential extrapolation for larger values is chosen, as described in Ref. [182], to infer the number of expected events for each value of the α parameter.

As previously mentioned, γ NPs parameterize the effect of MC statistical uncertainties. Their size, δ_γ, corresponds to the relative MC statistical uncertainty in a given bin. Also these parameters have a gaussian constraint, and the total MC yields vary in a continuous way between the nominal value and the $\pm 1\sigma$ variations. Gamma parameters are treated as fully uncorrelated, as it is assumed that every $p_{\mathrm{T}}^{\mathrm{recoil}}$ of every region is an independent counting experiment. These parameters are included only if the relative MC statistical uncertainty of the total background in one bin, σ_i^{exp}, is such that $\sqrt{N^{\mathrm{obs}_{ri}}} < 10 \cdot \sigma_{ri}^{\mathrm{exp}}$. For this reason, gamma parameters are included for the bins at large $p_{\mathrm{T}}^{\mathrm{recoil}}$ values, where the equivalent integrated luminosity of simulated samples is necessarily limited.

4.7.3 Fit strategies

Two set of fits are performed to the data, called hereafter exclusive and inclusive. Exclusive fits adopt the bins defined in Table 4.6, and are performed in three consecutive steps. First, a *control-region-only* fit is performed. This allows an unbiased estimate of the total SR background, and of the impact of systematic uncertainties on it. If no significant deviations from SM predictions are observed, a *signal-plus-control-region* (SR+CRs) fit in the background-only hypothesis, i.e. fixing $\mu = 0$, is performed. This gives a feeling on how much the predictions change by introducing also the SR in the fit. Finally, a SR+CR fit under different BSM hypotheses is performed introducing the signal predictions and floating the signal strength. Upper limits are set on the parameters of such models.

Thirteen inclusive fits are performed by considering single-binned regions. These are called IM, from 0 to 12. These regions are built by integrating the expected yields over the $p_{\mathrm{T}}^{\mathrm{recoil}}$ bins for the different thresholds. From such fits, model-independent limits on the visible cross-section, defined as $\sigma_{\mathrm{sig}}^{\mathrm{vis}} = \sigma_{sig} \times A \times \varepsilon$ with A the acceptance and ε the reconstruction efficiency, are derived.

4.8 Systematic uncertainties

The overall normalization and shape of the $p_{\mathrm{T}}^{\mathrm{recoil}}$ distributions used in the fit can vary for the effect of systematic uncertainties. Sources of uncertainty can be divided in two groups. One associated with the measurement of physics objects, i.e. experimental. One due to uncertainties on the theoretical predictions used in the MC simulation, i.e. modelling.

4.8.1 Experimental uncertainties

Experimental uncertainties are related to the measurement of the energy and momentum scales of the reconstructed objects, as well as to the reconstruction, identification and selection efficiencies. These affect all the MC simulated samples, thus the multijet and NCB processes are excluded, as they are data-driven. Variations of the $p_{\mathrm{T}}^{\mathrm{recoil}}$ spectrum are obtained by propagating the effect of each NP through the monojet analysis selection.

Luminosity. An uncertainty of 1.7% is set on the combined full-Run 2 ATLAS data set. The evaluation is documented in Ref. [123]. Such uncertainty is expected to cancel out in the background estimation procedure, as it assumes the same value for every process, and is flat as a function of $p_{\mathrm{T}}^{\mathrm{recoil}}$.

Jets. The jet energy scale (JES) calibration and the jet energy resolution (JER) measurement are affected by uncertainties, as described in Section 3.3. Five NPs are associated to the η inter-calibration procedure, 30 NPs are associated to the JES in-situ measurement and 13 NPs to the JER one. The latter cover both the case in which the resolution is higher in MC than in data, and vice versa. Additional systematic uncertainties account for the jet composition, the single particle response at high-p_{T}, possible punch-through effects and the efficiency of the JVT cut requirement. The JES uncertainty of b-jets (BJES) is treated separately.

Flavour tagging of jets. Fifteen NPs are related to the flavour-tagging procedure. Three, four and five NPs account for the variation of FTAG SF respectively of b-, c- and light-flavour jets. Two separate NPs account for the extrapolation of the tagging SF from the calibrated range to high p_{T} jets, and from c-quark to τ-lepton originated jets.

Missing transverse momentum. Uncertainties on the measurement of the scale and resolution of the TST of $\vec{E}_{\mathrm{T}}^{\mathrm{miss}}$ are propagated through the monojet analysis. These account for the effects described in Section 3.4. Three independent NPs are introduced: one for the uncertainty on the resolution of the measurement of the longitudinal component, one for the transverse component and one for the scale measurement.

Electrons. Two NPs are introduced to take into account uncertainties associated to the trigger procedure. Concerning electron identification, two different systematic schemes have been adopted for the regions which require reconstructed electrons and for the ones which set a veto on such objects. This choice is motivated by the fact that different identification working points are used to identify the electrons the two cases. In regions requiring *signal* electrons, the *Simplified* scheme adopted include respectively 16 and 18 correlated and uncorrelated variations of the identification scale factors across different (p_{T}, η) bins. This reflects a more accurate description of the identification performance, and therefore of the systematic uncertainty effects. In SR, single and di-muon CR instead, a simpler scheme, called *Total*, is used, and it includes only one single NP to parameterize electrons identification uncertainties.

Reconstruction and isolation efficiency uncertainties are taken into account by two separate NPs. Two additional NPs describe the energy scale and energy resolution uncertainties.

Muons. Systematic uncertainties on the muon reconstruction and identification efficiency are separated for $p_{\mathrm{T}}(\mu)$ below and above 15 GeV. NPs are introduced to take into account uncertainties on the track-to-vertex association performed for the reconstruction of combined muons, and on the resolution of the p_{T} measurement performed with the ID and the MS. Two NPs parameterize the uncertainty in the

measurement of the sagitta due to the alignment of the ID.

To cover differences in the identification efficiency of *Medium* muons with $p_{\mathrm{T}} > 300\,\mathrm{GeV}$, as measured in data and MC, additional uncertainties are derived in 5 bins of muon-p_{T} and 3 $|\eta|$ intervals. These contributions add up to fifteen extra NPs, whose effect is mainly present in the tail of the $p_{\mathrm{T}}^{\mathrm{recoil}}$ distribution of the $Z(\rightarrow \mu\mu)$+jets CR.

Tau leptons. Two NPs are introduced to take into account uncertainties in the τ_{had} reconstruction, while six reflect uncertainties in the identification procedure, as parameterized in different bins of τ p_{T}. Separate contributions are derived for one- and three-prong tracks. Additional three NP account for uncertainties in the calibration procedure.

Pileup modelling. One nuisance parameter takes into account the uncertainty associated to the pileup-reweighting procedure adopted to match in simulation the distribution of the average number of interactions per bunch-crossing observed in data.

A summary of all the systematic uncertainties, along with the name of the NP used in the technical implementation of the fit, is shown in Table 4.8 and Table 4.7.

The pre-fit effect of experimental systematic uncertainties, defined as the variation of the total background in each bin, is presented for the SR and all the CR in Figure 4.11, and compared to the data statistical uncertainty. NPs belonging to the same category are summed in quadrature. Sub-dominant contributions are neglected, as described in the next Section. Flavour-tagging-related systematic uncertainties affect the background predictions only in the regions where either a veto or a selection on b-jets is present.

Smoothing and pruning of systematic uncertainties

Systematic uncertainties can modify the shape of the $p_{\mathrm{T}}^{\mathrm{recoil}}$ distribution. Therefore its crucial to ensure that non-physical fluctuations due to limited MC statistic are removed. Moreover, large changes in the expected yields for a given background in two consecutive bins can lead to instabilities in the numerical minimization of the likelihood during the fit procedure. For these purposes, a smoothing of the systematic shapes is performed. Two algorithms have been adopted: the monotonic and the parabolic rebinning. Both evaluate the MC statistical uncertainty in each bin of the $p_{\mathrm{T}}^{\mathrm{recoil}}$ distribution. For the bins in which this is above a fixed threshold, the monotonic (parabolic) algorithm rebins until no extrema (at most one local extremum) in the shape is left.

Sub-percent-level uncertainties on processes contributing at the percent level to the total background have no power at all in the fit, nor impact on the final result. Instead, they introduce numerical instabilities in the likelihood minimization procedure. Therefore, NPs parameterizing uncertainties which have negligible impact on the final result are not included in the likelihood model. In the previous iteration of the analysis pruning was performed on a bin-by-bin basis. If the associated variation of the process in one bin was below 0.1% (pre-fit), the NP was removed

from only that bin. In the analysis presented in this thesis a new *global-aware* pruning is developed. It is based on three consecutive steps:

1. the integrated $p_{\mathrm{T}}^{\mathrm{recoil}}$ distribution of the process must be greater than 0.2% of the total integrated background of the region considered;
2. the systematic variation must be greater than 0.2% in at least one $p_{\mathrm{T}}^{\mathrm{recoil}}$ bin;
3. the effect of the systematic variation on the process considered must vary its yields by more than 0.002% of the total background in at least one $p_{\mathrm{T}}^{\mathrm{recoil}}$ bin.

If all the conditions above are satisfied, then the systematic shape is included in the likelihood model for every bin of the region considered. Pruning and smoothing are applied only to experimental systematic uncertainties, and largely improve the numerical stability of the fit. The systematic uncertainty associated to the luminosity measurement is always applied.

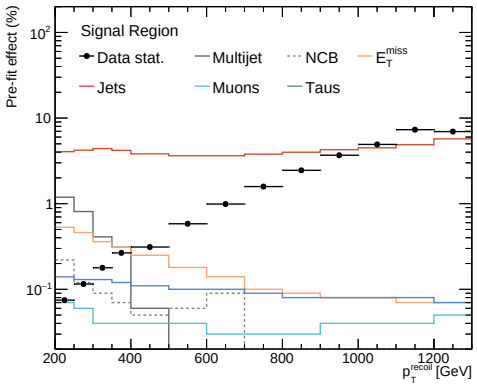
Most of the systematic uncertainties associated to the reconstruction of τ_{had} leptons are removed from the likelihood model, as well as the ones associated with low p_{T} muons (below 15 GeV).

Table 4.7. Summary of the experimental systematic uncertainties related to leptons.

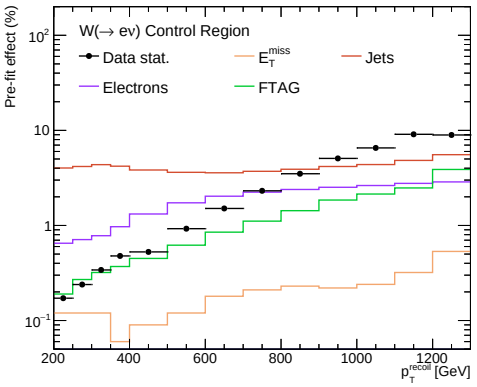
Systematic uncertainty	Short description
Electrons	
EL_EFF_Trigger_TOTAL_1NPCOR_PLUS_UNCOR EL_EFF_TriggerEff_TOTAL_1NPCOR_PLUS_UNCOR	trigger efficiency unc.
EL_EFF_Reco_TOTAL_1NPCOR_PLUS_UNCOR	unc. on the reconstruction efficiency
EL_EFF_ID_CorrUncertaintyNP	16 correlated identification efficiency uncertainties of *signal* electrons
EL_EFF_ID_UncorrUncertaintyNP	18 uncorrelated identification efficiency uncertainties of *signal* electrons
EL_EFF_ID_TOTAL_1NPCOR_PLUS_UNCOR	identification efficiency unc. of *baseline* electrons
EL_EFF_Iso_TOTAL_1NPCOR_PLUS_UNCOR	isolation efficiency unc.
EG_SCALE_ALL	energy scale unc.
EG_RESOLUTION_ALL	energy resolution unc.
Muons	
MUON_EFF_RECO_STAT MUON_EFF_RECO_SYS	reconstruction unc. for $p_{\mathrm{T}}(\mu) > 15\,\mathrm{GeV}$
MUON_EFF_RECO_STAT_LOWPT MUON_EFF_RECO_SYS _LOWPT	reconstruction and ID efficiency unc. for $p_{\mathrm{T}}(\mu) < 15\,\mathrm{GeV}$
MUON_ISO_STAT MUON_ISO_SYS	isolation efficiency unc.
MUON_TTVA_STAT MUON_TTVA_SYS	track-to-vertex association efficiency unc.
MUONS_SCALE	transverse momentum scale unc.
MUONS_SAGITTA_RHO MUONS_SAGITTA_RESBIAS	variations in the scale of the momentum from the sagitta measurement
MUONS_ID	momentum resolution unc. from inner detector
MUONS_MS	momentum resolution unc. from muon system
MUON_EFF_ID_HighPT	unc. to cover mismodelling of *Medium* muons at high p_{T}
Tau leptons	
TAUS_TRUEHADTAU_EFF_RECO_HIGHPT	reconstruction unc. for 3-prong taus with $p_{\mathrm{T}} > 100\,\mathrm{GeV}$
TAUS_TRUEHADTAU_EFF_RECO_TOTAL	τ_{had} reconstruction unc.
TAUS_TRUEHADTAU_EFF_JETID_1PRONGSTATSYSTUNCORR2025	statistical unc. on the identification eff. for 1-prong taus with $20 < p_{\mathrm{T}} < 25\,\mathrm{GeV}$
TAUS_TRUEHADTAU_EFF_JETID_1PRONGSTATSYSTUNCORR2530	statistical unc. on the identification eff. for 1-prong taus with $25 < p_{\mathrm{T}} < 30\,\mathrm{GeV}$
TAUS_TRUEHADTAU_EFF_JETID_1PRONGSTATSYSTUNCORR3040	statistical unc. on the identification eff. for 1-prong taus with $30 < p_{\mathrm{T}} < 40\,\mathrm{GeV}$
TAUS_TRUEHADTAU_EFF_JETID_1PRONGSTATSYSTUNCORRGE40	statistical unc. on the identification eff. for 1-prong taus with $p_{\mathrm{T}} > 40\,\mathrm{GeV}$
TAUS_TRUEHADTAU_EFF_JETID_3PRONGSTATSYSTUNCORR2030	statistical unc. on the identification eff. for 3-prong taus with $20 < p_{\mathrm{T}} < 30\,\mathrm{GeV}$
TAUS_TRUEHADTAU_EFF_JETID_3PRONGSTATSYSTUNCORRGE30	statistical unc. on the identification eff. for 3-prong taus with $p_{\mathrm{T}} > 30\,\mathrm{GeV}$
TAUS_TRUEHADTAU_EFF_JETID_HIGHPT	statistical unc. on the identification efficiency of taus with $p_{\mathrm{T}} > 100\,\mathrm{GeV}$
TAUS_TRUEHADTAU_EFF_JETID_SYST	systematic unc. on the identification of τ_{had}
TAUS_TRUEHADTAU_SME_TES_DETECTOR	unc. on the τ energy scale due to detector effects
TAUS_TRUEHADTAU_SME_TES_INSITU	unc. on the τ energy scale due to in-situ corrections
TAUS_TRUEHADTAU_SME_TES_MODEL	unc. on the τ energy scale due the MC modelling

Table 4.8. Summary of the experimental systematic uncertainties related to jets, missing transverse momentum and other effects.

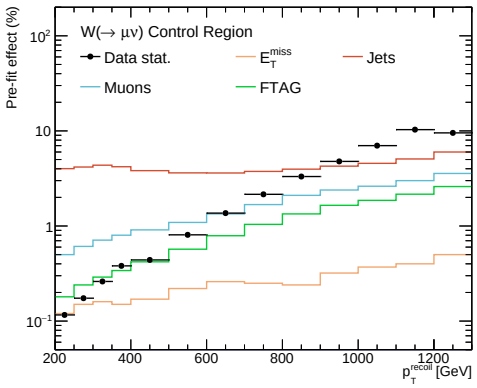
Systematic uncertainty	Short description
Luminosity	unc. on the total integrated luminosity
Pileup	
PRW_DATASF	unc. on the pileup reweighting procedure
Jets	
JET_EffectiveNP	JES uncertainties, 30 NP
JET_EtaIntercalibration	calibrate the scale of forward jets with respect to central jets, 5 NP
JET_FullJER_EffectiveNP	JER uncertainties, 13 NP
JET_Flavour_Composition	uncertainties on the fraction of HF hadrons in a jet
JET_Flavour_Response	uncertainties on the particle originating the jet (quark vs gluon)
JET_SingleParticle_HighPt	effect on the in-situ calibration of single particle response unc.
JET_PunchThrough_MC16	Punch-through unc.
JET_Pileup	uncertainties associated to the pileup energy corrections
JvtEfficiency	JVT efficiency unc.
JET_BJES	JES for b-quark originated jets
Flavour tagging	
FT_EFF_EIGEN_B	unc. on the tagging SF derived for b-jets, 3 NP
FT_EFF_EIGEN_C	unc. on the tagging SF derived for c-jets, 4 NP
FT_EFF_EIGEN_Light	unc. on the tagging SF derived for light-flavour jets, 5 NP
FT_EFF_EIGEN_extrapolation	b-tagging efficiency unc. on the extrapolation on high p_{T}-jets
FT_EFF_EIGEN_extrapolation_from_charm	b-tagging efficiency unc. on τ-jets
Missing transverse momentum	
MET_SoftTrk_Scale	track-based soft term related to longitudinal scale unc.
MET_SoftTrk_ResoPerp	resolution unc. of the TST transverse component
MET_SoftTrk_ResoPara	resolution unc. of the TST longitudinal component



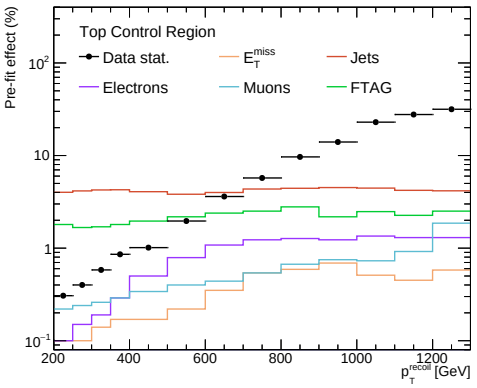
(a) Signal Region



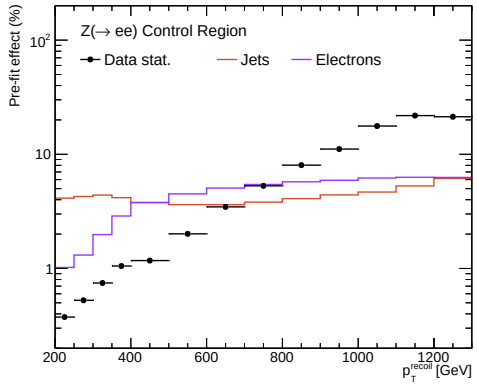
(b) $W(\rightarrow e\nu)$ Control Region



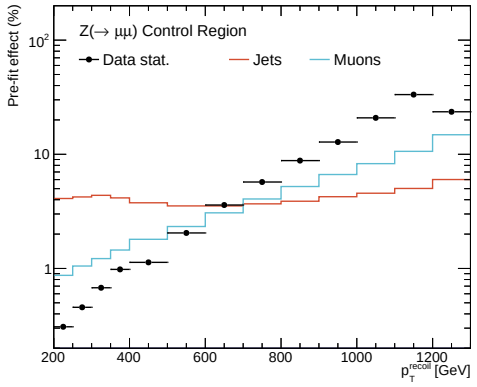
(c) $W(\rightarrow \mu\nu)$ Control Region



(d) Top Control Region



(e) $Z(\rightarrow ee)$ Control Region



(f) $Z(\rightarrow \mu\mu)$ Control Region

Figure 4.11. Pre-fit effect of experimental systematic uncertainties on the total background expectations of each region. The data statistical uncertainty is also shown. NPs are grouped in different categories and the total effect is obtained from the sum in quadrature of the various effects.

4.8.2 Modelling uncertainties

V+jets processes. A set of systematic uncertainties is provided by the authors of the prescriptions [167] used to reweight V+jets predictions to higher order.

Three systematic uncertainties cover pure QCD effects. The first one ($\delta_1 K$) accounts for the truncation of the perturbative series in α_s. This is evaluated by varying the renormalization and factorization scales both independently and simultaneously by a factor 0.5 and 2. The half-width of the resulting band is taken as an uncertainty. A second systematic uncertainty ($\delta_2 K$) is used to cover possible biases in the extrapolation between low and high p_{T}. It is estimated via a shape distortion of the scale variations band. The last pure QCD uncertainty ($\delta_3 K$) accounts for the non universality of NNLO QCD corrections between W and Z+jets processes. All the systematic uncertainties mentioned are correlated between the V+jets processes.

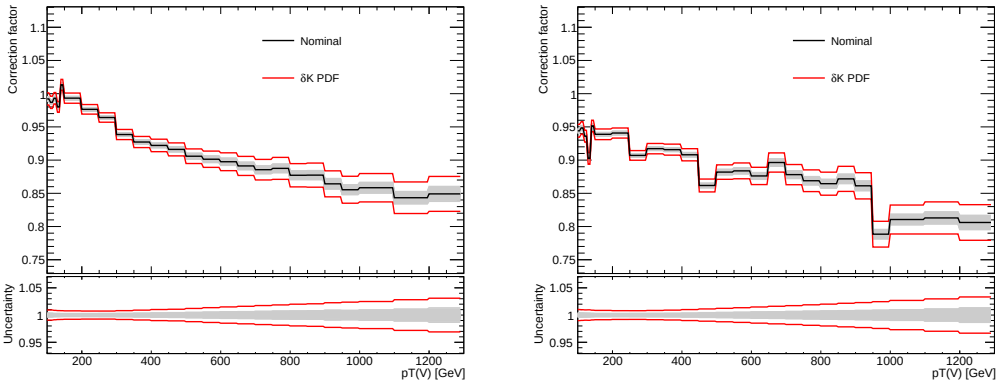
Three systematic uncertainties cover pure EW effects: $\delta_1\kappa$ accounts for higher order Sudakov logarithms beyond the two loops calculation. The second one, $\delta_2\kappa$, accounts for NLO EW terms at high-p_{T} not taken into account in the corrections. Since these might be different for $W(\to \ell\nu)$+jets, $Z(\to \ell\ell)$+jets and $Z(\to \nu\bar{\nu})$+jets processes, the corresponding NP is decorrelated between the three. The last pure EW uncertainty ($\delta_3\kappa$) accounts for the approximations adopted in the calculation of the two-loop Sudakov logarithms. The unknown effects might differ between W and Z+jets processes, thus the NP is decorrelated between the two vector bosons.

An uncertainty takes into account alternative ways of implementing mixed QCD+EW corrections (namely the additive and multiplicative schemes, whose description can be found in Ref. [183]). Its size is equal to 5% of the difference observed between the two methods. The authors provide also 100 variations associated with the PDF set used in the calculations, PDF4LHC NNLO supplemented with QED effects from the `LuxQED` set. To reduce the degrees of freedom included in the fit, and improve its numerical stability, the variations obtained on the $p_{\mathrm{T}}(V)$ spectrum are summed in quadrature. As shown in Figure 4.12 for $Z(\to \nu\bar{\nu})$+jets and $W(\to e\nu)$+jets processes, this is a conservative approach. Similar pre-fit impact is observed for the other processes. An additional uncertainty has been set on processes including τ leptons. This is due to differences between the τ definition in the parton level calculations and the one available in MC simulation.

The pre-fit effect on the total SR background of the systematic uncertainties discussed is shown in Figure 4.13. The effect of the $Z(\to \ell\ell)$+jets $\delta_2\kappa$ systematic uncertainty is null since the $Z(\to \ell\ell)$+jets background is negligible in SR.

Electroweak V+jets production Electroweak production of vector bosons is simulated using the Herwig 7 generator. No alternative setups of the same generator is available to evaluate modelling uncertainties. Renormalization and factorization scale variations, α_s and PDF uncertainties are propagated from the ones evaluated in a Sherpa 2.2.1 Vjj+0,1,2 jets @ LO setup. Such uncertainties are expected to be conservative, since the nominal setup is simulated at an higher level of perturbative accuracy (NLO). Moreover, the EW production of V+jets processes is subdominant with respect to the strong mode.

Renormalization and factorization scales are varied by a factor 0.5 and 2 one at



(a) $Z(\to \nu\bar{\nu})$+jets (b) $W(\to e\nu)$+jets

Figure 4.12. Effect of PDF variations on (a) $Z(\to \nu\bar{\nu})$+jets and (b) $W(\to e\nu)$+jets process as a function of the $p_{\mathrm{T}}(V)$. Gray lines indicate each single variation, while the red lines indicate the sum in quadrature of the components.

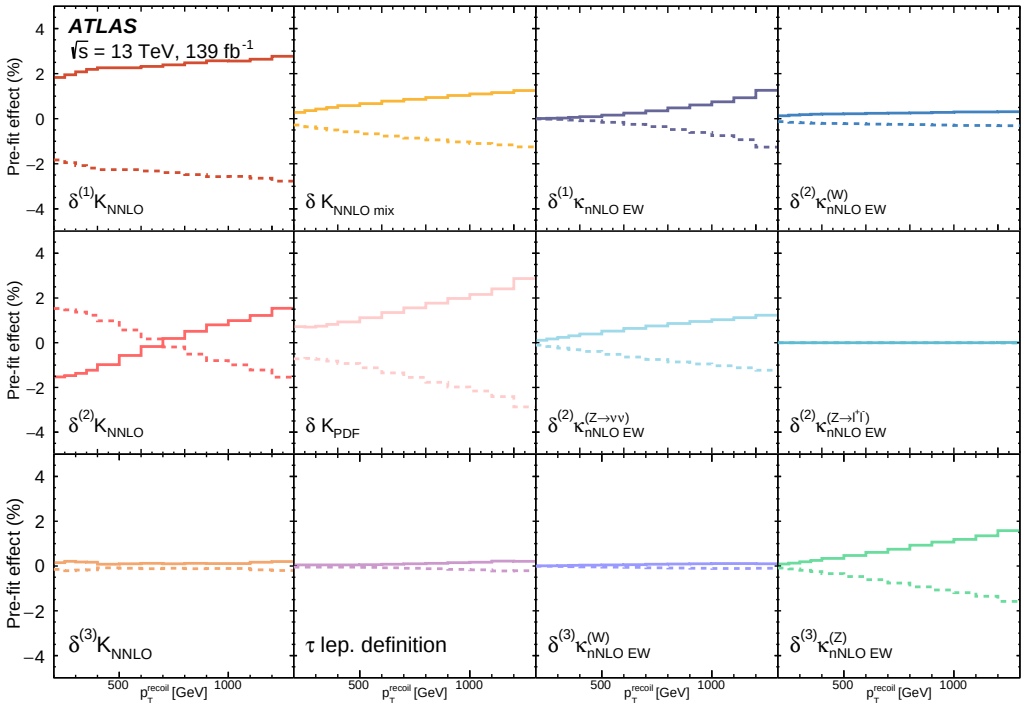
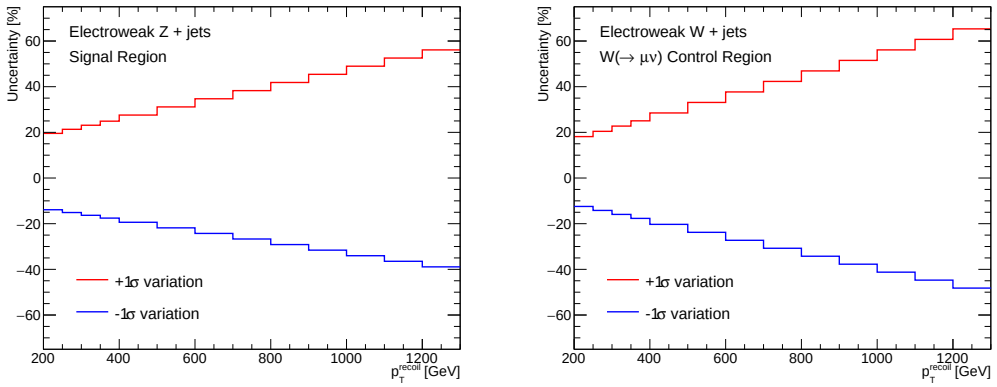


Figure 4.13. Pre-fit effect of the systematic uncertainties associated to the V+jets processes on the total SR background, shown as a function of $p_{\mathrm{T}}^{\mathrm{recoil}}$. Figure from the auxiliary material of Ref. [4].

a time and simultaneously. Half the width of the obtained envelope has been taken as the uncertainty. PDF uncertainties are evaluated by summing in quadrature the variations obtained from the 100 replicas included in the NNPDF3.0NNLO set. α_s has been varied between the nominal value, $\alpha_s = 0.118$ and two values,

$\alpha_s = 0.117, 0.119$ and the corresponding variation observed in the $p_{\mathrm{T}}^{\mathrm{recoil}}$ distribution is taken as an uncertainty. The three uncertainties are summed in quadrature to obtain the total $\pm 1\sigma$ combined variations. In Figure 4.14, the total uncertainty associated to EW Z+jets in SR and EW W+jets in single muon CR is shown as a function of $p_{\mathrm{T}}^{\mathrm{recoil}}$. Uncertainties between 20% to 60% are obtained. Similar contributions are observed in the other control regions for both samples.



(a) (b)

Figure 4.14. Total modelling uncertainty associated to the electroweak production of Z+jets and W+jets, respectively evaluated in (a) SR and (b) single muon CR as a function of $p_{\mathrm{T}}^{\mathrm{recoil}}$.

Dibosons production. Uncertainties on double vector-boson production are evaluated using the internal weights variations available in the adopted SHERPA samples. These are the same renormalization and factorization scale, α_s and PDF variations described for the SHERPA electroweak V+jets setup.

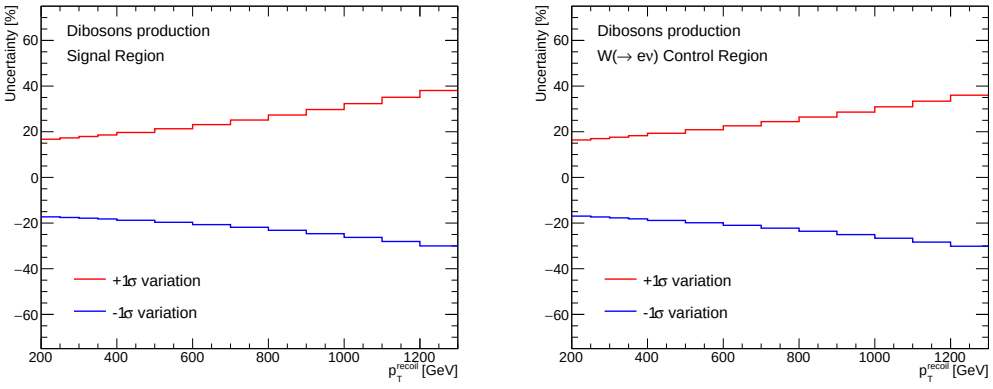
Additional systematic uncertainties are considered to take into account the variations of the resummation and matching scales. Such variations require the production of alternative samples. These are available only at truth level, and only for $W(\to \ell\nu)Z(\to \ell\ell)$ final states. The variation of the cross-section prediction is evaluated inclusively in a tri-lepton enriched region after requiring the SR preselection cuts. The matching scale is varied from the nominal value of 20 GeV to 15 and 30 GeV, and the resummation scale is varied by a factor 0.25,4. Moreover, the parton shower dipole recoil scheme is switched between the default setting [184], and an alternative one [162]. The impact of these three effects on the cross-section is reported in Table 4.9.

All the variations are summed in quadrature with the scale, α_s and PDF ones. The total uncertainty on dibosons production, as a function of $p_{\mathrm{T}}^{\mathrm{recoil}}$, is shown in Figure 4.15(a) and 4.15(b) for the SR and the single electron CR respectively. It ranges between 15% and 40% with increasing $p_{\mathrm{T}}^{\mathrm{recoil}}$.

Top-quark processes. Modelling uncertainties on $t\bar{t}$ and single-t quark production are evaluated by means of alternative available MC samples.

Table 4.9. Modelling systematic uncertainties due to alternative setups of the dibosons MC simulation.

Alternative setup	Variation [%]
Resummation scale variation × {0.25, 4}	{10.8, -4.4}
Matching scale {15,30} GeV	{0.7, -1.6}
Dipole recoil scheme variation	5.1



(a) (b)

Figure 4.15. Total modelling uncertainty associated to the production of vector boson pairs, evaluated respectively in (a) SR and (b) single electron CR, shown as a function of $p_{\mathrm{T}}^{\mathrm{recoil}}$.

The nominal setup for $t\bar{t}$ simulation is described in Section 4.2.1. Powheg is used to generate the ME process and Pythia8 for parton showering. Uncertainties are estimated by comparing to alternative simulations. Uncertainties on the hard-scatter process (HS) modelling and matching to the PS derive from comparison with a MadGraph5 aMC@NLO plus Pythia 8 setup. The parton shower and hadronisation model are compared to a setup based on Powheg and the Herwig7 PS.

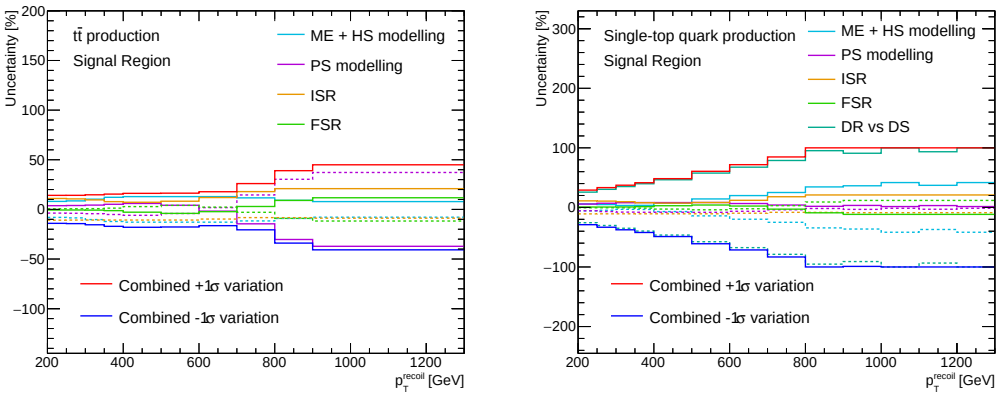
Uncertainties are set on the choice of the h_{damp} factor, which controls the matching between the Powheg ME generation and the showering performed by Pythia8. This parameter regulates the ISR which recoils against the $t\bar{t}$ system. Alternative samples, generated varying the nominal h_{damp} parameter from its nominal value of $1.5 \cdot m_{\mathrm{top}}$ to $\{0.5, 3\} \cdot m_{\mathrm{top}}$ are compared to the nominal setup.

Final-state-radiation uncertainties are derived by varying the value of α_s in the PS of the nominal setup. PDF uncertainties are negligible with respect to the effects mentioned before.

Uncertainties on the ME, HS, PS, hadronization and fragmentation modelling of the single-t processes are evaluated in the same way. An additional uncertainty is derived for the tW process by comparing the $p_{\mathrm{T}}^{\mathrm{recoil}}$ distribution obtained by switching to the diagram removal scheme to remove the overlap with the $t\bar{t}$ sample. The difference is expected to be large at high $p_{\mathrm{T}}^{\mathrm{recoil}}$. It is the dominant source of

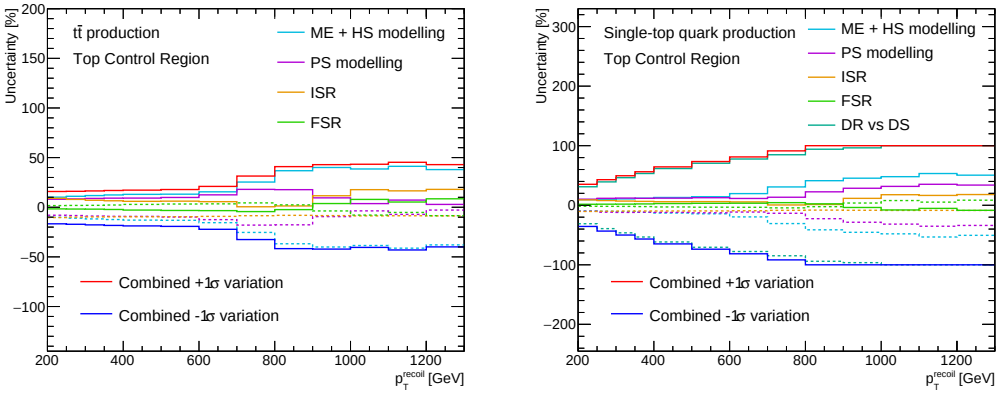
uncertainty for the single-t production.

The different variations obtained on the $p_{\mathrm{T}}^{\mathrm{recoil}}$ spectrum are summed in quadrature to derive two combined systematic uncertainties, one for $t\bar{t}$ production and one for single-t processes. These two uncertainties are shown in Figure 4.16 and 4.17 for the SR and the top CR respectively.



(a) (b)

Figure 4.16. Combined modelling uncertainty associated to the (a) $t\bar{t}$ and (b) single-top quark production in SR, as a function of $p_{\mathrm{T}}^{\mathrm{recoil}}$.



(a) (b)

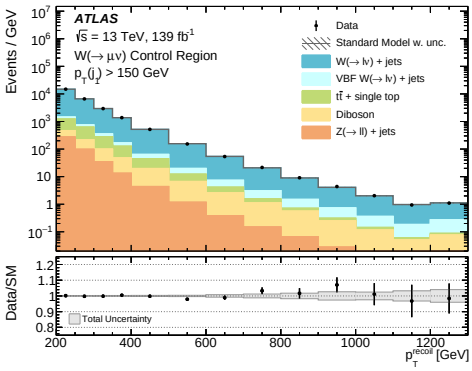
Figure 4.17. Combined modelling uncertainty associated to the (a) $t\bar{t}$ and (b) single-top quark production in top CR, as a function of $p_{\mathrm{T}}^{\mathrm{recoil}}$.

The impact of including one NP for each source of systematic uncertainty is tested in the fit. No differences on the final results is observed with respect to a two-NP-only setup. Thus, for the sake of simplicity, only two nuisance parameters are included in the likelihood model

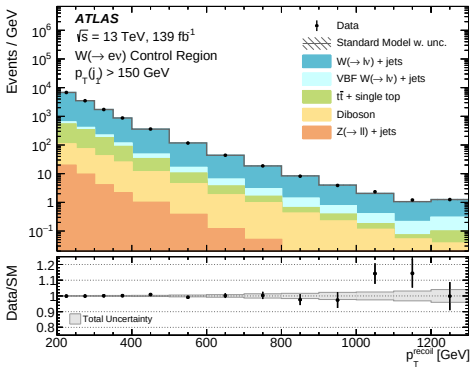
4.9 Background estimation results

After a CR only fit is performed, a good agreement between data and SM predictions is observed overall in the CR $p_{\mathrm{T}}^{\mathrm{recoil}}$ distributions. In figure 4.18 the results obtained in the single-lepton control regions are presented. A deviation of -2σ, evaluated as $(\mathrm{Data}-\mathrm{SM})/\sqrt{\sigma_{data}^2+\sigma_{MC}^2}$ is observed in the $[500, 600]$ GeV $p_{\mathrm{T}}^{\mathrm{recoil}}$ bin of the single muon CR. In two bins of the single-electron CR a slight excess of data is observed. The deviation, below the level of 2σ, might be due to mis-reconstructed jets faking electrons, or to fluctuations in the background MC templates.

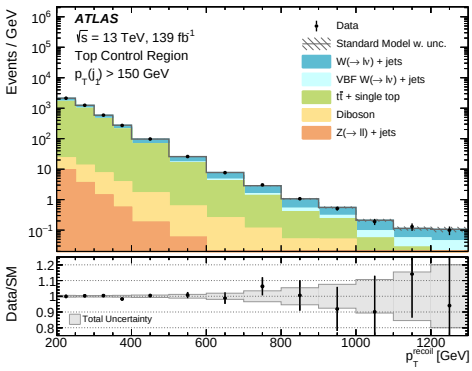
The level of uncertainty in the single muon (electron) CR on the total background ranges between 0.25% (0.27%) to 4% (4.1%). In the top-quark CR the MC mismodelling due to top quark processes are fixed, and a total uncertainty of 0.57% to 20% respectively at low and high $p_{\mathrm{T}}^{\mathrm{recoil}}$ is reached.



(a) Single muon CR.



(b) Single electron CR.

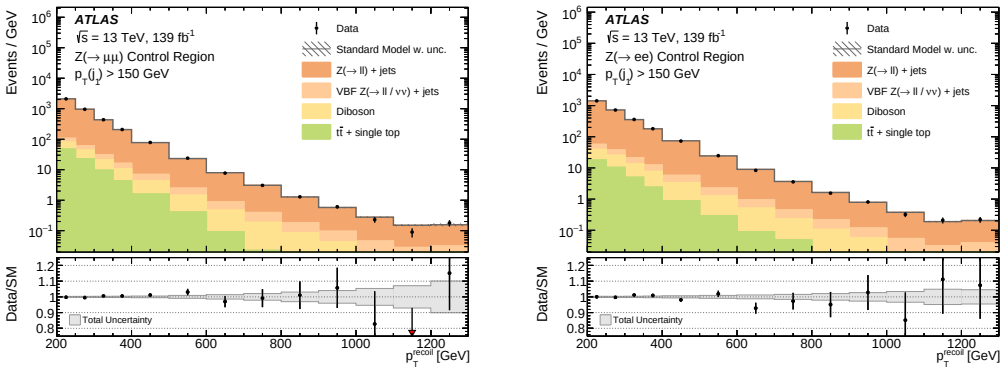


(c) Top CR.

Figure 4.18. Comparison between data and MC predictions of the $p_{\mathrm{T}}^{\mathrm{recoil}}$ distribution, in single-lepton CR, after a CR only fit is performed. The last bin in the distributions include the overflow. The band in the bottom pane includes both the statistical and systematic uncertainties on the background predictions. Figures from Ref. [4].

Di-lepton CR $p_{\mathrm{T}}^{\mathrm{recoil}}$ distributions are presented in Figure 4.19. Also in this case good agreement between data and the background predictions is observed. In the di-electron CR a similar level of uncertainty to the single-lepton one is observed, ranging

between 0.37% and 4.5%. The di-muon CR is affected in the tail by large additional systematic uncertainties included to correct mismodelling of high-p_{T} muons. Thus, the total uncertainty ranges between 0.31% and 10%. In Table 4.10 the yields before and after the fit in each region, split for background components, are reported. These are obtained inclusively for $p_{\mathrm{T}}^{\mathrm{recoil}} > 200\,\mathrm{GeV}$.



(a) Di-muon CR. (b) Di-electron CR.

Figure 4.19. Comparison between data and MC predictions for the $p_{\mathrm{T}}^{\mathrm{recoil}}$ distribution, in di-lepton CR, after a CR only fit is performed. The last bin in the distributions include the overflow. The band in the bottom pane includes both the statistical and systematic uncertainties on the background predictions. Figures from Ref. [4].

The $p_{\mathrm{T}}^{\mathrm{recoil}}$ distribution observed in the SR are shown in Figure 4.20, and compared to SM predictions obtained after performing a CRs-only or SR+CRs fit. Agreement is observed between data and SM predictions. The total level of uncertainty varies between 1.2%, at $p_{\mathrm{T}}^{\mathrm{recoil}}$ 200 GeV, and 4.2% for $p_{\mathrm{T}}^{\mathrm{recoil}} > 1.2\,\mathrm{TeV}$. The effect of adding the SR to the fit for the background estimation, in the background-only hypothesis, is shown in the same figure. The background predictions are not significantly affected. However, the uncertainty on the background predictions is reduced by almost half of the value obtained after a CR only fit. This is due to the fact that the SR has a non-negligible statistical power, and allows to further constrain modelling systematic uncertainties.

After the CR-only fit, an inclusive effective k factor, defined as the ratio between the post-fit and pre-fit yields, of 1.13 ± 0.01 is observed for V+jets backgrounds in the SR. In the same region, the $t\bar{t}$ background is corrected by a multiplicative factor of 0.9 ± 0.1, and the single-t background overall gets scaled by a factor 1.6 ± 0.4. These values do not correspond to the best-fit value of the normalization factors included in the likelihood model, due to non-zero post-fit values of the NPs, which imply non-zero effects on the overall normalization of these backgrounds. Systematic uncertainties, in fact, can not only modify the shape of the $p_{\mathrm{T}}^{\mathrm{recoil}}$ distributions, but also their overall normalization. The values of the normalization factors obtained in the CR-only and background-only SR+CR fit are reported in Table 4.11.

The value obtained for the normalization factor of the single-t quark processes is balanced by a negative *pull* of the NP which parameterize the single top combined uncertainty. The best-fit value of all the α NPs included in the fit are reported in Figure 4.21. The constrains observed on the 'VBF theo sys', 'singletop combined

Table 4.10. Data and expected events for $p_{\mathrm{T}}^{\mathrm{recoil}} > 200\,\mathrm{GeV}$ in each CR. The top part shows the post-CR-only fit predictions, while in the bottom one the pre-fit expected events are reported. Negligible contributions are indicated by a dash. Table from Ref. [4].

$\mathbf{p_T^{recoil} > 200\,GeV}$	$W \to \mu\nu$	$W \to e\nu$	Top	$Z \to \mu\mu$	$Z \to ee$
Data events (139 fb^{-1})	1 364 958	699 674	225 606	196 800	145 531
SM prediction (post-fit)	1 364 800 ± 3300	699 700 ± 1800	225 600 ± 1100	197 000 ± 600	145 500 ± 500
Fitted $W \to e\nu$	–	578 800 ± 3400	16 100 ± 900	–	–
Fitted $W \to \mu\nu$	1 149 000 ± 6000	–	31 600 ± 1700	–	–
Fitted $W \to \tau\nu$	71 500 ± 800	45 200 ± 500	3380 ± 180	–	–
Fitted VBF W + jets	26 200 ± 3100	14 300 ± 1700	2020 ± 340	–	–
Fitted $Z \to ee$	–	–	–	–	138 100 ± 700
Fitted $Z \to \mu\mu$	21 500 ± 500	–	778 ± 20	185 200 ± 900	–
Fitted $Z \to \tau\tau$	–	1900 ± 50	–	–	–
Fitted $Z \to \nu\nu$	–	–	–	–	–
Fitted VBF Z + jets	–	–	–	3300 ± 400	2530 ± 320
Fitted single-t	22 000 ± 6000	13 200 ± 3500	33 000 ± 10 000	350 ± 170	110 ± 60
Fitted $t\bar{t}$	52 000 ± 4000	34 000 ± 2800	137 000 ± 9000	4000 ± 400	1790 ± 180
Expected dibosons	23 000 ± 4000	12 400 ± 1900	1880 ± 340	4000 ± 700	2900 ± 500
MC exp. SM events	1 220 000 ± 60 000	623 000 ± 32 000	233 000 ± 31 000	175 000 ± 9000	127 000 ± 7000
Fit input $W \to e\nu$	–	509 000 ± 27 000	14 200 ± 1200	–	–
Fit input $W \to \mu\nu$	1 010 000 ± 50 000	–	28 000 ± 2300	–	–
Fit input $W \to \tau\nu$	63 000 ± 3400	39 800 ± 2100	2970 ± 250	–	–
Fit input VBF W + jets	22 000 ± 4000	11 700 ± 2300	1500 ± 500	–	–
Fit input $Z \to ee$	–	–	–	–	120 000 ± 7000
Fit input $Z \to \mu\mu$	18 900 ± 1100	–	689 ± 23	163 000 ± 9000	–
Fit input $Z \to \tau\tau$	–	1680 ± 60	–	–	–
Fit input $Z \to \nu\nu$	–	–	–	–	–
Fit input VBF Z + jets	–	–	–	2700 ± 500	2000 ± 400
Fit input single-t	16 000 ± 6000	10 000 ± 4000	28 000 ± 13 000	700 ± 500	280 ± 210
Fit input $t\bar{t}$	60 000 ± 7000	39 000 ± 5000	155 000 ± 27 000	4600 ± 1300	2000 ± 700
Fit input dibosons	23 000 ± 4000	12 600 ± 2300	1900 ± 400	4100 ± 800	3000 ± 600

Table 4.11. Best fit value of the free-floating normalization factors obtained in the CR only and SR+CR background-only fits.

Normalization factor	CR only fit	SR+CR ($\mu = 0$) fit
κ_V	1.13 ± 0.04	1.15 ± 0.04
$\kappa_{t\bar{t}}$	$0.85^{+0.10}_{-0.09}$	$0.87^{+0.10}_{-0.09}$
κ_t	$2.88^{+0.44}_{-0.42}$	$2.84^{+0.46}_{-0.43}$

sys' and 'ttbar combined sys' NP are due to the fact that the corresponding pre-fit uncertainties are very large. In a similar way, data are able to constrain the effect of some of the systematic uncertainties associated to jets, electrons and muons. Pulls of the NP away from the α pre-fit value of 0 reflect shape corrections which are applied to the $p_{\mathrm{T}}^{\mathrm{recoil}}$ spectrum in the various control regions. The impact of pulls and constrains of systematic uncertainties on the background estimation is discussed in Section 4.9.1.

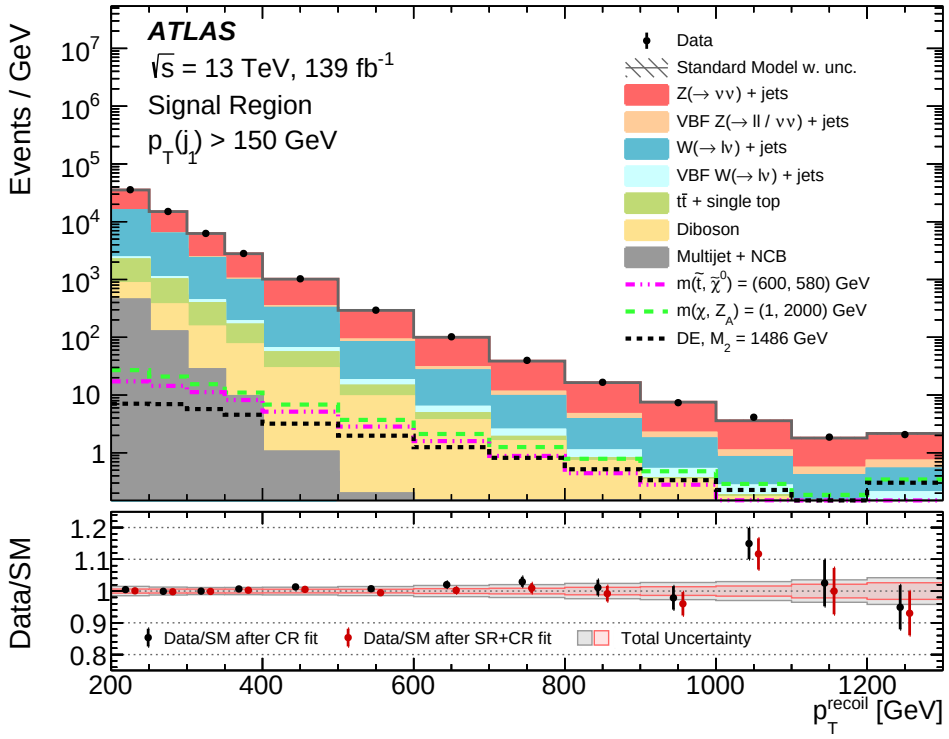
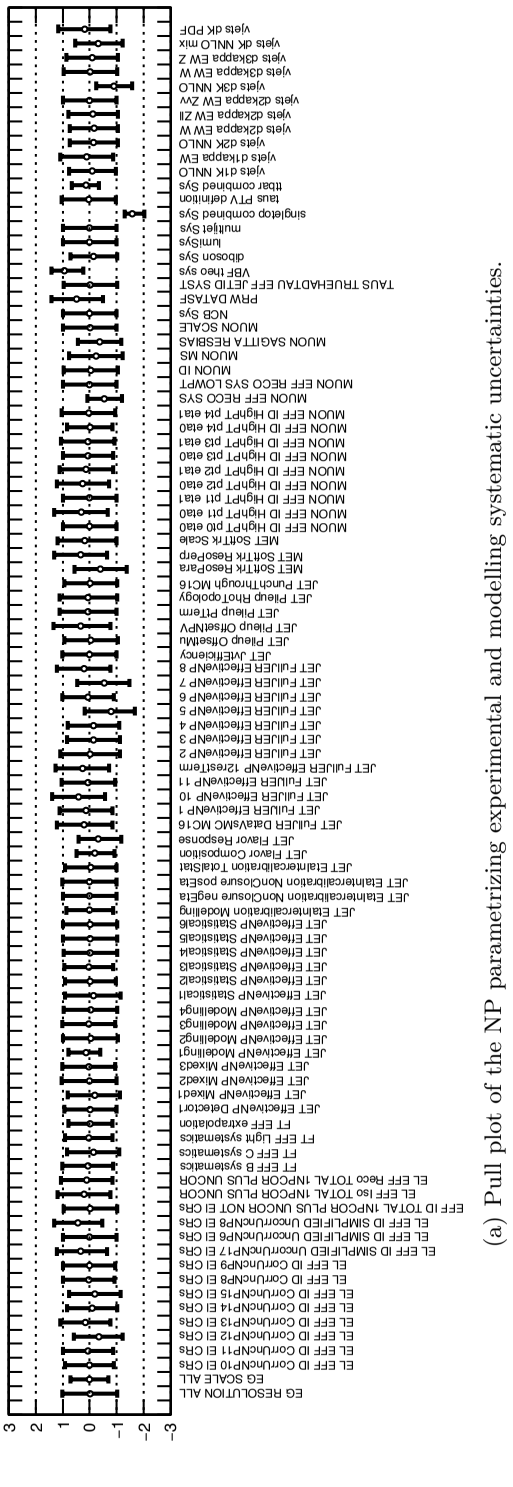
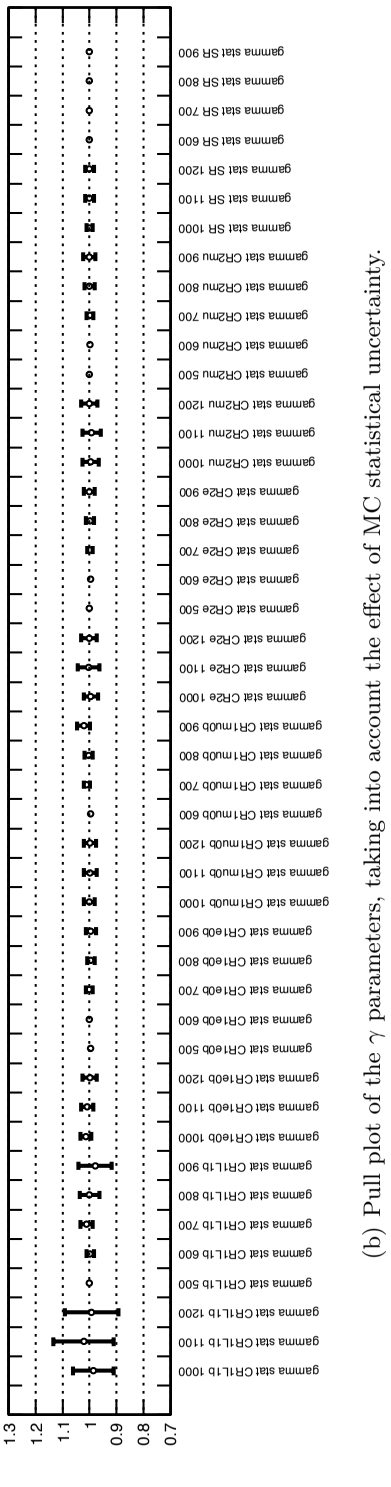


Figure 4.20. Observed $p_{\mathrm{T}}^{\mathrm{recoil}}$ distribution in the signal region compared to background predictions as estimated in a CR only fit. The total uncertainty on the background predictions is reported in the bottom pane, where the data-to-SM ratio is presented. The black (red) points and band represent this ratio and the background total relative uncertainty as obtained from the CR (SR+CR in the null signal hypothesis) fit. The expected $p_{\mathrm{T}}^{\mathrm{recoil}}$ spectrum for three benchmark BSM signals is also reported. Figure from Ref. [4].



(a) Pull plot of the NP parametrizing experimental and modelling systematic uncertainties.



(b) Pull plot of the γ parameters, taking into account the effect of MC statistical uncertainty.

Figure 4.21

The correlation matrix between the various NPs, after a CR-only fit is performed, is presented in Figure 4.22. Only the NPs with at least a correlation $\rho_{ij} > 0.2$ are shown. A strong anti-correlation is observed between the normalization factor of the $t\bar{t}$ process and its combined modelling systematic uncertainty. This is due to the normalization component carried by the latter. The nuisance parameter is pulled to correct the $p_{\mathrm{T}}^{\mathrm{recoil}}$ shape of the background, and the shift in the normalization is balanced by the κ factor. A similar interplay is observed between the NP of the single-t quark combined modelling systematic and κ_t.

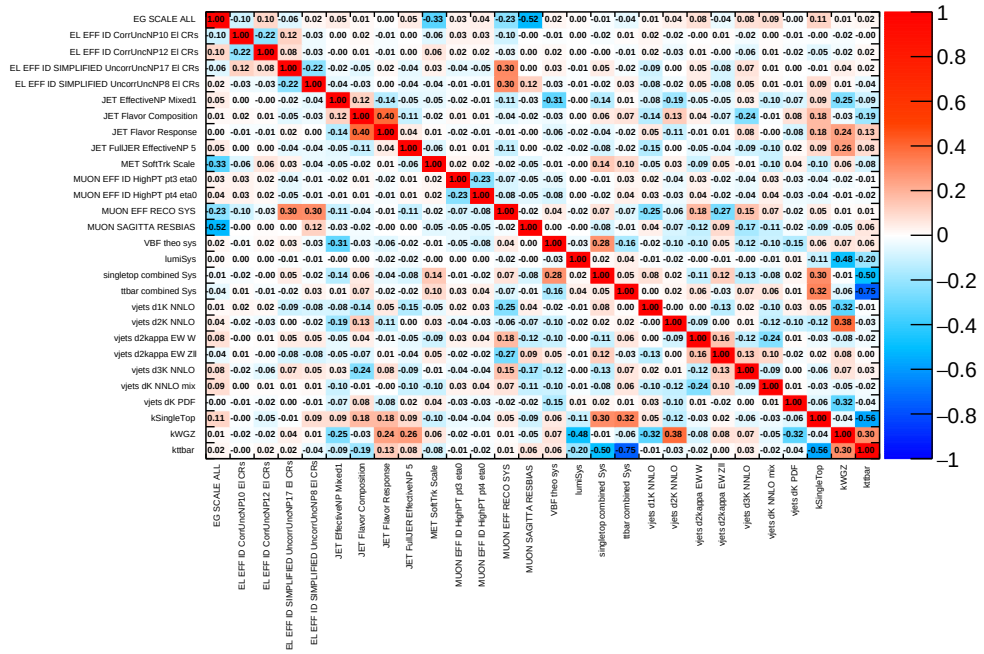


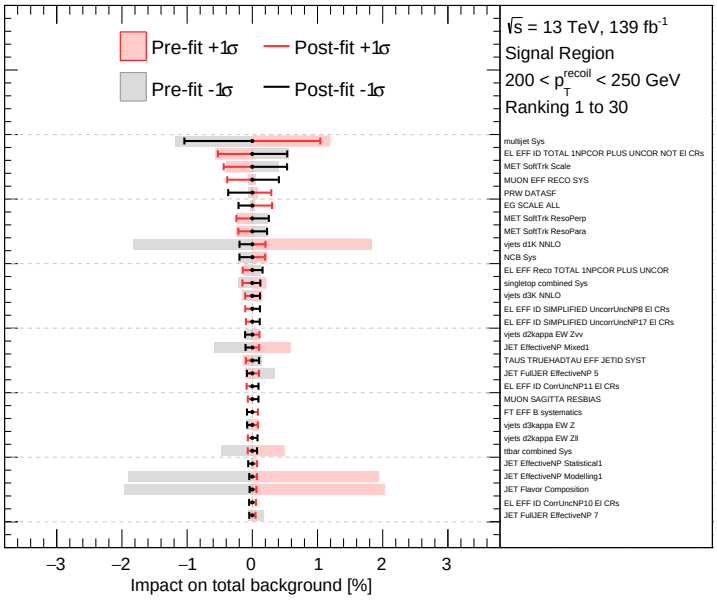
Figure 4.22. Correlation matrix of the parameters included in the likelihood model, after a CR-only fit is performed.

The correlation between the luminosity NP and the normalization factor is expected, as the former is flat in $p_{\mathrm{T}}^{\mathrm{recoil}}$, as the κ factors. A correlation is observed between NPs parameterizing electron and muon systematic uncertainties. This is expected due to the fact that electron- and muon-enriched regions are linked by the unique normalization factor applied to V+jets processes.

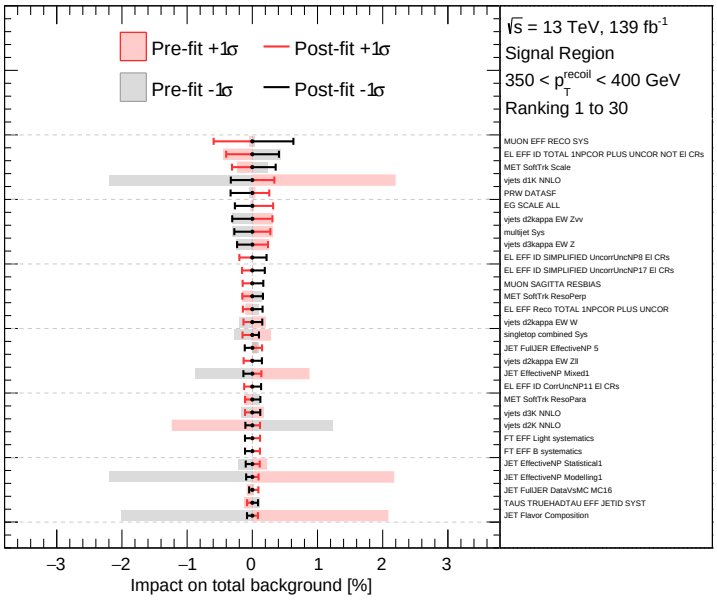
4.9.1 Post-fit systematic uncertainties

The effect of systematic uncertainties on the SR background estimation is evaluated by comparing the nominal background estimation with the one obtained in two fits for each NP α_i. These are done fixing the NP at its best-fit value plus or minus its uncertainty as obtained in a CR-only fit, $\hat{\alpha}_i \pm \sigma_{\hat{\alpha}_i}$, and repeating the CR-only fit. The total background shift, relative to the post-CR-only fit one, represents the impact of the systematic uncertainty on the background estimate. This can be visualized as in Figures 4.23 and 4.24 for bins of increasing $p_{\mathrm{T}}^{\mathrm{recoil}}$. The effect of MC statistical uncertainty, taken into account in the likelihood via the γ parameters, is also evaluated but is not shown in the plots below. This choice is made because

neither partial cancellation, nor constrain can happen on such parameters, since they are decorrelated among regions and bins.

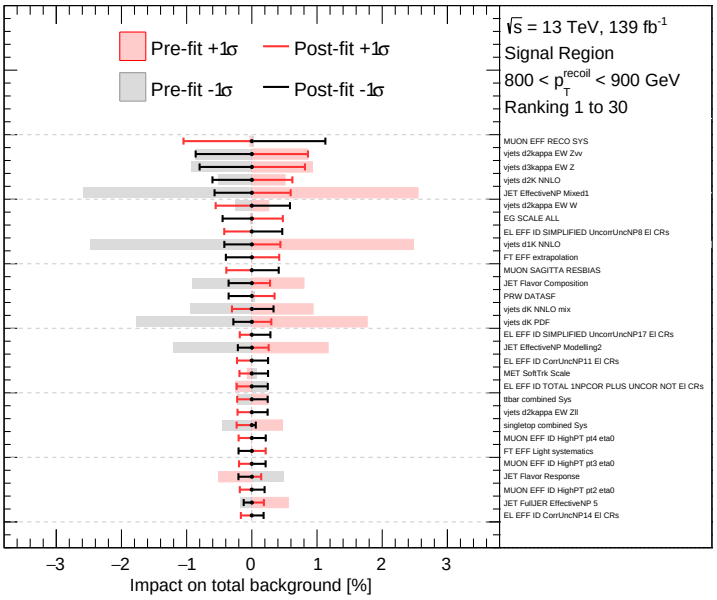


(a) $200 < p_{\mathrm{T}}^{\mathrm{recoil}} < 250\,\mathrm{GeV}$

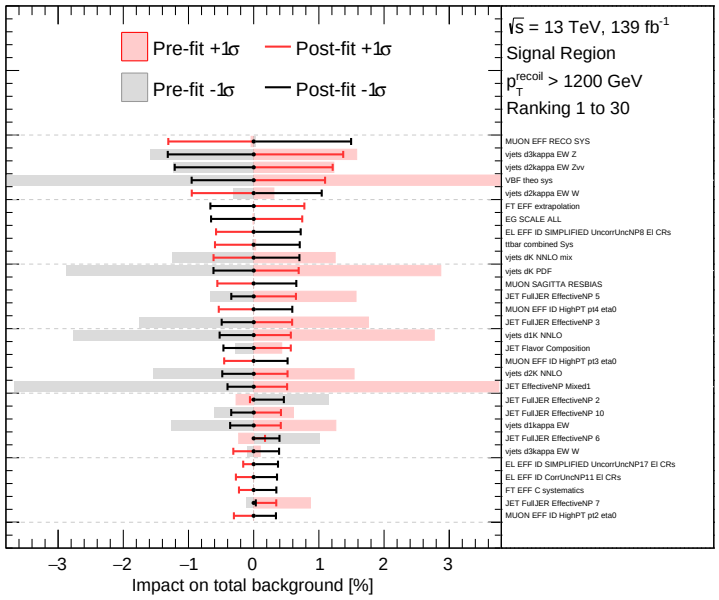


(b) $350 < p_{\mathrm{T}}^{\mathrm{recoil}} < 400\,\mathrm{GeV}$

Figure 4.23. Representation of the impact of the largest 30 systematic uncertainties on the background estimate for two medium-$p_{\mathrm{T}}^{\mathrm{recoil}}$ bins.



(a) $800 < p_{\mathrm{T}}^{\mathrm{recoil}} < 900\,\mathrm{GeV}$



(b) $p_{\mathrm{T}}^{\mathrm{recoil}} > 1.2\,\mathrm{TeV}$

Figure 4.24. Representation of the impact of the largest 30 systematic uncertainties on the background estimate for two high-$p_{\mathrm{T}}^{\mathrm{recoil}}$ bins.

In these plots, the pre-fit effect indicates the shift in the total background observed when the nominal template is switched with the varied one. Electron-

and muon-related systematic uncertainties are expected to have a negligible pre-fit effect on the total SR background[2]. Though, such uncertainties have a non-zero impact on the post-fit estimated yields. This is due to the fact that SR backgrounds are estimated via CRs in which those systematic uncertainties are dominant. For this reason, NPs associated to muon and electron reconstruction and identification efficiencies are expected to be among the top-ranked systematic uncertainties.

In the lowest bin, $200 < p_{\mathrm{T}}^{\mathrm{recoil}} < 250\,\mathrm{GeV}$, the dominant source of uncertainty is related to the multijet background. It is followed by the uncertainty on the identification of electrons in the region which have a veto on such objects, as it is for the SR. Among the top-ranked, systematic uncertainties on the TST of the $E_{\mathrm{T}}^{\mathrm{miss}}$ are present. This term, in fact, is mostly relevant at low $p_{\mathrm{T}}^{\mathrm{recoil}}$. Some NPs show a large difference between the pre-fit and post-fit effect, as some of the jet-related ones. This is due to the fact that, in the background estimation procedure, NPs which have the same effect between the signal and CRs tend to cancel. In the $350 < p_{\mathrm{T}}^{\mathrm{recoil}} < 400\,\mathrm{GeV}$ bin, the multijet background becomes subdominant, and so its uncertainty. Uncertainties on the resolution of the $E_{\mathrm{T}}^{\mathrm{miss}}$ TST also become less important.

At higher $p_{\mathrm{T}}^{\mathrm{recoil}}$, as in the $800 < p_{\mathrm{T}}^{\mathrm{recoil}} < 900\,\mathrm{GeV}$ bin shown in Figure 4.24(a), V+jets modelling uncertainties start to dominate the total one. The second- and third-ranked NPs are in fact related to uncertainties on the EW corrections of such processes. In the highest $p_{\mathrm{T}}^{\mathrm{recoil}}$ bin this is also true. The single dominant component though is however still related to the muon muon reconstruction efficiency, but nine out of 12 V+jets modelling uncertainties are among the top 30 ranked ones. The EW V+jets backgrounds modelling uncertainty is also among the five top-ranked, due to its large pre-fit effect.

In Table 4.12, the effect of systematic uncertainties grouped by category is presented for each SR $p_{\mathrm{T}}^{\mathrm{recoil}}$ bin. The grouping is performed by summing in quadrature the impact of each NP belonging to each category. This table also shows the effect of having a limited amount of simulated events. As it can be seen from the last row of the Table, the combined impact on the background uncertainty of the γ parameters is the second-dominant one in the last two $p_{\mathrm{T}}^{\mathrm{recoil}}$ bins. Innovative methods to efficiently populate the tails of the $p_{\mathrm{T}}(V)$ distributions are discussed in this thesis in Chapter 6.

[2]Represented by the almost invisible filled bars

Table 4.12. Summary of the effect of systematic uncertainties on the SR background estimation, presented for different $p_{\mathrm{T}}^{\mathrm{recoil}}$ bins, indicated by EM. Table from the auxiliary material of Ref. [4].

Source (%)	EM0	EM1	EM2	EM3	EM4	EM5	EM6	EM7	EM8	EM9	EM10	EM11	EM12
Flavor tagging	0.1	0.13	0.15	0.17	0.19	0.25	0.33	0.41	0.49	0.57	0.62	0.7	0.87
Jet energy scale	0.17	0.2	0.27	0.25	0.28	0.39	0.5	0.63	0.8	0.89	0.9	1.0	0.97
Jet energy resolution	0.15	0.2	0.21	0.25	0.32	0.37	0.4	0.37	0.31	0.34	0.43	0.62	1.28
Jet JVT efficiency	0.0	0.0	0.01	0.01	0.01	0.01	0.01	0.01	0.0	0.01	0.01	0.02	0.03
Pile-up reweighting	0.37	0.35	0.34	0.33	0.32	0.3	0.32	0.34	0.36	0.33	0.26	0.24	0.3
$E_{\mathrm{T}}^{\mathrm{miss}}$ resolution	0.34	0.31	0.25	0.2	0.18	0.14	0.08	0.05	0.04	0.05	0.05	0.06	0.07
$E_{\mathrm{T}}^{\mathrm{miss}}$ scale	0.53	0.46	0.4	0.36	0.31	0.27	0.26	0.26	0.25	0.26	0.27	0.27	0.3
Electron and photon energy resolution	0.0	0.0	0.0	0.0	0.0	0.01	0.01	0.02	0.02	0.03	0.04	0.05	0.08
Electron and photon energy scale	0.3	0.3	0.31	0.32	0.33	0.36	0.4	0.44	0.48	0.54	0.6	0.66	0.74
Electron identification efficiency	0.58	0.56	0.54	0.54	0.54	0.56	0.6	0.67	0.73	0.8	0.85	0.92	1.06
Electron reconstruction efficiency	0.16	0.16	0.16	0.16	0.16	0.15	0.15	0.16	0.16	0.17	0.18	0.18	0.2
Muon identification efficiency	0.06	0.07	0.07	0.04	0.03	0.11	0.2	0.29	0.38	0.48	0.58	0.7	0.9
Muon reconstruction efficiency	0.41	0.48	0.56	0.63	0.73	0.82	0.92	1.03	1.13	1.21	1.27	1.35	1.49
Muon momentum scale	0.1	0.12	0.15	0.17	0.2	0.26	0.31	0.37	0.42	0.48	0.53	0.58	0.66
τ-lepton identification efficiency	0.1	0.1	0.09	0.09	0.08	0.07	0.06	0.06	0.05	0.06	0.06	0.06	0.07
Luminosity	0.01	0.01	0.01	0.01	0.01	0.01	0.02	0.02	0.02	0.02	0.02	0.03	0.05
Diboson theory	0.04	0.04	0.04	0.04	0.04	0.02	0.01	0.04	0.04	0.05	0.06	0.1	0.22
Noncollision background	0.2	0.1	0.08	0.06	0.05	0.05	0.08	0.0	0.0	0.0	0.0	0.0	0.0
Multijet background	1.04	0.72	0.36	0.28	0.06	0.02	0.01	0.0	0.01	0.0	0.0	0.0	0.0
Single-top theory	0.15	0.15	0.14	0.15	0.17	0.22	0.24	0.22	0.23	0.17	0.13	0.13	0.28
$t\bar{t}$ theory	0.07	0.07	0.06	0.06	0.08	0.13	0.18	0.22	0.24	0.33	0.4	0.52	0.71
V+jets τ lepton definition	0.05	0.04	0.04	0.04	0.04	0.04	0.06	0.07	0.08	0.1	0.12	0.16	0.13
V+jets pure QCD corrections	0.24	0.28	0.33	0.39	0.44	0.5	0.61	0.73	0.83	0.9	0.89	0.96	1.07
V+jets pure EW corrections	0.17	0.25	0.35	0.45	0.58	0.78	0.96	1.15	1.36	1.53	1.69	1.89	2.2
V+jets mixed QCD - EW corrections	0.02	0.04	0.06	0.08	0.12	0.18	0.23	0.28	0.33	0.4	0.45	0.54	0.7
V+jets PDF	0.02	0.03	0.01	0.03	0.04	0.08	0.16	0.23	0.3	0.35	0.39	0.48	0.69
VBF EW V+jets backgrounds	0.02	0.03	0.04	0.06	0.09	0.13	0.17	0.16	0.16	0.03	0.24	0.53	1.1
Limited MC statistics	0.05	0.06	0.06	0.06	0.08	0.13	0.56	0.6	0.9	1.0	1.21	1.76	1.86
Total bkg. unc.	1.48	1.26	1.13	1.14	1.22	1.42	1.76	2.03	2.41	2.69	2.98	3.53	4.21

A further grouping of the systematic uncertainties is done in Figure 4.25. The top pane presents the contributions to the total uncertainty due to detector related effects; in the bottom one, modelling uncertainties are grouped.

It is possible to see, also in this case, how the dominant sources of uncertainty at low $p_{\mathrm{T}}^{\mathrm{recoil}}$ are the one associated with data-driven estimated backgrounds. Contributions from muon and electron detector-related uncertainties arise from the background estimate strategy, which adopts lepton-enriched CRs. At high $p_{\mathrm{T}}^{\mathrm{recoil}}$, instead, the modelling of V+jets processes is the dominant term. The other contributions are below the percent level. Data statistical uncertainties ranges between the sub-permille level and 7%.

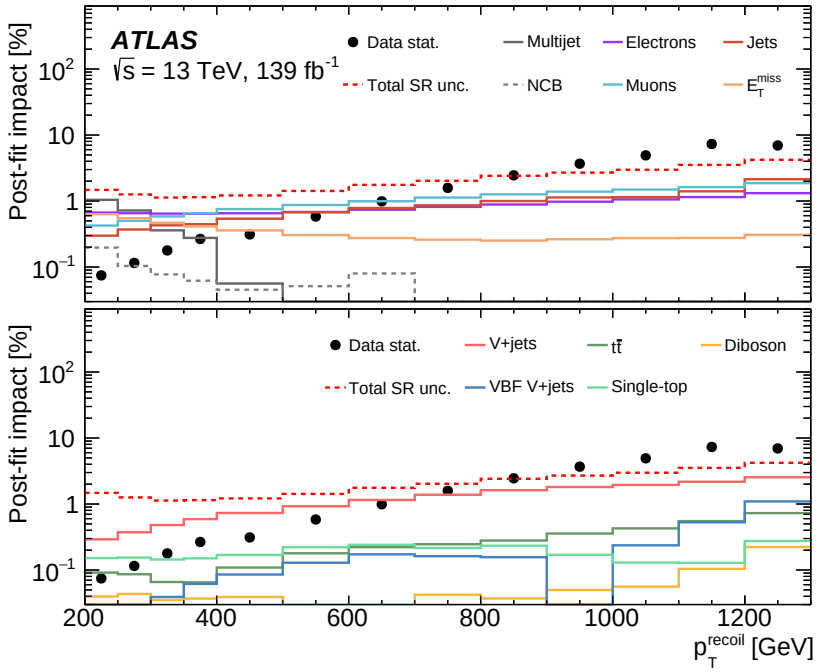


Figure 4.25. Summary of the sources of uncertainty on the background estimation in SR. The data statistical uncertainty is overlaid in both panes, and shown by black dots. Figure from the auxiliary material of Ref. [4].

4.9.2 Inclusive fit

As anticipated in Section 4.7.3, inclusive fits are performed to derive model-independent limits. Before this step, discussed in Section 4.10.1, CR-only fits are performed. Since in a cut-and-count setup the shape of the $p_{\mathrm{T}}^{\mathrm{recoil}}$ is not adopted, the likelihood model is slightly modified. Instead of having two separate normalization factors for top quark processes, a single one is used since two NFs would be degenerate being the regions single-binned. The two background contributions are therefore summed together, and the effect of systematic uncertainties is derived by weighting the pre-fit effect on each sample by its fraction to the total yields. In Table 4.13 the best fit value of the normalization factors obtained after a CR-only fit is reported. Each column corresponds to a separate fit.

The statistical power of the highest $p_{\mathrm{T}}^{\mathrm{recoil}}$ bins of the top-quark CR is poor, therefore the normalization factor is extracted with large uncertainty. Moreover, the large value observed for the $p_{\mathrm{T}}^{\mathrm{recoil}} > 1\,\mathrm{TeV}$ is balanced by a pull at the 1σ level of the combined top-quark modelling NP.

Since the shape information is not available in the fit, the NPs are less constrained, and in general the total expected uncertainty on the background estimate is larger. A comparison of the expected and observed yields between the inclusive and exclusive fits is presented in Table 4.14.

While a direct comparison of the yields is not meaningful, the relative uncertainty

Table 4.13. Best-fit value of the normalization factor in each of the 13 single-bin inclusive fits performed to the CR only.

	IM0	IM1	IM2	IM3	IM4	IM5	IM6
κ_V	$1.14^{+0.06}_{-0.06}$	$1.14^{+0.06}_{-0.06}$	$1.14^{+0.06}_{-0.06}$	$1.14^{+0.06}_{-0.06}$	$1.13^{+0.06}_{-0.06}$	$1.13^{+0.07}_{-0.07}$	$1.13^{+0.08}_{-0.07}$
κ_t	$0.92^{+0.17}_{-0.12}$	$0.89^{+0.18}_{-0.12}$	$0.85^{+0.18}_{-0.13}$	$0.82^{+0.21}_{-0.13}$	$0.81^{+0.23}_{-0.15}$	$0.73^{+0.31}_{-0.17}$	$0.73^{+0.52}_{-0.24}$
	IM7	IM8	IM9	IM10	IM11	IM12	
κ_V	$1.16^{+0.09}_{-0.09}$	$1.16^{+0.10}_{-0.10}$	$1.20^{+0.12}_{-0.11}$	$1.11^{+0.15}_{-0.14}$	$1.20^{+0.16}_{-0.18}$	$1.21^{+0.19}_{-0.17}$	
κ_t	$0.59^{+0.62}_{-0.22}$	$0.47^{+0.94}_{-0.23}$	$0.42^{+1.57}_{-0.27}$	$5.3^{+6.6}_{-3.8}$	$0.6^{+4.9}_{-0.5}$	$0.2^{+1.7}_{-0.2}$	

Table 4.14. Comparison of data and SM predictions obtained in a CR-only fit to the $p_{\mathrm{T}}^{\mathrm{recoil}}$ spectrum performed using inclusive and exclusive bins. In the inclusive case the table refers to the result of 13 separate fits with increasing $p_{\mathrm{T}}^{\mathrm{recoil}}$ threshold. Table from Ref. [4].

Inclusive Signal Region			**Exclusive Signal Region**		
Region	Predicted	Observed	Region	Predicted	Observed
IM0	3 120 000 ± 40 000	3 148 643	EM0	1 783 000 ± 26 000	1 791 624
IM1	1 346 000 ± 16 000	1 357 019	EM1	753 000 ± 9000	752 328
IM2	597 000 ± 8000	604 691	EM2	314 000 ± 3500	313 912
IM3	286 000 ± 4000	290 779	EM3	140 100 ± 1600	141 036
IM4	146 400 ± 2300	149 743	EM4	101 600 ± 1200	102 888
IM5	45 550 ± 1000	46 855	EM5	29 200 ± 400	29 458
IM6	16 800 ± 500	17 397	EM6	10 000 ± 180	10 203
IM7	7070 ± 240	7194	EM7	3870 ± 80	3986
IM8	3180 ± 130	3208	EM8	1640 ± 40	1663
IM9	1560 ± 80	1545	EM9	754 ± 20	738
IM10	720 ± 60	807	EM10	359 ± 10	413
IM11	407 ± 34	394	EM11	182 ± 6	187
IM12	223 ± 19	207	EM12	218 ± 9	207

on the prediction gives a feeling of the power of the shape fit in constraining systematics. The level of uncertainty on the background predictions is similar in the first three IM and EM regions. Above $p_{\mathrm{T}}^{\mathrm{recoil}} = 350\,\mathrm{GeV}$ the predictions in exclusive bins are affected by a lower uncertainty. For this reason the sensitivity of an exclusive shape fit to new phenomena is higher. On the other hand, the inclusive fit can be used to set limits on the visible cross-section and it does not need as an input the $p_{\mathrm{T}}^{\mathrm{recoil}}$ shape of a new physics processes.

4.10 Interpretation of the results

In this Section, the constrains set on BSM phenomena using the monojet analysis are presented. To derive such upper limits, in the likelihood model introduced in Equation 4.4 the term parametrizing the signal yields is considered.

4.10.1 Model-independent limits

Model independent limits on the visible cross-section, defined as σ multiplied by acceptance times efficiency, are derived by considering inclusive SR+CR fits. Using the modified frequentist approach described in Ref. [185], an upper limit at 95% of

confidence level is obtained on the signal yields. This is converted into a cross-section value dividing by the integrated luminosity, 139 fb^{-1}. Results are presented in Table 4.15.

Table 4.15. Upper limits on the visible cross-section, as obtained from the inclusive SR+CR fits. Table from Ref. [4].

Selection	$\langle\sigma\rangle^{95}_{\text{obs}}$ [fb]	S^{95}_{obs}	S^{95}_{exp}
$p_{\text{T}}^{\text{recoil}} > 200$ GeV	736	102 274	$83\,000^{+22\,000}_{-23\,000}$
$p_{\text{T}}^{\text{recoil}} > 250$ GeV	296	41 158	$33\,800^{+11\,300}_{-9400}$
$p_{\text{T}}^{\text{recoil}} > 300$ GeV	150	20 893	$15\,400^{+5900}_{-4300}$
$p_{\text{T}}^{\text{recoil}} > 350$ GeV	86	11 937	8300^{+3100}_{-2300}
$p_{\text{T}}^{\text{recoil}} > 400$ GeV	52	7214	4700^{+1800}_{-1300}
$p_{\text{T}}^{\text{recoil}} > 500$ GeV	21	2918	1930^{+730}_{-540}
$p_{\text{T}}^{\text{recoil}} > 600$ GeV	10	1391	940^{+360}_{-260}
$p_{\text{T}}^{\text{recoil}} > 700$ GeV	4.1	574	490^{+190}_{-140}
$p_{\text{T}}^{\text{recoil}} > 800$ GeV	2.1	298	277^{+106}_{-77}
$p_{\text{T}}^{\text{recoil}} > 900$ GeV	1.2	164	168^{+65}_{-47}
$p_{\text{T}}^{\text{recoil}} > 1000$ GeV	1.3	186	119^{+45}_{-33}
$p_{\text{T}}^{\text{recoil}} > 1100$ GeV	0.5	73	75^{+28}_{-21}
$p_{\text{T}}^{\text{recoil}} > 1200$ GeV	0.3	40	49^{+19}_{-14}

A comparison with existing limits, obtained in the previous iteration of the monojet analysis performed by the ATLAS collaboration with the partial Run 2 data set [180], is shown in Figure 4.26. The stronger upper limits obtained are mainly due to the increase in data statistics available, since no information on the shape is used in inclusive fits. However, two improvements of the analysis presented in this thesis are visible here: the additional bin at low $p_{\text{T}}^{\text{recoil}}$ and an improved binning at high $p_{\text{T}}^{\text{recoil}}$.

4.10.2 Constraints on simplified dark matter models

MC simulated samples are produced according to the simplified DM models introduced in Section 1.6.1.

$pp \to \chi\chi + j$ events are generated in the hypothesis of the exchange of a $s-$channel axial vector (DMA) or pseudo-scalar mediator (DMP), at NLO and LO in QCD respectively, using Powheg-Box [89]. The revision 3049 of the models, documented in Ref. [88] is adopted. NNPDF3.0NLO (NNPDF2.3LO) is the PDF set used in the ME generation for the DMA (DMP) signal. The renormalization and factorization scales are taken equal to $\sqrt{m^2_{\chi\chi} + p_{\text{T},j_1}} + p_{\text{T},j_1}$, where p_{T,j_1} is the transverse momentum of the hardest jet at ME level. The mediator width is set to the minimal allowed, as discussed in Section 1.6.1. For the DMA (DMP) model, the coupling between the mediator and SM particles is set to the benchmark value of $g_q = 0.25$ ($g_q = 1$), while the coupling with DM particles is set to $g_\chi = 1$ ($g_\chi = 1$). Events are generated with a truth $E_{\text{T}}^{\text{miss}}$ filter of 150 GeV, which is checked to be fully efficient at reconstruction level above 200 GeV. The ME calculation is interfaced with Pythia 8.205 for the

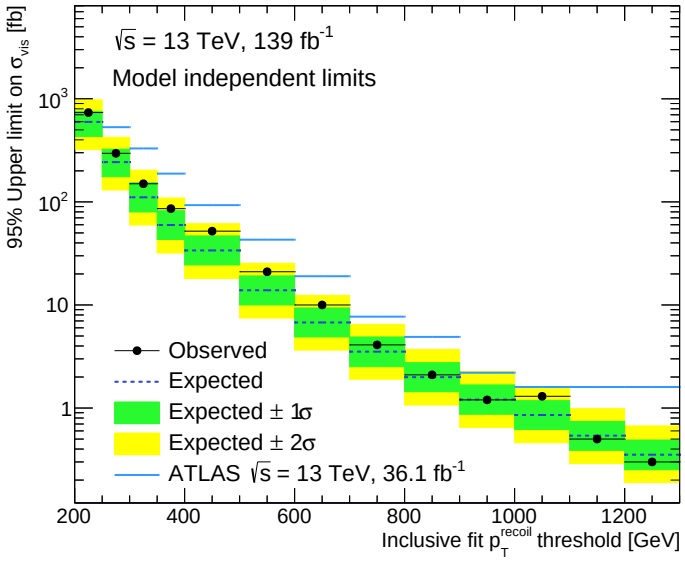
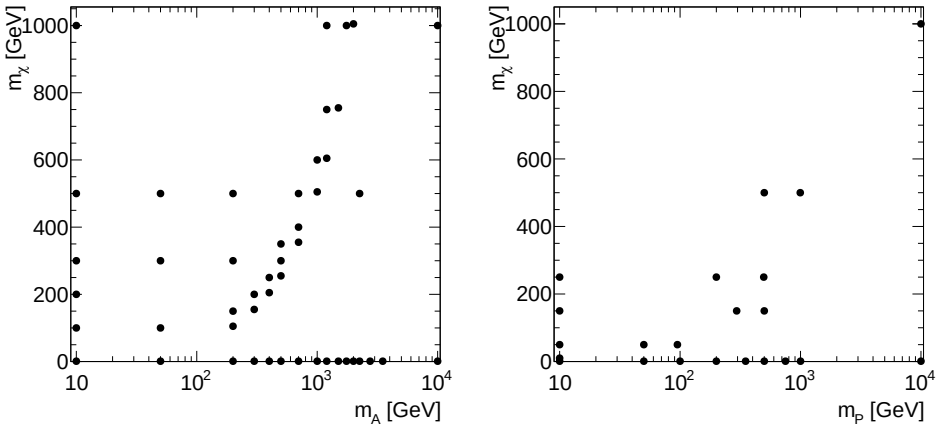


Figure 4.26. Observed upper limits on the visible cross-section, compared to the expected value, and results obtained in the previous iteration of the monojet analysis by the ATLAS collaboration partial Run 2 data set.

parton showering, with the NNPDF2.3LO set of PDF and the A14 tune of the parameters.

A grid of signal points is generated, as shown in Figure 4.27. Since in the on-shell regime the signal acceptance is constant for different values of the mass of the WIMPs [86], simulated samples are produced for several values of the mediator mass fixing $m_\chi = 1\,\text{GeV}$. Fewer events are generated only at truth level to evaluate the cross-sections for $m_\chi \neq 1$ to perform a rescaling of the obtained limits up to the diagonal of the (m_{med}, m_χ) plane.

Signal systematic uncertainties. Since DM particles escape undetected from ATLAS, experimental systematic uncertainties are derived in the same way as it is done for the SM background samples. The main source of systematic is due JES and JER. Variations of the pre-fit signal yields due to detector-related uncertainties are presented for two benchmark signals in Table 4.16. Uncertainties on lepton reconstruction and identification are due to the presence of the veto in SR on such objects. However, they have a subdominant effect.



(a) DMA model (b) DMP model

Figure 4.27. Simulated signal samples grid for DM model dependent interpretation. Credits to Giuliano Gustavino.

Table 4.16. Pre-fit impact of systematic uncertainties on the SR expected signal yields for two DM benchmark signals.

	$p_{\mathrm{T}}^{\mathrm{recoil}}$ interval [GeV]												
Source (%)	[200,250]	[250,300]	[300,350]	[350,400]	[400,500]	[500,600]	[600,700]	[700,800]	[800,900]	[900,1000]	[1000,1100]	[1100,1200]	[1200,+∞)
DMA, $m_\chi = 1\,\mathrm{GeV}$, $m_{Z_A} = 2\,\mathrm{TeV}$													
Muons	0.01	0.01	0.0	0.01	0.02	0.02	0.02	0.02	0.02	0.02	0.02	0.02	0.02
Electrons	0.03	0.03	0.03	0.03	0.03	0.03	0.03	0.03	0.03	0.03	0.03	0.04	0.05
Jets	1.32	1.56	1.85	1.88	1.78	1.79	1.85	1.98	2.15	2.34	2.84	3.55	4.18
$E_{\mathrm{T}}^{\mathrm{miss}}$	0.2	0.2	0.19	0.19	0.2	0.22	0.21	0.19	0.18	0.19	0.19	0.2	0.27
DMP, $m_\chi = 1\,\mathrm{GeV}$, $m_{Z_P} = 100\,\mathrm{GeV}$													
Muons	0.01	0.0	0.01	0.01	0.02	0.02	0.04	0.07	0.08	0.08	0.08	0.08	0.08
Electrons	0.04	0.05	0.05	0.06	0.08	0.12	0.15	0.16	0.21	0.25	0.25	0.25	0.25
Jets	4.37	4.41	4.53	4.5	4.83	4.93	5.02	6.09	6.76	6.81	6.81	6.81	6.81
$E_{\mathrm{T}}^{\mathrm{miss}}$	0.38	0.29	0.11	0.06	0.11	0.29	0.53	0.69	0.73	0.73	0.73	0.73	0.73

The effect of modelling systematic uncertainties can be divided in an overall normalization and an acceptance component. The latter can affect how events are distributed among different $p_{\mathrm{T}}^{\mathrm{recoil}}$ bins, and therefore is included in the likelihood fit. The former instead is an uncertainty on a somehow arbitrary cross-section, therefore its effect is only shown a posteriori on the exclusion contour.

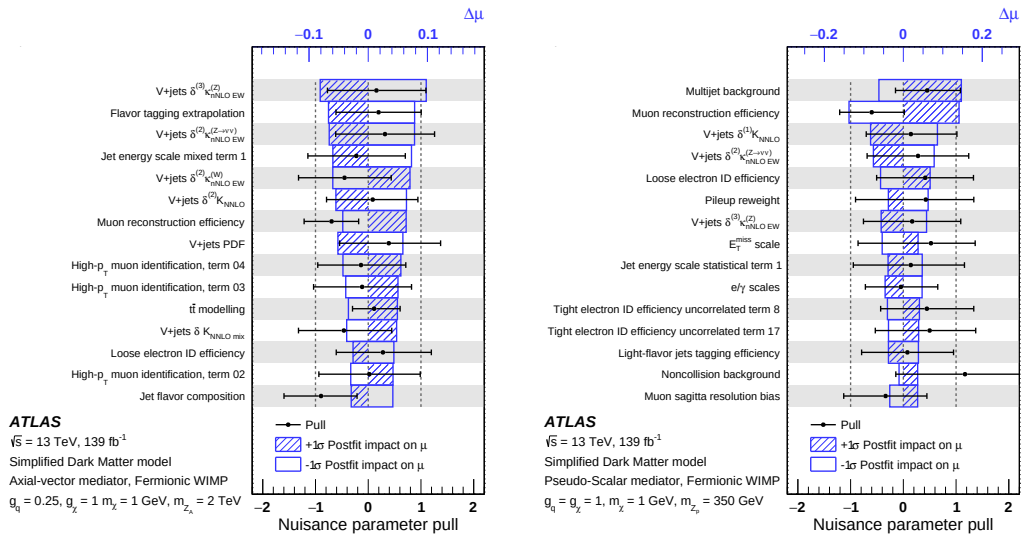
Uncertainties on the truncation of the perturbative QCD series are estimated by varying the renormalization and factorization scales. Six variations, both individual and simultaneous by a factor 0.5 and 2 are performed on μ_r and μ_f. Cases in which one scale is varied by a factor 0.5 and the other by a factor 2 are not included. Half of the width of the obtained envelope is taken as the uncertainty. Scale variation uncertainties range between 0.1% and 6.5% for DMA signal samples. Lower uncertainties are obtained for samples with higher DM and mediator mass. On DMP samples, uncertainties range between 0.4% and 21%; also in this case higher mediator masses lead to lower scale uncertainties.

PDF acceptance uncertainties are evaluated from the 100 replicas available in the NNPDF sets. Each variation is summed in quadrature to form a final uncertainty. No significant dependencies on the mediator or DM mass is observed for the DMA model. Uncertainties range between 0.1% and 10%. For the DMP signal samples, lower uncertainties are observed for higher DM mass. Overall, PDF uncertainties are between 0.2% and 20%. In both cases, such uncertainties increase as a function of $p_{\mathrm{T}}^{\mathrm{recoil}}$.

Additional modelling uncertainties are evaluated on the tuning of ISR, FSR and multiple-parton interactions parameters. Five independent schemes are tested, and the variation of each scheme with respect to the nominal one is summed in quadrature to the other to obtain a combined uncertainty. An effect of around 3% (6%) is observed for DMA (DMP) signal samples.

As already mentioned, overall cross-section uncertainties are applied to the exclusion contour directly. Scale (PDF) uncertainties on the total cross-section give a 5% (20%) variation of the cross section of DMA signal samples, and 10% ($^{+50\%}_{-30\%}$).

The effect of systematic uncertainties on the signal strength, measured in the SR+CR fit including signal MC predictions, can be evaluated by means of the *ranking plots*. The idea behind is similar to the one presented in Section 4.9.1. The best fit value of the signal strength is compared to the one obtained in a fit in which a single NP is fixed to its best fit value $\pm 1\sigma$ post-fit. The absolute shift of the signal strength, $\Delta\mu$, shows the impact of the systematic uncertainty on the measurement. The ranking plots of two benchmark signals are presented in Figure 4.28. As already mentioned, DMA signals have an harder spectrum than SM backgrounds. Among the top-ranked NPs, in fact, V+jets modelling ones are found, since most of the sensitivity comes from the tail of the $p_{\mathrm{T}}^{\mathrm{recoil}}$ distribution. On the contrary, DMP signals have a softer $p_{\mathrm{T}}^{\mathrm{recoil}}$ spectrum than SM processes, thus the signal strength is expected to be more affected by systematic uncertainties dominant at low $p_{\mathrm{T}}^{\mathrm{recoil}}$. The top-ranked NP in this case is the one associated with the multijet background estimate. However, all the $p_{\mathrm{T}}^{\mathrm{recoil}}$ shape is used in the fit, thus also in this case V+jets modelling uncertainties have a leading impact on the measured signal strength.



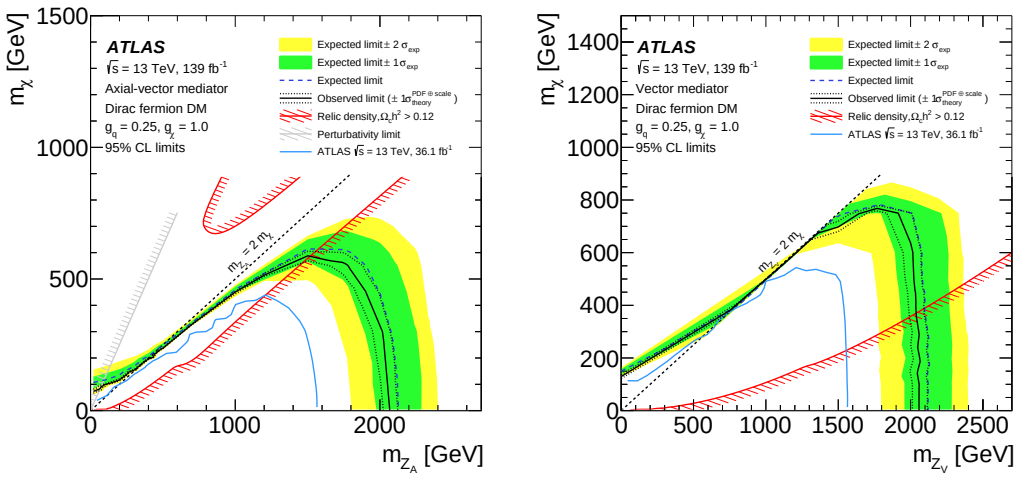
(a) DMA, $m_\chi = 1\,\text{GeV}$, $m_{Z_A} = 2\,\text{TeV}$ (b) DMP, $m_\chi = 1\,\text{GeV}$, $m_{Z_P} = 350\,\text{GeV}$

Figure 4.28. Ranking plots obtained for a DMA (a) and DMP (b) benchmark signal point. Ranking of the systematic uncertainties on the measured cross-section σ for a DMA (a) and DMP (b) benchmark signal point. The figure shows the effect of the fifteen most significant uncertainties. Further details on the procedure to derive the effect are provided in the text. Figures from the auxiliary material of Ref. [4].

Exclusion contours. In Figure 4.29(a) the exclusion contour obtained for the DMA model is presented. Results are shown in the (m_{Z_A}, m_χ) plane; the shaded in the bottom-left corner indicates values of the parameters for which the theory is no longer perturbative. The red line indicates the value of the parameters of the model considered which would match the observed relic density observed in the universe by WMAP. The evolution as a function of the model parameters is evaluated with the `MadDM` tool [186]. Values of the parameters where $\Omega_c h^2 < 0.12$ would imply that this model is not able to account for all the observed relic density.

Values of the axial-vector mediator mass up to 2067 GeV are excluded for WIMPs of 1 GeV of mass. The largest value of m_χ excluded is 585 GeV, for a mediator with $m_{Z_A} \simeq 1.5\,\text{TeV}$. The sensitivity rapidly drops in the off-shell-regime since the cross-section of the interaction is suppressed by a factor $1/m_{Z_A}^4$. Compared to previously obtained results [180], the excluded value of the mediator mass is increased by about 450 GeV. Results are obtained also under the hypothesis of the exchange of a vector mediator (DMV). Since the acceptance of the DMA and DMV models is the same, exclusion limits obtained on the former model are rescaled by the ratio of the cross-sections. Obtained results in the DMV hypothesis are presented in Figure 4.29(b).

The DMA exclusion contour is further converted into a limit on the interaction cross-section between WIMPs and SM nucleons. Due to the axial-vector nature of the mediator, limits are set under a spin-dependent interaction hypothesis. The translation of the limits is done as described in Section 1.6.1 of this thesis, and the



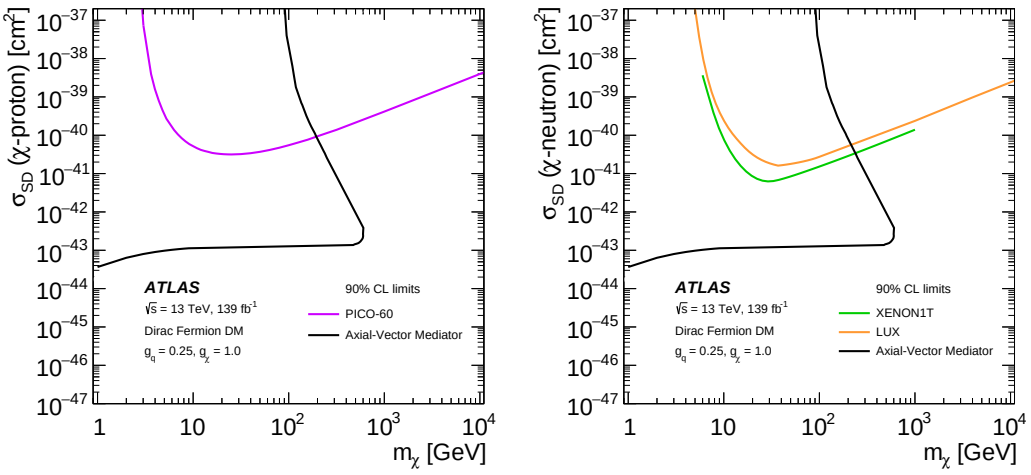
(a) DMA model (b) DMV model

Figure 4.29. Exclusion contours in the (m_{med}, m_χ) plane for the (a) DMA and (b) DMV simplified models, for fixed values of the coupling constants, $g_q = 0.25$, $g_\chi = 1$. Figures from Ref. [4] and its auxiliary material.

obtained results are presented in Figure 4.30.

In this case, limits are shown at 90% of CL, to be compared with direct detection (DD) search results. Compared to the ones of the PICO-60 [187], Lux [188] and XENON-1T [189] experiments, ATLAS results are able to exclude lower values of the interaction cross-section, and to expand current boundaries to lower WIMP mass values. However, ATLAS results strongly depend on the assumptions made on the value of the couplings between the mediator and WIMPs, and on the width of the mediator. Different choices, in fact, can drastically affect the monojet exclusion power. Direct detection contours instead remain unchanged.

Following the procedure described in Section 1.6.1, the DMV exclusion contour is translated into boundaries on the spin independent WIMP-nucleon scattering cross section at 90% CL. This is presented in Figure 4.31 as a function of the WIMP mass. Results are compared to recent results from DD search, provided by the XENON-1T [190, 191], PandaX [192] and DarkSide [193] experiments. Stronger limits are obtained at low WIMP mass values. Again though, ATLAS results are strongly model-dependent, and might change drastically under different assumptions with respect to those made in the considered DMV model.



(a) (b)

Figure 4.30. Exclusion contours in the WIMP mass, interaction cross section with protons (a) and neutrons (b) plane, in the spin dependent interaction hypothesis. Limits are compared with the ones obtained by DD search. ATLAS results depend on the assumptions made on the value of the couplings between the mediator and WIMPs, and on the width of the mediator. Figures from Ref. [4].

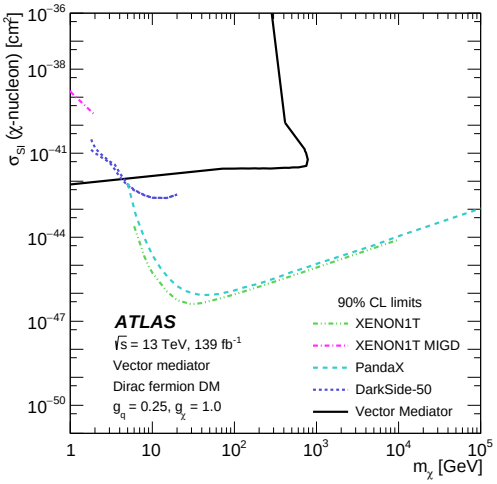
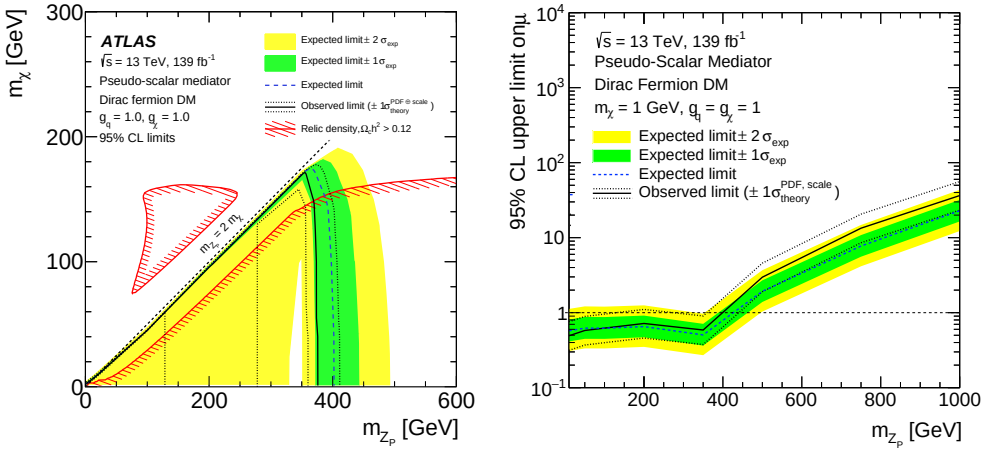


Figure 4.31. Exclusion contours in the WIMP mass, scattering cross-section with SM particles plane, in the spin independent interaction hypothesis. Limits are compared with the ones obtained by DD search. ATLAS results depend on the assumptions made on the value of the couplings between the mediator and WIMPs, and on the width of the mediator. Figures from the auxiliary material of Ref. [4].

Exclusion contours on the DMP model are presented in Figure 4.32(a) at 95% CL. This is the first time that the monojet analysis of the ATLAS collaboration is able to close an exclusion contour for such model in the (m_{Z_P}, m_χ) plane. This is possible thanks to the lower p_T^{recoil} and leading jet p_T thresholds adopted in this

version of the analysis.

Values of the mass of the mediator up to 376 GeV are excluded for 1 GeV WIMPs. The shape of the $+2\sigma$ expected band and $+1\sigma_{obs}$ uncertainty can be better understood by looking at Figure 4.32(b). This shows the 95% CL upper limit on the signal strength, as measured for models of different mediator mass and fixed $m_\chi = 1$ GeV. The $+2\sigma$ band is above 1 for values of the mediator mass up to around 300 GeV. The cross-section of these processes rapidly increases around the two m_{top} threshold, since additional diagrams including the top quark have to be considered. Thus, the sensitivity also increases, and the resulting limits are stronger.



(a) (b)

Figure 4.32. (a) Exclusion contour in the (m_{Z_P}, m_χ) plane for the DMP model (figure from Ref. [4]). (b) Upper limit on the signal strength (μ) obtained for the DMP model with a fixed value of $m_\chi = 1$ GeV. In both plots the coupling constants are fixed to the benchmark value of $g_q = g_\chi = 1$.

The results obtained for a pseudo-scalar mediator are translated into upper limits on the WIMP-pair annihilation rate, as described in Section 1.6.1. This quantity is defined as the product of the interaction cross-section times the relative velocity of DM particles, averaged over the DM velocity distribution ($\langle \sigma v_{\text{rel}} \rangle$). Upper limits on this quantity are shown in Figure 4.33 as a function of the WIMP mass. The obtained result is compared to the indirect detection DM search performed by the Fermi-LAT experiment [194]. Values above the drawn lines are excluded at 95% of CL. Also in this case, ATLAS results depend on the assumptions made in the DMP simplified model considered.

Comparison to other ATLAS dark matter searches

In the wider ATLAS picture, the monojet analysis provides complementary results to other DM searches [195]. In the on-shell regime, it is the most sensitive mono-X search on DMA, DMV and DMP models. Searches which target the resonant production of the new mediator, instead, like the dijet one [196], exclude higher

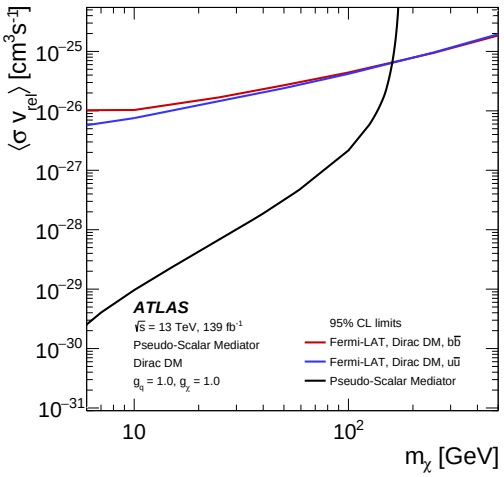


Figure 4.33. 95% CL exclusion contour on the WIMP pair annihilation rate shown as a function of the WIMP mass. Results are compared to the limits obtained by the Fermi-LAT experiment [194]. Figure from the auxiliary material of Ref. [4].

values of its mass. A summary plot of ATLAS constraints on the DMA model is presented in Figure 4.34. The off-shell region for mediator masses below 500 GeV is not covered by the standard dijet search due to limitations of trigger thresholds. This lower part is covered instead by tri-jet searches or by trigger-level-analyses, which can afford lower trigger thresholds at the cost of limited amount of information read out from the detector. References to the mentioned searches are given in the figure.

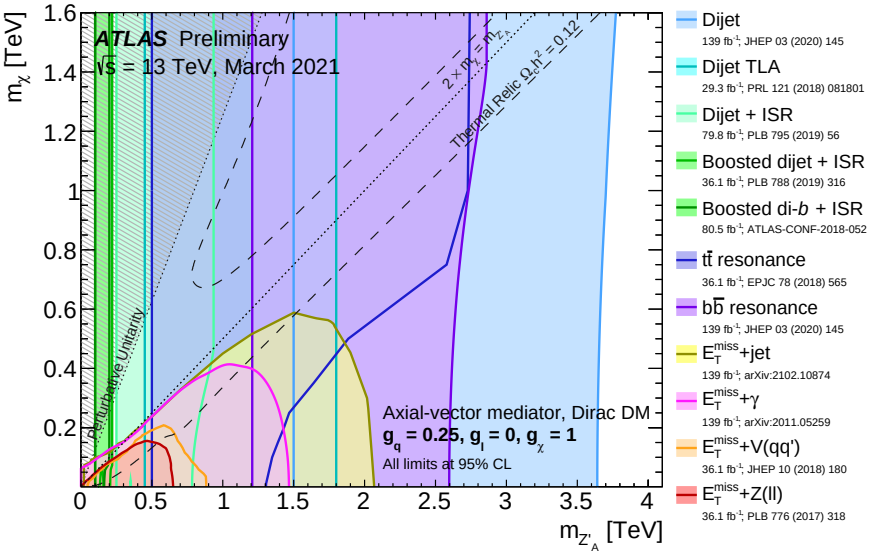


Figure 4.34. Comparison of the constraints obtained by various ATLAS analyses on the parameters of the DMA model. Figure from Ref. [195].

Concerning the DMP model, also in this case other ATLAS searches provide

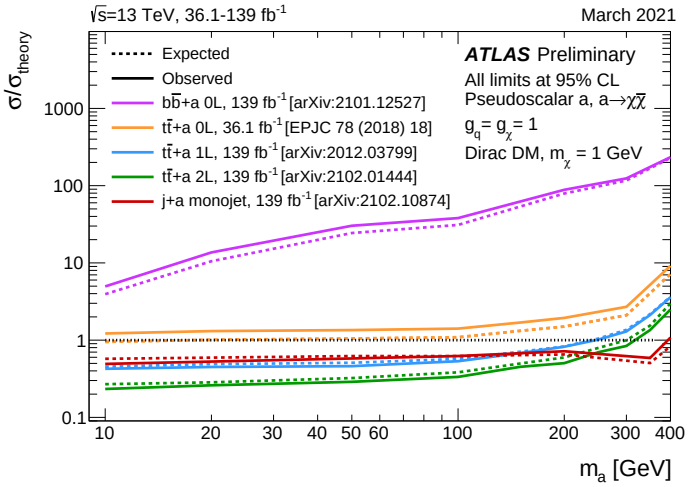


Figure 4.35. Comparison of the constraints obtained by various ATLAS analyses on the parameters of the DMP model. Figure from Ref. [195].

complementary sensitivity to its parameter space. In Figure 4.35, the upper limit on the signal strength for WIMP masses of 1 GeV is presented as a function of the mediator mass. Even if the monojet analysis is not setting the strongest limits on the signal strength at low m_{med}, it is the one that excludes the largest value, up to $m_{Z_P} = 376\,\text{GeV}$.

4.10.3 Constraints on compressed SUSY scenarios

Simulated signal samples of the SUSY models introduced in Section 1.6.1 have been generated for several benchmark points of $m_{\tilde{q}}$ and $m_{\tilde{\chi}_1^0}$. The hard scattering process is generated with MadGraph v2.2.3 including up to two additional partons at LO in QCD. The NNPDF23LO PDF set is used, and the renormalization and factorization scales are set to $\mu = \sqrt{\sum_i m_i^2 + p_{\text{T},i}^2}$, where the sum includes all the final state particles generated at ME level. The ME is interfaced with Pythia 8.186 for the parton showering using the CKKW-L prescription; the matching scale is set to $m_{\tilde{q}}/4$. Signal samples cross-sections have been normalized at approximate NNLO+NNLL accuracy following Ref. [197, 198].

As already discussed in Section 1.6.1, the monojet analysis is sensitive in the so-called *compressed scenario*, which foresee a small mass difference between the decaying squark and the neutralino. Signal samples have been thus generated for $\Delta(m_{\tilde{q}}, m_{\tilde{\chi}_1^0}) \simeq 5 \div 50\,\text{GeV}$, while the mass of the squarks is varied between 300 and 1200 GeV.

Signal systematic uncertainties. As for the simplified DM models, the produced neutralinos do not interact with the ATLAS detector, thus experimental systematic uncertainties are derived as done for SM backgrounds. Pre-fit signal yields of the models considered vary mainly for the effect of systematic uncertainties associated with the jet measurements, with contributions ranging between 2% and 5% at low at high $p_{\text{T}}^{\text{recoil}}$, respectively.

Signal modelling uncertainties are also taken into account. Due to lack of Monte Carlo statistics, modelling uncertainties are evaluated by looking at the inclusive yields variations, thus no $E_{\mathrm{T}}^{\mathrm{miss}}$ dependence is taken into account. The effect of a variation in the renormalization and factorization scales, or in the PDF set adopted in the signal generation are evaluated following the prescriptions reported in Ref. [199].

PDF uncertainties include both an intra- and an inter-PDF set component. The former effect is evaluated by taking the RMS of the 100 replicas variations available in the NNPDF set. The latter is derived by a comparison of the yields obtained using the CT10 and MMHT2014lo68c PDF sets. The two variations are then summed in quadrature. Scale and PDF variations are consistent between different mass points and between the different SUSY models considered. Thus the uncertainties calculated from the $(m_{\tilde{t}}, m_{\tilde{\chi}_1^0}) = (700, 693)$ GeV point of the direct stop decay process simulation is used for all the SUSY signal samples.

Additional uncertainties are derived for the variation of PS parameters which impact the modelling of ISR, FSR and multi-parton interactions. Such contributions are summed in quadrature into a single systematic uncertainty.

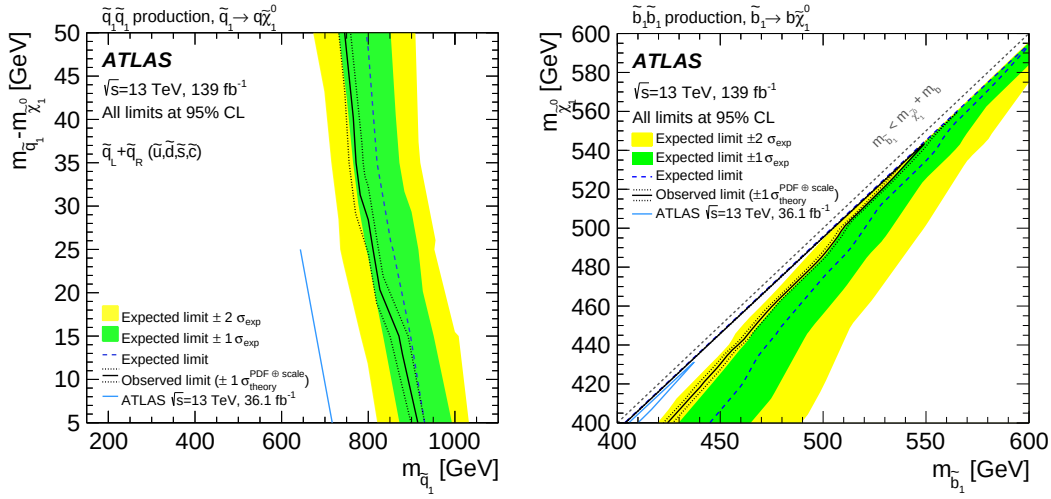
The effect of modelling uncertainties is summarised in Table 4.17. Merging scale variations are also reported, and are derived by comparing the nominal predictions with the ones from alternative choices.

Table 4.17. Modelling systematic uncertainties due to alternative setups of the SUSY signal samples MC simulation.

Modelling uncertainty	Variation [%]
Renormalization scale	±2.8
Factorization scale	±2.8
Merging scale	±7.0
ISR+FSR+MPI	±7.6
PDF	±5.1

Exclusion contours. The exclusion contour obtained for the squark pair production model is reported in Figure 4.36(a). Limits are shown in the plane in which the x-axis corresponds to the squark mass, $m_{\tilde{q}}$, and the y-axis is the mass difference between the decaying squark and the neutralino. Squark masses below $800 \div 900$ GeV are excluded for mass splittings between 5 and 50 GeV, with most stringent limits obtained in the most compressed scenario. The results obtained by the monojet analysis presented in this thesis is compared to the previous iteration of this analysis, and as can be seen largest mass splittings have been investigated in the newer result. In Figure 4.36(b) constraints on the sbottom pair production model are presented in the $(m_{\tilde{b}_1}, m_{\tilde{\chi}_1^0})$ plane. Limits on the sbottom quarks of mass are extended up to around 550 GeV for low mass splittings.

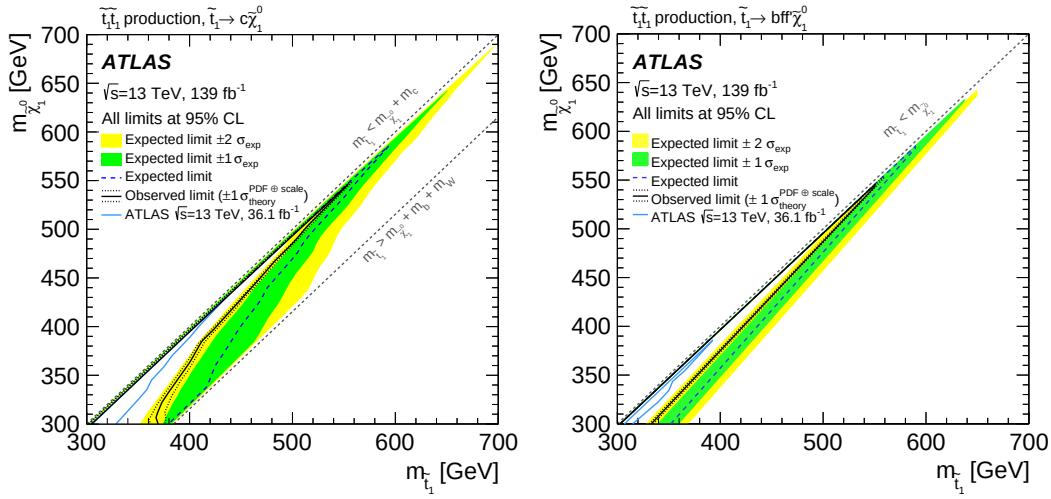
Similar exclusion contours are presented in Figure 4.37 for the search of top-squarks. In particular, in Figure 4.37(a) the constraints set on the mass values considering the direct stop quark decay into a charm quark and a neutralino, while Figure 4.37(b) shows the limit obtained considering four-body decays of the top-



(a) (b)

Figure 4.36. Exclusion contour in the $(m_{\tilde{q}_1}, m_{\tilde{q}_1} - m_{\tilde{\chi}_1^0})$ plane (a) and $(m_{\tilde{b}_1}, m_{\tilde{\chi}_1^0})$ plane (b) for the squark and sbottom pair production models, respectively. Figure from Ref. [4].

squarks. Stop masses up to around 560 GeV are excluded by the presented analysis, extending significantly previous limits set by the monojet analysis performed with part of the LHC Run 2 data-set [180].



(a) (b)

Figure 4.37. Exclusion contour in the $(m_{\tilde{t}_1}, m_{\tilde{\chi}_1^0})$ plane (a) and $(m_{\tilde{t}_1}, m_{\tilde{\chi}_1^0})$ plane (b) for the squark pair production and the direct and four-body decays, respectively. Figure from Ref. [4].

4.10.4 Constraints on the $H \to$ inv. branching ratio

The Higgs boson branching fraction to invisible final states ($\mathcal{B}(H \to \text{inv.})$) via the $H \to ZZ^* \to \nu\bar{\nu}\nu\bar{\nu}$ process, is predicted by the standard model to be 0.1% [35]. Any deviations from such value might hint that new phenomena not accounted for in the SM lead to the production of invisible particles, such as DM ones. Direct searches for the $H \to$ inv. decay have been performed in different topologies in ATLAS, and the latest combination of such results was able to constrain the $\mathcal{B}(H \to \text{inv.})$ below the 10% level at 90% of CL [41]. These results however do not include the ones from the full Run 2 monojet search, which are provided by the analysis presented in this thesis.

All the production modes of the Higgs boson are taken into account. The leading one is the gluon-gluon fusion (ggF) which accounts for 73% of the total accepted SR events. The second contribution is due to vector boson fusion (VBF) production, 18%, followed by the VH topology (including $gg \to ZH$), 8% and the $t\bar{t}H$ process, 1%. Simulated samples are produced at NLO in QCD using Powheg-Box v2 for all the aforementioned processes, except for the ggF and $gg \to ZH$ one. For the former Powheg NNLOPS [200, 201] is used to generate events at NNLO in QCD, while the latter is generated in Powheg at LO. The PDF4LHC_NLO PDF set has been used in all cases for the nominal predictions. The ggF, VBF and VH samples are interfaced with Pythia 8.230 (8.212 for $gg \to ZH$) for the parton showering, and use the AZNLO tune and the CTEQ6L1 PDF set. The $t\bar{t}H$ sample uses the A14 tune and NNPDF2.3LO as PDF set instead. All the simulated samples are interfaced with EvtGen, which handles the HF hadrons description. Samples cross-sections are normalized to the highest order available. Gluon-gluon fusion production is normalized to the next-to-NNLO QCD and NLO EW cross-section, VBF production to the NNLO QCD and NLO EW one. Events produced in the VH (excluding $gg \to ZH$) and $t\bar{t}H$ topologies are normalized to the NLO QCD and NLO EW cross-section, while the $gg \to ZH$ process to the NLO+NLL QCD accuracy.

In all samples, the Higgs boson is forced to decay in four neutrinos, via the process $H \to ZZ^* \to \nu\bar{\nu}\nu\bar{\nu}$, 100% of the times. Upper limits on the signal strength of such a process is directly converted into a limit on $\mathcal{B}(H \to \text{inv.})$.

Experimental systematic uncertainties can vary the pre-fit event yields of the $H \to$ inv. signal. The largest effects are related to JES and JER uncertainties. Modelling uncertainties are also considered. PDF uncertainties are derived taking in each $p_{\mathrm{T}}^{\mathrm{recoil}}$ bin the standard deviation of the 30 PDF4LHC_NLO eigenvector variations. Scale uncertainties are derived as recommended by the LHC Higgs working group. Uncertainties on the PS model are evaluated by comparing the nominal sample to alternative predictions obtained varying the renormalization and factorization scales, the value of α_s, and the hadronization model. Uncertainties on higher order EW corrections are applied to the VBF sample. An overview of the size of the different contributions is presented in Table 4.18.

The observed (expected) upper limit on the $\mathcal{B}(H \to \text{inv.})$ is $34\%(39^{+16}_{-11}\%)$ at 95% CL. This is the third most stringent limit, up to date, set by a single ATLAS analysis.

Table 4.18. Pre-fit effect of experimental and modelling systematic uncertainties associated with the $H \to$ inv. signal sample, as a function of the $p_{\mathrm{T}}^{\mathrm{recoil}}$ bin.

	$p_{\mathrm{T}}^{\mathrm{recoil}}$ bin [GeV]												
Source (%)	[200,250]	[250,300]	[300,350]	[350,400]	[400,500]	[500,600]	[600,700]	[700,800]	[800,900]	[900,1000]	[1000,1100]	[1100,1200]	[1200+)
Experimental uncertainties													
Muons	0.02	0.04	0.06	0.09	0.11	0.22	0.45	0.77	0.91	0.91	0.91	0.91	0.91
Electrons	0.08	0.09	0.11	0.14	0.16	0.25	0.43	0.56	0.59	0.59	0.59	0.59	0.59
Jets	3.68	4.19	4.61	4.79	4.74	4.8	5.37	6.41	6.91	6.91	6.91	6.91	6.91
$E_{\mathrm{T}}^{\mathrm{miss}}$	0.26	0.24	0.08	0.23	0.37	0.43	0.66	0.85	0.9	0.9	0.9	0.9	0.9
Modelling uncertainties													
Scale variation	10												
PDF variations	0.38	0.39	0.39	0.41	0.45	0.47	0.50	0.55	0.6	0.67	0.68	0.70	0.76
Parton shower uncertainties	3.0	3.3	3.6	3.9	4.2	4.7	5.3	6.0	6.6	7.6	7.9	8.3	8.8
EW corrections	1.4	1.7	2.1	2.5	3.0	3.8	4.6	5.4	6.2	6.9	7.9	8.5	10

4.11 Monojet and Long-Lived-Particles

Simulated signal events of the FRVZ (Hss) model are generated at LO in QCD using MadGraph5 aMC@NLO v2.6.2 generator [202], using Pythia v8.212 (v8.230) for parton showering, with the NNPDF2.3LO PDF set and the A14 tune. In the FRVZ model, hidden-sector particles masses are set to the benchmark values of $m_{f_d} = 5\,\mathrm{GeV}$ and $m_{\mathrm{HLPS}} = 2\,\mathrm{GeV}$. The simulated γ_d mass is chosen to be 400 MeV. Events are generated for three benchmark dark photon mean lifetime values, expressed in terms of $c\tau_{\sim}$, 5, 50 and 500 mm.

A lifetime reweighting procedure (LTR) is used to emulate a new signal sample characterized by a different value of the mean lifetime, such that it is possible to probe the model as a function of $c\tau$. For a simulated sample of a given $c\tau_{\mathrm{sim}}$, the lifetime of each γ_d , indicated by t_i, follows the probability distribution function

$$f(t_i|\tau_{\mathrm{sim}}) = \frac{1}{\tau_{\mathrm{sim}}} \exp\left(-\frac{t_i}{\tau_{\mathrm{sim}}}\right). \tag{4.7}$$

To correct the total event weight defined in Section 4.2.2, a LTR weight is calculated by multiplying weights obtained for each dark photon given their proper lifetimes. The weight for each γ_d is calculated from the ratio of the exponential probability distributions with mean proper lifetime τ_{sim} and the one with the new mean proper lifetime value τ_{new}, given the lifetime of the considered dark photon. It can be written as

$$w_i(t_i|\tau_{\mathrm{sim}} \to \tau_{\mathrm{new}}) = \frac{\tau_{\mathrm{sim}}}{\tau_{\mathrm{new}}} \exp\left[-t_i\left(\frac{1}{\tau_{\mathrm{new}}} - \frac{1}{\tau_{\mathrm{sim}}}\right)\right]. \tag{4.8}$$

However, if this procedure is applied in order to reweight a sample from τ_{sim} to tau_{new} with $\tau_{\mathrm{new}} \gg \tau_{\mathrm{sim}}$ or $\tau_{\mathrm{new}} \ll \tau_{\mathrm{sim}}$, to reproduce the expected decay time distribution many events will be weighted with a very small LTR weight, while a few will be weighted with a very large LTR weight. For this reason, the resulting re-weighted sample will be affected by large statistical uncertainty.

In order to overcome such a limitation, if multiple generated samples are available it is possible to adopt a multi-sample LTR. This method uses part of the events of the samples with mean lifetime $\tau_{\mathrm{sim}_1} \ldots \tau_{\mathrm{sim}_n}$ to build a new one characterized by τ_{new}. The multi-sample LTR consists in applying the simple-LTR, but the events are taken from the different samples such that no large LTR weights appear.

As previously mentioned, in the case of the investigated FRVZ model three samples of different mean proper lifetime were generated. Since in the events there

are two dark photons, for a sample with fixed mean proper-lifetime τ_{sim_1}, the distribution of the sum of the decay times of the two dark photons is given by

$$f(t_1 + t_2|\tau_{\text{sim}_1}) = \frac{1}{\tau^2_{\text{sim}_1}} \exp\left(-\frac{t_1 + t_2}{\tau_{\text{sim}_1}}\right). \tag{4.9}$$

The $c\tau$ value for which the distributions with mean lifetime $c\tau_{\text{sim}_1}$ and τ_{sim_2} are equal is called *critical time*, and its used to decide whether or not to use the events of each generated sample to build the new one, with a mean lifetime $c\tau_{\text{new}}$. With N generated samples, $N - 1$ critical times can be found, and are given by

$$\tau_{c_{ij}} = 2 \ln\left(\frac{\tau_j}{\tau_i}\right) \Big/ \left(\frac{1}{\tau_i} - \frac{1}{\tau_j}\right), \tag{4.10}$$

were i and j represent two consecutive simulated $c\tau$ values (that are for example in this case 5 mm and 50 mm, or 50 mm and 500 mm). The factor 2 is associated to the fact that there are 2 LLPs in the final states. It can be trivially derived by imposing the equivalence of two Equations 4.9, written for two benchmark $c\tau$ values.

For each event of the generated sample with $c\tau_{\text{sim}_1}$, the sum of the decay times of the dark photons, $t_1 + t_2$, is evaluated. If $t_1 + t_2 < c\tau_{12}$, the event is kept and a LTR weight is evaluated per each dark photon via Equation 4.8, using $\tau_{\text{sim}} = \tau_{\text{sim}_1}$. If $t_1 + t_2 > c\tau_{12}$ the events are not used. A similar procedure is adopted to re-weight the events of the other two generated sample, and in the end the re-weighted one is produced. This procedure can be easily extended to N samples or M long-lived-particles in the final states, and allows to maximise the available MC statistics wile keeping the LTR weight limited.

The procedure can be further understood by looking at Figure 4.38, which shows the distribution of the sum of the lifetime of two dark photons for $c\tau_1 = 5$ mm, $c\tau_2 = 50$ mm and $c\tau_3 = 500$ mm. The distribution for the hypothetical re-weighted sample with $c\tau = 225$ mm is shown by the dashed line. In each interval of $t_1 + t_2$, below $c\tau_{12}$, between $c\tau_{12}$ and $c\tau_{23}$, and above $c\tau_{23}$, only the events from the most populated generated sample are used to build the re-weighted one.

The LTR procedure has been cross-validated by re-weighting one generated sample (e.g. the one with $c\tau = 5$ mm) to the mean lifetime of another generated one (e.g $c\tau = 50$ mm). A perfect closure is observed between the $p_{\text{T}}^{\text{recoil}}$ distributions of the generated and reweighted samples.

For the Hss model, three different values of the mass of the scalar particle s have been considered, 15, 35 and 55 GeV. For each mass value, two simulated signal samples at different lifetime values, ranging between a few cm and 5.5 m, are available. Also in this case, the multi-sample LTR is performed to produce more samples in order to test multiple $c\tau$ hypotheses.

In both models, only the gluon-gluon fusion production of the SM Higgs boson is considered. At very large lifetime values, one would expect that the upper limit on such model converges to the monojet constraint on the $\mathcal{B}_{H\to\text{inv}}$. This does not happen for two reasons: the first is that VBF and VH production modes of the Higgs boson, taken into account in the result presented in Section 4.10.4, account for a non-negligible contribution to the total expected number of events. The second

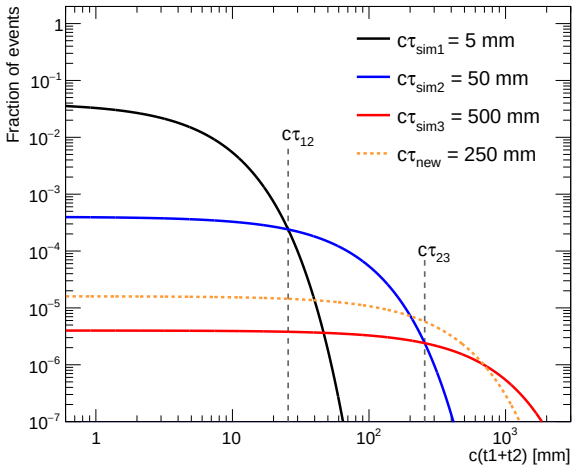


Figure 4.38. Distributions of the sum of the decay time of two dark photons, indicated by $t1$ and $t2$ respectively, for the three generated benchmark samples. These are compared to the distribution of an hypothetical new sample of $c\tau = 225\,\text{mm}$. The vertical lines represent the critical times, as defined in the text.

one is that in monojet the simulation of the ggF process is done at NNLO in QCD, while for this LLP models is done at LO. The difference between the differential $p_{\text{T}}^{\text{recoil}}$ event yield can be up to 50% at high transverse momentum. To correct for the latter effect, a one dimensional reweight of the $p_{\text{T}}^{\text{recoil}}$ distribution is performed in LLP signal samples. It is based on the p_{T} of the truth Higgs boson in each event, such that particle-level distributions of the $p_{\text{T}}(H)$ obtained in the LO QCD samples match the distribution predicted by the NNLO one. After this correction, samples are normalized to the N^{3}LO QCD and NLO EW cross-section.

The $p_{\text{T}}^{\text{recoil}}$ shape for samples with very large $c\tau$ values is found to be consistent with the one used in the monojet analysis for the ggF $H \to$ inv. process. This allows to extrapolate the limits obtained as a function of $c\tau$ of the LLP up to very large lifetime values. Such extrapolation is also performed to mitigate the impact of the MC statistical uncertainty. In fact, as previously mentioned the LTR procedure does not yield reliable results when a MC sample is re-weighted to a significantly different lifetime value. For weighted events the relative MC statistical uncertainty σ_{rel} is given by

$$\sigma_{\text{rel}} = \frac{\sqrt{\sum_i^{N_{\text{gen}}} w_i^2}}{\sum_i^{N_{\text{gen}}} w_i} = \frac{1}{\sqrt{N_{\text{gen}}}} \sqrt{1 + \frac{\sigma_{w_i}^2}{\langle w \rangle^2}}, \tag{4.11}$$

where N_{gen} is the number of generated events, w_i is the weight of each event, $\sigma_{w_i}^2$ the variance of the event weights, and $\langle w \rangle$ their mean value. By looking at the distribution of $\sigma_{w_i}/\langle w \rangle$ it is possible to see the effect of the LTR procedure on the MC statistical uncertainty of the emulated benchmark samples. This is presented in Figure 4.39. As can be easily seen, the MC statistical uncertainty will increase when moving far from the $c\tau$ values of the generated samples, where instead $\sigma_{w_i}/\langle w \rangle$ reaches a minimum.

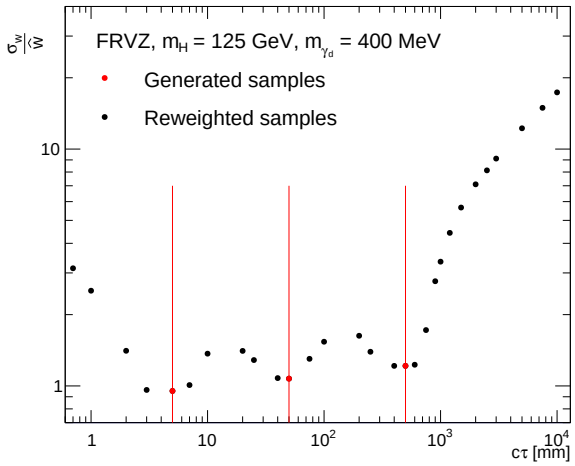


Figure 4.39. Distribution of the ratio between the standard deviation of the event weights and their mean (in the plot indicated with $\hat{w}$), as a function of the mean lifetime of the benchmark signal samples tested for the FRVZ model. The red lines indicate the values of $c\tau$ of the generated signal samples.

Signal systematic uncertainties. Experimental systematic uncertainties are taken into account for the FRVZ and Hss models. It is assumed that the standard description of physics objects holds also for these models, since the decay product of LLPs are visible SM particles. The pre-fit effect is reported for two benchmark signal models in Table 4.19. Only jet and $E_{\mathrm{T}}^{\mathrm{miss}}$ reconstruction effects are non negligible. For these two models, theoretical uncertainties are not taken into account.

Table 4.19. Effect of detector-related systematic uncertainties on the pre-fit event yields of two benchmark LLP signal samples. Table from Ref. [5].

Source of uncertainty and impact on the prefit signal yields (%)	
FRVZ model, m_H = 125 GeV, m_{γ_d} = 400 MeV, $c\tau_d$ = 500 mm	
Jet energy scale	1.8 – 2.4
Jet energy resolution	1.0 – 2.1
Jet quark/gluon composition and response	0.9 – 2.8
$E_{\mathrm{T}}^{\mathrm{miss}}$ scale and resolution	1.2 – 2.6
Hss model, m_H = 125 GeV, m_s = 5 GeV, $c\tau_s$ = 411 mm	
Jet energy scale	1.7 – 2.3
Jet energy resolution	1.0 – 3.3
Jet quark/gluon composition and response	0.7 – 3.1
$E_{\mathrm{T}}^{\mathrm{miss}}$ scale and resolution	0.1 – 2.9

Results

Upper limits at 95% of CL on the branching fraction of the Higgs boson into a pair of γ_d are reported in Figure 4.40, as a function of $c\tau_d$. The analysis efficiency varies for the different dark-photon decay modes: a γ_d decaying into two muons may go

completely undetected in the final state if the *baseline* muon requirements, as defined in Section 4.3, are not satisfied. Analogously, a γ_d decaying into electrons or light hadrons in the outer layer of the calorimeter can deposit only a portion of its energy in the detector, thus originating low-p_{T} jets which do not pass the selection criteria. For these reasons, three separate channels are considered. These are based on the truth decay products of the dark photon in the events:

- **Muonic channel:** both γ_d in the event decay into a pair of muons;
- **Hadronic channel:** both γ_d decay into a pair of electrons or light hadrons;
- **Mixed channel:** a γ_d decays into a pair of muons and the other decays into either a pair of electrons or into light hadrons.

These definitions are closely related to the ones adopted in Ref. [99], which are based on reconstructed objects in the final states. While a large hierarchy in the sensitivity is observed in the dedicated analysis, the sensitivity of the monojet reinterpretation is similar in all the channels for large dark photon lifetimes, where it is expected to set new constraints.

Existing constrains are improved by the monojet analysis for $c\tau_d < 0.9\,\mathrm{mm}$. The sensitivity in this regime is due to the fact that decay products of the γ_d are not properly identified in the final states. In particular, the sensitivity of the Muonic channel derives from the fact that standard reconstruction algorithms target prompt muons. Indeed, *baseline* muons, as defined as in Section 4.3, are required to have an inner-detector track matched to muon spectrometer hits, and to be associated to the primary vertex. Thus, even for small lifetimes, the boost of the γ_d in the final states is such that their decay products may not satisfy these criteria, escaping from the interaction point not-identified. However, the sensitivity decreases rapidly in more prompt-like regimes.

The sensitivity loss observed in the hadronic channel below $c\tau_d = 10^2\,\mathrm{mm}$ is mainly due to the photon veto present in the monojet SR definition. This has the largest impact in events with displaced electrons. These in fact lead to energy deposits in the electromagnetic calorimeter which are not associated to any track, which is indeed the signature of the prompt production of a photon.

At large lifetime values, $c\tau_d > 10^2$ mm, the observed limits tend to be flat, since most of the LLPs decay outside the fiducial volume of the ATLAS experiment. For this reason, the upper limits are extrapolated to very large lifetimes from the value of cτ_d for which the $p_{\mathrm{T}}^{\mathrm{recoil}}$ distribution matches the one expected from the $gg \to H \to$ inv process. The observed upper limit on the $\mathcal{B}(H \to \mathrm{inv})$ is checked to be consistent with the ones obtained with the FRVZ benchmark signal samples with very long lifetime values, and corresponds to $\mathcal{B}(H \to 2\gamma_d + X) < 50\%$ at 95%.

The results of both this reinterpretation and the displaced jets ATLAS search in the Higgs sector are also shown in Figure 4.41 as a function of the γ_d kinetic mixing parameter ε and the γ_d mass. In this case, limits are shown at 90% CL to be compared with the results of other non-ATLAS searches [203]. To obtain such result, it is assumed that the $p_{\mathrm{T}}^{\mathrm{recoil}}$ shape of the FRVZ signal does not change significantly for different γ_d masses. Therefore, the limit obtained for a 400 MeV γ_d in the three aforementioned channels has been rescaled according the γ_d BR.

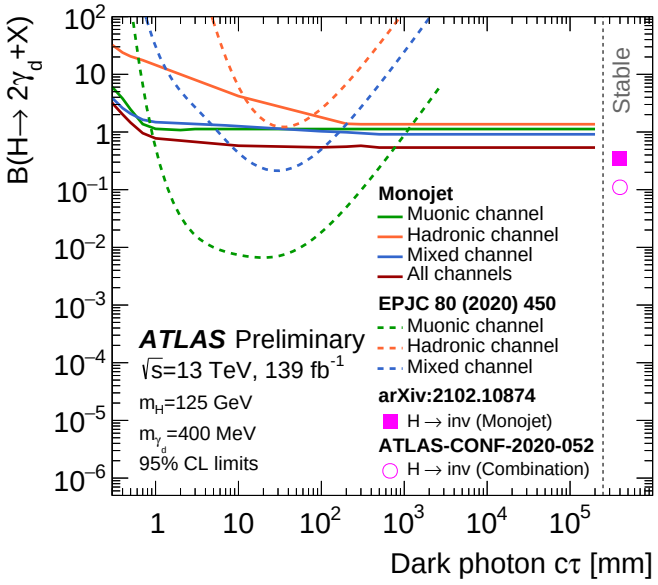


Figure 4.40. Exclusion contours obtained for a γ_d with $m_{\gamma_d} = 400\,\text{MeV}$ in the Muonic (green), Hadronic (orange) and Mixed (blue) channels, produced in the decay of SM Higgs boson. The red line shows the upper limit obtained in this reinterpretation when considering one single inclusive channel. The results are compared to the exclusion limits of the dedicated ATLAS search (dashed lines with same colour scheme) [99]. $\mathcal{B}(H \to \text{inv})$ upper limits from the monojet analysis [4] and the combination of ATLAS Run 1 and Run 2 results [41] are shown in the asymptotic regime of $c\tau$. Figure from Ref. [5].

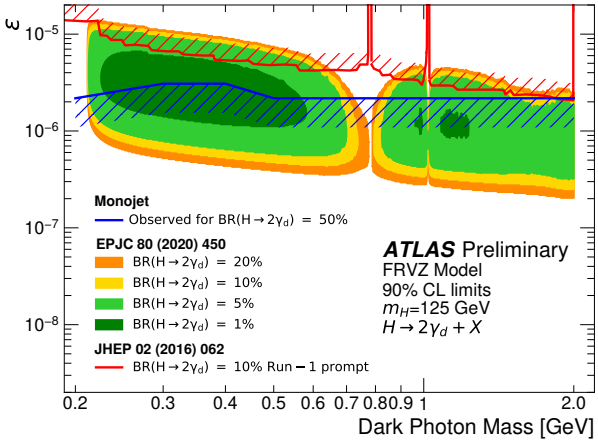


Figure 4.41. Exclusion contours shown in the dark photon mass - kinetic mixing parameter (ε) plane. Previous results from the dedicated prompt [98] and displaced [99] ATLAS searches are also shown. Figure from Ref. [5].

The exclusion contour corresponding to $\mathcal{B}(H \to 2\gamma_d + \text{X}) = 50\%$ is used as a benchmark value. In the range of γ_d mass [0.2, 2] GeV, the monojet analysis can exclude values of the kinetic mixing parameters below 10^{-6} for very light dark

photons, and $\varepsilon \leq 2 \cdot 10^{-6}$ for γ_d with $m_{\gamma_d} = 2\,\text{GeV}$. The shape of the contour is directly related to the branching fractions of the γ_d decays: for masses of the γ_d below 0.5 GeV the sensitivity slightly increases because the BR of the γ_d in pairs of muons increases. As can be seen from Figure 4.40, in fact the most sensitive channels are the Muonic and the Mixed ones. Figure 4.41 highlights the complementarity of the searches carried out by the ATLAS experiment. In the future, more stringent limits in this regime might be set from the Higgs to invisible search carried out via the VBF production mechanism, obtaining a similar contour to the one from the monojet analysis, but at much lower values of $\mathcal{B}(H \to 2\gamma_d + \text{X})$.

Results obtained on the Hss model are presented in Figure 4.42. These are compared to the constraints obtained by other ATLAS searches tuned for such signatures [204, 205, 206]. The complementarity among the several analyses can be observed for all the mass values of the scalar particles s, for which different lifetimes regimes are probed by different detection techniques. As for the FRVZ model, the monojet analysis extends current limits to higher $c\tau_s$ values.

Differences on the exclusion contours between the several scalar mass hypotheses are expected because of their different boost in the Higgs boson decay. In the asymptotic regime (i.e. for ∼infinite lifetimes) the monojet result approaches $\mathcal{B}(H \to ss) = 50\%$ @95% CL, which, again, is the value obtained by probing the $H \to$ inv process produced via ggF only. Hence, such a process is used to extrapolate the contours at lifetime values higher than the one corresponding to the $c\tau$ reweighted sample having a compatible $p_{\text{T}}^{\text{recoil}}$ distribution. Also in this case, constraints on the invisible branching fraction of the Higgs boson are shown for a comparison. The difference between the value obtained in this reinterpretation for large lifetime values is entirely due to the additional production mechanisms considered in the Higgs to invisible interpretation presented in Section 4.10.4.

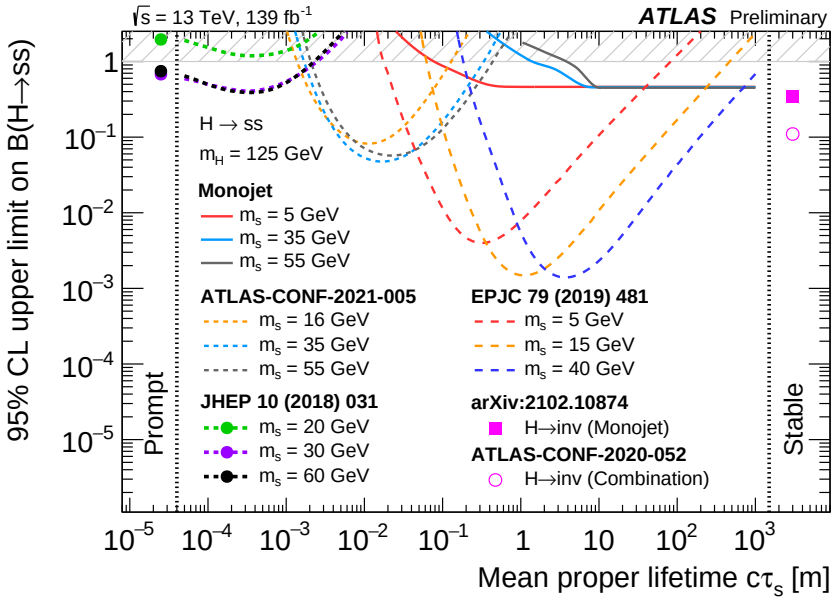


Figure 4.42. Exclusion contours on $\mathcal{B}(H \to ss)$ at 95% CL obtained in the monojet analysis reinterpretation shown as a function of the decay length of the s particle, compared to dedicated searches [204, 205, 206]. The results based on the prompt [204] and displaced ID vertex [206] techniques assume negligible signal efficiency for decays other than $s \to b\bar{b}$. The $\mathcal{B}(H \to \text{inv.})$ limit from the monojet [4] analysis and the combination of ATLAS Run 1 and Run 2 results [41] are also shown in the asymptotic regime of infinite lifetime. Figure from Ref. [5].

Chapter 5

Measurement of the $VH(b\bar{b})$ process

The Higgs boson has been only recently discovered, in 2012, and its properties are still today being studied. As introduced previously in Section 1.1.1, the decay to a $b\bar{b}$ pair is the most probable for the SM Higgs boson, being $\mathcal{B}(H \to b\bar{b}) = 58.2\%$ [207]. Without an efficient identification of the b-jets which arise from the hadronisation of the b-quarks, such process would be impossible to distinguish from the QCD multijet background of the LHC collisions. To further suppress this process, it is possible to look at the VH production mode of the Higgs boson. Indeed, even if the cross-section is approximately fifteen (WH) to fifty (ZH) times lower than the gluon-gluon fusion one, the presence of the vector boson allows to tag the events via its leptonic decays.

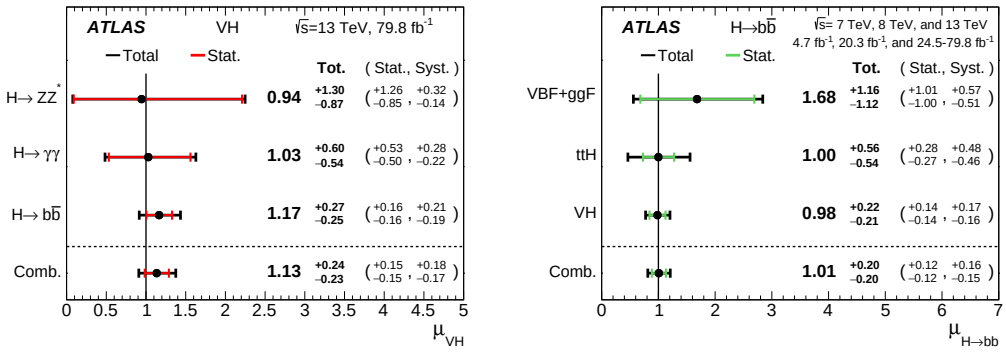
Measurements of the $VH(\to b\bar{b})$ process are discussed in this Chapter. After a general overview of the channel, in Section 5.2 the latest results obtained by the ATLAS collaboration are reviewed, and the main limitations of them are discussed. Studies carried out in preparation for an analysis of the data which will persist for several years as a legacy of the Run 2 of the LHC are presented in Section 5.3. In this Section I discuss how latest improvements in the flavour tagging procedure can improve the analysis, and I present studies to find an optimal combination of alternative reconstruction techniques to improve the sensitivity to the signal process. Furthermore, in Section 5.3.2 an innovative method to reduce the effect of limited MC statistics is presented.

As the results in preparation will remain as a legacy of the Run 2 period of the LHC it is important to extract as much information as possible from the data being analysed. A complementary approach to the simplified-template-cross-section measurements (STXS) is presented in Section 5.4, where the measurement of a fiducial differential cross-section of the $Z(\to \nu\bar{\nu})H(\to b\bar{b})$ process is discussed. Preliminary results are also shown. This study provides foundations for a more complete measurement of the $VH(\to b\bar{b})$ process considering all the leptonic decay modes of the vector boson produced in association with the Higgs boson, which will be included in the upcoming results.

5.1 The $H \to b\bar{b}$ observation

Three distinct channels can be exploited and combined to maximise the sensitivity to the signal by considering the VH production mode. These correspond to the $Z(\to \nu\bar{\nu})H(\to b\bar{b})$, $W(\to \ell\nu)H(\to b\bar{b})$ and $Z(\to \ell\ell)H(\to b\bar{b})$ ($\ell = e, \mu$) processes, which define the 0-, 1- and 2-lepton (L) channels, respectively. The main background process of the 0- and 2-L channels is the production of a Z boson in association with heavy-flavour (HF) jets. Minor contribution in the 0L channel arise also from $t\bar{t}$ and W+HF production. In the 1L channel, instead, the main backgrounds are due to $t\bar{t}$ and W+HF production.

The observation of the VH production mode and of the $H \to b\bar{b}$ decay has been reported by the ATLAS and CMS collaborations in Refs. [28, 29]. Partial LHC Run 2 results in the $b\bar{b}$, $\gamma\gamma$ and $ZZ^* \to 4\ell$ ($\ell = e, \mu$), obtained with a data set corresponding to 79.8 fb^{-1}, allowed ATLAS to observe the VH process with a significance of 5.5σ (5.4 expected). To achieve the 5σ threshold for the $H \to b\bar{b}$ decay, partial LHC Run 2 results from the $VH(\to b\bar{b})$ analysis reported in Ref. [28] were combined with results from other searches carried out in other production channels, performed with both LHC Run 1 and Run 2 data. The combination of the VH, $t\bar{t}H$ and VBF production modes, with the latter also carrying a non-negligible signal component from the gluon-gluon fusion process, resulted in a 5.4σ excess over the background-only hypothesis, above the 'observation' threshold. Results for the observation of both the VH and $H \to b\bar{b}$ process are reported in Figure 5.1, showing the contribution of each mentioned production- and decay-mode of the Higgs boson.



(a) VH production mode

(b) $H \to bb$ decay mode

Figure 5.1. Breakdown of the different contributions to the signal strength, given by $\mu = \sigma/\sigma_{\text{SM}}$, which provides the observation of the (a) VH and (b) $H \to b\bar{b}$ processes, as measured by the ATLAS collaboration. Figures from Ref. [28].

As it can be seen in Fig. 5.1(a), the $H \to b\bar{b}$ decay provides the best sensitivity to the VH production mode, thanks to the large branching fraction of the Higgs boson in such channel. On the other hand, the VH process provides the best sensitivity for $H \to b\bar{b}$ decays, thanks to an equilibrium between the cross-section value and the cleanliness of the final state.

The first observation of the $VH(\to b\bar{b})$ combined process was achieved by the

ATLAS collaboration with the full LHC Run 2 data set, corresponding to 139 fb^{-1} of integrated luminosity. A significance of 6.7σ is reported in Ref. [42], which also provided for the ZH and WH production modes a rejection of the background-only hypothesis with 5.3σ and 4.0σ, respectively.

5.2 The starting point: preliminary $VH(\to b\bar{b})$ analyses

The latest ATLAS $VH(\to b\bar{b})$ measurements, performed with the full LHC Run 2 data set, adopted two different techniques to reconstruct the Higgs boson candidate in the events. In the *resolved* analysis [42], Higgs boson candidates are formed by pairs of b-tagged anti-k_T $R = 0.4$ jets. At large $p_T(H)$, however, the Higgs boson decay products are emitted closer to each other, thus the efficiency of reconstructing two well-separated jets in the final state is reduced. The *boosted* analysis [208] exploits large-R jets, introduced in Section 3.3 of this thesis, to better catch such final states. The two published analyses are not completely orthogonal: while the resolved one is sensitive for $p_{\text{T}}(V)$ above 150 GeV (75 GeV for $Z(\to \ell^-\ell^+)H(\to b\bar{b})$ process), the boosted analysis requires a vector boson p_{T} of at least 250 GeV. In the range between 250 and 500 GeV, the overlap in the events used in the two analyses is non-negligible. In this range, in fact, both the reconstruction techniques provide a good signal reconstruction efficiency. Strategies to remove such overlap in the combination of the two methods, foreseen for the *Legacy* Run 2 analysis, are discussed in Section 5.3.3, where different options are presented.

In this section the workflow of the two published analysis is reviewed, and their main limitations are discussed. Methods and improvements to overcome such limitations are discussed in Section 5.3.

5.2.1 Signal and background simulations

Simulated MC samples are used to model the SM backgrounds as done in the monojet analysis. Such predictions are also in this case corrected by means of orthogonal control regions, which are defined in the next Section. The same generator configurations adopted in the monojet analysis, and described in Section 4.2.1, are used in the resolved and boosted $VH(\to b\bar{b})$ analyses. However, the V+jets reweighting is not applied in this case, since it was developed originally for the monojet phase space only. Moreover, the impact of NLO EW corrections to the background predictions are expected to be small in the $VH(\to b\bar{b})$ analysis, since the $p_{\text{T}}(V)$ is low.

VH signal processes initiated by quark pairs are simulated with the Powheg generator and the Multiscale Improved NLO procedure (MiNLO) [209]. The $gg \to ZH$ signal process instead is simulated at LO in QCD with Powheg. Both simulations are interfaced to Pythia8 for the parton showering, and the AZNLO set of tuned parameters, described in Ref. [210], is adopted. Both the ME and PS algorithms use the NNPDF3.0 PDF set, but the ME calculations are reweighted to the PDF4LHC15NLO PDF set via the internal algorithm of Powheg-Box v2.

Signal samples are normalized to the state-of-the-art cross-section calculations. The $qq \to ZH$ and $qq \to WH$ processes are normalized to NNLO QCD + NLO EW accuracy [211, 212]. The NLO EW differential cross-section is computed as a

function of $p_{\mathrm{T}}(V)$ using the Hawk package [213], and a correction function is used to re-weight the signal events. A shape uncertainty of the size of the correction is then introduced in the likelihood fit to take into account this reweight. The $gg \to ZH$ process cross-section instead is calculated at NLO+NLL in QCD [214, 215].

5.2.2 Object definition

Both analyses consider three leptonic channels, as introduced in Section 5.1, defined by the number of identified electrons or muons from the leptonic decay of the V produced in association with the Higgs boson. Electrons and muons are reconstructed in the final states as described in Section 3.2. As done in the monojet analyses, two categories of these objects are defined: *VH-loose* and *VH-signal* leptons.

VH-loose electrons are required to have $p_{\mathrm{T}} > 7\,\mathrm{GeV}$, $|\eta| < 2.47$, and to satisfy the *Loose&Blayer* identification WP (cf. Section 3.2.1). They are also required to have $|d_0/\sigma_{d_0}| < 5$, $|z_0 \sin\theta| < 0.5\,\mathrm{mm}$, and to satisfy the fixed-cut Loose isolation WP as defined in Section 3.2.1.

On top of such requirements, *VH−signal* electrons are required to have $p_{\mathrm{T}} > 27\,\mathrm{GeV}$. For the 1L channel, *WH−signal* electrons are defined by requiring stricter identification and isolation WPs to better suppress the multijet background. The Tight identification and *Fixed-Cut-High-Pt-Calo-Only* isolation WP are required. The latter is based on a differential cut on the $E_{\mathrm{T,cone}}^{\mathrm{isol,R=0.2}}$ variable, defined in Section 3.2.1, which is required to be less than 3.5 GeV.

VH-loose muons are required to be reconstructed within $|\eta| < 2.7$, and to have $p_{\mathrm{T}} > 7\,\mathrm{GeV}$. Moreover, the *Loose* selection WP, defined in Section 3.2.2, is required along with $|d_0/\sigma_{d_0}| < 3$, $|z_0 \sin\theta| < 0.5\,\mathrm{mm}$. Muons are also required to pass the *loose* fixed cut isolation WP, which requires $E_{\mathrm{T,cone}}^{\mathrm{isol,R=0.2}}/p_{\mathrm{T}} < 0.3$, and $p_{\mathrm{T,var\text{-}cone}}^{\mathrm{isol,R=0.3}}/p_{\mathrm{T}} < 0.15$.

As for the electrons, *ZH−signal* muons are required to pass the *loose* selection and to have at least $p_{\mathrm{T}} > 27\,\mathrm{GeV}$. *WH−signal* muons are defined by stricter requirements on the identification, *Medium* quality, and on the isolation, *Fixed-Cut-High-Pt-Calo-Only* WP (cf. Section 3.2.2). For these muons, the p_{T} threshold is reduced to 25 GeV.

Hadronically decaying τ-leptons are used only in the evaluation of the missing transverse momentum of the event, and in the overlap removal procedure. Differently to what is done in the monojet analysis, a τ-lepton veto is not applied in the $VH(\to b\bar{b})$ analysis, because it would reduce significantly the $W(\to \tau\nu)H(\to b\bar{b})$ signal component.

The reconstruction of such objects is performed according to Section 3.2.3, and candidates are required to have $p_{\mathrm{T}} > 20\,\mathrm{GeV}$, $|\eta| < 2.5$ (excluding the crack region), and to pass the *Medium* identification WP.

Hadronic jets are reconstructed as described in Section 3.3. The resolved analysis adopts only anti-k_t $R = 0.4$ EMTopo jets, while in the boosted one large-R jets and VR track-jets are also used. The requirements applied on these objects are reported

below separately for each topology.

Resolved analysis. In the resolved $VH(\to b\bar{b})$ analysis, jets are defined as *signal* and *forward*. The former are required to be central, $|\eta| < 2.5$, and have $p_{\mathrm{T}} > 20\,\mathrm{GeV}$. Below 60 GeV a further requirement of $|\eta| < 2.4$ and JVT > 0.59 is applied to suppress pileup contributions. *Forward* jets are required to have at least $p_{\mathrm{T}} > 30\,\mathrm{GeV}$, and $2.5 < |\eta| < 4.5$. A *loose* jet cleaning requirement, as described for the monojet analysis in Section 4.3, is applied to all jets in the events.

Two corrections are applied to b-jets, aiming to improve their energy scale and resolution. These take into account the undetected energy deposits in the calorimeter of some of the decay products of the b-hadrons, such as neutrinos, or muons produced in semi-leptonic decays of unstable hadrons. The first correction is related to muons, which loose only part of their energy in the calorimeters, and they are typically removed in the overlap removal procedure with jets. The criteria for such a removal are described later in this section. To correct the jet energy measurement, the four momentum of the reconstructed muon is summed together with the one of the reconstructed jet, and the corresponding energy deposit in the calorimeter is removed. If more than one muon is found within a jet, only the one closer to its axis is considered for the application of the correction. This procedure is applied both to data and simulated events.

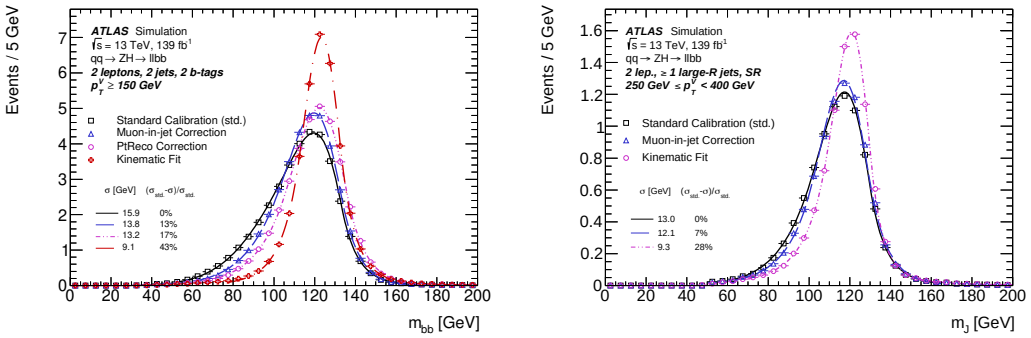
The second correction applies only to simulated events, and takes into account the missing energy deposit of the neutrinos. The size of the correction is different between semi-leptonic and hadronic decays of the b-hadrons. Two functions are derived from particle-level jets. An effect of around 10%, decreasing with the jet p_{T}, and almost vanishing at 70 GeV, is found for *hadronic* decays of the b-hadrons. Semi-leptonic decay corrections are found to be of the same size, however a constant off-set of $\sim 7\%$ is observed. Thus at low jet p_{T}, the total size of the correction is about 20%.

Such a correction is applied only in the 0 and 1L channels. In the 2L channel, instead, a kinematic fit to the $\ell\ell b\bar{b}$ system is applied. This allows to exploit percent-level resolution on the reconstruction of the lepton energy and momentum scale to improve the JES, which is of the level of $5 \div 10\%$. The four-body system is balanced in the transverse plane, thus the transverse momenta of the jets and leptons are fitted including constraints on the resolution of the transverse momentum, on $m_{\ell\ell}$ and a term which accounts for the lower response of b-jets due to the presence of neutrinos.

Both the corrections mentioned in this sub-section are applied after the event selection is performed. The event $\vec{E}_{\mathrm{T}}^{\mathrm{miss}}$ is built using uncorrected jets. The performance of the corrections on the m_{bb} scale and resolution are presented for the resolved analysis in Figure 5.2(a) for the simulated $qq \to Z(\to \ell\ell)H(\to b\bar{b})$ process.

Boosted analysis. To better catch the Higgs boson decay products at high $p_T(H)$, the boosted analysis adopts large-R jets reconstructed with the anti-k_t algorithm with $R = 1.0$. At least one large-R jet with $p_{\mathrm{T}} > 250\,\mathrm{GeV}$ and $|\eta| < 2$ is required in the events. Moreover, its invariant mass is required to be $m_{\mathrm{J}} > 50\,\mathrm{GeV}$, since below this threshold no calibration of the JMS is provided.

VR track-jets of $p_{\mathrm{T}} > 10\,\mathrm{GeV}$ and $|\eta| < 2.5$ are used to identify, within the



(a) (b)

Figure 5.2. Effect of the corrections applied to EMTopo jets in the resolved analysis [42] (a) and to the large-R jet in the boosted analysis [208] (b). Further details on the event selection applied to obtain these distributions are presented in Section 5.2.3 and 5.2.4,respectively.

large-R jet, the hadronisation products of the two highly-energetic b-quarks. Ghost association with the large-R jet of the VR track jets is performed, and at least two of them are required in the events.

Anti-k_t $R = 0.4$ EMTopo jets are used in the boosted analysis only in the event categorization. These are retained in the events if they have $p_{\mathrm{T}} > 30\,\mathrm{GeV}$ and $|\eta| < 4.5$. Jets within $|\eta| < 2.5$ and below 120 GeV of p_{T} are required to pass a requirement on the JVT discriminant, JVT > 0.59, to suppress pileup contributions.

As done in the resolved analysis, to account for muons originating in b-hadron decays, the large-R-jet four momentum is corrected too. All muons within the track-jets which are ghost associated with the large-R jet are considered. The m_{calo} term of the combined mass (cfr. Equation 3.7 in Section 3.3) is corrected after the sum of the large-R jet and muon four momenta. The m_{TA} term is evaluated using the new $p_{\mathrm{T}}^{\mathrm{calo}}$ value, and then the new combined mass is calculated. No corrections for neutrinos are applied in the boosted analysis. In the 2L channel, the kinematic-fit already described for the resolved analysis is additionally performed. The impact of such correction on the m_{J} distribution is presented in Figure 5.2(b).

Overlap removal

An overlap removal procedure of pre-selected objects is done to avoid a double counting of detector signals, as already described also for the monojet analysis in Section 4.3.

At first, the overlap between hadronically decaying τ-leptons and electrons (e) / muons (μ) is solved by removing τ candidates if they have $\Delta R(\tau, e/\mu) < 0.2$.

If a muon which is not identified as *combined* (cfr. Section 3.2.2) is found within a cone of $\Delta R = 0.2$ of a τ-lepton candidate of $p_{\mathrm{T}} > 50\,\mathrm{GeV}$, then the latter is retained and the muon is removed.

Combined muons which share an ID track with an electron, are retained, while the electron is removed. However, if the muon is *calorimeter tagged*, it is removed instead and the electron is kept.

EMTopo jets found within $\Delta R(j,e) = 0.2$ of an electron are removed, while if $\Delta R(j,e) < \max[0.2, \min(0.4, 0.04 + 10\,\text{GeV}/p_{\text{T}}(e))]$, then the electron is removed.

Concerning muon and EMTopo jets, if $\Delta R(j,\mu) < 0.2$ or the muon is ghost-associated with the jet then two conditions are evaluated. If the jet has less than three associated reconstructed ID tracks, or $p_{\text{T}}(\mu)/p_{\text{T}}(j) > 0.5$ and the ratio between the muon p_{T} and the scalar sum of the tracks associated with the jet is greater than 0.7, then the jet is removed. For any surviving jet, if $\Delta R(j,\mu) < \max[0.2, \min(0.4, 0.04 + 10\,\text{GeV}/p_{\text{T}}(\mu))]$ the muon is removed.

In the boosted analysis, an overlap removal is applied to large-R jets and electrons: if $\Delta R(e, \text{large-R}\, j) < 1.2$, the large-R jet is removed.

5.2.3 Flavour tagging strategy

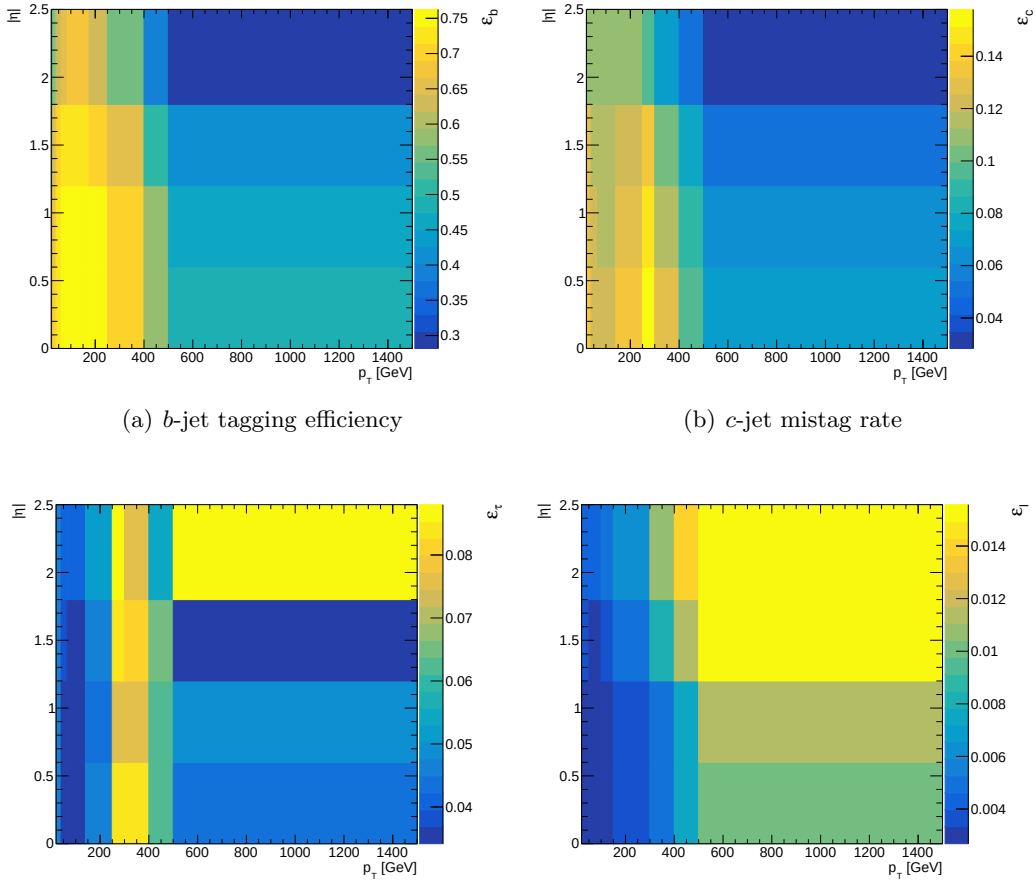
The identification of jets originating from b-quarks is central in this analysis. In MC simulated events, the flavour labelling procedure introduced in Section 3.3.2 is used. In the resolved analysis flavour tagging is applied to all the *signal* jets reconstructed in the event. In the boosted channels, the tagging is instead applied only to the leading two VR track-jets associated with the large-R jet. Such choice was done to optimise the signal significance. Flavour tagging is also applied to VR track-jets not matched with the Higgs boson large-R jet candidate.

The same discriminant algorithm adopted by the monojet analysis, MV2c10, is used. The chosen working point is the one providing an average efficiency of 70%. The corresponding c- and light-jet rejection factors are given in Table 3.3 of Section 3.3.2. This procedure is referred to in the following as *direct* tagging (DT). The calibration of the tagging algorithm has been performed on both the EMTopo and VR track-jets collections separately, and follows the method described in Ref. [149].

When applied to MC simulation, DT reduces the number of events available to describe the background processes. For event categories including jets which are c- or light-flavour labelled, due to the high rejection rates of the MV2c10 algorithm most of the MC events are rejected, thus large statistical fluctuations arise. To recover a smooth template of the kinematic distributions of background processes, an event-weighting technique called *truth tagging* (TT) can be used. This allows to keep all the MC events, which are re-weighted based on the characteristics of the jets in the events as follows. The flavour tagging performance are parameterised by means of two-dimensional efficiency maps derived from $t\bar{t}$ single- and di-lepton events. These maps provide the tagging efficiency ε binned as a function of jet p_{T} and $|\eta|$. This description is accurate enough for isolated jets, while lacks in capturing the correlations between close-by jets in boosted environments. For this reason, the TT cannot be used in the boosted analysis. A way to overcome such limitation is presented in Section 5.3.2.

Efficiency maps depend on the jet label, the jet reconstruction technique (EMTopo, PFlow, VR track-jets), the tagger (MV2, DL1, DL1r), the chosen working point, and most importantly on the MC generator used in their derivation. Efficiency maps obtained with Powheg+Pythia 8 $t\bar{t}$ events are presented in Figure 5.3(a). A different granularity is chosen to build such maps, taking into account the available MC statistics, and keeping the relative uncertainty below a few percent. This is also the main reason why the parameterization is performed only in two dimensions.

A bin-by-bin interpolation is then performed to obtain a smooth and continuous surface.



(a) b-jet tagging efficiency

(b) c-jet mistag rate

(c) τ-jet mistag rate

(d) light-flavour jet mistag rate

Figure 5.3. Efficiency maps obtained from single- and di-lepton $t\bar{t}$ events for the MV2c10 tagger algorithm and the 70% efficiency WP with the POWHEG+PYTHIA 8 generator for (a) $b-$labelled jets, (b) $c-$labelled jets, (c) τ-jets and (d) light-flavour jets.

For each jet in the event, the value ε_{tag} is read from the efficiency maps either to represent the b-tag probability or the mis-tag rate. In events with only two jets, the total corresponding weight is built as the product of the ε_{tag} values. If three jets are found, namely j_a, j_b and j_c, a choice of two-out-of-three to be considered as tagged is needed. Three combinations are thus produced: in each one, two jets are considered as tagged and the corresponding efficiency value is assigned, while for the third one $1 - \varepsilon_{\text{tag}}$ is assigned, representing an anti-tagging probability. For each case, the total weight is derived as $\varepsilon_{j_a} \cdot \varepsilon_{j_b} \cdot (1 - \varepsilon_{j_c})$ (and permutations of a, b, c). By normalising each combination weight to the sum of all of them, a probabilistic choice of one of the three configurations to represent the event can be done. This procedure can be extended to the case of n jets: all combinations of 2 jets out-of-n tagged and the rest not-tagged are made. A pair which will form the Higgs boson

candidate is then chosen based on its relative tagging probability.

In the application of TT in the resolved $VH(\to b\bar{b})$ analysis, a bias on the closure with the DT was found for $b\bar{b}$ final states, while a good description was observed for the others. This motivated the development of an *hybrid*-tagging (HT) strategy. It consists in the application of TT only to the non-b-labelled jets, for which DT is applied. Hybrid tagging proceeds in two steps: at first jets in the events are separated between b-labelled and not. To the first ones the DT is applied. If two jets are direct-tagged, the event weight associated to the truth-tagged jets is built by requiring the non-tag probability, i.e. $1-\varepsilon_{\text{tag}}$. Otherwise truth tagging is performed as outlined above, and the truth-tagged jets are selected via the aforementioned probabilistic algorithm.

HT is used in the resolved analysis for the training of the multivariate algorithm used as a discriminant in the maximum likelihood fit which is used in the extraction of the $VH(b\bar{b})$ signal (cf. Section 5.2.5). TT instead is used in both analyses in the derivation of modelling systematic uncertainties. Any bias introduced by this technique cancels in the ratio performed to estimate the effect of the considered variation.

5.2.4 Event selection and categorization

Data events are required to be in the *good run list* introduced in Section 4.4. For both data and simulated collisions, the presence of at least one reconstructed PV is required. Events of the 0, 1 and 2L channels are selected using the same $E_{\text{T}}^{\text{miss}}$ and single-electron triggers used in the monojet analysis, reported in Tables 4.1 and 4.2. In the 2L channel of the resolved analysis, single-muon triggers are also adopted. The combination of trigger chains is listed in Table 5.1. The 'iloose' and 'ivarmedium' suffixes refer to isolation criteria (cf. Section 3.2.2).

Table 5.1. Single-muon triggers used to select events for the 2L channel, combined via a logical *or*.

Period	Trigger chain
2015	HLT_mu20_iloose_L1MU15 *or* HLT_mu50
2016, '17, '18	HLT_mu50 *or* HLT_mu26_ivarmedium

Resolved analysis. In the 0 and 1L channels of the resolved analysis, only events with at least 2 signal jets, and at most 3 jets (including forward ones), are selected. To reduce the large $t\bar{t}$ background, events with 4 or more jets are vetoed. Since this background is sub-dominant in the 2L channel, events with more than 3 jets are allowed. Therein b-tagging is applied to all signal jets and exactly two tagged jets are required in the events. The leading one is required to have $p_{\text{T}} > 45\,\text{GeV}$. Additional selections, specific to each of the leptonic channel, are summarised below.

ZERO LEPTON: Events are required to have exactly 0 *VH-loose* leptons reconstructed, and $E_{\text{T}}^{miss} > 150\,\text{GeV}$ due to trigger limitations: the trigger efficiency, in fact, reaches around 90% at 150 GeV. To remove a known mismodelling in simulation due to an interplay between the $E_{\text{T}}^{\text{miss}}$ trigger and the number of jets in the events,

the scalar sum of the p_{T} of all the jets is required to be greater than 120 GeV (150 GeV) in events with two (three) jets.

To reduce multijet contributions, anti-QCD cuts based on the angular separation between jets and the $\vec{E}_{\mathrm{T}}^{\mathrm{miss}}$ are applied. The minimum angular distance between any jet and the $E_{\mathrm{T}}^{\mathrm{miss}}$ in the event is 0.2 (0.3) for two (three) jets events. In addition, the two jets forming the Higgs boson candidate (h) are required to satisfy $|\Delta\phi| < 140°$. Moreover, it is required that $|\Delta\phi(h, E_{\mathrm{T}}^{\mathrm{miss}})| > 120°$, and that the angular separation between the $E_{\mathrm{T}}^{\mathrm{miss}}$ and the track-$E_{\mathrm{T}}^{\mathrm{miss}}$ is below 90°. After such selection, the dominant background process is $Z(\to \nu\bar{\nu})$+HF, followed by $t\bar{t}$ production. The latter is more dominant in the 3 jet category.

One lepton: In the 1L channel, the transverse momentum of the vector boson produced in association with the Higgs boson is reconstructed from the vectorial sum of $E_{\mathrm{T}}^{\mathrm{miss}}$ and of the lepton momentum in the (x, y) plane. Events are required to include exactly one *WH-signal* lepton, as defined before, and no additional *VH-loose* leptons. In the electron channel, to reduce mis-reconstructed cases, $E_{\mathrm{T}}^{\mathrm{miss}}$ is required to be greater than 30 GeV. The main background processes of the 1L channel after event selection are $t\bar{t}$ and W+HF production. A sub-dominant multijet component is present, and estimated in a data-driven way as documented in Ref. [42].

Two leptons: Exactly two same-flavour leptons are required in the events. At least one of those is required to pass the stricter *ZH−signal* requirement. The invariant mass of the two lepton system is required to be close to the Z-pole, $81 < m_{\ell\ell} < 101$ GeV. The vector boson p_{T} is determined by the sum of the momenta of the two leptons. In this channel, the only background process is due to the Z+HF process. Top-quark pair production is a sub-dominant component, and it is estimated in a data-driven way in an orthogonal electron-muon CR.

In all three channels, minor backgrounds arise from the production of a pair of vector bosons, with one of them decaying into a pair of HF quarks (b or c). This process is very similar to the VH signal, and is exploited in the analysis to perform a validation of the fit and background model on the VV peak. Further details on the measurement of this process are provided in Ref. [42].

Boosted analysis. Events in the boosted topology are selected if at least one large-R jet is reconstructed. Two VR track-jets ghost-associated with it are required. The leading large-R jet is taken to be the Higgs boson candidate. b-tagging is applied to the two leading VR track-jets, and both are required to pass the WP defined above. The mass of the Higgs boson candidate is taken to be the one of the large-R jet. Specific selections applied to the three leptonic channels are summarised below. The background composition in each of these is very similar to what is observed in the resolved analysis.

Zero lepton: The $E_{\mathrm{T}}^{\mathrm{miss}}$ in the event, proxy for the reconstruction of the Z boson produced in association with the Higgs boson, is required to be at least 250 GeV. This value approximately corresponds to an angular separation (ΔR) of the two Higgs boson decay products of 1, therefore these can be reconstructed

within a single large-R jet with $R = 1.0$. As for the resolved analysis, exactly 0 VH-*loose* leptons are required in the events. To suppress the multijet background which could lead to fake $E_{\mathrm{T}}^{\mathrm{miss}}$, $\Delta\Phi(E_{\mathrm{T}}^{\mathrm{miss}}, H_{\mathrm{cand}}) > 120°$ is required. Moreover, the cuts $\Delta\Phi(E_{\mathrm{T}}^{\mathrm{miss}}, p_{\mathrm{T}}^{\mathrm{miss}} < 90°$ and $\min\Delta\Phi(j, E_{\mathrm{T}}^{\mathrm{miss}}) > 30°$ are applied. For the latter, only the EMTopo jets reconstructed outside the H candidate large-R jet, and with a p_{T} greater than 70 GeV, are considered.

One lepton: Events are selected requiring the same criteria of the resolved analysis and by tightening the $E_{\mathrm{T}}^{\mathrm{miss}}$ cut to 50 GeV. Additionally, a cut on the absolute rapidity separation between the large-R jet and the vector boson, $|\Delta y(W, H)| < 1.4$, is applied. To evaluate such quantity, the neutrino momentum is needed, and it is evaluated by imposing to the lepton-neutrino system a mass constraint of the W boson.

Two leptons: The same criteria of the resolved analysis concerning leptons are applied to select candidate events. The additional cut on the rapidity separation between the Z boson and the large-R jet, introduced in the 1L boosted channel, is applied also in this case. To improve the rejection of the Z+jets background, the leptons p_{T} imbalance, defined as $(p_{\mathrm{T}}^{\ell_1} - p_{\mathrm{T}}^{\ell_2})/p_{\mathrm{T}}^{Z}$, is required to be lower than < 0.8. This variable provides discrimination power between the Z+jets and VH processes [216].

Region definition

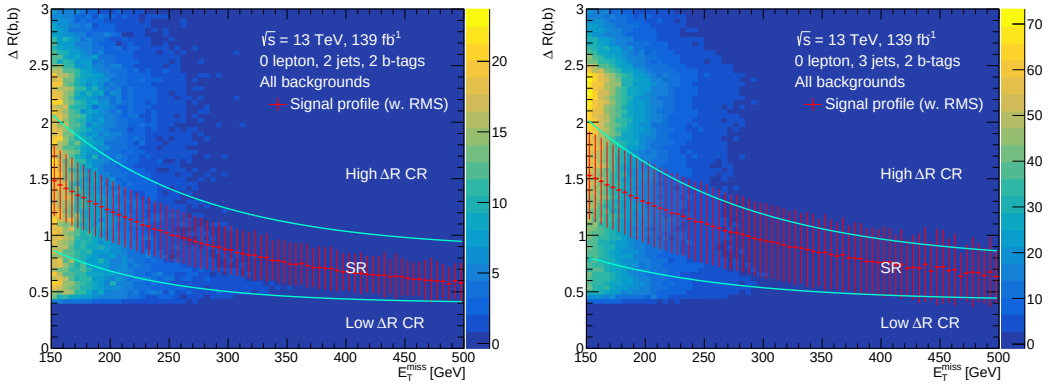
In each leptonic channel, events are further categorized in $p_{\mathrm{T}}(V)$ bins in both the resolved and boosted analyses to enhance the sensitivity to the Higgs boson signal. A set of signal and control regions are defined, and their definition in the two analyses is reported below.

Resolved analysis. The 0 and 1L channels are split in two $p_{\mathrm{T}}(V)$ bins, $150 < p_{\mathrm{T}}(V) < 250$ GeV and $p_{\mathrm{T}}(V) > 250$ GeV, while in the 2L one also the $75 < p_{\mathrm{T}}(V) < 150$ GeV interval is considered.

Furthermore, signal and control regions are defined with a requirement on the angular separation between the two b-tagged jets as a function of the vector boson p_{T}. This cut is motivated by the fact that in $H \to b\bar{b}$ decays, the angular separation of the decay products is given by $\Delta R(b, b) \simeq \frac{2m_H}{p_{\mathrm{T}}(H)}$. Such correlation is not present in V+jets and $t\bar{t}$ production. V+HF events are quite uniform, with a component which accumulates at low values of $\Delta R(b, b)$ due to the gluon-splitting phenomenon. In $t\bar{t}$ events, instead, the two b-jets tend to be produced in opposite hemispheres of the detector, thus events populate the higher values of $\Delta R(b, b)$. Such control regions are used in the maximum likelihood fit to correct the normalisation of the SM predictions.

In Figures 5.4(a), the contribution of background processes in the $(E_{\mathrm{T}}^{\mathrm{miss}}, \Delta R(b, b))$ plane in the $0L$ channel for the two- and three-jet categories is shown. The profile of the signal distribution, and its RMS, are overlaid to show the aforementioned correlation. Two functions define the signal region (SR) and the *High*-ΔR and *Low*-ΔR control regions. These have been optimised with the 1L selection, and used

in all lepton channels. The high-ΔR cut has been defined such that at least 95% (85%) of the signal events in the two (three) jet category are included in the SR. The lower boundary has been tuned such that 10% of the total dibosons events are included in the low-ΔR CR. This allows to keep the SR contamination from such processes low, yet enough contribution is present to perform the cross-check analysis on the VV peak, as described later in Section 5.2.5.



(a) Two jet category (b) Three jet category

Figure 5.4. Distribution of the ΔR between the two b-tagged jets in the events for the sum of the background processes as a function of $E_{\mathrm{T}}^{\mathrm{miss}}$ obtained in the (a) two- and (b) three-jet categories of the 0 lepton channel. The profile and RMS of the signal distribution is overlaid, and the functions which determine the separation between the low-ΔR, SR and high-ΔR regions are shown.

In the fit model, CRs consists of inclusive bins, while in the SR either a multivariate discriminant built via a boosted decision tree (BDT_{VH}), or the binned distribution of the invariant mass of the two b-jets system (m_{bb}) are used to enhance the sensitivity to the Higgs boson signal.

Considering the $p_T(V)$, jet multiplicity, and $\Delta R(b,b)$ splitting, a total of 28 CRs and 14 SRs are defined. A summary of the event categories is presented in Table 5.2.

Boosted analysis. Events are split in two $p_{\mathrm{T}}(V)$ bins, $[250, 400]$ GeV and $p_{\mathrm{T}}(V) > 400$ GeV. These intervals overlap with the ones defined in the resolved analysis, since especially up to 500 GeV events are efficiently reconstructed in both topologies. Studies to solve such overlap in the combination of the two analyses are presented in Section 5.3.3.

To suppress the $t\bar{t}$ background, the boosted analysis SRs are defined by requiring that any track-jet not matched with the large-R jet Higgs boson candidate is not tagged. In the 0 and 1L channels, a further splitting of the SR is done. The *High-purity* SR and *Low-purity* SR are defined by requiring either 0 or ≥ 1 EMTopo jet with $\Delta R > 1$ with the Higgs boson candidate jet. Such a categorization is performed using EMTopo jets since the associated systematic uncertainties can be used to estimate migrations of events between the two signal regions. The available statistics in the 2L channel is not enough to allow such categorization.

A set of control regions is defined in the 0 and 1L channels to constrain the $t\bar{t}$

Table 5.2. Summary of the defined signal and control regions of the resolved $VH(\to b\bar{b})$ analysis. In the single binned regions, here indicated with 'Yields', no shape information of either the BDT or the m_{bb} distribution is used, but only the inclusive number of events.

Channel	Region	Category					
		$75 < p_{\mathrm{T}}^{V} < 150\,\mathrm{GeV}$		$150 < p_{\mathrm{T}}^{V} < 250\,\mathrm{GeV}$		$p_{\mathrm{T}}^{V} > 250\,\mathrm{GeV}$	
		2-jets	$(\geq)$ 3-jets	2-jets	$(\geq)$ 3-jets	2-jets	$(\geq)$ 3-jets
0L	Low-ΔR-CR	–	–	Yields	Yields	Yields	Yields
	SR	–	–	Binned	Binned	Binned	Binned
	High-ΔR-CR	–	–	Yields	Yields	Yields	Yields
1L	Low-ΔR-CR	–	–	Yields	Yields	Yields	Yields
	SR	–	–	Binned	Binned	Binned	Binned
	High-ΔR-CR	–	–	Yields	Yields	Yields	Yields
2L	Low-ΔR-CR	Yields	Yields	Yields	Yields	Yields	Yields
	SR	Binned	Binned	Binned	Binned	Binned	Binned
	High-ΔR-CR	Yields	Yields	Yields	Yields	Yields	Yields

background. These are defined by changing the requirement of exactly 0 b-tagged track-jets outside the large-R jet, to at least an additional one. By construction these regions are enriched in the $t\bar{t}$ process. The large-R jet with two matched and b-tagged VR track-jets in such regions is most of the times reconstructed from the top-quark decay and the hadronic W boson, with one jet which mis-tagged as originated from a b quark.

In all regions of the boosted analysis, the invariant mass of the leading large-R jet, m_{J}, is the discriminant variable adopted to extract the Higgs boson signal via the statistical model described in the next Section.

5.2.5 Statistical model and fit strategies

The statistical analysis is performed with a binned likelihood function given by the product over all bins and regions, of the distributions considered, of Poisson terms. As in Equation 4.4, the number of expected events in each bin is given by the sum of the background and signal contributions. Both of these depend on gaussian-constrained nuisance parameters and freely-floating normalization factors. Signal events are scaled by the freely-floating signal strength, μ. The effect of experimental and modelling systematic uncertainties, along with the effect of limited MC statistics, is parameterized in the likelihood via gaussian-constrained NPs. The fit models of the resolved and boosted analyses is summarised below.

Resolved analysis. To maximise the sensitivity to the $VH(\to b\bar{b})$ signal, BDTs are used to build the main discriminant variable. A cross-check fit is also performed by looking at the less sensitive m_{bb} distribution. The improved sensitivity achieved with the BDT is due to the fact that it includes also the m_{bb} distribution of the events, in addition to other variables, as described in Ref. [42]. In this thesis the

BDT discriminant is not used as an effort to improve the MVA analysis is ongoing. Therefore, the studies presented to improve the current published results presented in Section 5.3.3 were performed by looking at the m_{bb} distributions. Moreover, the fiducial cross-section measurement study presented in Section 5.4 is based on the m_{bb} fit. The reader is referred to Ref. [42] for more details on the input variables and training procedure of the BDT.

In the likelihood model, the $V(\to \text{lep.})H(\to b\bar{b})$ signal, $t\bar{t}$ and single-t quark production, dibosons production and V+jets processes are considered. The latter are split in three sub-categories according to the flavour of the two leading jets in the event: V+light flavour jets, V+cl and V+HF, which includes V+[$b\bar{b}$, bc, bl, $c\bar{c}$] production. The data-driven multijet template, relevant only for the 1L channel, is also considered.

Eight freely-floating normalization factors (NFs) are included in the likelihood model to correct the background predictions. These NFs are decorrelated between two- and three-jet categories only, and correct the expected number of events of Z+HF, W+HF and $t\bar{t}$ processes. Two additional NFs are included in the lowest $p_{\text{T}}(V)$ bin of the 2L channel for the Z+HF process.

Different fits, involving a variable number of parameters of interest (POI), i.e. signal strengths, are performed. At first, the inclusive $\mu_{VH}^{b\bar{b}}$ is extracted by considering one single POI. A fit with two POIs is performed to extract the WH and ZH contributions separately. A five-POI setup is used to measure different STXS bins, three for the ZH process, and two for the WH process. The splitting does not correspond exactly to the Stage 1 bins presented in Figure 1.7, since a merging of various bins has been performed. Further details are provided in Ref. [42].

When considering m_{bb} as a discriminant, a single POI fit is performed to extract the inclusive $\mu_{VH}^{b\bar{b}}$ signal strength. This result is used as a cross-check of the main MVA analysis.

In order to validate the statistical model, an additional two-POI fit is performed by considering the WZ and ZZ processes as standard candles. This is done in an earlier stage of the analysis, before unblinding the data corresponding to m_{bb} values close to the Higgs boson peak. An uncertainty of 50% is assigned in this case to the VH signal, which is fixed at its SM expected predictions.

Boosted analysis. The discriminant variable used in the boosted analysis to extract the signal strength from the likelihood fit is the mass of the large-R jet of the Higgs boson candidate, m_{J}. An optimization of the binning has been performed such that the resolution is maximized given the limited MC statistics available, and empty bins either in the background templates or in the data distributions are avoided. The final binning of each region is reported in Ref. [208].

The background processes included in the likelihood are V+jets production, split in the three categories V+HF, $V+cl$ and $V+l$, $t\bar{t}$, and single top-quark production. The $s-$ and $t-$ channel processes are taken together, while the tW one is separate. Dibosons production is also considered. The multijet background is included in the $1L$ channel, and estimated in a data-driven way as done in the resolved analysis.

Four freely-floating NFs are included in the fit model: one for the $Z+bb$ component and one for the $W+bb$ component, both independently fully correlated

among different regions and bins. Two NFs are introduced for the $t\bar{t}$ process, one for the 0L and one for the 1L channel. These normalizations are fixed from the additional CRs.

To simultaneously extract the signal strength of the VZ and VH processes, a two-POI fit is performed. This is not done in the resolved analysis since the main analysis is performed using a BDT discriminant optimized to separate only one signal at the time from background processes.

Systematic uncertainties

Systematic uncertainties can be divided in experimental and modelling-related. The former are almost identical to the ones adopted in the monojet analysis and already described in Section 4.8.1. Differences and additional contributions are briefly discussed in this sub-section.

The derivation of modelling systematic uncertainties is based on the comparison with alternative MC predictions, based either on QCD scales or PDF variations, or on alternative ME generators and PS algorithms. The categorization of the events requires the derivation of migration and extrapolation uncertainties between different regions. Full details of the modelling uncertainties included in the resolved and boosted $VH(\to b\bar{b})$ analyses can be found in Refs. [42] and [208], respectively. However, the general method to derive such uncertainties is discussed below.

Experimental uncertainties. Concerning electron related uncertainties, both the resolved and boosted analyses adopt the same NP scheme used also by the monojet analysis in the regions which do not include *monojet-signal* leptons. Therefore, only one NP is used to parameterize the uncertainties on the SF for the identification efficiency.

On muons, two additional NPs are considered in the resolved analysis to parametrize the statistical and systematic uncertainties associated to the scale factors adopted to match in simulation the efficiencies observed in data. The presence of this uncertainty is due to the fact that in the 2L channel single-muon triggers are used to select events.

In both the $VH(\to b\bar{b})$ analyses presented, the same reduced set of NP used in the monojet analysis is used for the parameterization of JES uncertainties. JER uncertainties however are described in the $VH(\to b\bar{b})$ by a simpler scheme, composed by seven NP (instead of the 13 adopted in the monojet analysis) derived by the eigenvector decomposition method.

The jet flavour composition uncertainty, which accounts for response of the detector to jets originated from the hadronization of different quarks or gluons, in the resolved $VH(\to b\bar{b})$ analysis is kept uncorrelated between the top quark, V+jets and diboson plus signal processes, while in the monojet and boosted $VH(\to b\bar{b})$ ones is correlated among all processes. In the boosted analysis, a set of systematic uncertainties is introduced to cover uncertainties on the large-R JMR, JMS and on the derivation of the combined mass. JMR and JMS uncertainties are treated as uncorrelated between different background processes.

An extended scheme is adopted in the resolved $VH(\to b\bar{b})$ analysis to parameterize the flavour tagging uncertainties. A total of 45, 20 and 20 components are

included for the tagging of truth b-, c- and light-flavour jets, respectively. The boosted analysis adopts a scheme derived for VR track-jets, in which four NPs are provided for c- and light-flavour jets, and five for b-jets.

Uncertainties on the $E_{\mathrm{T}}^{\mathrm{miss}}$ trigger are included in the resolved $VH(\to b\bar{b})$ analysis due to the fact that the lower threshold on $E_{\mathrm{T}}^{\mathrm{miss}}$ is 150 GeV. In the $[150, 200]$ GeV range, SFs of the order of $0.9 \div 1$ are needed to take into account simulation mismodelling, and uncertainties on these SFs are included.

Modelling uncertainties. Uncertainties on the MC simulations adopted in the analysis have three effects: they can affect the normalization of the samples, impact the relative acceptance between the categories defined for the fit model and affect the shapes of the main discriminant variables such as m_{bb} and $p_T(V)$. These uncertainties are estimated by comparing the nominal MC samples with alternative ones, obtained under different hypotheses. Uncertainties are associated to different choices of the renormalization and factorization scales or of the α_s value used in the simulation, or to alternative PDF sets. Moreover, the effect of changing ME generator or PS model is also considered. These latter uncertainties are sometimes ill-defined since comparisons are, in some cases, made between samples which are generated at different perturbative orders. However, for some sources of uncertainty this is the only available approach to estimate a systematic.

The effect on the normalization, efficiency and acceptance is evaluated by a comparison of the integrated cross-section obtained in an alternative setup with the one used for the nominal predictions, and by summing in quadrature the largest effect of each category of variations.

Uncertainties on the relative acceptance of different event categories are derived by performing a double ratio as

$$\delta = \left(\frac{N_A}{N_B}\right)_{\text{Nominal}} \Big/ \left(\frac{N_A}{N_B}\right)_{\text{Alternative}}, \tag{5.1}$$

where $N_{A,B}$ indicate the yields in two different categories of events or regions of the analysis, and 'alternative' is referred to a different prediction of the process considered, provided for example by an alternative MC generator.

Shape uncertainties are obtained by comparing the normalized yields of one setup to several variations. In the resolved analysis, these are derived on the m_{bb} and $p_{\mathrm{T}}(V)$ distributions, which are the main discriminants between signal and background events, and are propagated to the final discriminant in the MVA analysis. For the Z+jets process, shape uncertainties are derived in a data-driven way from the $2L$ channel. For the W+jets and $t\bar{t}$ processes, uncertainties on m_{bb} and on the final MVA discriminant are derived by reweigthing the nominal MC predictions to alternative ones via a set of BDTs in a procedure called BDT-reweighting. More details on such technique are presented in Ref. [42]. In the boosted analysis, shape uncertainties are derived on the m_{J} distribution, which is the discriminant adopted in the maximum likelihood fit.

5.2.6 Main limitations

This section focuses on the main limitations of the resolved and boosted $VH(\to b\bar{b})$ analyses, while the results obtained are reported in Ref.[42] and Ref. [208], respectively.

Resolved analysis. In Table 5.3 the breakdown of the effect of uncertainties on the $VH(\to b\bar{b})$ signal strength, as measured by the resolved analysis, is presented. The impact on the signal strength measurement is derived by subtracting in quadrature the uncertainty on μ obtained in the nominal fit, and in a fit in which all the NPs belonging to one category are fixed to their best-fit value. The statistical error reported in the first part of the table is the uncertainty on μ obtained in a fit in which all the nuisance parameters are fixed to their best-fit value. The systematic component is given by the difference in quadrature of the latter uncertainty with the one obtained in the nominal fit. From the latter two numbers it is possible to state that the analysis is starting to become systematics-dominated, but yet the two contributions are very similar.

Table 5.3. breakdown of the sources of uncertainty on the measurement of the inclusive $\mu^{b\bar{b}}_{VH}$ and exclusive $\mu^{b\bar{b}}_{WH}$ and $\mu^{b\bar{b}}_{ZH}$ signal strengths. Table from Ref. [42].

Source of uncertainty		σ_μ VH	WH	ZH
Total		0.177	0.260	0.240
Statistical		0.115	0.182	0.171
Systematic		0.134	0.186	0.168
Statistical uncertainties				
Data statistical		0.108	0.171	0.157
$t\bar{t}$ $e\mu$ control region		0.014	0.003	0.026
Floating normalisations		0.034	0.061	0.045
Experimental uncertainties				
Jets		0.043	0.050	0.057
$E_{\mathrm{T}}^{\mathrm{miss}}$		0.015	0.045	0.013
Leptons		0.004	0.015	0.005
b-tagging	b-jets	0.045	0.025	0.064
	c-jets	0.035	0.068	0.010
	light-flavour jets	0.009	0.004	0.014
Pile-up		0.003	0.002	0.007
Luminosity		0.016	0.016	0.016
Theoretical and modelling uncertainties				
Signal		0.072	0.060	0.107
Z + jets		0.032	0.013	0.059
W + jets		0.040	0.079	0.009
$t\bar{t}$		0.021	0.046	0.029
Single top quark		0.019	0.048	0.015
Diboson		0.033	0.033	0.039
Multi-jet		0.005	0.017	0.005
MC statistical		0.031	0.055	0.038

Concerning experimental uncertainties, the largest contributions are associated with jets measurements and the flavour tagging procedure. The former term can be reduced by the adoption new reconstruction techniques for the jets, i.e. the PFlow method described in Section 3.3, affected by lower uncertainties. This allows to reduce the uncertainties on jets below 100 GeV thanks to the combination of ID and

calorimeter information in the jet reconstruction procedure.

Uncertainties on the flavour tagging procedure can be reduced in several ways. The largest source of uncertainty originates in the calibration of the tagging algorithms, and therefore an improved treatment of the uncertainties which are then propagated to the SFs can help in reducing such contribution. Furthermore, better MC simulation of processes involving HF jets can lead to SFs, and in particular MC-to-MC scale factors closer to unity. The latter are used in this analysis to propagate the calibration of the tagging procedure from the default sample, based on Powheg+Pythia 8, to the various MC generators adopted for the simulation of background processes. Moreover, the rejection of c- and light-flavour jets can be enhanced by using a more performant tagger, such as DL1r. The PFlow algorithm for jet reconstruction can also improve the performance of b-tagging especially at low p_{T}, where the mistag rates of non b-jets is largest. Further details on studies of the performance of b-tagging with PFlow jets are reported in Section 5.3.1.

Among modelling systematic uncertainties, the largest ones are associated to the signal simulation. The leading contribution to this term is associated with the generation of $gg \to ZH$ simulated events, whose MC predictions are available only at LO. Further details on this are discussed in Ref. [42]. The simulation of V+jets processes, and in particular of V+HF, has also a large impact on the signal strength measurement. Its effect is split into a component due to alternative modelling schemes, thus the comparison with alternative generation parameters and alternative generators, and a component due to the data modelling discrepancies, which have been already discussed for the monojet analysis. To correct the inclusive cross-section predictions, freely-floating NFs are needed, and introduce additional uncertainties in the background determination. Such effect could be reduced by improved MC simulations which provide a better description of data. Updated configurations of the Sherpa MC generator for the simulation of V+jets processes are discussed in Section 6.1.4 and 6.1.5, where improvements on the V+HF process modelling are presented.

The MC statistical uncertainty has been, in previous iteration of this analysis, one of the leading contributions. Its effect was reduced significantly thanks to extended generation of simulated samples. Truth tagging also helps in reducing such contributions. As already mentioned in Section 5.2.3, non-closures observed in $b\bar{b}$ final states required the introduction of the hybrid tagging. This is mainly due to the fact that flavour tagging emulation via two-dimensional efficiency maps is a good but not perfect parameterization of the complete procedure. Such limitations can be overcome by adopting new techniques, as presented in Section 5.3.2, where a neural network (NN) approach to the truth tagging is proposed. Moreover, a reduction of the MC statistical uncertainty can be also achieved by adopting new event generation techniques, which can provide a larger equivalent luminosity for fixed number of raw events. Further details on this methods, related to the simulation of V+jets processes, are discussed in Section 6.2.

Boosted analysis. In Table 5.4, the sources of uncertainty on the measurement of $\mu_{VH}^{b\bar{b}}$ in the boosted topology are presented. The breakdown of the various contributions is obtained as described for the resolved analysis. The analysis is currently dominated by the statistical uncertainty, but the total systematic term is

only slightly lower than that one.

Table 5.4. breakdown of the sources of uncertainty on the measurement of the $\mu_{VH}^{b\bar{b}}$ signal strength in the boosted $VH(\to b\bar{b})$ analysis. Table from Ref. [208].

Source of uncertainty		Avg. impact
Total		0.372
Statistical		0.283
Systematic		0.240
Experimental uncertainties		
Small-R jets		0.038
Large-R jets		0.133
$E_{\mathrm{T}}^{\mathrm{miss}}$		0.007
Leptons		0.010
b-tagging	b-jets	0.016
	c-jets	0.011
	light-flavour jets	0.008
	extrapolation	0.004
Pile-up		0.001
Luminosity		0.013
Theoretical and modelling uncertainties		
Signal		0.038
Backgrounds		0.100
$\hookrightarrow Z$ + jets		0.048
$\hookrightarrow W$ + jets		0.058
$\hookrightarrow t\bar{t}$		0.035
$\hookrightarrow$ Single top quark		0.027
$\hookrightarrow$ Diboson		0.032
$\hookrightarrow$ Multijet		0.009
MC statistical		0.092

Among the experimental systematic uncertainties, the leading one is related to large-R jets, and in particular the dominant source comes from the JMR due to the fact that a 20% conservative term is included to take into account its calibration. The impact of flavour tagging uncertainties is lower in the boosted analysis than in the resolved one, due to the fact that in the former VR track-jets are adopted. These jets can be used to better catch the sub-jets in the large-R one, but are less common in ATLAS analyses, therefore studies have been mainly focused on the EMTopo reconstruction technique.

Concerning modelling systematic uncertainties, the signal contribution is subdominant with respect to the one associated to the background processes. The largest contributions come from the simulation of V+jets processes. In such a boosted regime, in fact, large normalization factors are needed to correct the mismodelling of MC simulation, as also shown in the ATLAS measurement of the $Z + b(b)$ process [217].

A significant contribution to the total uncertainty is due to the limited amount of MC statistics available for V+jets processes. To reduce such large impact TT is a viable approach. However, as already mentioned in Section 5.2.3, two-dimensional efficiency maps yield only an approximation of the flavour tagging procedure. In particular, such maps are derived in events with isolated jets, therefore they intrinsically fail in modelling the boosted topologies where the effects of close-by

jets have a non-negligible impact in the tagging. These effects did not allow to use TT for the background simulation, thus the limited amount of events available in simulated MC samples reflects in such a large uncertainty. A way to overcome the limitations of TT in boosted topologies is presented in Section 5.3.2.

5.3 Towards a Run 2 VH *legacy* analysis

A first combination of the resolved and boosted topologies has been performed recently [218] to provide a simultaneous STXS measurement across multiple $p_T(V)$ bins exploiting the two analyses. However, such work is based on the state of the art results presented in the previous section, thus no optimization of the objects reconstruction or of the tagging procedure has been performed. Moreover, the overlap between the two analysis has been solved introducing an hard cut at 400 GeV of vector boson p_{T}. Below such threshold the resolved analysis is considered, while above the boosted regions are adopted. This strategy can be improved in view of a Run 2 legacy result for the $VH(\rightarrow b\bar{b})$ process measurement. The studies I performed on possible alternative strategies are presented in Section 5.3.3. Expected improvements in the flavour tagging, thanks to the adoption of new taggers and PFlow jets are summarised in Section 5.3.1, where the studies I performed are presented. An innovative method we proposed in [219] for the implementation of TT via NN is described in Section 5.3.2.

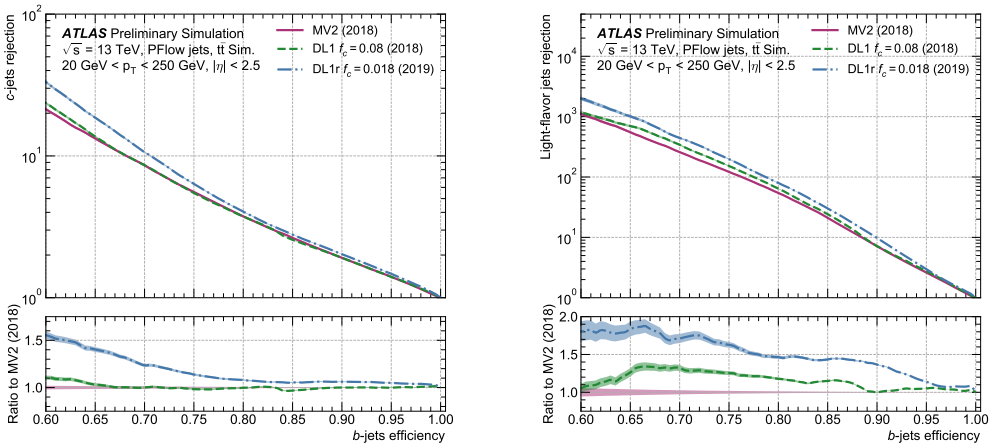
5.3.1 Improving flavour tagging

The adoption of the PFlow algorithm for the reconstruction of hadronic jets requires a re-tuning of the flavour tagging algorithms. This is done as documented in Ref. [149] using the PFlow jets as inputs. The b-tagging efficiency achieved in various algorithms, introduced in Section 3.3.2 of this thesis, is presented for PFlow jets in Figures 5.5(a) and 5.5(b) in terms of c- and light-flavour jets rejection[1], respectively. The performance is tested on a $t\bar{t}$ MC sample for isolated jets. In both cases, jets are required to be within the interval $20\,\mathrm{GeV} < p_{\mathrm{T}} < 250\,\mathrm{GeV}$, which is the range for which c-jets are calibrated using data. Light-flavour jets are calibrated up to 300 GeV of p_{T}, while b-jets up to 400 GeV. Above those values, an extrapolation of the calibration SF is performed.

In general, for fixed b-tagging efficiency the DL1 and DL1r algorithms provide an increased rejection for all values of the $b-$tagging efficiency. At a fixed value of $\varepsilon_b = 70\%$, which corresponds to the WP chosen in the resolved analysis, the c-jet rejection of MV2c10 can be improved inclusively of around 25% by DL1r. The light-flavour jet rejection, at fixed 70% of b-tagging efficiency again, is improved significantly in DL1r with respect to the one obtained with the MV2c10 algorithm up to a factor 1.7. For these reasons, DL1r is chosen as the algorithm to be used in the Run 2 legacy $VH(\rightarrow b\bar{b})$ analysis.

The performance of DL1r on the tagging procedure are presented in Figure 5.6 as a function of the jet p_{T} for various single-cut operating points (OP) which provide an average efficiency of 60, 70, 77, 85%. The b-tagging efficiency increases as a function

[1]The c- and light-flavour jet rejections are defined as the inverse of the mistag rate.



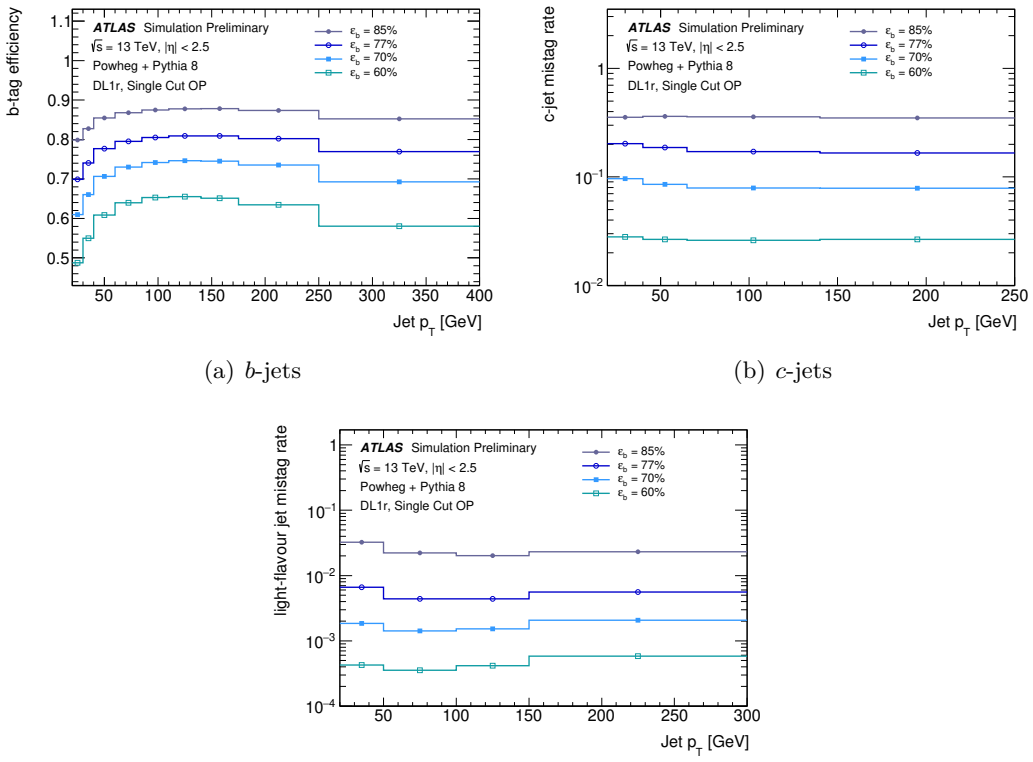
(a) (b)

Figure 5.5. Performance of different flavour tagging algorithms evaluated on PFlow jets. Figure (a) shows the inverse of the c-jet mistag rate as a function of the b-jet tagging efficiency, Figure (b) the inverse of the light-flavour jet mistag rate, again as a function of the b-jet tagging efficiency. More details are provided in the text. Figures from Ref. [149].

of the jet p_{T}, since the effect of multiple-scattering on the tracks is reduced and the decay length of b-hadrons is increased. At high p_{T} the efficiency decreases due to lower performance in the tracking procedure. The mistag rate of c- as b-jets is almost constant as a function of the jet p_{T}: for the $\varepsilon_b = 70\%$ WP it varies between 10 and 8%. Light-flavour jets are characterized by high rejection factors, as shown in Figure 5.5(b), and the mistag rate is slightly lower in the $50\,\mathrm{GeV} < p_{\mathrm{T}} < 150\,\mathrm{GeV}$ range. The binning and p_{T} range shown correspond to the ones adopted in the calibration procedure.

From the comparison between data and MC events, data-to-MC SFs (or simply SFs) are derived to correct the modelling of the flavour tagging procedure in the simulation. These are obtained for each algorithm and each WP, and provided to all ATLAS physics analyses under the form of official recommendations. If an alternative MC generator, with respect to the one adopted in the calibration procedure (Powheg+Pythia 8) is used, a correction needs to be applied. In fact, as shown in Figure 5.7, different ME generators and PS algorithms show a different modelling of quantities relevant for the flavour tagging procedure, such as the fraction of energy in a b-jet carried by the b-hadron, or the b-hadron p_{T}. MC-to-MC scale factors are defined for this purpose, and are obtained from the ratio of the measured efficiency in a different generator with the one used in the calibration. These are applied as

$$\mathrm{SF}_{\text{Alternative MC}}(p_{\mathrm{T}}) = \frac{\varepsilon_{\text{Data}}(p_{\mathrm{T}})}{\varepsilon_{\text{Nominal MC}}(p_{\mathrm{T}})} \times \frac{\varepsilon_{\text{Nominal MC}}(p_{\mathrm{T}})}{\varepsilon_{\text{Alt. MC}}(p_{\mathrm{T}})} = \frac{\mathrm{SF}_{\text{Data-MC}}(p_{\mathrm{T}})}{\mathrm{SF}_{\text{MC-MC}}(p_{\mathrm{T}})}. \quad (5.2)$$



(a) b-jets

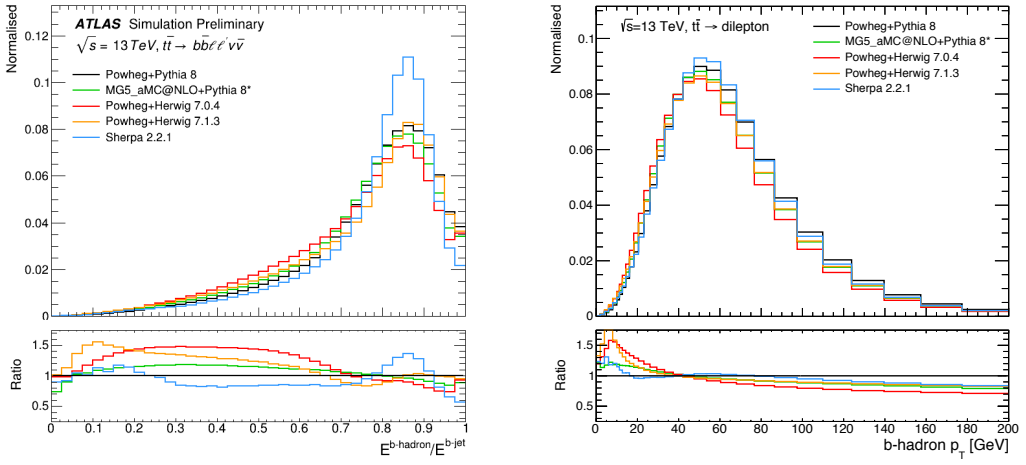
(b) c-jets

(c) light-flavour jets

Figure 5.6. Performance of the DL1r algorithm shown on the b-jet tagging efficiency (a) and c- (b) and light-flavour jet (c) mistag rates, shown as a function of the jet p_{T} for different single cut OPs. Figures from Ref. [6].

MC-to-MC scale factors are used under the assumption that relative differences in the flavour tagging efficiency are internal to each jet, and thus are factorized from any difference in the event topology. For this reason, these are evaluated from isolated jets in $t\bar{t}$ dilepton events only, and applied to any other process. Moreover, as done for the calibration SF, these are assumed to be independent on the jet pseudo-rapidity.

MC-to-MC SF derived for PFlow jets and the $\varepsilon_b = 70\%$ WP of the DL1r algorithm are presented in Figure 5.8. The nominal simulated sample is Powheg+Pythia 8, while alternative MC setups considered are based on the MadGraph 5 and Powheg ME generator, as well as the Powheg ME interfaced with the Herwig PS algorithm. MC-to-MC SF are derived also for the Sherpa 2.2.1 generator. On the same plots, the data-to-MC SF obtained in the calibration procedure are also shown. The uncertainty for the MC simulated samples is only statistical, while for the data calibration points the total uncertainty is shown. This does not always cover the differences observed between the several setups. For the b-jet tagging efficiency, larger corrections are observed when the PS algorithm is varied, i.e. in the Powheg+Herwig setups. MC-to-MC SF are provided for two versions of the Herwig PS. Values closer to one are observed for the latest version.



(a) (b)

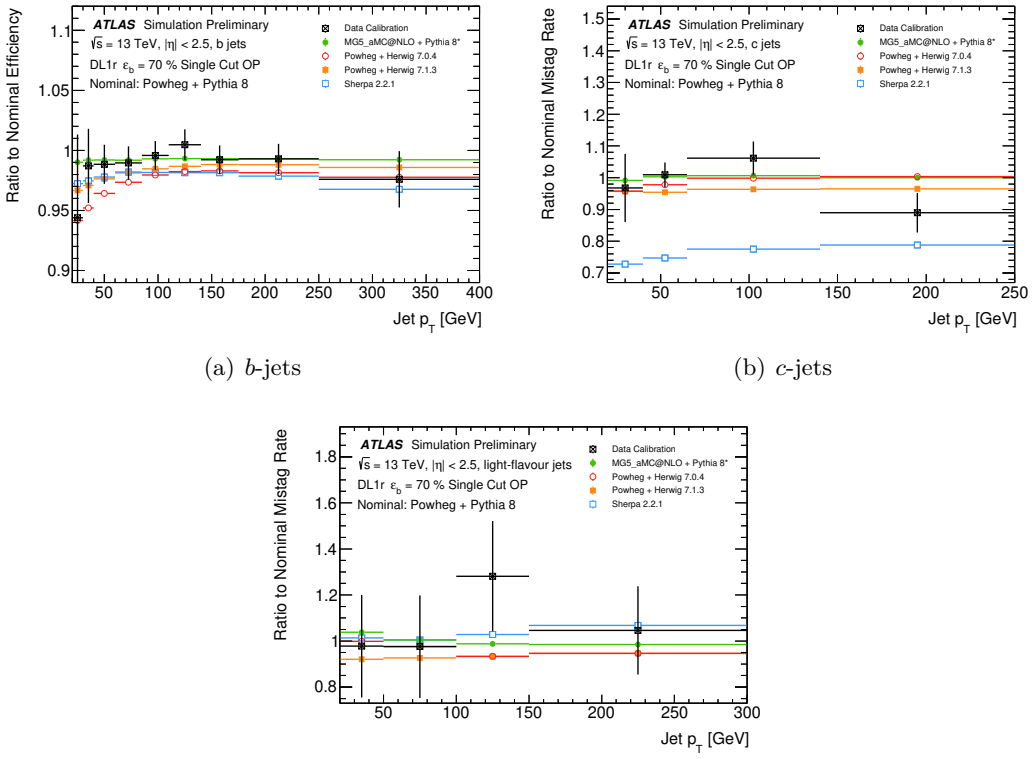
Figure 5.7. Normalized distribution (a) of the fraction of energy of a jet carried by the b-hadron matched to it (figure from Ref. [6]), and (b) of the b-hadron p_{T} (b), as obtained in $t\bar{t}$ dilepton events simulated with different MC generators.

Values of the MC-to-MC SF significantly different from unity are needed to correct the mistag rate of c-jets observed in Sherpa 2.2.1. The reason for such a large value is due to large differences in the production rates of the species of hadrons produced in the fragmentation of the c-quark between Sherpa and the nominal sample. Further details on this, and how this issue is addressed in newer versions of the Sherpa MC generator, are presented in Section 6.1.4. Differences in the mistag rates between the various generators are covered at low p_{T} by the uncertainty of the measured data-to-MC SF. In the highest p_{T} bin, above 140 GeV, some differences are observed. In particular, all the MC predictions (with the exception of the ones based on Sherpa) seem to over-estimate the mistag rate observed in data.

For the light-flavour jet mistag rate, MC-to-MC SFs close to unity are observed for all the MC generators studied, and in general differences are well within the data-to-MC SF uncertainty. In the 100 GeV $< p_{\mathrm{T}} <$ 150 GeV bin, a larger data-to-MC SF is observed, but in agreement with 1 within slightly more than 1σ. This is presumably due to a statistical fluctuation observed in the calibration SF.

5.3.2 Enhancing the truth tagging method

The truth tagging (TT) method, introduced in Section 5.2.3, is an event weighting technique which allows to reduce the MC statistical uncertainty when applying the flavour tagging procedure. The relative uncertainty of a sample on which direct tagging is applied is $1/\sqrt{N_{\mathrm{tag}}}$. Event weighting techniques lead to a final uncertainty $\sqrt{\sum_i w_i^2}/N_{\mathrm{all}}$ instead, where the numerator and denominator include all the events available in the simulated samples. Such method improves the statistical uncertainty if the uncertainty component due to weights distribution is small enough, which is usually the case.



(a) b-jets

(b) c-jets

(c) light-flavour jets

Figure 5.8. MC-to-MC SF obtained for different MC generators, and compared to data-to-MC SF derived by a comparison of the efficiency and mistag rate values observed in data and the nominal MC simulation (based on POWHEG+PYTHIA 8). Figures from Ref. [6].

Up to now, in the $VH(\to b\bar{b})$ analyses TT has been implemented using a two dimensional parameterization of the b-tagging efficiencies, based on jet p_{T} and $|\eta|$. These two variables are good enough for topologies involving isolated jet, in which close-by jets effects are irrelevant. However, in dense environments this approach fails to catch the correlations which arise between different jets. A multi-dimensional parameterization of the efficiency maps could solve this issue, but this is not viable due to the limited available MC statistics.

We proposed [219] a new approach to TT, based on graph neural networks [220] (GNN). This model aims to prove an higher-dimensional parameterization of the tagging efficiency. GNN are particularly useful since are able to cope with a variable size of the inputs, such as a different number of jets in each event. In a GNN, the order of the inputs is not relevant, and pair-wise dependencies of the reconstructed objects are exploited to derive the per-jet efficiency value. In particular, jet-by-jet dependencies variables such as $\Delta R(j_1, j_2)$ are not given as an input, but are rather inferred from single-jet properties during the training procedure. The per-jet efficiency is inferred from the following variables which are given as an input: p_{T}, η, ϕ and the truth flavour (b, c or light-flavour).

Simulated samples. The GNN has been developed on a generic simulation of the production of jets from pp collisions. For this work, the same coordinate system of the ATLAS experiment, as described in Section 2.2, has been adopted. Events are simulated in two different topologies with the aim to probe the generalization of the proposed method.

To test and validate this new approach, a synthetic dataset has been produced. The number of jets in each event is extracted from an exponential function, $e^{-N_j/4}$, which roughly models what is expected for the background processes of the $VH(\to b\bar{b})$ signal. At least two jets are required, and their p_{T} is extracted from Gaussian distribution with mean 20 GeV and $\sigma = 200$ GeV, imposing $p_{\mathrm{T}} > 20$ GeV. The leading-jet η is extracted from a Gaussian distribution defined in the interval $[-2, 2]$, mimicking the ATLAS detector acceptance, and using $\mu = 0$, $\sigma = 0.5$. The azimuthal angle is extracted from a uniform distribution in $[0, 2\pi]$. The angular variables of the other jets (j) in the events is sampled uniformly from the (η, ϕ) plane, given a ΔR constraint which is evaluated with respect to the leading jet, and sampled from the $\sqrt{\Delta R(1, j)}$ distribution. The mass value of the jet is set arbitrarily to 2 GeV. This choice is made such that the obtained m_{jj} distribution is close to the one observed in W/Z+jets events. The sample is split in three truth flavours, b-, c- and light-flavour, in equal fraction.

The alternative data sample, used to probe the generalization power of the model, has been generated with slightly different kinematics. Boosted decays of a scalar particle into a pair of jets, which can be with a probability of 33% of b, c or light-flavour, has been considered. The p_{T} of the two jets has been extracted from an exponential distribution, while the mass of the particle is extracted from a gaussian distribution centered at 90 GeV. The p_{T}, η and $\Delta R(i, j)$ distributions for both samples are presented in Figure 5.9.

Efficiency maps similar to the one introduced in Section 5.3.1, have been considered to parameterize the flavour tagging procedure. To obtain these, the *true b-tagging efficiency* for a single jet has been evaluated as

$$\varepsilon_j = \varepsilon_{f_j}(p_{\mathrm{T}}, \eta) \prod_i \varepsilon_{ij}(\Delta R(i, j), f_j), \tag{5.3}$$

where the first term of right hand side is the efficiency value read from the two dimensional map corresponding to the flavour f of the jet. The additional term is introduced to take into account a reduction in the tagging performance when two jets are close to each other. The form of the parameterization adopted is presented in Figure 5.9, and depends on the truth flavour f of the jet. Such curve is defined to mimic the ATLAS and CMS flavour tagging performance.

This true efficiency is used to assign to each jet a flag if it is considered tagged or not. An ISTAG flag is assigned by extracting a random number uniformly between 0 and 1: if this is smaller than the true efficiency, the jet is considered tagged (ISTAG= 1), otherwise it is not (ISTAG= 0). From the efficiency and the ISTAG flag, the event weight is built. For each jet failing the tag requirement, a (1-ε) term is considered in the event weight term, while for each tagged one the total weight is multiplied by ε. The efficiencies obtained in this way are referred to as *true* distribution in the following.

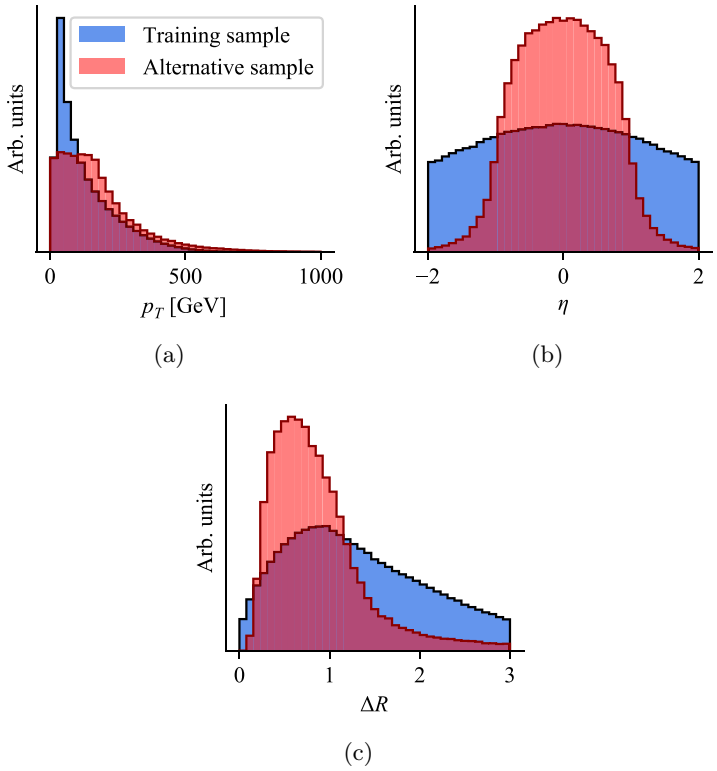


Figure 5.9. Comparison of the normalized p_{T} (a), η (b) and ΔR (c) distributions between the two simulated samples, labelled *Training* and *Alternative*, respectively. Figures adapted from Ref. [219].

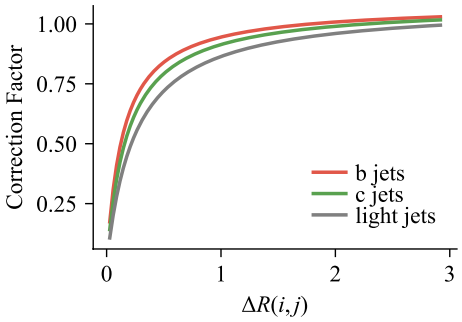


Figure 5.10. Correction factor included in the true tagging efficiency to take into account a reduction when considering two close-by jets. Figure from Ref. [219].

As anticipated, from the ISTAG flag *evaluation* efficiency maps are built to emulate what is currently done in ATLAS: on an inclusive sample, the two-dimensional distributions (p_{T},$|\eta|$) of the jets passing the b-tagging procedure are divided by the same distribution obtained considering all jets, and efficiency maps are built based on the true flavour of such jets.

The true underlying distribution, the one obtained by applying DT (using the

flag ISTAG), and the one applying the *evaluation* efficiency maps are compared to the distribution obtained weighting events via the NN to asses the performance of each method.

Model architecture and training. The developed neural network is represented in Figure 5.11. It is made of two components, the GNN and a deep neural network (DNN). Details on the GNN and DNN models are provided in Ref. [219]. The GNN takes as input the vector $\vec{\theta} = (p_{\mathrm{T}}, \eta, \phi, \text{flavour})$ of each jet, and builds an hidden representation of those by taking into account the properties of all the other jets in the event. The dimension of the hidden representation (d_{hidden}) of each jet is an hyper parameter of the model, fixed to $d_{hidden} = 256$.

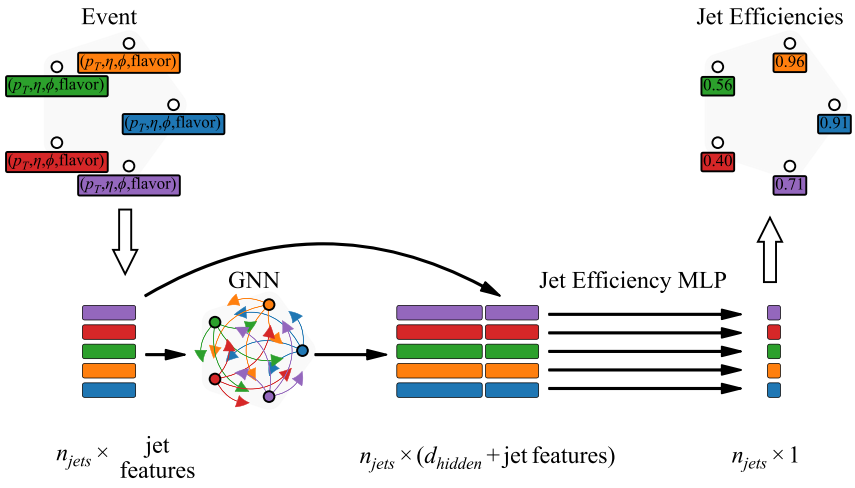


Figure 5.11. Illustration of the architecture of the neural network model. Figure adapted from Ref. [219].

The DNN, also called *Jet Efficiency MLP* (multi-layer-perceptron), acts on each jet singularly. The inputs are the hidden representation of the jet and its original quantities vector $\vec{\theta}$, and the network outputs a single value, the tagging efficiency.

The loss function used in the training procedure is the weighted binary cross-entropy (BCE), defined as

$$\begin{aligned} \mathrm{BCE} = \frac{1}{N_{\mathrm{jets}}} \sum_{i}^{N_{\mathrm{jets}}} & \left[-\mathrm{ISTAG}_i \log\left(\varepsilon_i^{NN}(\boldsymbol{\Theta})\right)\right] \\ & - \left[\mu(1-\mathrm{ISTAG}_i)\log\left(1-\varepsilon_i^{NN}(\boldsymbol{\Theta})\right)\right]. \end{aligned} \tag{5.4}$$

The sum runs over all the jets in the event which have ISTAG equal to 1 (0) if they pass (do not pass) the DT. The efficiency that the network has to predict is ε^{NN}, which depends on $\boldsymbol{\Theta}$, the vector formed by the $\vec{\theta}$ of all jets in the event. The factor μ introduced in front of the second term can be used to weight the relevance of the non-tagged category, and can be useful in cases in which this category is much larger than the tagged one in the training sample. In this application μ was set to unity.

The actual loss function which is minimized in the training procedure is the sum of the per-event BCE, defined in Equation 5.4, over a batch of events. The chosen batch size is 5000 events. This needs to be large enough to include a significant number of both tagged and non-tagged jets in order to reduce statistical fluctuations in the training procedure.

As described in Ref. [221], the training of a NN with the BCE as loss function provides an efficiency value

$$\varepsilon_i^{NN}(\boldsymbol{\Theta}) \simeq \frac{p_i^{\text{tag}}(\boldsymbol{\Theta})}{p_i^{\text{tag}}(\boldsymbol{\Theta}) + p_i^{\text{non-tag}}(\boldsymbol{\Theta})} \simeq \varepsilon_{\text{jet}}, \tag{5.5}$$

i.e. for each jet, the network provides an estimate of the tagging probability without calculating explicitly the p_i^{tag} and $p_i^{\text{non-tag}}$ terms.

In the training procedure, two sources of uncertainties arise. The first is related to the statistical fluctuations of the training sample. The second one is due to the fact that the minimization of the loss function is not performed in an analytical way. Moreover, its initial value depends on the random parameters of the weights in the NNs, thus different starting values might lead to slightly different final ones. Further details on how such uncertainties have been evaluated can be found in the appendix of Ref. [219].

The network is trained for 40 epochs over 1.5 million events; 500k events are used for the validation step performed at the end of each one. The model which provides the smallest value of the loss function, among the 40 epochs, is retained as the final one.

Results. The performance on the efficiency prediction for a single jet are compared in Figure 5.12 between NN result and the TT based on *evaluation* efficiency maps. Residuals on the prediction, defined as $(\varepsilon_{\text{true}} - \varepsilon_{\text{predicted}})/\varepsilon_{\text{true}}$, are shown for the two methods.

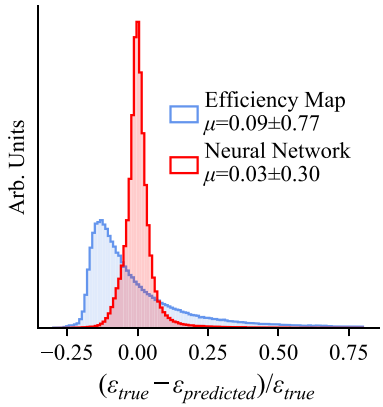


Figure 5.12. Residuals on the prediction of the efficiency, as obtained from the efficiency maps and from the NN model. Figure from Ref. [219].

It is possible to see how the TT based on efficiency maps is not able to catch the jet-by-jet dependencies, which can lead to either an over- or an under-prediction of the efficiency. The NN instead provides a good description of such effect, since to

evaluate the efficiency of a single jet it adopts the information of also the other ones in the event.

Further comparisons between the two methods with the DT and the true efficiency values are performed in the case in which two b-tagged jets are required in the event by using the ISTAG flag. Non b-labelled jets might also be included if these are mistagged (i.e. they pass the DT). Events are split in components based on the true flavour of the leading and sub-leading jets, and the invariant mass is reported in Figure 5.13. In the *light light* category, the large rejection factors of light-flavour jets is such that very few events pass the DT procedure. Even if this is a sub-dominant component of the total background, TT is needed to have a sufficient description of the background.

Overall, the NN description of the tagging procedure is more accurate than the one achieved via the efficiency maps. These plots also show how relevant is to have TT to achieve a smooth description of the backgrounds in categories which lack MC statistics.

Figure 5.14 presents a comparison of the three aforementioned tagging methods when evaluating the performance on events of the *alternative* setup, which are characterized by different kinematic distributions with respect to the one adopted in the NN training. It shows that the NN approach does not depend on the training sample. The discrepancy observed between the true distribution and the one obtained via the efficiency maps originates from the fact that the $\Delta R(j, j)$ dependency is not taken into account in the map approach, as it can be seen from Figure 5.14(b).

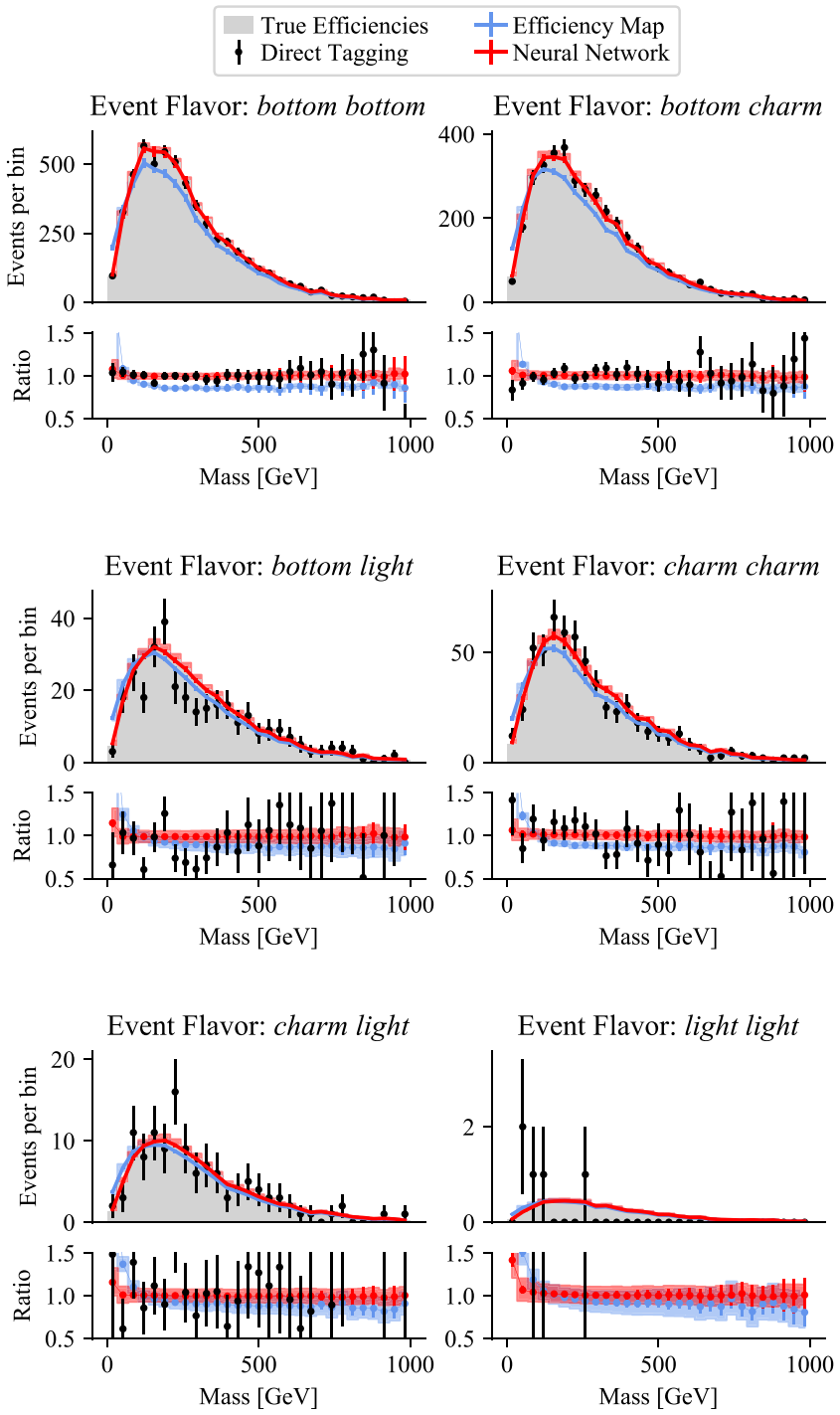
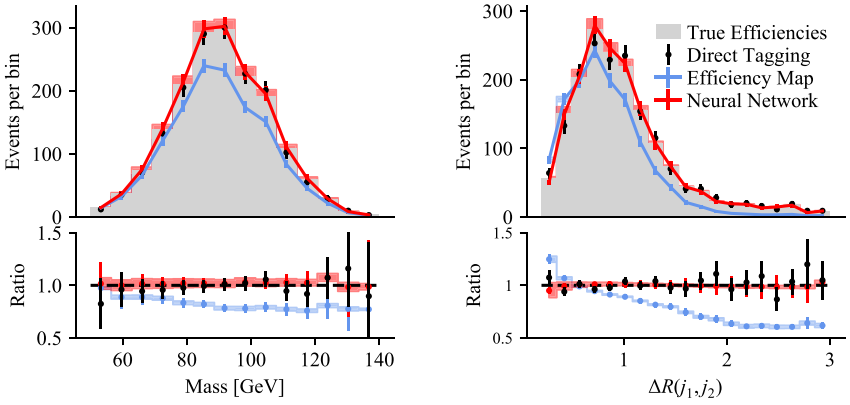


Figure 5.13. Invariant mass distribution of the two leading jets in various event categories, as described by different tagging techniques. The uncertainty on the efficiency maps predictions is statistical, while the one on the NN predictions is derived as reported in Appendix of Ref. [219]. The grey area is the result of weighting the events by their true efficiency as $\varepsilon_1 \cdot \varepsilon_2$, while the black dots represent the effect of DT. Figures from Ref. [219].



(a) (b)

Figure 5.14. Performance of the three tagging techniques compared to the true efficiency in the description of the di-jet invariant mass and $\Delta R(j, j)$ distributions obtained for the *alternative* simulated sample. Figures from Ref. [219].

5.3.3 Solving the overlap between resolved and boosted decays

The removal of the overlap between the resolved and boosted $VH(\to b\bar{b})$ analyses has been performed in the first combination of the two results [218] by selecting the former (latter) analysis below (above) $p_{\mathrm{T}}(V) = 400\,\mathrm{GeV}$. However, as it can be seen from Figure 5.15, the efficiency of reconstructing events in the resolved topology is around 40% at this value, and becomes lower than the one of the boosted analysis only above 600 GeV. Thus, in view of the legacy analysis, a study of different strategies to solve the overlap between the two regimes is performed in the 0 lepton channel.

While the first combination was based on previous published results, thus using the EMTopo jet reconstruction and the MV2c10 b-tagging algorithm, the study presented in this Section is based on improved techniques. In the resolved analysis, PFlow jets are used to build the Higgs boson candidate, and in both the resolved and boosted topologies the DL1r tagging algorithm is adopted.

The presented studies are performed on MC simulated events only, and compare the statistical significance computed in the various signal regions defined in Section 5.2.4, for various setups. To further improve the sensitivity of the analysis, an additional $p_T(V)$ splitting at 600 GeV is proposed. This could also allow to define an additional STXS bin, $400 < p_{\mathrm{T}}(H) < 600\,\mathrm{GeV}$, to be probed. The choice of such threshold is based on the fact that, according to the approximate relation $\Delta R(b,b) \simeq 2m_H/p_{\mathrm{T}}(H)$, the angular separation of the two Higgs boson decay products is expected to be smaller than 0.4 above $\sim 625\,\mathrm{GeV}$. Above such threshold the reconstruction efficiency of Higgs boson candidates via two $R = 0.4$ PFlow jets is expected to drop significantly.

Due to the issues discussed in Section 5.3.1, the TT is not adopted in this study because the NN presented in the previous section is not implemented yet in the analysis framework. However, once available it will become the baseline method to apply TT. Since the optimization of the MVA strategy for both the resolved and boosted analyses is ongoing, the studies are performed by looking at the m_{bb} and m_{J} distributions, respectively. A significant improvement of the performance is expected from the adoption of a multivariate analysis (MVA). However, the comparison presented in this Section can be considered fair, and the ratio of the significance between different setups is expected to remain the same.

The metric adopted to compare different strategies is the binned statistical significance under the assumption that each bin corresponds to a separate independent experiment. It is defined as

$$S\left(\vec{s},\vec{b}\right) = \sqrt{\sum_i 2\left[(s_i+b_i)\ln\left(1+\frac{s_i}{b_i}\right)-s_i\right]}, \tag{5.6}$$

where the sum runs over all the bins i, s_i and b_i indicate the expected signal and background yields, respectively. The uncertainty on this quantity can be evaluated via error propagation as

$$\Delta S = \sqrt{\sum_i \left[\left(\frac{\partial \tilde{S}_i(s_i,b_i)}{\partial s_i}\Delta s_i\right)^2 + \left(\frac{\partial \tilde{S}_i(s_i,b_i)}{\partial b_i}\Delta b_i\right)^2\right]}, \tag{5.7}$$

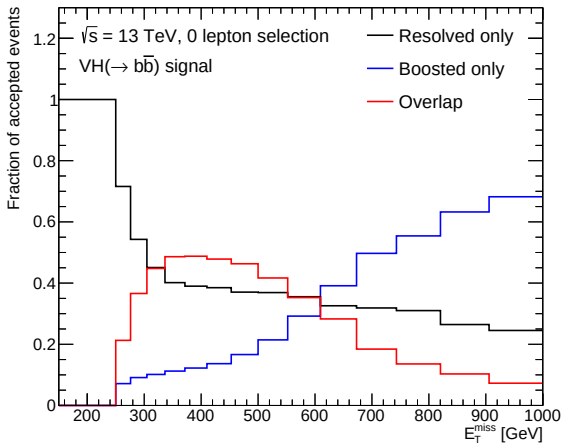


Figure 5.15. Fraction of accepted events reconstructed in the resolved only, boosted only topologies, or with both methods (Overlap) in the 0 lepton channel.

with

$$\begin{aligned} \frac{\partial \tilde{S}_i}{\partial s_i} &= \frac{1}{S} \cdot \left[\ln\left(1 + \frac{s_i}{b_i}\right) \right] \\ \frac{\partial \tilde{S}_i}{\partial b_i} &= \frac{1}{S} \cdot \left[\ln\left(1 + \frac{s_i}{b_i}\right) - \frac{s_i}{b_i} \right]. \end{aligned} \tag{5.8}$$

The expected m_{bb} distributions for the 0 lepton, resolved selection SRs are presented in Figure 5.16 for both the two and three jet event categories. The expected signal distribution is stacked on top of the backgrounds, and overlaid to show the expected shape. In the bottom pad the bin-by-bin significance, evaluated as the square root of the term inside the sum of Equation 5.6, is presented. The integrated significance, summed over all the bins, is also shown. Up to $E_{\mathrm{T}}^{\mathrm{miss}} = 400\,\mathrm{GeV}$, a bin width of 10 GeV is adopted. In the $400 < E_{\mathrm{T}}^{\mathrm{miss}} < 600\,\mathrm{GeV}$ range it is set to 20 GeV, while above 600 GeV a single bin is used. This region is not shown in Figure 5.16. The description of the backgrounds is expected to significantly improve for $E_{\mathrm{T}}^{\mathrm{miss}} > 400\,\mathrm{GeV}$ once TT is applied. As expected, most of the sensitivity comes from the two jet regions, where the leading background is the $Z(\to \nu\bar{\nu}) + bb$ process. The contribution of the $t\bar{t}$ background is large mainly in the lowest $E_{\mathrm{T}}^{\mathrm{miss}}$ bin, while for larger values the dominant contribution is Z+jets.

The distribution of the large-R jet mass is presented in Figure 5.17 after the boosted 0L selection is applied, for both the high-purity (HP) and low-purity (LP) signal regions and in the various $E_{\mathrm{T}}^{\mathrm{miss}}$ bins. For $E_{\mathrm{T}}^{\mathrm{miss}}$ values above 600 GeV a rebinning of the distribution is needed to keep the number expected events above 1. This leads to a loss of information which can be extracted from the binned m_{J} distribution. However, one should keep in mind that the approach via the mass distributions will be kept as a cross-check of the analysis, and the main approach will make use of MVA techniques which enhance the signal to background ratio. Moreover, the definition of the HP and LP regions can be revisited if the number of additional reconstructed jets outside the leading large-R jet is given as an input to

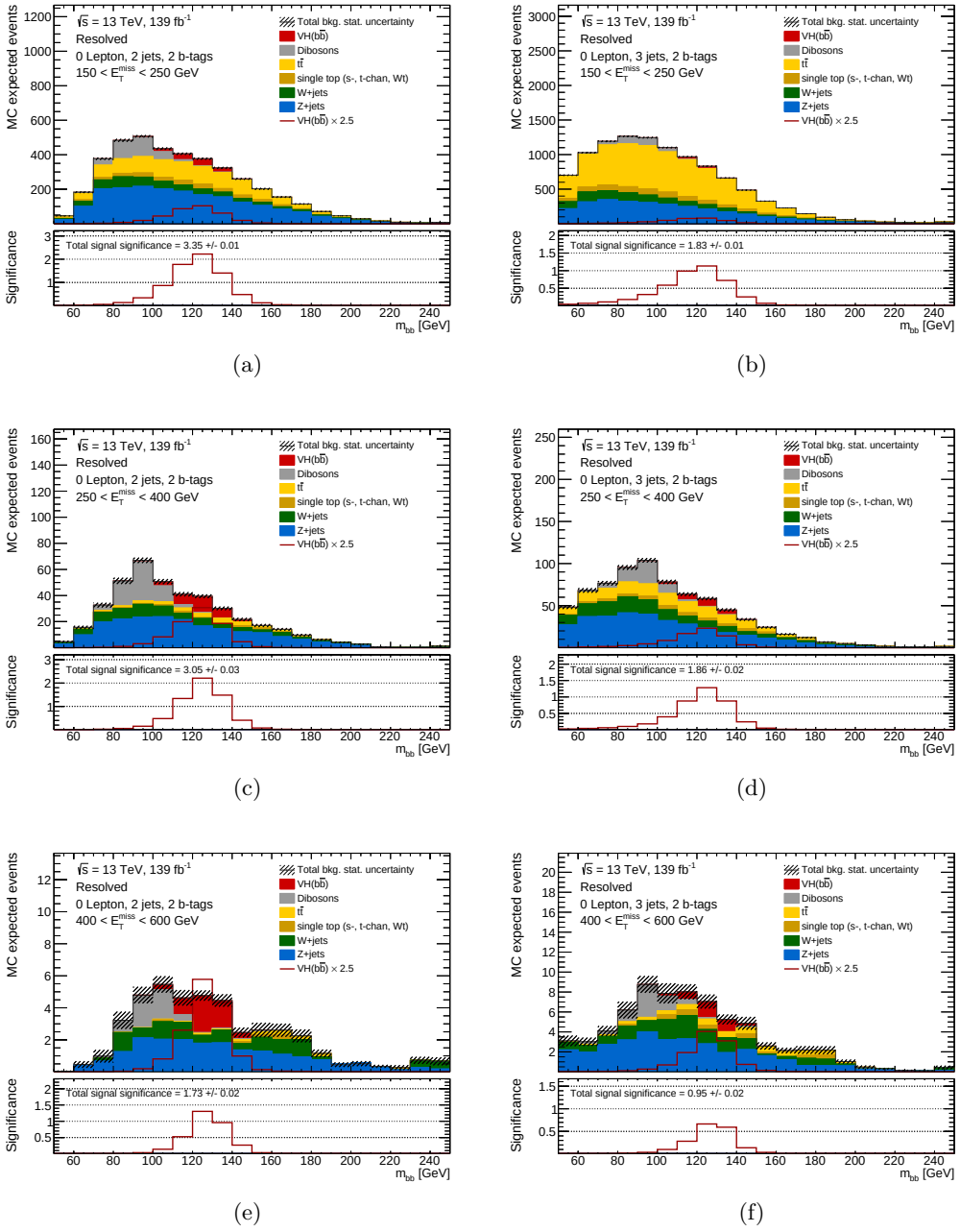


Figure 5.16. Di-jet invariant mass expected distribution for the signal and background processes after applying the 0L resolved selection. In figures (a), (c) and (e) the 2 jet category is presented, while the 3 jet one is presented in figures (b), (d) and (f), respectively. Further details are provided in the text.

the MVA. In this study, the splitting is kept.

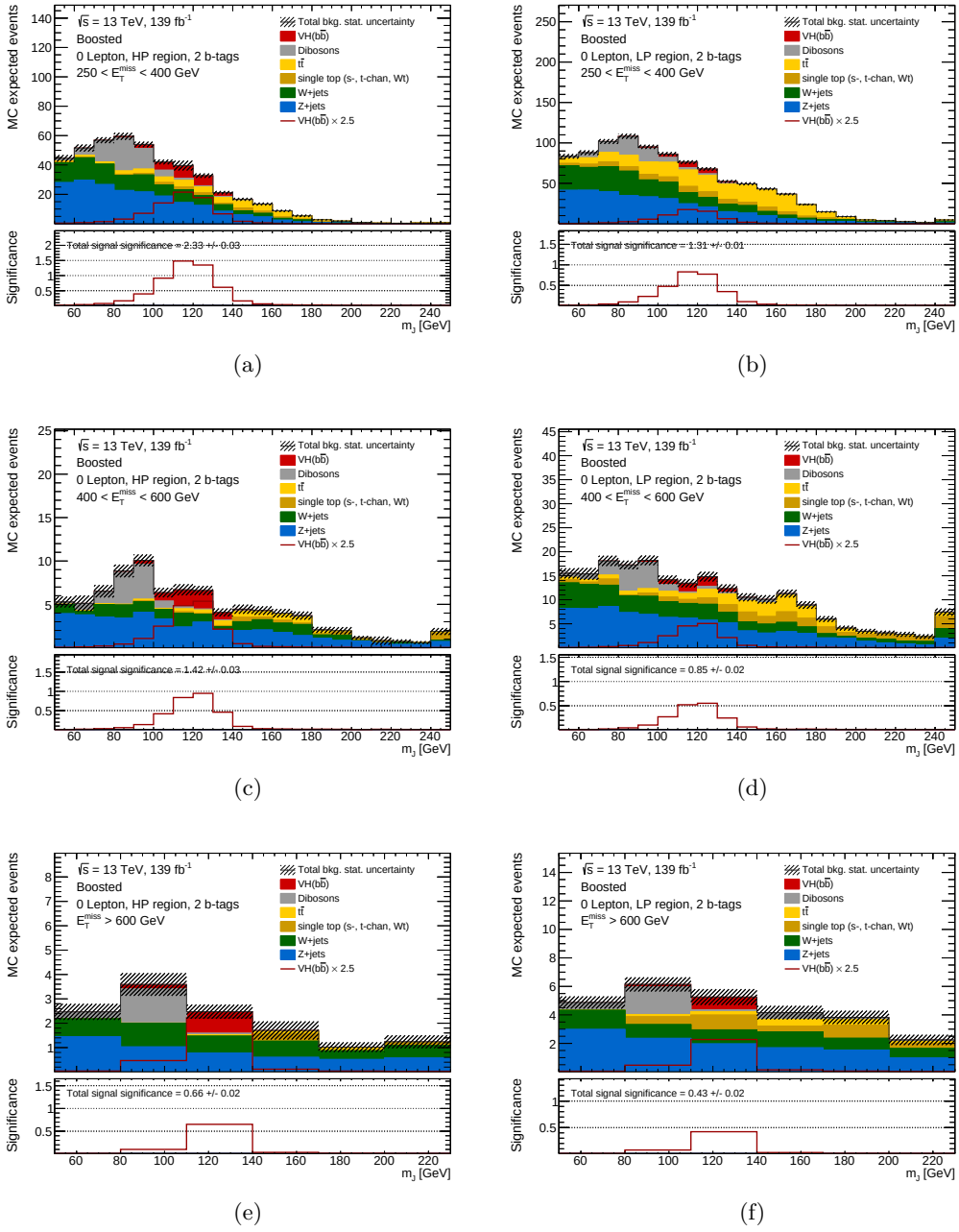


Figure 5.17. Large-R jet invariant mass expected distribution for the signal and background processes after applying the 0L boosted selection. In figures (a), (c) and (e) the HP region are presented, while in figures (b), (d) and (f) the LP ones. Further details are provided in the text.

Combination strategies

A simple way to remove the overlap between the resolved and boosted selection is to apply a fixed cut at one E_T^{miss} value. The choice can be driven by physical reasons, such as the angular separation between the Higgs boson decay products, or

by experimental reasons, such as the resolution on the measurement of the invariant mass of the system with different techniques (PFlows compared to large-R jets). Moreover, statistical reasons might lead to lower boundaries, since otherwise the available statistics in the ATLAS Run 2 data set might not allow for a proper description of the background processes at high $E_{\mathrm{T}}^{\mathrm{miss}}$, and a constrain of the associated uncertainties. As already mentioned, in the first resolved plus boosted combination [218] this approach was chosen, with a threshold value driven by the boundaries of the SRs of the boosted analysis, 400 GeV. An alternative boundary at 600 GeV is also tested in this Section. These two strategies are called either 'split' or 'simple-merge' in the following.

Ideal combination. The best selection one could apply is the logical *or* of the resolved and boosted ones. This, in principle, leads to the highest achievable sensitivity since the signal acceptance is maximised. However, such selection implies that flavour tagging would be applied twice on the same ensemble of tracks forming a jet, which in the resolved analysis is reconstructed via the PFlow algorithm, while in the boosted one is built as a VR track-jet. As already mentioned in Section 5.3.1, each time the flavour tagging technique is adopted, a SF needs to be applied to correct the response in MC. Such calibration scale factors however are not evaluated in a nested configuration of the taggers, as in this case. The simple product of two SF is not a viable option since the tracks on which the tagging algorithm is ran are the same, therefore a correlation between the two SFs would need to be considered, together with a proper comparison with data. Anyway, such strategy is a useful benchmark to compare to, thus its performance are evaluated. In the cases in which an event is selected by both analyses, it is arbitrarily assigned to the resolved (boosted) one if $E_{\mathrm{T}}^{\mathrm{miss}}$ is below (above) 600 GeV.

Priority strategy. A way to solve the mentioned issue with the flavour tagging procedure is to postpone the application of such requirement to a later stage in the selection. This leads to a *priority* strategy. The workflow is briefly presented in Figure 5.18. Two possible strategies arise, in which either the resolved or boosted analyses are prioritised. In the following, these two strategies are referred to as 'Resolved priority' and 'Boosted priority', respectively.

The selection would be applied in two steps: at first all the selection criteria of either the resolved or boosted analysis, except b-tagging, are required to be passed. If these, also referred to as *kinematic selections*, are not satisfied, the other analysis selections are tested. Once the kinematic selection is passed, the b-tagging requirement is applied, either to PFlow jets or VR track-jets. The priority strategy allows to recover events that in a simple-merge approach would be lost. Thus, an improved significance over the split strategies is expected.

In Figures 5.19 (a:d), the boosted regions included in the resolved priority strategy are presented. These are combined with the resolved regions presented in Figure 5.16, improving the overall significance. In the same way, in Figures 5.19 (e:h), the resolved regions recovered via the boosted priority approach are reported. These are combined with Figures 5.17. In this strategy, the first $E_{\mathrm{T}}^{\mathrm{miss}}$ bin ($150 \leq E_{\mathrm{T}}^{\mathrm{miss}} < 250$ GeV) is taken from the resolved selection. At low $E_{\mathrm{T}}^{\mathrm{miss}}$ values large sensitivity is recovered by considering the reconstruction of the Higgs candidate via two PFlow jets. This can be understood by the fact that the cross-section decreases rapidly in $E_{\mathrm{T}}^{\mathrm{miss}}$, and from Figure 5.15, it is possible to see that a large

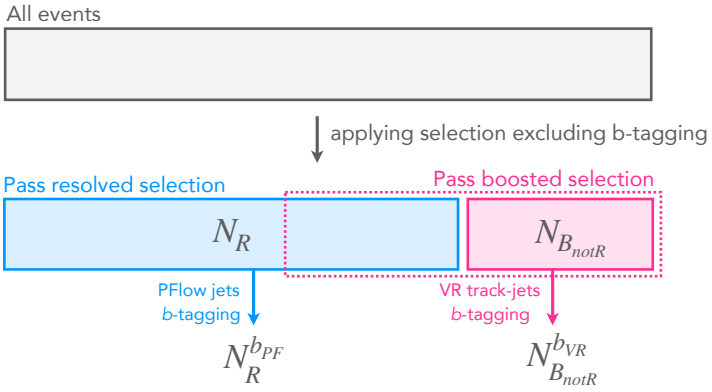


Figure 5.18. Representation of the Resolved priority strategy. The application of the b-tagging requirement is postponed to a second stage, after a *kinematic-only* selection is applied.

amount of events in the $250 \leq E_{\mathrm{T}}^{miss} < 400\,\mathrm{GeV}$ range are reconstructed by the resolved analysis only.

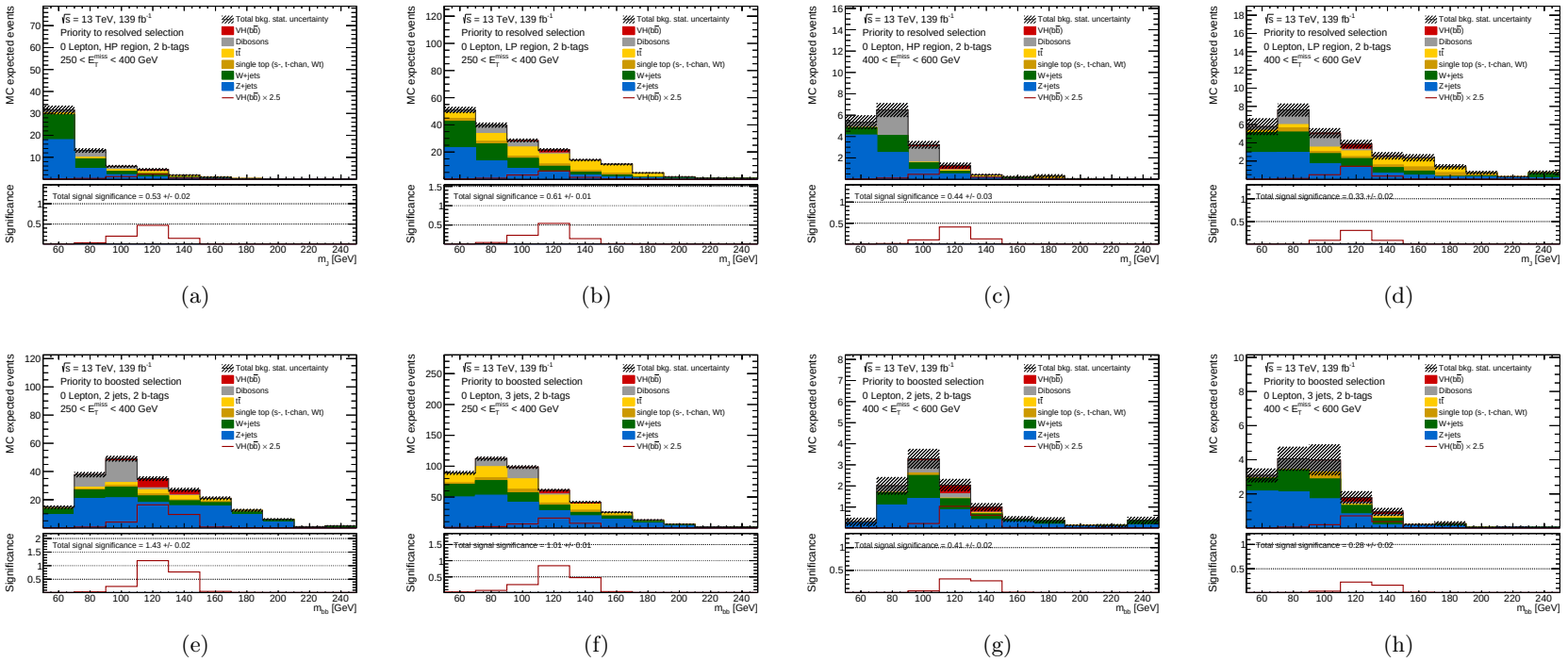


Figure 5.19. (a-d) Large-R jet mass distribution for the boosted regions recovered in a *resolved priority* strategy. (e-h) Di-jet invariant mass distribution for the resolved regions recovered in a *boosted priority* strategy.

Tag VR strategy. The possibility to match reconstructed PFlow jets to VR track-jets built in the ID is investigated. In this way, it would be possible to adopt a strategy close to the *ideal* one, but with the application of b-tagging only to VR track-jets, such that the tagging algorithm is common between the resolved and boosted analyses. The workflow of the strategy is presented in Figure 5.20.

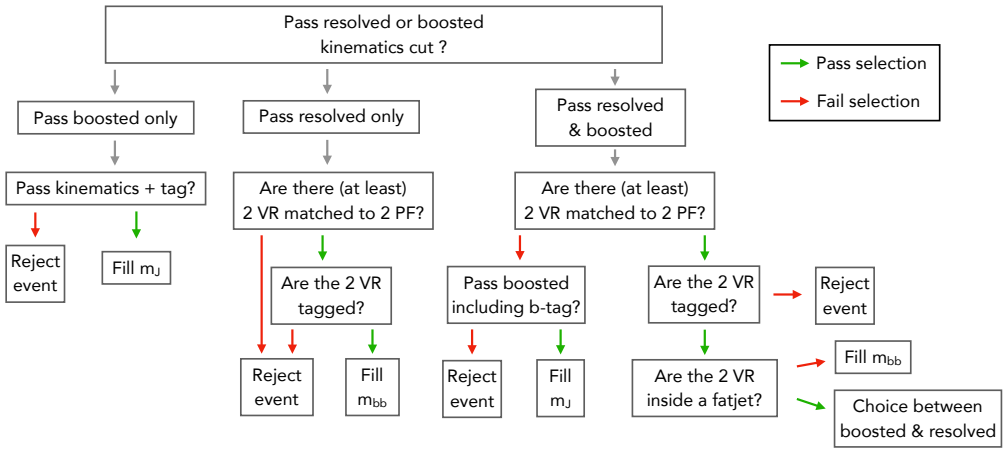


Figure 5.20. Illustration of the selection workflow for the *TagVR* strategy.

For the events passing only the boosted selection, the tagging requirement is applied to the two leading VR track-jets ghost-associated to the leading large-R jet, considered to be the Higgs boson candidate. If the kinematic selection of the resolved topology is passed, events are required to have at least two PFlow jets matched, with the criterion $\Delta R < 0.4$, with two VR track-jets. If this condition is also satisfied, then b-tagging is applied to the latter. Otherwise the event is rejected.

The same kind of requirement is also applied to events passing both the resolved and boosted kinematic selections. In the very rare case ($< 1\%$) in which two matched PFlow-to-VR track-jets are not found, the event can still be recovered by the boosted selection. If at least there are two matches, flavour tagging is applied to all the VR track-jets in the event, and exactly two b-tagged VR track-jets are required. If these two VR track-jets are outside the large-R jet, the boosted selection is failed (since it requires the two b-tagged VR track-jets to be within the large-R jet). Therefore, in these cases m_{bb} is chosen as the mass of the Higgs boson candidate. Otherwise, it means that the Higgs boson candidate is reconstructed simultaneously as a large-R jet and as two separate PFlow jets contained in it. This topology is, strictly speaking, the overlap between the resolved and boosted analyses, and a choice between the two reconstruction techniques is to be made. As done for the priority strategy, both the resolved (based on m_{bb}) and boosted (based on m_{J}) reconstructions are tested for these cases.

Performance comparison. The significance obtained in the various $E_{\mathrm{T}}^{\mathrm{miss}}$ ranges, in the different strategies, are presented in Figure 5.21(a). A sum in quadrature of the statistical significance obtained in different categories, two-, three-jets, HP and LP, is performed for each $E_{\mathrm{T}}^{\mathrm{miss}}$ bin. The total combined significance

is shown in the bottom part of the plot. Figure 5.21(b) shows a comparison of the various strategies in terms of equivalent luminosity. Under the assumption that $\mathcal{S} = s/\sqrt{b} = \sqrt{\mathcal{L}}$, where $\mathcal{L}$ is the integrated luminosity, it can be written

$$\frac{\mathcal{L}}{\mathcal{L}_{\text{ref.}}} = \left(\frac{\mathcal{S}}{\mathcal{S}_{\text{ref.}}}\right)^2. \tag{5.9}$$

The *split* strategy, with a threshold set at $E_{\text{T}}^{\text{miss}} = 400\,\text{GeV}$, is taken here as the reference result, and to which the other investigated options are compared.

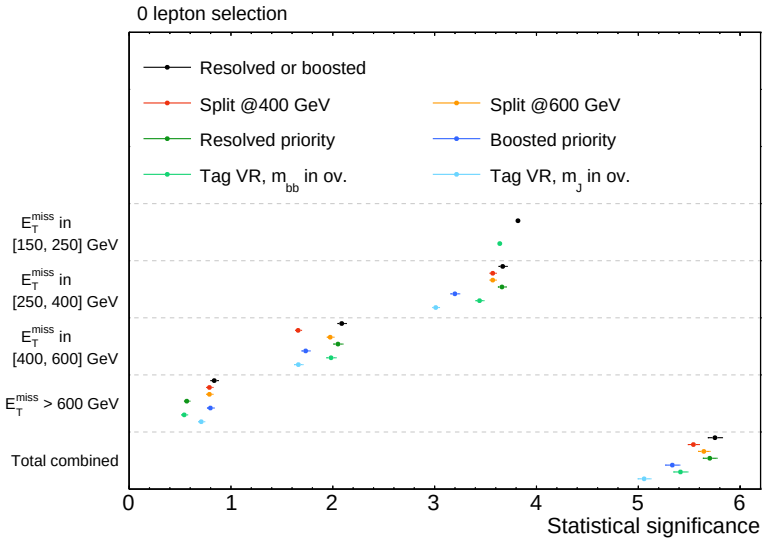
As expected, Figure 5.21 shows that the largest significance is achieved by the logical *or* of the resolved and boosted selections, also referred to as *ideal* strategy. By considering the resolved analysis selection in the $400 < E_{\text{T}}^{\text{miss}} < 600\,\text{GeV}$ regime, an improvement over the boosted analysis of $\sim 19\%$ can be achieved, which corresponds to a gain of more than 40% in terms of equivalent luminosity. However, considering only the highest $E_{\text{T}}^{\text{miss}}$ bin for the boosted analysis, the 'Split @600 GeV' might be sub-optimal, since the available statistics to constrain large JMR uncertainties might be insufficient. The impact of such systematic uncertainty could be reduced in an MVA analysis, thus the strategy might be viable.

The closest result to the significance achieved in the *ideal* case is provided by the resolved-priority strategy. An overall improvement of 3% and 23% over the *split* strategy can be obtained in the $[250, 400]\,\text{GeV}$ and $[400, 600]\,\text{GeV}$ $E_{\text{T}}^{\text{miss}}$ bins, respectively. In the highest $E_{\text{T}}^{\text{miss}}$ bin a drop in significance is observed because the categorisation becomes sub-optimal. In fact, events are split between the m_{bb} and m_J distributions with a slightly higher percentage to the boosted regions, and the acceptance is such that only few bins can be used in both distributions. However, as it can be seen from Figure 5.21(a), the highest $E_{\text{T}}^{\text{miss}}$ bin contributes in a sub-dominant way to the overall inclusive significance.

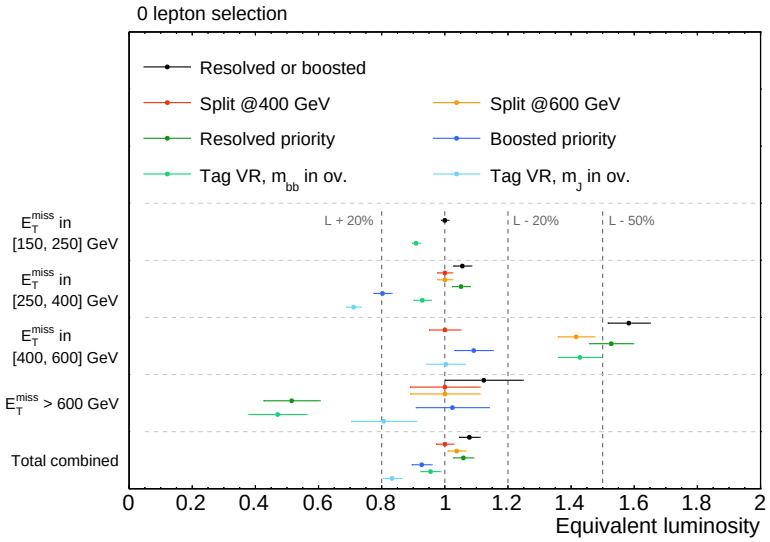
The boosted-priority strategy in general leads to a significant loss in performance, and overall a decrease of 5% in significance is observed. This is mainly due to the $[250, 400]\,\text{GeV}$ $E_{\text{T}}^{\text{miss}}$ bin (-10%), and can be due to three effects: sub-optimal categorisation of the events in the boosted analysis with respect to the resolved one, worse resolution on the Higgs peak and different background composition. The latter two effects are investigated later in this Section.

The performance of the *TagVR* strategy is also shown. In general a reduced significance with respect to the priority strategy is observed. The main reason for this is due to a different background composition and total background shape in the considered regions, especially at low $E_{\text{T}}^{\text{miss}}$. A comparison of the lowest $E_{\text{T}}^{\text{miss}}$ bin resolved region, obtained when flavour tagging is applied to PFlow or to VR track-jets, is presented in Figure 5.22.

A 4.5% lower significance with respect to the former is observed in the latter case. This is due to the fact that both the signal and background events efficiencies are slightly lower in the *TagVR* strategy, thus a reduction in sensitivity is expected. As can be better observed in Figure 5.21(b), the gap between the *TagVR* and the priority strategies is smaller at higher $E_{\text{T}}^{\text{miss}}$ values. This is thanks to the fact that with the shrinking cone, the VR track-jets can better catch the flight direction of the b-hadrons, thus slightly improving the tagging efficiency at higher p_{T}.



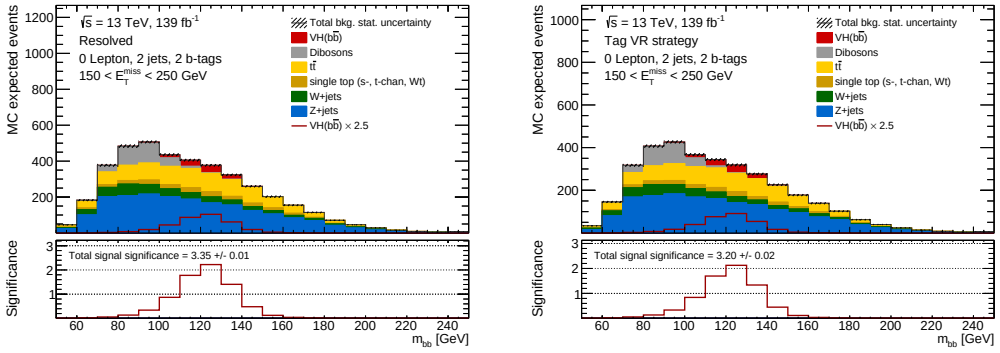
(a)



(b)

Figure 5.21. Comparison of the investigated strategies in terms of (a) the statistical significance and (b) the equivalent integrated luminosity. In the latter plot, $L-20\%$ and $L-50\%$ mark the values of the x-axis corresponding to a reduced integrated luminosity of 20% and 50%, respectively, while $L+20\%$ refers to an increased data statistics of 20% with respect to the one collected by the ATLAS experiment during Run 2 of the LHC.

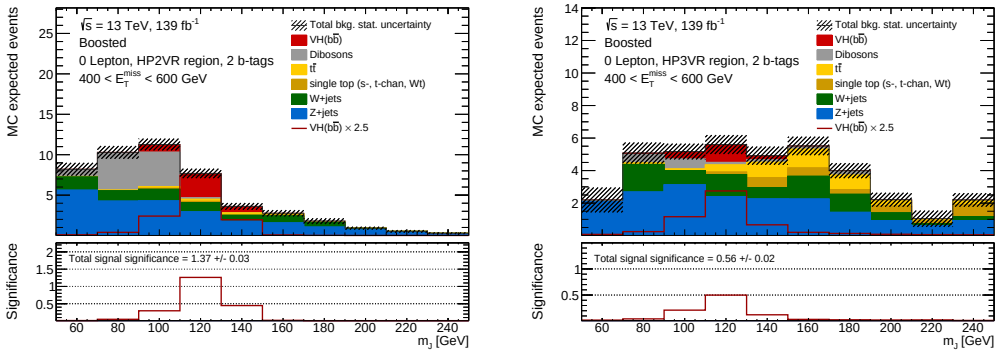
To better understand the differences observed between the resolved and boosted analysis in the overlap region, mainly in the $[400, 600]$ GeV range, two effects are investigated. The first one consists in testing a different event categorization for the boosted analysis, to see if the significance can be improved. An additional split of the HP SR is tested. Events are further categorized based on the number of VR



(a) (b)

Figure 5.22. Di-jet invariant mass distribution for the case in which flavour tagging is applied to the (a) PFlow jets and (b) to VR track-jets.

track-jets matched to the large-R jet. Higgs boson decays into $b\bar{b}$ pairs will more likely be observed in events with only two VR track-jets, while background processes such as $t\bar{t}$ are characterized by a larger jet multiplicity within the large-R jet. The effect of splitting the HP region in the $[400, 600]$ GeV $E_{\mathrm{T}}^{\mathrm{miss}}$ bin is presented in Figure 5.23.

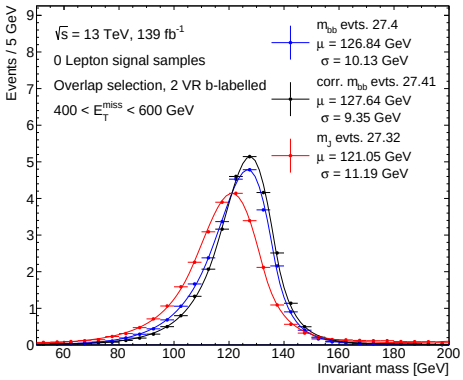


(a) (b)

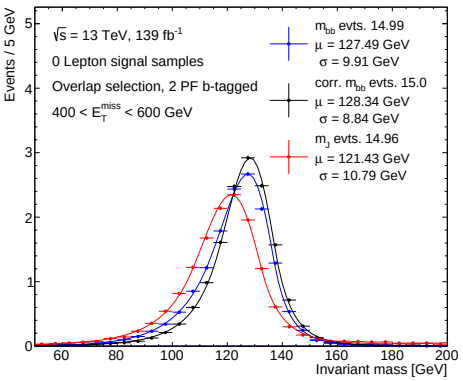
Figure 5.23. Large-R jet mass distribution of the improved HP region categorization for events with (a) two and (b) three VR track-jets matched, and defined HP2VR and HP3VR, respectively.

An improvement of around 8% is observed with respect to the HP region presented in Figure 5.17 for the same $E_{\mathrm{T}}^{\mathrm{miss}}$ range. In an MVA approach of the analysis the same improvement can be achieved by including in the input variables the number of VR track-jets matched to the large-R jet. Thus, it can be concluded that the categorization of the events accounts roughly for half of the difference of the statistical significance between the resolved and boosted analysis in the $400 < E_{\mathrm{T}}^{\mathrm{miss}} < 600\,\mathrm{GeV}$ bin.

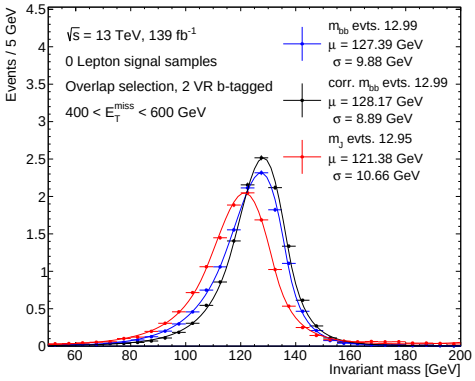
The signal mass resolution also plays a role in the sensitivity estimate. A comparison between the large-R jet and PFlow jets invariant mass distributions is done in the *overlap* region, i.e. when at least two PFlow jets are matched to two VR track-jets and located within the large-R jet and b-tagged. The comparison is done prior to the categorisation of the events in signal and control regions. Results are presented in Figure 5.24 for the $[400, 600]$ GeV $E_{\mathrm{T}}^{\mathrm{miss}}$ bin when either truth labelling or flavour tagging to PFlow or VR track-jets are applied. In the plots, a comparison between the PFlow jets invariant mass distributions obtained before and after applying the corrections outlined in Section 5.2.2 is also presented. The large-R jet is corrected for the possible presence of muons from b-hadrons semi-leptonic decays. The inclusion of such corrections, as already mentioned, helps in improving the resolution of the peak.



(a) Applying b-labelling



(b) Applying b-tag to PFlow jets



(c) Applying b-tag to VR track-jets

Figure 5.24. Higgs candidate mass distribution comparison between PFlow jets and large-R jets in the overlap region between the resolved and boosted $VH(\to b\bar{b})$ analyses, in the 0L channel. The integral of the distributions, reported in the legend, is the same modulo negligible effects due to under-flow or over-flow events. The comparison is performed either requiring the two matched jets to be b-labelled (a), or the two PFlow jets (b) or VR track-jets (c) to be b-tagged.

The difference in the integral of the distributions of the three plots is due to different efficiencies of the b-labelling and b-tagging procedures adopted.

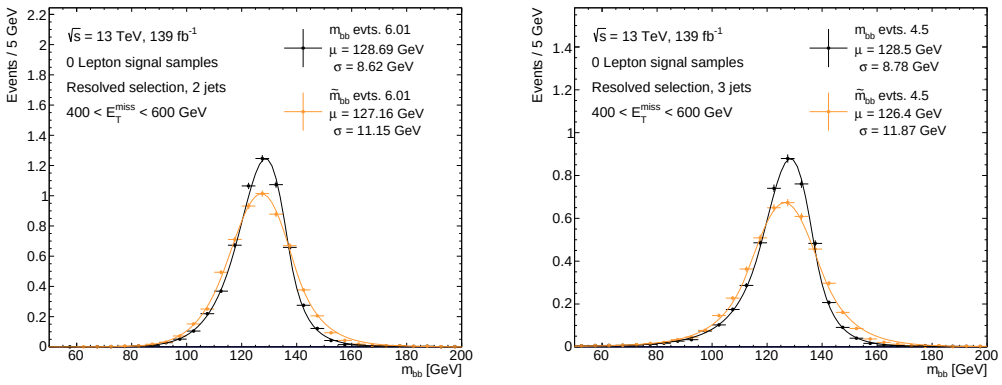
A sharper peak is observed for Higgs boson candidates reconstructed using PFlow jets. To give a quantitative estimate of the effect, a fit with the Bukin function [222], suitable for the fit of asymmetric peaks, is performed. The probability density function is given by the convolution of a gaussian and an exponential function as

$$F_{\mathrm{B1}}(x, x_g, \sigma_g, \lambda) = \frac{1}{2|\lambda|}\left[1 - \mathrm{erf}\left(-\frac{(x-x_p)\lambda}{\sigma_g|\lambda|\sqrt{2}} + \frac{\sigma_g}{|\lambda|\sqrt{2}}\right)\right] \exp\left(-\frac{x-x_g}{\lambda} + \frac{\sigma_g}{2\lambda^2}\right), \tag{5.10}$$

where x_g determines the position of the peak, σ_g is the standard deviation of the gaussian function, λ is the asymmetry parameter, and

$$\mathrm{erf}(x) = \frac{2}{\sqrt{\pi}}\int_0^x e^{-\xi^2} d\xi. \tag{5.11}$$

A difference of around 20% is observed between the two mass distributions in this $E_{\mathrm{T}}^{\mathrm{miss}}$ range. The effect is consistent among all the three tagging methods. The impact of a worse resolution on the mass of the reconstructed Higgs boson candidate is tested on the resolved analysis regions. A smearing of the resolution of $20 \div 25\%$ is performed as presented in Figure 5.25.



(a) (b)

Figure 5.25. Effect of the smearing introduced on the resolution of the di-jet invariant mass distribution to test its impact on the significance.

The new signal distribution is used to evaluate the statistical significance in the two and three jet event categories for the $[400, 600]$ GeV $E_{\mathrm{T}}^{\mathrm{miss}}$ bins. A reduced significance of about 10% is observed in both categories, which corresponds to a result obtained with an equivalent $\sim 20\%$ less integrated luminosity. Thus, it can be concluded that in this $E_{\mathrm{T}}^{\mathrm{miss}}$ range the difference in the resolution of the reconstructed Higgs boson candidate mass accounts for about half of the difference in

significance between the boosted and resolved analysis. Combined with the impact of a different categorization of the events, these two effects are able to explain most of the difference between the two analyses. However, some of the differences will be reduced when an optimised MVA strategy will be in place for both topologies.

5.4 A first fiducial cross-section measurement

The measurement of fiducial cross-sections allows to investigate the properties of the Higgs boson in a complementary way to the STXS framework. The aim of such a measurement is to be as model independent as possible, such that results can be sensitive to the presence of new BSM phenomena, and compared to state-of-the-art predictions of the SM. Fiducial cross-section measurements also have the advantage that they provide a particle-level result. Therefore, they do not depend on a particular configuration of the ATLAS detector and can be directly compared with theoretical calculations without having to process the events through the entire simulation and reconstruction chain.

Differential cross-section measurements in the Higgs sector have been already performed by both the ATLAS and CMS collaborations in four-lepton [223, 224] and di-photon final states [225, 226]. Recently, CMS published results in di-tau final states [227].

In this Section, a first fiducial cross-section measurement performed in $b\bar{b}+E_{\mathrm{T}}^{\mathrm{miss}}$ final states is presented. Results have been obtained via a re-definition of the fit model of the published resolved $VH(\to b\bar{b})$ analysis [42]. An in-likelihood unfolding, as discussed in Section 5.4.3, is performed. To reduce the model-dependency of the measurement, the fiducial cross-section is extracted via a fit to the invariant mass distribution of two b-tagged hadronic jets, m_{bb}.

The published resolved $VH(b\bar{b})$ analysis will be referred to as the *detector-level analysis* in the following. The definition of the particle-level objects and of the fiducial phase-space is presented in the next Section.

5.4.1 Particle-level definitions

Particle-level objects and selections have been chosen to be as close as possible to the ones adopted in the detector-level analysis. This allows model-dependent corrections to be minimized when comparing with detector-level objects such as jets. It also reduces extrapolations of the cross-section measurement into phase-spaces that are not explored at the detector-level.

Object definitions

Only collider-stable final-state particles are used in the definition of the fiducial phase-space. These are characterized by a mean life-time $c\tau_0 > 10\,\mathrm{mm}$.

Leptons. Electrons and muons are defined as *prompt* if they are not produced in hadron decays. To account for the possible emission of QED radiation by such particles, the four-momentum of photons located within $\Delta R < 0.1$ of leptons is added to that of leptons, so that *dressed-leptons* are considered.

In the definition of the fiducial phase-space, electrons are considered if they have $p_{\mathrm{T}} > 7\,\mathrm{GeV}$ and $|\eta| < 2.47$. Similarly, muons are also considered if they have $p_{\mathrm{T}} > 7\,\mathrm{GeV}$ and $|\eta| < 2.7$. The chosen thresholds for transverse momenta mimic the ones used in the definition of 0-lepton channel events in the detector-level analysis. No isolation requirements are imposed at particle-level, but overlap removal with jets is performed, as described later in this Section.

τ-leptons are not collider-stable particles and decay either in leptons or hadrons, plus a neutrino. In the former case, electrons and muons from the decay are stable particles which do not originate in hadron decays, thus are used as the prompt ones in the fiducial phase-space definition. The particles produced in hadronic decays of τ-leptons are instead clustered as particle-level jets. As discussed later in this Section, an overlap removal procedure between jets and $\tau_{\mathrm{had.}}$ is applied.

Jets. Particle-level jets are formed using the anti-k_t algorithm with radius parameter $R = 0.4$. Prompt leptons, photons and neutrinos not originating from hadronic decays are excluded from the particles used to form jets. These objects are referred to also as *Truth WZ* jets. To define the flavour of the jet, the labelling procedure described in Section 3.3.2 is used.

Overlap removal between jets and leptons, which are not considered to be constituents of the jets themselves, is performed at the particle-level to mimic what happens at the detector-level. Prompt leptons found within $\Delta R < 0.4$ of a particle-level jet are removed. In addition, jets that are labelled as originated from a hadronically decaying τ-lepton are not included in the ensemble of particle-level jets.

In a similar way to what is done in the resolved $VH(\to b\bar{b})$ analysis, jets are categorized based on their p_{T} and $|\eta|$ as signal- or forward-jets. Particle-level signal jets are required to be within $|\eta| < 2.5$ and to have at least $p_{\mathrm{T}} > 20\,\mathrm{GeV}$. Particle-level forward jets are characterized by $2.5 < |\eta| < 4.5$ and $p_{\mathrm{T}} > 30\,\mathrm{GeV}$.

Missing transverse momentum. At particle-level, the $\vec{E}_{\mathrm{T}}^{\mathrm{miss}}$ is defined as the negative vectorial sum of the p_{T} of all stable and interacting particles produced in the events up to $|\eta| < 5$. This definition emulates the calorimetric measurement of $E_{\mathrm{T}}^{\mathrm{miss}}$. Muons are included in the calculation of the $\vec{E}_{\mathrm{T}}^{\mathrm{miss}}$only if they have $p_{\mathrm{T}} > 6\,\mathrm{GeV}$, as they leave a non-negligible amount of $E_{\mathrm{T}}^{\mathrm{miss}}$ in the calorimeters.

5.4.2 Fiducial phase-space definition

The fiducial phase-space of the measurement is defined by a series of particle-level cuts on the previously defined objects. The event selection of the detector-level analysis is mimicked as much as possible, such that any extrapolation in the cross-section measurement is reduced.

In this study, $b\bar{b} + E_{\mathrm{T}}^{\mathrm{miss}}$ final states are targeted, thus the presence of exactly 0 leptons is required. Events are required to have at least 150 GeV of $E_{\mathrm{T}}^{\mathrm{miss}}$. At least two signal jets are required in the events, and at most the presence of one extra signal- or forward-jet is allowed. Moreover, exactly two of the identified signal jets are required to be b-labelled; the leading one needs to have $p_{\mathrm{T}} > 45\,\mathrm{GeV}$. As done at detector-level, the scalar sum of the transverse momenta of the jets is required to be at least 120 GeV (150 GeV) for two- (three-) jet events.

Anti-QCD cuts are applied at detector-level to reduce the amount of $E_{\mathrm{T}}^{\mathrm{miss}}$ produced by mis-measurements of jets, and therefore the multijet background. Similar cuts are used in the definition of the fiducial phase-space. In two- (three-) jet events the minimum angular distance between the particle-level $\vec{E}_{\mathrm{T}}^{\mathrm{miss}}$ and any jet is required to be at least 20° (30°). Moreover, defining $\vec{b}_1$ and $\vec{b}_2$ the transverse momentum of the two b-labelled jets in the event, $\Delta\phi\left(\vec{b}_1, \vec{b}_2\right) < 140°$ and $\Delta\phi\left(\vec{E}_{\mathrm{T}}^{\mathrm{miss}}, \vec{b}_1 + \vec{b}_2\right) > 120°$ are required.

In the resolved $VH(\to b\bar{b})$ analysis, signal and control regions are defined by a differential cut on the ΔR between the two candidate b-jets as a function of the missing transverse momentum in the events. Such a requirement is not applied in the definition of the fiducial phase-space because it is only adopted in the detector-level analysis to define the signal and control regions.

A comparison between the detector- and particle-level objects definitions and event selection is presented in Table 5.5.

Table 5.5. Comparison between the detector-level and particle-level objects definitions and event selection.

Selection	Detector-level	Particle-level
Leptons	No electrons or muons $p_{\mathrm{T}} > 7\,\mathrm{GeV}$ Electrons: $\lvert\eta\rvert < 2.47$, Loose&Blayer ID, $\lvert d_0/\sigma_{d_0}\rvert < 5$, $\lvert z_0 \sin\theta\rvert < 0.5\,\mathrm{mm}$ Muons: $\lvert\eta\rvert < 2.7$, Loose ID, $\lvert d_0/\sigma_{d_0}\rvert < 3$, $\lvert z_0 \sin\theta\rvert < 0.5\,\mathrm{mm}$ FC loose isolation	No electrons or muons $p_{\mathrm{T}} > 7\,\mathrm{GeV}$ Electrons: $\lvert\eta\rvert < 2.47$ Muons: $\lvert\eta\rvert < 2.7$ $\Delta R(e/\mu, j) > 0.4$
Hadronic τ	$p_{\mathrm{T}} > 20\,\mathrm{GeV}$ $\lvert\eta\rvert < 1.37$ or $\lvert\eta\rvert > 1.52$ Medium ID WP	τ-labelled jets
Anti-k_t R = 0.4 Jets	EMTopo jets ≥ 2 *Signal* jets *Signal*: $p_{\mathrm{T}} > 20\,\mathrm{GeV}$, $\lvert\eta\rvert < 2.5$ *Forward*: $p_{\mathrm{T}} > 30\,\mathrm{GeV}$, $2.5 < \lvert\eta\rvert < 4.5$	TruthWZ jets ≥ 2 *Signal* jets *Signal*: $p_{\mathrm{T}} > 20\,\mathrm{GeV}$, $\lvert\eta\rvert < 2.5$ *Forward*: $p_{\mathrm{T}} > 30\,\mathrm{GeV}$, $2.5 < \lvert\eta\rvert < 4.5$
b-jets	2 b-tagged *Signal* jets, MV2c10 70% ε WP leading b-tagged jet $p_{\mathrm{T}} > 45\,\mathrm{GeV}$	2 b-labelled *Signal* jets leading b-labelled jet $p_{\mathrm{T}} > 45\,\mathrm{GeV}$
Jet categories	Exactly 2 / exactly 3 jets	2 or 3 jets
$E_{\mathrm{T}}^{\mathrm{miss}}$	$> 150\,\mathrm{GeV}$	Negative vectorial sum of p_{T} of all stable interacting particles within $\lvert\eta\rvert < 5$, including muons with $p_{\mathrm{T}} > 6\,\mathrm{GeV}$ $> 150\,\mathrm{GeV}$
H_{T}	$> 120\,\mathrm{GeV}$ (2 jets), $> 150\,\mathrm{GeV}$ (3 jets)	$> 120\,\mathrm{GeV}$ (2 jets), $> 150\,\mathrm{GeV}$ (3 jets)
$\min \Delta\phi(\vec{E}_{\mathrm{T}}^{\mathrm{miss}}, \vec{j})$	$> 20°$ (2 jets), $> 30°$ (3 jets)	$> 20°$ (2 jets), $> 30°$ (3 jets)
$\Delta\phi(\vec{E}_{\mathrm{T}}^{\mathrm{miss}}, \vec{bb})$	$> 120°$	$> 120°$
$\Delta\phi(\vec{b}_1, \vec{b}_2)$	$< 140°$	$< 140°$
$\Delta\phi(\vec{E}_{\mathrm{T}}^{\mathrm{miss}}, \vec{p}_{\mathrm{T}}^{\mathrm{miss}})$	$< 90°$	–
$E_{\mathrm{T}}^{\mathrm{miss}}$ regions	$150 \leq E_{\mathrm{T}}^{\mathrm{miss}} < 250\,\mathrm{GeV}$ $E_{\mathrm{T}}^{\mathrm{miss}} \geq 250\,\mathrm{GeV}$	$150 \leq E_{\mathrm{T}}^{\mathrm{miss}} < 250\,\mathrm{GeV}$ $E_{\mathrm{T}}^{\mathrm{miss}} \geq 250\,\mathrm{GeV}$

To study the fiducial phase-space definition, the SM VH MC samples introduced in Section 5.2.1 are used. These include all the signal processes of the 0L channel of the reconstruction-level analysis.

Defining $N_{\mathrm{R\&T}}$ the number of events passing simultaneously both the detector- and particle-level selections, and N_{T} the number of the events in the fiducial phase-space, i.e. which pass the particle-level selection independently of the detector-level

one, the reconstruction efficiency is defined as

$$\varepsilon = \frac{N_{\mathrm{R\&T}}}{N_{\mathrm{T}}}. \tag{5.12}$$

The binned efficiency is shown in Figure 5.26 as a function of the particle-level $E_{\mathrm{T}}^{\mathrm{miss}}$. The *turn-on* effect observed around 150 GeV is due to the trigger and detector-level requirements on the $E_{\mathrm{T}}^{\mathrm{miss}}$, which is required to be at least 150 GeV. However, it is not possible to reduce the detector-level requirement due to the limitations imposed by the $E_{\mathrm{T}}^{\mathrm{miss}}$ trigger adopted to collect the data. Indeed, the trigger $E_{\mathrm{T}}^{\mathrm{miss}}$ threshold has been raised up to 120 GeV during the data taking to cope with the large instantaneous luminosity delivered by the LHC.

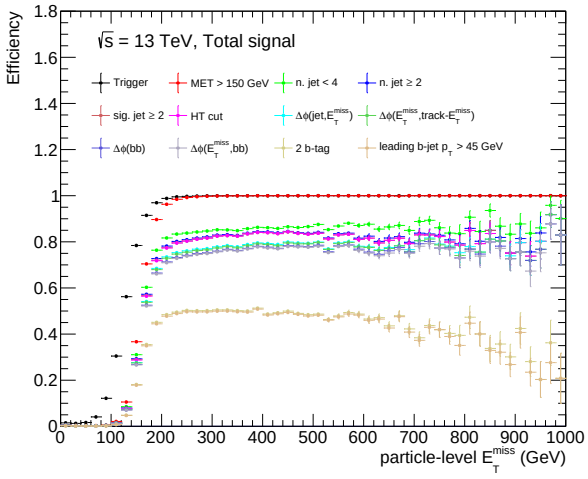


Figure 5.26. Reconstruction efficiency as a function of the particle-level $E_{\mathrm{T}}^{\mathrm{miss}}$ after applying each detector-level selection, evaluated on the total MC simulated signal sample adopted for the extraction of the cross-section.

Above 200 GeV of particle-level $E_{\mathrm{T}}^{\mathrm{miss}}$ the efficiency becomes roughly constant, and it is $\sim 50\%$. Such a value is mainly due to the requirement of exactly two b-tagged jets in the events applied at detector-level. The flavour-tagging procedure in fact is performed adopting a working point which provides an average tagging-efficiency of 70%, as described in Section 5.3.1.

Defining N_{R} the number of reconstructed events independently of the fact that they satisfy the particle-level requirements, $N_{\mathrm{R}} = N_{\mathrm{R\&T}} + N_{\mathrm{R\&!T}}$, the purity of the fiducial phase-space definition is given by

$$\mathcal{P} = \frac{N_{\mathrm{R\&T}}}{N_{\mathrm{R}}}. \tag{5.13}$$

This quantity determines how many reconstructed events belong to the fiducial phase-space we aim to measure. It is possible in fact that resolution effects on the measurement of physics objects, such as jets, leptons and the $\vec{E}_{\mathrm{T}}^{\mathrm{miss}}$, lead to a migration of the events from outside to inside the fiducial phase-space. Mismeasured jets, or leptons not reconstructed due to the presence of passive material in the

ATLAS detector, might lead to detector-level events which mimic the signal we want to measure. One example is given by events with leptons, such as the WH process, which are characterized by genuine $E_{\mathrm{T}}^{\mathrm{miss}}$ due to the presence of a neutrino. If the lepton from the W decay is not reconstructed, then it is possible that such process passes the selection at detector-level, and thus is included in the signal template we want to fit.

In figure 5.27 the invariant mass distribution of the Higgs-boson candidate is shown after requiring either both the detector- and particle-level selections simultaneously, or after requiring the detector-level selection without any conditions on its particle-level equivalent one. Events are categorized in the fit following the SRs and CRs of the 0L channel of the reconstructed-level analysis, thus in two $E_{\mathrm{T}}^{\mathrm{miss}}$ ranges and in the two- and three-jet categories. The ratio of the two distributions shown in each plot, presented in the bottom pad, is the definition of the purity.

In general, a larger purity is observed for the two-jet category with respect to the three jet one, and a ratio closer to 1 is observed in the $E_{\mathrm{T}}^{\mathrm{miss}} \geq 250\,\mathrm{GeV}$ bin. The loss observed in the lower $E_{\mathrm{T}}^{\mathrm{miss}}$ bin is due to the particle-level $E_{\mathrm{T}}^{\mathrm{miss}}$ selection, and to resolution effects which affect the detector-level quantity. In the higher detector-level $E_{\mathrm{T}}^{\mathrm{miss}}$ bin instead a purity higher than 90% is observed. The same effects are present in the three jet category.

To further study the out-of-fiducial events, i.e. reconstructed but not in the fiducial phase-space, which induce the loss in purity, the two main components of the detector-level total signal sample, namely the $qq \to Z(\nu\bar{\nu})H(b\bar{b})$ and $qq \to W(\ell\nu)H(b\bar{b})$ processes, are studied independently. The invariant mass distribution of the Higgs boson candidate after requiring the particle- and detector-level event selections simultaneously and requiring only the detector-level one are shown for the detector-level SRs categories in Figure 5.28 for both processes.

The $qq \to Z(\nu\bar{\nu})H(b\bar{b})$ matches the final state we are aiming to measure, namely the production of two b-jets in association with large missing transverse momentum. The purity for the lowest $E_{\mathrm{T}}^{\mathrm{miss}}$ detector-level bin is between 85% and 90% in roughly all m_{bb} bins in the two-jet category, while it is around 80% for the three-jet category.

In these two regions out-of-fiducial events arise from resolution effects in the measurement of the missing transverse momentum. The particle-level requirement of $E_{\mathrm{T}}^{\mathrm{miss}} > 150\,\mathrm{GeV}$ indeed is the one which is not fulfilled most of the times when applying the fiducial selection. Such effect is significantly reduced in the detector-level categories defined for $E_{\mathrm{T}}^{\mathrm{miss}} \geq 250\,\mathrm{GeV}$ as it can be seen in Figures 5.28(c) and 5.28(d). In particular, the purity of the two-jet category is above 95%, while in three-jet case it is around 90%. Out-of-fiducial events in this case arise from resolution effects in the measurements of jets and of missing transverse momentum. In fact, the selection requirement failed by these events is the one on the angular distance between jets and the $\vec{E}_{\mathrm{T}}^{\mathrm{miss}}$.

As shown in Figure 5.28 (e-h), the loss in purity of the total signal is mainly caused by the WH signal events, which roughly constitute 20% of the total detector-level signal. For the low $E_{\mathrm{T}}^{\mathrm{miss}}$ regions two effects lead to out-of-fiducial events: the already discussed requirement on the particle-level $E_{\mathrm{T}}^{\mathrm{miss}}$, and the presence of electrons and muons in the events. This might be either prompt from the W decay, or from the leptonic decay of τ-leptons. Reconstruction inefficiencies in particular regions of the ATLAS detector, or resolution effects at the boundaries of the fiducial

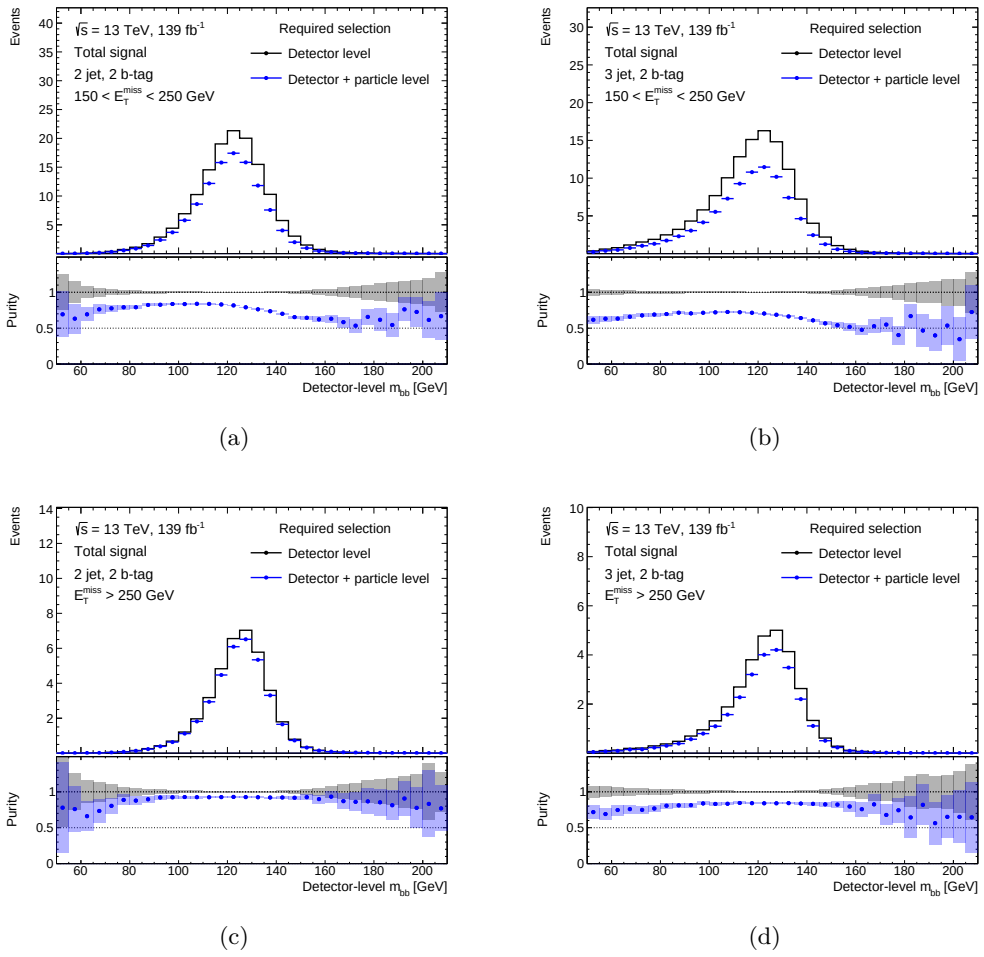


Figure 5.27. Invariant mass distribution of the Higgs boson candidate for the events simultaneously satisfying the detector- and particle-level selections and for the events passing the detector-level selection, without any requirement on the particle-level one. The four 0L channel SRs are presented, (a-b) show for the $150\,\text{GeV} \leq E_{\text{T}}^{\text{miss}} < 250\,\text{GeV}$ interval the 2 jet and 3 jet categories, respectively, while (c-d) show the $E_{\text{T}}^{\text{miss}} \geq 250\,\text{GeV}$ categories. The bottom pad of the plots shows the ratio between the two aforementioned distributions, which is the definition of the purity. The error band represents the relative MC statistical uncertainty.

phase-space, lead to out-of-fiducial events in which a particle-level electron or muon within the acceptance is not correctly identified. Hadronically-decaying τ-leptons are instead reconstructed as jets, which are τ-labelled and therefore do not enter in the particle-level jet collection.

In the larger detector-level $E_{\text{T}}^{\text{miss}}$ category, roughly $70 \div 75\%$ of the reconstructed events are also in the fiducial phase-space. Also in this case, the main component of out-of-fiducial events arises from the presence of leptons which are either not reconstructed at detector-level, or fall out of the acceptance. Minor effects are related to the resolution in the measurement of jets and $E_{\text{T}}^{\text{miss}}$, as for the $Z(\nu\bar{\nu})H(b\bar{b})$ process.

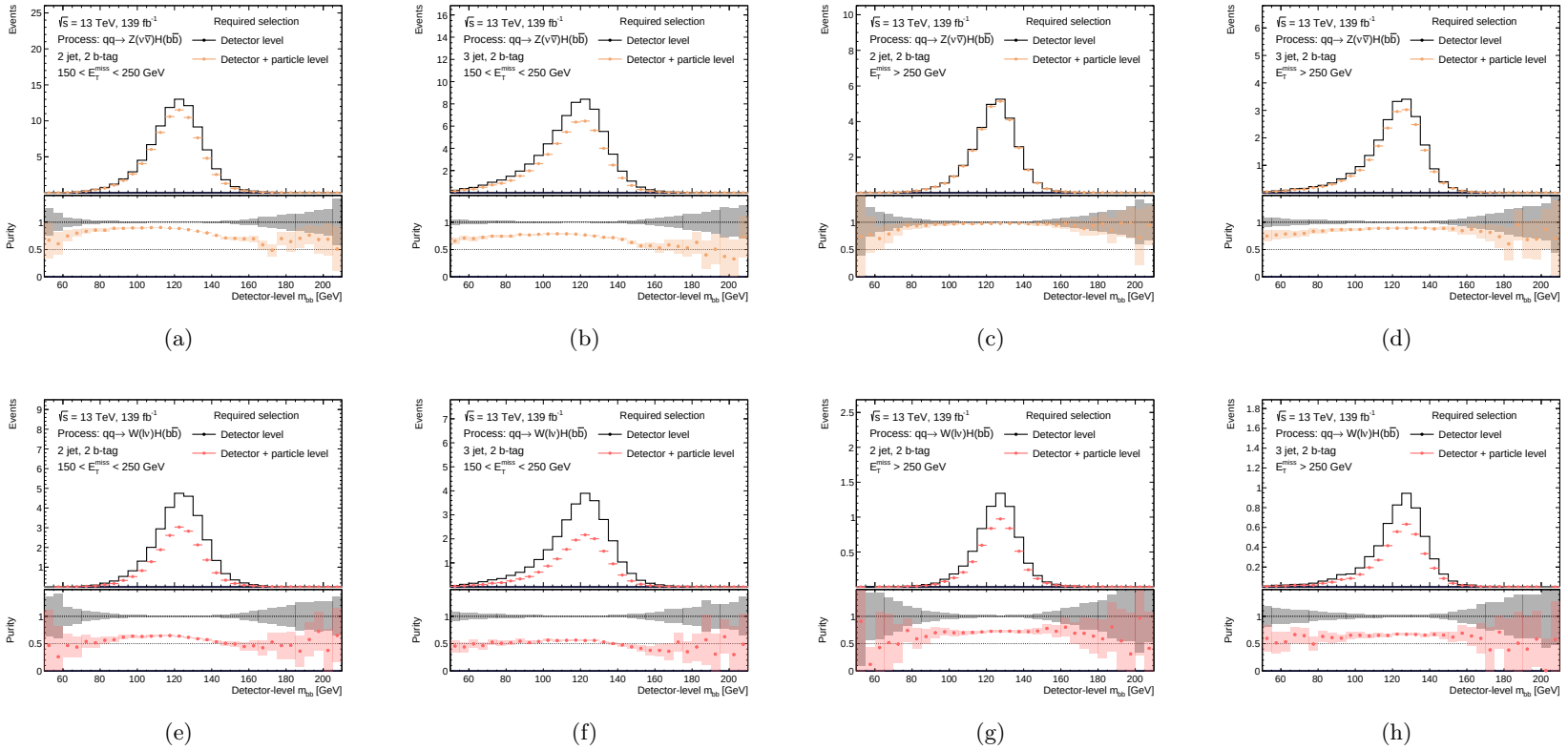


Figure 5.28. Invariant mass distribution of the Higgs boson candidate for $qq \to Z(\nu\bar{\nu})H(b\bar{b})$ (a-d) and $qq \to W(\ell\nu)H(b\bar{b})$ (e-h) simulated events in the four detector-level categories corresponding to the SR of the 0L channel defined in the resolved $VH(b\bar{b})$ analysis. In the bottom pad the ratio $N_{\mathrm{R\&T}}/N_{\mathrm{R}}$, which corresponds to the definition of purity, is shown. The error band represents the relative MC statistical uncertainty.

In order to reduce the number of out-of-fiducial events, the possibility to lower the particle-level $E_{\mathrm{T}}^{\mathrm{miss}}$ selection was investigated. It is important however to remark that such a modification would change the fiducial phase-space of the provided measurement.

While on the one hand the extension of the fiducial phase-space helps by construction in a reduction of out-of-fiducial events, on the other hand such a reduction introduces features in the measurement. In particular, as already shown in Figure 5.26, the reconstruction efficiency significantly drops for particle-level $E_{\mathrm{T}}^{\mathrm{miss}}$ below 150 GeV. This implies that only a tiny fraction of the real events are measured, thus a large extrapolation would be performed when providing the fiducial cross-section measurement. Moreover, in this case the effect of modelling uncertainties on the choice of the templates used to perform the measurement might wash-out the gain of a reduced number of out-of-fiducial events.

To quantify the gain in purity, and consequent reduction in reconstruction efficiency, the two quantities can be monitored simultaneously varying the particle-level $E_{\mathrm{T}}^{\mathrm{miss}}$ threshold. In Figure 5.29, the receiver operating characteristic (ROC) curve of the integrated purity and efficiency is presented.

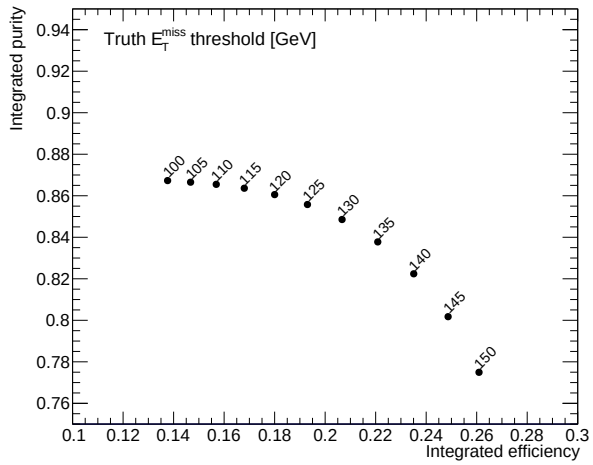


Figure 5.29. ROC curve obtained varying the particle-level $E_{\mathrm{T}}^{\mathrm{miss}}$ requirement in the definition of the fiducial phase-space. On the horizontal (vertical) axis, the integrated efficiency (purity) is shown. The $E_{\mathrm{T}}^{\mathrm{miss}}$ threshold is reported close to each point.

Both quantities are evaluated here in an inclusive way by considering all the detector-level categories, thus the curve is expected to be dominated by the lower detector-level $E_{\mathrm{T}}^{\mathrm{miss}}$ bin. However, no effect is expected on the purity of the $E_{\mathrm{T}}^{\mathrm{miss}} \geq 250$ GeV category by a variation of the particle-level $E_{\mathrm{T}}^{\mathrm{miss}}$ threshold. In Figure 5.30 (a,b) a comparison of the m_{bb} distributions obtained for the total signal in the two- and three-jet detector-level categories is presented for different values of the threshold. A minor dependence on m_{bb} is observed. Larger effects can be seen in the $\Delta R(b,b)$ distributions, where a larger gain is observed at high values. This is expected by the fact that the $E_{\mathrm{T}}^{\mathrm{miss}}$ and $\Delta R(b,b)$ variables are correlated in Higgs boson decays as $\Delta R(b,b) \sim 2m_H/p_{\mathrm{T}}(H) \sim 2m_H/E_{\mathrm{T}}^{\mathrm{miss}}$.

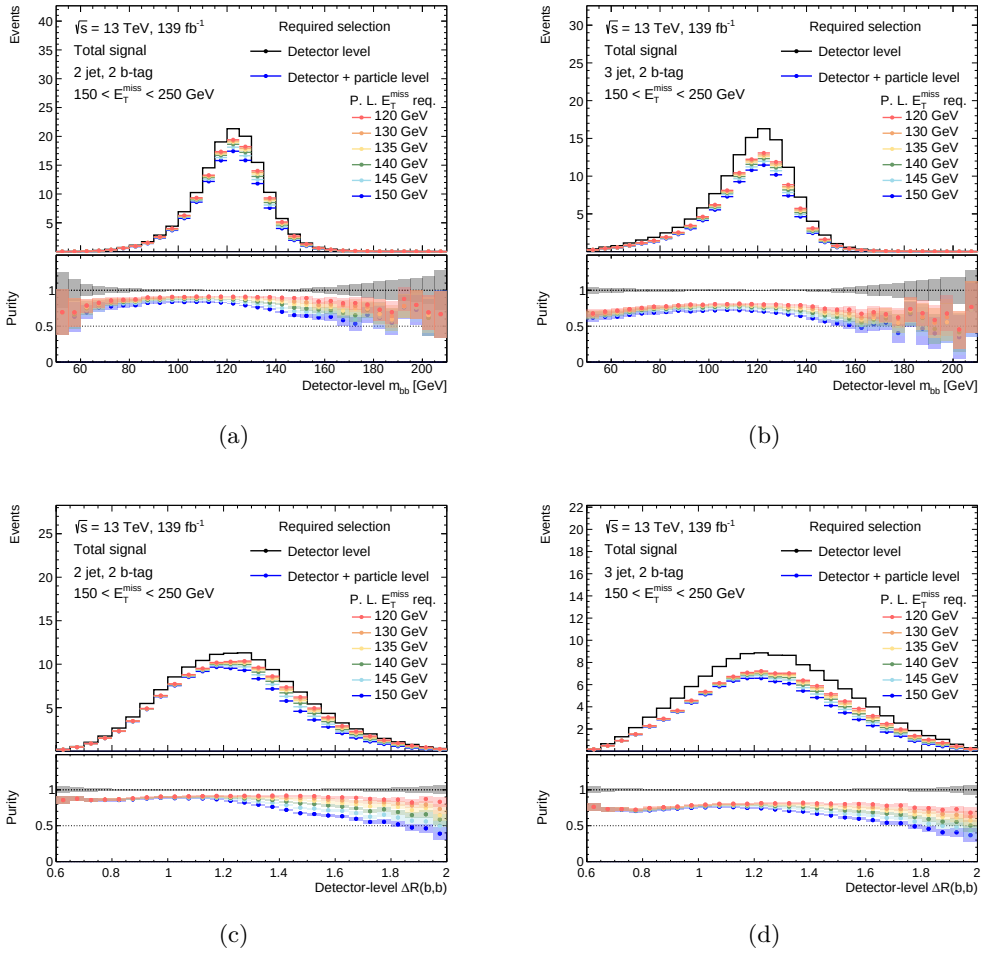


Figure 5.30. (a,b) Invariant mass distribution of the Higgs boson candidate and (c,d) ΔR distribution of the two b-jets for the events simultaneously satisfying the detector- and particle-level selections varying the particle-level $E_{\mathrm{T}}^{\mathrm{miss}}$ requirement (P. L. $E_{\mathrm{T}}^{\mathrm{miss}}$ req.), and for the events passing the detector-level selection. The ratio between the former and latter distributions is presented in the bottom pad, and corresponds to the definition of the purity. The uncertainty band shows the relative statistical uncertainty.

To reduce the effect of the efficiency turn-on presented in Figure 5.26 however it was chosen to keep the particle-level $E_{\mathrm{T}}^{\mathrm{miss}}$ threshold at 150 GeV. Out-of-fiducial events are considered in the fit model adopted to extract the cross-section values, and a comparison of the detector-level templates is presented in the next Section.

5.4.3 Fit model and unfolding strategy

The cross-section extraction is performed via a one-step method also referred to as in-likelihood unfolding. Signal-templates of each detector-level category adopted in the fit can be in fact re-parameterized as the sum of multiple templates defined by particle-level selections.

Events with a particle-level $E_{\mathrm{T}}^{\mathrm{miss}}$ lower than 150 GeV are referred to as *out-of-*

fiducial-off events, and labelled O^{Off}. Furthermore, events are split in a component with a particle-level $E_{\text{T}}^{\text{miss}} < 250\,\text{GeV}$ and one with $E_{\text{T}}^{\text{miss}} \geq 250\,\text{GeV}$. These are the bins in which we want to measure the differential cross-section. However, as already mentioned, some of the reconstructed events might be out of the fiducial phase-space. Therefore the events are split in a *in-fiducial*, N^{T_j}, and an *out-of-fiducial* component, O^{T_j}, where $j = 1$ corresponds to the particle-level $E_{\text{T}}^{\text{miss}}$ interval $[150, 250)\,\text{GeV}$, and $j = 2$ to the $[250+)\,\text{GeV}$ one.

The expected number of signal events in a detector-level category, N_{R_i}, is therefore given by

$$N_{\text{R}_i}(\vec{\alpha}) = \sum_{j=1}^{2} \left(N_{\text{R}_i}^{\text{T}_j}(\vec{\alpha}) + O_{\text{R}_i}^{\text{T}_j}(\vec{\alpha}) \right) + O_{\text{R}_i}^{\text{Off}}(\vec{\alpha}), \tag{5.14}$$

where the index i refers to either the signal- or control-regions of the 0L channel, as defined in Section 5.2.4. Each term of Equation 5.14 can vary under the effect of the nuisance parameters $(\vec{\alpha})$ which parameterize the effect of systematic uncertainties, and the dependency is made explicit in the equation.

The profile-likelihood (or one-step) unfolding method adopted in this work provides equivalent results to other unfolding methods commonly adopted to perform fiducial cross-section measurements, e.g. the iterative Bayesian method [228]. The difference is that there is not an explicit inversion of a resolution matrix, which in the latter method happens in a second separate stage with respect to the background subtraction procedure. Furthermore, the method chosen in this study allows to propagate in a straight-forward manner the pulls, constraints and correlations between the different NPs which parameterize the effect of systematic uncertainties in the maximum-likelihood fit.

As already mentioned, the number of in-fiducial events, whose associated signal strength is later converted in a cross-section value, is extracted from the detector-level regions of the 0L channel of the resolved $VH(b\bar{b})$ analysis. The number of in-fiducial events in the two bins are scaled inclusively in the fit by two independent freely-floating POI, μ_{T_j}. Out-of-fiducial events which belong to the same particle-level $E_{\text{T}}^{\text{miss}}$ interval, also referred to as *diagonal* out-of-fiducial component, can be either fixed to SM predictions or scaled by the same signal strength parameters. This latter case foresees that if the measured cross-section deviates from the SM predictions, out-of-fiducial events increase accordingly. However if the number of these events is not negligible, the latter parameterization might lead to reduced uncertainties on the signal strength parameter which scales the in-fiducial component, thus artificially reducing the uncertainty on the measured fiducial cross-section.

In Figure 5.31 a summary of the categorization of the events in the different detector-level SR categories given their particle-level origin is presented.

As expected from what discussed previously, in the lowest detector-level $E_{\text{T}}^{\text{miss}}$ bin most of the out-of-fiducial events are characterized by a particle-level $E_{\text{T}}^{\text{miss}}$ below 150 GeV, thus fall in the O^{Off} category.

Furthermore, from the same plot by looking at only the first two columns, and considering the sum of the first-and-second line and the third-and-fourth ones, a migration matrix in the $E_{\text{T}}^{\text{miss}}$ variable is obtained.

A comparison between the in-fiducial and out-of-fiducial detector-level templates

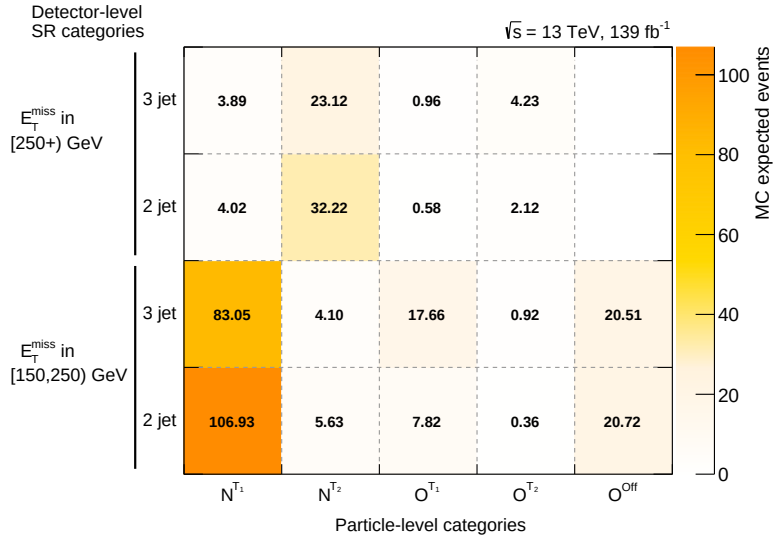


Figure 5.31. Categorization of the MC events adopted to build the signal template used in the fit in the different detector-level SRs, given their particle-level categorization.

is presented in Figure 5.32. In the detector-level categories requiring $150 \leq E_{\mathrm{T}}^{\mathrm{miss}} \leq 250\,\mathrm{GeV}$ it is possible to observe that the in-fiducial off-diagonal component, i.e. N^{T_2}, is roughly 5% of the diagonal component N^{T_1}. Moreover, from the shape comparison it is possible to see that the former one has a lower mass scale. This is due to the fact that only events included in the detector-level SRs categories are shown. Therefore, to fall in the $150\,\mathrm{GeV} \leq E_{\mathrm{T}}^{\mathrm{miss}} < 250\,\mathrm{GeV}$ SR, events with large particle-level $E_{\mathrm{T}}^{\mathrm{miss}}$ will be characterized by a larger m_{bb} value such that the $\Delta R(b,b)$ constrain is matched.

The out-of-fiducial-off component, O^{Off}, is the largest one in these detector-level categories: as already mentioned, this is due to the migration of events across the $E_{\mathrm{T}}^{\mathrm{miss}}$ lower boundary of the fiducial phase-space. From the bottom pad of Figure 5.32(a) it is possible to see that this component has also a larger mass scale compared to the signal we aim to measure.

The diagonal out-of-fiducial component, (O^{T_1}), in the m_{bb} range where most of the events are expected, is almost degenerate in shape with N^{T_1}. Therefore it is not possible to assign in the maximum likelihood fit two independent normalization factors to normalize separately these components.

From Figures 5.32(a) and 5.32(b) it is also possible to see how the shape differences between the templates are larger in the two-jet category with respect to the three-jet one.

The latter conclusion holds also for the larger detector-level $E_{\mathrm{T}}^{\mathrm{miss}}$ bin. Also in the two categories of this $E_{\mathrm{T}}^{\mathrm{miss}}$ interval it is possible to see how the shape of the diagonal in-fiducial and out-of-fiducial components are almost degenerate. The off-diagonal in-fiducial component N^{T_1} is slightly larger in this case, reaching up to 17% in the three-jet category. However, no contribution from the out-of-fiducial-off component is expected here.

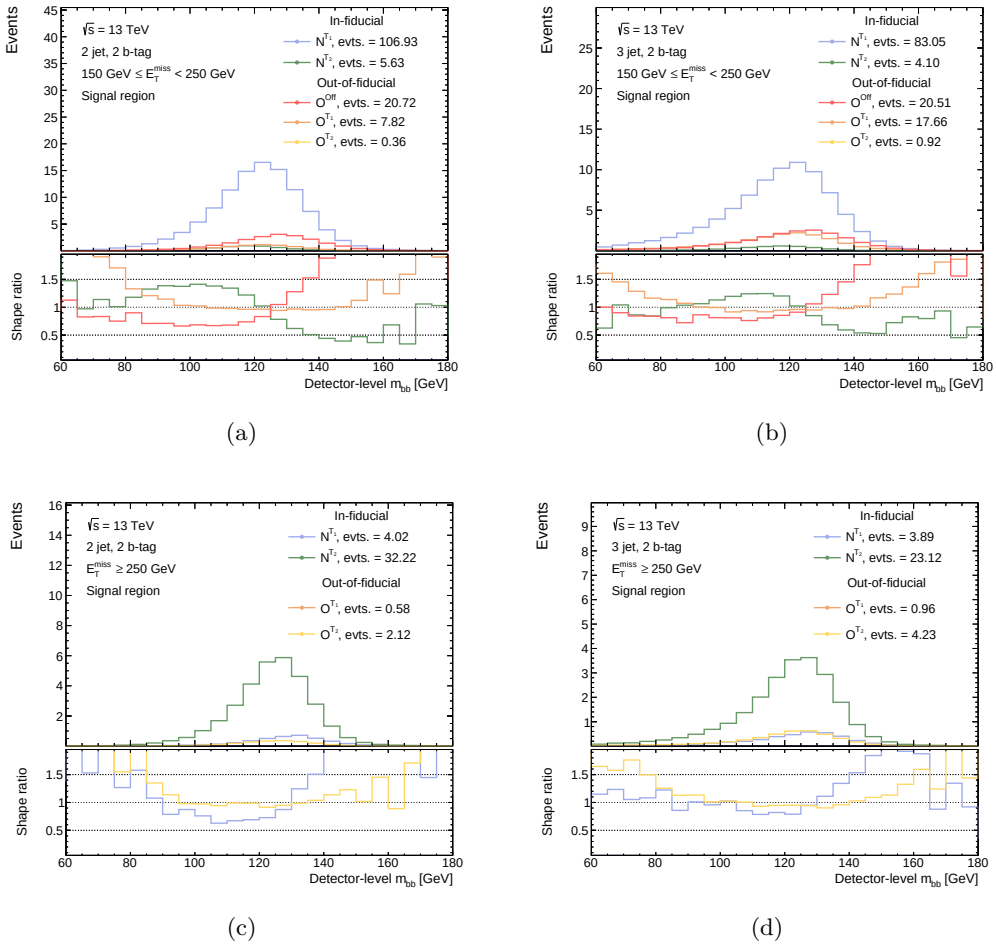


Figure 5.32. Signal templates adopted in the maximum likelihood fit for the four detector-level SRs. The top pad compares the expected distributions, while in the bottom one a shape comparison with respect to the largest contribution in the specific region is presented. Contributions with an integral, indicated in the legend, below 1 event are not shown in the shape comparison.

Statistical model. The fit model adopted in this work is entirely inherited from the published $VH(b\bar{b})$ resolved analysis [42], and is described in Section 5.2.5 of this Chapter. Therefore also the 1- and 2-lepton channels are included.

The other leptonic channels are included to obtain a more precise estimate of the Z+jets, W+jets and $t\bar{t}$ processes, since the former is driven by the 2L channel, and the latter two by the 1L one. Indeed, the MC simulations adopted are affected by a known mismodelling which needs to be corrected in control regions. Since the 1L and 2L channels are meant to be used as CRs only, the SRs of such channels are taken single-binned, and the SM $VH(b\bar{b})$ signal is considered as a background process and fixed to SM predictions (i.e. no freely-floating NF is applied to such a process).

The pre-fit distribution of the invariant mass distribution of the Higgs boson candidates in the four SRs adopted in the fit are presented in Figure 5.33. In Figure

5.34 the pre-fit comparison of the data and MC expected yields in the several CRs considered in the fit is shown, and as it can be seen the background predictions are not exactly reproducing the data. In particular an under-estimation of the data is observed in the 0L and 2L channels due to the mismodelling of the Z+jets process.

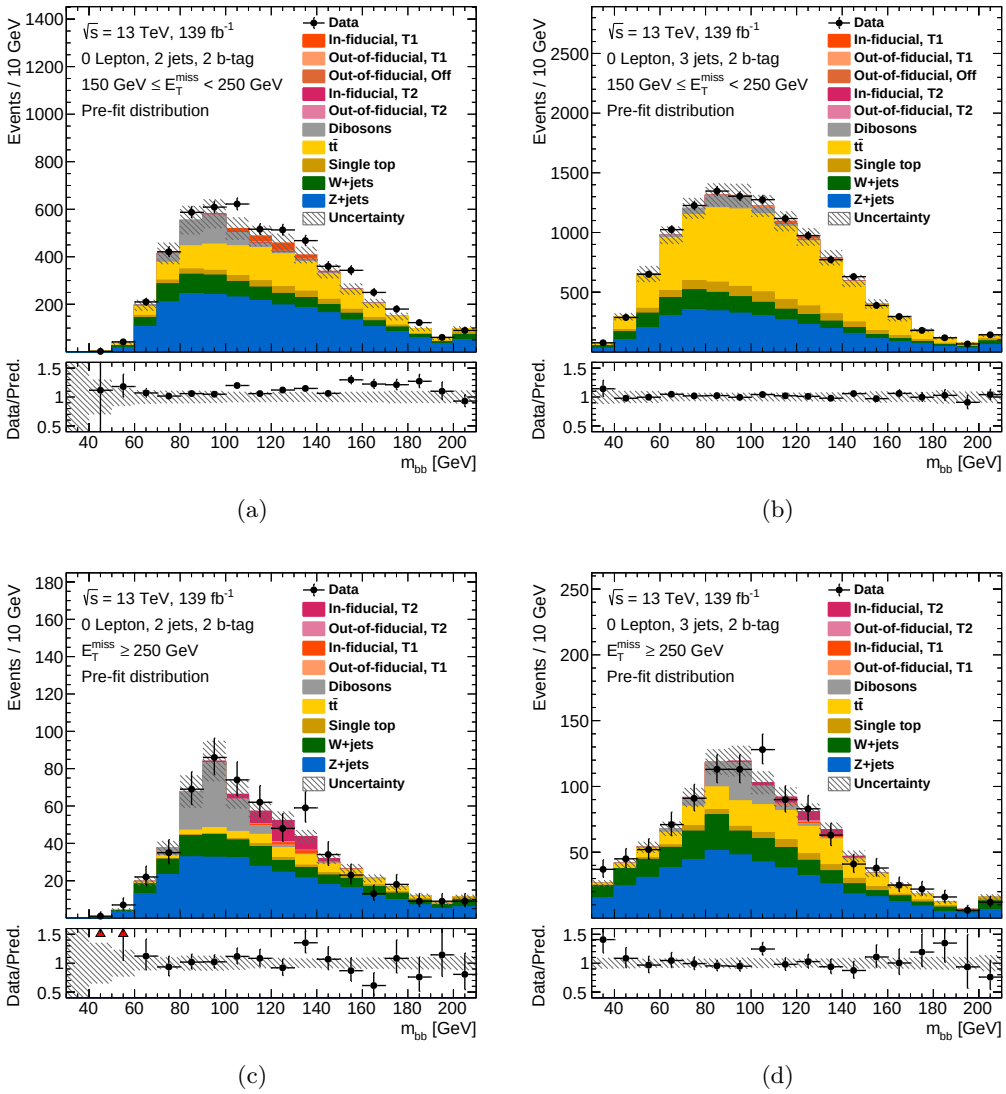


Figure 5.33. Pre-fit invariant mass distribution of the Higgs boson candidates for the four SRs of the 0L channel. The in-fiducial and out-of-fiducial components are shown on top of the SM backgrounds. The bottom pad shows the ratio between data and the SM predictions. The error band represents the total relative uncertainty on these.

Signal modelling uncertainties. Signal modelling uncertainties for the 1 and 2L channels are kept as in the published resolved $VH(b\bar{b})$ analysis, but the expected impact is negligible since the SRs of the aforementioned channels are taken as single-binned. In the 0L channel no modelling uncertainties are included initially. However, at least two components will need to be considered. The first one is related to the unfolding procedure, and in particular associated to the fact that the detector-level

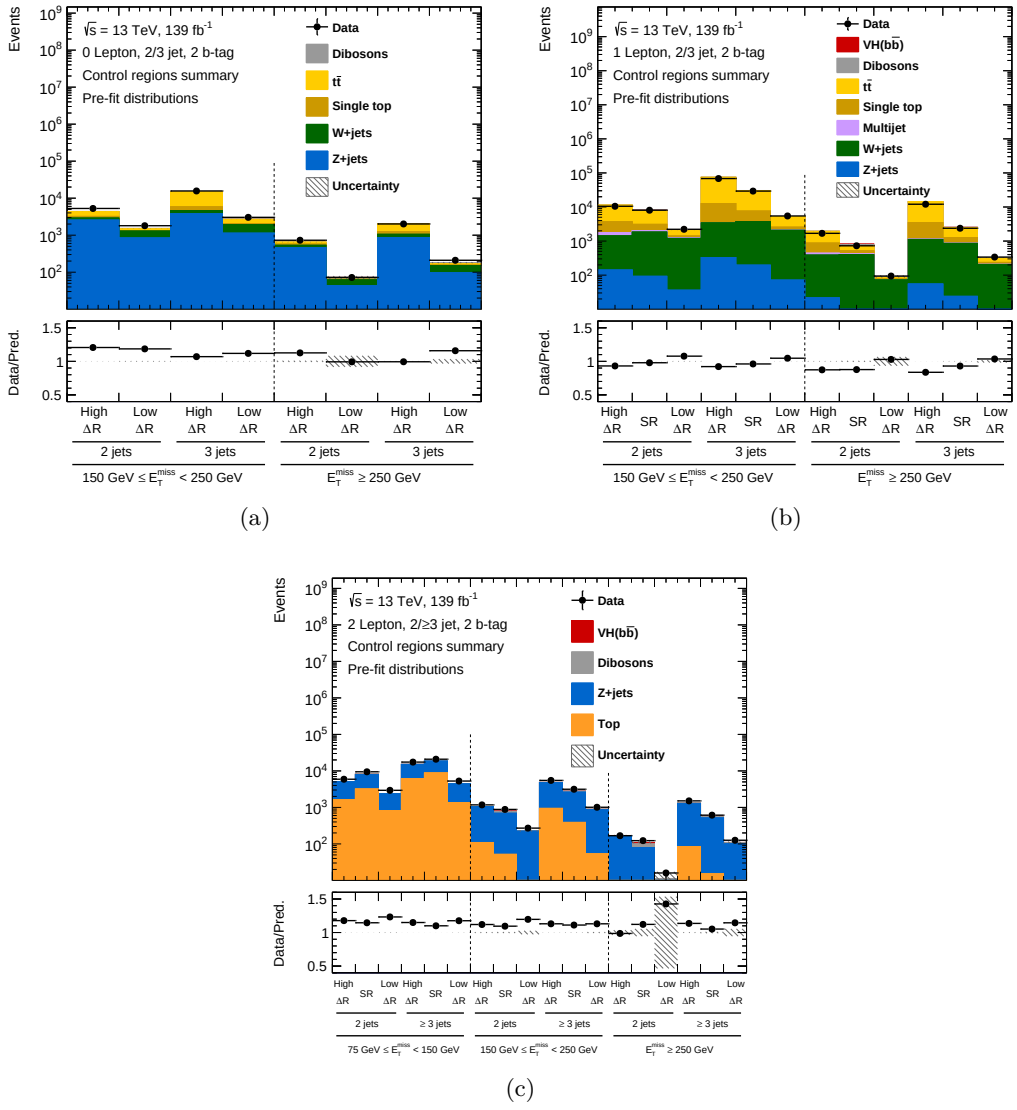


Figure 5.34. Pre-fit comparison of observed data and expected MC predictions for the 0L (a), 1L (b) and 2L (c) channels, respectively. The SRs of the 1L and 2L channel are taken single-binned, and kept separate with respect to the CRs. The bottom pad shows the ratio between data and the SM predictions, and the error band represents the total relative uncertainty on these. The effect of modelling uncertainties is not shown here.

templates used in the maximum likelihood fit have been derived using the nominal MC simulation (cfr. Section 5.2.1) of the $VH(b\bar{b})$ SM process.

Another modelling uncertainty which might need to be included is due to the definition of the fiducial phase-space, which allows either the presence of two or three jets in the events. Therefore, the ratio between the two- and three jet events is fixed by the model chosen in the simulation used to extract the cross-section value via the fit, i.e. by the SM. However, the statistical uncertainty is expected to dominate the measurement, especially in the higher particle-level $E_{\mathrm{T}}^{\mathrm{miss}}$ bin, therefore such an

effect might be sub-leading, and has been neglected in this sensitivity study.

5.4.4 Results

The post-fit m_{bb} distributions for the 0L channel SRs are presented in Figure 5.35. The signal component is split according to the categories defined in the previous section. The large contribution observed in the three-jet category of the $150 \leq E_{\mathrm{T}}^{\mathrm{miss}} < 250\,\mathrm{GeV}$ interval for the $t\bar{t}$ background motivated the adoption of the 1L channel as a control region of this measurement.

The difference which can be observed between the pre- and post-fit background distribution in the two-jet category of the $150 \leq E_{\mathrm{T}}^{\mathrm{miss}} < 250\,\mathrm{GeV}$ bin is due mainly to the Z+jets process. The inclusive cross-section is corrected by means of the high- and low-ΔR CRs of the 0L channel, and by the highly-pure regions of the 2L channel.

As already mentioned, the 1L and 2L channels of the $VH(b\bar{b})$ analysis are kept in this measurement as CRs in order to improve the estimates of the background processes. In Figure 5.36 summary plots showing the 36 resulting CRs are presented, split for each leptonic channel.

The normalization factors measured for the background processes are reported in Table 5.6. The precision with which such NF are measured is roughly proportional to the data statistics in the regions defined, and vary between $5 \div 10\%$. The $t\bar{t}$ background is better constrained in the three-jet category due to the large contribution observed also in the 0L channel, both in the high-ΔR CR and in the SR itself. The W+HF NF value is driven instead mainly by the low-ΔR CR of the 1L channel.

Table 5.6. Normalization factor of the background processes measured in the maximum likelihood fit.

Process and category	Normalization factor
Z+HF, 2 jet, $p_{\mathrm{T}}(V) < 150\,\mathrm{GeV}$	1.32 ± 0.08
Z+HF, 3 jet, $p_{\mathrm{T}}(V) < 150\,\mathrm{GeV}$	1.17 ± 0.05
Z+HF, 2 jet, $p_{\mathrm{T}}(V) > 150\,\mathrm{GeV}$	1.20 ± 0.07
Z+HF, 3 jet, $p_{\mathrm{T}}(V) > 150\,\mathrm{GeV}$	1.10 ± 0.04
W+HF, 2 jet	1.08 ± 0.12
W+HF, 3 jet	1.14 ± 0.10
$t\bar{t}$, 2 jet	0.98 ± 0.11
$t\bar{t}$, 3 jet	0.98 ± 0.06

The normalization factors measured for the signal processes are reported in Figure 5.37. A breakdown of the uncertainties on the POI is performed by fixing group of nuisance parameters, and looking at the difference in quadrature of the new best-fit-value for a particular POI with respect to the original one.

The statistical component of the uncertainty is evaluated by fixing all NPs to their best-fit-value. The total systematic component is then obtained by subtracting in quadrature from the total uncertainty the statistical one. The uncertainty on the POIs associated with the N^{T_1} component is affected by statistical and systematic

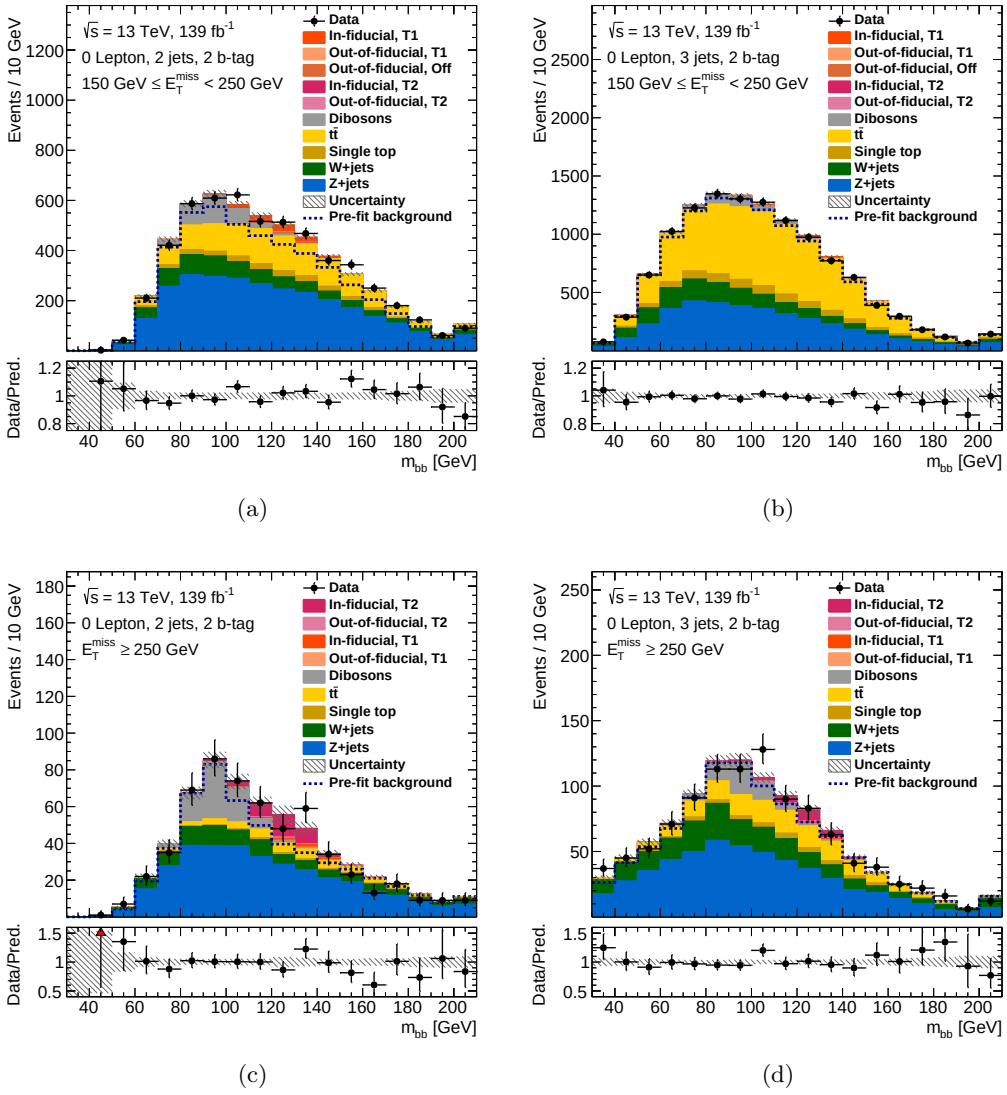


Figure 5.35. Post-fit invariant mass distribution of the Higgs boson candidates for the four SRs of the 0L channel. The in-fiducial and out-of-fiducial components are shown on top of the SM backgrounds. The bottom pad shows the ratio between data and the SM predictions. The error band represents the total relative uncertainty on these.

uncertainties of roughly the same size. The measurement of N^{T_2} is dominated by the statistical one instead.

In Table 5.7 a detailed breakdown of different sources of uncertainty on the POI used to extract the fiducial differential cross-section measurement is presented. The effect shown is the mean between the one associated with a plus 1σ and minus 1σ variation of the post-fit value of the NPs.

Among detector-related systematic uncertainties, the dominant effect on both the POI associated with the fiducial templates is due to the measurement of hadronic jets. The uncertainty is dominated by jet flavour composition and energy scale uncertainties. The second leading effect is associated with missing transverse momentum:

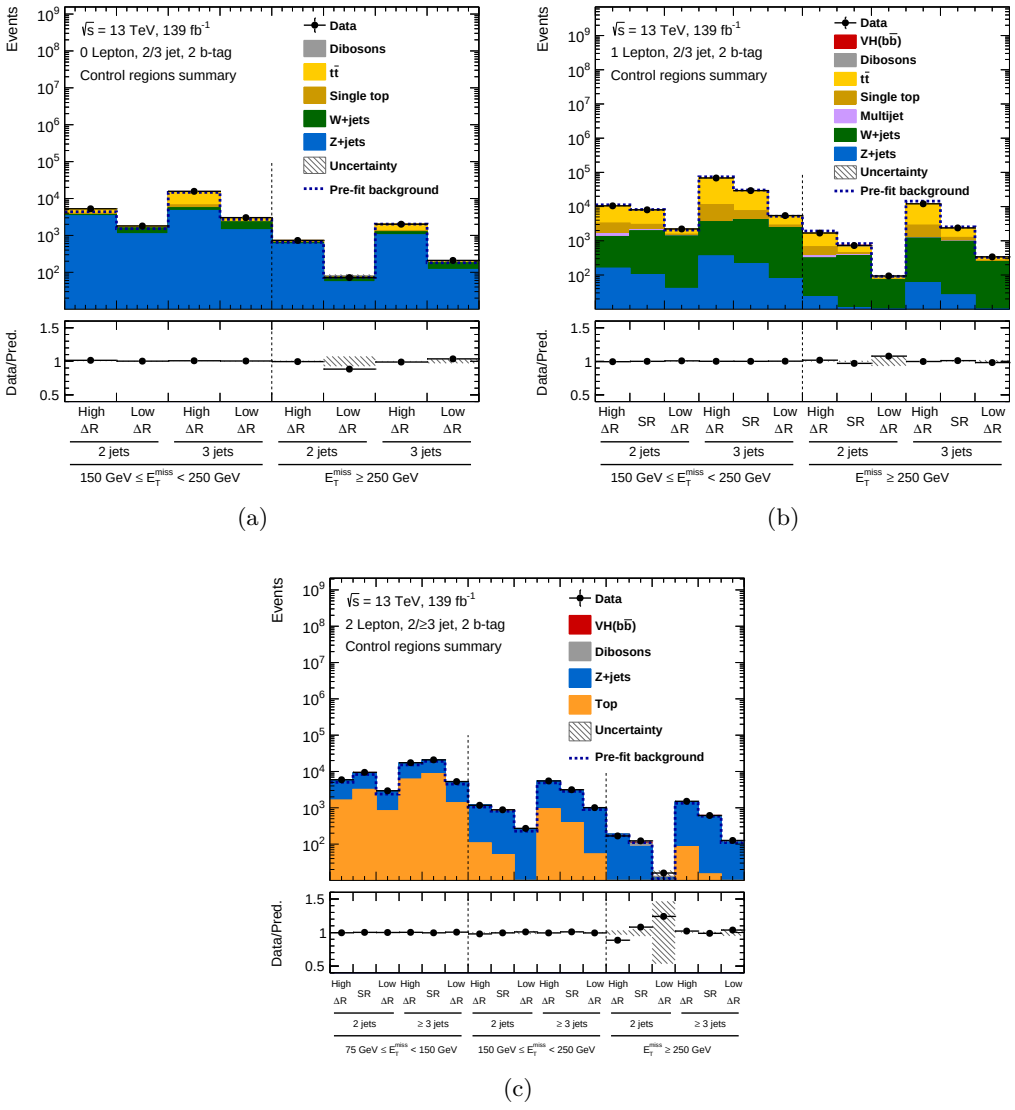


Figure 5.36. Post-fit comparison of observed data and expected MC predictions for the 0L (a), 1L (b) and 2L (c) channels, respectively. The SRs of the 1L and 2L channel are taken single-binned, and kept separate with respect to the CRs. The bottom pad shows the ratio between data and the SM predictions, and the error band represents the total relative uncertainty on these.

to this term both track-soft-term and trigger efficiency uncertainties contribute. The third effect is associated to the flavour tagging procedure, while uncertainties on leptons are subdominant, as they are only inherited by the inclusion of the 1L and 2L channel as CRs.

Concerning modelling systematic uncertainties, the one associated with the VH signal is almost negligible, and it is inherited by the inclusion of the other leptonic channels as CRs, since no uncertainty on the signal template adopted in the 0L channel to extract the fiducial cross-section measurement is assigned. The dominant

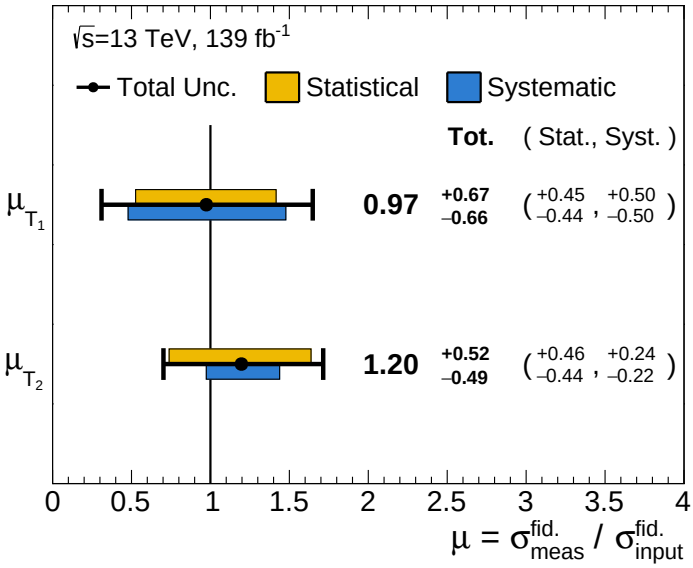


Figure 5.37. Best fit value of the freely-floating signal strength parameters included in the maximum likelihood fit, and breakdown of the statistical and systematic uncertainty components.

effect on the μ_{T_1} parameter arises from $t\bar{t}$ modelling, and is due to the fact that the three-jet category of the $150\,\text{GeV} \leq E_T^{\text{miss}} < 250\,\text{GeV}$ detector-level bin has a large background component coming from $t\bar{t}$ events. Furthermore, the μ_{T_1} parameter uncertainty is largely affected by the modelling of the dibosons processes. This effect is mainly due to the resolution of the m_{bb} distribution. As it can be seen in Figure 5.35(a) part of the in-fiducial template overlaps with the diboson peak.

Both μ_{T_1} and μ_{T_2} are largely affected by the modelling uncertainties associated to the dominant and irreducible (under the Higgs boson peak) background process: Z+jets. The main effect arises from flavour composition uncertainties, i.e. how differently the nominal Sherpa MC generator and the alternative one, based on MadGraph+Pythia 8, model the ratio of the $Z+[bc]/Z+[bb]$ and $Z+[bl]/Z+[bb]$ processes. For the same reason, uncertainties on the W+jets processes arise, but their effect in the 0L channel is sub-dominant. Moreover, the effect of mismodelling of the V+jets processes is also propagated to non-unit floating normalization factors.

A non negligible component of the uncertainty is also due to the MC statistical uncertainty. With respect to the published resolved $VH(b\bar{b})$ analysis [42], this component has a larger impact on the POIs because the signal templates are split in smaller components. For this reason, their measured value is more affected by the presence of gamma-parameters (as defined in Sec. 4.7.2) which parameterize the effect of the MC statistical uncertainty in the fit.

The correlation matrix between the POIs is presented in Figure 5.38. The two parameters adopted to normalize the fiducial templates, μ_{T_1} and μ_{T_2}, exhibit a slight negative correlation of -9.5%. This effect is due to the presence of non-diagonal terms in the E_T^{miss} migration matrix, as discussed in the previous Section.

Table 5.7. Breakdown of the uncertainties on the POIs associated to the templates adopted for the extraction of the fiducial differential cross-section. The effects of the statistical and systematic component add in quadrature to the total uncertainty, while the single components do not due to the presence of correlations between the different NPs.

Set of NPs	Effect on the uncertainty $\Delta\mu_{T_1}$	$\Delta\mu_{T_2}$
Total	0.67	0.51
Statistical	0.45	0.45
Systematic	0.50	0.23
Experimental uncertainties		
Leptons	0.01	0.04
Missing transverse momentum	0.06	0.05
Jet	0.16	0.10
FTAG b-jet	0.06	0.06
FTAG c-jet	0.06	0.04
FTAG *light*-flavour-jet	0.03	0.01
Pileup	0.02	0.02
Luminosity	0.02	0.02
Modelling uncertainties		
Single top-quark	0.07	0.04
$t\bar{t}$	0.17	0.06
W+jets	0.10	0.03
Z+jets	0.12	0.08
Dibosons	0.14	0.06
VH signal	0.01	≤ 0.01
Floating normalizations	0.15	0.06
MC stat	0.17	0.11

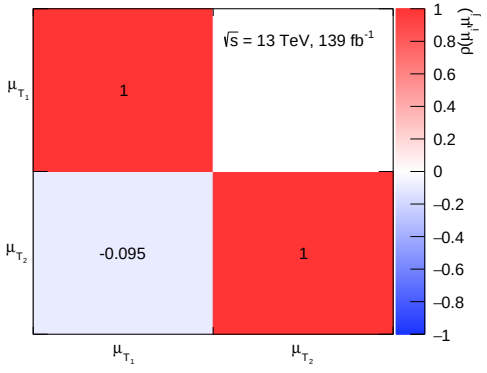


Figure 5.38. Correlation matrix of the NFs associated to the signal templates adopted in the maximum likelihood fit to extract the fiducial differential cross-section.

Finally, the measured fiducial differential cross-section for the $E_{\mathrm{T}}^{\mathrm{miss}} + b$-jets process is reported in Table 5.8. The total error for each term is given by the sum in quadrature of its statistical and systematic uncertainties.

Table 5.8. Measured values of the fiducial cross-section in the two particle-level $E_{\mathrm{T}}^{\mathrm{miss}}$ bins.

$\sigma_{\mathrm{fid}}(150 \leq E_{\mathrm{T}}^{\mathrm{miss}} < 250\,\mathrm{GeV})$	$5.58 \pm 2.55\,(\mathrm{stat.}) \pm 2.86\,(\mathrm{syst.})\,\mathrm{fb}$
$\sigma_{\mathrm{fid}}(E_{\mathrm{T}}^{\mathrm{miss}} \geq 250\,\mathrm{GeV})$	$1.83 \pm 0.69\,(\mathrm{stat.}) \pm 0.35\,(\mathrm{syst.})\,\mathrm{fb}$

The study presented in this Section provides for the first time a fiducial cross-section measurement of the $H(b\bar{b})+E_{\mathrm{T}}^{\mathrm{miss}}$ process. As mentioned at the beginning of the Chapter, these results provide foundations for a more complete and refined work to be performed in the context of a Run 2 legacy $VH(b\bar{b})$ analysis.

Chapter 6

Next generation V+jets Monte Carlo simulations

The importance of the V+jets process modelling has been highlighted several time in this thesis, as they often form the dominant background of new physics searches and Higgs boson measurements.

The following Chapter summarises a new Sherpa V+jets configuration developed within the ATLAS collaboration in conjunction with the Sherpa authors. Both the statistical precision and modelling performance are evaluated. Improvements in the parton shower model, and the inclusion of virtual NLO EW corrections as on-the-fly weights are of particular interest for the aforementioned $VH(b\bar{b})$ and monojet analyses. These can be found in Section 6.1. Moreover, HF modelling improvements in the form of a hybrid flavour scheme, in which a 4-flavour scheme NLO Z+bb calculation is matched with an inclusive 5-flavour Z+jets calculation, is presented.

The possibility to generate events via cross-section biasing has been introduced in recent versions of the Sherpa event generator. The performance of this method are presented in Section 6.2, as well as the results which guided the development of improved methods. The statistical power of the final configuration chosen for the *bulk* production of MC events in ATLAS is discussed in Section 6.2.3, along with a comparison to the previous recommended setup.

Part of the results presented in this Chapter have been published in the paper arXiv:2112.09588 (submitted to JHEP) which documents modelling and computational improvements to the simulation of V+jets processes.

6.1 The impact of improved calculations

The default Sherpa V+jets MC configuration adopted by several ATLAS Run 2 analyses, referred to in this Chapter as the Legacy setup, corresponds to the description provided in Section 4.2.1 and summarised here. The configuration is based on Sherpa version 2.2.1, in which matrix elements accurate up to 2-jets at NLO, and up to 4-jets at LO in QCD are calculated in a 5-flavour scheme [229], considering massless c/b-quarks. NNPDF3.0NNLO is the PDF set chosen as nominal, with a set of 100 replicas available as alternative MC weights to evaluate PDF-related

uncertainties. To estimate the effect of missing higher orders in the calculation, variations of the renormalization and factorization scales are also parameterized as alternative MC weights. The final inclusive V+0,1,2j@NLO, 3,4j@LO is merged and matched to the Sherpa PS, based on the Catani-Seymour dipole description, with the MC@NLO algorithm using the CKKW procedure [164]; a merging scale $Q_{\text{cut}} = 20\,\text{GeV}$ is adopted. This procedure is briefly summarised in Section 6.1.3. The updated configuration chosen by ATLAS, also referred to as Final setup in this Chapter, is based on Sherpa 2.2.11. An additional fifth emission at LO is included in the ME calculation. The PDF set and the matching and merging procedures are the same of the previous setup.

A summary of the changes between the two versions of the MC generator is presented in Table 6.1. All the mentioned topics are discussed in further detail below.

Table 6.1. Summary of the Legacy and Final Sherpa configurations.

Feature	Legacy	Final
Generator version	Sherpa 2.2.1	Sherpa 2.2.11
PDF set	NNPDF3.0nnlo	NNPDF3.0nnlo
EW input scheme	Effective	$\sin\theta_{W,\text{eff}}$
QCD accuracy	0-2j@NLO+3,4j@LO	0-2j@NLO+3,4,5j@LO
NLO_{virt} corrections	No	Yes
Subtraction scheme	Default	Modified Catani-Seymour
Unordered histories allowed	Yes	No
Gluon colour/spin exact matching	Yes	No
Generation strategy	Sliced in $\max(H_{\text{T}}, p_{\text{T}}^{V})$	Analytic Enhancement

6.1.1 Next-to-leading-order virtual electroweak corrections

Electroweak corrections to the production of vector bosons in association with jets can have a significant effect on the predicted cross-section at large transverse momentum. This is due to the appearing in the calculation of large Sudakov logarithms which take into account the possible emissions of virtual vector bosons.

The possibility to include virtual NLO electroweak corrections [183] in the predictions by means of alternative internal weights have been included in latest Sherpa versions. These corrections are similar to the one adopted by the monojet analysis described in Section 4.2.1.

NLO EW virtual corrections can be expressed as

$$\delta\sigma^{\text{NLO}}_{n,\text{EW}_{\text{virt}}} = [B_n(\Phi_n) + V_{n,\text{EW}}(\Phi_n) + I_{n,\text{EW}}(\Phi_n)]\, d\Phi_n, \tag{6.1}$$

where Φ_n represents the phase-space of the n-particle final state. B_n represents the Born process of order α_s^n and α^2 in the strong and electroweak coupling constants, respectively. $V_{n,\text{EW}}$ is the exact virtual one-loop correction of the Born process with α^3 in the EW coupling, and $I_{n,\text{EW}}$ is the approximated subtraction term used to make the cross-section finite. It has been shown that the approximations used in

the derivation of the subtraction term agree well with the full NLO EW calculation given in Ref. [183], except in phase-spaces dominated by the real emission of an additional vector boson.

The net effect of virtual NLO EW corrections on the cross-section is a reduction in the predictions at high $p_T(V)$ as shown by Figure 6.1. Three alternative ways of implementing the corrections are available: additive ($\mathrm{QCD}_{\mathrm{NLO}} + \delta_{\mathrm{EW}}$), multiplicative ($\mathrm{QCD}_{\mathrm{NLO}} \times \delta_{\mathrm{EW}}$) and exponentiated ($\mathrm{QCD}_{\mathrm{NLO}} \times \exp\delta_{\mathrm{EW}}$). The first two are described in Ref. [183], while the latter in Ref. [230].

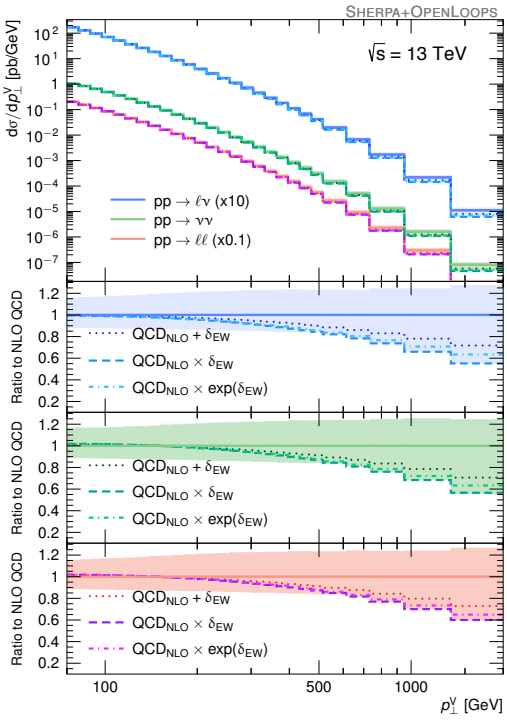


Figure 6.1. Effect of NLO EW corrections on cross-section predictions for V+jets processes, shown as a function of the vector boson p_{T}. Credits to Matthew Gignac and Christian Gutschow.

Results obtained in the three different methods are consistent with each other for both W+jets and Z+jets processes. As already mentioned in Chapter 4, NLO EW corrections include different terms for $Z(\to \ell^-\ell^+)$ and $Z(\to \nu\bar{\nu})$, thus these processes are shown separately. The size of the corrections is similar to the one observed in the reweighting procedure adopted by the monojet analysis, though in that case the calculations were reweighted to NNLO QCD + NLO EW accuracy.

The availability of such corrections as internal weight variations allows, in principle, the to be used in the MC predictions adopted in every ATLAS analysis. The availability of these higher-order corrections as on-the-fly weights reduces our needs in terms of both CPU, disk space and computing time.

6.1.2 Electroweak parameter input scheme

In the EW sector of the SM, relations between parameters such as m_W, m_Z, α, and those related to the Higgs sector are fixed for a given perturbative accuracy. Three independent parameters are given as an input to the SHERPA Event generator. For the LEGACY configuration, these are $m_W = 80.399\,\text{GeV}$, $m_Z = 91.1876\,\text{GeV}$ and $m_H = 125.09\,\text{GeV}$, following Ref. [231]. The weak mixing angle (or Weinberg angle) is then derived using tree level relations using the input vector boson masses:

$$\sin^2\theta_W = 1 - \frac{m_W^2}{m_Z^2} = 0.222. \tag{6.2}$$

However, when evaluating this quantity at the Z pole, higher order corrections due to bosonic and fermionic loops need to be included. These shift the value of the weak mixing angle to $sin^2\theta_{W,\text{eff}}$, which is called *effective* mixing angle. Combined measurements from ATLAS, CMS and LHCb provide [73] $sin^2\theta_{W,\text{eff}} = 0.23113$. This value is set in the generator configuration.

τ-lepton polarization in Z boson decays arises in the EW theory from the mixing of the A_μ and W_μ^3 fields, as introduced in Chapter 1.1, which depends on the $\sin^2\theta_W$ value. The polarization ($\mathcal{P}$) measured at the Z pole in a simulated $Z(\to\tau^-\tau^+)$+jets sample produced with the LEGACY setup, is found to be in tension with the measurement of such quantity performed at LEP [232]. $\mathcal{P}$ is measured as

$$\mathcal{P}(\tau^-) = \frac{\sigma_R - \sigma_L}{\sigma_R + \sigma_L}, \tag{6.3}$$

where $\sigma_{L(R)}$ are the cross-sections measured for left- and right-handed τ-leptons. Its value can be extracted from MC events by looking at the τ visible four-momentum fraction (x_π) in $\tau \to \pi\nu$ decays, parameterizing the cross-section according to

$$\frac{1}{N}\frac{dN}{dx_\pi} = 1 + P(2x_\pi - 1). \tag{6.4}$$

In the LEGACY sample $P = -0.2$, while the measured value from LEP is $-0.14 \pm 0.02(\text{stat.}) \pm 0.04(\text{syst.})$ [232]. In order to correct such a discrepancy, the FINAL configuration for Z+jets adopted an EW scheme in which the effective value of $\sin^2\theta_W$ is given as an input, together with the mass of the Z boson and $\alpha(m_Z)$. This is called the $\sin^2\theta_W$ *scheme*. Using PDG values and tree level EW relations, a slight tension is found for the value of the mass of the W boson. However, this is not relevant in the simulation of Z+jets processes.

The G_μ scheme was chosen for the simulation of W+jets even if the predicted mixing angle is the same of the LEGACY setup, $\sin^2\theta_w = 0.222$. The EW input parameters in this scheme are the Fermi constant G_μ, and the mass values of the W and Z bosons. Figure 6.2 shows the particle level measurement of the τ-lepton polarization in $Z(\to\tau^-\tau^+)$+jets events generated in the two aforementioned schemes. As expected, the $\sin^2\theta_W$ result is consistent with the LEP measurement, while the G_μ one is not, yielding a value similar to the one observed in the LEGACY setup.

Such choice of the scheme of EW input parameters has almost no effect on the MC distributions. However, in Drell-Yan events ($(Z \to \ell^-\ell^+)$ with $\ell = e, \mu$), the forward-backward asymmetry in the polar angle of the leptons (with respect to the

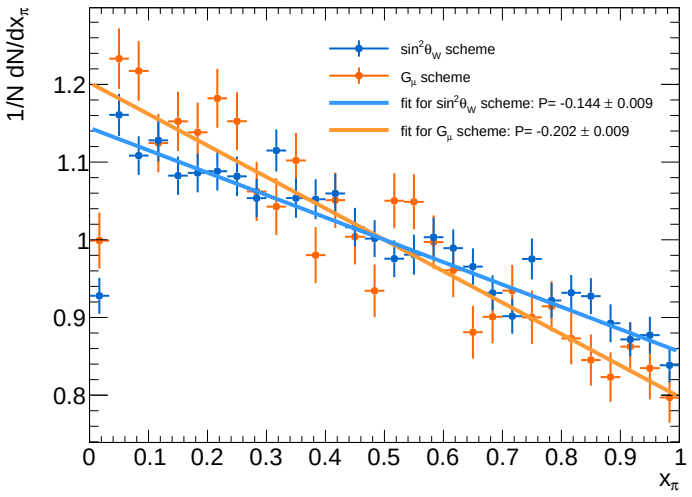


Figure 6.2. Particle level measurement of the τ-lepton polarization in $Z \to \tau^-\tau^+$+jets MC events generated with the G_μ and $\sin^2\theta_W$ schemes in orange and blue, respectively, as a function of the visible momentum fraction of τ leptons in $\tau \to \pi\nu$ decays, x_π. The fitted values of $\mathcal{P}$ are indicated in the legend, along with their uncertainty. The dip observed in the first bin is expected due to the finite mass of the τ lepton, and it is excluded from the fit. Credits to Janina Anna Krzysiak

beam direction) defined in the rest frame of the dilepton system, is sensitive to the weak mixing angle. Such measurement was performed by the ATLAS collaboration at $\sqrt{s} = 7\,\text{TeV}$ [233]. A cross-check with samples generated at such centre-of-mass energy was performed. Both the two schemes were found to be in good agreement with data.

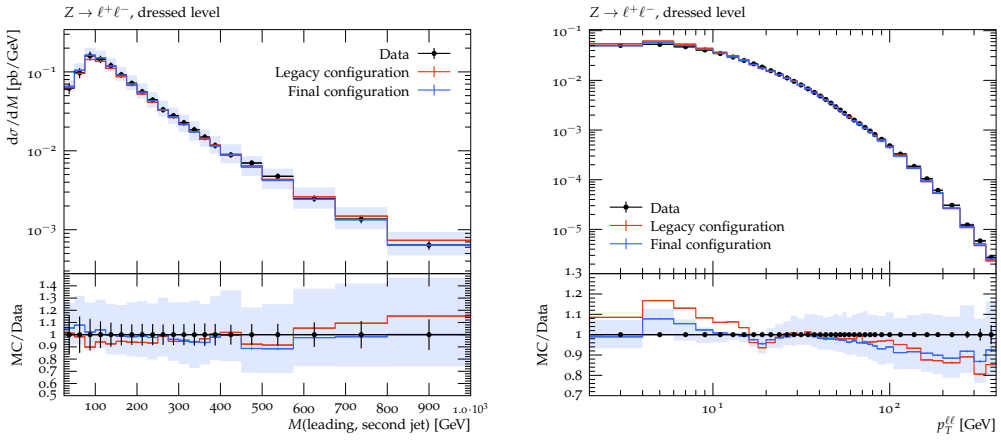
6.1.3 Improved performance of the parton shower model

In multijet merged setups, such as Sherpa, the ME and PS are combined such that the strength of each algorithm is exploited. Matrix elements accurately describe hard emissions at a fixed order in α_s, while PS generates QCD radiation patterns down to the Λ_{QCD} scale (cf. Section 1.1.1). Merging and matching algorithms allow to reweight the ME to the accuracy of the PS, by taking into account Sudakov factors for the non-emission of additional partons [234] and avoid double counting of the processes. Furthermore, Sudakov factors include the effect of unresolved-real- and virtual-corrections, which are needed to maintain the logarithmic accuracy of the overall prediction [164].

The CKKW-L matching procedure adopted by Sherpa re-interprets the final states obtained from the ME as a core process accompanied by parton emissions. A backward clustering is performed with a k_t algorithm by inverting the parton shower kinematics, as described in Ref. [235]. This procedure is applied iteratively according to Feynman rules until a core process is identified. A series of nodes (n) in which parton emissions happen are found. In each of those, the strong coupling constant is evaluated at the branching scale Q_n, i.e. the energy of the emitting

parton, as determined in the clustering process. Sudakov factors are then included to veto additional emissions between two nodes. One of the determined parton shower histories is chosen, in a probabilistic way, to represent the event. From such a starting configuration, the PS algorithm is run. Emissions in the PS above the Q_{cut} scale are vetoed.

In the clustering procedure outlined above, the branching scales increase towards the core process as $Q_n \leq Q_{n-1} \leq .. \leq Q_1 \leq Q_{\text{core}}$. However, in extreme regions of the phase space, it may happen that unordered scales are found, i.e. the scale Q_{m-1} is lower than Q_m. In such cases no Sudakov factor can be evaluated, thus the differential cross-section might become uncontrollably large. In the FINAL configuration, such unordered scales (or *unordered histories*) are no longer allowed. If these appear, the largest previously identified scale is used for the evaluation of α_s. This leads to a reduction in the predicted cross-section in phase spaces dominated by multiple parton emissions with similar p_{T}, such as at large m_{jj} values. In Figure 6.3(a) the particle-level distribution of m_{jj} obtained in the LEGACY and FINAL setups is compared to measured data by the ATLAS collaboration in Z+jets events [179]. The over-prediction observed in the LEGACY setup in the tail of the distribution is significantly reduced in the FINAL one, thanks to the veto on unordered PS histories.



(a) (b)

Figure 6.3. Comparison of generator level predictions from the LEGACY and FINAL setups of the (a) m_{jj} distribution against data measured by ATLAS in the inclusive Z+jets measurement [179], and (b) of the transverse momentum of lepton pairs in Drell-Yan events as measured from ATLAS [236]. Both measurements have been performed at $\sqrt{s} = 13\,\text{TeV}$. The uncertainty band is built from the envelope of the variations obtained changing the renormalization and factorization scales of a factor one-half and two, both simultaneously and independently. The cases in which one scale is varied of a factor two and the other one of a factor one-half are excluded. Credits to Matthew Gignac.

Another improvement of the FINAL SHERPA configuration concerns the Catani-Seymour dipole operators [237] which are used to subtract the overlapping phase space between the ME and PS. These were slightly modified to better reflect the known soft limits of the hard matrix elements. These changes are made consistently

in both the parton shower, the NLO fixed-order and NLO matched calculations, and mainly affect the physics in the parton shower and are thus relevant for p_{T}^{V} around and below the merging scale, 20 GeV. As it can be observed in Figure 6.3(b), which shows the differential cross-section as a function of the transverse momentum of the pair of leptons in Drell-Yan $Z(\to e^{-}e^{+})$ events, a discrepancy in the predictions from the PS and the ME components of the calculation leads to a bump around the merging scale 20 GeV. In the FINAL configuration, the aforementioned modified dipole operators are adopted, therefore a better agreement with data measured by the ATLAS collaboration [236] is obtained. Such an improvement is also expected to reduce the modelling uncertainties associated to the variation of the merging scale.

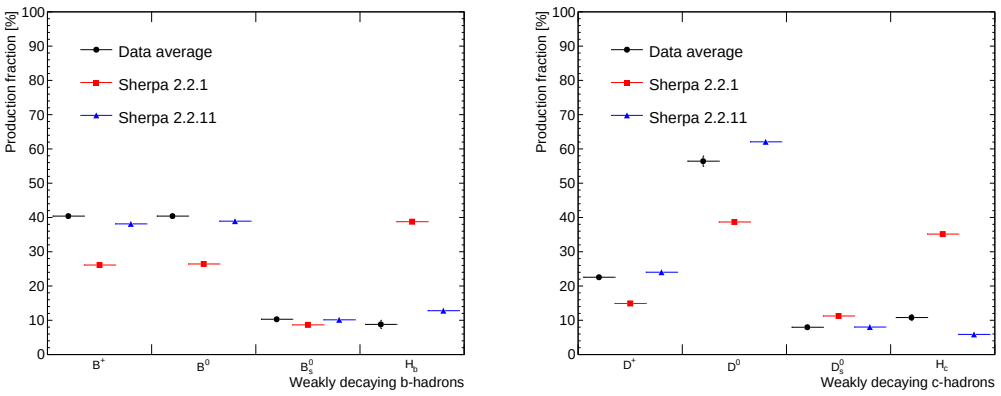
Negative-weighted events are needed to take care of divergences which appear beyond the LO. A reduction in the fraction of these over all the events has been achieved in SHERPA 2.2.7, and following versions, by running the PS in the leading colour approximation, i.e. neglecting terms which are suppressed by a power of N_c. This approximation has no effect on the differential cross-section predictions. In the LEGACY setup, in $Z(\to e^{-}e^{+})$+jets events, an overall negative weights fraction (NWF) of 18% is observed. In the FINAL setup, instead, this has been reduced to 9%, with a significant reduction at low values of H_{T}. This quantity is defined as the scalar sum of the transverse momenta of particle-level jets, built from stable particles (as defined in Section 5.4.1) using the anti-k_t algorithm with $R = 0.4$. The impact on the statistical power of the MC samples of such improvement is discussed in Section 6.2.3.

6.1.4 Heavy flavour modelling

The production fraction of weakly-decaying b- and c-hadrons in SHERPA has been checked in $t\bar{t}$ samples, and compared data measurements and to predictions from alternative samples [238]. The values are found to be in tension with the predictions from other MC generators and the world-average data. These discrepancies, which are present also in the V+jets setups, have a direct effect on quantities relevant for the flavour tagging procedure, such as track multiplicities, or the kinematics of the decays. A consequence of this was shown already in this thesis in Section 5.3, where large MC-to-MC SFs are needed to correct the mistag rate of c-jets.

From the 2.2.4 version of the SHERPA event generator onwards, the modelling of HF decays has been improved thanks to updated decay rates and better tuning of the parameters which impact the b- and c-jets fragmentation functions. These describe the longitudinal momentum distribution of hadrons inside jets, and are defined as $z_{b,c} \equiv \vec{p}_{b,c} \cdot \vec{p}_{\mathrm{jet}}/|p_{\mathrm{jet}}|^2$. In Figure 6.4, the production fraction for different weakly-decaying b- and c-hadrons, as measured from particle-level jets of W+jets events, is presented for the LEGACY configuration (based on SHERPA 2.2.1) and the FINAL one (based on SHERPA 2.2.11). These are compared to world-average data from Refs. [239, 240]. A better agreement with measured data is observed in the latest version of the event generator. In general, in the SHERPA 2.2.1 setup an over-production of Λ_b^0 and Λ_c^+ baryons, grouped in the $H_{b,c}$ category, was observed.

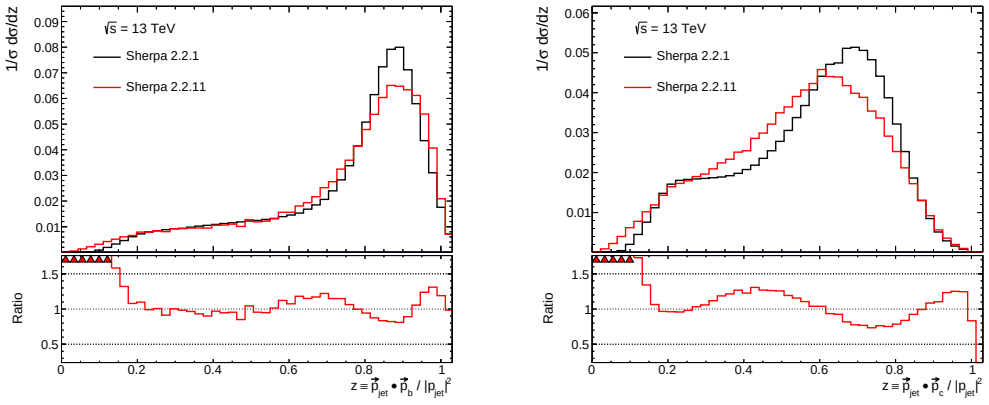
These discrepancies lead to differences in the jet fragmentation functions introduced above. In Figure 6.5, the distribution of z as measured at particle-level in W+jets simulated samples is compared between SHERPA 2.2.1 and 2.2.11 for b- and



(a) (b)

Figure 6.4. Production fractions of weakly-decaying (a) b- and (b) c-hadrons as measured from simulated SHERPA 2.2.1 and 2.2.11 W+jets samples, compared to world average data from Refs. [239, 240].

c-jets. In the events, hadrons are associated to jets with an exclusive $\Delta R < 0.3$ matching, as introduced in Section 3.3.2. In SHERPA 2.2.11, the b-hadron fragmentation function is less peaked, while the step structure observed in SHERPA 2.2.1 for the c-hadron fragmentation function is smoothed. The differences observed between the two setups have an impact on the flavour tagging procedure, as described in the case of $t\bar{t}$ events in Section 5.3. In particular, MC-to-MC SFs are expected to be closer to unity.



(a) (b)

Figure 6.5. Particle-level comparison of the z distribution, defined in the text, as observed for b- and c-jets in W+jets SHERPA 2.2.1 and 2.2.11 simulated events.

6.1.5 Heavy flavour fusing

As presented in Section 5.3, the modelling of vector boson production in association with heavy flavour (HF) jets is highly relevant to $VH(\to b\bar{b})$ measurements. The Sherpa event generator adopts a five-flavour number scheme (5FS) calculation, in which b-quarks are considered as mass-less particles and included in the PDF. Therefore, such a particle can appear both in the initial and final states of the calculations. The mass of the b-quarks is then restored in the parton showering by means of a kinematic reshuffling. This is needed otherwise an excess of $g \to b\bar{b}$ splittings would be observed. A five-flavour massive scheme has been proposed in Ref. [241], but is not yet part of multijet merged event generators. An alternative way of including the b-quark mass in the ME calculation is to use only four active flavours in the PDFs (4FS), thus neglecting the b contribution in the initial state.

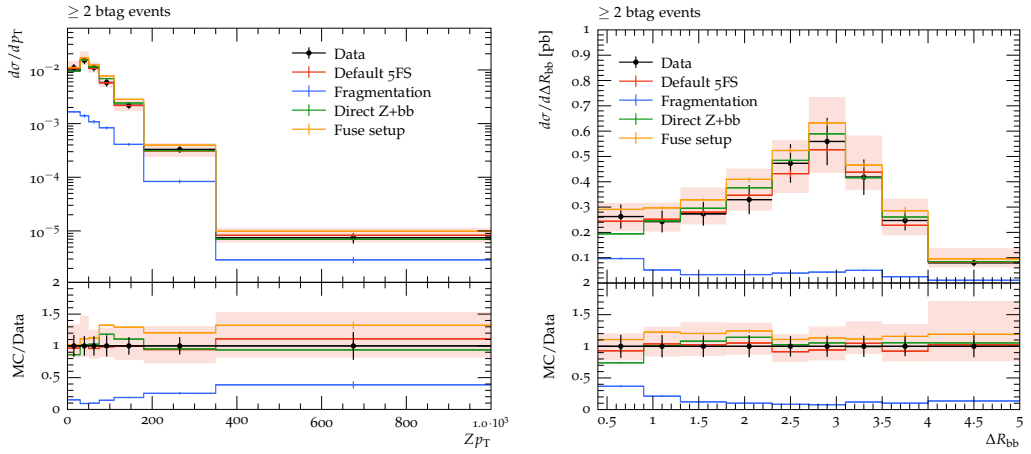
From Sherpa 2.2.8 onwards, a method to combine a 4FS $Z + b\bar{b}$ calculation at NLO QCD with a 5FS Z+jets predictions, called *heavy flavour fusing*, is available [242]. The removal of overlapping events is treated separately in the two samples. $Z + b\bar{b}$ events are treated as if they are part of an inclusive multijet merged sample. When the MEPS@NLO algorithm is run on them, the overlap with the 5FS calculation is taken into account by the Sudakov logarithms, which express the differential radiation probability of the final state partons. In the 5FS calculation, instead, a veto on parton shower histories which would lead to a configuration allowed also by the 4FS calculation is set. In such a way, two separated and non-overlapping samples are obtained, which form the *direct* and the *fragmentation* component, respectively. The first one describes the production of $Z + b\bar{b}$ events via 4FS ME calculation considering massive b quarks. The latter includes events in which b pairs are produced via gluon splitting. The *fragmentation* component of the 5FS sample can be isolated in the generated events by means of alternative MC-event-weights available in the simulated sample of events: such weight is either 0 or equal to the nominal MC weight. The sum of the two samples yields the 4+5FS *fused* setup.

A first validation set of events was produced in ATLAS to allow modelling comparisons with available data. In Figure 6.6 the *fused* setup and the 5FS samples are compared to the ATLAS measurement of $Z + b(\bar{b})$ differential cross-sections performed at 13 TeV [217]. Both the setups presented in this comparison are based on a version of Sherpa (2.2.10) which does not include the improvements discussed in Section 6.1.3.

Moreover, the default 5FS sample includes up to 4 jets @LO in the ME, not 5 jets @LO as in the Final configuration. Overall, a similar modelling of data is achieved in the two setups, with the fuses one predicting a slightly higher cross-section than the 5FS configuration. In the $\Delta R(b, b)$ distribution presented in Figure 6.6(b), it is possible to see how the fragmentation component is mainly dominant at lower values, hinting at the gluon splitting ($g \to b\bar{b}$) process.

Resolved $Z(\to \nu\bar{\nu})H(\to b\bar{b})$ phase space.

The *fused* setup has been also tested at particle level by requiring the 0-lepton channel event selection of the $VH(b\bar{b})$ measurement. Since unfolded data are not available in such phase space yet, only a MC to MC comparison has been performed.



(a) (b)

Figure 6.6. Particle level comparison of the *fused* and 5FS setups against data measured by ATLAS [217] at $\sqrt{s} = 13\,\text{TeV}$ in $Z + b(\bar{b})$ final states, for the Z boson p_T (a) and $\Delta R(b, b)$ distributions in events with two or more b-tagged jets (b). The uncertainty band shown around the default setup is built from the envelope of the renormalization and factorization scale variations.

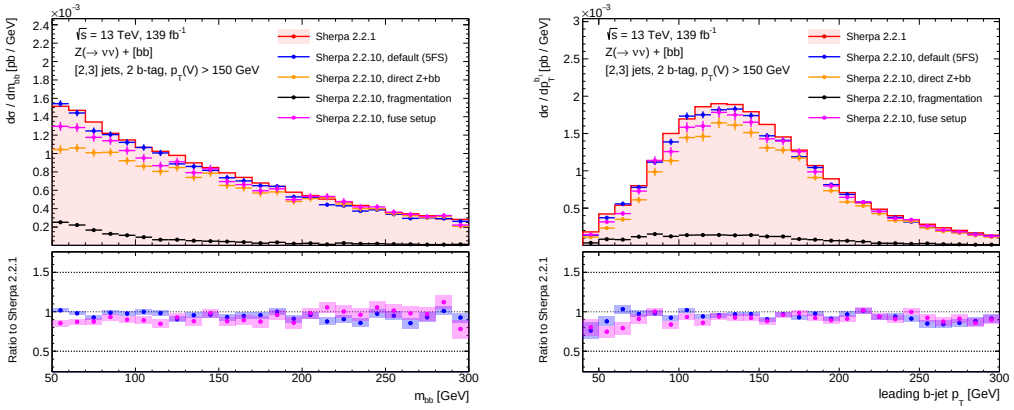
Events are required to have at least 150 GeV of truth missing transverse momentum, built as defined in Section 5.4. Central (forward) jets are selected if they have at least 20 GeV (30 GeV) of p_T, and $|\eta| < 2.5$ ($2.5 < |\eta| < 4.5$). At least two central jets are required in the events.

To emulate the performance of the flavour tagging procedure, the truth tagging method, introduced in Section 5.2.3 is used. In order not to introduce in the modelling comparison any dependence on the efficiency maps used, the same set is used for all the configurations. The leading b-truth-tagged jet in the event is then required to have $p_T > 45\,\text{GeV}$.

As for the detector-level analysis presented in Section 5.2, events are categorized based on the number of leptons found in the final state. Particle-level electrons (muons) are considered if they have $|\eta| < 2.47$ ($|\eta| < 2.7$) and at least $p_T > 7\,\text{GeV}$. Moreover, leptons are required to have $\Delta R > 0.4$ from any jet in the event. Only events with exactly 0 leptons passing these selections are considered. To improve the statistical uncertainty of the adopted samples, the 2 and 3 jet categories are merged together in a single region, and no categorization in signal and control regions is performed.

A comparison of the Legacy setup with the 5FS Sherpa 2.2.10 and the 4+5FS *fused* setups is performed for $Z(\to \nu\bar{\nu})$+jets events. The distribution of the invariant mass of the two jets forming the Higgs candidate (m_{bb}), and of the leading b-jet p_T are shown in Figure 6.7 for events in which the two jets are both b-labelled.

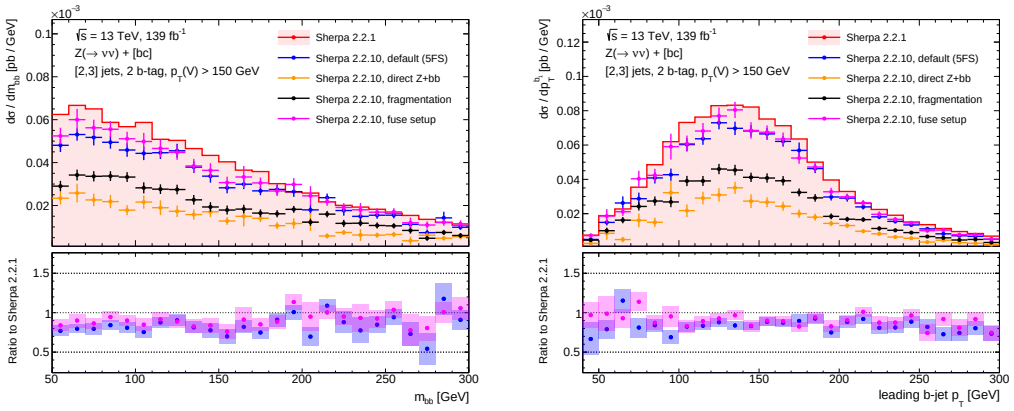
Similar modelling by the three configurations is observed. In the plots, it is possible to see how in $Z + [bb]$ events the *fused* setup is mainly composed by the *direct* component, while the fragmentation part has a larger effect at low values of m_{bb}.



(a) (b)

Figure 6.7. MC-MC comparison of the LEGACY, default (5FS) and *fused* (4+5FS) setups in the $Z(\to \nu\bar{\nu})H(\to b\bar{b})$ phase space in events with two b-labelled jets. Only the statistical uncertainty is shown.

In Figure 6.8, the same distributions are presented, but for events in which the two jets forming the Higgs-candidate are b- and c-labelled, respectively. This is, in fact, the second leading background for the $Z(\to \nu\bar{\nu})H(\to b\bar{b})$ measurement. In this case, the *direct* and *fragmentation* components contribute half each to the *fused* setup.



(a) (b)

Figure 6.8. MC-MC comparison of the LEGACY, default (5FS) and *fused* (4+5FS) setups in the $Z(\to \nu\bar{\nu})H(\to b\bar{b})$ phase space, in events with one b- and one c-labelled jet. Only the statistical uncertainty is shown.

From the previous comparisons, no significant differences are observed between the default and *fused* setup. However, the possibility to adopt such method in the Legacy $VH(b\bar{b}/c\bar{c})$ analysis will be investigated as samples in the FINAL configuration will be available.

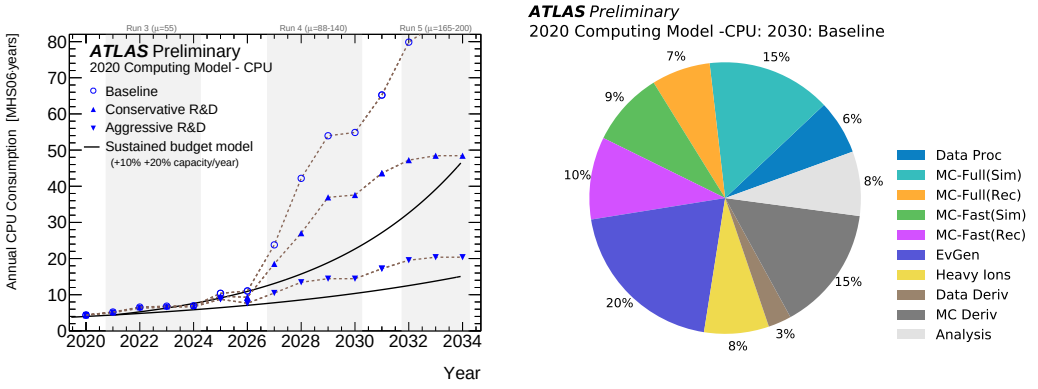
One additional advantage of the *fused* setup, is that the predictions for Z+bb are performed only at a fixed order, and therefore the simulation is much lighter with respect to the bulk sample. This is relevant to address one of the limiting factor of the $VH(\to b\bar{b})$ analyses: the amount of available MC statistics. In fact, as it is discussed in Section 6.2, the LEGACY setup has been extended several times in the past years to achieve enough statistical precision for the various ATLAS analyses. Events have been generated in three separate setups using HF filters. These require either the presence of a b-hadron with at least 0 GeV of p_{T} and $|\eta| < 4$, or a c-hadron with $p_{\mathrm{T}} > 4$ GeV and $|\eta| < 3$, joint with a b-hadron veto, or a veto on both type of hadrons. The b-filter efficiency is $\varepsilon_{\mathrm{filt.}} \sim 6 \div 18\%$, therefore to obtain one event passing the filter $1/\varepsilon_{\mathrm{filt.}}$ events are need to be generated on average. This time- and resources-consuming process could be improved significantly by switching to the *fused* setup as the default.

6.2 Towards a more efficient event generation

In preparation of the future LHC runs, the computing and software framework of the ATLAS collaboration has been reviewed, and a conceptual design report has been produced [243]. A significant amount of resources, both in terms of CPU consumption and disk usage is highlighted to be due to simulated Monte Carlo simulated samples. In particular, Figure 6.9(a) shows a projection of the CPU requirements of the ATLAS collaboration between 2020 and 2034, based on 2020 data. The Figure shows how the current model, indicated by *baseline*, is not sufficient to respect the projected budget availability increase, and that an aggressive research and development (R&D) is needed in preparation of the Run 4 of the LHC, the first stage of the High-Luminosity phase (HL-LHC). Figure 6.9(b) shows the projected breakdown of CPU requirements as extrapolated to 2030 for the baseline scenario. About 20% of the CPU consumption is expected to be associated with the generation of MC events. Moreover, about 41% of the CPU will be required for the simulation of MC events through the ATLAS detector, to provide predictions which can be compared directly with reconstructed data.

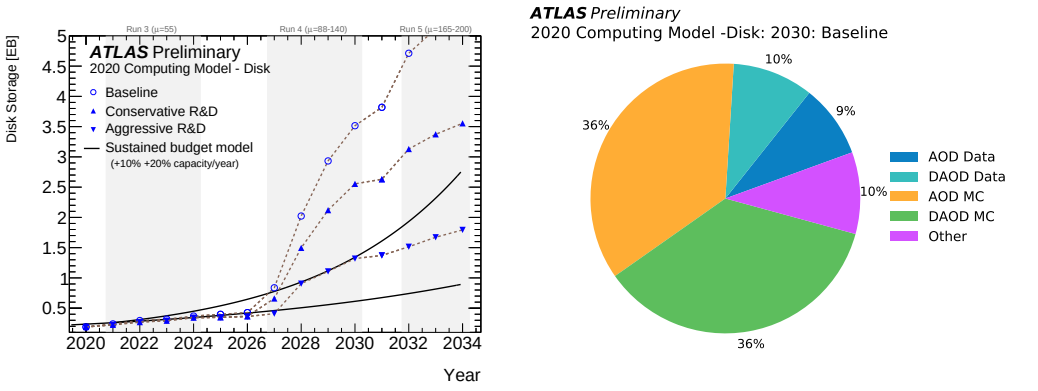
Another key point to take into account, is that the amount of data which is expected to be collected during the HL-LHC will require a very large amount of simulated samples to perform meaningful comparisons. Such samples will therefore have a non-negligible impact on the storage resources. Figure 6.10(b) shows the expected evolution of storage requirements in the timeline already mentioned, as projected from 2020 data. Similar conclusion to the CPU results can be drawn: an aggressive R&D is needed to respect the budget evolution. The amount of MC events to be stored is thus another key aspect, as represented by Figure 6.10(b). It shows that more than 70% of the expected disk occupation in 2030, as projected from 2020 data, will be due to MC events, stored under the AOD and DAOD formats. These are the standard formats in which ATLAS data and MC events are organised; in particular, DAOD is a reduced version of AOD in which only partial information about the reconstructed events are retained.

The above-mentioned studies motivate the usage of innovative and efficient event generation techniques. Of crucial importance is that the produced MC samples of



(a) (b)

Figure 6.9. (a) Projected CPU requirements, expressed in millions of HS06 seconds per year, for the ATLAS collaboration between the 2020 and 2034, based on 2020 studies. HS06 is a standard CPU performance metric, developed to make assessments independent on the hardware on which the studies are performed. The continuous black lines present the expected budget increases of +10% and +20% respectively. (b) Breakdown of the expected CPU requirements by different activities of the ATLAS collaboration, as extrapolated in the baseline scenario. Figures from Ref. [243].



(a) (b)

Figure 6.10. (a) Projected disk storage requirements, expressed in exabytes, for the ATLAS collaboration between the 2020 and 2034, based on 2020 studies. The black continuous lines present the expected budget increases of +10% and +20% respectively. (b) Breakdown of the expected storage requirements by different activities of the ATLAS collaboration, as extrapolated in the baseline scenario. Figures from Ref. [243].

events are not affected by large statistical dilutions, which can be caused by the presence of an excessive fraction of negative weights, or by a large variance of the event weights distributions. These aspects are discussed in the next Section.

6.2.1 Phase-space slicing

As already described in Section 4.2.1, the events of the LEGACY setup were generated via a phase space slicing procedure, which is performed in the hard-scattering calculation. This is needed because the cross-section is steeply falling, thus if events were generated according to their real probability, the tail of the $p_{\mathrm{T}}(V)$ (or H_{T}) distribution would never be populated.

In Figure 6.11, the raw distribution of the events is presented as a function of $\log_{10}(\max(H_{\mathrm{T}}, p_{\mathrm{T}}(V)))$. To better catch the features of the slicing procedure, the quantities here have been evaluated at the parton-level. The p_T^V is built from the sum of the four-momenta of ME-level leptons, before they emit any QED radiation, while H_T is given by the scalar sum of the transverse momenta of the partons produced in the hard-scattering process. Different colours indicate different slices; the right axis shows the parton-level cross-section.

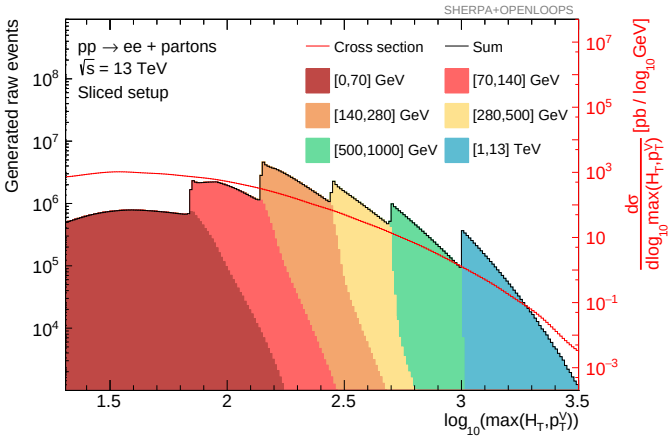


Figure 6.11. Raw events distribution for the LEGACY setup in a $Z(\to e^-e^+)$+jets sample, shown as a function of the logarithm of $\max(H_{\mathrm{T}}, p_{\mathrm{T}}(V))/1\,\mathrm{GeV}$ evaluated at parton-level. The right axis refers to the cross-section, shown in red.

As it can be seen from the peaked structure, a different number of raw events has been generated in each slice. This is due to several MC simulation campaigns which happened in the past years to help analyses mitigate uncertainties related to MC statistics. However, once event weights are taken into account, a smooth distribution is obtained, as shown by the cross-section distribution. The generation was performed mainly above 100 GeV of H_{T}, since in this phase space a ME description of multiple emissions is needed. Analysis targeting lower values of H_{T} (or $p_T(V)$) rely instead on inclusive NLO samples, based on Powheg, which allows to efficiently simulate a larger number of events with respect to the ones expected from the collected data.

6.2.2 Phase-space biasing

The *phase-space biasing* for the generation of events has been recently introduced in the SHERPA MC generator. The idea behind this is to populate the tail of the $p_{\mathrm{T}}(V)$ or H_{T} distributions by sampling events according to a biased, or *enhanced*, value of

the cross-section. Phase-space biasing is achieved by multiplying, in the integration step, the cross-section of a process $ab \to m$ by a function $e(\mathcal{O}, \Phi_m(\vec{x})) = \frac{d\sigma}{d\mathcal{O}_m}$ as

$$\sigma_{ab\to m} \to \sigma'_{ab\to m} = \int_\Omega d\hat{\sigma}_{ab\to m} e(\mathcal{O}, \Phi_m(\vec{x}))^{-1}. \tag{6.5}$$

This function depends on one observable, $\mathcal{O}$, and on the phase space element $\Phi_m(\vec{x})$ of the $ab \to m$ process. To restore the correct cross-section distribution, each event weight is multiplied by an additional biasing component given by

$$w_{i,m}^{\text{bias}} = e(\mathcal{O}, \Phi_m(\vec{x})) = \frac{d\sigma}{dO_m}, \tag{6.6}$$

which depends on the core process ($ab \to m$). This method is called *differential enhancement* and is associated to the *Enhance Observable* feature of the SHERPA event generator. It allows to flatten the raw statistical uncertainty as a function of an observable defined by the user.

The cross-section enhancement can be activated in a well-defined range of the chosen observable. For the generation of V+jets processes it was chosen to enhance all the different $2 \to X$ ME processes (except for the $2 \to 2$ one) in the interval between 1 and 3.3 of the $\mathcal{O} = \log_{10}(\max(H_\text{T}, p_\text{T}(V)))$ observable. The distribution of raw events generated in such a setup, overlaid to the cross-section, is presented in Figure 6.12 for a $Z(\to e^-e^+)$+jets sample. As already stated, the generation is enhanced up to 3.3, which corresponds to $\max(H_\text{T}, p_\text{T}(V))) \sim 2\,\text{TeV}$. Above this value, the sampling rate is governed by the normal cross-section again, thus a steeply falling distribution is observed.

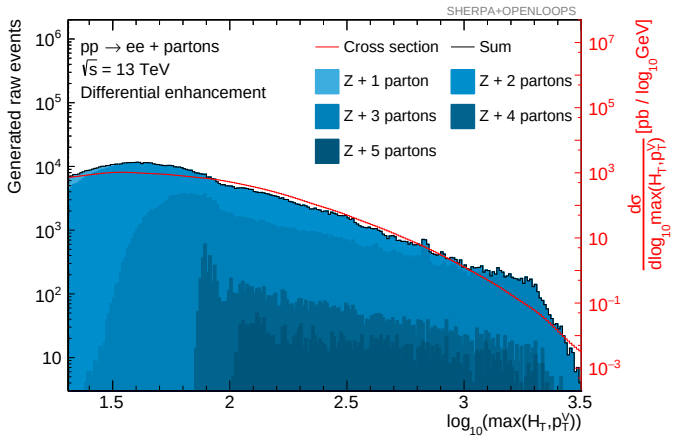


Figure 6.12. Raw events distribution for the FINAL setup, generated using the *enhance observable* method. $Z(\to e^-e^+)$+jets raw events are shown as a function of the logarithm of $\max(H_\text{T}, p_\text{T}(V))/1\,\text{GeV}$, evaluated at parton-level, for different parton multiplicities. The right axis refers to the partonic cross-section, shown in red.

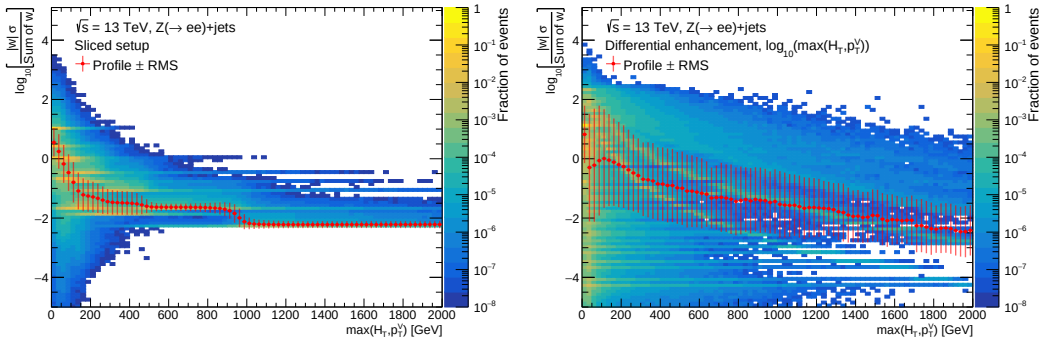
In the plot, different parton-multiplicities are highlighted. This variable is a proxy for the ME quantities used in the phase space biasing, thus the obtained raw distribution is not exactly flat. The biased generation over-samples the high $\max(H_\text{T}, p_\text{T}(V))$ phase-space at the expense of the lower one. Indeed, as it can

be seen from the Figure, while the cross-section falls for medium values of p_{T} of two order of magnitude, the raw distribution falls only of one order of magnitude. A smoother coverage with respect to the slicing technique is obtained with this technique.

The MC statistical uncertainty of such a sample has been evaluated and compared to the one obtained in the LEGACY setup as a function of $\max(H_{\mathrm{T}}, p_{\mathrm{T}}(V))$ and $p_{\mathrm{T}}(V)$. As already mentioned in Section 4.11, when dealing with weighted events the relative statistical uncertainty can be expressed as

$$\sigma_{\mathrm{rel}} = \frac{\sqrt{\sum_i^{N_{\mathrm{raw}}} w_i^2}}{\sum_i^{N_{\mathrm{raw}}} w_i} = \frac{1}{\sqrt{N_{\mathrm{raw}}}} \sqrt{1 + \frac{\sigma_{w_i}^2}{\langle w \rangle^2}}, \tag{6.7}$$

where the w_i are the weights of each event, $\sigma_{w_i}^2$ their variance, and $\langle w \rangle$ their mean. In the right-hand term of Equation 6.7 there is a clear separation of two components entering the MC statistical uncertainty: the number of raw generated events, N_{raw}, and how these events are generated, i.e. how their weights are distributed. The square root term can be interpreted as a dilution factor. An intrinsic one is included in NLO samples, since negative event weights are needed to implement correctly the NLO subtraction terms. However, the dilution factor can also be impacted by the event generation technique. From a comparison between the LEGACY setup, and the one obtained with the differential enhancement, a significantly larger dilution factor was observed in the latter. This can be understood by looking at the distribution of event weights. To improve the visualization of such quantity, in Figure 6.13 the normalized distribution of the logarithm of the absolute value of event weights is shown as a function of particle-level $\max(H_{\mathrm{T}}, p_{\mathrm{T}}(V))$ for the two setups. The weights are also scaled by the cross-section, such that it is possible to visualize the various components of the LEGACY sliced setup. In an inclusive sample, the cross-section provides only an offset on the y-axis.



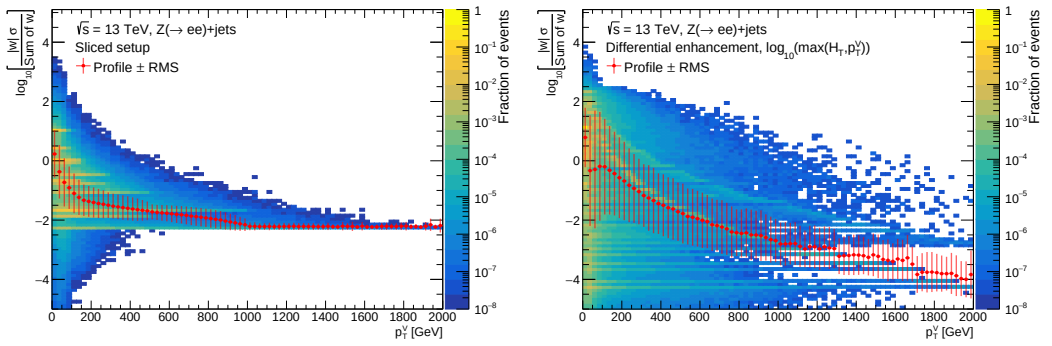
(a) (b)

Figure 6.13. Normalized distribution of the logarithm of the absolute value of event weights, normalised to the sum performed over all the events and scaled by the cross-section, shown as a function of particle-level $\max(H_{\mathrm{T}}, p_{\mathrm{T}}(V))$ for (a) the LEGACY setup and (b) for the one produced with differential enhancement of the cross-section. Further details on the structures observed in the two figures are provided in the text.

The accumulation of events on horizontal lines observed for the LEGACY setup is due to the different slices which form the complete sample. These roughly extend in the range of $\max(H_{\mathrm{T}}, p_{\mathrm{T}}(V))$ of the various slices. A spread of the weights within each one arises from different $2 \to X$ processes and from the HF filters applied in generation phase, described in Section 6.1.5. The mean value and the RMS of the weights are represented by the red points. A larger variance is observed in correspondence of the boundaries of each slice.

For the setup adopting the differential enhancement, Figure 6.13(b) highlights the presence of a multi-prong structure which results in a significantly larger RMS of the event weights. Such structure is a by-product of having a biasing function for each of the 2 to X processes, i.e. $e(\mathcal{O}, \Phi_m) = d\sigma_m / d\mathcal{O}$, thus dependent on the parton multiplicity of the final state process.

In Figure 6.14, the two-dimensional distribution of event weights is presented for the LEGACY and the differential enhanced setup as a function of $p_T(V)$, which is an interesting quantity for both the monojet and the $VH(\to b\bar{b})$ analyses presented in this thesis. This variable is correlated with $\max(H_{\mathrm{T}}, p_{\mathrm{T}}(V))$, and in fact the same multi-prong structure is observed in the enhanced setup. The presence of this feature depends on the fact that the observable chosen for the cross-section enhancement has a strong dependence on the parton multiplicity of the final states. By choosing a less parton-dependent observable, such as $p_T(V)$, the differential enhancement yields to a smaller spread of the event weights. However, the purpose of biasing in a variable dependent on H_{T} is to provide enough statistical power for analysis looking at final states with one or more jets. The impact of such feature on the statistical power of the sample is further discussed in Section 6.2.3.



(a) (b)

Figure 6.14. Normalized distribution of the logarithm of the absolute value of the event weights, normalised to the sum performed over all the events and scaled by the cross-section, shown as a function of particle-level $p_{\mathrm{T}}(V)$ for (a) the LEGACY setup and (b) for the one produced with differential enhancement of the cross-section. Further details on the structures observed in the two figures are provided in the text.

Analytic enhancement. To overcome the limitations of the differential enhancement, a new feature was provided by the SHERPA authors, namely the *analytic enhancement*, implemented via the *enhance function* method available in the SHERPA version 2.2.11. The biasing function, in this case, is parameterised such

that it is independent of the final state parton-multiplicity m of the hard-scattering process, $e(\mathcal{O}, \Phi_m) \to e(\mathcal{O})$. Events of the FINAL setup have been generated using this technique, choosing $e(\mathcal{O}) = (\max(H_T, p_T(V))/\mathcal{R})^2$. The value $\mathcal{R}$ at the denominator is a regularization factor for the cross-section biasing procedure, and determines how much the generation of raw events is shifted from the low- to the high-p_T phase-space. For the final setup, $\mathcal{R} = 20\,\text{GeV}$ was chosen. The raw distribution of the events obtained with this technique is shown in Figure 6.15 as a function of the parton-level $\log_{10}(\max(H_T, p_T(V)))$.

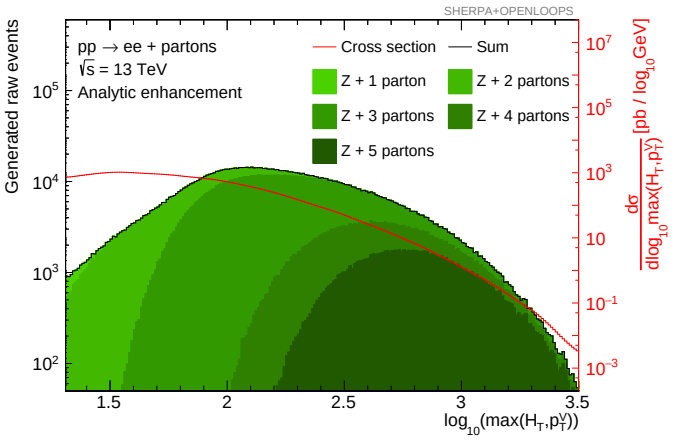


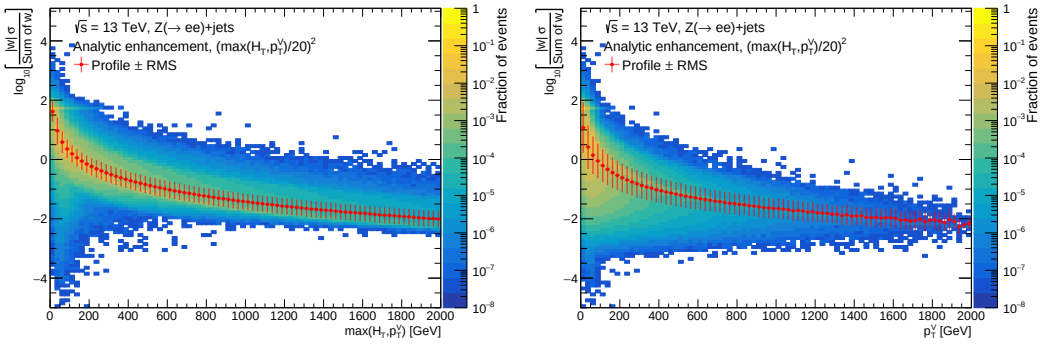
Figure 6.15. Raw events distribution for the FINAL setup, generated using the *enhance function* method. $Z(\to e^-e^+)$+jets raw events are shown as a function of the logarithm of parton-level $\max(H_T, p_T(V))/1\,\text{GeV}$ for different parton multiplicities. The right axis refers to the partonic cross-section, shown in red.

As for the differential enhancement, the high $\max(H_T, p_T(V))$ phase-space is over-sampled at the expenses of the low one. However, comparing Figure 6.15 with Figure 6.12 it is clear that the former method provides a coverage of the phase space closer to the one of the LEGACY setup.

The distribution of the event weights obtained in this setup is presented in Figure 6.16 as a function of particle-level $\max(H_T, p_T(V))$ and of $p_T(V)$. The multi-prong structure observed in the differential enhanced setup is no more present thanks to the new parameterization of the biasing function. Similar performance are observed in both the shown variables. The presence of a fraction of events with roughly constant event weight at low $\max(H_T, p_T(V))$ (and therefore also $p_T(V)$) is due to the fact that the biasing is not applied to the $2 \to 2$ process.

Slicing vs biasing. The two approaches presented for the generation of MC events are characterized by both strengths and weaknesses. The slicing of the phase space allows to control in an efficient manner the raw statistics in each of the different ranges, but it introduces non-negligible dilution factors at the boundaries of each slice. Moreover, the granularity of the slicing is determined at the beginning of the generation stage, and care is needed when merging such generation with inclusive samples.

The cross-section biasing method is a versatile way of shifting the bulk of the



(a) (b)

Figure 6.16. Distribution of the logarithm of the absolute value of event weights, normalised to the sum performed over all the events and scaled by the cross-section for the setup based on the analytic enhancement, shown as a function of particle-level (a) $\max(H_{\mathrm{T}}, p_{\mathrm{T}}(V))$ and (b) $p_{\mathrm{T}}(V)$.

event generation in the desired phase space, thanks to the fact that the biasing function can be tuned for different needs. An example of this is presented in Section 6.2.4. Furthermore, the statistical power of the event generation is fully predictable, since the cross-section biasing induces a flat dilution effect in the enhancement variable.

6.2.3 Assessing the statistical power

As introduced by Equation 6.7, the statistical uncertainty of a set of weighted events depends at least on four terms. Three of them are explicit in the equation and are the number of raw events generated (N_{raw}), the mean of the event weights ($\langle w \rangle$) and their variance s_w^2, respectively. The fourth component is the fraction of events with negative weights (f_{nw}), which is defined as

$$f_{\mathrm{nw}} = \frac{\sum_i^{N_{\mathrm{neg}}} |w_i|}{\sum_i^{N_{\mathrm{all}}} |w_i|}. \tag{6.8}$$

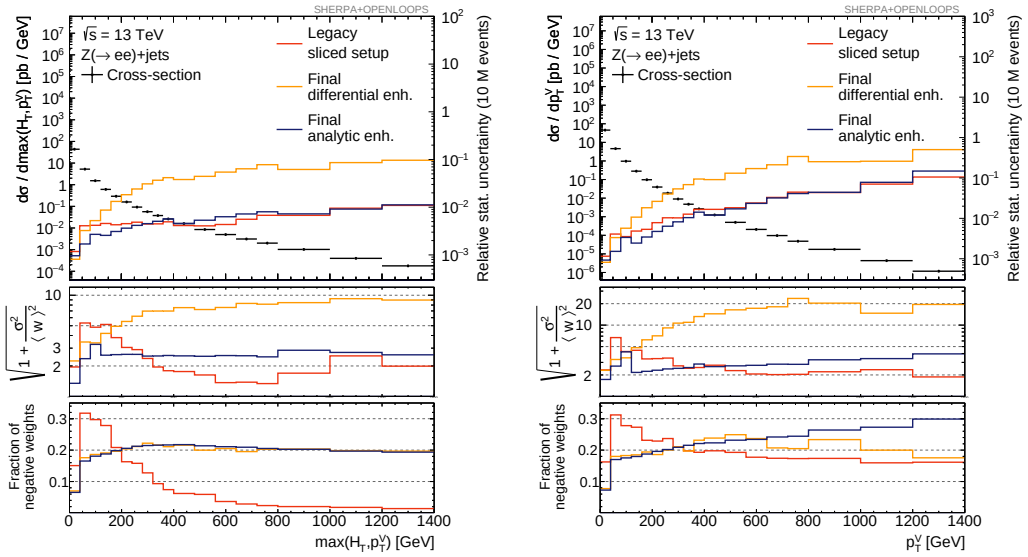
In this equation, N_{neg} indicates the raw events characterized by a negative weight, while N_{all} refers to all the events in the sample.

To see how the fraction of events with negative weights affects the statistical precision of a sample of N_{gen} weighted events, in the limit of constant weights one can write

$$\frac{\sqrt{\sum_i w_i^2}}{\sum_i w_i} = \frac{1}{\sqrt{N_{\mathrm{gen}}}} \frac{1}{(1 - 2f_{\mathrm{nw}})}. \tag{6.9}$$

This shows that for a negative weights fraction of 0.5 the MC statistical uncertainty diverges, therefore the sample is not usable.

Figures 6.17(a) and 6.17(b) summarize in one plot the effect of all the aforementioned components as a function of $\max(H_{\mathrm{T}}, p_{\mathrm{T}}(V))$ and $p_{\mathrm{T}}(V)$, respectively.



(a) (b)

Figure 6.17. Summary plots comparing the statistical power of the LEGACY setup, and the two samples generated biasing the cross-section, as a function of particle-level (a) $\max(H_{\mathrm{T}}, p_{\mathrm{T}}(V))$ and (b) $p_{\mathrm{T}}(V)$. The top pane shows the differential cross-section of $Z(\to e^-e^+)$+jets events and a comparison of the statistical uncertainties (referred to the right axis) obtained in the three setups, normalised to the same number of raw events. The middle pane shows the dilution factor, while the bottom pane shows the differential fraction of negative weights, as defined in Equation 6.8.

In the top pad the differential cross-section of inclusive $Z \to e^-e^+$+jets events is presented as a function of $\max(H_{\mathrm{T}}, p_{\mathrm{T}}(V))$ and $p_{\mathrm{T}}(V)$. The MC statistical uncertainty of the three discussed setups is reported on the right axis, and is normalised to the same number of total raw events, 10^7. The sum of all the slices of the LEGACY setup is normalized to such value to achieve a fair comparison between the sliced and continuous samples. A large difference is observed between the setup generated using the differential enhancement and the other two, for which the statistical uncertainty is comparable. From the middle pad it is possible to see that this difference is due to a significantly higher dilution factor. The origin of this was tracked down to the spread of event weights presented in Figures 6.13(b) and 6.14(b). The slightly larger fraction of negative weights observed, in the lower pad, in the tail of the distributions for the FINAL setup plays a minor role in the dilution factor, as it can be seen from the difference in the middle pad between the analytic enhanced setup and the LEGACY one. The lower pad highlights also the reduction of negative weights obtained in the low p_{T} regime thanks to the improved parton shower model discussed in Section 6.1.3. Differences between the two FINAL setups in the tail of the $p_{\mathrm{T}}(V)$ distribution of f_{nw} are due to statistical fluctuations of the differential enhanced sample.

The performance of the three discussed setups can be further assessed by evaluating the equivalent luminosity corresponding to each of these. This quantity is

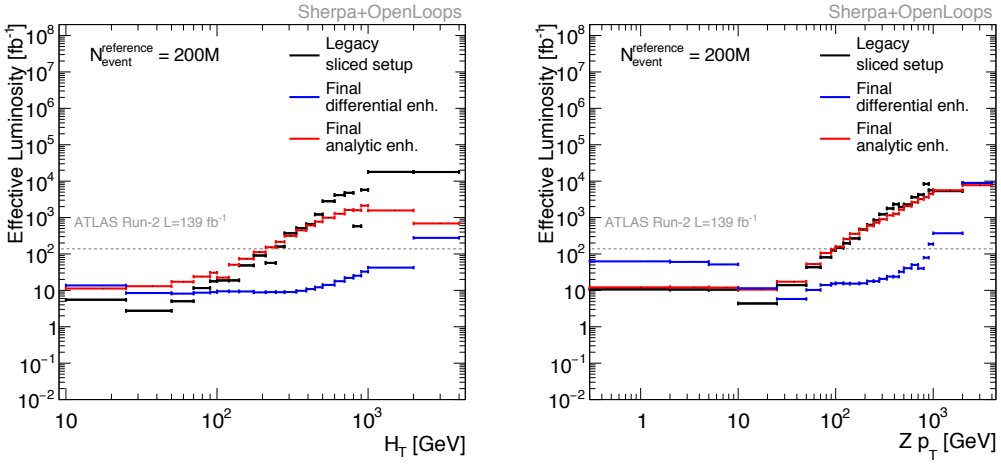
defined as

$$\mathcal{L}(x) = \sum_b \frac{N(x)_{b,\text{eff}}}{d\sigma_b/dx}, \tag{6.10}$$

where x is an observable with bins b, and $d\sigma_b/dx$ is the differential cross-section. $N(x)_{b,\text{eff}}$ is the effective number of events in the bin b, defined as

$$N(x)_{b,\text{eff}} = \left(\sum_i w_i\right)^2 / \sum_i w_i^2, \tag{6.11}$$

where w_i is the weight of the i-th event. A comparison of the LEGACY setup and the FINAL, generated with both the differential and analytic enhancement of the cross-section, is shown in Figure 6.18 as a function of the particle-level H_T and $p_T(Z)$ for $Z(\to e^-e^+)$+jets events. The comparison is performed here for a benchmark of $2 \cdot 10^8$ raw events. Again, to perform a fair comparison between the sliced and continuous enhanced sample, the sum of all slices of the LEGACY setup is normalized to such value.



(a) (b)

Figure 6.18. Comparison of the equivalent luminosity corresponding to $2 \cdot 10^8$ raw events generated in the LEGACY, or FINAL setup using two different methods of cross-section biasing, as a function of particle-level (a) H_T and (b) $p_\text{T}(V)$. Credits to Matthew Gignac.

In the low H_T and $p_T(V)$ phase space, as already stated in this Chapter, the integrated luminosity of multijet merged setups is not enough to compete with data. Indeed, inclusive NLO samples are used by analyses interested in this regime. At around 100 GeV the collected data luminosity is matched by the LEGACY and the analytic enhanced setups, while the differential one is about one order of magnitude lower. However, the latter shows a larger equivalent luminosity in the low $p_T(V)$ phase space. In the tail of the distributions, all the three configurations exceed the data luminosity by at least one order of magnitude, with similar performance observed in the LEGACY and analytic enhanced setup. In the H_T distribution, the LEGACY sample presents localised dips in correspondence of the slices boundaries. These are not present when the cross-section is biased in a continuous way.

An interpretation of these plots in terms of the computing resources costs is presented in Ref. [244].

6.2.4 Mass enhancement for new physics searches

The FINAL setup described in previous sections is suitable for the majority of ATLAS physics analyses, and is usually referred to as the *bulk* sample. However, new physics searches might be interested in the tail of the $m_{\ell\ell}$ or m_W distributions. The LEGACY and FINAL setups do not provide enough coverage in the tail of such distribution. Indeed large dilution factors arise in this phase space because the generation of the events has been optimised for the H_{T} tail instead.

Phase-space biasing allows to go beyond such a limitation. Events have been generated with the analytic enhancement and the biasing function $e(\mathcal{O}) = (m_V/100\,\mathrm{GeV})^2$, with a cut $m_{\ell\ell} > 120\,\mathrm{GeV}$ applied at matrix-element-level. This sample can be then combined with the *bulk* one after the removal of the overlapping phase space. This is resolved by applying a cut on $m_{\ell\ell}$ evaluated using matrix-element-level leptons. The statistical power of this new configuration is compared to the FINAL setup in an inclusive $Z(\to \mu^-\mu^+)$+jets sample in Figure 6.19.

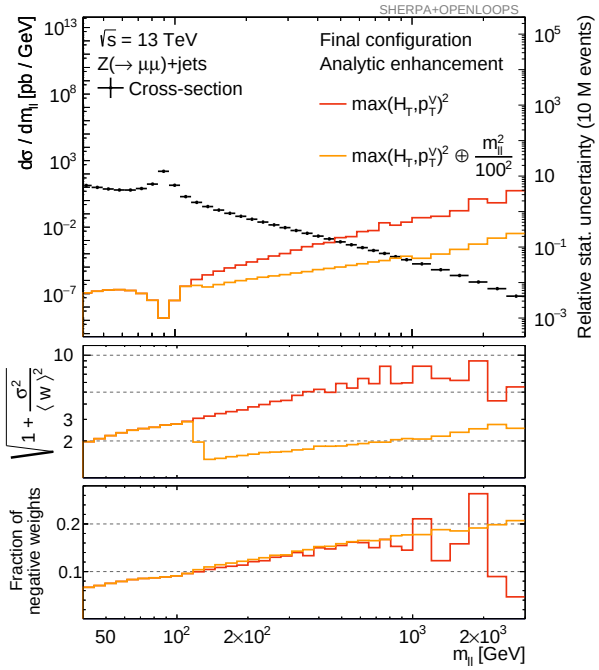
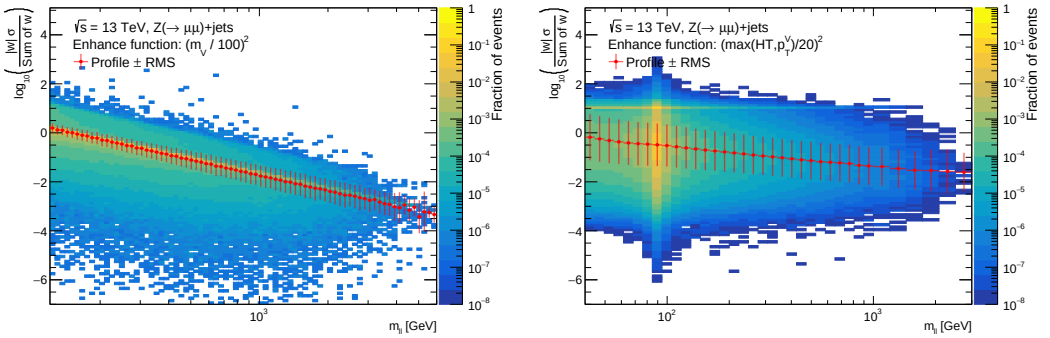


Figure 6.19. Comparison of the statistical power achieved in the FINAL configuration between the *bulk* sample, generated using the analytic enhancement and the $(\max(H_{\mathrm{T}}, p_{\mathrm{T}}(V))/20\,\mathrm{GeV})^2$ biasing function, and one sample with dedicated mass enhancement. The comparison is done for a $Z(\to \mu^-\mu^+)$+jets sample as a function of particle-level $m_{\ell\ell}$.

As it can be seen from the black points, the cross-section rapidly falls in the off-shell regime. The adoption of the analytic enhancement method with the mass as

observable allows to probe such low values of the cross-section, and to significantly reduce the statistical uncertainty of the resulting ensemble of events. Around the threshold where the mass enhanced sample is merged with the *bulk* one the dilution factor is indeed halved. The fraction of negative weights is the same in the two setups since they are both based on the FINAL SHERPA 2.2.11 configuration.

The action of the biasing procedure on the mass distribution is clearly visible in the weights distributions presented in Figures 6.20(a) and 6.20(b) for the mass enhanced sample and the *bulk* sample, respectively. The latter one is cut at $m_{\ell\ell} = 120\,\text{GeV}$ due to the presence of the matrix-element-level filter.



(a) $e(\mathcal{O}) = (m_{\ell\ell}/20\,\text{GeV})^2$ (b) $e(\mathcal{O}) = (\max(H_\text{T}, p_\text{T}(V))/20\,\text{GeV})^2$

Figure 6.20. Normalized distribution of the logarithm of the absolute value of event weights, scaled by the cross-section and the total sum of event weights, as a function of the particle-level $m_{\ell\ell}$, obtained in a $Z(\to \mu^-\mu^+)$+jets sample generated with the FINAL SHERPA 2.2.11 configuration using the analytic enhancement with different functions.

A significant reduction in the spread of the event weights is observed in the sample generated biasing the cross-section by a $m_{\ell\ell}$ based function. Since more events are generated in the high $m_{\ell\ell}$ phase space in the latter setup, their weights is smaller in magnitude. Figure 6.20(b) shows instead how for the *bulk* sample most of the events are generated around the Z peak, and that the high $m_{\ell\ell}$ tail is sampled following the cross-section. Therefore, only an almost negligible fraction of the total events is included in this extreme phase-space.

These results highlights the high flexibility of the cross-section biasing method also for the generation of V+jets processes. In future, such a method could be used to provide theoretical predictions in corner of the phase space, which are largely expensive in terms of CPU requirements for sliced setups.

Chapter 7

Conclusions

In this thesis, the nature of dark matter and of the Higgs boson were investigated by studying pp collisions produced by the LHC at $\sqrt{s} = 13\,\text{TeV}$ and recorded by the ATLAS experiment between 2015 and 2018.

Monojet final states are the golden channel to search for the production of DM particles at the LHC, because the latter are assumed not to interact with the ATLAS detector and therefore lead to unbalanced final states. The monojet analysis targets final states with at least one energetic jet of $p_{\text{T}} > 150\,\text{GeV}$ recoiling against a large amount of missing transverse momentum. A semi-data-driven technique based on statistically-independent control regions to correct the SM prediction of irreducible and reducible background processes is applied, allowing to constrain both the modelling and the detector-related systematic uncertainties affecting the SM background predictions.

Compared to the previous iteration of the analysis [180], which was performed using only part of the LHC Run 2 data set, the analysis presented in this thesis was performed with an integrated luminosity of $139\,\text{fb}^{-1}$. The monojet analysis shown in this thesis was published in Phys. Rev. D 103 (2021) 112006.

To further improve the sensitivity of the analysis to new physics phenomena, especially those predicted to have a softer $E_{\text{T}}^{\text{miss}}$ spectrum compared to the SM background, the $E_{\text{T}}^{\text{miss}}$ and leading jet p_{T} threshold values were lowered from 250 GeV to 200 GeV and 150 GeV, respectively. The p_{T} thresholds for identifying leptons in the final states were also lowered from 20 GeV to 7 GeV. Combined with the introduction of a τ_{had} veto, this allows to reduce the background of W+jets events in the SR between 10% and 40%, depending on the leptonic decay considered.

The definition of the top-quark processes enriched control region was extended to include final states with one electron plus b-jets final states, increasing the available statistics by 30%. In addition, a CR enriched in two-electron plus jets events was introduced, which increases the data statistics of the $Z(\to \ell\ell)$+jets CRs by about 40%.

The V+jets MC predictions have been reweighted using updated NNLO QCD and NLO EW predictions [167] that provide a set of systematic uncertainties to account for the effects of missing higher orders and differences between the W+jets and Z+jets processes. These allow the use of highly statistical W+jets CRs, in addition to Z+jets ones, to estimate the irreducible $Z(\to \nu\bar{\nu})$+jets process.

Together with the updated reconstruction algorithms, all these improvements lead to a significant improvement in the background prediction estimate known with an uncertainty of $\sim 1.2 \div 4\%$. These result were used to establish model-independent limits on the visible cross-section and model-dependent limits for models providing a WIMP DM candidate. The results presented in this thesis improved the range of excluded parameters of simplified dark matter models by about 30% when a vector or an axial-vector mediator is considered. For the first time, the ATLAS monojet analysis was also able to constrain the parameters of simplified models introducing a pseudo-scalar mediator, follow the recommendations of the LHC DM working group. The results on simplified dark matter models have been reformulated as limits on the scattering cross-section between WIMPs and nucleons and on the annihilation rate of WIMPs in pairs of SM particles. A comparison with the state of the art results provided by both direct- and indirect-detection searches for WIMP DM was performed. The reach on compressed SUSY scenarios have been further extended by this analysis: the constraints on the mass of light-squarks have been extended by more than 50%, while the range of the sbottom- and stop-quark mass values, also in the compressed scenario, has been extended by about 25%.

For the first time, the ATLAS monojet analysis probed the properties of the Higgs boson by targeting its invisible decays. An upper limit on the invisible branching fraction of 34% was set at 95% CL. This result is the third most stringent one provided by a single analysis of the ATLAS collaboration and will be included in a Legacy Run 1 + Run 2 combination. In addition, this is the first time the monojet analysis has examined scenarios for long-lived particles. Complementary results for scenarios involving LLPs production in Higgs boson decays were provided: within the FRVZ model, current constraints on the dark-photon mean proper life-times ($c\tau$) have been extended for values above 1 m. Simplified models in which a new scalar particle s is produced were also investigated, and current limits were extended for life-times larger than ~ 10 m. These results have been documented in an ATLAS public note, ATL-PHYS-PUB-2021-020.

Jet plus $E_{\mathrm{T}}^{\mathrm{miss}}$ final states can also be used to study the nature of the Higgs boson. In particular, to study the dominant Higgs boson decay mode $H(\to b\bar{b})$, the associated production with a leptonically-decaying vector boson can be targeted. The state of the art has explored both regimes in which the Higgs boson decay products appear as resolved in the final states [42] or as a single-jet of large radius [208]. A first combination of the two regimes was recently published [218], but it is based on a simple merge of the two analyses with a fixed cut at $p_{\mathrm{T}}(V) = 400$ GeV. In this thesis, studies on the optimal combination of the two regimes have been reported, and a possible increase of up to $\sim 20\%$ of sensitivity in the $250\,\mathrm{GeV} < E_{\mathrm{T}}^{\mathrm{miss}} < 400\,\mathrm{GeV}$ range is presented by adopting a priority strategy which is not based exclusively on either one of the two experimental technique only. This will allow more accurate measurements of the VH production mode in the context of STXS framework.

Towards a Run 2 legacy $VH(b\bar{b})$ analysis, new developments in flavour tagging performance will help in improving the precision of the measurements made. The expected gain in c- and light-flavour jets has been illustrated and the performance of flavour tagging using particle-flow jets has been investigated. Some of these results were also documented in an ATLAS public note ATL-PHYS-PUB-2020-009.

To further reduce the statistical uncertainty of MC simulations in highly boosted environments, the truth tagging method plays a central role. Namely, it allows overcoming event generation constraints by keeping all simulated events but weighting them according to the corresponding probability that they contain one or more b-tagged jets. This method is based on two-dimensional efficiency maps that parameterize the flavour tagging performance based on jet p_{T} and η. However, such a parameterization does not capture the proximity effects of boosted environments, since the efficiency maps are derived from isolated jets. We proposed a neural network approach to the truth tagging method in Comput.Softw.Big Sci. 5 (2021) 1, 14. A graph neural network is used to assign a weight to each jet, which takes into account the presence of other jets in the events and therefore is able to provide a good closure to the direct-tagging method even in boosted environments. This approach allows the truth tagging method to be used in the boosted $VH(b\bar{b})$ analysis as well. Therefore a reduction of one of the leading sources of uncertainty, namely the Monte Carlo statistical uncertainty, is expected in the legacy result.

A first fiducial differential cross-section measurement of the $H(b\bar{b})$+$E_{\mathrm{T}}^{\mathrm{miss}}$ process is also presented in this thesis. The results were obtained by reparameterizing the signal templates of the 0L channel of the published resolved $VH(b\bar{b})$ analysis [42]. The profile-likelihood unfolding method was used to extract from the m_{bb} distribution in different statistically-independent categories the fiducial cross-section in two ranges of particle-level $E_{\mathrm{T}}^{\mathrm{miss}}$, $[150, 250)$ GeV and $[250, +)$ GeV. In the first range, the statistical and systematic uncertainty contributions are approximately equal, while in the second range the statistical uncertainty dominates the precision of the measurement. The obtained results provide foundations for a more complete and refined work to be carried out in the context of a Run 2 legacy $VH(b\bar{b})$ analysis.

The leading irreducible background of both the analyses presented in this thesis is the $Z(\to \nu\bar{\nu})$+jets process, and in general large contributions are due to V+jets production. In the last part of this thesis I presented the implications of recent developments in the Sherpa MC generator on ATLAS analyses. In summary, virtual NLO EW corrections as on-the-fly weights, an improved parton shower model, updated HF decay tables and the availability of a new $4 + 5$ flavour-scheme merged calculations characterize the latest developments. All ATLAS analyses will benefit from these improvements, which are included in the ongoing mass production of events.

The simulation of V+jets processes also has a non-negligible impact on the computational resources available to the ATLAS collaboration. Therefore, the statistical power of the new samples has been studied in detail. In particular, it was found that the performance of a cross-section biasing via the *enhance observable* method available in latest versions of Sherpa is inadequate for the scheme intended for the mass production of V+jets events. An alternative method to bias the sampling cross-section, namely the *analytic enhancement* - available from version 2.2.11 of the Sherpa MC generator - was found to achieve a statistical power comparable to that obtained by slicing techniques. The analytical enhancement was finally chosen for the new generation of V+jets samples for the ATLAS collaboration.

Cross-section biasing is a powerful way to generate MC events in regions of phase space not adequately covered by the main sample. Z+jets events were generated

by biasing the cross-section as a function of the invariant mass of muon pairs. The statistical power of such a sample was compared to that of the bulk generation, and a significantly reduced dilution factor was observed. This result is a first example of what can be achieved when generating V+jets events with a biased cross-section. In future such an approach will open new possibilities for the search for new physics phenomena in extreme regions of phase space.

Part of the results presented in this final part of the thesis have been included in the paper arXiv:2112.09588, submitted to JHEP for publication, which documents the modelling and computational improvements to the simulation of V+jets processes for the ATLAS collaboration.

Appendix A

New Small Wheels for the upgrade of the ATLAS experiment

For the LHC Run 3 and Phase 2 the innermost stations of the end-cap of the ATLAS muon spectrometer (MS) which cover the $|\eta|$ range between 1.3 and 2.7, i.e. the *small wheels* described in Section 2.2.1, will be replaced by new detectors featuring different technologies.

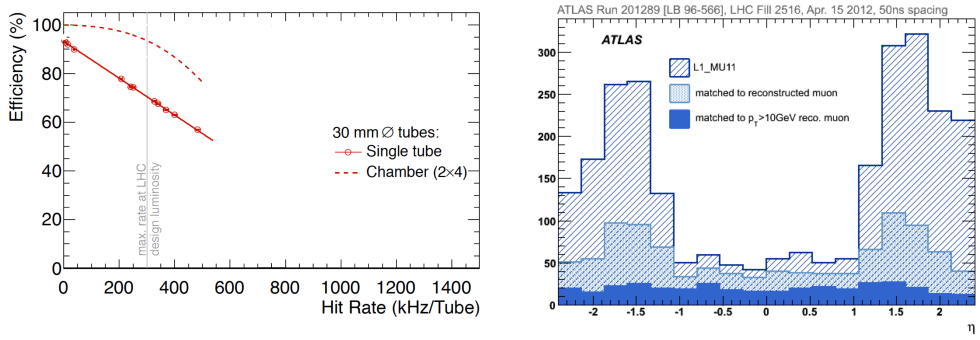
The development of innovative detectors to cope with the expected high rates of the upcoming runs of the LHC started more than 10 years ago, and resulted in the ATLAS New Small Wheels (NSW). The Italian institute of Nuclear Physics, INFN, was involved in this effort and has been responsible for the production of the tracking chambers, based on MicroMegas concept [245]. The ones built by INFN, referred to as SM1 modules, will be located closest to the beam-pipes. In the context of this effort, I participated to the validation of modules of MicroMegas detectors at the national laboratories of Frascati during 2019.

After an overview of the motivation for NSWs and of the featured systems presented in Section A.1, a description of the SM1 modules is provided in Section A.2. In Section A.3 a summary of the measurements performed to validate the SM1 modules are reported, along with the results of the data collected with a cosmic ray stand to quantify the reconstruction efficiency.

A.1 Motivation and system overview

During LHC Run 3 and Phase 2, the expected hit rates due to cavern background is expected to increase significantly. This has two impacts: first the tracking efficiency and resolution of the detectors decrease. In figure A.1(a) the efficiency of MDT detectors is shown as a function of the Hit Rate, as measured with test-beam data. A significant reduction is observed for the single tube, however the efficiency can be increased when considering multiple layers. Secondly, since the level-1 muon trigger in the forward region is on segments built from the hits in the middle and outer stations of the end-caps of the MS, higher background rates lead to an increase in the fake triggers due to low-energy particles which mimic muons pointing to the

interaction point. Such backgrounds is repsonsible for a trigger rate about 8 times larger in the end-caps than in the barrel of the muon spectrometer, and limit the ATLAS performance. Figure A.1(b) shows the distribution in η of the level-1 muon signals, as measured using a threshold of 11 GeV, and how this evolves after requiring the matching with a reconstructed muon ($\Delta R < 0.2$) and after requiring a muon p_{T} larger than 10 GeV. The number of final muons available is significantly reduced with respect to the initial ones, indicating the presence of a significant fraction of fakes.



(a) (b)

Figure A.1. (a) Degradation in the efficiency of reconstruction of hits in MDT chambers for increasing hit rate as measured in test-beam data.. (b) η distribution of level-1 muons requiring the L1_MU11 trigger to be fired, or after matching the hits with a reconstructed muon, as measured from 2012 ATLAS data. Figures from Ref.[246].

To cope with such problems, CSCs and MDT chambers will be replaced by small thin gap chambers (sTGCs) and MicroMegas chambers (MM). The former will provide, in addition to tracking, an additional information which can be used at trigger level to reject fake hits in the forward region. The latter detectors instead will be used for precision tracking. The choice of MicroMegas and sTGCs was based on two facts: gas detectors are used to cover in a limited expensive way a large portion of the space, and micro-pattern detectors in particular are suitable to cope with the high interaction rates expected.

A single NSW features 16 sectors, divided in 8 large (L) and 8 small (S) sectors with a small overlapping region, such that a full coverage of the along the ϕ direction is obtained. Modules of sTGC detectors and of MM detectors are organised in wedges. An sTGC wedge features three modules, referred in this appendix to as L/S1, 2 and 3, while a MM wedge features two modules, referred to as SM1 and SM2 in the small sectors, and LM1 and LM2 in the large sectors. The lower number is always referred to the module closer to the beam pipe. MicroMegas wedges are assembled together to form the so-called double wedges, which are then dressed externally by two sTGC wedges, as represented in Figure A.2.

As presented in next section, MM modules include each four detection layers; sTGC also feature multiple planes on which it is possible to record an hit. Such an high redundancy of the readout system, 16 detection planes, allows to keep the identification and reconstruction efficiencies high.

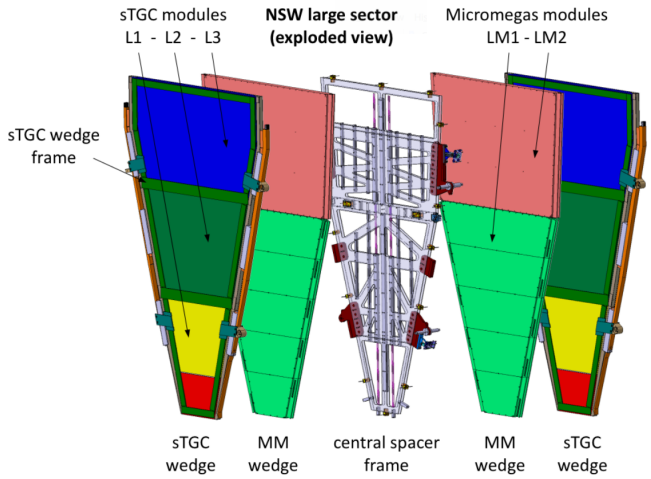


Figure A.2. Exploded view of a NSW sector, with highlights over the three modules which compose each sTGC wedge, and two MicroMegas modules which form a MM wedge. Figure adapted from Ref. [247].

The production of detector modules has been divided by several different communities participating to the ATLAS experiment. In particular, the Italian community was responsible for the construction, validation and transportation at CERN of 32 MicroMegas modules denoted SM1, i.e. the ones of the small sectors, located in the innermost radial part. Since my work focused on the validation of such modules, a description of the MicroMegas chambers is provided in the next Section.

A.2 SM1 modules of MicroMegas detectors

A representation of a single MicroMegas chamber is presented in Figure A.3. The active volume of the detector is formed by a $\sim 5\,\text{mm}$ gas gap, filled with an $Ar : CO_2$ gas mixture $(93 : 7)$. This volume, delimited by two electrodes, is divided in two by a metallic micromesh placed on top of isolating pillars with an height of about $130\,\mu\text{m}$. The wider part is called *conversion and drift gap* while the part between the micromesh and the electrode is called *amplification gap*. The micromesh is grounded, the drift electrode, located roughly $5\,\text{mm}$ from it is kept at $-300\,\text{V}$, while on the electrode located closer to the mesh a high voltage is applied. The optimal value for the MicroMegas adopted in ATLAS was found to be $570\,\text{V}$. Further details on this are provided later in this appendix.

The working principle of a MicroMegas chamber is the following. When a charged particle traverse the conversion gap, electrons are produced via the ionization of the gas mixture. These electrons are guided by an electric field of about $600\,\text{V/cm}$ towards the mesh. Once this is passed, the electrons enter in a region where an electric field of more than $40\,\text{kV/cm}$ is located. In the amplification gap, the interaction of the accelerated electrons with other gas molecules produce an avalanche such that the number of electrons is amplified of roughly 10^4. The presence of CO_2 in the gas mixture allows to absorb, via the excitation of rotational modes of the molecule, extra

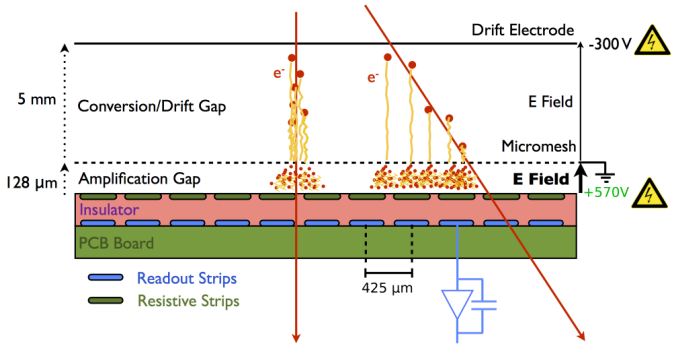


Figure A.3. Drawn of the working principle of a MicroMegas detector. Figure adapted from Ref. [248].

photons produced in the multiplication stage, which could lead to larger avalanches and damage the detector itself. The signal induced by the electrons is read out in a capacitive way by the readout strips characterised by a pitch of 425 µm, positioned under resistive ones, which are instead located in the actual chamber and to which the high voltage is applied. The two kind of strips are separated by an insulator.

Thanks to the small distance between this region and the metallic mesh, the ions produced in this avalanche are fast evacuated, and therefore the detector is able to cope with very high rates. The pitch of the detector instead allows for a fine measurement along the axis in which the strips are separated between each other.

SM1 modules

A schematic view of a MicroMegas module is presented in Figure A.4. The same setup is adopted for all the four type of chambers, SM1, SM2, LM1 LM2. The only difference between the four is the dimension of the active volume.

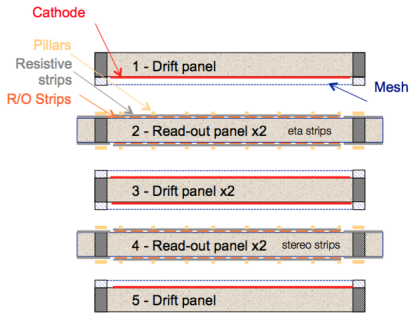


Figure A.4. Schematic view of a MicroMegas module as built for the ATLAS NSW. Figure adapted from Ref. [249].

Each module is formed by 4 gas gaps. At the edge of each one a readout printed circuit board is located. The four gas gaps are obtained from 3 drift panel, one referred to as *central*, and indicated with the number 3 in Figure A.4, and two outer. Two readout panels instead feature the pillars, the resistive strips and the readout strips. The panels are assembled together such that each of the gas gap corresponds

to the dimensions reported in Figure A.3.

Modules are shaped as trapezoids, as represented in Figure A.2, and each PCB of the read out sides is split in two along the basis of it. Furthermore, along the height of the trapezoid, the HV is supplied in 5 different sectors, such that for each of the readout layers 10 sectors are identified.

Two of the readout layers feature strips parallel to the basis of the trapezoid, while the other two feature strips tilted of $\pm 1.5°$ with respect to the bases. The former are called η-layers, while the latter are called stereo-layers. This choice was made because the main goal of the tracking of the detectors is to measure the η direction of muons, which is parallel to the height of the trapezoid. The ϕ coordinate can instead be recovered by a combination of the two stereo layers via simple trigonometric relations.

A schematic view of a muon travelling across an SM1 module is presented in Figure A.5, where the angle of the strips of the stereo layers has been highly exaggerated.

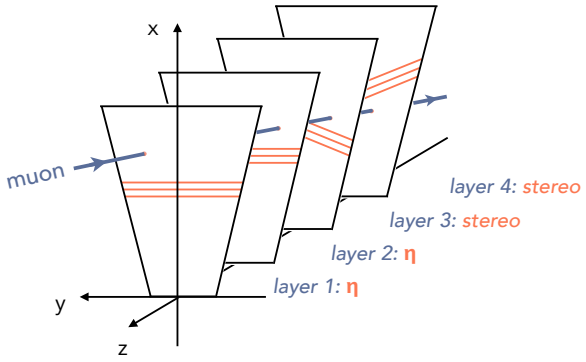


Figure A.5. Schematic view of the four layers of a MicroMegas quadruplet. The reference frame indicated is the one adopted in the studies at the cosmic ray stand, presented in Section A.3.2

.

A.3 Validation of SM1 modules at LNF

I joined for one year the effort at Laboratori Nazionali di Frascati (LNF) to validate the SM1 modules produced by the Italian community. I helped in the validation of 14 SM1 modules which are now installed on the NSW A, which has been lowered in the pit of the ATLAS experiment at CERN on the 12th of July 2021.

In Frascati several tests were performed before moving the MicroMegas quadruples to the Cosmic Ray Stand. In this context, I developed a summary document in which, for each validated chamber, all the validation measurements were collected. Such documents where included when the chambers were sent at CERN, such that the measurements performed there, before the assembly in wedges, could be repeated and compared.

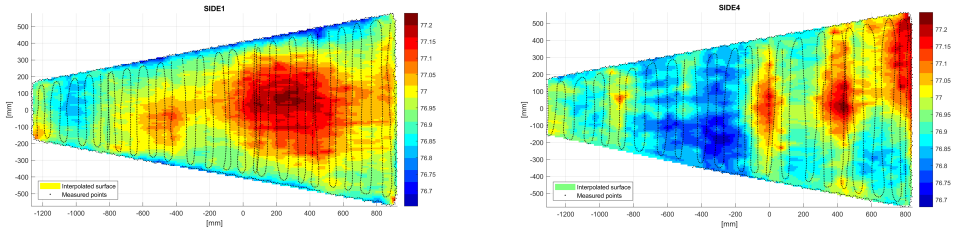
A.3.1 Preliminary checks

The first set of tests carried out concerned the construction stage of the MicroMegas quadruplets, with the aim to check that all the construction requirements were met. A second set of checks was performed on the stability of the high-voltage system, and the electronics noise.

Assembly checks

A map of the planarity of the modules was produced for the external layers, to check that deviations were within 80 µm, with values up to 200 µm tolerated. This measurement is performed on a granite table with a laser system which provides a set of measurements with respect of a reference point. From this, the maximum, minimum, RMS and average values of the thickness of the module are derived.

An example of such maps is presented in Figure A.6, as obtained for the SM1 M7 module.



(a) (b)

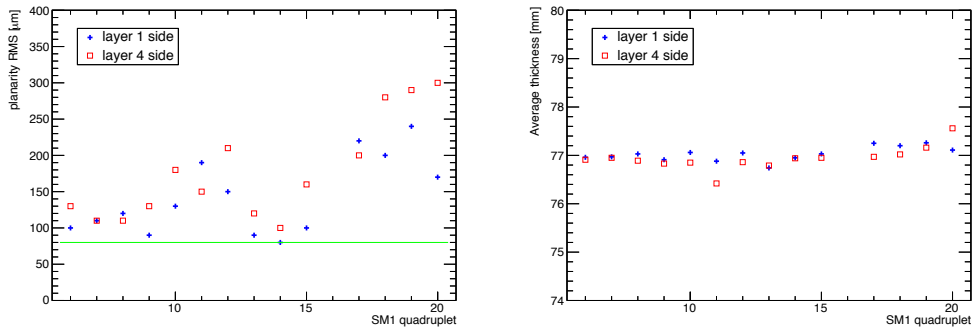
Figure A.6. Measurements of the height of SM1 M7 module with respect to the reference plane. Credits to LNF staff.

In Figure A.7 instead a summary of the values of the RMS of the planarity and the average thickness, measured for the modules which I validated, is presented.

The second assembly quality check is associated with the orientation of the various PCB among different layers. The displacement and rotational effects between η and stereo layers is measured via a so-called *rasfork mask*. Such a displacement is measured in 3 positions for each PCB, and a map, as reported in Figure A.8 in the case of SM1 M9, is produced for each quadruplet.

In general rotational effects induce a non zero value in the shift of a single side, while displacement effect lead to a sum of the displacements as measured in the two sides of each PCB which sums to a value different from zero.

The initial requirement on such a displacement was set to ± 60 µm, but was later relaxed. A summary of the values measured for the SM1 quadruplets M7 $\rightarrow$ M20 is presented in Figure A.9 for only the middle point of each PCB. Indeed, these are the most relevant points for the final geometry.



(a) (b)

Figure A.7. (a) RMS of the planarity and (b) average thickness of the two external layers with respect to the reference point, as measured for fourteen SM1 modules.

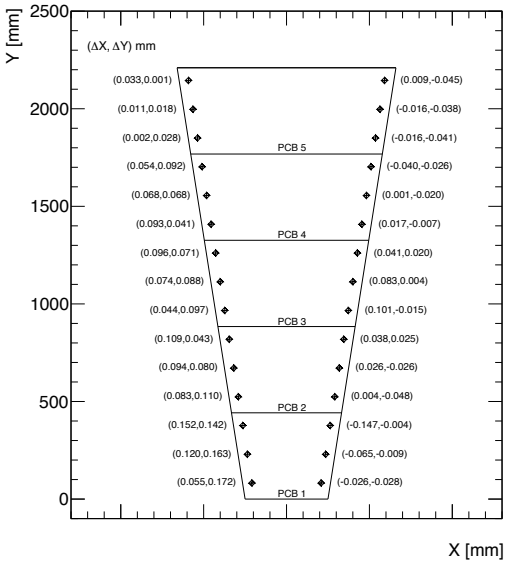


Figure A.8. Measurement of the displacement between the η-layers and the stereo-layers, as performed on SM1 M9.

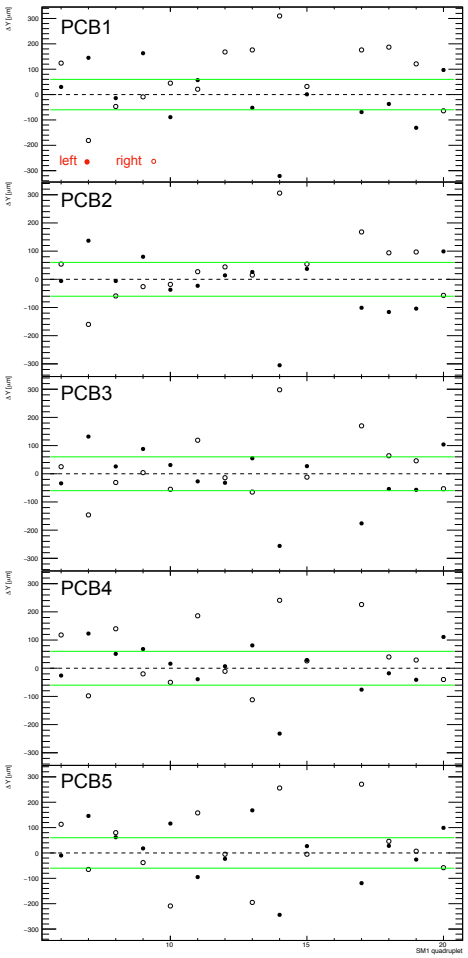
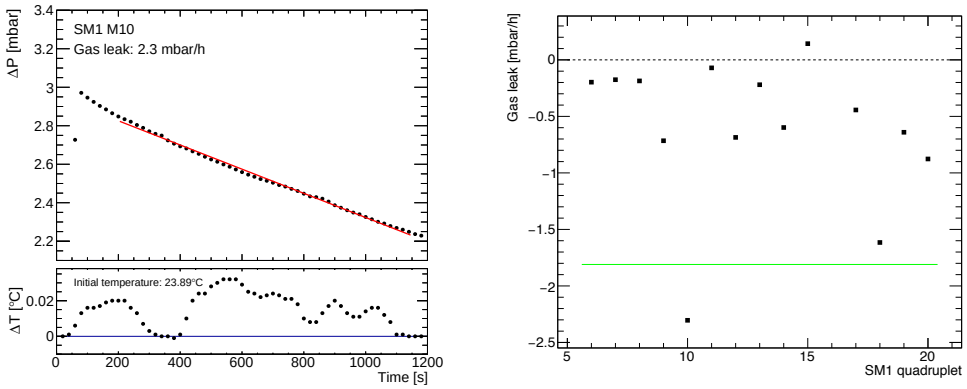


Figure A.9. Summary of the measurements of the displacement between the η-layers and stereo-layers, as measured from the middle point of each PCB, for SM1 quadruplets M7 $\rightarrow$ M20. The green lines represent the initial requirement on the maximum displacement.

The last assembly test carried out concerned the gas tightness of the chamber. Leaks might arise from issues which might arise during the assembly procedure. To test the gas tightness, the chamber is over-pressurised at about 3 millibar, and the pressure is monitored as a function of time. Via a linear fit to the distribution of the variation of the pressure versus time, it is possible to extract a loss of pressure per hour. During such a test, the environment temperature is monitored, such that it is possible to correlate eventual effects observed in the measurement.

An example of the measurement of the gas leak is presented for SM1 M10 in Figure A.10(a), while in Figure A.10(b) a summary of the measured values for SM1 M7 → M20 is presented.



(a) (b)

Figure A.10. (a) Measurement of the gas leak for SM1 M10. (b) Summary of the measured values of gas leaks for for SM1 quadruplets M7 → M20.

The initial requirement from the ATLAS collaboration was set to loss lower than 0.6 mbar/h, but then was moved to 1.8 mbar/h. Most of the values reported for the modules reported in this appendix are within the requirements. SM1 M15 showed the bizzare thing that the pressure was increasing during the measurement. This was tracked down to temperature effects, and the measurement was reproduced, but not reported on this plot.

High-voltage stability tests

As already mentioned in Section A.2, MM chambers are operated in the ATLAS experiment with an high voltage of the readout layer of 570 V. Eventual sparks or trips of high-voltage channels can lead to a reduced performance of the detector, thus is important to monitor the high-voltage modules which provide the power to the detector. Two parameters are monitored versus time, the current IMON, and the voltage VMON. Noise in the detector can lead to an increase current flow, which is usually localised in time, thus referred to as sparks. Values greater than 50 nA can damage the detector and lead to reduced performance, therefore it is important to monitor the number of time the current is above such threshold. Module trips instead are associated to a drop in the VMON value. An example of the monitoring

of these quantities is reported in Figure A.11. For each SM1 quadruplet, there are a total of 40 plots like this, one for each PCB of each layer (10 PCB × 4 layers). From such plots it is possible to identify issues with particular locations of the detector and correlate these with observed reduced efficiencies.

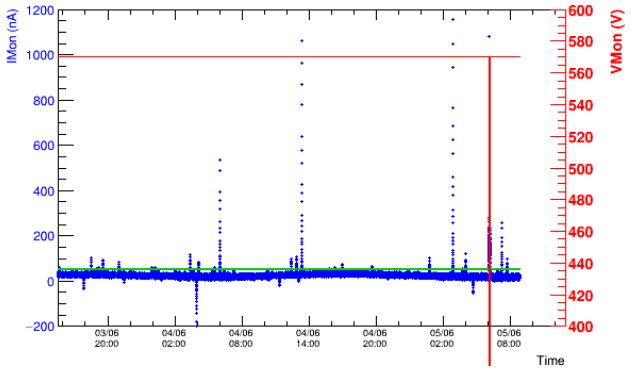


Figure A.11. High voltage (HV) stability monitoring for one example sector of SM1 M13. Sparks are defined for the cases in which IMON is above the threshold of 50 nA, while one trip of the HV channel can be seen, identified by the drop in VMON. The x-axis shows the time. Credits to Chiara Arcangeletti.

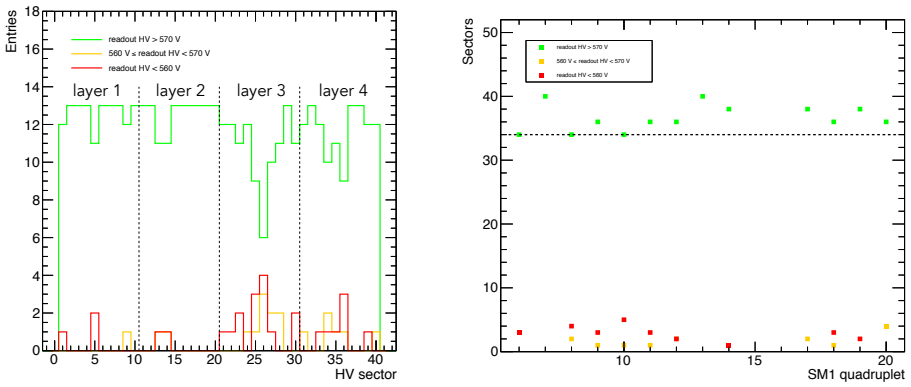
Not all the channels were able to reach the working voltage value. This was due to continuous sparks, especially for the stereo layer, as can be seen from Figure A.12(a), in which a summary of the readout HV values is shown as a function of the number of the HV sector. The layer 1 and 2 are the η ones, while 3 and 4 are the stereo ones. The feature of layer 3 being most of the times a problematic one was tracked down to a possible issue in the design of the PCB which might occur in some industrial production. To cope with this, a procedure to passivate part of the strips close to the border size of the PCB was developed, reducing significantly the issues with the HV stability. The requirement from the ATLAS collaboration was to have at least 85% of the sectors at the nominal working point tension value of 570 V. As can be seen in Figure A.12(b), this was achieved by all the tested modules. In both the figures presented SM1 M15 is not shown as it was tested with an alternative gas mixture.

Once the readout HV was declared stable, and the tension of the sectors not able to reach the nominal one were defined, it was possible to collect data at a cosmic ray stand and measure the identification efficiency.

A.3.2 Cosmic ray stand results

A picture of the cosmic ray stand of the Frascati National Laboratories were these modules were validated is presented in Figure A.13. Starting from the bottom part it is possible to see two set of plastic scintillators, separated by about 35 cm of iron, which allowed to absorb all the cosmic rays with roughly an energy below 600 MeV. In the top part of the slides it is possible to see one MicroMegas SM1 module.

Preliminary checks were carried out on the readout electronics to check whether it was correctly installed or not. To do so, data were collected with a random trigger,



(a) (b)

Figure A.12. High voltage readout summary plots for SM1 M7 → M20. M15 is not included as it was tested with a different gas mixture.

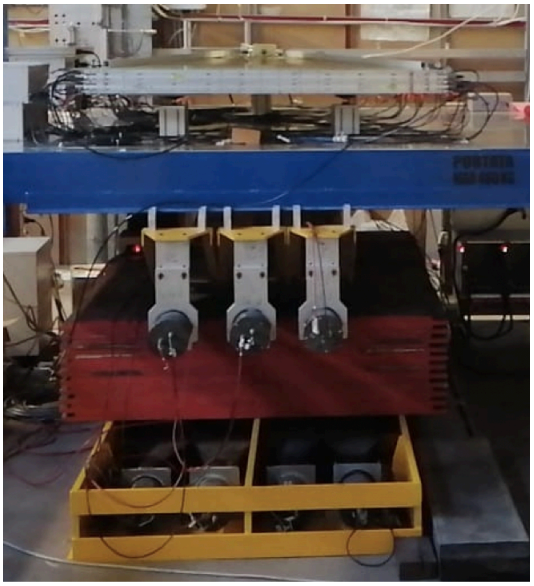
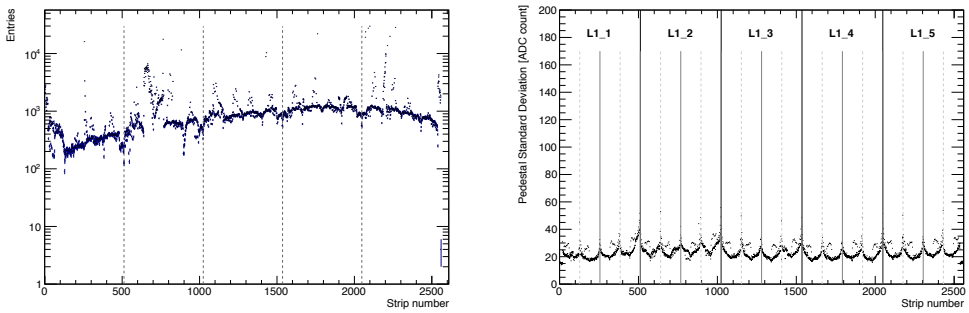


Figure A.13. Picture of the experimental setup at the cosmic ray stand of the national laboratories of Frascati (LNF). Credits to Giada Mancini.

and the occupancy of the strips, the mean value of the measured charges and the RMS of them were checked. One example distribution is presented for the occupancy of the strips in Figure A.14(a), while one example of the RMS of the pedestal charge is presented in Figure A.14(b). These distributions show on the horizontal axis the number of the strip, where 0 indicates the first strip from the side of the lower basis of the trapezoid. For each module, one distribution for each layer is obtained. All the distributions were included in the report form previously mentioned.



(a) (b)

Figure A.14. (a) Occupancy and (b) RMS of the pedestal of the collected charge, as a function of the strip number for the layer 1 (η-layer) of one of the tested SM1 modules. The vertical dashed lines on Figure (a) represent the separation point between different PCBs. This is indicated by a continuous black line in Figure (b), where instead the dashed line define the intervals corresponding to different readout electronic boards installed on the detector.

Efficiency measurements

Once the checks on the electronics installation were performed data were collected to measure the efficiency of the detectors. The trigger was performed by requiring a coincidence between the two plastic scintillators: the trigger rate was about 50 Hz.

To remove noise, only strips with at least 60 ADC counts where considered, and the charge deposit of a strip was required to be three times larger than the standard deviation of the measured value from the pedestal checks. To not take strips with saturated readout electronics, only strips with a charge below 2500 ADC counts were considered. Clusters were built by clustering adjacent strips. The charge of each cluster was required to be at least 100 ADC count. To not build clusters from strips with very low charge deposit, the strips in a cluster were required to be within 90 ADC count from the largest one. In a single cluster, two maximum non-consecutive holes, i.e. missing strips, were allowed. After a pre-selection of clusters, only the ones with at least two strips, and a charge above 400 ADC counts were considered.

Since no external tracker was available, to measure the efficiency of the detector a *self-tracking* method was used. The idea behind it is to use the information of an hit on three out of four layers to build a track, which was extrapolated to the fourth layer to look for an hit near to the expected one. In this extrapolation procedure, a maximum angle of 28° with respect to the vertical direction was allowed. Tracks with larger angles were rejected since out of the acceptance of the trigger system.

The main thing to check was the efficiency as a function of the x coordinate, defined in Figure A.5, as it is the η coordinate in the ATLAS experiment, direction in which muons are deflected for the effect of the magnetic field generated by the end-cap toroids. When testing one η-layer, the other is used in combination with a super-point built from the combination of the two stereo-layers to build the track, and a window of ± 10 mm was adopted to look for the presence of an hit on the tested layer. When instead testing a stereo-layer, the two hits on the η-layers are

used, and the hit on the other stereo one is used only to extrapolate the y direction.

The efficiency measured for all the layers of SM1 M7 is presented in Figure A.15, along with the weighted average value as evaluated on each PCB. This is done because each of these could be set at a different voltage if there were any issues with the spark rate or in general with the HV stability.

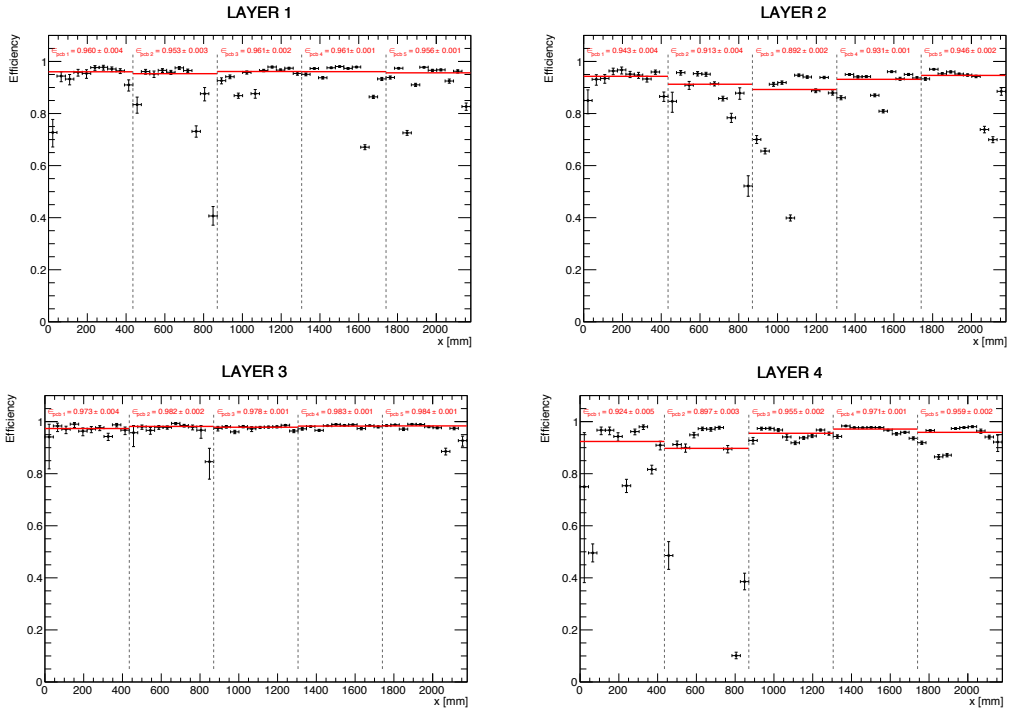
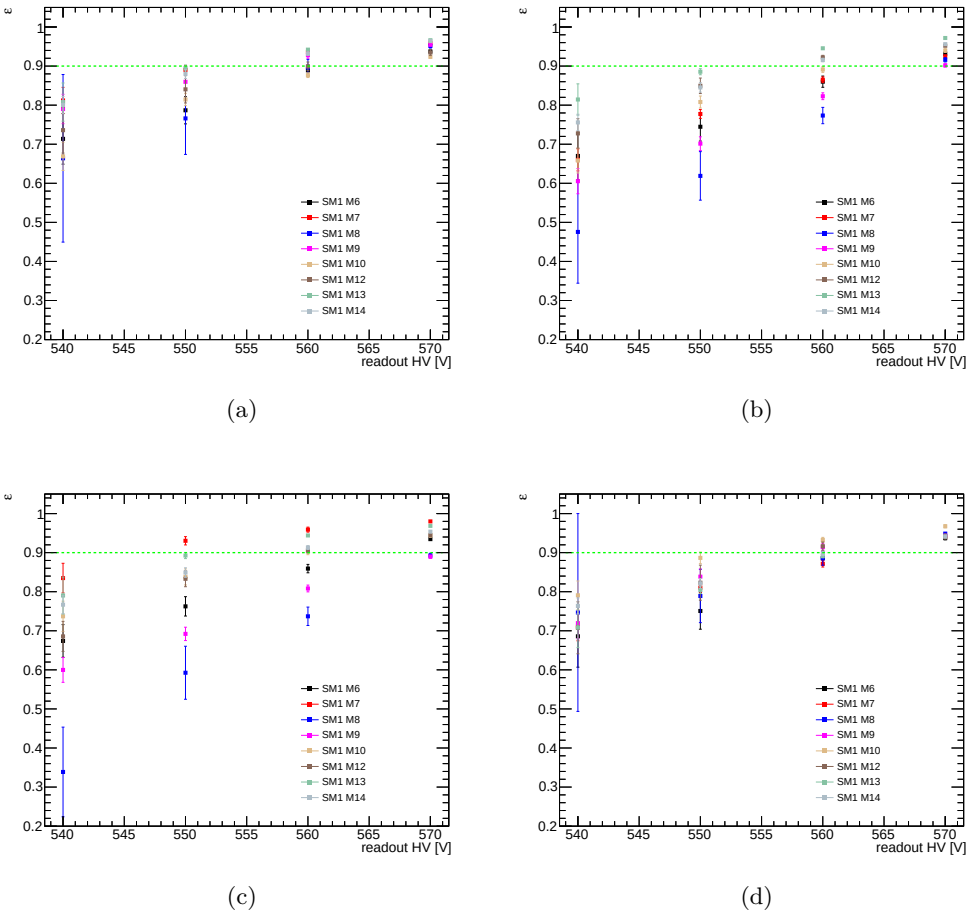


Figure A.15. Measured efficiency for SM1 M7 as a function of the x coordinate for all the layers. The weighted average of the efficiency of each PCB for each layer is reported in red within the figure. The error bars shown for each point indicate the statistical uncertainty. The dashed vertical line identify the separation between the different PCB.

High voltage scans

The performance of these detectors have been also tested, for some of the SM1 quadruplets, as a function of the readout HV value. In Figure A.16, a summary of the mean efficiency of each layer is presented. This is evaluated as the mean over the PCB of each layer, and a maximum of three PCB per chamber could be excluded. The required efficiency value from the ATLAS collaboration was of at least 90% at the nominal working value of 570 V. In general similar performance are observed for the various tested quadruplets.



(a) (b)

(c) (d)

Figure A.16. Mean efficiency shown as a function of the readout HV value for several tested SM1 MM quadruplets. The green line corresponds to an efficiency value of 90%, minimum value to be reached at the nominal working HV value of 570 V. The error bars indicate the statistical uncertainty.

Appendix B

Popular scientific description

In this Appendix you will find a popular scientific description of my thesis. The idea for such an appendix is not mine, I took it from the PhD thesis of Trine Poulsen [250], a physicist working on the same experiment I do, a thesis in which I accidentally stumbled into while browsing technical material. This part is mainly intended for my family and my non-physicist friends, and is generally aimed at piquing the curiosity of readers who are not experts.

General context

My work is embedded in the context of high-energy physics, which aims to investigate the fundamental properties of the Universe in which we all live. For hundreds or even thousands of years, people have been making observations, theorising to explain measured phenomena, and building experiments to reproduce them.

Particle physics is a fairly young field that has developed rapidly in the last century. In the beginning, experiments were based only on radioactive materials or cosmic rays. These are high-energy particles that travel in the universe and pass through the Earth every second, including you who are reading this, and interact only weakly, so special detectors are needed to observe them. Physicists have succeeded to reproduce the particles observed in the cosmic rays in laboratories, and making them collide such that their interactions can be studied.

The concept of the collision of particles and the creation of new particles through their interaction is by no means trivial. Its first formulation goes back to Albert Einstein's famous equation, $E = mc^2$, which basically says that all objects with non-zero mass have intrinsic energy associated with their mass. Thus, when high-energy particles are made to collide, the available energy can be used to create new particles that are even heavier than the colliding particles, and, again, their properties and interactions can be studied.

Fundamental interactions and elementary particles

From the various experiments briefly mentioned, people have come to understand that the things we deal with every day are basically made up of three particles: the proton, the neutron, and the electron. However, the proton and the neutron are

not fundamental particles, because it is possible to break them and see that they are made of a sea of *quarks*. Quarks instead appear as the smallest components of what we touch every day, but it is not possible to observe them alone. The strong force acts between two quarks as a rubber band: if you try to take them apart, the force will tend to recall them together. At some point, what happens is that a similar pair of quarks is created. In the rubber band example, this would mean that you do not manage to separate the two extrema of it, but instead a new copy of it, not stretched, is created. This strange property is associated with the *strong force*, one of the four known fundamental forces of nature. This force enables us and most non-point things to exist because it binds protons and neutrons through the continuous exchange of particles called *gluons*, which are called the *mediators* of the fundamental force. Thanks to them, protons and neutrons are bound in heavier nuclei that basically form everything you can see.

Protons and electrons have a common intrinsic property: they carry a non-zero electric charge. Because of this, they can also 'talk' to each other via *electromagnetic interactions*, another fundamental force. These electromagnetic interactions are also responsible for you being able to read this appendix. In fact, at this moment there is a stream of fundamental particles called *photons*, the mediators of the electromagnetic interaction or simply the constituents of light, travelling from your screen (or paper) to your eyes and interacting with them via the electromagnetic force. These particles carry the information about the presence of tiny black characters that our brain can convert into thoughts through extremely complex phenomena.

Neutrons, as mentioned earlier, are an important component of atomic nuclei because they help protons hold together through strong interactions; otherwise, the protons would repel each other due to the electromagnetic forces just mentioned. Neutrons, however, are distinguished by the bizarre fact that when not bound in nuclei, they tend to decay within about 15 minutes in most cases. This phenomenon is due to the third known fundamental interaction, the *weak force* that converts free neutrons into a proton, an electron, and another fundamental particle, the *neutrino*. The name of this force is derived from the fact that it is characterised by the lowest intensity among the three mentioned. Even if you have not heard about it before, this force is responsible for our Sun to be shining, since decays as the one briefly mentioned are key processes in complex nuclear reactions happening in the Sun right now.

The last fundamental force known to mankind is the gravitational force. It is responsible for the fact that we are currently on Earth and not flying aimlessly around the universe, as well as for the existence of large collections of matter, such as planets and stars. But while there is a fundamental particle that mediates the interactions for the other forces, hypothetical particles called *gravitons* have not yet been observed. For some physicists, gravity is not even a fundamental interaction, but rather a property of space-time itself. Such a description is truly fascinating, but beyond the scope of this thesis.

Most of the fundamental particles are characterized by a non-zero mass value. However, it is impossible to write a theory that includes such a property and at the same time presupposes that the observed physical phenomena are independent of the people measuring them. For this reason, the Standard Model includes what is known as the Brout-Englert-Higgs mechanism. This describes why particles have

mass, which is acquired via an interaction with a field which permeates all the Universe (a sort of magnetic field with which you might be more familiar, but with different characteristics). Furthermore, the Brout-Englert-Higgs mechanism predicts the existence of a particle, the famous Higgs boson. This particle is unique in the Standard Model as the strength of its interaction with other particles depends on the mass of the latter. As part of my thesis, I also investigated some of the properties of the Higgs boson, which I discuss in more detail later in this appendix.

The Standard Model of particle physics is an extremely successful theory that describes all known fundamental interactions except gravity. Physicists have been able to predict hundreds of interaction probabilities between fundamental particles that are now even measured to the precision of the percent. Is it all over then? No.

In fact, there are still many open questions to be answered, and most of them are raised by experimental observations. In my doctoral thesis I tried to answer one of these open questions: the nature of so-called *dark matter*.

The mystery of dark matter

For the last hundred years or so, astrophysicists have been looking up at the sky and noticing that there is something strange going on in the Universe. The motion of many systems like stars or even some galaxies is not consistent with what you would expect from gravitational interactions with the objects that we can observe from Earth. There must be something more which we cannot see via any kind of light, therefore this is called *dark matter*. We know that dark matter is there, and we can see only indirectly its effects, but we do not really understand its nature yet. Nowadays there are multiple evidences for the existence of dark matter and even quantitative estimates that lead to the conclusion that all we can see and understand is only 5% of the total energy content of the observed Universe. Pretty scary, isn't it?

Experiments have been able to rule out the possibility that the dark matter is made up of large planets or stars of matter, which are so cold that they do not emit light at all, so it is likely that dark matter is composed by particles. However, the intensity of the interactions of such particles with the ordinary particles we know should be very low (otherwise we would have seen an evidence of them already). You need to imagine that the Milky Way, the galaxy in which our planet is located, is immersed in a halo of dark matter particles through which we travel together with the Sun and its tiny planets with some velocity, so you would expect a sort of wind of dark matter particles coming towards us.

To search for these dark matter particles, physicists have developed three main types of experiments. Direct detection experiments try to find the rare recoil of known particles forming the target particles due to their interactions with dark matter ones. For this reason, it is imperative to reduce as much as possible the radioactivity of the materials used to build the detectors (everything is radioactive, also you!), and the interactions of the cosmic rays. For these reasons, these experiments are very complex and are located under very large mountains, such as the Gran Sasso in Italy, as they can act as a shield against these rays. Another way to look for these dark matter particles is to hypothesise that sometimes they interact with each other in particular regions of the Universe and produce an excess of Standard

Model particles that we can measure either with special telescopes or with detectors installed on orbiting satellites. The last way to investigate the nature of dark matter is the approach I took in my thesis: using particle accelerators. The hypothesis we rely on is that it is possible to create unknown particles in high-energy collisions. Dark matter would then leave our experiment undetected because it interacts with a very low probability with normal matter.

The Large Hadron Collider

The research I reported in my thesis was possible thanks to collisions between protons accelerated in the Large Hadron Collider. This is the largest particle accelerator ever built by humans, and it is about a circle 27 km long. However, such a large distance however is travelled more than 11000 times per second by the protons accelerated in it, as they travel at about 0.9999 times the speed of light[1].

The protons are accelerated to the highest technically achievable energy, which for the data used in this thesis is $6.5 \cdot 1\,000\,000\,000\,000$ electronvolts, and are brought into collisions head-on. Contrary to what most people think, or at least what I thought a few years ago, the colliding beams are not a continuous stream of particles, but many *sausages* of protons organised into what are called *bunches*. Each of these bunches contains about 100 billion protons in a cylinder as long as 30 centimeters, and less thick than a single hair, about 0.00 000 4 meters. The protons are packed by extremely high magnetic fields, and kept on a circular orbit in the LHC with a time separation of 0.0 000 000 25 seconds in two opposite directions, such that they can collide in the middle of the experiments. To put things in perspective, a bunch of protons travelling under the mentioned above conditions has as much energy as a 10-carriage railway train traveling 320 kilometers per hour (source Parking the LHC proton train by Zack Savitsky, posted on Symmetry magazine on 17/09/2020). With that much energy, the LHC re-creates the conditions of the Big-Bang, i.e. the process hypothesised to be the origin of the formation of our Universe.

The ATLAS experiment

The ATLAS Collaboration, of which I am a member, is investigating such collisions with A Toroidal LHC ApparatuS, i.e. the ATLAS experiment. An overview of the ATLAS experiment is shown in Figure B.1. As you can see from the comparison with the drawn human beings, it is really huge. In fact, the ATLAS experiment is a cylinder 44 meters long and 24 meters high. To put things into perspective it is about as long as 13 Fiat Panda (2002 model), and as high as 17 of them.

Our experiment is usually associated to a big camera which takes pictures of the collisions happening in the middle of the cylinder. However, as you might need different lenses or lights to take photographs under different conditions, different detector technologies are needed to detect the presence of different particles. Most importantly, the experiment is built such that most of the particles produced in the collisions can be identified. This is central to my work (and in general to many ATLAS analyses), because if we want to look for the production of particles that do

[1] The speed of light is a value that cannot be reached by massive particles, such as the protons accelerated in the LHC.

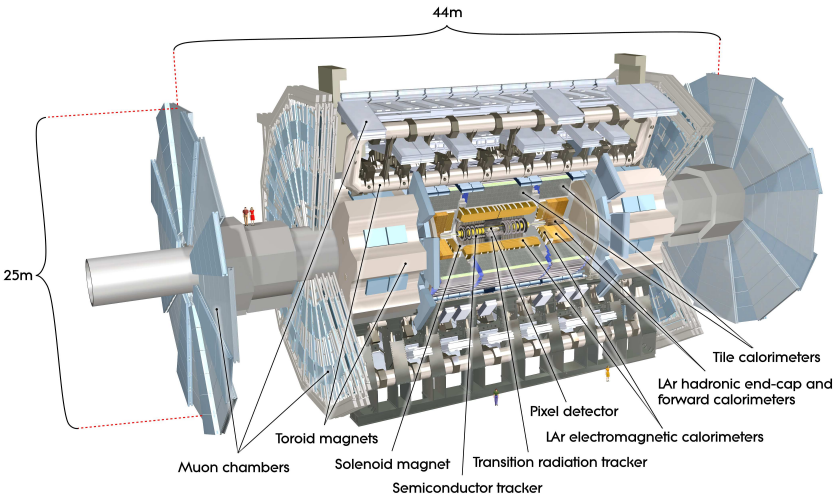


Figure B.1. Overview of the ATLAS experiment. Figure from Ref. [102].

not interact with the experiment, we want to be sure that we are seeing is everything we expect to see, i.e. ordinary particles.

The sub-detectors of the experiment are placed hierarchically with respect to the collision point, so it is possible to identify the point of the interaction between two protons via *tracking* detectors. The energy of all particles produced is measured by the so-called *calorimeters*, which absorb most of the outgoing particles by destroying them. Detectors located in the outer part of the experiment are used to measure *muons*. These are particles similar to electrons, but characterized by a larger mass and the fact that they lose only a small part of their energy when interacting with the detectors they meet along their flight path. Since charged particles moving in a magnetic field bend in proportion to their energy, there are magnetic fields in ATLAS located in different parts of the experiment and generated by many big coils powered by more than 20000 ampere. Even though the magnetic fields are more than ten thousand times stronger than those of the planet Earth itself, i.e. what makes compasses work, the very energetic muons produced in the collisions are only deflected by a few hundreds of microns. However, this is enough to measure their energy with an accuracy of one percent. All the reconstructed particles produced after the collisions, what we call the *final states* of the collisions, are then used to analyse the events.

Search for dark matter with jets and missing transverse momentum

Most of my research is based on a particular kind of final states of the collisions, which includes what is called the *missing transverse momentum*.

As mentioned earlier, the particles in the LHC experiments are collided head-on. This means that the protons only move in one direction, and therefore do not

move in the plane orthogonal to that direction[2]. If we then measure the transverse momentum of all the particles produced after a collision, we should find something pretty close to zero if no invisible particles are produced. We do not expect to measure exactly zero, since particle measurements are subject to some uncertainty and we cannot measure particles with energies below a certain threshold.

The point is that if we produce dark matter in the collision, we will not see it. So what could happen is that we collide the particles and see nothing in our detector. This is, of course, an idealization of collisions because, as mentioned in the section of this appendix on the LHC, multiple protons are accelerated together and can interact in a single crossing of the bunches. To tag these events, we can exploit a property of elementary particles, namely that they can convert some of their energy into the production of another particle.

This phenomenon, which may sound quite strange, is very common in particles with a non-zero electric charge. Indeed, when a charged particle is accelerated it emits electromagnetic radiation in the form of photons. Similarly, the components of the protons (the quarks) that actually interact with each other in collisions can also emit radiation. However, it is more likely that they emit the radiation associated with the strong force, i.e. the *gluons* mentioned earlier. Similar to the *quarks*, the gluons do not appear as free particles in our detector. Rather, they convert their energy into the production of many others particles, which end up appearing in our detectors as collimated sprays called *jets*.

Due to the conservation of momentum in the transverse plane, such a jet recoils in the opposite direction of the missing transverse momentum of the invisible particles, resulting in a striking signature often referred to as *monojet*. An example of what such an event looks like in the ATLAS experiment is shown in Figure B.2.

We have found many such events in the proton-proton collisions we have studied, but this does not mean that we have found dark matter. In fact, there are several other physics processes that can lead to the same final state signature. Our goal is to compare the state-of-the-art theoretical predictions with the observed data and to understand whether or not there is a significant excess of them. To look for such an excess, we do not simply count the events, but we count the events in different range of the values of the missing transverse momentum. This increases the sensitivity to dark matter and other new phenomena.

To achieve this, I have spent a lot of time trying to understand the sources of uncertainty in the predictions from theoretical physicists that we then compare to the data. In practice, theoretical physicists produce theories which describe how our Universe works, make calculations and tells us what we can measure. At that point, we experimental physicists verify these predictions. We perform measurements and compare with what the best predictions look like. Since these theoretical calculations are really hard to compute with pen and paper, we need computer simulations which perform these calculations.

Everything in physics is about uncertainties, and especially systematical uncertainties, which are those due for example to how well we know the underlying physics

[2]What actually collide is not the protons, but rather their constituents, the partons, but we do not know exactly how much they move in the direction of the protons. In any case, they are (mostly) steady in the transverse plane.

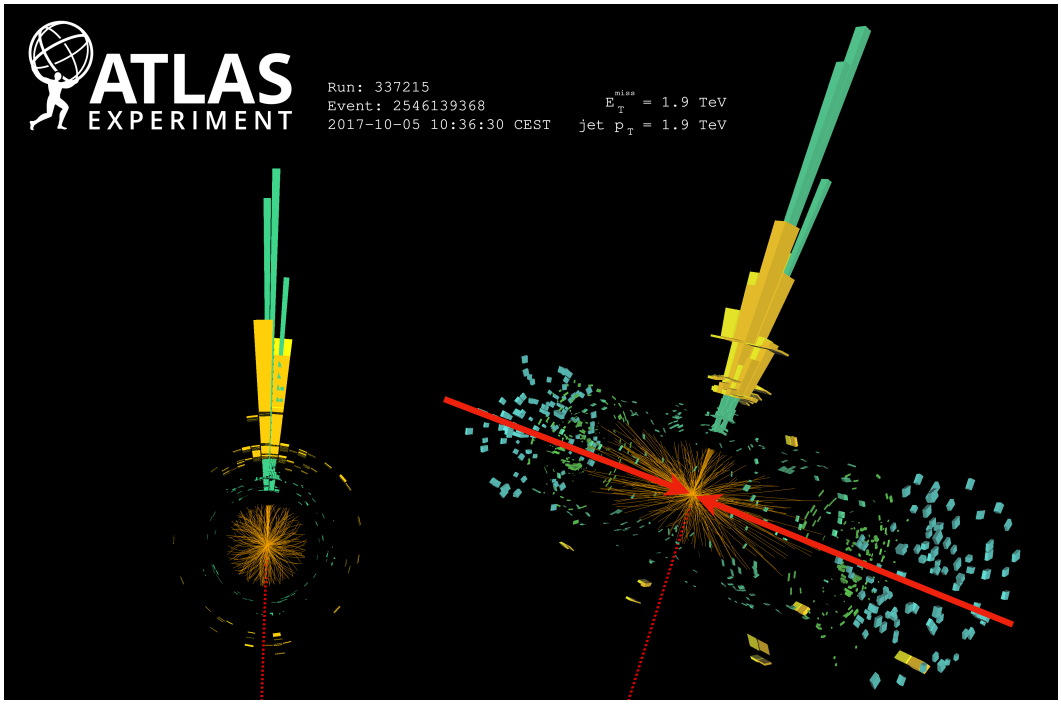


Figure B.2. A view of a monojet event is presented on the left part of the figure as it appears in the transverse plane, and on the right part from a view in which it is possible to see the direction of the colliding beams, indicated by the red arrows. This event was recorded by the ATLAS experiment during the 2017 data taking campaign. The length of the green and yellow bars is proportional to the energy deposits in the calorimeter cells associated with the jet produced in the interaction. Reconstructed tracks of charged particles measured with the innermost detector of the ATLAS experiment are represented by orange lines. The direction of missing transverse momentum is represented by the red dotted line. In the transverse plane view of the event it is possible to see how the direction of the missing transverse momentum is aligned with the energy deposits measured in the calorimeters. Figure adapted from the auxiliary material of Ref. [4].

behind these processes, and how well we can model with a computer the response of the various ATLAS sub-detectors.

The theoretical calculations are then corrected using statistically independent data selected differently from the data that might contain dark matter particles. I was responsible for this phase of the analysis in which the goal was to understand how well our predictions agree with data.

The main picture of this part of my thesis is shown in Figure B.3, where a comparison of the observed data with the expected number of events due to Standard Model processes is given.

Each of the filled regions, stacked above those below, represents the expected number of events for a given hypothesis on how protons and dark matter interact between protons that leads to the production of the particles indicated in the legend. The dashed lines represent the expected number of events from models which describe how protons and dark matter interact. In the lower part of the Figure, the ratio between the measured data and the total Standard Model predictions is

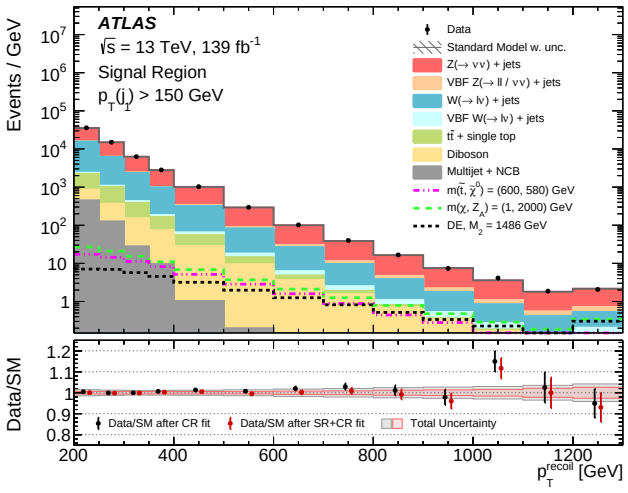


Figure B.3. Comparison of the measured missing transverse momentum distribution with the Standard Model predictions. More details on the figure are provided in the text. Figure from Ref.[4].

given. The black and red dots correspond to two different ways of answering the question "How much the data are in agreement with our background expectation?" which are described in detail in my thesis in Chapter 4. The coloured band in this part represents the uncertainty of the Standard Model predictions. It lies between one and four percent, an accuracy that is not usually achieved in searches for new physical phenomena.

No significant deviation from the background predictions, i.e. what we expect to see, is observed. Therefore, it is possible to compare the obtained result with different hypotheses of new physical phenomena using different theoretical models which depend on complicated physical parameters. In my thesis I have presented several different interpretations of the results, but many more derived by colleagues of mine will follow in the years. This is what I like about this analysis: once you have solid background predictions, the data can be interpreted in a wide range of new scenarios.

Higgs boson measurements in the $VH(\to b\bar{b})$ channel

As mentioned in the initial part of this appendix, the Higgs boson is truly a special particle in the Standard Model because it is characterized by unique properties that other particles do not have. Moreover, it was discovered only recently, in 2012, and its properties are still being studied. It is even possible that Higgs boson decays can produce dark matter particles.

The Higgs boson is not a stable particle, and when it is produced it immediately decays into lighter particles that can be used to reconstruct the so-called *Higgs boson candidates*. For example, it is possible to reconstruct the mass of the decaying particle, whose distribution tends to peak around the mass of the Higgs boson. By measuring the number of signal Higgs boson events we see in data we can compare wit the theoretical calculation and see if they are in agreement with the experimental

results.

In my work, I have focused on the main decay mode of the Higgs boson, which consists of a pair of bottom quarks (b quarks), particles very similar to the main constituents of protons, but characterized by a larger mass. Since these particles have the feature that have a mass that is small enough so that the Higgs boson can decay into them[3] but high enough that the decay probability of the Higgs in two bottom quarks, via the process $H \to b + \bar{b}$, is the highest. Like the gluons, the b quarks also produce jets in the final states, but very special ones. Namely, these include some interesting particles that do not decay immediately after their creation, but instead travel several hundred microns away from the interaction point before they decay in turn into other particles. By identifying these particles, a process called b-tagging, it is possible to isolate Higgs boson candidates that have decayed via the $H \to bb$ process.

This process is very difficult to study at the LHC because many other Standard Model processes can mimic the signal we are looking for. However, it is possible to search for events very similar to the monojet one shown in Figure B.2, where another special particle of the Standard Model, a W or Z *vector boson*, often referred to as V, is produced together with the Higgs boson. In the transverse plane, the two particles lie back to back, and if one considers Z decays neutrinos (i.e. the process $Z \to \nu + \nu$), one again obtains a striking signature, and can more easily identify the events.

My work on this topic is embedded in a larger project of performing an analysis of the dataset collected between the years 2015 and 2018 by the ATLAS experiment, which will endure in the years to come as a legacy from this period (and conditions) of data taking. In this context, I have conducted several studies aimed at improving the sensitivity to the $H \to b\bar{b}$ signal.

For this long-lasting result, we propose a new way of analysing the data which was never used before for this process. It consists of providing a measurement of the interaction probability, a term we call *cross-section* in physics, in which the effect of having a detector of limited size and performance are removed as much as possible. This procedure is known as *unfolding*, and consists in removing from the data the effect of reconstructing the particles in the detector. This is a really powerful result because it can be immediately compared to theoretical predictions.

This result is obtained from a comparison of the distribution of the invariant masses of two b-jets observed in the data and in the simulation, after applying a specific event selection. One example distribution is shown in Figure B.4. Similarly to the monojet case, the different colors represent different Standard Model processes, and the signal we wanted to extract is shown at the top, near the 125 GeV value of the x-axis, value which corresponds to the mass of the Higgs boson candidates.

Next generation of W/Z+jets events simulations

A central component of many analyses of the ATLAS collaboration is the simulation of the physical process by which a W or Z boson is produced in association with

[3] Actually, particles cannot decay in particles whose sum of the mass is higher than the mass of the decaying one.

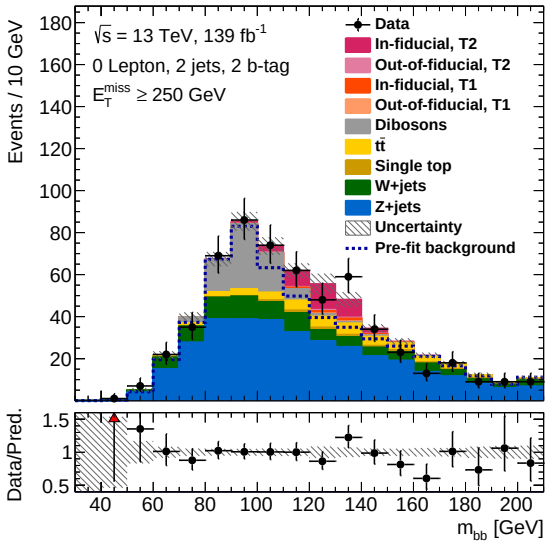


Figure B.4. Mass distribution of the Higgs boson candidates for one particular category of the events considered. More details on the figures are provided in the text and in Section 5.4 of Chapter 5.

jets. This is a process that can lead to the same final states of the sought signal in both the monojet and $VH(\to b\bar{b})$ analyses I have studied, and for this reason is also referred to as the *background process*, as opposed to the *signal process*.

In the last part of my thesis, I reported on the impact of improvements made to the simulations used for the main background process in the analyses I studied. In this chapter, I also reported on the studies I conducted to define a strategy for efficiently generating a large number of events. To quantify this a bit: for the next generation of simulated events, the collaboration plans to generate more than a billion simulated events for W/Z+jets processes. This is by no means trivial, as the ATLAS collaboration has a limited budget in terms of computational resources. Moreover, the simulation is performed in several steps. In one, the actual physical process is generated as it would occur in vacuum, and in a second step, the interaction with the ATLAS detectors is emulated. My work focuses on the first part. For more details, see Section 6.2 of the Chapter 6.2.4.

Final remarks

If you are reading this after having read even a small portion of this appendix and found it fascinating, I am happy, because this is exactly what I wanted. This appendix turned out much longer than I had originally planned, but a lot of things came to mind while I was writing it, and I found that I really enjoyed learning new things during my PhD.

Bibliography

[1] S. Weinberg. "A Model of Leptons". *Phys. Rev. Lett.* 19 (1967). DOI: 10.1103/PhysRevLett.19.1264.

[2] ATLAS Collaboration. "Observation of a new particle in the search for the Standard Model Higgs boson with the ATLAS detector at the LHC". *Phys. Lett. B* 716 (2012). DOI: 10.1016/j.physletb.2012.08.020. arXiv: 1207.7214 [hep-ex].

[3] CMS Collaboration. "Observation of a New Boson at a Mass of 125 GeV with the CMS Experiment at the LHC". *Phys. Lett. B* 716 (2012). DOI: 10.1016/j.physletb.2012.08.021. arXiv: 1207.7235 [hep-ex].

[4] ATLAS Collaboration. "Search for new phenomena in events with an energetic jet and missing transverse momentum in pp collisions at $\sqrt{s}$ =13 TeV with the ATLAS detector". *Phys. Rev. D* 103.11 (2021). DOI: 10.1103/PhysRevD.103.112006. arXiv: 2102.10874 [hep-ex].

[5] ATLAS Collaboration. "Constraining the Dark Sector with the monojet signature in the ATLAS experiment". ATL-PHYS-PUB-2021-020. 2021. URL: http://cds.cern.ch/record/2772627.

[6] ATLAS Collaboration. "Monte Carlo to Monte Carlo scale factors for flavour tagging efficiency calibration". ATL-PHYS-PUB-2020-009. 2020. URL: http://cds.cern.ch/record/2718610.

[7] R. P. Feynman. "A New Approach to Quantum Theory". Ed. by Brown Laurie M. World Scientific Publishing Co. Pte. Ltd, 2005.

[8] W. Greiner et al. "Quantum Chromodynamics". Springer Berlin Heidelberg, 2007.

[9] X. G. Wu et al. "The QCD renormalization group equation and the elimination of fixed-order scheme-and-scale ambiguities using the principle of maximum conformality". *Prog. Part. Nucl. Phys.* 108 (2019). DOI: 10.1016/j.ppnp.2019.05.003. arXiv: 1903.12177 [hep-ph].

[10] P. A. Zyla et al. "Review of Particle Physics". *PTEP* 2020.8 (2020). DOI: 10.1093/ptep/ptaa104.

[11] J. C. Collins et al. "Factorization of Hard Processes in QCD". *Adv. Ser. Direct. High Energy Phys.* 5 (1989). DOI: 10.1142/9789814503266_0001. arXiv: hep-ph/0409313.

[12] A. V. Manohar et al. "The Photon Content of the Proton". *JHEP* 12 (2017). DOI: 10.1007/JHEP12(2017)046. arXiv: 1708.01256 [hep-ph].

[13] L. Buonocore et al. "Leptons in the proton". *JHEP* 08.08 (2020). DOI: 10.1007/JHEP08(2020)019. arXiv: 2005.06477 [hep-ph].

[14] S. D. Ellis et al. "Successive combination jet algorithm for hadron collisions". *Phys. Rev. D* 48 (1993). DOI: 10.1103/PhysRevD.48.3160. arXiv: hep-ph/9305266.

[15] M. Cacciari et al. "The anti-k_t jet clustering algorithm". *JHEP* 04 (2008). DOI: 10.1088/1126-6708/2008/04/063. arXiv: 0802.1189 [hep-ph].

[16] Y. L. Dokshitzer. "Calculation of the Structure Functions for Deep Inelastic Scattering and e+ e- Annihilation by Perturbation Theory in Quantum Chromodynamics." *Sov. Phys. JETP* 46 (1977).

[17] V. N. Gribov et al. "Deep inelastic e p scattering in perturbation theory". *Sov. J. Nucl. Phys.* 15 (1972).

[18] G. Altarelli et al. "Asymptotic Freedom in Parton Language". *Nucl. Phys. B* 126 (1977). DOI: 10.1016/0550-3213(77)90384-4.

[19] S. Alekhin et al. "Fixed target Drell-Yan data and NNLO QCD fits of parton distribution functions". *Phys. Rev. D* 74 (2006). DOI: 10.1103/PhysRevD.74.054033. arXiv: hep-ph/0606237.

[20] S. Alekhin et al. "The PDF4LHC Working Group Interim Report" (2011). arXiv: 1101.0536 [hep-ph].

[21] A. Buckley et al. "General-purpose event generators for LHC physics". *Phys. Rept.* 504 (2011). DOI: 10.1016/j.physrep.2011.03.005. arXiv: 1101.2599 [hep-ph].

[22] ATLAS Collaboration. "Standard Model Summary Plots June 2021". ATL-PHYS-PUB-2021-032. 2021. URL: http://cds.cern.ch/record/2777014.

[23] ATLAS Collaboration. "Study of the spin and parity of the Higgs boson in diboson decays with the ATLAS detector". *Eur. Phys. J. C* 75.10 (2015). [Erratum: Eur.Phys.J.C 76, 152 (2016)]. DOI: 10.1140/epjc/s10052-015-3685-1. arXiv: 1506.05669 [hep-ex].

[24] ATLAS Collaboration. "Cross-section measurements of the Higgs boson decaying into a pair of τ-leptons in proton-proton collisions at $\sqrt{s} = 13$ TeV with the ATLAS detector". *Phys. Rev. D* 99 (2019). DOI: 10.1103/PhysRevD.99.072001. arXiv: 1811.08856 [hep-ex].

[25] CMS Collaboration. "Observation of the Higgs boson decay to a pair of τ leptons with the CMS detector". *Phys. Lett. B* 779 (2018). DOI: 10.1016/j.physletb.2018.02.004. arXiv: 1708.00373 [hep-ex].

[26] ATLAS Collaboration. "Observation of Higgs boson production in association with a top quark pair at the LHC with the ATLAS detector". *Phys. Lett. B* 784 (2018). DOI: 10.1016/j.physletb.2018.07.035. arXiv: 1806.00425 [hep-ex].

[27] CMS Collaboration. "Observation of $t\bar{t}H$ production". *Phys. Rev. Lett.* 120.23 (2018). DOI: 10.1103/PhysRevLett.120.231801. arXiv: 1804.02610 [hep-ex].

[28] ATLAS Collaboration. "Observation of $H \to b\bar{b}$ decays and VH production with the ATLAS detector". *Phys. Lett. B* 786 (2018). DOI: 10.1016/j.physletb.2018.09.013. arXiv: 1808.08238 [hep-ex].

[29] CMS Collaboration. "Observation of Higgs boson decay to bottom quarks". *Phys. Rev. Lett.* 121.12 (2018). DOI: 10.1103/PhysRevLett.121.121801. arXiv: 1808.08242 [hep-ex].

[30] CMS Collaboration. "Evidence for Higgs boson decay to a pair of muons". *JHEP* 01 (2021). DOI: 10.1007/JHEP01(2021)148. arXiv: 2009.04363 [hep-ex].

[31] ATLAS Collaboration. "A search for the dimuon decay of the Standard Model Higgs boson with the ATLAS detector". *Phys. Lett. B* 812 (2021). DOI: 10.1016/j.physletb.2020.135980. arXiv: 2007.07830 [hep-ex].

[32] ATLAS Collaboration. "Direct constraint on the Higgs-charm coupling from a search for Higgs boson decays to charm quarks with the ATLAS detector". ATLAS-CONF-2021-021. 2021. URL: http://cds.cern.ch/record/2771724.

[33] ATLAS Collaboration. "Combined measurements of Higgs boson production and decay using up to 80 fb^{-1} of proton–proton collision data at $\sqrt{s} = 13$ TeV collected with the ATLAS experiment". ATLAS-CONF-2019-005. 2019. URL: https://cds.cern.ch/record/2668375.

[34] J. R. Andersen et al. "Handbook of LHC Higgs Cross Sections: 3. Higgs Properties" (2013). Ed. by S Heinemeyer et al. DOI: 10.5170/CERN-2013-004. arXiv: 1307.1347 [hep-ph].

[35] D. de Florian et al. "Handbook of LHC Higgs Cross Sections: 4. Deciphering the Nature of the Higgs Sector". 2/2017 (2016). DOI: 10.23731/CYRM-2017-002. arXiv: 1610.07922 [hep-ph].

[36] J. R. Andersen et al. "Les Houches 2015: Physics at TeV Colliders Standard Model Working Group Report". *9th Les Houches Workshop on Physics at TeV Colliders*. 2016. arXiv: 1605.04692 [hep-ph].

[37] ATLAS Collaboration. "Search for invisible Higgs boson decays with vector boson fusion signatures with the ATLAS detector using an integrated luminosity of 139 fb^{-1}". ATLAS-CONF-2020-008. 2020. URL: https://cds.cern.ch/record/2715447.

[38] ATLAS Collaboration. "Search for a scalar partner of the top quark in the all-hadronic $t\bar{t}$ plus missing transverse momentum final state at $\sqrt{s} = 13$ TeV with the ATLAS detector". *Eur. Phys. J. C* 80.8 (2020). DOI: 10.1140/epjc/s10052-020-8102-8. arXiv: 2004.14060 [hep-ex].

[39] ATLAS Collaboration. "Search for new phenomena in events with two opposite-charge leptons, jets and missing transverse momentum in pp collisions at $\sqrt{s} = 13$ TeV with the ATLAS detector". ATLAS-CONF-2020-046. 2020. URL: https://cds.cern.ch/record/2728056.

[40] ATLAS Collaboration. "Constraints on new phenomena via Higgs boson couplings and invisible decays with the ATLAS detector". *JHEP* 11 (2015). DOI: 10.1007/JHEP11(2015)206. arXiv: 1509.00672 [hep-ex].

[41] ATLAS Collaboration. "Combination of searches for invisible Higgs boson decays with the ATLAS experiment". ATLAS-CONF-2020-052. 2020. URL: http://cds.cern.ch/record/2743055.

[42] ATLAS Collaboration. "Measurements of WH and ZH production in the $H \to b\bar{b}$ decay channel in pp collisions at 13 TeV with the ATLAS detector". *Eur. Phys. J. C* 81.2 (2021). DOI: 10.1140/epjc/s10052-020-08677-2. arXiv: 2007.02873 [hep-ex].

[43] P. Fisher et al. "Neutrino mass and oscillation". *Ann. Rev. Nucl. Part. Sci.* 49 (1999). DOI: 10.1146/annurev.nucl.49.1.481. arXiv: hep-ph/9906244.

[44] J. E. Kim et al. "Axions and the Strong CP Problem". *Rev. Mod. Phys.* 82 (2010). [Erratum: Rev.Mod.Phys. 91, 049902 (2019)]. DOI: 10.1103/RevModPhys.82.557. arXiv: 0807.3125 [hep-ph].

[45] C. W. Misner et al. "Gravitation". W. H. Freeman, 1973.

[46] A. Bilal. "Introduction to supersymmetry" (2001). arXiv: hep-th/0101055.

[47] P. Fayet. "Supersymmetry and Weak, Electromagnetic and Strong Interactions". *Phys. Lett. B* 64 (1976). DOI: 10.1016/0370-2693(76)90319-1.

[48] C. Csaki. "The Minimal supersymmetric standard model (MSSM)". *Mod. Phys. Lett. A* 11 (1996). DOI: 10.1142/S021773239600062X. arXiv: hep-ph/9606414.

[49] K. Garrett et al. "Dark Matter: A Primer". *Adv. Astron.* 2011 (2011). DOI: 10.1155/2011/968283. arXiv: 1006.2483 [hep-ph].

[50] J. H. Oort. "The force exerted by the stellar system in the direction perpendicular to the galactic plane and some related problems". *Bulletin of the Astronomical Institutes of the Netherlands* 4 (1932).

[51] F. Zwicky. "On the masses of nebulae and clusters of nebulae". *ApJ* 86 (1937).

[52] V. C. Rubin et al. "Rotational properties of 21 SC galaxies with a large range of luminosities and radii, from NGC 4605 R = 4kpc to UGC 2885 R = 122 kpc". *ApJ* Part 1, vol. 238 (June 1, 1980). DOI: 10.1086/158003.

[53] T. Treu. "Strong Lensing by Galaxies". *Annu. Rev. Astron. Astrophys.* 48.1 (2010). DOI: 10.1146/annurev-astro-081309-130924.

[54] M. Bartelmann. "Gravitational Lensing". *Class. Quant. Grav.* 27 (2010). DOI: 10.1088/0264-9381/27/23/233001. arXiv: 1010.3829 [astro-ph.CO].

[55] J. A. Tyson et al. "Detailed Mass Map of CL 0024+1654 from Strong Lensing". *ApJ* 498.2 (1998). DOI: 10.1086/311314.

[56] D. Clowe et al. "A direct empirical proof of the existence of dark matter". *ApJ Lett.* 648 (2006). DOI: 10.1086/508162. arXiv: astro-ph/0608407.

[57] A. A. Penzias et al. "A Measurement of Excess Antenna Temperature at 4080 Mc/s." *ApJ Lett.* 142 (1965). DOI: 10.1086/148307.

[58] R. H. Dicke et al. "Cosmic Black-Body Radiation." *ApJ Lett.* 142 (1965). DOI: 10.1086/148306.

[59] A. Einstein. "The Field Equations of Gravitation". *Sitzungsber. Preuss. Akad. Wiss. Berlin (Math. Phys.)* 1915 (1915).

[60] E. Hubble. "A relation between distance and radial velocity among extra-galactic nebulae". *Proc. Nat. Acad. Sci.* 15 (1929). DOI: 10.1073/pnas.15.3.168.

[61] J. D. Barrow et al. "The homogeneity and isotropy of the Universe." *Monthly Notices of the Royal Astronomical Society* 181 (1977). DOI: 10.1093/mnras/181.4.719.

[62] A. Friedman. "On the Curvature of space". *Z. Phys.* 10 (1922). DOI: 10.1007/BF01332580.

[63] J. C. Mather et al. "Measurement of the Cosmic Microwave Background spectrum by the COBE FIRAS instrument". *ApJ* 420 (1994). DOI: 10.1086/173574.

[64] Planck Collaboration. "Planck 2018 results. I. Overview and the cosmological legacy of Planck". *Astron. Astrophys.* 641 (2020). DOI: 10.1051/0004-6361/201833880. arXiv: 1807.06205 [astro-ph.CO].

[65] Planck Collaboration. "Planck 2018 results. VI. Cosmological parameters". *Astron. Astrophys.* 641 (2020). [Erratum: Astron.Astrophys. 652, C4 (2021)]. DOI: 10.1051/0004-6361/201833910. arXiv: 1807.06209 [astro-ph.CO].

[66] Y. B. Zeldovich. "Survey of Modern Cosmology". *Adv. Astron. Astrophys.* 3 (1965). DOI: 10.1016/b978-1-4831-9921-4.50011-9.

[67] G. Steigman et al. "Precise Relic WIMP Abundance and its Impact on Searches for Dark Matter Annihilation". *Phys. Rev. D* 86 (2012). DOI: 10.1103/PhysRevD.86.023506. arXiv: 1204.3622 [hep-ph].

[68] J. Billard et al. "Direct Detection of Dark Matter – APPEC Committee Report" (2021). arXiv: 2104.07634 [hep-ex].

[69] XENON Collaboration. "Dark Matter Search Results from a One Ton-Year Exposure of XENON1T". *Phys. Rev. Lett.* 121.11 (2018). DOI: 10.1103/PhysRevLett.121.111302. arXiv: 1805.12562 [astro-ph.CO].

[70] DarkSide Collaboration. "Low-Mass Dark Matter Search with the DarkSide-50 Experiment". *Phys. Rev. Lett.* 121.8 (2018). DOI: 10.1103/PhysRevLett.121.081307. arXiv: 1802.06994 [astro-ph.HE].

[71] SuperCDMS Collaboration. "Search for Low-Mass Dark Matter with CDMSlite Using a Profile Likelihood Fit". *Phys. Rev. D* 99.6 (2019). DOI: 10.1103/PhysRevD.99.062001. arXiv: 1808.09098 [astro-ph.CO].

[72] CRESST Collaboration. "First results from the CRESST-III low-mass dark matter program". *Phys. Rev. D* 100.10 (2019). DOI: 10.1103/PhysRevD.100.102002. arXiv: 1904.00498 [astro-ph.CO].

[73] Particle Data Group. "Review of Particle Physics". *Progress of Theoretical and Experimental Physics* 2020.8 (2020). 083C01. DOI: 10.1093/ptep/ptaa104.

[74] D. N. Spergel. "Motion of the Earth and the detection of weakly interacting massive particles". *Phys. Rev. D* 37 (1988). DOI: 10.1103/PhysRevD.37.1353.

[75] F. Mayet et al. "A review of the discovery reach of directional Dark Matter detection". *Phys. Rept.* 627 (2016). DOI: 10.1016/j.physrep.2016.02.007. arXiv: 1602.03781 [astro-ph.CO].

[76] IceCube Collaboration. "Search for dark matter annihilations in the Sun with the 79-string IceCube detector". *Phys. Rev. Lett.* 110.13 (2013). DOI: 10.1103/PhysRevLett.110.131302. arXiv: 1212.4097 [astro-ph.HE].

[77] Super-Kamiokande Collaboration. "An Indirect Search for WIMPs in the Sun using 3109.6 days of upward-going muons in Super-Kamiokande". *ApJ* 742 (2011). DOI: 10.1088/0004-637X/742/2/78. arXiv: 1108.3384 [astro-ph.HE].

[78] Fermi-LAT Collaboration. "Searching for Dark Matter Annihilation from Milky Way Dwarf Spheroidal Galaxies with Six Years of Fermi Large Area Telescope Data". *Phys. Rev. Lett.* 115.23 (2015). DOI: 10.1103/PhysRevLett.115.231301. arXiv: 1503.02641 [astro-ph.HE].

[79] AMS collaboration. "First Result from the Alpha Magnetic Spectrometer on the International Space Station: Precision Measurement of the Positron Fraction in Primary Cosmic Rays of 0.5–350 GeV". *Phys. Rev. Lett.* 110 (2013). DOI: 10.1103/PhysRevLett.110.141102.

[80] PAMELA Collaboration. "An anomalous positron abundance in cosmic rays with energies 1.5-100 GeV". *Nature* 458 (2009). DOI: 10.1038/nature07942. arXiv: 0810.4995 [astro-ph].

[81] AMS Collaboration. "Antiproton Flux, Antiproton-to-Proton Flux Ratio, and Properties of Elementary Particle Fluxes in Primary Cosmic Rays Measured with the Alpha Magnetic Spectrometer on the International Space Station". *Phys. Rev. Lett.* 117 (2016). DOI: 10.1103/PhysRevLett.117.091103.

[82] J. Goodman et al. "Constraints on Dark Matter from Colliders". *Phys. Rev. D* 82 (2010). DOI: 10.1103/PhysRevD.82.116010. arXiv: 1008.1783 [hep-ph].

[83] ATLAS Collaboration. "Search for new phenomena in final states with an energetic jet and large missing transverse momentum in pp collisions at $\sqrt{s}$ =8 TeV with the ATLAS detector". *Eur. Phys. J. C* 75.7 (2015). [Erratum: Eur.Phys.J.C 75, 408 (2015)]. DOI: 10.1140/epjc/s10052-015-3517-3. arXiv: 1502.01518 [hep-ex].

[84] CMS Collaboration. "Search for dark matter, extra dimensions, and unparticles in monojet events in proton–proton collisions at $\sqrt{s} = 8$ TeV". *Eur. Phys. J. C* 75.5 (2015). DOI: 10.1140/epjc/s10052-015-3451-4. arXiv: 1408.3583 [hep-ex].

[85] J. Abdallah et al. "Simplified Models for Dark Matter Searches at the LHC". *Phys. Dark Univ.* 9-10 (2015). DOI: 10.1016/j.dark.2015.08.001. arXiv: 1506.03116 [hep-ph].

[86] D. Abercrombie et al. "Dark Matter benchmark models for early LHC Run-2 Searches: Report of the ATLAS/CMS Dark Matter Forum". *Phys. Dark Univ.* 27 (2020). Ed. by Antonio Boveia et al. DOI: 10.1016/j.dark.2019.100371. arXiv: 1507.00966 [hep-ex].

[87] D. Berdine et al. "Breakdown of the Narrow Width Approximation for New Physics". *Phys. Rev. Lett.* 99 (2007). DOI: 10.1103/PhysRevLett.99.111601. arXiv: hep-ph/0703058.

[88] U. Haisch et al. "QCD effects in mono-jet searches for dark matter". *JHEP* 12 (2013). DOI: 10.1007/JHEP12(2013)007. arXiv: 1310.4491 [hep-ph].

[89] S. Alioli et al. "A general framework for implementing NLO calculations in shower Monte Carlo programs: the POWHEG BOX". *JHEP* 06 (2010). DOI: 10.1007/JHEP06(2010)043. arXiv: 1002.2581 [hep-ph].

[90] T. Sjostrand et al. "A Brief Introduction to PYTHIA 8.1". *Comput. Phys. Commun.* 178 (2008). DOI: 10.1016/j.cpc.2008.01.036. arXiv: 0710.3820 [hep-ph].

[91] A. Boveia et al. "Recommendations on presenting LHC searches for missing transverse energy signals using simplified s-channel models of dark matter". *Phys. Dark Univ.* 27 (2020). Ed. by Oliver Buchmueller et al. DOI: 10.1016/j.dark.2019.100365. arXiv: 1603.04156 [hep-ex].

[92] H. Cai et al. "A quirky little Higgs model". *Journal of High Energy Physics* 2009.05 (2009). DOI: 10.1088/1126-6708/2009/05/045.

[93] Z. Chacko et al. "The Twin Higgs: Natural electroweak breaking from mirror symmetry". *Phys. Rev. Lett.* 96 (2006). DOI: 10.1103/PhysRevLett.96.231802. arXiv: hep-ph/0506256.

[94] G. Burdman et al. "Folded supersymmetry and the LEP paradox". *Journal of High Energy Physics* 2007.02 (2007). DOI: 10.1088/1126-6708/2007/02/009.

[95] A. Falkowski et al. "Hidden Higgs Decaying to Lepton Jets". *JHEP* 05 (2010). DOI: 10.1007/JHEP05(2010)077. arXiv: 1002.2952 [hep-ph].

[96] A. Falkowski et al. "Discovering Higgs Decays to Lepton Jets at Hadron Colliders". *Phys. Rev. Lett.* 105 (2010). DOI: 10.1103/PhysRevLett.105.241801. arXiv: 1007.3496 [hep-ph].

[97] C. Cheung et al. "Kinetic Mixing as the Origin of Light Dark Scales". *Phys. Rev. D* 80 (2009). DOI: 10.1103/PhysRevD.80.035008. arXiv: 0902.3246 [hep-ph].

[98] ATLAS Collaboration. "A search for prompt lepton-jets in pp collisions at $\sqrt{s} = 8$ TeV with the ATLAS detector". *JHEP* 02 (2016). DOI: 10.1007/JHEP02(2016)062. arXiv: 1511.05542 [hep-ex].

[99] ATLAS Collaboration. "Search for light long-lived neutral particles produced in pp collisions at $\sqrt{s} = 13$ TeV and decaying into collimated leptons or light hadrons with the ATLAS detector". *Eur. Phys. J. C* 80.5 (2020). DOI: 10.1140/epjc/s10052-020-7997-4. arXiv: 1909.01246 [hep-ex].

[100] D. Curtin et al. "Exotic decays of the 125 GeV Higgs boson". *Phys. Rev. D* 90 (2014). DOI: 10.1103/PhysRevD.90.075004.

[101] L. Evans et al. “LHC Machine”. *JINST* 3.08 (2008). DOI: 10.1088/1748-0221/3/08/s08001.

[102] ATLAS Collaboration. “The ATLAS Experiment at the CERN Large Hadron Collider”. *JINST* 3.08 (2008). DOI: 10.1088/1748-0221/3/08/s08003.

[103] CMS Collaboration. “The CMS Experiment at the CERN LHC”. *JINST* 3.08 (2008). DOI: 10.1088/1748-0221/3/08/S08004.

[104] ALICE Collaboration. “The ALICE experiment at the CERN LHC”. *JINST* 3.08 (2008). DOI: 10.1088/1748-0221/3/08/S08002.

[105] LHCb Collaboration. “The LHCb Detector at the LHC”. *JINST* 3.08 (2008). DOI: 10.1088/1748-0221/3/08/S08005.

[106] E. Mobs. “The CERN accelerator complex - 2019. Complexe des accélérateurs du CERN - 2019” (2019). General Photo. URL: https://cds.cern.ch/record/2684277.

[107] S. Gilardoni et al. “The Long-Term Beam Losses in the CERN Injector Chain” (2015). URL: https://cds.cern.ch/record/2131161.

[108] R. Bruce et al. “Review of LHC Run 2 Machine Configurations” (2019). URL: https://cds.cern.ch/record/2750415.

[109] ATLAS Collaboration. “Measurement of the Inelastic Proton-Proton Cross Section at $\sqrt{s} = 13$ TeV with the ATLAS Detector at the LHC”. *Phys. Rev. Lett.* 117.18 (2016). DOI: 10.1103/PhysRevLett.117.182002. arXiv: 1606.02625 [hep-ex].

[110] ATLAS Collaboration. “Operation of the ATLAS trigger system in Run 2”. *JINST* 15.10 (2020). DOI: 10.1088/1748-0221/15/10/P10004. arXiv: 2007.12539 [physics.ins-det].

[111] ATLAS Collaboration. “ATLAS inner detector: Technical Design Report, 1”. Technical design report. ATLAS. CERN, 1997. URL: https://cds.cern.ch/record/331063.

[112] J. Pequenao. “Computer generated image of the ATLAS inner detector”. 2008. URL: https://cds.cern.ch/record/1095926.

[113] ATLAS Collaboration. “ATLAS Insertable B-Layer Technical Design Report”. CERN-LHCC-2010-013, ATLAS-TDR-19. 2010. URL: https://cds.cern.ch/record/1291633.

[114] A. La Rosa. “The ATLAS Insertable B-Layer: from construction to operation”. *Journal of Instrumentation* 11.12 (2016). DOI: 10.1088/1748-0221/11/12/c12036.

[115] A. Ahmad et al. “The silicon microstrip sensors of the ATLAS semiconductor tracker”. *Nucl. Instrum. Methods Phys. Res. A* 578.1 (2007). DOI: https://doi.org/10.1016/j.nima.2007.04.157.

[116] ATLAS Collaboration. “Performance of the ATLAS Transition Radiation Tracker in Run 1 of the LHC: tracker properties”. *JINST* 12.05 (2017). DOI: 10.1088/1748-0221/12/05/P05002. arXiv: 1702.06473 [hep-ex].

[117] ATLAS Collaboration. "Track Reconstruction Performance of the ATLAS Inner Detector at $\sqrt{s} = 13$ TeV". ATL-PHYS-PUB-2015-018. 2015. URL: https://cds.cern.ch/record/2037683.

[118] ATLAS Electromagnetic Barrel Liquid Argon Calorimeter Group. "Construction, assembly and tests of the ATLAS electromagnetic barrel calorimeter". *Nucl. Instrum. Methods Phys. Res. A* 558.2 (2006). DOI: https://doi.org/10.1016/j.nima.2005.11.212.

[119] ATLAS Collaboration. "Expected Performance of the ATLAS Experiment - Detector, Trigger and Physics" (2009). arXiv: 0901.0512 [hep-ex].

[120] ATLAS Collaboration. "Performance of the missing transverse momentum triggers for the ATLAS detector during Run-2 data taking". *JHEP* 08 (2020). DOI: 10.1007/JHEP08(2020)080. arXiv: 2005.09554 [hep-ex].

[121] M. Schaumann et al. "Proceedings of the 2019 Evian workshop on LHC beam operations" (2019). URL: https://cds.cern.ch/record/2706427.

[122] G. Avoni et al. "The new LUCID-2 detector for luminosity measurement and monitoring in ATLAS". *Journal of Instrumentation* 13.07 (2018). DOI: 10.1088/1748-0221/13/07/p07017.

[123] ATLAS Collaboration. "Luminosity determination in pp collisions at $\sqrt{s} = 13$ TeV using the ATLAS detector at the LHC". ATLAS-CONF-2019-021. 2019. URL: http://cds.cern.ch/record/2677054.

[124] ATLAS Collaboration. "ATLAS data quality operations and performance for 2015–2018 data-taking". *Journal of Instrumentation* 15.04 (2020). DOI: 10.1088/1748-0221/15/04/p04003.

[125] ATLAS Collaboration. "The ATLAS Simulation Infrastructure". *Eur. Phys. J. C* 70 (2010). DOI: 10.1140/epjc/s10052-010-1429-9. arXiv: 1005.4568 [physics.ins-det].

[126] S. Agostinelli et al. "GEANT4–a simulation toolkit". *Nucl. Instrum. Meth. A* 506 (2003). DOI: 10.1016/S0168-9002(03)01368-8.

[127] J. Allison et al. "Recent developments in Geant4". *Nucl. Instrum. Meth. A* 835 (2016). DOI: 10.1016/j.nima.2016.06.125.

[128] T. G. Cornelissen, et al. "Updates of the ATLAS Tracking Event Data Model (Release 13)". ATL-SOFT-PUB-2007-003, ATL-COM-SOFT-2007-008. 2007. URL: https://cds.cern.ch/record/1038095.

[129] ATLAS Collaboration. "Performance of the ATLAS Track Reconstruction Algorithms in Dense Environments in LHC Run 2". *Eur. Phys. J. C* 77.10 (2017). DOI: 10.1140/epjc/s10052-017-5225-7. arXiv: 1704.07983 [hep-ex].

[130] R. Frühwirth. "Application of Kalman filtering to track and vertex fitting". *Nucl. Instrum. Methods Phys. Res. A* 262.2 (1987). DOI: https://doi.org/10.1016/0168-9002(87)90887-4.

[131] ATLAS Collaboration. "Topological cell clustering in the ATLAS calorimeters and its performance in LHC Run 1". *Eur. Phys. J. C* 77 (2017). DOI: 10.1140/epjc/s10052-017-5004-5. arXiv: 1603.02934 [hep-ex].

[132] ATLAS Collaboration. "Electron and photon performance measurements with the ATLAS detector using the 2015–2017 LHC proton-proton collision data". *JINST* 14.12 (2019). DOI: 10.1088/1748-0221/14/12/P12006. arXiv: 1908.00005 [hep-ex].

[133] ATLAS Collaboration. "Measurement of the photon identification efficiencies with the ATLAS detector using LHC Run 2 data collected in 2015 and 2016". *Eur. Phys. J. C* 79.3 (2019). DOI: 10.1140/epjc/s10052-019-6650-6. arXiv: 1810.05087 [hep-ex].

[134] ATLAS Collaboration. "Muon reconstruction and identification efficiency in ATLAS using the full Run 2 *pp* collision data set at $\sqrt{s} = 13$ TeV". *Eur. Phys. J. C* 81 (2021). DOI: 10.1140/epjc/s10052-021-09233-2. arXiv: 2012.00578 [hep-ex].

[135] ATLAS Collaboration. "Muon reconstruction performance of the ATLAS detector in proton–proton collision data at $\sqrt{s}$ =13 TeV". *Eur. Phys. J. C* 76.5 (2016). DOI: 10.1140/epjc/s10052-016-4120-y. arXiv: 1603.05598 [hep-ex].

[136] ATLAS Collaboration. "Measurement of the tau lepton reconstruction and identification performance in the ATLAS experiment using *pp* collisions at $\sqrt{s} = 13$ TeV". ATLAS-CONF-2017-029. 2017. URL: https://cds.cern.ch/record/2261772.

[137] ATLAS Collaboration. "Reconstruction, Energy Calibration, and Identification of Hadronically Decaying Tau Leptons in the ATLAS Experiment for Run-2 of the LHC". ATL-PHYS-PUB-2015-045. 2015. URL: https://cds.cern.ch/record/2064383.

[138] ATLAS Collaboration. "Jet energy scale and resolution measured in proton-proton collisions at $\sqrt{s} = 13$ TeV with the ATLAS detector" (2020). arXiv: 2007.02645 [hep-ex].

[139] M. Cacciari et al. "Pileup subtraction using jet areas". *Phys. Lett. B* 659 (2008). DOI: 10.1016/j.physletb.2007.09.077. arXiv: 0707.1378 [hep-ph].

[140] ATLAS Collaboration. "Determination of the jet energy scale and resolution at ATLAS using Z/γ–jet events in data at $\sqrt{s} = 8$ TeV". ATLAS-CONF-2015-057. 2015. URL: https://cds.cern.ch/record/2059846.

[141] ATLAS Collaboration. "Jet energy measurement and its systematic uncertainty in proton-proton collisions at $\sqrt{s} = 7$ TeV with the ATLAS detector". *Eur. Phys. J. C* 75 (2015). DOI: 10.1140/epjc/s10052-014-3190-y. arXiv: 1406.0076 [hep-ex].

[142] ATLAS Collaboration. "Jet reconstruction and performance using particle flow with the ATLAS Detector". *Eur. Phys. J. C* 77.7 (2017). DOI: 10.1140/epjc/s10052-017-5031-2. arXiv: 1703.10485 [hep-ex].

[143] J. M. Butterworth et al. "Jet substructure as a new Higgs search channel at the LHC". *Phys. Rev. Lett.* 100 (2008). DOI: 10.1103/PhysRevLett.100.242001. arXiv: 0802.2470 [hep-ph].

[144] ATLAS Collaboration. "In situ calibration of large-radius jet energy and mass in 13 TeV proton–proton collisions with the ATLAS detector". *Eur. Phys. J. C* 79.2 (2019). DOI: 10.1140/epjc/s10052-019-6632-8. arXiv: 1807.09477 [hep-ex].

[145] D. Krohn et al. "Jet Trimming". *JHEP* 02 (2010). DOI: 10.1007/JHEP02(2010)084. arXiv: 0912.1342 [hep-ph].

[146] D. Krohn et al. "Jets with Variable R". *JHEP* 06 (2009). DOI: 10.1088/1126-6708/2009/06/059. arXiv: 0903.0392 [hep-ph].

[147] ATLAS Collaboration. "Tagging and suppression of pileup jets with the ATLAS detector". ATLAS-CONF-2014-018. 2014. URL: http://cds.cern.ch/record/1700870.

[148] A. Hoecker et al. "TMVA - Toolkit for Multivariate Data Analysis" (2007). arXiv: physics/0703039 [physics.data-an].

[149] ATLAS Collaboration. "ATLAS b-jet identification performance and efficiency measurement with $t\bar{t}$ events in pp collisions at $\sqrt{s} = 13$ TeV". *Eur. Phys. J. C* 79.11 (2019). DOI: 10.1140/epjc/s10052-019-7450-8. arXiv: 1907.05120 [hep-ex].

[150] ATLAS Collaboration. "Optimisation and performance studies of the ATLAS b-tagging algorithms for the 2017-18 LHC run". ATL-PHYS-PUB-2017-013. 2017. URL: http://cds.cern.ch/record/2273281.

[151] ATLAS Collaboration. "Secondary vertex finding for jet flavour identification with the ATLAS detector". ATL-PHYS-PUB-2017-011. 2017. URL: https://cds.cern.ch/record/2270366.

[152] ATLAS Collaboration. "Topological b-hadron decay reconstruction and identification of b-jets with the JetFitter package in the ATLAS experiment at the LHC". ATL-PHYS-PUB-2018-025. 2018. URL: https://cds.cern.ch/record/2645405.

[153] ATLAS Collaboration. "Identification of Jets Containing b-Hadrons with Recurrent Neural Networks at the ATLAS Experiment". ATL-PHYS-PUB-2017-003. 2017. URL: https://cds.cern.ch/record/2255226.

[154] ATLAS Collaboration. "Measurement of b-tagging Efficiency of c-jets in $t\bar{t}$ Events Using a Likelihood Approach with the ATLAS Detector". ATLAS-CONF-2018-001. 2018. URL: http://cds.cern.ch/record/2306649.

[155] ATLAS Collaboration. "Calibration of light-flavour b-jet mistagging rates using ATLAS proton-proton collision data at $\sqrt{s} = 13$ TeV". ATLAS-CONF-2018-006. 2018. URL: http://cds.cern.ch/record/2314418.

[156] ATLAS Collaboration. "Performance of missing transverse momentum reconstruction with the ATLAS detector using proton-proton collisions at $\sqrt{s} = 13$ TeV". *Eur. Phys. J. C* 78.11 (2018). DOI: 10.1140/epjc/s10052-018-6288-9. arXiv: 1802.08168 [hep-ex].

[157] UA1 Collaboration. "Experimental observation of events with large missing transverse energy accompanied by a jet or a photon (S) in pp collisions at s = 540 GeV". *Physics Letters B* 139.1 (1984). DOI: https://doi.org/10.1016/0370-2693(84)90046-7.

[158] E. Bothmann et al. "Event Generation with Sherpa 2.2". *SciPost Phys.* 7.3 (2019). DOI: 10.21468/SciPostPhys.7.3.034. arXiv: 1905.09127 [hep-ph].

[159] T. Gleisberg et al. "Comix, a new matrix element generator". *JHEP* 12 (2008). DOI: 10.1088/1126-6708/2008/12/039. arXiv: 0808.3674 [hep-ph].

[160] F. Cascioli et al. "Scattering Amplitudes with Open Loops". *Phys. Rev. Lett.* 108 (2012). DOI: 10.1103/PhysRevLett.108.111601. arXiv: 1111.5206 [hep-ph].

[161] R. D. Ball et al. "Parton distributions for the LHC Run II". *JHEP* 04 (2015). DOI: 10.1007/JHEP04(2015)040. arXiv: 1410.8849 [hep-ph].

[162] S. Schumann et al. "A Parton shower algorithm based on Catani-Seymour dipole factorisation". *JHEP* 03 (2008). DOI: 10.1088/1126-6708/2008/03/038. arXiv: 0709.1027 [hep-ph].

[163] J. C. Winter et al. "A modified cluster-hadronization model". *Eur. Phys. J. C* 36 (2004). DOI: 10.1140/epjc/s2004-01960-8. arXiv: hep-ph/0311085.

[164] S. Catani et al. "QCD matrix elements + parton showers". *JHEP* 11 (2001). DOI: 10.1088/1126-6708/2001/11/063. arXiv: hep-ph/0109231.

[165] S. Höche et al. "QCD matrix elements + parton showers: The NLO case". *JHEP* 04 (2013). DOI: 10.1007/JHEP04(2013)027. arXiv: 1207.5030 [hep-ph].

[166] C. Anastasiou et al. "High precision QCD at hadron colliders: Electroweak gauge boson rapidity distributions at NNLO". *Phys. Rev. D* 69 (2004). DOI: 10.1103/PhysRevD.69.094008. arXiv: hep-ph/0312266.

[167] J. M. Lindert et al. "Precise predictions for V+ jets dark matter backgrounds". *Eur. Phys. J. C* 77.12 (2017). DOI: 10.1140/epjc/s10052-017-5389-1. arXiv: 1705.04664 [hep-ph].

[168] M. Bahr et al. "Herwig++ Physics and Manual". *Eur. Phys. J. C* 58 (2008). DOI: 10.1140/epjc/s10052-008-0798-9. arXiv: 0803.0883 [hep-ph].

[169] K. Arnold et al. "Vbfnlo: A parton level Monte Carlo for processes with electroweak bosons". *Computer Physics Communications* 180.9 (2009). DOI: https://doi.org/10.1016/j.cpc.2009.03.006.

[170] A. D. Martin et al. "Parton distributions for the LHC". *Eur. Phys. J. C* 63 (2009). DOI: 10.1140/epjc/s10052-009-1072-5. arXiv: 0901.0002 [hep-ph].

[171] S. Frixione et al. "Angular correlations of lepton pairs from vector boson and top quark decays in Monte Carlo simulations". *JHEP* 04 (2007). DOI: 10.1088/1126-6708/2007/04/081. arXiv: hep-ph/0702198.

[172] T. Sjöstrand et al. "An introduction to PYTHIA 8.2". *Comput. Phys. Commun.* 191 (2015). DOI: 10.1016/j.cpc.2015.01.024. arXiv: 1410.3012 [hep-ph].

[173] R. D. Ball et al. "Parton distributions with LHC data". *Nucl. Phys. B* 867 (2013). DOI: 10.1016/j.nuclphysb.2012.10.003. arXiv: 1207.1303 [hep-ph].

[174] ATLAS Collaboration. "ATLAS Pythia 8 tunes to 7 TeV data". ATL-PHYS-PUB-2014-021. 2014. URL: https://cds.cern.ch/record/1966419.

[175] D. J. Lange. "The EvtGen particle decay simulation package". *Nucl. Instrum. Methods Phys. Res. A* 462.1 (2001). BEAUTY2000, Proceedings of the 7th Int. Conf. on B-Physics at Hadron Machines. DOI: https://doi.org/10.1016/S0168-9002(01)00089-4.

[176] S. Frixione et al. "Single-top hadroproduction in association with a W boson". *JHEP* 07 (2008). DOI: 10.1088/1126-6708/2008/07/029. arXiv: 0805.3067 [hep-ph].

[177] ATLAS Collaboration. "Selection of jets produced in 13TeV proton-proton collisions with the ATLAS detector". ATLAS-CONF-2015-029. 2015. URL: https://cds.cern.ch/record/2037702.

[178] ATLAS Collaboration. "Performance of electron and photon triggers in ATLAS during LHC Run 2". *Eur. Phys. J. C* 80.1 (2020). DOI: 10.1140/epjc/s10052-019-7500-2. arXiv: 1909.00761 [hep-ex].

[179] ATLAS Collaboration. "Measurements of the production cross section of a Z boson in association with jets in pp collisions at $\sqrt{s} = 13$ TeV with the ATLAS detector". *Eur. Phys. J. C* 77.6 (2017). DOI: 10.1140/epjc/s10052-017-4900-z. arXiv: 1702.05725 [hep-ex].

[180] ATLAS Collaboration. "Search for dark matter and other new phenomena in events with an energetic jet and large missing transverse momentum using the ATLAS detector". *JHEP* 01 (2018). DOI: 10.1007/JHEP01(2018)126. arXiv: 1711.03301 [hep-ex].

[181] ATLAS Collaboration. "Characterisation and mitigation of beam-induced backgrounds observed in the ATLAS detector during the 2011 proton-proton run". *JINST* 8 (2013). DOI: 10.1088/1748-0221/8/07/P07004. arXiv: 1303.0223 [hep-ex].

[182] M. Baak et al. "HistFitter software framework for statistical data analysis". *Eur. Phys. J. C* 75 (2015). DOI: 10.1140/epjc/s10052-015-3327-7. arXiv: 1410.1280 [hep-ex].

[183] S. Kallweit et al. "NLO QCD+EW predictions for V + jets including off-shell vector-boson decays and multijet merging". *JHEP* 04 (2016). DOI: 10.1007/JHEP04(2016)021. arXiv: 1511.08692 [hep-ph].

[184] S. Höche et al. "Hard photon production and matrix-element parton-shower merging". *Phys. Rev. D* 81 (2010). DOI: 10.1103/PhysRevD.81.034026. arXiv: 0912.3501 [hep-ph].

[185] A. L. Read. "Presentation of search results: the CLs technique". *Journal of Physics G: Nuclear and Particle Physics* 28.10 (2002). DOI: 10.1088/0954-3899/28/10/313.

[186] M. Backović et al. "Direct Detection of Dark Matter with MadDM v.2.0". *Phys. Dark Univ.* 9-10 (2015). DOI: 10.1016/j.dark.2015.09.001. arXiv: 1505.04190 [hep-ph].

[187] PICO Collaboration. "Dark matter search results from the complete exposure of the PICO-60 C_3F_8 bubble chamber". *Phys. Rev. D* 100 (2019). DOI: 10.1103/PhysRevD.100.022001.

[188] LUX Collaboration. "Limits on Spin-Dependent WIMP-Nucleon Cross Section Obtained from the Complete LUX Exposure". *Phys. Rev. Lett.* 118 (2017). DOI: 10.1103/PhysRevLett.118.251302.

[189] XENON Collaboration. "Constraining the Spin-Dependent WIMP-Nucleon Cross Sections with XENON1T". *Phys. Rev. Lett.* 122 (2019). DOI: 10.1103/PhysRevLett.122.141301.

[190] XENON Collaboration. "First Dark Matter Search Results from the XENON1T Experiment". *Phys. Rev. Lett.* 119.18 (2017). DOI: 10.1103/PhysRevLett.119.181301. arXiv: 1705.06655 [astro-ph.CO].

[191] XENON Collaboration. "Search for Light Dark Matter Interactions Enhanced by the Migdal Effect or Bremsstrahlung in XENON1T". *Phys. Rev. Lett.* 123 (2019). DOI: 10.1103/PhysRevLett.123.241803.

[192] PandaX-II Collaboration. "Dark Matter Results from First 98.7 Days of Data from the PandaX-II Experiment". *Phys. Rev. Lett.* 117.12 (2016). DOI: 10.1103/PhysRevLett.117.121303. arXiv: 1607.07400 [hep-ex].

[193] DarkSide Collaboration. "First results from the DarkSide-50 dark matter experiment at Laboratori Nazionali del Gran Sasso". *Physics Letters B* 743 (2015). ISSN: 0370-2693. DOI: https://doi.org/10.1016/j.physletb.2015.03.012.

[194] Fermi-LAT Collaboration. "Searching for Dark Matter Annihilation from Milky Way Dwarf Spheroidal Galaxies with Six Years of Fermi Large Area Telescope Data". *Phys. Rev. Lett.* 115 (2015). DOI: 10.1103/PhysRevLett.115.231301.

[195] ATLAS Collaboration. "Dark matter summary plots for s-channel mediators". ATL-PHYS-PUB-2021-006. 2021. URL: http://cds.cern.ch/record/2758386.

[196] ATLAS Collaboration. "Search for new resonances in mass distributions of jet pairs using 139 fb^{-1} of pp collisions at $\sqrt{s} = 13$ TeV with the ATLAS detector". *JHEP* 03 (2020). DOI: 10.1007/JHEP03(2020)145. arXiv: 1910.08447 [hep-ex].

[197] W. Beenakker et al. "Supersymmetric top and bottom squark production at hadron colliders". *JHEP* 08 (2010). DOI: 10.1007/JHEP08(2010)098. arXiv: 1006.4771 [hep-ph].

[198] W. Beenakker et al. "NNLL resummation for stop pair-production at the LHC". *JHEP* 05 (2016). DOI: 10.1007/JHEP05(2016)153. arXiv: 1601.02954 [hep-ph].

[199] C. Borschensky et al. "Squark and gluino production cross sections in pp collisions at $\sqrt{s}$ = 13, 14, 33 and 100 TeV". *Eur. Phys. J. C* 74.12 (2014). DOI: 10.1140/epjc/s10052-014-3174-y. arXiv: 1407.5066 [hep-ph].

[200] K. Hamilton et al. "NNLOPS simulation of Higgs boson production". *JHEP* 10 (2013). DOI: 10.1007/JHEP10(2013)222. arXiv: 1309.0017 [hep-ph].

[201] K. Hamilton et al. "Finite quark-mass effects in the NNLOPS POWHEG+MiNLO Higgs generator". *JHEP* 05 (2015). DOI: 10.1007/JHEP05(2015)140. arXiv: 1501.04637 [hep-ph].

[202] J. Alwall et al. "The automated computation of tree-level and next-to-leading order differential cross sections, and their matching to parton shower simulations". *JHEP* 07 (2014). DOI: 10.1007/JHEP07(2014)079. arXiv: 1405.0301 [hep-ph].

[203] P. Ilten et al. "Serendipity in dark photon searches". *JHEP* 06 (2018). DOI: 10.1007/JHEP06(2018)004. arXiv: 1801.04847 [hep-ph].

[204] ATLAS Collaboration. "Search for the Higgs boson produced in association with a vector boson and decaying into two spin-zero particles in the $H \to aa \to 4b$ channel in pp collisions at $\sqrt{s} = 13$ TeV with the ATLAS detector". *JHEP* 10 (2018). DOI: 10.1007/JHEP10(2018)031. arXiv: 1806.07355 [hep-ex].

[205] ATLAS Collaboration. "Search for long-lived neutral particles in pp collisions at $\sqrt{s} = 13$ TeV that decay into displaced hadronic jets in the ATLAS calorimeter". *Eur. Phys. J. C* 79.6 (2019). DOI: 10.1140/epjc/s10052-019-6962-6. arXiv: 1902.03094 [hep-ex].

[206] ATLAS Collaboration. "Search for exotic decays of the Higgs boson to long-lived particles in pp collisions at $\sqrt{s} = 13$ TeV using displaced vertices in the ATLAS inner detector". ATLAS-CONF-2021-005. 2021. URL: http://cds.cern.ch/record/2759209.

[207] B. Mellado Garcia et al. "CERN Report 4: Part I Standard Model Predictions" (2016). URL: https://cds.cern.ch/record/2150771.

[208] ATLAS Collaboration. "Measurement of the associated production of a Higgs boson decaying into b-quarks with a vector boson at high transverse momentum in pp collisions at $\sqrt{s} = 13$ TeV with the ATLAS detector". *Phys. Lett. B* 816 (2021). DOI: 10.1016/j.physletb.2021.136204. arXiv: 2008.02508 [hep-ex].

[209] G. Luisoni et al. "$HW^{\pm}$/HZ + 0 and 1 jet at NLO with the POWHEG BOX interfaced to GoSam and their merging within MiNLO". *JHEP* 10 (2013). DOI: 10.1007/JHEP10(2013)083. arXiv: 1306.2542 [hep-ph].

[210] ATLAS Collaboration. "Measurement of the Z/γ^* boson transverse momentum distribution in pp collisions at $\sqrt{s} = 7$ TeV with the ATLAS detector". *JHEP* 09 (2014). DOI: 10.1007/JHEP09(2014)145. arXiv: 1406.3660 [hep-ex].

[211] G. Ferrera et al. "Associated ZH production at hadron colliders: the fully differential NNLO QCD calculation". *Phys. Lett. B* 740 (2015). DOI: 10.1016/j.physletb.2014.11.040. arXiv: 1407.4747 [hep-ph].

[212] J. M. Campbell et al. "Associated production of a Higgs boson at NNLO". *JHEP* 06 (2016). DOI: 10.1007/JHEP06(2016)179. arXiv: 1601.00658 [hep-ph].

[213] A. Denner et al. "HAWK 2.0: A Monte Carlo program for Higgs production in vector-boson fusion and Higgs strahlung at hadron colliders". *Comput. Phys. Commun.* 195 (2015). DOI: 10.1016/j.cpc.2015.04.021. arXiv: 1412.5390 [hep-ph].

[214] L. Altenkamp et al. "Gluon-induced Higgs-strahlung at next-to-leading order QCD". *JHEP* 02 (2013). DOI: 10.1007/JHEP02(2013)078. arXiv: 1211.5015 [hep-ph].

[215] R. V. Harlander et al. "Soft gluon resummation for gluon-induced Higgs Strahlung". *JHEP* 11 (2014). DOI: 10.1007/JHEP11(2014)082. arXiv: 1410.0217 [hep-ph].

[216] D. Goncalves et al. "Role of the Z polarization in the $H \to b\bar{b}$ measurement". *Phys. Rev. D* 98.9 (2018). DOI: 10.1103/PhysRevD.98.093005. arXiv: 1805.06385 [hep-ph].

[217] ATLAS Collaboration. "Measurements of the production cross-section for a Z boson in association with b-jets in proton-proton collisions at $\sqrt{s} = 13$ TeV with the ATLAS detector". *JHEP* 07 (2020). DOI: 10.1007/JHEP07(2020)044. arXiv: 2003.11960 [hep-ex].

[218] ATLAS Collaboration. "Combination of measurements of Higgs boson production in association with a W or Z boson in the $b\bar{b}$ decay channel with the ATLAS experiment at $\sqrt{s} = 13$ TeV". ATLAS-CONF-2021-051. 2021. URL: http://cds.cern.ch/record/2782535.

[219] F. A. Di Bello et al. "Efficiency Parameterization with Neural Networks". *Comput. Softw. Big Sci.* 5.1 (2021). DOI: 10.1007/s41781-021-00059-x. arXiv: 2004.02665 [hep-ex].

[220] P. Battaglia et al. "Relational inductive biases, deep learning, and graph networks" (2018). arXiv: 1806.01261 [cs.LG].

[221] M. Sugiyama et al. "Density Ratio Estimation in Machine Learning". Cambridge University Press, 2012. DOI: 10.1017/CBO9781139035613.

[222] A. D. Bukin. "Fitting function for asymmetric peaks". 2007. arXiv: 0711.4449 [physics.data-an].

[223] ATLAS Collaboration. "Measurements of the Higgs boson inclusive and differential fiducial cross sections in the 4ℓ decay channel at $\sqrt{s} = 13$ TeV". *Eur. Phys. J. C* 80.10 (2020). DOI: 10.1140/epjc/s10052-020-8223-0. arXiv: 2004.03969 [hep-ex].

[224] CMS Collaboration. "Measurements of production cross sections of the Higgs boson in the four-lepton final state in proton–proton collisions at $\sqrt{s} = 13\,\text{TeV}$". *Eur. Phys. J. C* 81.6 (2021). DOI: 10.1140/epjc/s10052-021-09200-x. arXiv: 2103.04956 [hep-ex].

[225] ATLAS Collaboration. "Measurements and interpretations of Higgs-boson fiducial cross sections in the diphoton decay channel using 139 fb^{-1} of pp collision data at $\sqrt{s} = 13$ TeV with the ATLAS detector". ATLAS-CONF-2019-029. 2019. URL: http://cds.cern.ch/record/2682800.

[226] CMS Collaboration. "Measurement of inclusive and differential Higgs boson production cross sections in the diphoton decay channel in proton-proton collisions at $\sqrt{s} = 13$ TeV". *JHEP* 01 (2019). DOI: 10.1007/JHEP01(2019)183. arXiv: 1807.03825 [hep-ex].

[227] CMS Collaboration. "Measurement of the inclusive and differential Higgs boson production cross sections in the decay mode to a pair of τ leptons". CMS-PAS-HIG-20-015. 2021. URL: https://cds.cern.ch/record/2771692.

[228] G. D'Agostini. "Improved iterative Bayesian unfolding" (2010). arXiv: 1010.0632.

[229] F. Febres Cordero et al. "Electroweak Gauge-Boson Production in Association with b Jets at Hadron Colliders". *Int. J. Mod. Phys. A* 30.16 (2015). DOI: 10.1142/S0217751X15300422. arXiv: 1504.07177 [hep-ph].

[230] E. Bothmann et al. "Automated evaluation of electroweak Sudakov logarithms in Sherpa". *Eur. Phys. J. C* 80.11 (2020). DOI: 10.1140/epjc/s10052-020-08596-2. arXiv: 2006.14635 [hep-ph].

[231] A. Denner et al. "Standard Model input parameters for Higgs physics" (2015). URL: https://cds.cern.ch/record/2047636.

[232] ALEPH Collaboration. "Measurement of the tau polarization at LEP". *Eur. Phys. J. C* 20 (2001). DOI: 10.1007/s100520100689. arXiv: hep-ex/0104038.

[233] ATLAS Collaboration. "Measurement of the forward-backward asymmetry of electron and muon pair-production in pp collisions at $\sqrt{s} = 7$ TeV with the ATLAS detector". *JHEP* 09 (2015). DOI: 10.1007/JHEP09(2015)049. arXiv: 1503.03709 [hep-ex].

[234] A. Schalicke et al. "Implementing the ME+PS merging algorithm". *JHEP* 07 (2005). DOI: 10.1088/1126-6708/2005/07/018. arXiv: hep-ph/0503281.

[235] S. Höche et al. "QCD matrix elements and truncated showers". *JHEP* 05 (2009). DOI: 10.1088/1126-6708/2009/05/053. arXiv: 0903.1219 [hep-ph].

[236] ATLAS Collaboration. "Measurement of the transverse momentum distribution of Drell–Yan lepton pairs in proton–proton collisions at $\sqrt{s} = 13$ TeV with the ATLAS detector". *Eur. Phys. J. C* 80.7 (2020). DOI: 10.1140/epjc/s10052-020-8001-z. arXiv: 1912.02844 [hep-ex].

[237] S. Catani et al. "The Dipole formalism for next-to-leading order QCD calculations with massive partons". *Nucl. Phys. B* 627 (2002). DOI: 10.1016/S0550-3213(02)00098-6. arXiv: hep-ph/0201036.

[238] ATLAS Collaboration. "Studies on top-quark Monte Carlo modelling with Sherpa and MG5_aMC@NLO". 2017. URL: http://cds.cern.ch/record/2261938.

[239] Y. Amhis et al. "Averages of b-hadron, c-hadron, and τ-lepton properties as of summer 2016". *Eur. Phys. J. C* 77.12 (2017). DOI: 10.1140/epjc/s10052-017-5058-4. arXiv: 1612.07233 [hep-ex].

[240] E. Lohrmann. "A Summary of Charm Hadron Production Fractions" (2011). arXiv: 1112.3757 [hep-ex].

[241] F. Krauss et al. "Towards a fully massive five-flavor scheme". *Phys. Rev. D* 98 (2018). DOI: 10.1103/PhysRevD.98.096002.

[242] S. Höche et al. "Multijet Merging in a Variable Flavor Number Scheme". *Phys. Rev. D* 100.1 (2019). DOI: 10.1103/PhysRevD.100.014011. arXiv: 1904.09382 [hep-ph].

[243] ATLAS collaboration. "ATLAS HL-LHC Computing Conceptual Design Report". CERN-LHCC-2020-015. 2020.

[244] ATLAS Collaboration. "Modelling and computational improvements to the simulation of single vector-boson plus jet processes for the ATLAS experiment" (2021). arXiv: 2112.09588 [hep-ex].

[245] Y. Giomataris et al. "MICROMEGAS: A High granularity position sensitive gaseous detector for high particle flux environments". *Nucl. Instrum. Meth. A* 376 (1996). DOI: 10.1016/0168-9002(96)00175-1.

[246] T. Kawamoto et al. "New Small Wheel Technical Design Report". CERN-LHCC-2013-006, ATLAS-TDR-020. 2013.

[247] P. Scholer. "Test Beam Results and Performance Studies of ATLAS Micromegas Production Modules". 1498 (2020). DOI: 10.1088/1742-6596/1498/1/012053.

[248] Y Kataoka et al. "Performance studies of a micromegas chamber in the ATLAS environment". 9.03 (2014). DOI: 10.1088/1748-0221/9/03/c03016.

[249] I. Manthos et al. "The Micromegas Project for the ATLAS New Small Wheel". *AIP Conf. Proc.* 2075.1 (2019). Ed. by Todor M. Mishonov et al. DOI: 10.1063/1.5091211. arXiv: 1901.03160 [physics.ins-det].

[250] T. Poulsen. "Searches for new phenomena in inclusive and tagged dijet distributions at $\sqrt{s} = 13$ TeV". CERN-THESIS-2020-124. 2020. URL: https://cds.cern.ch/record/2734072.

Acknowledgements

It's hard to believe that three years have already passed and I am finishing my PhD. These years have been a roller coaster of emotions and have given me the opportunity to meet incredible people, which has made it all easier and more fun. This work was only possible thanks to many of them, whom I would like to thank here.

I can not start this section without thanking Valerio Ippolito, who was much more than a supervisor during these years. I was truly impressed when I followed his seminar on dark matter searches at ATLAS in November 2017. His brilliance and kindness really inspired me. His guidance, constant support and patience during my PhD meant a lot to me, and this work would not have been possible without all that. I consider myself very lucky to have met him.

Many thanks to Giuliano Gustavino. Without his constant help, patience and willingness to answer all my questions and doubts, much of this work would not have been possible. I feel that I have grown a lot in this work because of him, and working with him has been a real pleasure.

Another large part of my work would not have been possible without the help of Marumi Kado and Francesco A. Di Bello, whom I would like to thank here. Their passion for this field has always inspired me, and their attention to me and support have been truly valuable. I found our meetings very helpful and I was able to learn a lot through them.

Thank you to Valerio Dao, Paolo Francavilla, Giulia di Gregorio and Milène Calvetti for the fruitful discussions on the work we have done together in the VH($b\bar{b}$) group.

Thank you to Stephen Jiggins for always being available to discuss any question or doubt I had about LHC physics and Monte Carlo generators, I always appreciated his kindness. Thanks also to Matthew Gignac for his availability and help in understanding these topics.

Many thanks to Stefano Giagu who gave me the opportunity to join the ATLAS Roma 1 group in March 2018 for my master thesis, which led to all this. I would also like to thank him for his support and presence in our student office. It was always nice to have the opportunity to discuss any topic with him and hear his funny stories.

I had the pleasure of sharing my PhD journey with Iacopo Longarini and Luigi Sabetta, who went through many things with me, from the most boring ones like bureaucracy to the most pleasant ones like sharing the office or more exotic work trips. I really enjoyed sharing my time and thoughts with them. Thank you to Simone Francescato for always being available to answer my questions and for his friendship. He helped me a lot during my time in Geneva and I am very grateful for his support. Many thanks to Cristiano Sebastiani and Damiano Vannicola, I have always appreciated their spirit and shared many funny moments with them. Thank you to Giovanni Padovano, Elena Pompa Pacchi, Maria Carnesale and Lorenzo Santi for sharing with me the last period of my PhD in our common office, it made it even sweeter. I would like to thank Matteo Bauce for his kindness and his willingness to discuss with me any physical or non-physical topic. I enjoyed every time we talked. Many thanks to all the people with whom I have shared the office, our Saletta*, during*

these years. I think it is a very special place where I always found someone to help me during my PhD. I really enjoyed my time there.

A special thanks goes to Francesco Giuli, who was a good friend and helped me with the many questions I had, especially in the last phase of my PhD.

Many thanks to Luca Martinelli for our friendship. Special thanks to Dario Baffari, Andrea Ciarma, Chiara Arcangeletti, Valerio D'Amico, Nico Giangiacomi, Anita Burattini, Lorenzo Massa, Federica Riti and all the other people I shared my stay in Geneva with. I really enjoyed spending my time with them and would like to thank them for their support. Thank you to Maria Giovanna Foti for being available to discuss our doubts about future prospects and for her support during my stay in Geneva.

Many thanks to my old friends Francesco Finelli, Flavio Di Clemente, Valerio Gilles, Andrea Franceschini, Francesco Di Giulio, Alessio Dastoli and Izat Baybusinov. Even though we do not talk as much as we used to, it's always nice to know that I can share my thoughts with them. A special thanks goes to Francesco Finelli. If it was not for him sharing our early days of study during bachelor and master, I probably would not be here writing this acknowledgements.

I would like to thank Elvira Biasioli, my high school physics teacher. She inspired me to pursue this profession.

Grazie Zio Paolo e Zia Giovanna per il vostro supporto e la vostra compagnia. Grazie Marzia per esserci sempre stata.

Infine voglio ringraziare mio fratello Giacomo, mia madre Ilaria e mio padre Antonio. Questo lavoro è dedicato a voi perché siete la cosa più preziosa che ho. Grazie per aver sempre creduto in me.